

Repair Systems for Deteriorated Bridge Piles:

Final Report

University of Houston

Mina Dawood
Hossein Karagah
Cheng Shi
Abdeldjelil Belarbi
Cumaraswamy Vipulanandan

Texas Tech University (TechMRT)

Sang-wook Bae
Sangwook Lee

**Both FRP repair systems described in this study are patented by
Professor Mo Ehsani; U.S. Patent #8,650,831 and #9,376,782**

Both FRP repair systems described in this study are patented by Professor Mo Ehsani; U.S. Patent #8,650,831 and #9,376,782

Technical Report Documentation Page

1. Report No. FHWA/TX-17/0-6731-1		2. Government Accession No.		3. Recipient's Catalog No.	
4. Title and Subtitle Repair Systems for Deteriorated Bridge Piles: Final Report				5. Report Date December 2015; Published April 2017	
				6. Performing Organization Code	
7. Author(s) Univ of Houston: Mina Dawood, Hossein Karagah, Cheng Shi, Abdeldjelil Belarbi, Kumaraswamy Vipulanandan Texas Tech University: Sang-wook Bae, Sangwook Lee				8. Performing Organization Report No. 0-6731-1	
9. Performing Organization Name and Address Cullen College of Engineering Building 1 Civil and Environmental Engineering 4726 Calhoun Road, Room N107 Houston, TX 77204-4003				10. Work Unit No. (TRAIS)	
				11. Contract or Grant No. 0-6731	
12. Sponsoring Agency Name and Address Texas Department of Transportation Research and Technology Implementation Office P.O. Box 5080 Austin, TX 78763-5080				13. Type of Report and Period Covered Technical Report September 2011–August 2015	
				14. Sponsoring Agency Code	
15. Supplementary Notes Project performed in cooperation with the Texas Department of Transportation and the Federal Highway Administration.					
16. Abstract The objective of this research project is to develop a durable repair system for deteriorated steel bridge piles that can be implemented without the need for dewatering. A rigorous survey of the relevant practice nationwide was conducted to inform and direct the remaining research efforts. The current state-of-practice was critically reviewed and the most promising alternatives were identified for detailed investigation. The structural performance, constructability, and economy of the existing systems were considered. A simplified but reliable framework for assessing the condition of deteriorated piles is proposed. The framework was used to direct the full-scale testing of artificially deteriorated and repaired piles. Accelerated environmental exposure tests were conducted to evaluate the durability of the different repair systems. The results of the full-scale tests and the environmental durability tests were used to inform a life-cycle cost analysis to identify the most economical repair systems based on initial costs, life-cycle costs, agency costs, and user costs. To evaluate the performance of the repair systems in 'real' applications, a field installation was conducted. Based on the research findings, guidelines for the design, construction, and maintenance of the systems will be developed to facilitate transfer of the technology to TxDOT bridge maintenance operations.					
17. Key Words Condition surveys, Deterioration, Dewatering, Life cycle costing, Piles (Supports), Steel bridges				18. Distribution Statement No restrictions. This document is available to the public through the National Technical Information Service, Springfield, Virginia 22161; www.ntis.gov .	
19. Security Classif. (of report) Unclassified	20. Security Classif. (of this page) Unclassified	21. No. of pages 538		22. Price	

TxDOT Project 0-6731
Repair Systems for Deteriorated Bridge Piles

Final Report

University of Houston
Mina Dawood
Hossein Karagah
Cheng Shi
Abdeldjelil Belarbi
Cumaraswamy Vipulanandan

Texas Tech University
Sang-wook Bae
Sangwook Lee

December 2015

Acknowledgements

The research reported herein was conducted as part of Texas Department of Transportation Research Project 0-6731. Additional resources were provided by the University of Houston, Department of Civil and Environmental Engineering and Texas Tech University, Department of Civil Environmental, and Construction Engineering. Support was also provided by Delta Structural LLC, Epoxy Design Systems Inc., Fyfe Co. LLC, and QuakeWrap Inc. Some of the techniques presented in this report are protected under US Patent Number 8,650,831, registered to Mohammad R. Ehsani. The technical and administrative support that were provided by the members of the Texas Department of Transportation Project Management Committee is gratefully acknowledged. Specifically, the contributions of Wade Odell, Leon Flournoy, and Aaron Garza are gratefully acknowledged. The experimental components of this research could not have been successfully completed without the contributions of Gerald McTigret and Jeffery Miller. The assistance of Oswaldo Russian in the preparation of this report is also gratefully acknowledged.

Both FRP repair systems described in this study are patented by Professor Mo Ehsani; U.S. Patent #8,650,831 and #9,376,782

Table of Contents

Chapter 1. Introduction.....	29
1.1. Problem.....	29
1.2. Scope.....	30
1.3. Layout of the Report	31
Chapter 2. Background	34
2.1. Global Buckling of Concentrically Loaded Columns	34
2.2. Local Buckling of Cross-Sectional Elements	37
2.3. Existing Design Specifications	39
2.3.2. AISI Effective Width Method (AISI-EWM)	42
2.3.3. AISI Direct Strength Method (AISI-DSM).....	44
2.3.4. Local Buckling of Slender Elements.....	46
2.4. Evaluation of Deteriorated Steel Members	49
2.4.1. Effect of Corrosion on Steel Structures	49
2.4.2. Effect of Corrosion on Plate Elements.....	51
2.4.3. Thickness Measurement of Corroded Elements	51
2.5. Repair of Steel Compression Members with FRP	52
2.5.1. FRP-Bonded Directly to Steel Compression Members	53
2.5.3. Bond Behavior at Steel-Concrete Interface.....	61
2.6. Repair of Steel Compression Members with Steel Based Systems	62
2.7. Numerical Simulation of Axially Loaded Steel Members	64

2.7.1.	FEA of steel channel columns	66
2.7.2.	FEA of steel angles	68
2.7.3.	FEA of hollow section columns	69
2.7.4.	FEA of W-shaped columns	72
2.7.5.	FEA of steel frames.....	73
Chapter 3.	Small-scale Pile Tests	74
3.1.	Small-Scale Experimental Study of Piles with Localized Corrosion.....	74
3.1.1.	Test Specimens	74
3.1.2.	Materials	79
3.1.3.	Test Setup.....	80
3.1.4.	Instrumentation	81
3.1.5.	Results.....	84
3.2.	Discussion of the Results	98
3.2.1.	Independent Reduction of Flange or Web Thickness	100
3.2.2.	Simultaneous Reduction of Flange and Web Thickness.....	101
3.2.3.	Unsymmetric Reduction of Flange Thickness	102
3.2.4.	Reduction of Flange Width	103
3.2.5.	Through-Web Corrosion	103
Chapter 4.	Full-scale Pile Tests.....	105
4.1.	Test Matrix.....	105
4.1.1.	Section Size and Effective Length	105

4.1.2.	Deterioration Pattern	107
4.2.	Test Specimens	108
4.3.	Materials	110
4.4.	Test Setup.....	111
4.5.	Instrumentation	112
4.6.	Results.....	113
4.7.	Discussion of the results	131
4.7.1.	Failure Mode	132
4.7.2.	Axial Capacity.....	133
Chapter 5.	Comparison to Existing Design Specifications	135
5.1.	Comparison with Existing Design Specifications.....	135
5.1.1.	AASHTO Method.....	137
5.1.2.	AISI-EWM.....	139
5.1.3.	AISI-DSM.....	142
5.1.4.	Comparison	144
Chapter 6.	Finite Element Simulations	147
6.1.	Description of the Finite Element Model.....	147
6.1.1.	Element Types and Mesh Size	147
6.1.2.	Initial Out-of-Straightness.....	150
6.1.3.	Material Properties.....	152
6.1.4.	Effect of residual stresses.....	153

6.2.	Validation of the Finite Element Model	155
6.2.1.	Small-scale piles	155
6.2.2.	Full-scale piles	160
6.3.	Parametric Study	164
6.3.1.	Effect of Degree of Flange Corrosion, Web Corrosion, and Pile Slenderness	165
6.3.2.	Effect of the Location of the Corroded Region.....	167
6.3.3.	Effect of the Extent of the Corroded Region	168
6.3.4.	Effect of Residual Stresses.....	170
Chapter 7.	Design of FRP-based and Steel-Based Repair Systems for Corroded Steel H-Piles	
	173	
7.1.	Design Approach for FRP-Confined Grout Repair System.....	173
7.1.1.	Failure Modes	176
7.1.2.	Design Considerations and Calculations.....	178
7.2.	Design Approach for Steel-based Repair System	185
7.2.1.	Failure Modes	186
7.2.2.	Design Considerations	187
Chapter 8.	Experimental Evaluation of Repaired Full-scale Steel H-Piles.....	193
8.1.	Grouted FRP-Jacket Repair System.....	193
8.1.1.	Materials	193
8.1.2.	Details and Construction of the Retrofitted Piles.....	197
8.1.3.	Test Setup.....	212

8.1.4.	Instrumentation	213
8.2.	Steel Plate Based Repair System	214
8.2.1.	Materials	215
8.2.2.	Details and Construction of the Retrofitted Piles.....	221
8.2.3.	Test setup	222
8.2.4.	Instrumentation	223
8.3.	Results for Grout-filled FRP Jacket Repair System.....	224
8.3.1.	Pile Group 0/20	224
8.3.2.	Pile Group 40/20	228
8.3.3.	Pile Group 40/60	232
8.3.4.	Pile Group 80/60	235
8.3.5.	Pile Group 80/60/V	244
8.3.6.	Pile Group 80/60/3	248
8.3.7.	Comparison and Discussion.....	253
8.4.	Results for Steel Plate Based Repair System	261
8.4.1.	Pile 0/20-S.....	261
8.4.2.	Pile 40/20-S.....	262
8.4.3.	Pile 40/60-S.....	265
8.4.4.	Piles 80/60-S(1) and 80/60-S(2)	268
8.4.5.	Pile 80/60/V-S.....	271
8.4.6.	Pile 80/60/3-S.....	272

8.4.7.	Comparison and Discussion.....	275
Chapter 9.	Finite Element Analysis of Repaired Piles.....	279
9.1.	Finite Element Modeling of Grouted FRP Jacket Repairs.....	279
9.1.1.	Description of the Finite Element Model.....	280
9.1.2.	Results Comparison and Discussion: FRP-Confined Grout Repair System.....	301
9.2.	Finite Element Modeling of Steel-based Repair System	313
9.2.1.	Simulation of Corroded Piles.....	314
9.2.2.	Simulation of Steel Plates	315
9.2.3.	Simulation of High-Strength Bolts.....	316
9.2.4.	Simulation of the Interface Properties.....	317
9.2.5.	Comparison to Experimental Results and Discussion	318
9.2.6.	Parametric Study.....	326
Chapter 10.	Experimental Evaluation of Durability of the Proposed Repair Systems.....	332
10.1.	Design of Small-Scale Test Piles.....	332
10.1.1.	Size of the Small-Scale Test Piles.....	332
10.1.2.	Damage Levels and Locations of the Test Piles	333
10.1.3.	Design of FRP-Confined Grout Repair Systems	337
10.1.4.	Design of Steel-Based Repair Systems - Repair System 3	339
10.2.	Fabrication of Test Piles	341
10.2.1.	Simulation of Corrosion Damage	341
10.2.2.	Repair System 1	342

10.2.3.	Repair System 2	345
10.2.4.	Repair System 3	350
10.3.	Environmental Cycles.....	352
10.4.	Accelerated Corrosion Process	354
10.5.	Failure Test Set-Up and Instrumentation	359
10.6.	Test Matrix.....	361
10.6.1.	Group 1 - Control Test Piles	361
10.6.2.	Group 2 - Test Piles Conditioned under the Environmental Cycles	362
10.6.3.	Group 3 - Test Piles for Evaluating Corrosion Rate	363
10.7.	Results and Discussion.....	364
10.7.1.	Failure Mode	366
10.7.2.	Axial Load Capacity of Undamaged Control Piles.....	375
10.7.3.	Reduction in Axial Load Capacity Due to Simulated Corrosion-Damage	375
10.7.4.	Restoration of Axial Load Capacity by Repair System 1	376
10.7.5.	Restoration of Axial Load Capacity by Repair System 2	377
10.7.6.	Restoration of Axial Load Capacity by Repair System 3	379
10.7.7.	Effects of Environmental Cycles	380
10.7.8.	Corrosion of the Test Piles.....	381
10.8.	Concluding Remark	390
Chapter 11.	Life-Cycle Cost Analysis.....	391
11.1.	Introduction.....	391

11.2.	Evaluation Criteria	394
11.3.	Introduction of Selected LCCA Programs	395
11.3.1.	BLCCA	395
11.3.2.	BridgeLCC	396
11.3.3.	RealCost	396
11.3.4.	BridgeLCC	397
11.3.5.	RealCost	401
11.3.6.	Bridge Life-cycle Cost Analysis (BLCCA)	404
11.4.	Analysis and Comparison of Three Programs	406
11.4.1.	Comparison of Inputs	406
11.4.2.	Comparison of Outputs	414
11.4.3.	Assesment of the Three Programs	419
11.5.	Summary of Evaluation	427
11.6.	Implementation of LCCA for FRP-based and Steel-based Repair Systems for Corroded Steel H-Piles	428
11.6.1.	Part I: Survey Questionnaire	429
11.7.	LCCA of Five Bridge Pile Repair Solutions	444
11.7.1.	Introduction	444
11.7.2.	Implementation of RealCost	445
11.7.3.	Analysis of Life-Cycle Costs	463
11.7.4.	Parametric Study	468

Chapter 12.	Field Implementation.....	482
12.1.	Identification of Bridge Site.....	482
12.2.	Evaluation of Existing Piles and Site Conditions	482
12.3.	Repair Design.....	490
12.4.	Repair Installation.....	491
12.4.1.	Installation of the Grouted FRP Jacket Repair System.....	493
12.4.2.	Steel Plate Based Repair System.....	497
Chapter 13.	Summary, Conclusions and Recommendations for Future Work	502
13.1.	Summary and Conclusions.....	503

List of Figures

Figure 1.1: Scope of the study	31
Figure 2.1: Comparison of multiple column curves (Bjorhovde, 1988)	37
Figure 2.2: Correlation between Plate Buckling Coefficient and Aspect Ratio (adapted from Timoshenko, 1961)	38
Figure 2.3: Slender un-stiffened element reduction factor (AISC, 2010)	41
Figure 2.4: Effective width method (AISI, 2012)	42
Figure 3.1: Schematic drawing and designation of the piles in phase I	75
Figure 3.2: Schematic drawing and designation of the piles in phase II	78
Figure 3.3: Test setup for small-scale piles	81
Figure 3.4: Instrumentation of the small-scale compression test	82
Figure 3.5: Facet size, facet step, and computational size	84
Figure 3.6: Failure mode and load-deformation response of pile 0/0	86
Figure 3.7: Failure mode and load-deformation response of pile 0/30	87
Figure 3.8: Failure mode and load-deformation response of pile 0/60	88
Figure 3.9: Failure mode and load-deformation response of pile 50/0	89
Figure 3.10: Failure mode and load-deformation response of pile 50/30	90
Figure 3.11: Failure mode and load-deformation response of pile 75/0	91
Figure 3.12: Failure mode and load-deformation response of pile 75/60	92
Figure 3.13: Failure mode and load-deformation response of pile 75/60/NV/US	93
Figure 3.14: Failure mode and load-deformation response of pile 75/60/NV/US/WR	94

Figure 3.15: Failure mode and load-deformation response of pile 75/60/V/S.....	95
Figure 3.16: Failure mode and load-deformation response of pile 75/60/V/S/WR	96
Figure 3.17: Failure mode and load-deformation response of pile 75/60/V/US	97
Figure 3.18: Failure mode and load-deformation response of pile 75/60/V/US/WR	98
Figure 3.19: Correlation between the loss of axial capacity and loss of cross section	102
Figure 4.1: Schematic view of bridge piles and buckling modes	106
Figure 4.2: Corrosion simulation using CNC milling machine	108
Figure 4.3: Schematic drawing of the location and geometry of the milled region.....	109
Figure 4.4: Designation of the full-scale piles	110
Figure 4.5: 600-kip Self-reacting compression test frame	112
Figure 4.6: Instrumentation of the full-scale compression test.....	113
Figure 4.7: Axial load-shortening response of the un-corroded control pile	114
Figure 4.8: Global deformation and strain contours of the un-corroded control pile	115
Figure 4.9: Axial load-shortening response of pile 0/20.....	116
Figure 4.10: Global deformation and strain contours of pile 0/20	117
Figure 4.11: Axial load-shortening response of pile 40/20.....	118
Figure 4.12: Global deformation, local deformation, and strain contours of pile 40/20.....	119
Figure 4.13: Buckled flange of pile 40/20	120
Figure 4.14: Axial load-shortening response of pile 40/60.....	121
Figure 4.15: Global deformation, local deformation, and strain contours of pile 40/60.....	122
Figure 4.16: Flange and web local buckling of pile 40/60.....	123

Figure 4.17: Axial load-shortening response of pile 80/60.....	124
Figure 4.18: Global deformation, local deformation, and strain contours of pile 80/60.....	125
Figure 4.19: Flange and web local buckling of pile 80/60.....	126
Figure 4.20: Axial load-shortening response of pile 80/60/V.....	127
Figure 4.21: Global deformation, local deformation, and strain contours of pile 80/60/V.....	128
Figure 4.22: Flange and web local buckling of pile 80/60/V.....	129
Figure 4.23: Axial load-shortening response of pile 80/60/3.....	130
Figure 4.24: Global deformation, local deformation, and strain contours of pile 80/60/3.....	131
Figure 4.25: Correlation between the loss of axial capacity and loss of cross section	133
Figure 5.1: Strong and weak-axis effective length factor	137
Figure 5.2: Comparison of the measured and predicted axial capacities for small-scale piles.....	144
Figure 5.3: Comparison of the measured and predicted axial capacities for full-scale piles.....	145
Figure 6.1: Sensitivity study for element type and mesh size.....	150
Figure 6.2: Shapes initial global and local imperfections from elastic buckling analysis	151
Figure 6.3: Effects of initial global imperfection on pile axial capacity.....	152
Figure 6.4: Stress-strain relationship of steel used in FEA.....	153
Figure 6.5: Distribution of residual stresses on the flange and web	154
Figure 6.6: Effects of residual stresses on axial capacity.....	154
Figure 6.7: Deformation of small-scale piles from FEA and tests.....	157
Figure 6.8: Comparison of axial load-shortening responses from tests and FEA of W4×13	160
Figure 6.9: Deformation of full-scale piles from FEA and test	162

Figure 6.10: Comparison of axial load-deformation responses from test and FEA of HP12×53	164
Figure 6.11: Axial peak loads for piles with different reduction on flange and web.....	166
Figure 6.12: Axial peak loads of piles with different corroded extents	169
Figure 6.13: Axial peak loads of piles with different residual stresses.....	171
Figure 7.1: Design approach to repair corroded HP12×53 with 60% loss of web thickness.....	174
Figure 7.2: Classification of the repair systems	176
Figure 7.3: F1 and F2 jacket configurations	179
Figure 7.4: Length of the FRP jacket.....	181
Figure 7.5: Headed-stud anchor configuration	183
Figure 7.6. Configuration of the longitudinal reinforcing bars in the repaired pile.....	184
Figure 7.7: Friction-type bolted plate-based repair system.....	186
Figure 7.8. Cross section of repaired pile (clamping plates not shown for clarity)	191
Figure 8.1: Schematic drawing of the location and geometry of the milled region.....	198
Figure 8.2: Installation of end-caps.....	202
Figure 8.3: Installation of reinforcing bars	202
Figure 8.4: Installation of headed-stud anchor.....	203
Figure 8.5: Tank used to simulate underwater repair process.....	204
Figure 8.6: Installing FRP jacket for F1 FRP-based repair system.....	205
Figure 8.7: Installing FRP jacket for F2 FRP-based repair system.....	207
Figure 8.8: Grout casting	208
Figure 8.9: Filling the two piles with end-void.....	209

Figure 8.10: Sealing condition of the piles repaired with F2 repair system.....	210
Figure 8.11: Designation of the repaired piles	211
Figure 8.12: Instrumentation of repaired corroded piles.....	214
Figure 8.13: Specimen of slip resistance tests	219
Figure 8.14: Load-slip relationships from slip resistance tests	220
Figure 8.15: Fabrication of the repair system	222
Figure 8.16: Test instrumentation used in the of the test of the repaired piles	223
Figure 8.17: Axial load-shortening behavior of 0/20 pile group.....	225
Figure 8.18: Piles 0/20 repaired with the F1 and F2 repair systems after testing	226
Figure 8.19: Comparing the slip at steel-grout interface of 0/20 repaired piles.....	227
Figure 8.20: Comparing FRP hoop strain of 0/20 repaired piles	228
Figure 8.21: Axial load-shortening behavior of 40/20 pile group.....	229
Figure 8.22: Piles 40/20 repaired with the F1 and F2 repair systems after testing	230
Figure 8.23: Comparing the slip at steel-grout interface of 40/20 repaired piles.....	231
Figure 8.24: Comparing FRP hoop strain of 40/20 repaired piles	231
Figure 8.25: Axial load-shortening behavior of 40/60 pile group.....	232
Figure 8.26: Piles 40/60 repaired with the F1 and F2 repair systems after testing	233
Figure 8.27: Comparing the slip at steel-grout interface of 40/60 repaired piles.....	234
Figure 8.28: Comparing FRP hoop strain of 40/60 repaired piles	235
Figure 8.29: Axial load-shortening behavior of 80/60 pile group.....	236

Figure 8.30: Comparing the slip at steel-grout interface of 80/60 repaired piles (a) piles without mechanical anchors, and (b) piles with mechanical anchors.	238
Figure 8.31: Comparing FRP hoop strain of 80/60 repaired piles	239
Figure 8.32: Pile 80/60(1)-F1/R after testing.....	240
Figure 8.33: Pile 80/60(1)-F2/R after testing.....	241
Figure 8.34: Pile 80/60*-F1/RA after testing	242
Figure 8.35: Pile 80/60(2)-F2/RA after testing.....	243
Figure 8.36: Axial load-shortening behavior of 80/60/V pile group.....	244
Figure 8.37: Comparing the slip at steel-grout interface of 80/60/V repaired piles.....	245
Figure 8.38: Comparing FRP hoop strain of 80/60/V repaired piles	246
Figure 8.39: Pile 80/60/V-F1/RA after testing.....	247
Figure 8.40: Pile 80/60/V-F2/RA after testing.....	248
Figure 8.41: Axial load-shortening behavior of 80/60/3 pile group	249
Figure 8.42: Comparing the slip at steel-grout interface of 80/60/3 repaired piles	250
Figure 8.43: Comparing FRP hoop strain of 80/60/3 repaired piles	250
Figure 8.44: Pile 80/60/3-F1/RA after testing	252
Figure 8.45: Pile 80/60/3-F2/RA after testing	253
Figure 8.46: Ratio of the axial capacity of the repaired piles to the control un-corroded pile.....	255
Figure 8.47: Comparison of Pile 0/20 and Pile 0/20-S	262
Figure 8.48: Comparison of Pile 40/20 and Pile 40/20-S	263
Figure 8.49: Observed local failure on Pile 40/20-S.....	263

Figure 8.50: Axial strains of the plate and the reduced flange of Pile 40/20-S	264
Figure 8.51: Slip of the steel repair plates of Pile 40/20-S	265
Figure 8.52: Comparison of Pile 40/60 and Pile 40/60-S	266
Figure 8.53: Buckled flange and web and damaged bolts of Pile 40/60-S	266
Figure 8.54: Axial strains of the plate and the reduced flange of Pile 40/60-S	267
Figure 8.55: Slip of the steel repair plates of Pile 40/60-S	268
Figure 8.56: Comparison of Pile 80/60 and Piles 80/60-S(1) and 80/60-S(2)	269
Figure 8.57: Buckled flange and web and coating damage of Pile 80/60-S(1) and 80/60-S(2).....	270
Figure 8.58 Slip of the steel repair plates of Pile 80/60-S(1).....	270
Figure 8.59: Comparison of Pile 80/60/V and Pile 80/60/V-S	271
Figure 8.60: Observed failure on Pile 80/60/V-S and Pile 80/60/V	272
Figure 8.61: Slip of the steel repair plates of Pile 80/60/V-S	272
Figure 8.62: Comparison of Pile 80/60/3 and Pile 80/60/3-S	273
Figure 8.63: Observed failure on Pile 80/60/3-S	274
Figure 8.64: Slip of the steel repair plates of Pile 80/60/3-S	274
Figure 8.65: Comparison of axial load capacities between corroded and retrofitted piles	277
Figure 8.66: Comparison of axial stiffness between corroded and retrofitted piles	278
Figure 9.1: Components of modeled repaired piles	281
Figure 9.2: Sensitivity of load-shortening response to different mesh size and type.....	284
Figure 9.3: Applied boundary conditions to FE model.....	285
Figure 9.4: Applied initial global imperfection to FE models	286

Figure 9.5: Effect of initial imperfection on axial load-shortening response.....	286
Figure 9.6: Residual stress magnitude and distribution	288
Figure 9.7: Effect of residual stress on axial load-shortening response.....	289
Figure 9.8: Cohesive and friction properties in tangential direction.....	292
Figure 9.9: Comparing of the proposed model (Liu et al., 2005) and simplified model.....	293
Figure 9.10: Comparison of full-bond, low friction, and Liu et al. bond-slip relationship.....	294
Figure 9.11: Effect of tangential bond stiffness on axial load-shortening response	295
Figure 9.12: Changing the pile deformation by decreasing the bond strength	296
Figure 9.13: Effect of tangential bond strength on axial load-shortening response.....	297
Figure 9.14: Effect of fracture energy on axial load-shortening response	298
Figure 9.15: Effect of coefficient of friction on axial load-shortening response	299
Figure 9.16: Effect of normal bond stiffness and strength on axial load-shortening response	300
Figure 9.17: Comparison of the test and FE load-shortening response for the piles repaired with F1 jacket	304
Figure 9.18: Comparison of the test and FE load-shortening response for the piles repaired with F2 jacket	305
Figure 9.19: Comparison of the deformation of the tested and modeled pile 40/60-F1/R.....	307
Figure 9.20: Comparison of the deformation of the tested and modeled piles with 80% reduction of the flange thickness.....	308
Figure 9.21: Stress contours in FRP jacket and grout cylinder.....	311
Figure 9.22: Comparison of measured and predicted slip at grout/steel interface for the piles repaired with F1 jacket.....	312

Figure 9.23: Comparison of measured and predicted slip at grout/steel interface for the piles repaired with F2 jacket.....	313
Figure 9.24: Cross sectional views of the repaired piles simulated in FEA.....	316
Figure 9.25: Relationship of friction force and normal force defined in FEA.....	318
Figure 9.26: Axial load-deformation responses of repaired piles from tests and FEA.....	321
Figure 9.27: Comparison of deformations of FEA and experiments for repaired piles.....	325
Figure 9.28: Axial peak loads of repaired piles as function of different slip resistances.....	328
Figure 9.29 Failure within the corroded region	328
Figure 9.30 Failure outside the repair system.....	329
Figure 9.31 Axial peak loads of repaired piles as function of varying bolt pretension	330
Figure 9.32 Axial peak loads of repaired piles with different lengths of plates	331
Figure 10.1: Damage level for minor repair case.....	334
Figure 10.2: Damage level for major repair case.....	335
Figure 10.3: FRP jacket configuration for Repair System 1	338
Figure 10.4: Length of the FRP jackets used for the minor repair case and the minor repair case.....	338
Figure 10.5: FRP jacket configuration for Repair System 2	339
Figure 10.6: Configuration the Repair System	340
Figure 10.7: Design of Repair System 3 for the minor repair case.....	340
Figure 10.8: Design of Repair System 3 for the major repair.....	341
Figure 10.9: Small-scale test piles with minor/moderate corrosion damage and major corrosion damage.	342

Figure 10.10: Fabrication of FRP jackets for Repair System 1	344
Figure 10.11: Fabricated FRP jackets for Repair System 1	345
Figure 10.12: Fabrication of Repair System 1	345
Figure 10.13: Fabrication of cylindrical GFRP shells	347
Figure 10.14: Installed Pre-Fabricated Cylindrical GFRP shells.....	348
Figure 10.15: Grout injection into the voids between the GFRP shell and the pile.....	348
Figure 10.16: Application of CFRP Sheets using wet lay-up technique.....	350
Figure 10.17: Fabrication of Repair System 3	352
Figure 10.18: Environmental chamber and the small-scale test piles placed inside.....	353
Figure 10.19: One year environmental cycle.....	354
Figure 10.20: Schematic of accelerated corrosion process	356
Figure 10.21: Actual set-up of accelerated corrosion process	358
Figure 10.22: Loading frame for failure testing of the test piles.....	359
Figure 10.23: Schematic of the test set-up.....	360
Figure 10.24: Actual test set-up for failure testing	360
Figure 10.25: Failure of an undamaged control column (CONTs).....	366
Figure 10.26: Failure of 4-in. damaged control piles (DCONT-4) and 12-in. damaged control piles (DCONT-12).....	367
Figure 10.27: Failure of 4-in damaged piles repaired with Repair System 1 (S1-4-CONT and S1-4-Env)	368

Figure 10.28: Failure of 12-in damaged piles repaired with Repair System 1 (S1-12-CONT and S1-12-Env).....	369
Figure 10.29: Failure of 4-in damaged piles repaired with Repair System 2 (S2-4-CONT and S2-4-Env)	370
Figure 10.30: Failure of 4-in damaged piles repaired with Repair System 2 (S2-12-CONT and S2-12-Env)	371
Figure 10.31: Crushing of 4-in. damaged region of the test piles repaired with Repair System 3	372
Figure 10.32: Crushing of 12-in. damaged region of the test piles repaired with Repair System 3	373
Figure 10.33: Global buckling of the piles repaired with Repair System 3	374
Figure 10.34: Global buckling of the piles repaired with Repair System 3	374
Figure 10.35: Axial load vs. axial deformation curves of the control piles (CONT).....	375
Figure 10.36: Axial load vs. axial deformation curves of the damaged control piles (DCONT-4 and DCONT-12)	376
Figure 10.37: Axial load vs. axial deformation curves of the damaged piles repaired with Repair System 1	377
Figure 10.38: Axial load vs. axial deformation curves of the damaged piles repaired with Repair System 2	378
Figure 10.39: Axial load vs. axial deformation curves of the damaged piles repaired with Repair System 3	379
Figure 10.40: Comparisons of the performance of the repaired piles with/without being exposed to the environmental cycles	381
Figure 10.41: Undamaged pile (CONT-Cor) showing the rust build-up	382

Figure 10.42: A damaged pile repaired with Repair System 1 (S1-4-Cor) showing no evidence of corrosion	383
Figure 10.43: A damaged pile repaired with Repair System 2 (S2-12-Cor) showing no evidence of corrosion	384
Figure 10.44: Accelerated corrosion test set-up for the piles repaired with System 3 (S3-4-Cor)	385
Figure 10.45: Bolt and web corrosion of Repair System 3 (S3-4-Cor).....	386
Figure 10.46: Web corrosion of Repair System 3 (S3-4-Cor)	387
Figure 10.47: Accelerated corrosion test set up for Repair System 3 (S3-12-Cor).....	388
Figure 10.48: Web and bolt corrosion for Repair System 3 (S3-12-Cor)	389
Figure 10.49: Web and bolt corrosion of Repair System 3 (S3-12-Cor)	390
Figure 11.1: Corroded Steel Bridge Piles (Deep Water Case and Shallow Water Case)	432
Figure 11.2: Repair Duration of Five Repair Systems.....	439
Figure 11.3: Repair System of Service Life for Shallow and Deep Water Cases.....	440
Figure 11.4: Cost Data of Repair Systems in Shallow Water Case	443
Figure 11.5: Cost Data of Repair Systems in Deep Water Case.....	443
Figure 11.6: Total Cost of Repair Systems in Shallow and Deep Water Case	444
Figure 11.7: The Alternative-Level Input Example of RealCost ($n = 75$, $i = 2.5\%$, Shallow Water).....	446
Figure 11.8: Repair Plans for Five repair alternatives ($t=10, 20$ and 30 , $n=35$)	448
Figure 11.9: Repair Plans for Five repair alternatives ($t=10, 20$ and 30 , $n=50$)	449
Figure 11.10: Repair Plans for Five repair alternatives ($t=10, 20$ and 30 , $n=75$)	450
Figure 11.11: Life-Cycle Costs in NPV (Shallow Water Case, $n=35$)	457

Figure 11.12: Life-Cycle Costs in NPV (Deep Water Case, n=35)	458
Figure 11.13: Life-Cycle Costs in NPV (Shallow Water Case, n=50)	459
Figure 11.14: Life-Cycle Costs in NPV (Deep Water Case, n =50)	460
Figure 11.15: Life-Cycle Costs in NPV (Shallow Water Case, n =75)	461
Figure 11.16: Life-Cycle Costs in NPV (Deep Water Case, n=75)	462
Figure 11.17: NPVs of Deterministic LCCA under Different Discount Rates (n =35)	470
Figure 11.18: NPVs of Deterministic LCCA under Different Discount Rates (n=50)	471
Figure 11.19: NPVs of Deterministic LCCA under Different Discount Rates (n=75)	472
Figure 11.20: Probability Scales of LCCs for Five Companies under Probabilistic Interest Rates (Shallow Water, n=75)	473
Figure 11.21: Probability Scales of LCCs for Five Companies under Probabilistic Interest Rates (Deep Water, n=75)	474
Figure 11.22: NPVs of Deterministic LCCA under Different Repair Time (n=35)	475
Figure 11.23: NPVs of Deterministic LCCA under Different Repair Time (n=50)	476
Figure 11.24: NPVs of Deterministic LCCA under Different Repair Time (n=75)	476
Figure 11.25: Probability Distributions of LCCs for Five Companies under Probabilistic Repair Time (Shallow Water, n=75)	477
Figure 11.26: Probability Distributions of LCCs for Five Companies under Probabilistic Repair Time (Deep Water, n=75)	478
Figure 11.27: NPVs of Deterministic LCCA under Different Analysis Periods and Initial Repair Time (Shallow Water, i=2.5%)	480

Figure 11.28: NPVs of Deterministic LCCA under Different Analysis Periods and Initial Repair Time (Deep Water, $i=2.5\%$).....	481
Figure 12.1: Candidate piles at bent 2 from northeast abutment, view towards northeast.	483
Figure 12.2: Measured thickness profiles of flanges and webs of three candidate bridge piles for field installation of repairs.....	487
Figure 12.3: Site conditions on November 30, 2015	492
Figure 12.4: Updated high water levels and relative repair system positions.....	493
Figure 12.5: Positioning of GFRP jackets	494
Figure 12.6: Coating the GFRP jacket with epoxy	495
Figure 12.7: Installation of the CFRP overwrap	496
Figure 12.8: Completed installation of grouted FRP-jacket	497
Figure 12.9: Initial positioning of steel plates.....	498
Figure 12.10: Bolt tightening sequence	499
Figure 12.11: Torque wrench calibration curve.....	500
Figure 12.12: Steel based repair system.....	501

List of Tables

Table 3.1: Measured Geometry and Designations of the Tested Piles in Phase I	76
Table 3.2: Measured Geometry and Designations of the Tested Piles in Phase II	79
Table 3.3: Properties of Steel Piles	80
Table 3.4: Cross-Sectional Properties of the Small-Scale Piles.....	99
Table 3.5: Measured Capacities and Observed Failure Modes of the Small-Scale Piles.....	100
Table 4.1 Measured Clear Lengths of Bridge Piles	107
Table 4.2: Measured Geometry and Designations of the Control H-Piles at Milled Section	110
Table 4.3: Measured Properties of Steel Piles	111
Table 4.4: Degradation of the Specifications of the Tested Piles due to Corrosion.....	132
Table 5.1: Prediction of the Axial Capacity of Small-Scale Columns using AASHTO	138
Table 5.2: Prediction of the Axial Capacity of Full-Scale Columns using AASHTO	138
Table 5.3: Effective Width of the Corroded Web and Flange – Small-Scale	139
Table 5.4: Effective Width of the Corroded Web and Flange – Full-Scale	140
Table 5.5: Prediction of the Axial Capacity of Small-Scale Columns using AISI-EWM	142
Table 5.6: Prediction of the Axial Capacity of Full-Scale Columns using AISI-EWM	142
Table 5.7: Prediction of the Axial Capacity of the Small-Scale Columns using AISI-DSM.....	143
Table 5.8: Prediction of the Axial Capacity of the Small-Scale Columns using AISI-DSM.....	144
Table 6.1: Material Properties of W4×13 and HP12×53	153
Table 6.2: Axial Peak Loads and Failure Modes of W4×13 from FEA and tests.....	156
Table 6.3: Axial peak loads and failure modes of HP12×53 from FEA and tests	161

Table 6.4: Comparison of Axial Capacities for Different Locations of Reduction	168
Table 8.1: Properties of the FRP Material used for F1 (PileMedic LLC) and F2 (Fyfe Co. LLC) Repair Systems as Reported by the Manufacturers	194
Table 8.2: Properties of the Adhesive used for F1 (QuakeWrap LLC) and F2 (Fyfe Co. LLC) Repair Systems as Reported by the Manufacturers	195
Table 8.3: Properties of the Grout used for the Repair Systems	195
Table 8.4: Properties of the longitudinal reinforcing bars used for the repair systems.....	196
Table 8.5: Material properties of steel piles.....	197
Table 8.6: Measured Geometry and Designations of the Repaired H-piles at Milled Section	199
Table 8.7: Prediction of the Remaining Nominal Axial Capacity, $P_{n,c}$, of the Deteriorated Piles	200
Table 8.8: Geometric Specification of the F1 and F2 Repair Systems	212
Table 8.9: Test Matrix of Repaired H-piles	215
Table 8.10: Material Properties of the Steel Repair Plates	216
Table 8.11: Test matrix of coefficient of friction.....	218
Table 8.12: Experimental results of coefficient of friction test	221
Table 8.13: Axial Capacities and Failure Modes of the Tested Repaired and Un-Repaired Piles.....	254
Table 8.14: Comparing the Failure Mode of the Steel Piles Tested with and without the Repair	257
Table 8.15: Experimental results of full-scale corroded and repaired piles.....	276
Table 9.1: Type of elements used to model each part in sensitivity study.....	282
Table 9.2: Comparison of the number of nodes, elements, and computational time for different mesh sizes and element types.....	283

Table 9.3: Selected element type and mesh size for FE modeling.....	284
Table 9.4: Assigned properties to steel flange and web elements.....	287
Table 9.5: Assigned properties to reinforcing bar elements	289
Table 9.6: Assigned properties to anchor elements	290
Table 9.7: Assigned properties to grout elements.....	290
Table 9.8: Assigned properties to FRP elements	291
Table 9.9: Existing interfaces in FE model.....	291
Table 9.10: Bond characteristics of the existing models.....	293
Table 9.11: Assumed bond characteristic for FE modeling.....	300
Table 9.12: Comparison of the Test and FE peak load for piles repaired with F1 jacket.....	302
Table 9.13: Comparison of the Test and FE peak load for piles repaired with F2 jacket.....	302
Table 9.14: Maximum and Minimum Principal Stresses Observed in FRP jacket in FE Model for the Pile Repaired with F1 System.....	310
Table 9.15: Maximum and Minimum Principal Stresses Observed in FRP jacket in FE Model for the Pile Repaired with F2 System.....	310
Table 9.16: Axial peak loads and failure modes of repaired piles from FEA and tests.....	319
Table 10.1: Comparison of Small-Scale Test Piles and Full-Scale Test Piles.....	333
Table 10.2: Summary of the FE Model Analysis to Determine the Effects of Damage Locations	336
Table 10.3: Group 1 - Control Test Piles	362
Table 10.4: Test matrix for test piles subjected to environmental cycles	363
Table 10.5: Test matrix for test piles subjected to environmental cycles	364

Table 10.6: Summary of the failure test results	365
Table 11.1: FHWA LCCA Steps and corresponding RealCost Forms	403
Table 11.2: The Comparison of Project-Level Inputs for Each Program	408
Table 11.3: The Comparison of Alternative-Level Inputs for Each Program.....	412
Table 11.4: The Comparison of Outputs for Each Program	415
Table 11.5: The Comparison of the Analysis Performed by Each Program.....	417
Table 11.6: Description of Two Alternatives.....	425
Table 11.7: Activities and Cost.....	426
Table 11.8: LCCA Results in Present Value from Three Programs	426
Table 11.9: Detailed User Cost Component Results from RealCost (Base Case)	427
Table 11.10: Cost Comparison of Shallow Water Case.....	436
Table 11.11: Cost Comparison of Deep Water Case	437
Table 11.12: LCCA Results for Shallow Water Case and Deep Water Case (n=35)	451
Table 11.13: LCCA Results for Shallow Water Case and Deep Water Case (n=50)	453
Table 11.14: LCCA Results for Shallow Water Case and Deep Water Case (n=75)	455
Table 11.15: Ranking Orders of LCCs for Each Condition (Shallow Water)	467
Table 11.16: Ranking Orders of LCCs for Each Condition (Deep Water)	468
Table 12.1: Measured Properties and Calculated Capacities of Candidate Piles.....	489
Table 12.2: Details of FRP-based Repair System ^a	490
Table 12.3: Details of Steel-based Repair System.....	491

Chapter 1. Introduction

1.1. Problem

Deterioration of civil infrastructures including bridges has raised concerns in the engineering community. Deterioration due to corrosion is one of the concerns particularly for those bridges constructed over waterways.

To maintain the functionality and safety of bridges with corroded piles, steel H-piles are inspected and evaluated on a regular basis. Based on the assessment outcomes and progress of corrosion, various courses of action may be considered. One possible course of action is to leave the pile as-is and 'load post' the bridge. That is, reduce the allowable live load on the structure. However, load postings reduce the functionality of the roadway, could have significant social or economic implications, and are difficult to enforce. Another course of action is the replacement of the piles or the entire structure. If repair is an option, there are several retrofit methods, such as FRP jacketing, concrete encasement, and adding bolted or welded steel plates. These methods are often developed and implemented based on best engineering practice.

This report presents the findings of a research project that was conducted to investigate the behavior of different repair systems, as well as evaluating their suitability, developing a rational approach for their specification, and providing guidelines for their implementation.

The objectives of the research are:

- 1) To determine an accurate method to quantify the remaining capacity of steel H-piles with localized corrosion, which can be implemented without the need for involved numerical simulation.

- 2) To evaluate the effectiveness of different types of repair systems that can be implemented in underwater applications and which require minimal modification of the existing piles.
- 3) To evaluate the environmental durability of the repair systems and quantify the reduction of capacity that can be expected due to environmental exposure.
- 4) To quantify the expected life-cycle costs of the repair alternatives.
- 5) To establish rational approaches for the design the different types of repair systems.

1.2. Scope

This study aims to investigate the behavior of systems for underwater repair of steel H-piles with localized severe corrosion. Figure 1.1 summarizes the scope of the study. The study consisted of eight research tasks including both experimental and numerical components. The progression of the research is illustrated in the figure. The research was conducted as a joint effort between the University of Houston (UH) and Texas Tech University (Tech).

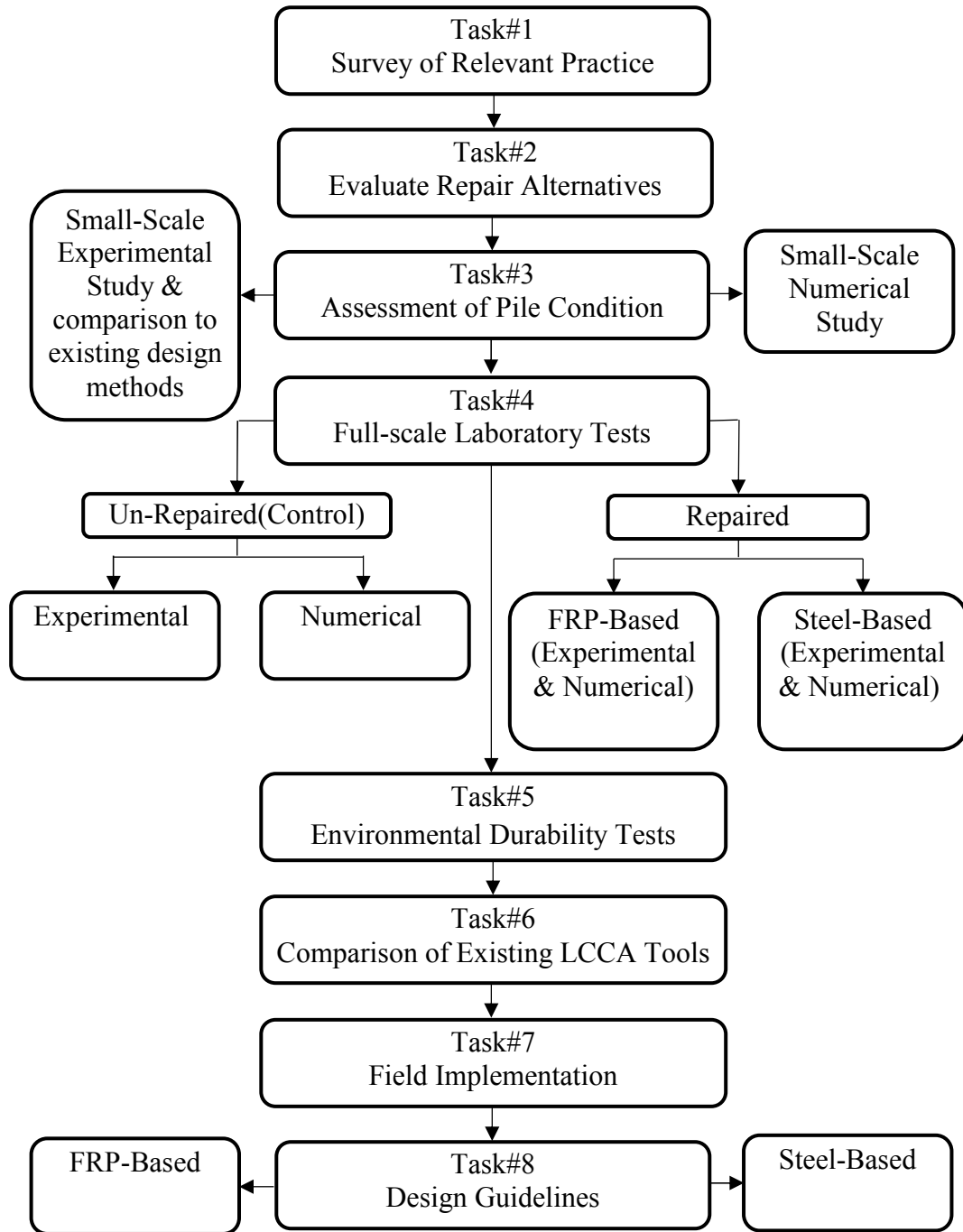


Figure 1.1: Scope of the study

1.3. Layout of the Report

This report consists of thirteen chapters, including this introductory chapter.

Chapter 2 presents a review of the literature and summarizes the relevant work that has been completed to date related to corrosion of steel members, their prevalent failure modes, existing specifications for remaining capacity determination and fundamentals of repair methods.

Chapter 3 presents the details and results of the experimental program that was implemented to study the effect of different corrosion patterns on the capacity of small-scale piles.

Chapter 4 presents the details and results of the experimental program that was implemented to study the effect of different corrosion patterns on the capacity of full-scale piles.

Chapter 5 compares the measured capacities of the tested small-scale and full-scale piles to the predicted capacities that were obtained using the currently available specifications for design of steel piles in the US.

Chapter 6 presents the details of the numerical modeling that was conducted to quantify the remaining capacity of corroded steel piles. The numerical model was validated using the experimental results that are presented in Chapters 3 and 4. The validated model was used to conduct a parametric study.

Chapter 7 presents the design approaches that were adopted to design the FRP-based and steel-based repair systems that were evaluated in this study. The basic failure modes and the corresponding design equations are summarized.

Chapter 8 presents the details and findings of the experimental program that was conducted to evaluate the effectiveness of the repair systems that were investigated in this project.

Chapter 9 presents the details of the numerical models that were implemented to study the behavior of the corroded and repaired piles. The models provide additional insight into aspects of the behavior that could not be fully observed during testing.

Chapter 10 describes the methodology and presents the detailed findings of the experimental study that was conducted to evaluate the environmental durability of the repaired piles.

Chapter 11 presents the methodology and results of the life-cycle cost analysis of the FRP-based and steel-based repair systems in different installation scenarios and environmental conditions.

Chapter 12 describes a field implementation of the repair systems that was conducted at the end of the project to identify technical challenges that should be considered when installing the repair systems on-site rather than in a laboratory setting.

Chapter 13 summarizes the main conclusions and limitations of the research project, and identifies specific areas requiring additional investigation.

Chapter 2. Background

Corrosion is an electro-chemical process that leads to metal loss, which may be uniformly distributed across exposed surfaces or localized in nature. From a structural standpoint, corrosion can lead to loss of capacity, functionality, and integrity of structures. Steel piles, especially those supporting bridges over waterways, are deteriorating due to localized corrosion within the tidal zone (in marine environments), in the splash zone, or in a zone between the high water level and below the mud line. This localized corrosion makes steel piles non-prismatic, reduces their capacity, and can change the failure mode.

This chapter presents a review of the existing literature in four relevant areas; summary of current column buckling formulations and design approaches, evaluation of deteriorated steel members due to corrosion, evaluation of FRP-based and steel-based repair systems to restore the capacity of corroded members, and numerical modeling of relevant structural elements.

2.1. Global Buckling of Concentrically Loaded Columns

The elastic critical buckling load, P_{cr} , of a perfectly straight slender prismatic column under concentric compression was first studied by Euler in 1744 (Galambos T, 1998). Euler developed and solved the differential equations for elastic buckling of an ideal column. However, Euler's equation cannot apply to non-slender columns whose material become nonlinear under compression prior to global buckling.

To predict inelastic buckling, the tangent modulus concept was introduced by Engesser in 1889 (Galambos and Surovek, 2008). However, this approach did not account for the different moduli of steel during loading and unloading. After buckling, due to the induced

bending moment, the compression side of the column experiences increased loading, while the opposite side of the column experiences unloading. According to Engesser's tangent modulus concept the tangent modulus was applied to both the loading and unloading sides of the column. This approach was later modified by Engesser and introduced as the reduced modulus concept in which different moduli are adopted on the loading and unloading sides of the column (Galambos and Surovek, 2008). According to this concept, the reduced modulus is a function of both material properties and geometric properties. Although the reduced modulus approach is conceptually correct, it led to unconservative predictions of axial capacity. Consequently, for about 50 years, engineers preferred to use the tangent-modulus approach although it was conceptually less rigorous than the reduced modulus approach.

To address this discrepancy a compression test was conducted on a small aluminum column composed of two rigid bars that were connected by a short deformable cell (Shanley, 1947). The deformable cell was made up of two flanges and no web in such a way that the elastic moduli of the two flanges were different. According to the test results, the measured load at the onset of buckling when the lateral deformation was zero was equal to the load that was predicted using the tangent modulus approach. By increasing the lateral deformation, the rate of increase in the axial load became smaller due to the decrease of the tangent modulus. It was concluded that the axial capacity of a perfectly straight column is between the tangent-modulus load and the reduced-modulus load.

Further improvements to the column buckling concept were made to include the effect of initial out-of-straightness and existence of residual stresses. In case of hot-rolled or welded built-up steel members, residual stresses are induced in the cross section due to uneven cooling. The induced tensile stress in the vicinity of the weld can approach or exceed the

yield strength of the welded material. Heat due to flame cutting also induces stresses that, in extreme cases, can exceed the yield strength of the parent metal (Galambos, 1998). Studies on the effect of residual stresses on column strength began in late 1940s by the guidance of the Column Research Council (CRC). The effect of residual stresses on concentrically loaded columns was studied at Lehigh University (Tall et al., 1960). Multiple column curves were developed to predict the axial capacity of steel columns accounting for the influence of residual stresses and initial out-of-straightness (Bjorhovde, 1972).

Bjorhovde (1972) performed deterministic and probabilistic analysis on the available data on axial strength, initial out-of-straightness, and residual stress obtained from previously tested columns. Subsequently, two series of column curves were produced based on assumed sinusoidal initial out-of-straightness patterns with maximum amplitudes of $L/1000$ and $L/1470$ where L was the length of the columns. Finally, the column curves were grouped into three categories, which were subsequently adopted as design curves by the Structural Stability Research Council (SSRC) to predict the axial strength of columns (see Figure 2.1). The selection criteria of the curves were the type of the cross section and specified minimum yield stress of the steel material. The load and resistance factor (LRFD) curve in the American Institute of Steel Construction (AISC) specification (2011) and the American Association of State, Highway, and Transportation Officials (AASHTO) LRFD Bridge Design Specifications (2015) is identical to the SSRC-2P curve (Tide, 2001; Ziemian, 2010). This curve, which was produced for columns with initial out-of-straightness of $L/1500$, provides an average reliability index of 3. This reliability index is lower than SSRC-2 curve adopted by the Canadian standard, which was prepared for initial out-of-straightness of $L/1000$ (Bjorhovde, 1988).

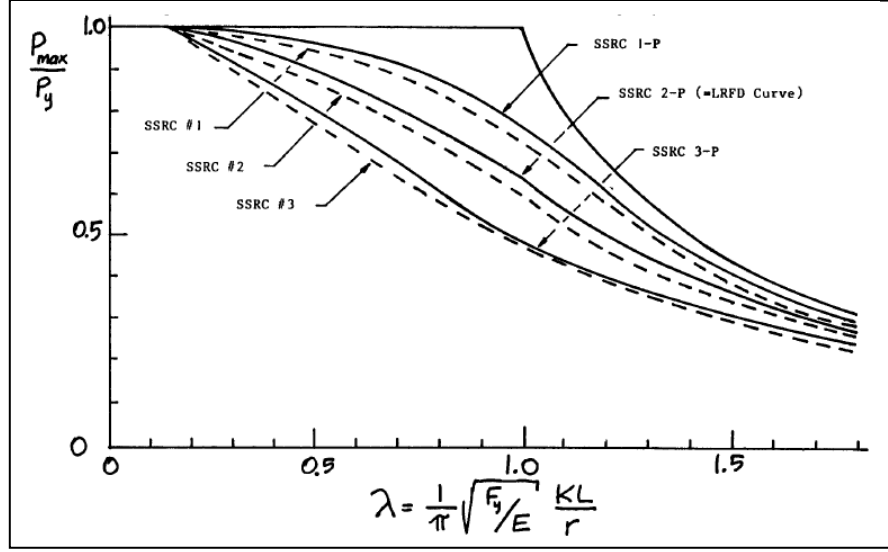


Figure 2.1: Comparison of multiple column curves (Bjorhovde, 1988)

2.2. Local Buckling of Cross-Sectional Elements

Columns with slender cross-sectional elements demonstrate local buckling prior to attaining their global strength. The elastic local buckling capacity of a plate is calculated as:

$$F_{cr1} = k \frac{\pi^2 E}{12(1-\nu^2)} \left(\frac{b}{t} \right)^2 \quad (\text{Eq. 2-1})$$

where ν is the Poisson's ratio of steel and k is the plate buckling coefficient (Timoshenko, 1961). Width and thickness of the plate are shown by b and t respectively. The value of the plate buckling coefficient depends on the boundary conditions and length-to-width ratio (aspect ratio) of the plate. Figure 2.2 shows the variation of the plate buckling coefficient (k) as a function of plate aspect ratio for a simply supported rectangular plate loaded axially along the width (Timoshenko and Gere, 1961). As the plate aspect ratio increases, the dominant buckling mode, m , increases and the plate buckling coefficient, k , decreases.

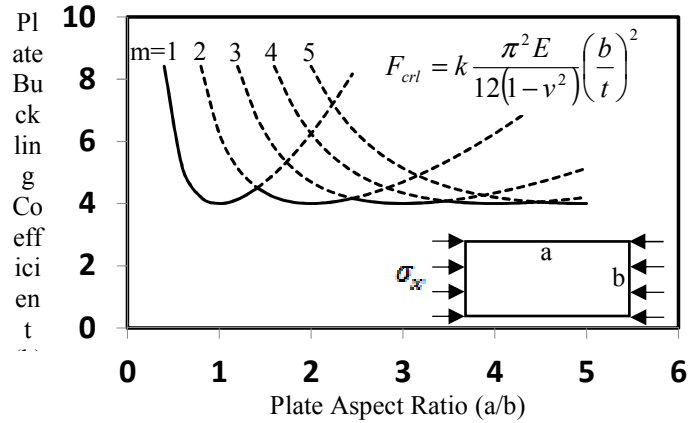


Figure 2.2: Correlation between Plate Buckling Coefficient and Aspect Ratio (adapted from Timoshenko, 1961)

To investigate the buckling stress of slender cross-sectional elements within the inelastic range, an analytical approach was proposed by Lundquist and Stowell (1942a and 1942b). They used a single overall effective plate modulus in substitution of Young's modulus to apply the approach to elements that buckle in the inelastic range. Lundquist (1939) conducted a study to obtain the effective plate modulus for aluminum. The effect of restraint provided by the adjacent element was considered by a restraint coefficient (Lundquist and Stowell, 1942c).

One approach to consider the effect of slender cross-sectional elements on the overall capacity of the columns is to reduce the global buckling stress by applying a reduction factor. This approach calculates the reduction factor based on the onset of buckling limit state (Johnson, 1985; AISC, 2010). Another approach is the effective width method which relies on post buckling strength of the slender cross-sectional elements (AISC, 2010; AISI, 2012). These approaches are explained in detail in the following sections.

2.3. Existing Design Specifications

2.3.1. AISC and AASHTO

AISC (2011) and AASHTO (2012) adopted the SSRC-2P curve to calculate global buckling strength (Ziemian, 2010). The design approach considers elastic buckling and inelastic buckling for hot-rolled steel members with or without slightly slender element. The elastic flexural buckling capacity is based on a modified Euler buckling equation which considers the effect of initial out-of-straightness. The inelastic flexural buckling capacity is calculated based on an empirical equation. Two multiplicative reduction factors, Q_s and Q_a , are adopted to account for the slenderness of unstiffened and stiffened elements, respectively. The nominal axial strength is calculated as

$$P_n = F_{cr} A_g \quad (\text{Eq. 2-2})$$

where A_g is the gross cross-sectional area of the compression member and

$$F_{cr} = Q \left(0.658^{\frac{QF_y}{F_e}} \right) F_y \quad \text{for} \quad \frac{KL}{r} \leq 4.71 \sqrt{\frac{E}{QF_y}} \quad (\text{Eq. 2-3})$$

$$= 0.877 F_e \quad \text{for} \quad \frac{KL}{r} > 4.71 \sqrt{\frac{E}{QF_y}} \quad (\text{Eq. 2-4})$$

$$F_e = \frac{\pi^2 E}{\left(\frac{KL}{r} \right)^2} \quad (\text{Eq. 2-5})$$

$$Q = Q_a Q_s \quad (\text{Eq. 2-6})$$

where F_y and E are the yield stress and elastic modulus of the material. The effective length factor, length of the member, and radius of gyration of the cross section are shown by K , L , and r respectively. Q_s and Q_a are stiffened and unstiffened element reduction factors. To consider the reduction of capacity due to local buckling of slender flanges and webs, AISC (2011) and AASHTO (2012) use stiffened and unstiffened element reduction factors. These factors are calculated as

$$Q_s = 1.0 \text{ for } \frac{b_f}{2t_f} \leq 0.56 \sqrt{\frac{E}{F_y}} \quad (\text{Eq. 2-7})$$

$$= 1.415 - 0.74 \left(\frac{b_f}{2t_f} \right) \sqrt{\frac{F_y}{E}} \text{ for } 0.56 \sqrt{\frac{E}{F_y}} < \frac{b_f}{2t_f} < 1.03 \sqrt{\frac{E}{F_y}} \quad (\text{Eq. 2-8})$$

$$= \frac{0.69E}{F_y \left(\frac{b_f}{2t_f} \right)^2} \text{ for } \frac{b_f}{2t_f} \geq 1.03 \sqrt{\frac{E}{F_y}} \quad (\text{Eq. 2-9})$$

where b_f and t_f are the width and thickness of the flange element respectively. The slender unstiffened element reduction factor, Q_s , is obtained for slender unstiffened elements, e.g. flanges of H-piles, based on the onset of local buckling as the governing limit state. Plate buckling coefficients, k , were assumed to be 0.7 for outstanding flange elements which reflects a state between simply supported ($k = 0.425$) and fixed ($k = 1.277$) on one edge and free on the opposite edge (AISC, 2010). There is no reduction in the overall axial capacity when the slenderness is above the limit defined by AISC, and flange elements can attain their yield stresses. Figure 2.3 illustrates the relationship between the reduction factor, Q_s , and the flange slenderness. The figure illustrates the

non-linear relationship in the elastic buckling region and the linear, empirical transition relationship in the inelastic buckling region.

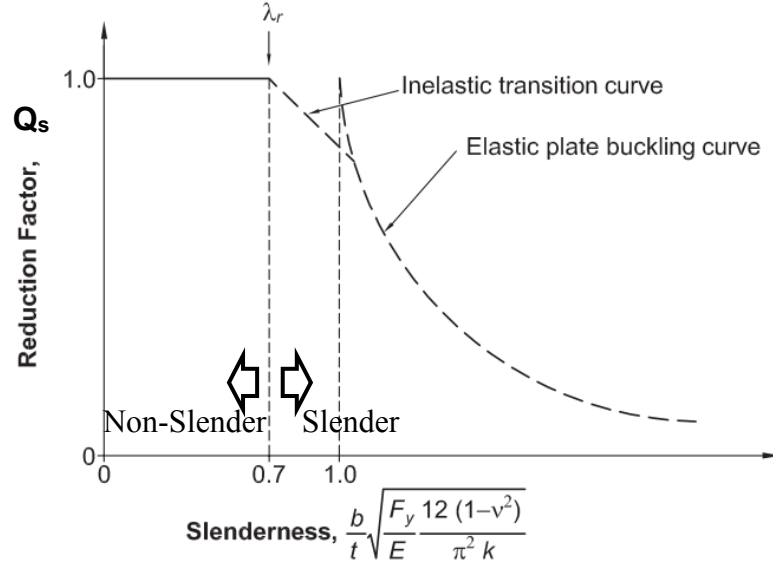


Figure 2.3: Slender un-stiffened element reduction factor (AISC, 2010)

The reduction factor, Q_a , for stiffened slender elements is defined as

$$Q_a = \frac{h_e}{h} \quad (\text{Eq. 2-10})$$

where,

$$h_e = 1.92t_w \sqrt{\frac{E}{f}} \left[1 - \frac{0.34}{\left(\frac{h}{t_w} \right)} \sqrt{\frac{E}{f}} \right] \leq h \quad (\text{Eq. 2-11})$$

where $f = F_{cr}$ which is calculated based on $Q = 1.0$. The actual width, effective width, and thickness of the web element are represented by h , h_e , and t_w respectively. AISC and AASHTO adopt the modified effective width method from (AISI, 2012) to calculate the

slender stiffened reduction factor, Q_a , based on the post buckling strength of the stiffened slender elements. This method is explained in the next section.

2.3.2. AISI Effective Width Method (AISI-EWM)

Using the AISI-EWM, the axial capacity is calculated by multiplying the effective area of the cross section by the nominal global buckling stress. The nominal global buckling stress is calculated according to the SSRC-2P curve. To account for slender elements the buckled portion of a slender plate element is assumed to be ineffective while the remaining effective portion of the plate is assumed to support a uniformly distributed stress as shown in Figure 2.4.

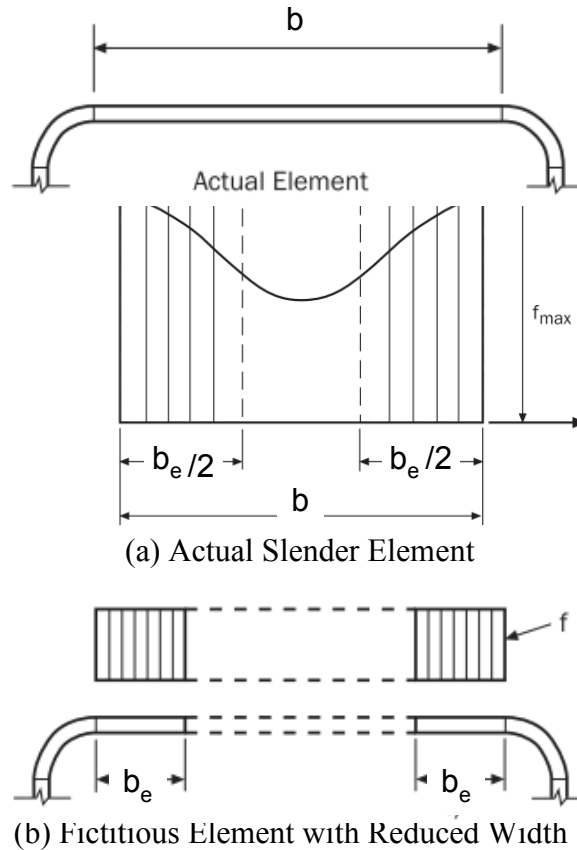


Figure 2.4: Effective width method (AISI, 2012)

The reduction of the axial capacity is taken into consideration by reducing the gross area of the cross-section to an effective area. This method determines the minimum local buckling strength of the cross section by examining each element individually. Thus, compatibility and equilibrium between cross-sectional elements are not considered by AISI-EWM in determining elastic buckling load (Schafer, 2008). The nominal axial strength is given by:

$$P_n = F_n A_e \quad (\text{Eq. 2-12})$$

where F_n is defined as

$$F_n = (0.658^{\lambda_c^2}) F_y \text{ for } \lambda_c \leq 1.5 \quad (\text{Eq. 2-13})$$

$$= \frac{0.877}{\lambda_c^2} F_y \text{ for } \lambda_c > 1.5 \quad = \frac{0.877}{\lambda_c^2} F_y \quad (\text{Eq. 2-14})$$

$$\lambda_c > 1.5$$

with,

$$\lambda_c = \sqrt{\frac{F_y}{F_e}} \lambda_c = \sqrt{\frac{F_y}{F_e}} \quad (\text{Eq. 2-15})$$

where F_y is the yield stress, F_e is the elastic buckling stress and the effective cross-sectional area, A_e , is calculated as

$$A_e = b_e \times t \quad (\text{Eq. 2-16})$$

where t is the thickness of the element and b_e is the effective width of the element defined as:

$$b_e = b \text{ for } \lambda \leq 0.673 \quad (\text{Eq. 2-17})$$

$$= \rho b \text{ for } \lambda > 0.673 = \rho b \quad (\text{Eq. 2-18})$$

$$\lambda_c > 0.673$$

where b is the actual width of the slender element, and the reduction factor ρ is defined as

$$\rho = \left(1 - \frac{0.22}{\lambda}\right) / \lambda \quad (\text{Eq. 2-19})$$

$$\lambda = \sqrt{\frac{F_n}{F_{cr1}}} \quad (\text{Eq. 2-20})$$

Where F_{cr1} is calculated using (Eq. 2-1)

2.3.3. AISI Direct Strength Method (AISI-DSM)

The direct strength method directly calculates the capacity of members with slender elements based on the properties of the entire cross-section rather than taking an element-by-element calculation approach. As a result, interaction between cross-sectional elements is considered in this method (Schafer, 2008). Three possible instabilities, global, local, and distortional, are considered in the AISI-DSM. The nominal axial strength is given by:

$$P_n = \min\{P_{ne}, P_{nl}, P_{nd}\} \quad (\text{Eq. 2-21})$$

where P_{ne} , P_{nl} , and P_{nd} are the nominal flexural, local, and distortional buckling strengths respectively. Flexural buckling is defined as

$$P_{ne} = (0.658^{\lambda_c^2}) P_y \text{ for } \lambda_c \leq 1.5 \quad (\text{Eq. 2-22})$$

$$\lambda_c \leq 1.5$$

$$= \frac{0.877}{\lambda_c^2} P_y \text{ for } \lambda_c > 1.5 \quad (\text{Eq. 2-23})$$

Where $\lambda_c > 1.5$

$$\lambda_c = \sqrt{\frac{P_y}{P_{cre}}} \quad (\text{Eq. 2-24})$$

$$P_y = F_y A_g \quad (\text{Eq. 2-25})$$

$$P_{cre} = F_e A_g \quad (\text{Eq. 2-26})$$

for local buckling,

$$P_{nl} = P_{ne} \text{ for } \lambda_l \leq 0.776 \quad (\text{Eq. 2-27})$$

$$\lambda_l \leq 0.776$$

$$= \left[1 - 0.15 \left(\frac{P_{crl}}{P_{ne}} \right)^{0.4} \right] \left(\frac{P_{crl}}{P_{ne}} \right)^{0.4} P_{ne} \text{ for } \lambda_l > 0.776 \quad (\text{Eq. 2-28})$$

$$F_n = \left[1 - 0.15 \left(\frac{F_{crl}}{F_{ne}} \right)^{0.4} \right] \left(\frac{F_{crl}}{F_{ne}} \right)^{0.4} F_{ne} \quad (\text{Eq. 2-29})$$

Where $\lambda_l > 0.776$

$$\lambda_l = \sqrt{\frac{P_{ne}}{P_{crl}}} \quad (\text{Eq. 2-30})$$

$$P_{crl} = F_{crl} A_g \quad (\text{Eq. 2-31})$$

where F_{crl} is the minimum local buckling stress of the cross-sectional elements calculated using (Eq. 2-1). For distortional buckling,

$$P_{nd} = P_y \text{ for } \lambda_d \leq 0.561 \quad (\text{Eq. 2-32})$$

$$\lambda_l \leq 0.776$$

$$= \left[1 - 0.25 \left(\frac{P_{crd}}{P_y} \right)^{0.6} \right] \left(\frac{P_{crd}}{P_y} \right)^{0.6} P_y \text{ for } \lambda_d > 0.561 \quad (\text{Eq. 2-33})$$

where $\lambda_l > 0.776$ P_{crd} is the elastic distortional buckling strength of the column which can be obtained numerically.

2.3.4. Local Buckling of Slender Elements

The failure mode of corroded steel piles changes as a result of increase in the slenderness of flange and web. This makes the piles more susceptible to localized buckling. In addition, the relative bending stiffness of the cross-sectional elements changes due to corrosion which in turn leads to changing the boundary conditions of the cross-sectional elements.

The provisions of existing specifications for designing H-piles, (AISC, 2011; AASHTO, 2012), do not consider the effect of varying the degree of web-flange interaction (Chen et al., 2013; Seif and Schafer, 2010a). Web-flange interaction was investigated using elastic

finite strip method (Seif & Schafer, 2010a). Using the results of the numerical analysis, the relationship between the predicted buckling stresses and flange-to-web slenderness ratios was studied. Consequently, a single plate-buckling coefficient for hot-rolled sections was developed. The introduced plate buckling coefficient was calibrated for plates with large aspect ratios. The applicability of this coefficient on predicting the axial capacity of columns with slender flanges and webs with small length-to-width or length-to-depth aspect ratios has not been studied.

Using nonlinear finite element analysis, the axial capacity of W-sections with modified flange and web slenderness ratios were calculated (Seif and Schafer, 2010b). The flange and web thicknesses of two long W-sections, W14×233 and W36×330 (US designations), were modified independently or in a fixed ratio over their entire length to investigate their influence on the local buckling mode. The axial capacities of these columns were compared with those predicted by current design specifications, AISC, AISI-EWM, and AISI-DSM. It was concluded that AISC provided a highly conservative prediction for columns with locally slender flanges due to ignoring the post-buckling strength of slender un-stiffened elements. The AISI-EWM resulted in the most accurate prediction among the other two methods. The AISI-DSM led to conservative prediction when one element became more slender than the other one. To improve the AISC prediction, an effective width method compatible with the AISC specification was proposed (Seif and Schafer, 2014).

Interaction between local, global, and distortional buckling of thin-walled members was studied by (Schafer, 2002), and design recommendations were proposed. Comparison of findings of numerical analysis with experimental results demonstrated minor local-

distortional interaction in C and Z sections. However, no conclusion was made for global-distortional interaction in these types of sections, and it was suggested to use the AISI-DSM which uses three separate design curves for global, local, and distortional buckling. To predict the local buckling strength of columns with slender elements using the AISI-DSM, an improved method based on strain energy distribution was suggested (Seif and Schafer, 2011).

In extreme cases, severe corrosion can lead to localized perforation of the column web. The effect of slotted perforations in the web of thin-walled, cold-formed C-channels under compression was studied by (Moen and Schafer, 2008). In a subsequent study equations were proposed to limit the distortional buckling strength to the net section strength. In addition, using these equations the predicted local-global buckling strength was limited to the capacity of the net section for the columns with low global and local slenderness (Moen and Schafer, 2011). However, none of these methods are applicable to I-shaped cross-sections and all of them require the use of finite element analysis making them too involved for typically day-to-day design and analysis.

Corrosion can make steel columns non-prismatic. Having corroded slender elements over a limited length introduces the aspect ratio of the plate as a new parameter which changes the plate buckling coefficient as illustrated in Figure 2.2. This effect could influence the plate buckling mode and failure capacity of steel columns with localized but severe corrosion. This effect could also influence the accuracy of the capacity predictions using existing design methods since, for local buckling, existing design methods assume that the plate aspect ratio is very large. However, for members with severe but localized

corrosion, the aspect ratio of the reduced portion of the flange or web in the corroded zone may be quite small in contrast.

2.4. Evaluation of Deteriorated Steel Members

Evaluating the remaining capacity of corroded piles is a challenging but important task for structural maintenance and rehabilitation activities. Corrosion makes steel members non-prismatic. It can also make the cross-sectional elements susceptible to localized buckling. The existing design specifications in North America do not provide prediction methods for members with localized degradation. Consequently, the behavior of corroded steel members has been studied by researchers to assess the suitability of current design tools, address their shortcomings, and propose revisions to the current approaches as necessary.

2.4.1. Effect of Corrosion on Steel Structures

Liu et al. (2005) tested seven I-shaped corroded columns with global slenderness of 213 under uniaxial compression. They machined two 25.42 in. \times 1.33 in. notches in both flanges to simulate corrosion. While this approach decreased the cross-sectional area of the member, the localized slenderness of flanges was also reduced. This made the flanges less susceptible to local buckling which may not be completely representative of all corrosion patterns. The degraded column demonstrated a 41% reduction of the axial capacity and failed by global buckling with a maximum lateral deflection occurring at mid-height at the location of the notches. Some of the corroded columns were subsequently repaired with FRP-confined concrete and tested under compression. Using an energy method, a closed-form equation was obtained to predict elastic buckling load of the repaired and un-repaired struts.

The effect of corrosion on the remaining axial compressive capacity of steel angles used in transmission towers was studied experimentally by Beaulieu et al. (2010). They utilized an accelerated procedure to create a random pattern of corrosion on sixteen steel angles. Three degrees of corrosion of 0%, 25%, and 40% and two levels of global slenderness of 40 and 110 were considered as the test parameters. Comparison of the experimental results with AISC (2005) showed that the code prediction was 68% lower than the measured capacity.

An investigation on the ultimate strength of corroded steel box girders, as a representation of members in ship construction, was conducted by Saad-Eldeen et al., (2010, 2011). Degradation of mid-ship beams was simulated by exposing three box girders to running seawater. During the corrosion process, weight loss measurements were conducted. Weight losses varied from 13% to 23% of the original weight. In addition, a survey of thickness measurement at 212 points was conducted. The corroded girders were attached to two supporting arms and tested under four-point bending to failure. Reduction in the thickness due to corrosion led to reduction of the ultimate capacity. The residual stresses in the corroded steel members reduced by 8% compared to those measured in an un-corroded girder. In addition, ultimate vertical load and bending moment, calculated by moment-curvature analysis using measured geometry, both reduced to 65% of the control one. Subsequently, the results of two numerical models, one with averaged thickness and the other with actual measured thickness from the survey, were compared against experimental data (Saad-Eldeen et al., 2014).

2.4.2. Effect of Corrosion on Plate Elements

The ultimate capacity of corroded plates has also been investigated by some researchers, and models were proposed to predict the remaining ultimate capacity based on the results of parametric studies. Empirical formulas were proposed by (Ok et al., 2007) to predict the ultimate strength of square plates with pitting corrosion under uniaxial compression. These formulas were obtained by applying a regression analysis to the results of a series of numerical analyses on square plates with various locations and sizes of pitting corrosion under uniaxial compression. The analyses showed that the effective depth, width, and location of the corrosion were the most important parameters affecting the ultimate compressive strength. Huang et al., (2010) studied the effect of pitting corrosion on the ultimate strength of hull plates under biaxial compression. Using the results of numerical analysis, a polynomial function was proposed to predict the reduction of ultimate strength based on volumetric loss and transverse-to-longitudinal in-plane stress ratio. Using the results of a non-linear finite element analysis, a semi-empirical method was developed to predict the capacity of corroded rectangular plates under biaxial compression (Jiang and Soares, 2012a and 2012b). Appuhamy et al. (2013) suggested equations to predict the reduction of yield strength, ultimate strength, and energy dissipation of corroded bridge girders under earthquake loading.

2.4.3. Thickness Measurement of Corroded Elements

In a harsh environment, corrosion is observed in the form of a pitting pattern on the surface of steel. For modelling purposes, it is more practical to model the pitting corrosion by applying a uniform reduction in the thickness and using an average reduced

thickness. Nakai et al. (2006) conducted a series of experimental and numerical investigations on web plates under patch loading. The comparison showed that using the average thickness loss provided an accurate evaluation of the web crippling behavior of members with pitting corrosion. An equivalent plate thickness approach was also suggested by (Seo et al., 2011) to predict the ultimate strength of stiffened panels with non-uniform corrosion under biaxial compression combined with lateral pressure. To investigate the relationship between the severity of corrosion and measurement techniques, a series of coupons were cut from a 100-year-old steel bridge girder with pitting corrosion and tested under tension (Appuhamy et al., 2013). Three different levels of corrosion, minor, moderate, and severe, were also defined corresponding to the values of minimum measured-to-initial thickness ratios. Minor and severe were the cases with the ratios above 0.75 and below 0.5 respectively. The moderate was corresponding to measured-to-initial thickness ratio between 0.5 and 0.75. Subsequently, several finite element models with different densities of thickness measurements were analyzed. Comparing the results showed that a coarse thickness measurements were adequate in the case of minor corrosion. However, in case of moderate or severe corrosion, dense thickness measurements including measurements at the location of minimum thickness are necessary to accurately predict the ultimate capacity and capture the effect of stress concentrations.

2.5. Repair of Steel Compression Members with FRP

The application of FRP in strengthening of concrete structure has been extensively studied (Hollaway and Cadei, 2002; Zhao and Zhang, 2007; Hollaway, 2010). However, its application in strengthening or retrofitting of steel structures has not been fully developed

(Zhao and Zhang, 2007). The majority of the studies that have been conducted to date were on FRP application in retrofitting of steel flexural members (Shulley et al., 1994; Gillespie et al., 1996; Tavakkolizadeh and Saadatmanesh, 2001; Shaat et al., 2004, Dawood et al., 2007). However, recently more attention has been paid to applying FRP for strengthening of compression members (Shaat and Fam, 2006a; Bambach and Elchalakani, 2007; Sundarraja and Sriram, 2014). These applications can be classified into two categories; applications in which FRP is bonded directly to steel substrate and applications in which FRP is used in conjunction with a cementitious core.

2.5.1. FRP-Bonded Directly to Steel Compression Members

This section summarizes the applications in which FRP materials are directly bonded to steel compressive members. These applications are categorized based on the shape of steel cross section into strengthening of closed-sections, open-sections, and concrete-filled steel hollow sections.

- **Strengthening of Closed-Sections**

FRP strengthening of two types of closed-section compression members, closed circular sections and square HSS, resulted in gain in axial capacity and change in failure mode. Strengthening of short steel tubular columns with FRP wraps under axial compression was studied experimentally and numerically by (Teng and Hu, 2005 and 2007). They tested two series of short columns, hollow steel tubular columns, and concrete-filled steel tubular columns with different number of FRP wraps under compression. Strengthening led to change in the failure mode of the steel tubes from elephant foot buckling to inward buckling occurring far from the end. FRP wrapping also resulted in 10% more ultimate

strength corresponding to the concrete-filled tubes and increased ductility up to 10 times corresponding to the hollow tube with three layers FRP wraps. A nonlinear finite element model was utilized to investigate the effect of using FRP wraps with different elastic moduli on the behavior of hollow steel tubular columns. According to the results, increasing the elastic modulus of FRP wraps led to increase of ultimate load. It was also evident that length of the buckled shape at the end reduced with increasing the modulus of elasticity.

Effect of CFRP wrapping in strengthening of short HSS columns with artificial corrosion was studied by (Sundarraja and Sriram, 2014). Corrosion was simulated on HSS columns by submerging the columns in acidic environment for 25 days which led to a maximum of 17% weight loss. Discrete CFRP strips were bonded to the surface of the HSS columns in hoop direction with different number of layers and spacing. The results demonstrated a maximum increase of 68% in the axial capacity compared to the control corroded HSS.

The behavior of HSS columns strengthened using FRP wraps under axial compression was studied by some researchers (Shaath and Fam, 2006a and 2009; Bambach and Elchalakani, 2007). FRP wraps were applied in the transvers and longitudinal directions on two opposite sides or four sides of a series of HSS columns. FRP strengthening led to changing the failure mode, increasing energy absorption, increasing axial stiffness and strength (Shaath and Fam, 2006a and 2009). Strengthening of the columns with higher global slenderness resulted in more gain in axial strength. Predictions were provided using a modified version of provisions of standard CAN/CSA S16-01. The test-to-predicted ratios varied between 0.97 and 1.22. An analytical model using finite difference approach was also developed and validated against the experimental results (Shaath et al.,

2006; Shaat and Fam, 2007a). The effect of non-linearity in material, geometric imperfection, and residual stresses were considered in the model. The ratio of the predicted to measured strengths varied between 0.76 and 1.25. This model was used to study the effect of parameters such as columns out-of-straightness, residual stresses, columns slenderness ratio, and number of FRP wraps. Finite element modeling followed by parametric study on HSS columns were also conducted by (Shaat and Fam, 2006b and 2007b). The results showed that the percentage gain in strength was highly dependent on slenderness ratio of the strengthened HSS columns and CFRP reinforcement ratio.

- Strengthening of Open-Sections

Application of FRP wraps for strengthening and stabilizing opened-sections such as channels, angles, or T-shaped sections was studied by (Silvestre et al., 2008; Harries et al., 2009; Kim and Harries, 2011). Experimental and numerical investigations have been conducted by (Silvestre et al., 2008) to study the behavior of short and long lipped channel steel columns strengthened with CFRP wraps. It was revealed that strengthening had no effect on buckling mode. However, average increases of 15% and 20% in axial capacity of the tested short and long columns were observed, respectively. Harries et al. (2009) studied the effect of FRP strengthening on increasing the stability of flanged steel compressive members. They conducted a series of tests on strengthened long and short steel T sections. Long columns were tested under concentric cyclic compressive loading, and stub columns were loaded under monotonic concentric compression. Only 9% increase in axial capacity was reported. Kim and Harries (2011) conducted a non-linear large displacement finite element modeling of CFRP-strengthened T-section columns, and the results were compared with those obtained from (Harries et al., 2009). It was

concluded that CFRP retrofitting was not efficient for T-sections with web aspect ratio more than 60.

- Strengthening of Concrete-Filled Steel Hollow Sections

FRP wraps were used to improve the behavior of concrete-filled tubular columns (CFT). In this application FRP is wrapped directly on the surface of the steel tube and provides confinement to the steel tube and restrains it from outward buckling. The axial capacity of short CFT columns wrapped with CFRP increased up to 2.2 times compared to the ones without FRP wrapping (Xiao et al., 2005). In addition, they studied the effect of CFRP sheets wrapped around potential plastic hinge regions in a series of long CFT columns under a constant axial load and cyclic lateral load applied at the top. Using CFRP wraps, confined CFT columns demonstrated more ductile and stable hysteretic behavior. Furthermore, local buckling and subsequent rupture of the steel tube was delayed by applying the CFRP wraps. Another study on CFRP confined CFT stub columns under impact load showed that the dynamic-to-static load ratio increased up to 53% under high strain rate loading (Shan, Chen, Zhang, Xiao, Yi, & Lu, 2007).

The effect of CFRP wrapping for repairing CFT columns exposed to fire under compression (Teng and Hu, 2007a), compression-flexure (Tao et al., 2007b), and combined constant axial compression and lateral cyclic load (Tao et al., 2008) was studied. The specimens were exposed to ISO-834 standard fire for 180 min before applying the CFRP confinement. Buckling of the steel tubes delayed due to the effect of CFRP confinement compared to the fire-exposed control specimen without CFRP wrapping. Strength enhancement of the fire-exposed columns after CFRP strengthening varied between 5.9% and 101.8% depending on slenderness, load eccentricity, and

number of CFRP layers. The authors concluded that in case of severely fire-exposed CFT with high slenderness ratio or bending moments, methods such as section enlargement would be more efficient than CFRP-wrapping.

2.5.2. Grouted FRP Jacket for Steel Compression Members

Another technique in strengthening of steel compression members is FRP jacketing. The annular space between the FRP jacket and steel column is subsequently filled with materials such as plain or reinforced concrete, grout, or any other filler material. FRP jackets act as stay-in-place forms, provide confinement, and prevent future deterioration.

The degraded region of a series of artificially corroded I-shaped struts were retrofitted using grout-filled FRP jacket and tested under axial compression (Liu et al., 2005). Corrosion of wide-flanged compression struts was simulated by reducing the flange width over a limited length at mid-height. The retrofitting system covered the degraded region and the two development regions above and below. The annular space between the FRP jacket and steel struts was filled with two different types of concrete, expansive and non-expansive light-weight concrete. All the columns failed by global buckling. The maximum lateral deformation of the un-repaired columns happened at mid-height while for the repaired columns it occurred at the section where the FRP jacket terminated. Comparing the axial capacity of the repaired columns showed that the longer the repair system, the higher the capacity. In addition, the columns repaired with expansive light-weight concrete demonstrated 15% more axial capacity due to the effect of active confinement. Using the test results, a simplified approach was proposed to design FRP-confined concrete systems for deteriorated columns.

An experimental study was conducted to investigate the behavior of strengthened thin steel plates with FRP jacketing repair systems (Ekiz and El-Tawil, 2006). The FRP jackets were filled with polyvinyl chloride (PVC) or mortar as a core material. Those specimens with PVC core were able to transfer the compression load from the steel plate to the repair system more effectively. The bond strength varied based on the type of filling material, level of confinement provided by FRP jacket, and surface condition of both materials in contact.

FRP jacketing was also used to strengthen bracing angles. Seven large-scale strengthened steel braces were tested under cyclic axial loading (El-Tawil and Ekiz, 2009). The strengthening was implemented by wrapping the steel angles with CFRP-wrapped mortar blocks. The number of CFRP layers, size of the mortar core, and presence of bond between steel and mortar were the test parameters. The results proved that the braces could attain the yield strength in compression using this strengthening technique. However, due to the small number of tested specimens the effects of steel-mortar bond and number of CFRP layers were not clear.

The composite action of FRP-encased I-shaped steel columns was studied experimentally by Karimi et al. (2011 and 2012). In these studies the FRP encasement was wrapped around the full-length of the steel columns, and compression was applied to the composite section including the confined concrete. A series of short compact GFRP-encased I-shaped steel columns were tested under axial compression (Karimi et al., 2011). Axial capacity and stiffness increased up to 5.5 and 4 times compared to the un-strengthened column, respectively. In addition, adding shrinkage reducing agent to the concrete mix resulted in 20% and 22% gain in axial capacity and stiffness compared to

those counterparts without shrinkage reducing agent. It was concluded that concrete should achieve a higher volumetric dilation to activate the FRP tube confinement and shrinkage delays the confinement action of FRP wraps.

In another study, the effect of FRP confinement and composite action were investigated by testing FRP-encased I-shaped steel columns with different slenderness (Karimi et al., 2012). Comparing the strengthened columns with corresponding control columns, an increase of 5-10 times in the axial capacity and 4-6 times in the axial stiffness were observed. Energy dissipation capacity, defined as the area underneath the axial load-deformation response, increased 15-25 times of the un-strengthened column. Increasing the slenderness of the columns led to reducing the contribution of confinement by the FRP jacket. Failure of the columns switched from FRP rupture to column global buckling as the slenderness increased. An analytical model was proposed to predict the axial capacity of these types of columns and validated against the experimental results (Karimi et al., 2013). Based on the parametric study conducted using the proposed analytical model, increasing parameters such as column-diameter-to-FRP-thickness ratio, axial stiffness of the FRP tube, and steel-to-concrete-area ratio resulted in gains in axial capacity of the strengthened columns.

Researchers also studied the behavior of FRP jacketing systems filled with other types of materials. A series of steel columns with different cross-sectional shapes were strengthened with FRP jackets filled with either bamboo sticks or mortar (Feng et al., 2013a and 2013b). The length of the retrofitting system was slightly shorter than the length of the steel columns so the axial load was only applied to the steel columns. The results showed increases in both axial capacity and ductility. Maximum gain in axial

capacity was 114% and 215% for the columns strengthened with bamboo sticks and mortar, respectively. Similarly, ductility increased 6.7 times and 9.8 times for the columns strengthened with bamboo sticks and mortar, respectively, compared to the un-strengthened column.

The application of FRP jacketing systems to repair buckled short steel columns with simulated corrosion was studied by Kaya et al. (2015). Thirteen 32 in. long W4x13 columns with different configurations of artificial corrosion on their flanges and webs were repaired and tested in this study. The columns failed under axial compression with visible initial global and local imperfections prior to applying the repair system as reported in (Karagah and Dawood, 2013). The repair system was composed of GFRP-confined grout with embedded longitudinal reinforcing bars. The results showed at least 90% increase in the axial capacity of the repaired columns compared to the capacity of the un-tested control column. The axial load-shortening response of the repaired columns demonstrated a hardening behavior after the onset of buckling. Also, increasing the diameter and the number of GFRP layers increased the axial capacity.

A series of numerical investigations on steel columns repaired with FRP-confined grout were performed by Griggs (2014), and the results were compared to the experimental counterpart obtained by Liu et al. (2005). Using a full-bond model between the steel column and confined grout, the developed finite element models predicted the failure mode and axial capacity accurately.

2.5.3. Bond Behavior at Steel-Concrete Interface

Strengthening or retrofitting creates a composite cross section. Based on the level of bond strength at the interface of the substrate material and the repair system, full or partial composite action is expected to form in the cross section. Researchers studied the bond behavior at the interface between repair systems and steel profile.

To estimate the bond stress capacity of Concrete-Filled Tubes (CFTs), an equation was developed providing a lower bond to the true bond stress for practical columns (Roeder et al. 1999). A series of push-out tests were conducted to investigate the effect of internal stiffeners on steel-concrete bond strength in CFT columns (Petrus et al., 2011). According to the results, bond strength varied from 0.058 ksi to 0.12 ksi based on configuration of the internal stiffeners and in-filled concrete strength. (AISC, 2010) Defines a nominal bond stress of 0.058 ksi for evaluating the direct bond interaction of filled composite members.

In numerical modeling of CFT columns, Coulomb friction model has been used widely with the coefficient of friction ranged from 0.05 to 0.55 (Hu et al., 2005; Ellobody and Young, 2006; Hu and Su, 2011; Gupta et al., 2014; Lai and Varma, 2015). For numerical modeling CFT columns, (Lai and Varma, 2015) used coefficient of friction of 0.55 with the maximum shearing stress of 0.058 ksi as recommended by (AISC, 2010). In this study no chemical bond or cohesive zone model was assigned to the interface. However, other studies such as (Liu et al., 2005) used bond-slip relationship for interface modeling.

A series of pull-out tests on GFRP-confined concrete specimens with an embedded smooth steel bar were conducted to obtain bond-slip relationship (Frauenberger et al.,

2003). The test parameters were type of the confined concrete, i.e. expansive and non-expansive, and embedment length. A bond-slip relationship was obtained with a maximum average bond strength of 0.47 ksi and 0.49 ksi for non-expansive and expansive light-weight concrete, respectively. Another bond-slip relationship for expansive and non-expansive grout resulted in 0.47 ksi and 0.52 ksi for non-expansive and expansive light-weight concrete, respectively, as a maximum average bond strength (Liu et al. 2005).

2.6. Repair of Steel Compression Members with Steel Based Systems

The development of a steel-based plating repair system and current plating rehabilitation methods are reviewed in this section. Traditional plating rehabilitation approaches for steel members are bolted and welded steel plates. The design procedures of these methods are straightforward and well specified in current codes and specifications. However, for underwater rehabilitation of steel piles, welding is not preferred due to cost and quality considerations. Bolting plates to original member is labor intensive and drilling many holes in an already corroded pile is often not preferred by engineers and owners.

FRP sheets have been investigated for steel member retrofit, due to their high strength-to-weight ratio and ease of application. Research on the use of FRP sheets to repair steel columns has been broadly conducted. Shaat and Fam (2006) investigated the behavior of CFRP sheets strengthened short and long square hollow section columns. The study investigated the effects of types of CFRP, fiber orientation, and number of layers by experimental study on 27 short columns and five long columns. The results indicated that while CFRP increased the axial capacity of short and long square hollow columns, transversely wrapped FRP was more efficient than FRP oriented in longitudinal direction for

short columns. Further, retrofitted long columns failed by excessive global buckling, which was more correlated to the initial imperfection than the number of layers of CFRP.

Teng and Hu (2007) demonstrated that GFRP jacket was effective for retrofit circular hollow steel tubes under axial compression. Both experimental and numerical results demonstrate that the FRP jackets significantly increase the ultimate load and ductility of circular hollow steel tubes; while FEA results indicate the effectiveness of FRP jacket strengthening thin cylindrical shells under combined axial compression and internal pressure.

Young et al. (2006), Silvestre et al. (2008) carried out both experimental and numerical investigations on lipped channel columns strengthened by CFRP. The study indicates that longitudinally oriented CFRP is more beneficial to increase ultimate loads than transversely oriented. Further, the increment of ultimate capacity is proportional to the number of layers of CFRPs.

Kim and Harries (2011) strengthened steel T-section members with CFRP strips and tested them in axial compression. The results indicated that the CFRP strips effectively reduced the stresses at the web-flange junction where critical hysteretic stress concentrations could occur. Increment of layers of CFRP had no influence on the tee-section axial members.

Siddique and Damatty (2012) studied the enhancement in buckling capacity of steel plates repaired by GFRP plates numerically. The retrofitted plate capacity was governed by the ultimate shear capacity of the adhesive, ultimate axial capacity of the GFRP, or instability of the system. The failure mode was found depending on the slenderness ratio of the plate and the thickness of the GFRP.

However, as one most critical factor that governs the failure, bond between FRP and steel is difficult to control on site (Teng et al., 2012). Since the adhesion strength of steel/adhesive interface is highly sensitive to the surface preparation, bonded FRP repair system may not be effective or applicable for underwater applications like bridge piles. In contrast, clamped steel plates attached to the steel piles through friction provided by pre-tensioned high strength bolts may not have this disadvantage. The method may be suitable for underwater rehabilitation of steel piles because it is easy to install, immediately effective after installation (does not require a curing time), and maintains the integrity of the original member. The friction-type bolted plates repair system has not been commonly used in practice. Therefore, the axial behavior of the repaired members was investigated and a design model for the repair system was proposed.

2.7. Numerical Simulation of Axially Loaded Steel Members

In order to develop a numerical framework to predict the axial behavior of corroded H-piles, numerical frameworks of different shapes of axial members were reviewed. The reviewed sections include steel channels, angles, hollow sections, and W-shaped sections.

For steel axial members, shell elements are commonly used over solid element, since the thickness is typically much smaller than other dimensions. In some cases, thin shell theory was adopted due to the negligible contribution of transverse shear deformation (Avery and Mahendran, 2000; Yan and Young, 2002; Gardner and Nethercot, 2004). Most of the cases used general-purpose shell elements which use thick shell theory as the shell thickness is over 1/15 of its characteristic length and becomes discrete Kirchhoff thin shell element as the thickness decreases (Yan and Young, 2004; Ellobody and Young, 2005; Zhu and Young, 2006; Dinis et al., 2007; Ellobody, 2007; Chan et al., 2008; Seif and Schafer, 2009; Dinis and

Camotim, 2011; Zhu and Young, 2012; Vani et al., 2013). Reduced integration was commonly used among other researchers to avoid shear locking and save computational time. However, full integration was also used as it does not require hourglass checking like reduced integration. Also, when distortional buckling occurs, elements with reduced integration underestimate the column distortional post-critical strength. This is due to the fact that the reduced integration procedure does not fully capture the column shear stiffness due to the nonlinearity of the wall warping displacements (Dinis and Camotim, 2003; Dinis and Camotim, 2004). Sensitivity studies on elastic buckling have been widely used as the way to determine the appropriate element type and mesh size. However, the determined element type and mesh size from elastic buckling analyses may not capture the inelastic behavior precisely. Geometric imperfections and residual stresses were implemented according to measurements or determined by sensitivity study on nonlinear inelastic buckling analysis in studies when measurements were not taken or the maximum tolerance defined in specifications and codes.

Two steps were typically included for numerical analysis of nonlinear stability problems: first, elastic eigenvalue analysis to obtain the lowest overall and local buckling modes, which were used as initial imperfection shapes in the following analysis; second, nonlinear inelastic analysis incorporated material and geometric nonlinearities to capture the full load-deformation response (Yan and Young, 2004; Ellobody and Young, 2005; Zhu and Young, 2006; Dinis et al., 2007; Ellobody, 2007; Chan et al., 2008; Dinis and Camotim, 2011; Zhu and Young, 2012; Vani et al., 2013). Another technique to capture the initial global imperfection was to apply a transverse load on the member to create a desired lateral deformation. However, initial local imperfections (i.e. flange/web out-of-square) are difficult

to represent using this approach. For elastic analysis, Newton-Raphson method was adopted as the solution scheme. For inelastic analysis, particularly for collapse analysis of members with very slender elements, the modified Riks method (arc length method) was used as it is more robust than Newton-Raphson method (Schafer and Moen, 2010).

2.7.1. FEA of steel channel columns

Young and Yan (2002) developed a nonlinear finite element model to investigate the strength and behavior of cold-formed lipped channel columns. A finite element nonlinear analysis program, ABAQUS, was used to simulate the fixed-ended cold-formed lipped channel columns. The model implemented the measured material properties and initial geometric imperfections from their experimental program (Young and Rasmussen, 1998). The material properties were determined from tensile coupon tests, and the initial local and overall imperfections were measured from the test specimens before loading. The geometric imperfections were included by using a linear perturbation analysis to establish the probable buckling modes of the column, and scaling the eigenvectors by a factor (measured maximum magnitudes of local and global imperfections) for nonlinear analysis. Residual stresses were not considered since the measurements obtained from Young and Rasmussen (1995, 1998) indicated they were negligible. A thin shell element, S4R5, with 4 nodes and 5 degrees of freedom per node, linear shape function, reduced integration, was used for the model. The element type and size were determined according to a sensitivity study which indicated that the chosen type and size provided best prediction. Details of the sensitivity study were not mentioned in the paper. However, the FEA predictions were compared to the experimental results from Young and Rasmussen (1998). The ultimate loads obtained from FEA closely predicted the

experimental results. The mean values of the experimental-to-FEA ultimate load ratio were 0.97 and 0.99 with corresponding coefficient of variation (COV) of 0.051 and 0.057 for two series of columns, respectively. The axial load-shortening curves from test and FEA correlated well except the post-buckling portion where FEA predicted higher capacity compared to test response. This might be caused by the lack of residual stresses in FEA and unintentional eccentricity of the test set-up.

Similarly, Yan and Young (2004) investigated the axial behavior of fixed-ended cold-formed steel channel columns with complex stiffeners using a non-linear finite element model in ABAQUS. The section consisted of simple lips with return lips. The measured dimensions, material properties, and geometric imperfections were implemented in the FE model. The model used a four-node shell element, S4R, with 6 degrees of freedom per node, linear shape function, general-purpose, reduced integration. The mesh size was chosen based on a sensitivity study conducted in Young and Yan's (2002) previous study. The model was validated by four series of experimental results of a total 30 specimens (Yan and Young, 2002). The differences of axial capacity obtained from experimental results and FEA predictions were no more than 12%. The FEA provided good agreement of failure modes as well.

Dinis et al. (2007) presented a numerical investigation about elastic and elastic-plastic post-buckling behavior of cold-formed steel lipped channel columns affected by local-plate/distortional buckling mode interaction. ABAQUS was used for finite element analysis. A four-node isoparametric fully integrated shell element (S4) was chosen for modeling. A preliminary investigation was carried out to determine the level of mesh refinement, according to which 0.394 in×0.394 in was adopted. Initial geometric

imperfections were implemented by scaling the elastic buckling mode shapes. The solution schemes for elastic and elastic-plastic analyses were Newton-Raphson method and Riks arc-length method, respectively.

In a later research conducted by Dinis and Camotim (2011), the elastic and elastic-plastic post-buckling behavior of cold-formed steel lipped channel columns affected by distortional/global (flexural-torsional) buckling interaction was investigated. ABAQUS was used for FEA using the 4-node shell element, fully integrated, with linear shape functions. Imperfections were implemented with both global and distortional shapes obtained from elastic buckling analysis.

Schafer et al. (2010) reviewed computational modeling of elastic buckling and nonlinear collapse analysis on cold-formed steel members. For nonlinear collapse analysis, an example of 47.2 in long cold-formed steel lipped channel column was performed by finite element analysis to evaluate the influences of element type, mesh density, solver, solution step size, plasticity model, number of integration points through thickness, and choice of commercial implementation (ABAQUS and ADINA). The results indicated that collapse analysis of cold-formed members was very sensitive to the above parameters. However, computational modeling still plays an important role in future research and design of cold-formed steel.

2.7.2. FEA of steel angles

Vani et al. (2013) explored the behavior of cold-formed steel angles under compression numerically using ABAQUS. The material properties were taken from tensile coupon test. The 4-node general purpose shell element, S4R, with reduced integration and linear shape functions was used for analysis. The mesh size was determined as 0.394 in×0.394

according to a convergence study. Measured values of initial imperfections were taken. The modified Riks method was used for nonlinear analysis. The model was validated by experimental results of 5 specimens as the differences between experimental and numerical results were less than 5.7%. The numerical predictions of member capacities were compared to the predictions by DSM and EWM from AISI (2012). Both design methods provided conservative predictions. In extreme cases, the EWM underestimated the capacity by 96%.

2.7.3. FEA of hollow section columns

Gardner and Nethercot (2004) conducted numerical modeling of structural response of steel hollow sections using ABAQUS, including square, rectangular, and circular hollow sections. The objective of the research was to develop a consistent approach to model stainless steel structures. The model was implemented with general expressions defined for material stress-strain relationship, enhanced strength corner properties, initial geometric imperfection modes and magnitudes, and residual stresses. A nine-node thin shell element with five degrees of freedom per node and quadratic shape function, S9R5, was used for analysis. The research considered the effects of residual stresses, initial imperfections (global and local), extent of corner regions. The initial global and local imperfection shapes were obtained from an eigenvalue analysis and taken as the lowest modes of global and local buckling. The complete initial imperfection comprised a superposition of the global and local modes. Initial out-of-straightness was taken as $L/2000$ according to a parametric study comparing FEA predictions to test results with changing magnitudes of overall imperfections. A similar parametric study was conducted to determine the residual stresses, although the results indicated that the influence of

residual stresses were relatively insignificant to the column response. The modified Riks method was used to solve the material and geometric nonlinearity.

To investigate the axial compressive behavior of hot-rolled elliptical hollow sections, Chan and Gardner (2008) developed a non-linear FE model using ABAQUS. A four-node shell element with 6 degrees of freedom per node, linear shape functions, and reduced integration, designated as S4R, was used for analysis. A sensitivity study based on elastic eigenvalue analysis was conducted to choose the suitable mesh size. Three values of initial imperfection were taken into consideration, $t/10$, $t/100$, and $t/500$. The value of $t/100$ was adopted as it showed the best agreement with the test results. Residual stresses were not considered. The modified Riks method was used to solve geometric and material nonlinearity. The comparisons of ultimate loads and axial load-shortening responses between experiments and FEA demonstrated the accuracy of the model. Similarly in their later researches, Chan and Gardner (2008) studied the bending behavior of elliptical hollow sections and Gardner et al. (2011) investigated the behavior of elliptical hollow sections under combined compression and uniaxial bending.

Zhu and Young (2006) investigated fix-ended aluminum alloy tubular columns of square and rectangular hollow sections using the finite element program ABAQUS. A four-node shell element with reduced integration (S4R) was used based on the evaluation from Yan and Young (2004) and Ellobody and Young (2005). Initial overall and local imperfections were implemented in the model based on measured geometry. The way of implementing initial imperfections was first to obtain the necessary eigenvectors as imperfection shapes from elastic eigenvalue analysis, and then scaled them as the imperfections in non-linear analysis. Residual stresses were not included because the

values were very small for extruded aluminum alloy profiles. This numerical model provided reliable predictions of the axial capacities of the studied members. The differences between experimental results and FEA predictions were no greater than 16% among a total of 36 specimens, and the differences were less than 10% for 28 out of 36 specimens (Zhu and Young, 2006).

In their later study, Zhu and Young (2012) developed a finite element model to simulate the fixed-ended steel column tests of oval hollow sections. The FE model incorporated the initial global and local imperfections and material nonlinearity. Comparing with the four series (four types of cross section dimensions) of their test results (Zhu and Young, 2011), the mean values of the experimental-to-FEA ultimate load ratio were 1.04, 1.02, 1.01, and 0.99 with corresponding coefficients of variation of 0.024, 0.053, 0.083, and 0.101 respectively. The FE model predicted the behavior of cold-formed steel oval hollow section columns accurately. A parametric study on a total of 100 columns was performed using the FE model. The FEA predicted capacities were compared to strengths calculated using current North American, Australian/New Zealand, and European specifications for cold-formed steel members. Generally the design methods from specifications overestimated the column strength. The mean values of ratios of FEA predictions to calculations from the three specifications were 0.89, 0.89, and 0.90, with the coefficients of variation (COV) of 0.076, 0.076, and 0.100, respectively. However, for compact oval hollow sections, the predictions from design specifications were slightly conservative.

Ellobody and Young (2005) developed a finite element model for prediction of stainless steel columns with square and rectangular hollow sections. The software ABAQUS was

used. Two steps of analyses were conducted: first a linear elastic eigenvalue analysis was performed to obtain the lowest buckling mode; second a nonlinear analysis was conducted and incorporated geometric and material nonlinearity. The initial imperfection shapes were adopted from the eigenvectors from elastic analysis. A general-purpose 4-node shell element, S4R, with 6 degrees of freedom, reduced integration, and linear shape functions was used for the model. Convergence studies were conducted to determine the mesh size. The results indicated that a 0.787 in.×0.394 in. mesh provided adequate accuracy and acceptable computational time. Measured residual stresses were implemented in the model as well. A total of 22 cold-formed high strength stainless steel hollow columns were analyzed and compared to the experimental results. A maximum difference of 8% was observed between experimental results and FEA predictions, which indicated the accuracy of the FE model. Ellobody (2007) further used this FE model to investigate the buckling behavior of cold-formed high strength steel stiffened slender square and rectangular hollow section columns.

2.7.4. FEA of W-shaped columns

Seif and Schafer (2009) conducted a FEA on hot-rolled steel members using AISC W14 and W36 sections. The study focused on collapse response of short columns and beams with slender elements that failed by local buckling. An elastic buckling analysis was used to perform a sensitivity study to investigate the influence of element type and mesh size. The study indicated that the “S4” element provided in ABAQUS with ten elements along the depth of web and ten elements along the width of flange delivered adequate accuracy for hot-rolled steel sections in their study. Local imperfections and residual stresses were considered in the model. The local imperfections were determined according to

manufacturing tolerances (ASTM A6/A6M-04b, 2003). Only local imperfections were taken into consideration.

2.7.5. FEA of steel frames

Avery and Mahendran (2000) presented a detailed description of shell finite element distributed plasticity model for steel frame structures composed of non-compact sections. The model was built in ABAQUS and a thin, shear flexible, isoparametric, quadrilateral shell with 4 nodes and 5 degrees of freedom per node, utilizing reduced integration and bilinear interpolation schemes element was used for analysis. Also a R3D4 rigid surface element was used to create pinned-member end restraints, which was a rigid quadrilateral element with 4 nodes and 3 translational degrees of freedom per node. The model was verified by experimental results conducted by the authors (Avery and Mahendran, 2000), which demonstrated that the shell finite element model accurately represented distributed plasticity resulting from the combined effects of applied axial force and bending moment, residual stresses, and local buckling.

The FEA accurately predicted the ultimate load, failure mode, and load-displacement response of axial members with different types of sections. However, the results were sensitive to parameters related to simulation techniques, including element type, mesh size, material modeling, initial imperfections and stresses, solver, and step size.

Chapter 3. Small-scale Pile Tests

To investigate the effect of partial degradation on the remaining axial capacity of compression members, small-scale piles were tested. The main objectives of the tests were to quantify the remaining axial capacity of steel piles with different corrosion patterns and to determine the suitability of existing design equations to predict the remaining capacity. The parameters of the study were the reduction of the thickness of the flanges and webs, presence of through-web void, unsymmetric reduction of the flange thickness, and flange width reduction. The outcome provided insight into the effect of the studied parameters on the reduction of the axial capacity of the tested piles and informed the subsequent full-scale pile tests that are described in the next chapter. This chapter describes the experimental program for the small-scale pile tests. The test results are also presented and discussed.

3.1. Small-Scale Experimental Study of Piles with Localized Corrosion

3.1.1. Test Specimens

Thirteen 32 in. long W4×13 steel piles were tested in two phases to investigate the effect of partial corrosion on the axial capacity of the compression members. The corrosion patterns were selected to be representative of corrosion patterns that were observed in the field.

The testing was conducted in two phases. In phase I the effect of flange and web corrosion on the axial capacity of the piles was evaluated. One of the piles in phase I was tested as an un-corroded control pile. For the remaining piles, localized corrosion was simulated by milling the flanges and webs along a 12 in. long region at the mid-height of

the piles. Figure 3.1 illustrates the simulated corrosion pattern for a pile with reductions of the flange and web thicknesses. Two levels of flange thickness losses, 50% and 75%, and two levels of web thickness losses, 30% and 60%, were considered in phase I of the study. Four piles, two with only web loss and two with only flange loss, were examined to study the effect of web and flange deterioration independently. To investigate the effect of flange and web degradation together, two piles with simultaneous loss of flanges and web were tested. The fillet region at the web-flange junction remained un-milled due to practical limitations. As shown in Figure 3.1, each pile in phase I was assigned a unique two-part identifier which indicates the percent reduction of the flange and web thicknesses, respectively.

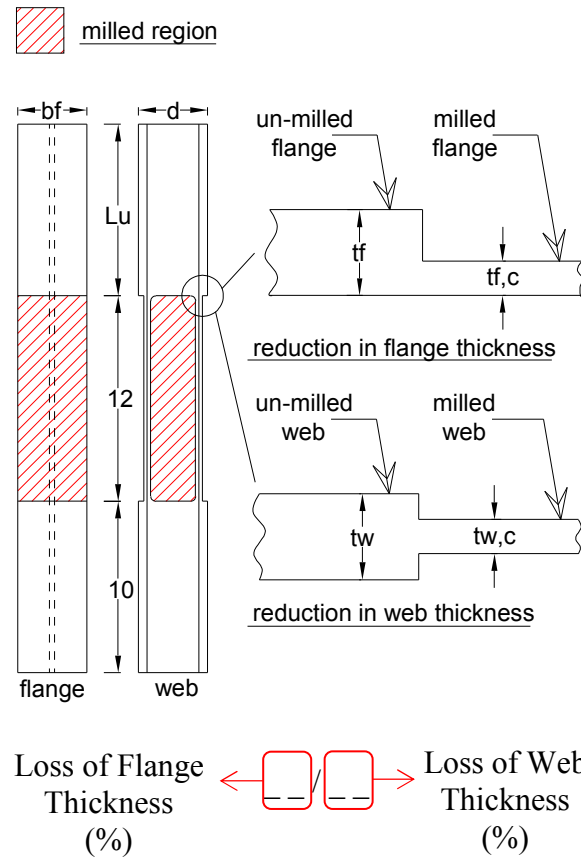


Figure 3.1: Schematic drawing and designation of the piles in phase I

Table 3.1 summarizes the measured geometry of the seven piles tested in phase I. Due to fabrication tolerances, the measured thicknesses varied from the target values by up to 17%. The total length of pile 50/30 was 27 in. (about 15% shorter than the other piles) and the length of the pile above the corroded region, L_u , was only 5 in. compared to 10 in. for the other piles.

Table 3.1: Measured Geometry and Designations of the Tested Piles in Phase I

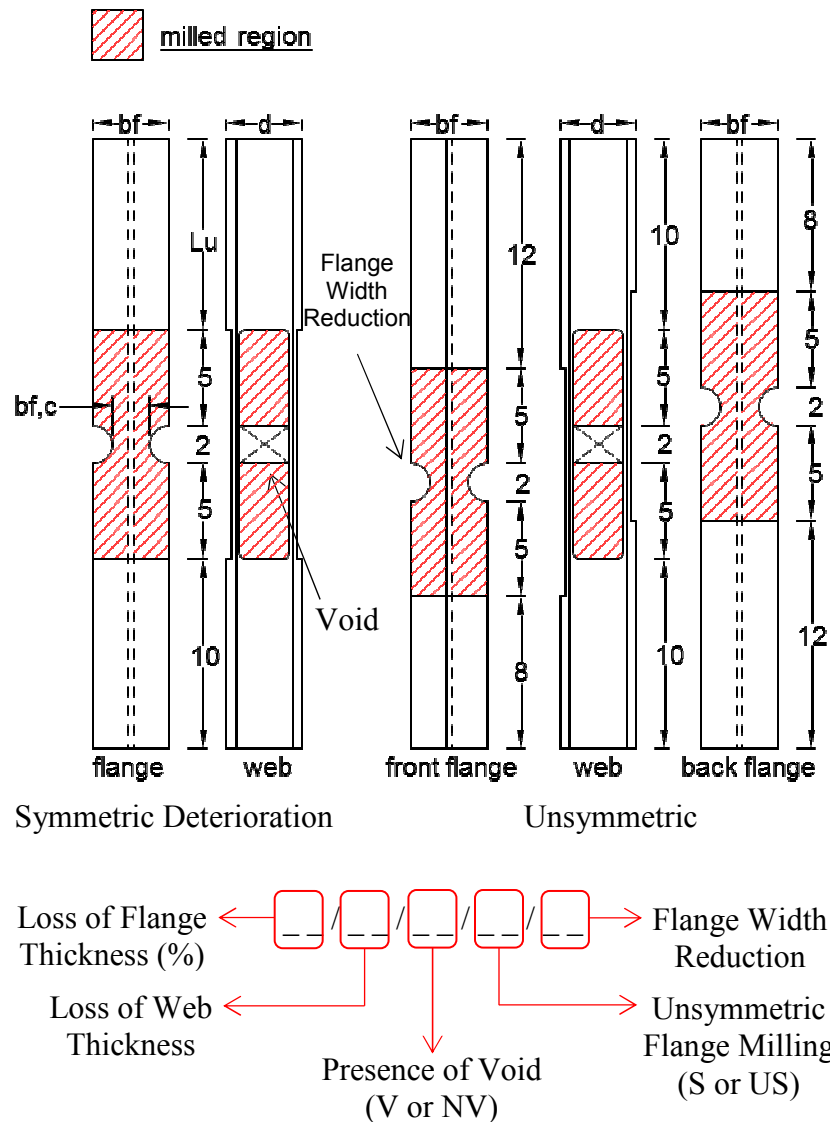
Pile	L_u	d	b_f	t_f	t_w	$t_{f,c}$	$t_{w,c}$
Designation	[in]	[in]	[in]	[in]	[in]	[in]	[in]
0/0	10.0	4.20	4.17	0.36	0.30	0.36	0.30
0/30	10.0	4.17	4.17	0.35	0.28	0.35	0.21
0/60	10.0	4.17	4.17	0.36	0.29	0.36	0.12
50/0	10.0	4.24	4.17	0.35	0.28	0.17	0.28
50/30	5.00	4.20	4.16	0.35	0.28	0.19	0.20
75/0	10.0	4.23	4.17	0.35	0.28	0.08	0.28
75/60	10.0	4.22	4.17	0.35	0.28	0.11	0.11

In phase II, piles with more complex corrosion patterns, closer to those observed in the field (see Figure 3.1(a)), were studied. In this phase six piles were tested with 75% flange thickness reduction and 60% web thickness reduction. Figure 3.2(b) illustrates a schematic drawing of the milling patterns of the tested piles in phase II. The influence of flange width reduction, through-web voids, and unsymmetric flange deterioration were studied in phase II. To simulate severe corrosion of the flanges, two 2-in. diameter semi-circular perforations were cut out of each flange in three of the tested piles. Four piles were machined with a 2 in. through-web void at mid-height. Also in four piles, the corroded region of each flange was offset by 2 in. towards opposite ends of the piles to simulate the cases with unsymmetric degradation, as illustrated in Figure 3.2(b). Each pile in phase II was assigned a unique four- or five- part identifier as shown in Figure 3.2(b). The first two parts indicate the reduction of the flange and web thicknesses,

respectively. The third part indicates the presence of a void in the web, “V”, or no void, “NV”. The fourth part indicates symmetric, “S”, or unsymmetric, “US”, corrosion of the flanges. The fifth part of the identifier, if present, indicates reduction of the width of the flanges “WR”.



(a) Reduction of Flange Width



(b) Milled Piles Tested in Phase II

Figure 3.2: Schematic drawing and designation of the piles in phase II

Table 3.2 summarizes the measured geometry of the seven piles tested in phase II. The nominal values of reduction of flange and web thicknesses were kept constant at 75% and 60% for the tested piles in phase II, respectively. However, the measured thicknesses varied from the target values by up to 10% due to fabrication tolerances.

Table 3.2: Measured Geometry and Designations of the Tested Piles in Phase II

Pile Designation	d [in]	b _f [in]	b _{f,c} [in]	t _f [in]	t _w [in]	t _{f,c} [in]	t _{w,c} [in]
75/60/NV/US	4.26	4.17	4.17	0.36	0.29	0.08	0.10
75/60/NV/US/WR	4.25	4.16	2.09	0.36	0.29	0.11	0.10
75/60/V/S	4.25	4.17	4.17	0.36	0.29	0.10	0.13
75/60/V/S/WR	4.26	4.16	2.15	0.35	0.30	0.10	0.12
75/60/V/US	4.23	4.19	4.19	0.35	0.29	0.10	0.13
75/60/V/US/WR	4.23	4.16	2.17	0.35	0.29	0.11	0.13

3.1.2. Materials

Six tension tests and a stub pile test were conducted to obtain the material properties of the steel piles. Four coupons from the flanges and two coupons from the web were tested under uniaxial tension according to ASTM A370 (2013). Displacement rates of 0.024 and 0.200 in/min were applied in the elastic and plastic regions, respectively. For the compression test, a 16 in. long segment of the pile was cut from the same W4x13 member as the test piles. The stub pile was loaded concentrically up to buckling at a rate of 0.008 in/min. The top was pinned about both axes while the bottom was fixed against rotation about both axes.

Table 3.3 shows the elastic modulus, yield stress, ultimate stress, and strain at ultimate stress of the tested tensile coupons and stub pile.

Table 3.3: Properties of Steel Piles

Location of Specimen	Test Type	Tensile Modulus (E_s) (ksi)	Yield Stress (f_{sy}) (ksi)	Ultimate Stress (f_{su}) (ksi)	Strain at Ultimate Stress ϵ_{su} (in/in)
Flange-1	Tension	N/A ^a	57.0	70.2	0.132
Flange-2	Tension	27100	54.5	68.4	0.139
Flange-3	Tension	28400	55.7	68.3	0.138
Flange-4	Tension	25200	57.1	70.5	0.123
Flange (average)		26900	56.1	69.4	0.13
Flange (STDV)		1310	1.06	0.99	0.01
Flange (C.O.V.)		0.0486	0.0189	0.0142	0.0531
Web-1	Tension	25810	66.70	78.88	0.0605
Web-2	Tension	26390	60.76	74.82	0.0787
Web (average)		26100	63.7	76.9	0.0696
Web (STDV)		290	2.97	2.03	0.0091
Web (C.O.V.)		0.0111	0.0466	0.0264	0.131
Stub Column	Compression	30160	53.51	N/A ^b	N/A ^b

^a Tensile modulus was not calculated due to receiving noisy signals in the elastic region.

^b Stub pile was not loaded to ultimate loading stage.

nominal material properties of the steel pile: f_{sy} =50 ksi, f_{su} =65 ksi, E_s =29000 ksi

3.1.3. Test Setup

All of the piles were tested under monotonic uniaxial concentric compression load using a servo-hydraulic Tinius-Olsen universal testing machine with a capacity of 400 kips. The piles were loaded until substantial inelastic deformations were observed using a constant displacement rate of 0.008 in/min. Figure 3.3(a) shows the test setup for small-scale piles. The piles were free to rotate about both axes at the top. The bottom ends of the piles were fixed against rotation about the strong axis and free to rotate about the weak axis as illustrated in Figure 3.3 (b) and (c). To level the ends of the piles, a thin layer of plaster was applied to both ends.

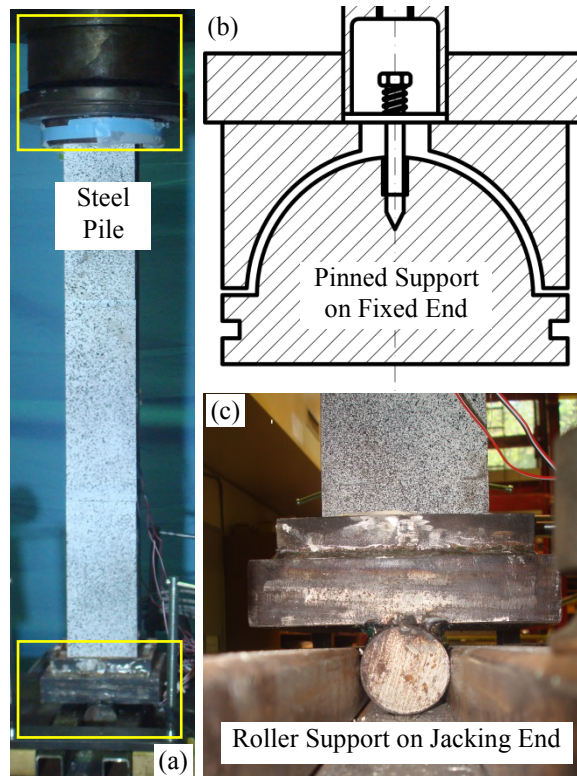


Figure 3.3. Test setup for small-scale piles

3.1.4. Instrumentation

The axial load was measured by the Tinius Olsen machine using a pressure transducer that was installed on the hydraulic pump which was calibrated using a load cell. A digital image correlation- (DIC) based non-contact measurement system (ARAMIS), shown in Figure 3.4(a), was used to measure full-field displacements on the front flange along the entire length of the piles. Figure 3.4(b) illustrates a schematic drawing of the test setup and the position of the DIC system. The axial shortening of the piles was measured by ARAMIS between two points located 4 in. from the top and bottom of the piles to eliminate the boundary effects.

As shown in Figure 3.4 (c), the surface of the front flange was painted with a black and white speckle pattern using a non-glossy spray paint to facilitate the use of the ARAMIS system. To produce the speckle pattern, first the surface of the flange was painted in white. Subsequently, the black dots were sprayed on the white background. The size of the black dots depends on the distance between the camera and the surface of the specimen. As the distance increases, the diameter of the dots should increase accordingly. The minimum diameter of the dots should be five pixels in the image.

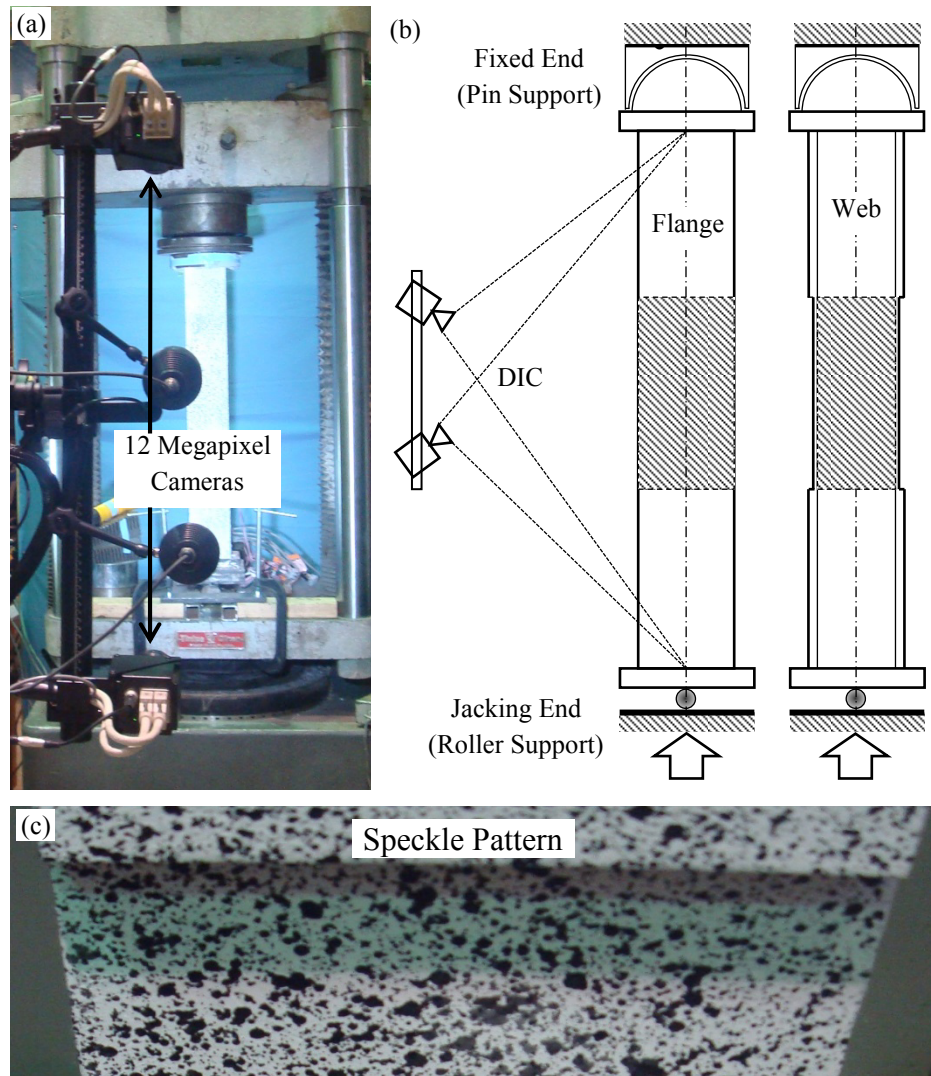


Figure 3.4: Instrumentation of the small-scale compression test

3.1.4.1. Non-Contact Measurement System

The DIC system consisted of a pair of 12 megapixel cameras connected to a sensor controller and a high performance image processing computer. The cameras captured images during the test every 20 sec. Then, using the ARAMIS tracking software, the computer processed the captured images and calculated the displacement and strain over the entire field of measurement. The motion of the speckle pattern on the surface of the specimen was tracked by the software. Then, comparing the subsequent images with the reference image, the deformation and strain were calculated (ARAMIS, 2011).

Figure 3.5 illustrates a set of four slightly overlapped square facets that are defined on a random speckle pattern. The individual facets are offset slightly to distinguish between adjacent facets, but in reality they all lie on the same horizontal line. As shown in Figure 3.5, to define a facet, two parameters, namely facet size and step were required. The facet size is the number of pixels along each edge of the facets. The facet step is the distance between the centroids of the adjacent facets, measured in pixels. The reference image is the image captured at a reference state of deformation which was an undeformed state under zero load. All the other subsequent images were then compared to this reference image to calculate the deformation. Strains were calculated by determining the relative displacements between different sets of facets and dividing them by the distance between the facets. The apparent ‘gauge length’ of the strain measurement can be controlled by changing the number of facets used in this calculation, known as the computation size. Figure 3.5 shows a case with a computation size of 3 which means the strain at the centroid of the middle

facet is calculated by considering the deformation over a distance between three consecutive facets. The relative displacement between the centroid of the two outer facets is used to determine the strain at the centroid of the middle facet. Increasing the computation size results in a more averaged strain (larger ‘gauge length’) while decreasing the computation size yields more accurate, but more noisy localized strains (smaller ‘gauge length’). Facet size, facet step, and computation size of 20, 16, and 7 respectively were selected to process the data of small-scale piles.

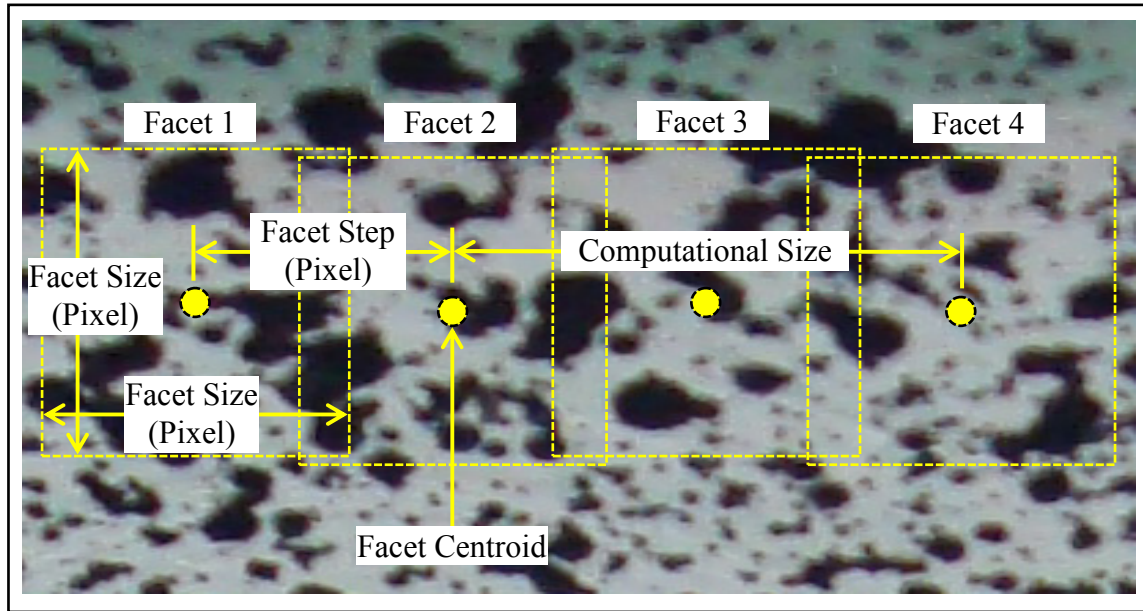


Figure 3.5: Facet size, facet step, and computational size

3.1.5. Results

This section presents the results of the piles that were tested in phases I and II. The axial load-shortening response, deformed shape, axial strain contours at peak load, and failure mode are reported for each pile. The axial strain contours are presented for the front flange and indicate the initiation of global or local deformation, although no visible sign of deformation was observed at this loading stage. The nominal axial capacity of the

undamaged piles, $P_{n,u}$, was calculated using the nominal geometry and material properties according to the equations presented in AISC (2011) and summarized previously in this report.

3.1.5.1. Pile 0/0

The un-corroded control pile, 0/0, had no artificial degradation and served as the basis of comparison for subsequent piles. Figure 3.6(a) shows the axial load-shortening response of the pile. The pile was loaded monotonically up to a peak load of 215 kips. The test was terminated when the axial load dropped to 182 kips. The capacity of the tested pile was 17% greater than calculated nominal axial capacity of the control pile due to having larger dimensions and higher elastic modulus and yield strength than the nominal values. Using the measured geometry of this pile and material properties of the stub pile, the predicted axial capacity according to AISC (2011) was calculated as 209 kips which is 3% smaller than the measured capacity. Figure 3.6 (b) shows the failure mode of pile 0/0 which failed by global buckling. Figure 3.6 (c) shows the axial strain contours on the front flange at the peak load. The lower axial strain on one side indicates the initiation of global buckling, although no visible sign of lateral deformation was observed at this loading stage.

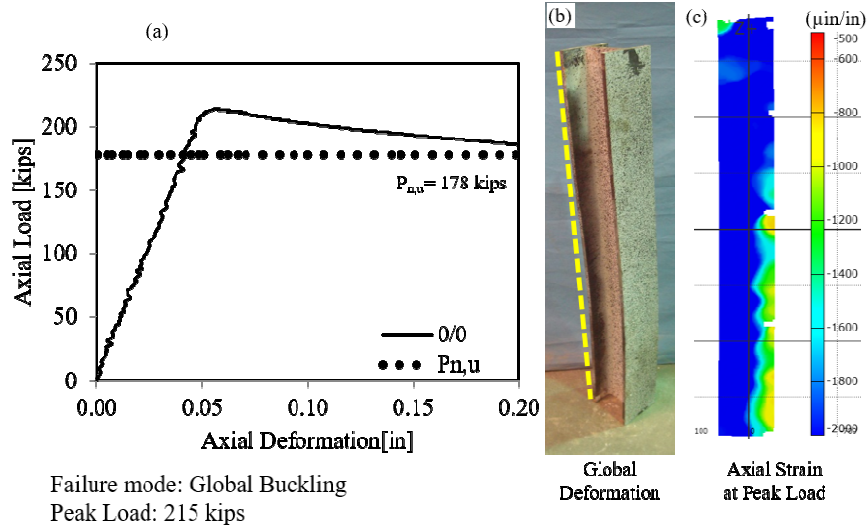


Figure 3.6: Failure mode and load-deformation response of pile 0/0

3.1.5.2. Pile 0/30

Pile 0/30, had no flange degradation and 30% reduction in the web thickness. Figure 3.7(a) shows the axial load-shortening response of the pile. The figure also shows the measured axial load-displacement response of the un-corroded control pile for comparison purposes. The 0/30 pile was loaded monotonically up to a peak load of 201 kips. The test was terminated when the axial load dropped to 173 kips. The measured capacity of the tested pile was 13% greater than the calculated nominal axial capacity of the control pile. Figure 3.7(b) shows the global deformation of pile 0/30 which failed by global buckling. Figure 3.7(c) shows the axial strain contours on the front flange at peak load. The lower axial strain on one side indicates the initiation of global buckling, although no visible sign of deformation was observed at this loading stage.

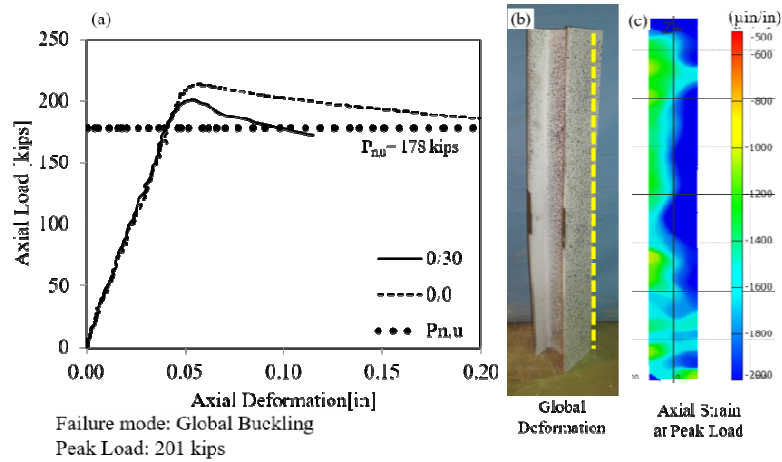


Figure 3.7: Failure mode and load-deformation response of pile 0/30

3.1.5.3. Pile 0/60

The pile 0/60, had no flange degradation and 60% reduction in the web thickness. This pile was loaded monotonically up to the peak load of 178 kips. The test was terminated when the axial load dropped to 92 kips. Figure 3.8(a) shows the axial load-shortening response of the pile. The figure also shows the measured axial load-displacement response of the un-corroded control pile for comparison purposes. Figure 3.8(b) shows the global deformation of pile 0/60 which failed by global buckling. Figure 3.8(c) shows the axial strain contours on the front flange at peak load. The lower axial strain on one side indicates the initiation of global buckling, although no visible sign of deformation was observed at this loading stage.

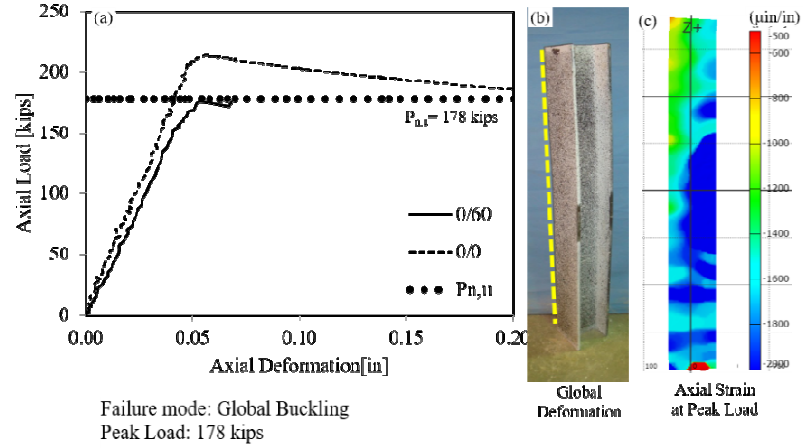


Figure 3.8: Failure mode and load-deformation response of pile 0/60

3.1.5.4. Pile 50/0

The pile 50/0 had no web degradation and 50% reduction in the flange thickness. This pile was loaded monotonically up to the peak load of 117 kips. The test was terminated when the axial load dropped to 90 kips. Figure 3.9(a) shows the axial load-shortening response of the pile. The figure also shows the measured axial load-displacement response of the un-corroded control pile for comparison purposes. The capacity of the tested pile is 34% less the nominal axial capacity of the control pile. Figure 3.9(b) and (c) shows the global and local deformation of pile 50/0 which failed by flange local buckling followed by global buckling. Figure 3.9(d) shows the axial strain contours on the front flange at peak load. The location of the strain concentration indicates the initiation of flange local buckling, although no visible sign of localized deformation was observed at this loading stage.

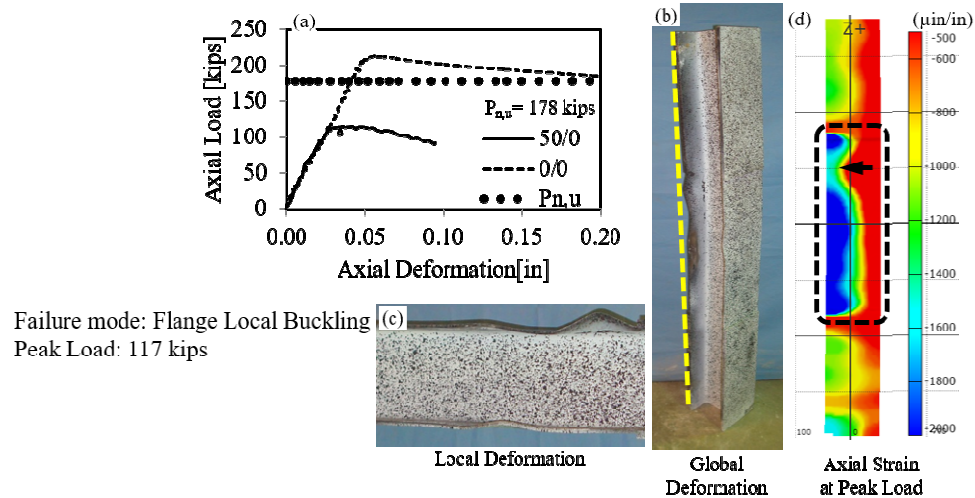


Figure 3.9: Failure mode and load-deformation response of pile 50/0

3.1.5.5. Pile 50/30

The pile 50/30 had 50% and 30% reduction in the flange and web thicknesses respectively. This pile was loaded monotonically up to the peak load of 130 kips. The test was terminated when the axial load dropped to 84 kips. Figure 3.10(a) shows the axial load-shortening response of the pile. Due to an unexpected complication during fabrication, the 50/30 pile was 5 in. shorter than the other piles in the testing program. Consequently, the nominal axial capacity of this pile was 4.5 kips greater than that of the other specimens. Figure 3.10(b) and (c) shows the global and local deformation of pile 50/30 which failed by flange and web local buckling. Figure 3.10(d) shows the axial strain contours on the front flange at peak load indicating the location of strain concentration.

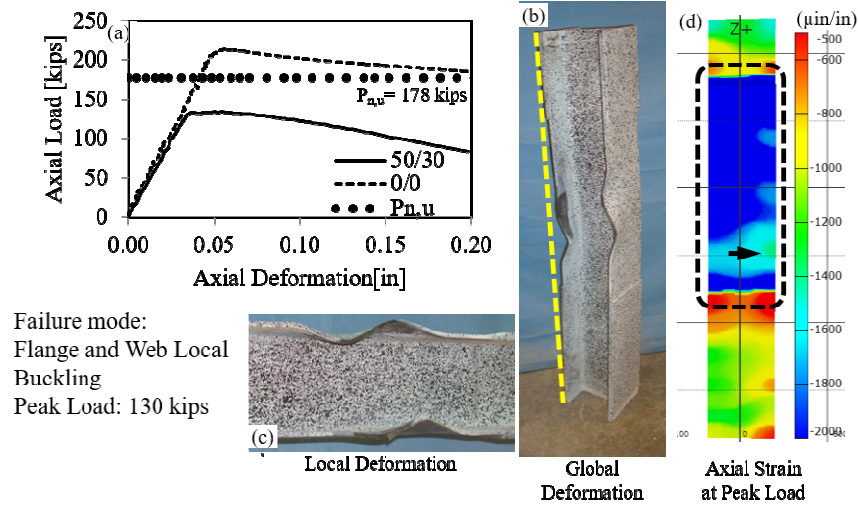


Figure 3.10: Failure mode and load-deformation response of pile 50/30

3.1.5.6. Pile 75/0

The pile 75/0 had no web degradation and 75% reduction in the flange thickness. This pile was loaded monotonically up to the peak load of 92 kips. The test was terminated when the axial load dropped to 73 kips. Figure 3.11(a) shows the axial load-shortening response of the pile. The pile attained the yield capacity at the corroded section. Figure 3.11(b) and (c) show the global and local deformation of pile 75/0 which failed by flange local buckling. Figure 3.11(d) shows the axial strain contours on the front flange at peak load indicating the locations of strain concentration. The strain contours also show increase of strain within the corroded region due to the reduced axial stiffness of the corroded region compared to the un-corroded portion of the pile.

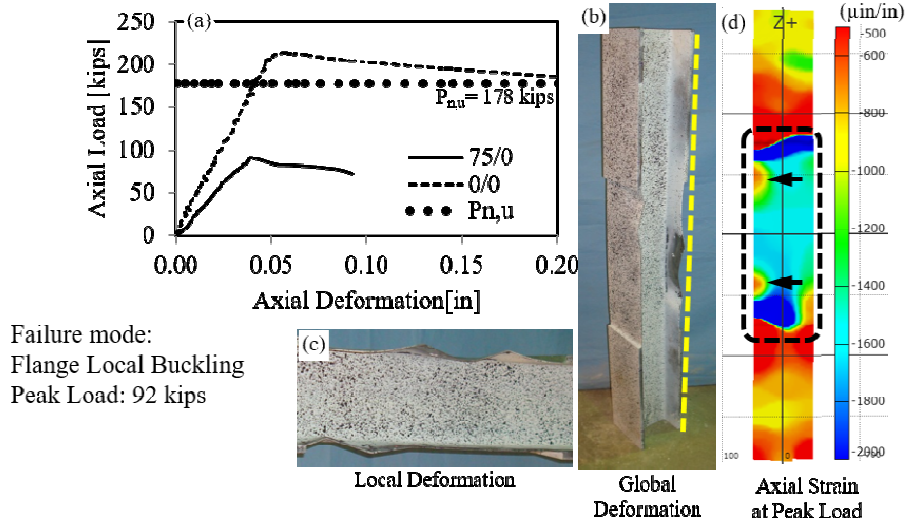


Figure 3.11: Failure mode and load-deformation response of pile 75/0

3.1.5.7. Pile 75/60

The pile 75/60 had 75% and 60% reduction in the flange and web thicknesses respectively. This pile was loaded monotonically up to the peak load of 70 kips. The test was terminated when the axial load dropped to 46 kips. Figure 3.12(a) shows the axial load-shortening response of the pile. The capacity of the tested pile is less than the nominal axial capacity of the control pile. Figure 3.12(b) and (c) shows the global and local deformation of pile 75/60 which failed by flange and web local buckling. Figure 3.12(d) shows the axial strain contours on the front flange at peak load indicating the location of strain concentration.

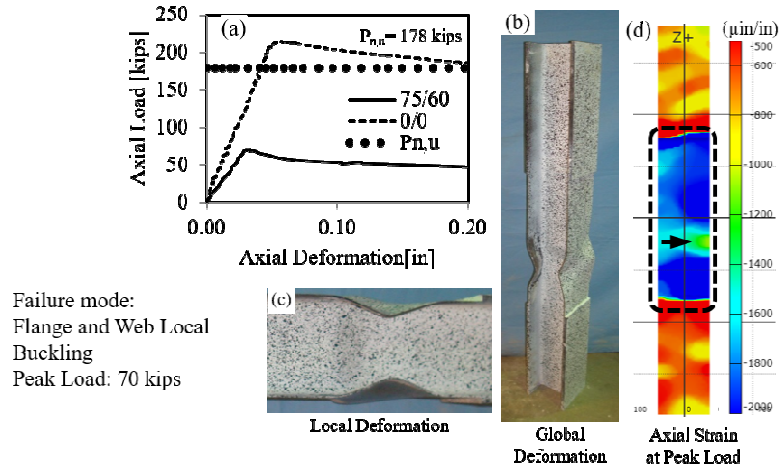


Figure 3.12: Failure mode and load-deformation response of pile 75/60

3.1.5.8. Pile 75/60/NV/US

The pile 75/60/NV/US had 75% and 60% reduction in the flange and web thickness respectively. No void was created in the web, but the milling of the flanges was offset by 2 in. towards opposite ends to achieve an unsymmetrical configuration. This pile was loaded monotonically up to the peak load of 57 kips. The test was terminated when the axial load dropped to 40 kips. Figure 3.13(a) shows the axial load-shortening response of the pile. Figure 3.13(b) and (c) shows the global and local deformations of pile 75/60/NV/US which failed by flange and web local buckling. Figure 3.13(d) shows the location of strain concentration which indicates initiation of localized deformation prior to the appearance of any visible indication on the pile.

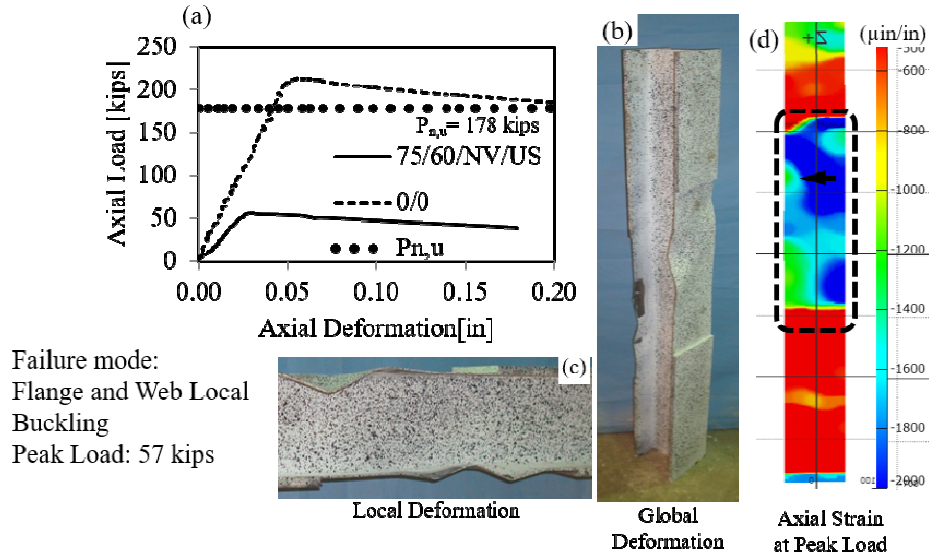


Figure 3.13: Failure mode and load-deformation response of pile 75/60/NV/US

3.1.5.9. Pile 75/60/NV/US/WR

The pile 75/60/NV/US/WR had 75% and 60% reduction in the flange and web thickness respectively. No void was created in the web, but the milling on the flanges was offset by 2 in. towards opposite ends resulting in an unsymmetrical degradation pattern. In addition, two 2 in. diameter semi-circular perforations were cut out of each flange. This pile was loaded monotonically up to the peak load of 70 kips. The test was terminated when the axial load dropped to 68.7 kips. Figure 3.14(a) shows the axial load-shortening response of the pile. Figure 3.14(b) and (c) show the global and local deformation of pile 75/60/NV/US/WR which failed by flange and web local buckling. Figure 3.14(d) shows the location of a strain concentration at the section with minimum flange width.

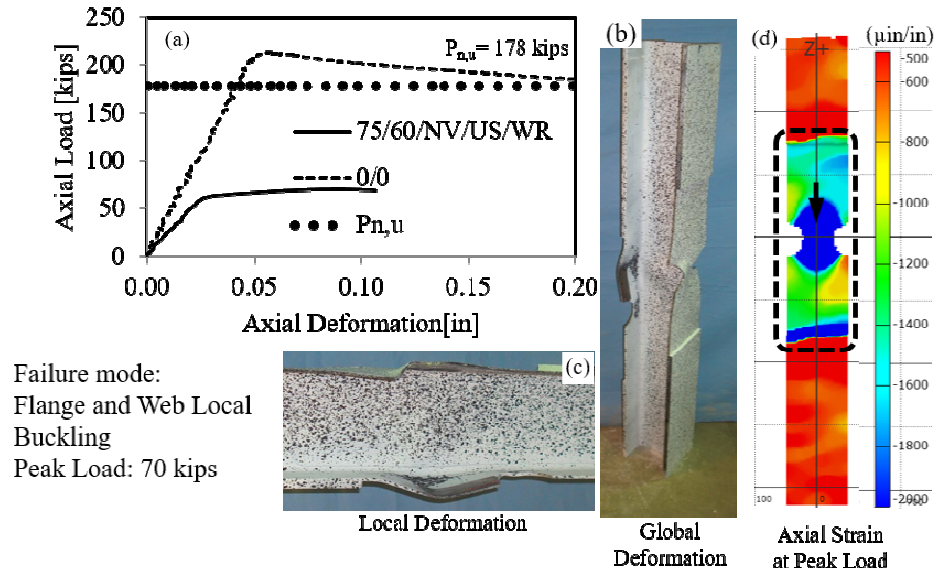


Figure 3.14: Failure mode and load-deformation response of pile 75/60/NV/US/WR

3.1.5.10. Pile 75/60/V/S

The pile 75/60/V/S had 75% and 60% reduction in the flange and web thickness respectively. A 2 in. long void was also created through the web. Milling on the flanges was symmetric, and there was no flange width reduction in the pile. This pile was loaded monotonically up to the peak load of 40 kips. The test was terminated when the axial load dropped to 15 kips. Figure 3.15(a) shows the axial load-shortening response of the pile. Figure 3.15(b) and (c) show the global and local deformations of pile 75/60/V/S which failed by flange local bending. Figure 3.15(d) shows the location of a strain concentration at the section with through-web void.

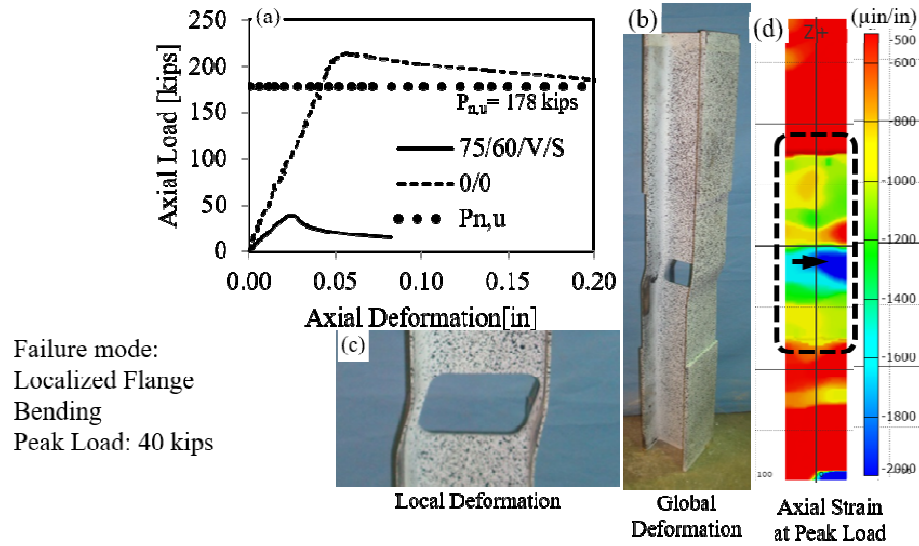


Figure 3.15: Failure mode and load-deformation response of pile 75/60/V/S

3.1.5.11. Pile 75/60/V/S/WR

The pile 75/60/V/S/WR had 75% and 60% reduction in the flange and web thickness respectively. A 2 in. long void was created through the web with symmetric milling of the flanges. In addition, two 2 in. diameter semi-circular perforations were cut out of each flange. This pile was loaded monotonically up to the peak load of 36 kips. The test was terminated when the axial load dropped to 14.4 kips. Figure 3.16(a) shows the axial load-shortening response of the pile. Figure 3.16(b) and (c) show the global and local deformations of pile 75/60/V/S/WR which failed by flange local bending. Figure 3.16(d) shows the location of strain concentration at the section with through-web void.

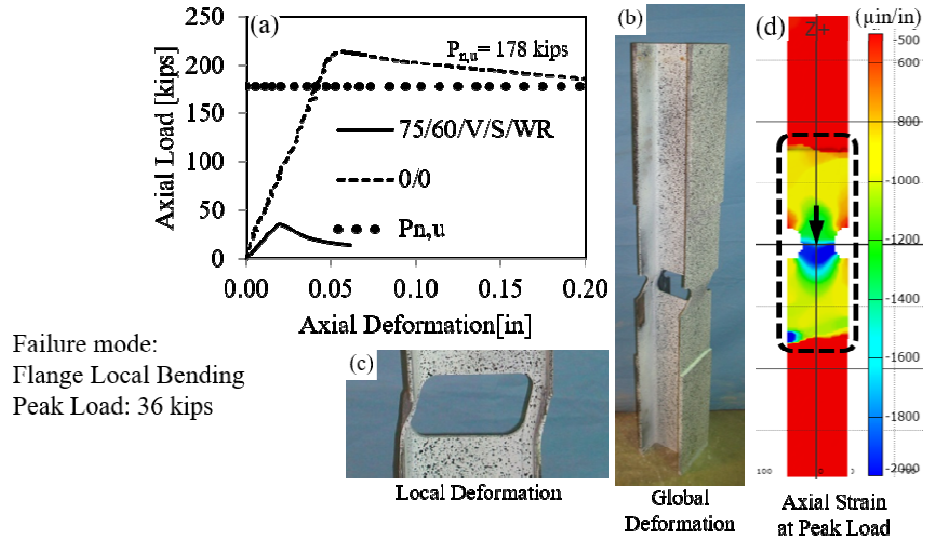


Figure 3.16: Failure mode and load-deformation response of pile 75/60/V/S/WR

3.1.5.12. Pile 75/60/V/US

The pile 75/60/V/US had 75% and 60% reduction in the flange and web thickness respectively. A 2 in. long void was created through the web. Milling on the flanges was offset by 2 in. towards opposite ends resulting in an unsymmetric degradation pattern, and there was no flange width reduction in the pile. This pile was loaded monotonically up to the peak load of 40 kips. The test was terminated when the axial load dropped to 14 kips. Figure 3.17(a) shows the axial load-shortening response of the pile. Figure 3.17(b) and (c) shows the global and local deformation of pile 75/60/V/US which failed by flange local bending. Figure 3.17(d) shows the location of a strain concentration at the section with the through-web void.

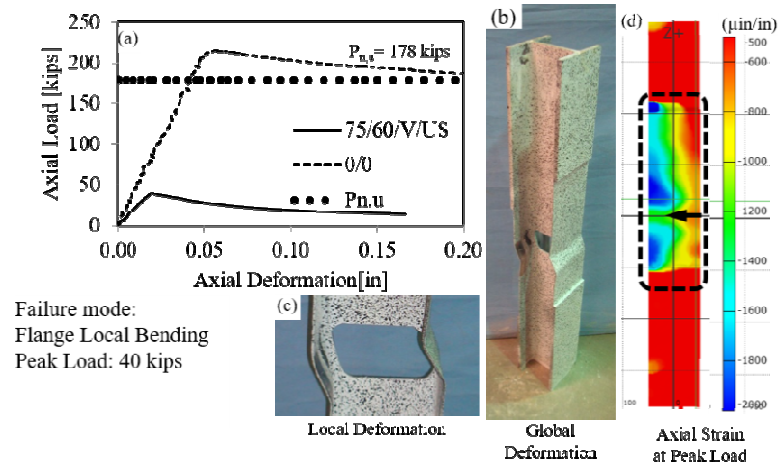


Figure 3.17: Failure mode and load-deformation response of pile 75/60/V/US

3.1.5.13. Pile 75/60/V/US/WR

The pile 75/60/V/US/WR had 75% and 60% reduction in the flange and web thickness respectively. A 2 in. long void was created through the web. Milling of the flanges was offset by 2 in. towards opposite ends to form an unsymmetric degradation pattern. In addition, two 2 in. diameter semi-circular perforations were cut out of each flange. This pile was loaded monotonically up to the peak load of 39 kips. The test was terminated when the axial load dropped to 14.6 kips. Figure 3.18(a) shows the axial load-shortening response of the pile. Figure 3.18(b) and (c) show the global and local deformations of pile 75/60/V/US/WR which failed by flange local bending. Figure 3.18(d) shows the location of a strain concentration at the section with the through-web void.

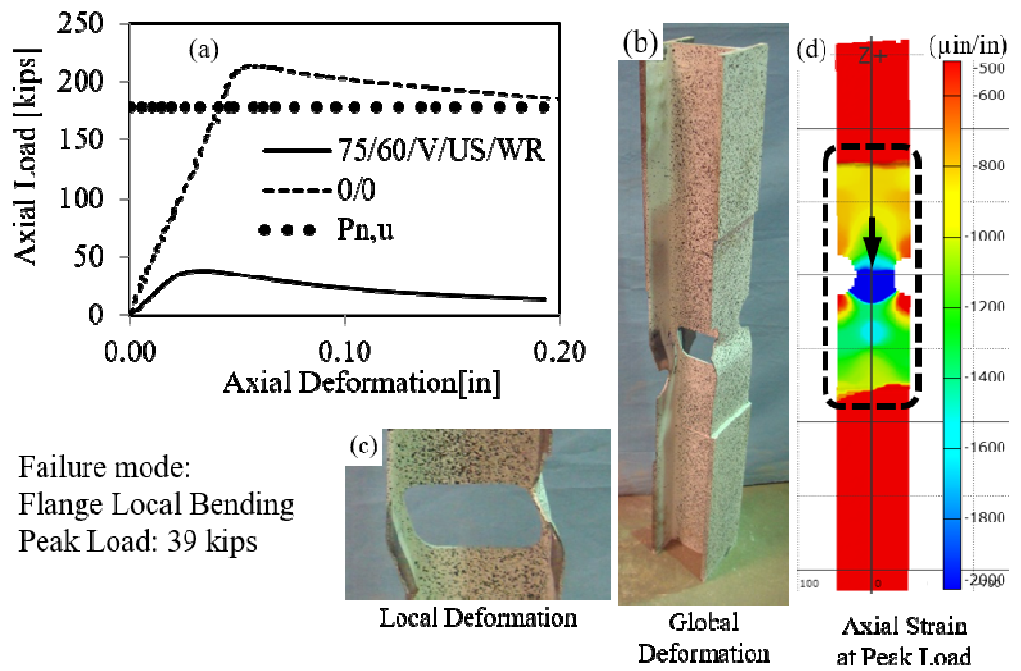





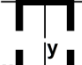



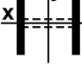
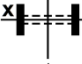




Figure 3.18: Failure mode and load-deformation response of pile 75/60/V/US/WR

3.2. Discussion of the Results

A summary of the cross-sectional properties found for the small-scale study piles is presented in Table 3.4. The results for the piles tested in the small-scale study, are summarized in Table 3.5.

Table 3.4: Cross-Sectional Properties of the Small-Scale Piles

Pile Designation	Shape	$A_{s,c}$ (in ²)	$I_{x,c}$ (in ⁴)	$I_{y,c}$ (in ⁴)	$r_{x,c}$ (in)	$r_{y,c}$ (in)	$b_f/2t_f$	h/t_w
Phase I								
0/0		4.05	12.16	4.35	1.73	1.04	5.79	9.93
0/30		3.68	11.48	4.28	1.77	1.08	5.91	14.00
0/60		3.39	11.24	4.30	1.82	1.13	5.84	24.60
50/0		2.41	5.86	2.05	1.56	0.92	12.30	10.70
50/30		2.27	5.96	2.24	1.62	0.99	11.20	14.60
75/0		1.64	3.10	0.94	1.37	0.76	27.10	10.70
75/60		1.27	3.34	1.31	1.62	1.01	19.30	28.60
Phase II								
75/60/NV/US		1.02	2.5467	0.9706	1.58	0.98	26.10	31.00
75/60/NV/US/WR		1.06	0.5622	0.7568	0.73	0.85	18.60	30.00
75/60/V/S ^b		0.40	0.5862	0.0003	0.85	0.02	N/A ^a	N/A ^a
75/60/V/S/WR ^b		0.21	0.0822	0.0002	0.44	0.02	N/A ^a	N/A ^a
75/60/V/US ^b		0.41	0.5910	0.0003	0.85	0.02	N/A ^a	N/A ^a
75/60/V/US/WR ^b		0.44	0.6319	0.0004	0.85	0.02	N/A ^a	N/A ^a

^a Flange and web slenderness ratios were not applicable to the pile with through-web void since only flexural buckling of a single flange ligament was considered

^b Geometric properties are reported for a single flange only.

$A_{s,c}$: cross-sectional area at corroded section

$I_{x,c}$ and $I_{y,c}$: strong and weak-axis moments of inertia, respectively

$r_{x,c}$ and $r_{y,c}$: strong and weak-axis radii of gyration, respectively

$(KL/r)_{max}$: maximum global slenderness ratio of the pile

$(b_f/2t_f)$ and (h/t_w) : flange and web slenderness ratios, respectively

Table 3.5: Measured Capacities and Observed Failure Modes of the Small-Scale Piles

Pile Designation	Peak Load (kip)	Corroded/ Control	Corroded/ Control	Failure Mode
		Peak Load	Cross- Sectional Area	
Phase I				
0/0	215	1.00	1.00	Global buckling
0/30	201	0.935	0.908	Global buckling
0/60	178	0.828	0.837	Global buckling
50/0	117	0.544	0.595	Flange local buckling
50/30	130	0.605	0.559	Flange and web local buckling
75/0	92.0	0.428	0.405	Flange local buckling
75/60	70.0	0.325	0.314	Flange and web local buckling
Phase II				
75/60/NV/US	57.0	0.265	0.251	Flange and web local buckling
75/60/NV/US/WR	70.0	0.325	0.261	Flange and web local buckling
75/60/V/S	40.0	0.186	0.200	Localized flange bending
75/60/V/S/WR	36.0	0.167	0.105	Flange local bending
75/60/V/US	40.0	0.186	0.200	Flange local bending
75/60/V/US/WR	39.0	0.181	0.216	Flange local bending

3.2.1. Independent Reduction of Flange or Web Thickness

Reduction of the flange thickness had a more significant effect on the capacity of the piles with simulated corrosion than reduction of the web thickness. The axial capacities of piles 0/30 (30% web thickness reduction) and 0/60 (60% web thickness reduction) were respectively 6% and 17% less than that of the un-corroded control pile, 0/0. However, piles with flange degradation, i.e. 50/0 (50% flange thickness reduction) and 75/0 (75% flange thickness reduction), had capacities that were respectively 46% and 57% less than the un-corroded control pile. This is due to the fact that reducing web thickness increases the weak-axis radius of gyration in contrast to reducing flange

thickness as shown in Table 3.4. Weak-axis radius of gyration increased 4% and 8% for piles 0/30 and 0/60, respectively, and decreased 11% and 27% for piles 50/0 and 75/0, respectively. This effect combined with reduction of the cross-sectional area led to less reduction of the axial capacity for the piles with only reduction of web thickness.

The piles with only web thickness reduction failed by global buckling, although the failure mode for the piles with only reduction of the flange thickness was flange local buckling. According to (AISC, 2011), a web element with 60% reduction of the thickness is still considered as a non-slender element. However, reducing the flange thickness by 50% made it just on the boarder of being considered as a slender element as shown in Table 3.4.

3.2.2. Simultaneous Reduction of Flange and Web Thickness

Simultaneous flange and web degradation led to a more substantial reduction in the axial capacity. Comparing piles 0/30 to 50/30 and 0/60 to 75/60 shows that reduction of the axial capacity was significant when reduction of the flange thickness was added to the section with existing reduction of the web thickness. In contrast, comparing 50/0 to 50/30 and 75/0 to 75/60 showed that adding reduction of the web thickness to the piles with existing flange thickness reduction did not dramatically reduce the axial capacity. This confirms that flange corrosion played a predominant role in determining the capacity reduction for the geometries and corrosion patterns considered in this study.

Figure 3.19 shows the correlation between the peak load and cross-sectional area of the tested piles normalized with respect to the peak load and cross-sectional area of the control pile for all of the piles that were tested in phase I and phase II. Reduction of the

cross-sectional area demonstrates a linear relationship with reduction in the axial capacity with a coefficient of determination, R^2 , of 0.985. This supports the rating approach of approximating the remaining axial capacity of corroded piles by assessment of the reduction of the cross section and proportionally reducing the initial design axial capacity for short piles.

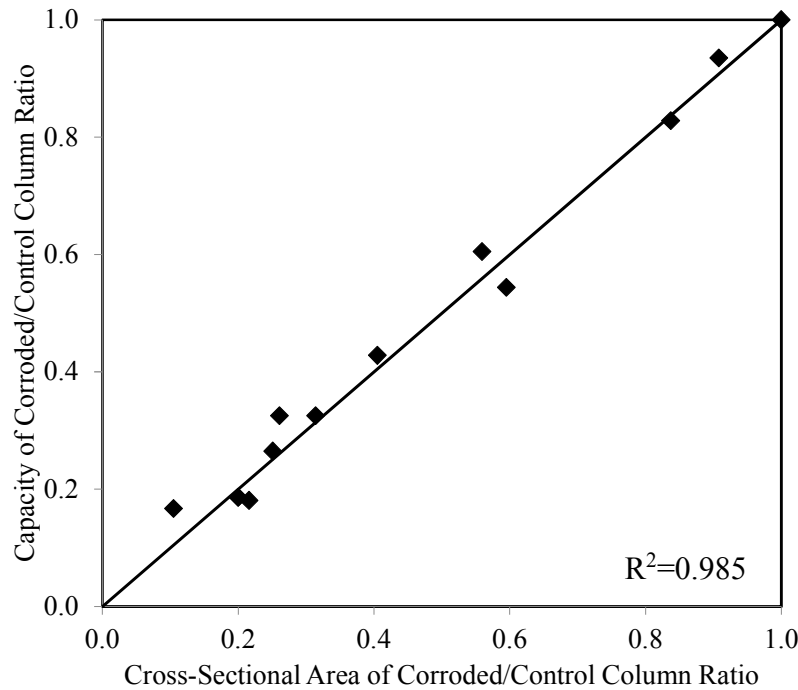


Figure 3.19: Correlation between the loss of axial capacity and loss of cross section

3.2.3. Unsymmetric Reduction of Flange Thickness

According to the test results, unsymmetric reduction of the flange thickness did not have significant effect on the axial capacity of the tested piles. Comparing piles 75/60 to 75/60/NV/US, 75/60/V/S to 75/60/V/US, and 75/60/V/S/WR to 75/60/V/US/WR showed a maximum of 10% variation in the axial capacities due to the unsymmetric nature of the corrosion pattern. Unsymmetric degradation of flange thickness did not change the failure mode compared to the symmetric counterparts.

3.2.4. Reduction of Flange Width

In severe cases of corrosion the width of flanges may be reduced at the most heavily corroded section due to extreme loss of material near the tips of the flanges. This effect was studied by testing three piles with two semi-circular perforations cut out of each flange. According to the test results reduction in the width of the flange did not have a significant influence on the axial capacity of the tested piles. Comparing the piles 75/60/V/S to 75/60/V/S/WR, 75/60/V/US to 75/60/V/US/WR, and 75/60/NV/US to 75/60/NV/US/WR demonstrated that reduction of flange width caused a maximum of 10% variation in the remaining axial capacity. This was attributed to the fact that the reduction of the flange width effectively decreased the flange slenderness at the section of the width reduction and failure occurred due to flange local buckling at the sections above or below the flange perforations where the flange slenderness was higher.

3.2.5. Through-Web Corrosion

Four piles with through-web voids and different configurations of deterioration otherwise were tested. All of the piles had axial load capacities between 36 and 40 kips which, on average, correspond to 18% of the capacity of the un-corroded control pile. This significant reduction of the axial capacity was due to the severe loss of the cross-sectional area of the pile which, at the most severely corroded locations was 78% to 90% loss of the cross-sectional area.

The failure mode for the four piles was bending of the two flange ligaments adjacent to the web void. Absence of the supporting web caused the flange ligaments to bend about

their weak axes in a beam buckling mode as opposed to the two-way bending that is associated with typical flange local buckling.

Chapter 4. Full-scale Pile Tests

To investigate the effect of partial degradation on the remaining axial capacity of compression members, seven full-scale piles were tested. The results from the small-scale pile tests (reported in the previous chapter) were used to direct the full-scale implementation. The main objectives of the tests were to quantify the remaining axial capacity of steel columns with different corrosion patterns and to determine the suitability of existing design equations to predict the remaining capacity. The parameters in the study were the reduction of the thickness of flanges and webs, the presence of through-web void, and the length of the corroded region. This chapter describes the experimental program for the full-scale tests and provides a discussion of the findings.

4.1. Test Matrix

4.1.1. Section Size and Effective Length

The research group visited four representative field sites in Texas and summarized the section sizes and clear lengths of observed piles in Table 4.1. The cross-section HP12×53 was selected for experimental study as it is a commonly used section in the TxDOT bridge inventory (L. Flournoy, personal communication, 2011).

Figure 4.1 shows a schematic view of a portion of bridge including a deck, bent caps, and two rows of piles. The clear length (l) of a pile is the distance from ground to the bottom surface of the bent cap. The top side of a pile, which is partially embedded in the bent cap, is considered to be able to rotate about both strong and weak axes but not translate. Since the base of the pile is embedded in the soil, the soil provides lateral restraint to the base of the pile. As such, the boundary conditions at the base of the pile must be carefully

considered. A commonly accepted approach is to define a depth of fixity (L_f) below the soil surface at which the pile can be assumed to be fully fixed (translations and rotations prevented) as illustrated in Figure 4.1. This length of fixity depends on the relative stiffnesses between the pile and the soil in which it is embedded. As such, it is a function of the soil type, and the flexural stiffness of the pile $E_p I_p$. The length of fixity L_f was calculated by the method adopted in AASHTO (2012) for soft clay soil type using:

$$L_f = 1.4 \left(\frac{E_p I_p}{E_s} \right)^{0.25} \quad (\text{Eq. 4-1})$$

where E_p and E_s are moduli of elasticity (tons per square foot) of the pile and soil, respectively, and I_p is the moment of inertia of the pile in the plane of buckling (ft^4).

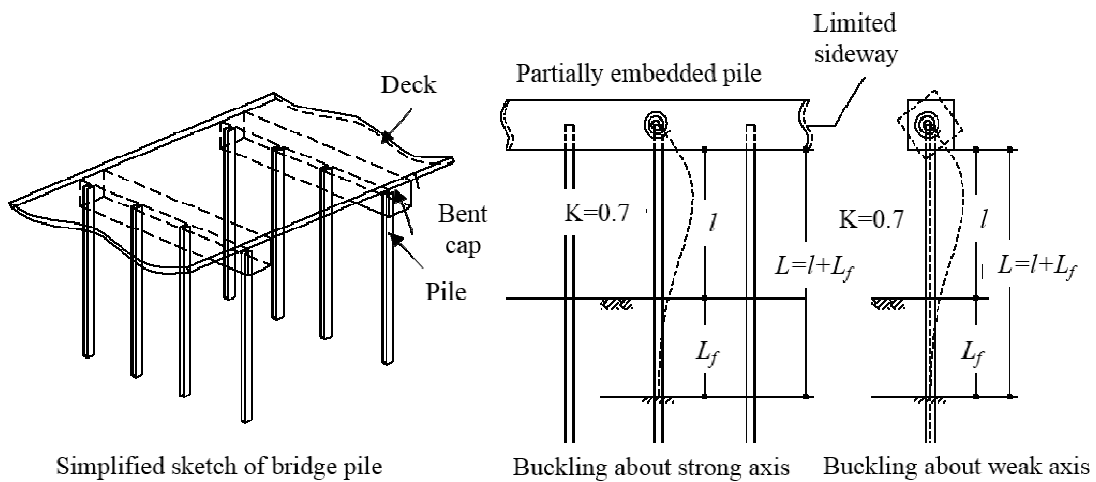


Figure 4.1: Schematic view of bridge piles and buckling modes

The effective length of the pile is calculated by adding the length of fixity, L_f , to the clear length of the pile, l , and multiplying by the effective length factor k , as recommended by AASHTO (2012). Table 4.1 presents the calculated effective lengths and slenderness ratios of the observed piles about their strong and weak axes. Inspection of Table 4.1 indicates that the failure of all the piles will be dominated by flexural buckling about their

weak axes. Considering that the TxDOT bridge inventory is reasonably expected to include longer piles than those observed, the maximum slenderness ratio of the HP12×53 piles was calculated as 38.0 and 59.8 about strong and weak axes, respectively. Hence, the pile was dominated by weak axis buckling with an effective length of 14.3 ft in that direction. Considering the limitation of the length of the test frame, the length of the tested piles were determined as 15ft with pin-pin boundary conditions corresponding to a slenderness ratio of 63 about the weak axis of the cross section.

Table 4.1 Measured Clear Lengths of Bridge Piles

Bridge	Pile Designation	Pile Clear Length [ft]	Pile Effective Length [ft]		Slenderness Ratio	
			Strong Axis	Weak Axis	Strong Axis	Weak Axis
1	HP 10x42	9.7	12.6	11.3	36.7	56.0
1	HP 12x53	6.2	11.2	9.5	26.7	39.8
1	HP 14x73	15.4	18.8	16.9	38.5	58.3
2	HP 12x53	10.5	14.2	12.5	33.8	52.5
2	HP 14x73	16.6	19.6	17.8	40.3	61.2
3	HP 12x53	12.5	15.6	13.9	37.2	58.3
4	HP 12x53	13	15.9	14.3	38.0	59.8

4.1.2. Deterioration Pattern

Except for the control pile with no corrosion, the degrees of section loss of the remaining six piles were determined based on the measurements from field observations: (1) the flange and web thickness reductions due to corrosion are of similar magnitudes and (2) degrees of corrosion are within a wide range from relatively minor corrosion to near total section loss. Therefore, three different degrees of flange thickness reduction were selected, 0%, 40%, and 80%; four different degrees of web thickness reduction were investigated, 0%, 20%, 60%, and 100% (which indicated a total section loss, a void in the web). For an HP12×53 section, the flange is at the limit of non-slender section and any

reduction of flange thickness results in a slender flange (AASHTO, 2012); the web becomes slender when the web thickness reduction exceeds 41%.

4.2. Test Specimens

Seven simply supported HP12×53 piles with lengths of 15 ft. were tested under concentric compression such that the behavior of the test piles was representative of the expected behavior of existing piles. One of the piles was tested as an un-corroded control pile. The other six piles were machined to represent different corrosion patterns. The corrosion patterns of the six piles were created by milling the thickness of the flanges and the web to simulate the loss of thickness associated with corrosion. Figure 4.2 shows the machining of the piles using a computer numerical control (CNC) milling machine.

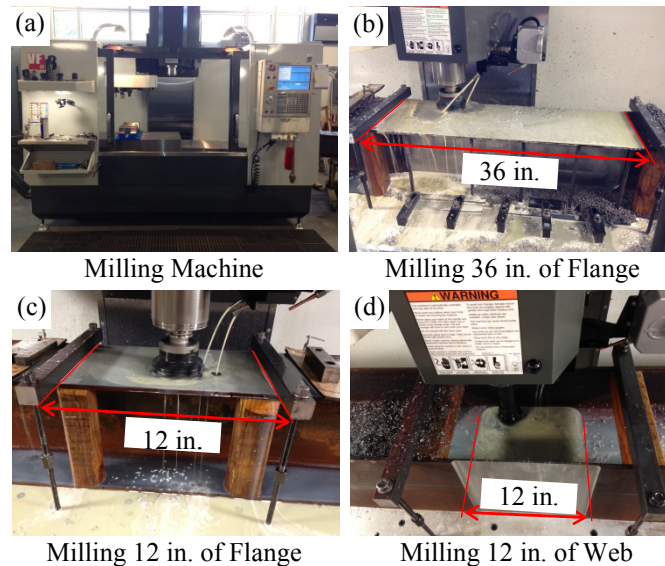


Figure 4.2: Corrosion simulation using CNC milling machine

For the piles that were observed in the field the corrosion was located closer to one of the points of inflection than the other. To represent this trend, the centroids of the corroded regions were located at 5 ft. from one end of the piles, that is, at the 1/3 length.. Figure 4.3

shows the schematic drawing of the corroded region. The nominal levels of reduction in the flange thicknesses were 0%, 40%, and 80%. The thicknesses of the webs were reduced by 20% and 60% distributed evenly between the two faces of the webs. As shown in Figure 4.3, one pile had a 2 in. through-web void. The extent of the corroded region was 12 in. for five piles and 36 in. for one pile.

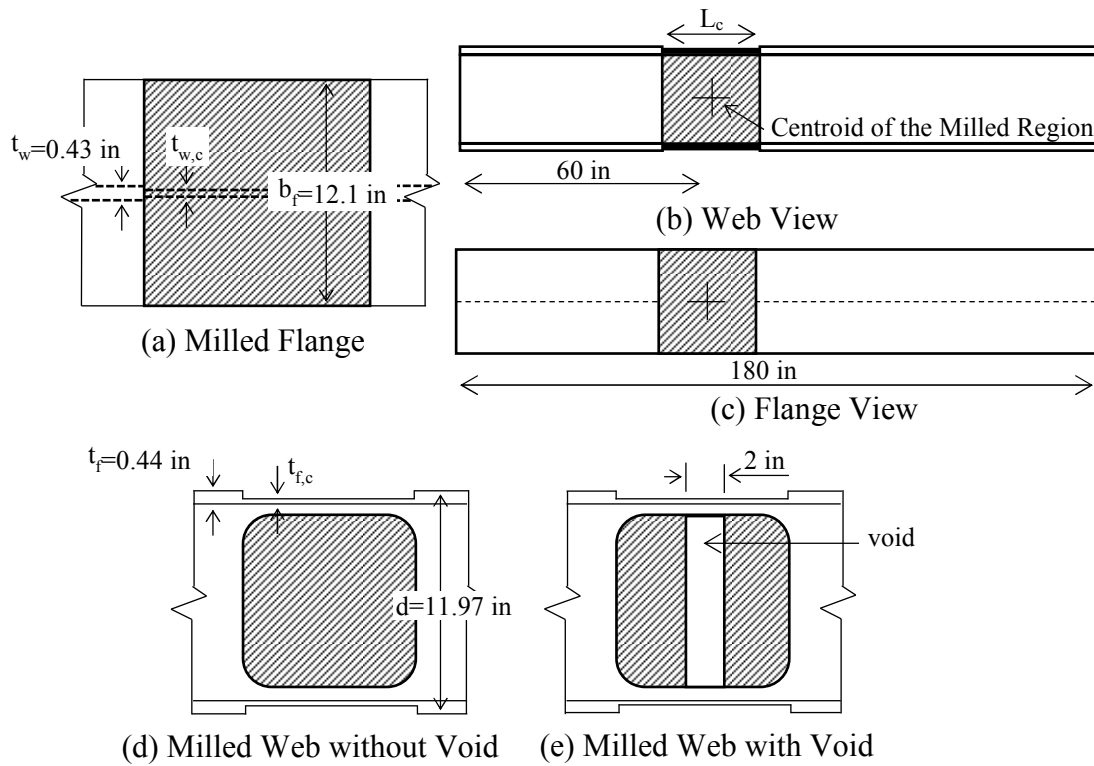


Figure 4.3: Schematic drawing of the location and geometry of the milled region

Figure 4.4 shows the identifier used to designate the corroded control piles. The first and second sections indicate the nominal reduction of the flange and web thicknesses, respectively, in percent. The third section indicates the presence of a through-web void (V) or that the milled region is three times longer than the basic case (3). Otherwise, the third section is omitted.

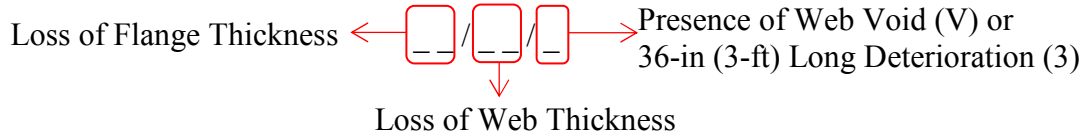


Figure 4.4: Designation of the full-scale piles

Table 4.2 summarizes the measured flange and web thicknesses, $t_{f,c}$ and $t_{w,c}$, respectively, in the milled regions of the piles. These thicknesses are the average of the measured values at several points using an ultrasonic thickness gauge. Table 4.2 also presents the calculated cross-sectional area, $A_{s,c}$, and weak-axis moment of inertia, $I_{y,c}$, at the reduced sections.

Table 4.2: Measured Geometry and Designations of the Control H-Piles at Milled Section

Pile Designation	$t_{f,c}$ [in]	$t_{w,c}$ [in]	$A_{s,c}$ [in]	$I_{y,c}$ [in ⁴]
0/0	0.46	0.43	15.9	135
0/20	0.46	0.37	15.3	136
40/20	0.29	0.31	10.4	85.3
40/60	0.24	0.16	7.64	71.4
80/60	0.10	0.19	4.53	29.8
80/60/V	0.11	0.19	2.77	33.9
80/60/3	0.14	0.18	5.38	41.8

4.3. Materials

To evaluate the material properties of the steel piles, three coupons from the flanges and one coupon from the web were tested according to ASTM A370 (2013).

Table 4.3 shows the tensile modulus, E_s , yield stress, f_{sy} , ultimate stress, f_{su} , and strain at ultimate stress, ϵ_{su} , of the steel piles. The average, standard deviation (STDV), and

coefficient of variation (C.O.V.) of the measured values for the flange coupons are also presented in

Table 4.3.

Table 4.3: Measured Properties of Steel Piles

Location of Coupons	Tensile Modulus (E_s) (ksi)	Yield Stress (f_{sy}) (ksi)	Ultimate Stress (f_{su}) (ksi)	Strain at Ultimate Stress ϵ_{su} (in/in)
Flange-1	28700	52.0	66.0	0.173
Flange-2	29400	53.0	67.0	0.186
Flange-3	27100	52.0	67.0	0.164
Flange (average)	28400	52.0	67.0	0.174
Flange (STDV)	969	0.55	0.58	0.0088
Flange (C.O.V.)	0.0341	0.011	0.0088	0.0505
Web	32000	60.5	71.0	0.0797
nominal material properties of the steel pile: f_{sy} =50 ksi, f_{su} =65 ksi, E_s =29000 ksi				

4.4. Test Setup

Figure 4.5(a) shows the 600-kip self-reacting test frame that was used for testing the full-scale piles. Both ends of the piles were free to rotate about the weak axis while rotation about the strong axis was prevented as shown in Figure 4.5(b) and (c). The piles were loaded up to the peak load in a horizontal configuration using a 10-ksi pump and 600-kip jack at a rate of 20 kip/min (see Figure 4.5(d)). The axial load was measured by three 200-kip load cells installed in a triangular configuration located behind, and concentric with the jack as shown in Figure 4.5(d) and (e). The centroid of each pile was aligned with the centroid of test frame using a pair of laser levels to minimize the unintentional eccentricity as shown in Figure

4.5(f). To maintain the piles in their vertical position, they were supported on two horizontal rollers located underneath the piles as shown in Figure 4.5(g).

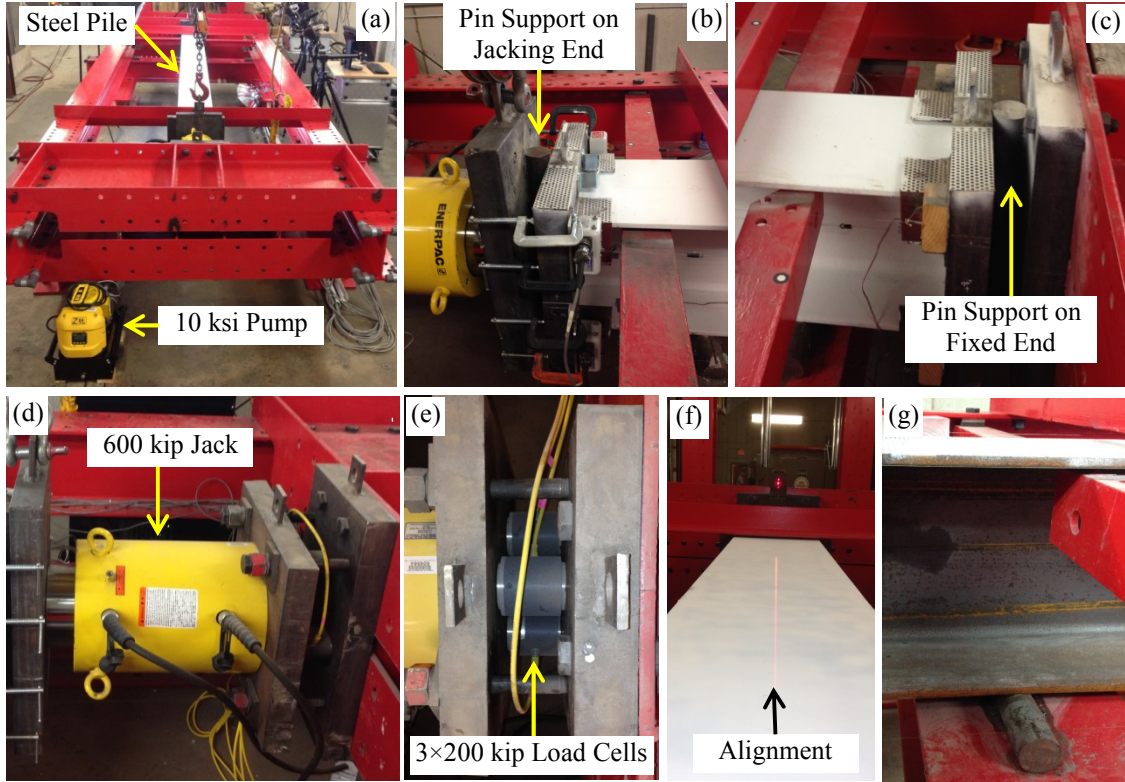
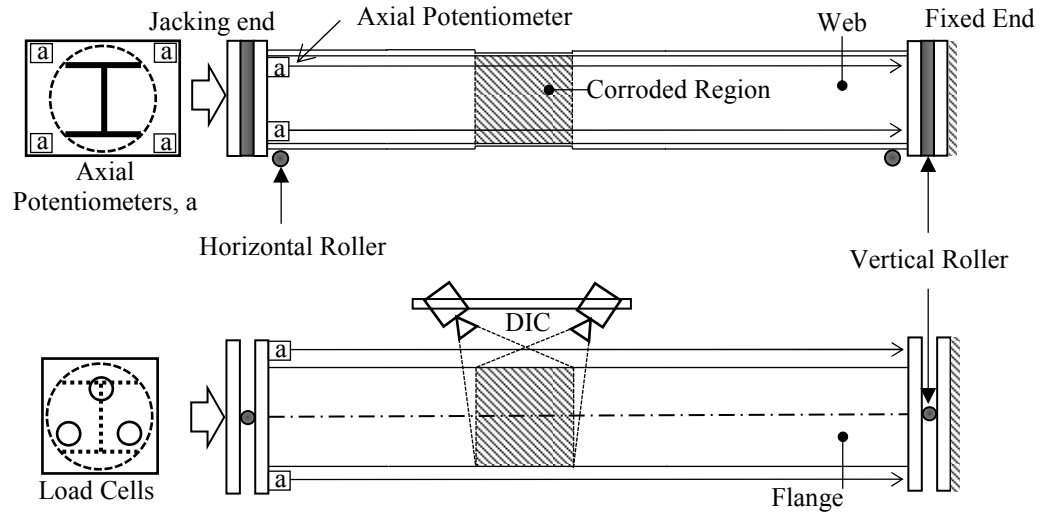


Figure 4.5: 600-kip Self-reacting compression test frame

4.5. Instrumentation

Figure 4.6(a) shows a schematic drawing of the instrumentation that was attached to the tested piles. The axial shortening of the piles was measured by taking the average of four linear string potentiometer measurements mounted symmetrically between the two end plates as shown in Figure 4.6(b). Full-field strain measurement over the top flange within the corroded region was achieved using a non-contact digital image correlation (DIC) system known as ARAMIS. As shown in Figure 4.6(c), the surface of the steel pile within the corroded region was painted with a black and white speckle pattern using a non-glossy spray paint to facilitate the use of the ARAMIS system. Facet size, facet step, and computational

size of 25 pixels, 20 pixels, and 5 facets were selected respectively for post-processing of the DIC images.



(a) Schematic Drawing of the Test Setup

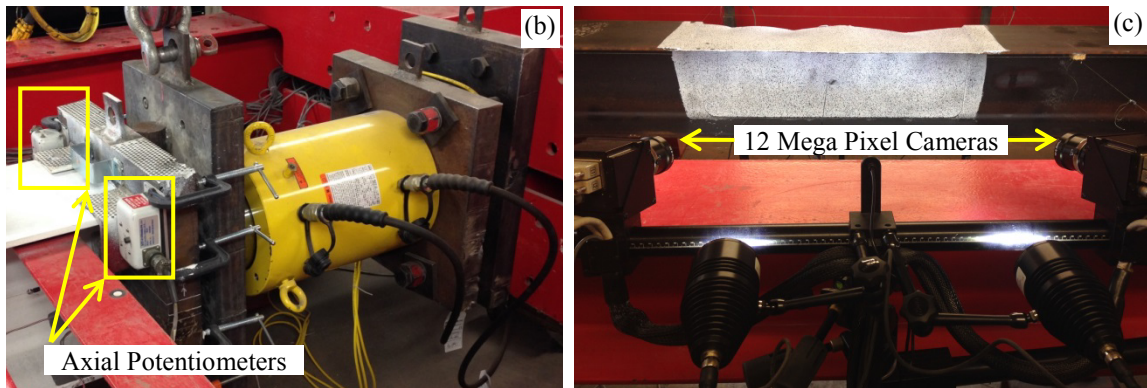


Figure 4.6: Instrumentation of the full-scale compression test

4.6. Results

The axial load-shortening response, global deformation and strain contours for the columns of the full-scale experimental program are presented in this section.

- **Pile 0/0**

Pile 0/0 was tested as an un-corroded control pile. Figure 4.7 shows the axial load-shortening response of the pile with the measured peak load of 623 kips. The dotted line indicates the nominal axial capacity, $P_{n,u}$, of a 15 ft. long HP12×53 pile calculated in accordance with (AISC, 2011) using nominal material properties and geometry. The measured capacity of the control pile is about 8% higher than the calculated nominal capacity due to the slightly higher cross sectional area, elastic modulus, and yield strength of the tested pile compared to the nominal values.

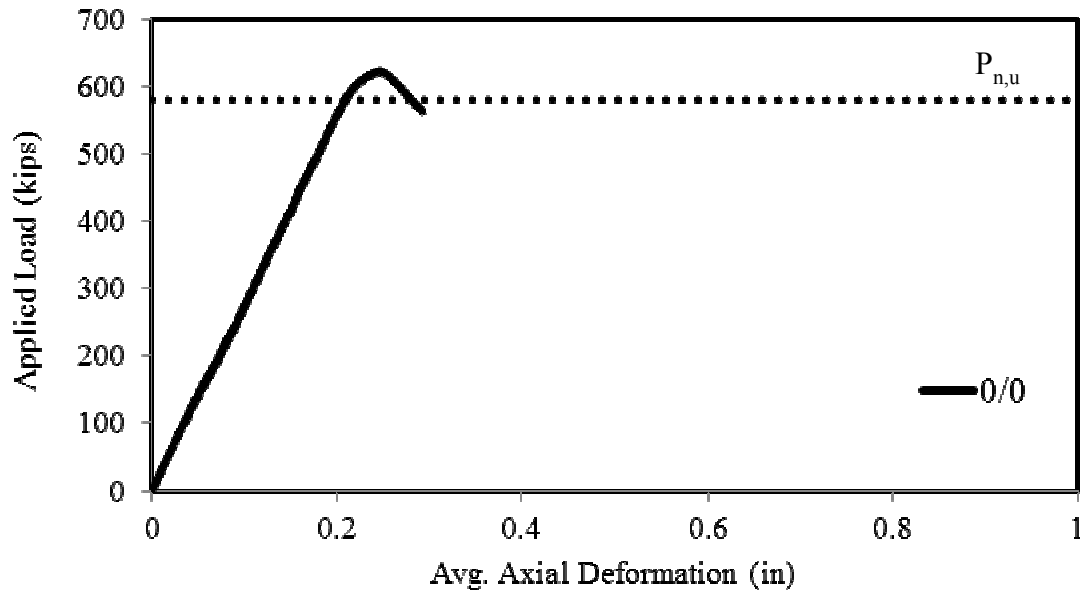


Figure 4.7: Axial load-shortening response of the un-corroded control pile

The un-corroded control pile, 0/0, was subjected to a seating load cycle up to 90 kips. Then, it was loaded up the peak load monotonically. No visible signs of lateral deformation were observed during the test up to the peak load. After attaining the peak load the pile began to buckle gradually. The test was terminated when the axial load dropped to 563 kips while the pile exhibited visible lateral deformation as shown in Figure 4.8(a). Figure 4.8(b) shows the longitudinal strain contours at peak load, as measured by the ARAMIS DIC system on the

top surface of the top flange of the pile. The measured longitudinal strain contours indicate the formation of a strain gradient across the width of the flange which is consistent with the initiation of global buckling, although at this stage no sign of lateral deformation was observed visually. Strain contours at the ultimate loading stage clearly indicate decompression on one side of the flange corresponding to excessive lateral deformation of the pile.

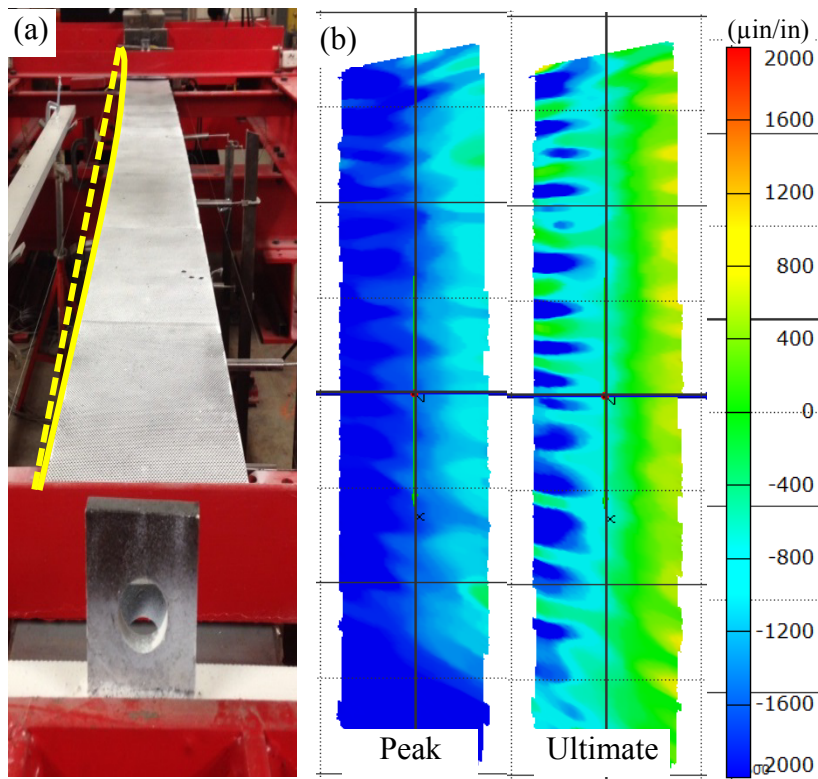


Figure 4.8: Global deformation and strain contours of the un-corroded control pile

- **Pile 0/20**

Pile 0/20 had no reduction of the flange thickness and 20% reduction of the web thickness along a 1 ft. length of the pile and represented the least severe case of corrosion that was considered in the full-scale experimental study. Figure 4.9 shows the axial load-shortening

response of the pile. The axial capacity of the tested pile, $P_{n,c}$, is about 5% higher than the nominal axial capacity of the un-corroded pile, $P_{n,u}$.

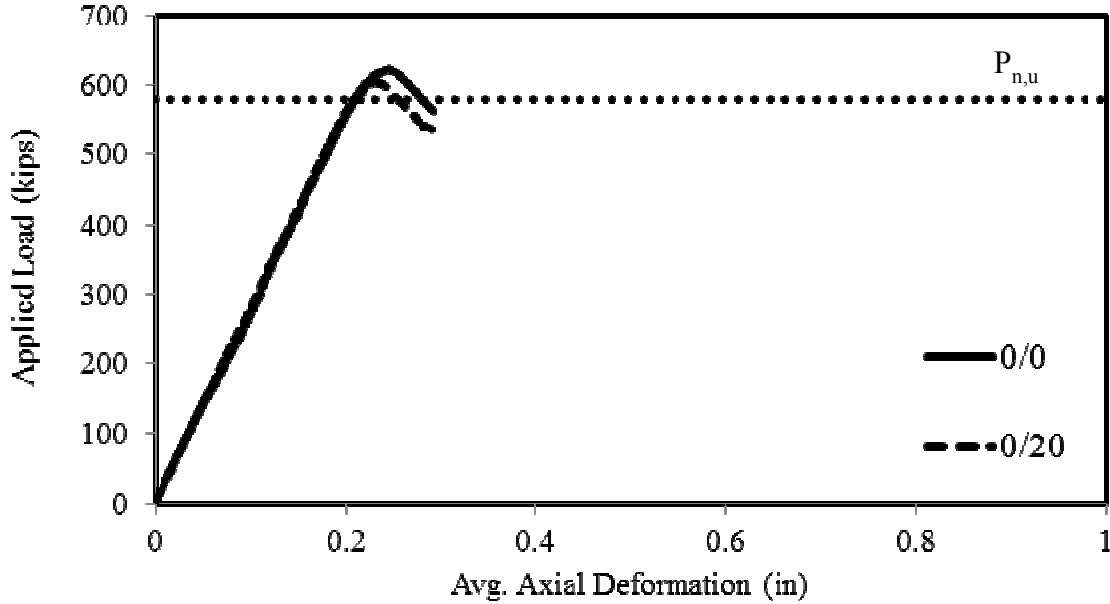


Figure 4.9: Axial load-shortening response of pile 0/20

The pile 0/20 was subjected to a seating load of 58 kips. Then, it was loaded up the peak load monotonically. No visible signs of lateral deformation were observed during the test up to the peak load. After attaining the peak load the pile began to buckle gradually. The test was terminated when the axial load dropped to 536 kips due to excessive visible lateral deformation as shown in Figure 4.10(a). The gradient of the longitudinal strain contours at the peak load on the top surface within the corroded region of the top flange, given in Figure 4.10 (b), indicates initiation of global buckling, although at this stage no sign of lateral deformation was observed visually. Longitudinal strain contours at the ultimate loading stage indicate decompression on one side of the flange corresponding to excessive lateral deformation of the pile.

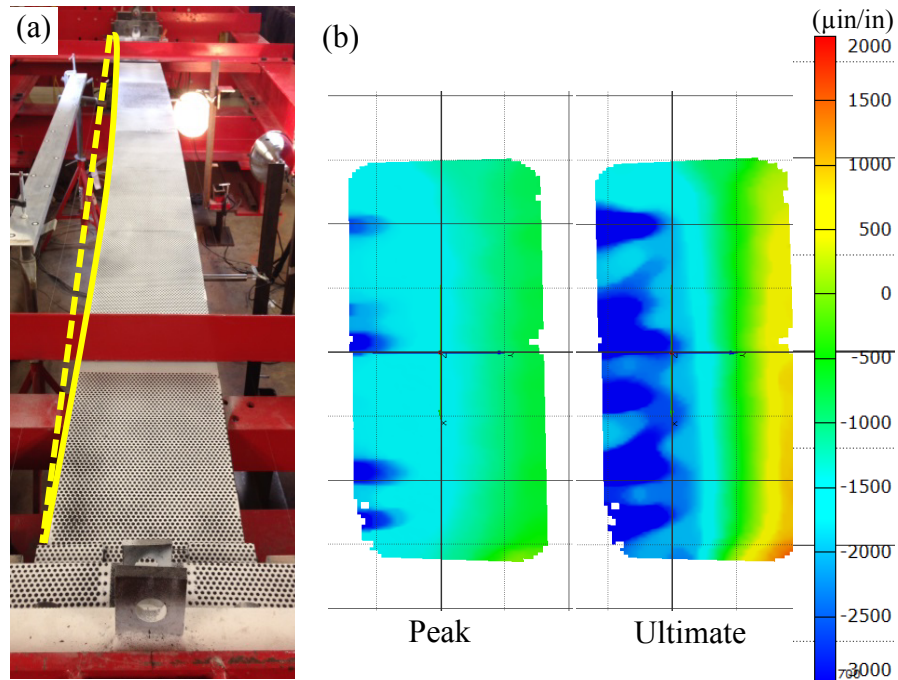


Figure 4.10: Global deformation and strain contours of pile 0/20

- **Pile 40/20**

Pile 40/20 had a 40% reduction of the flange thickness and a 20% reduction of the web thickness along a 1 ft. length of the pile.. The axial load-shortening response of the pile is shown in Figure 4.11. The axial capacity of the tested pile, $P_{n,c}$, is about 25% lower than the nominal axial capacity of the un-corroded pile, $P_{n,u}$.

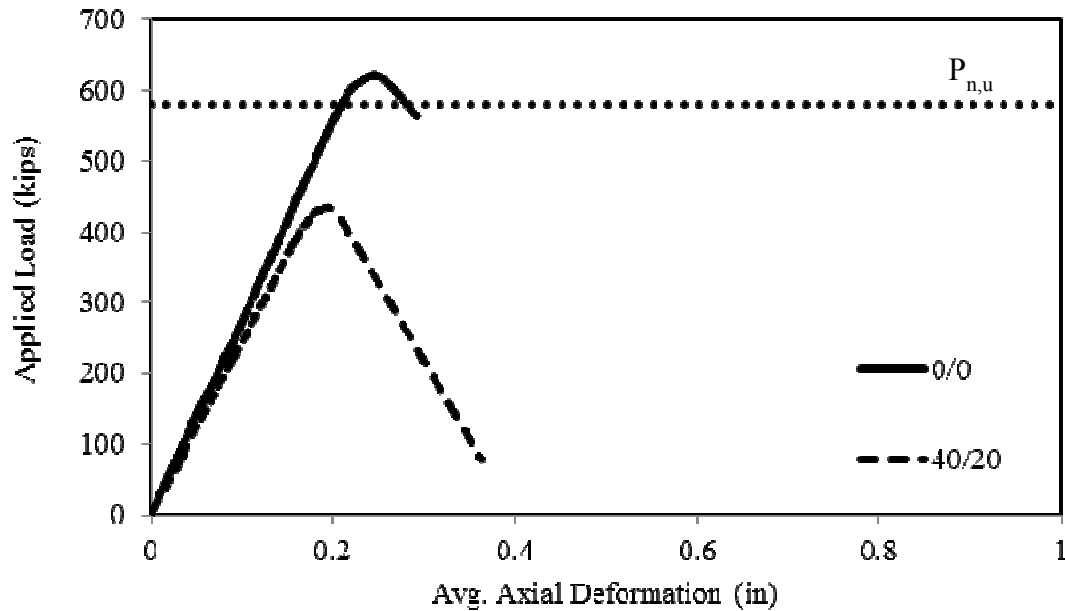


Figure 4.11: Axial load-shortening response of pile 40/20

After applying one loading cycle up to 99 kips to seat the specimen, the pile 40/20 was loaded up the peak load monotonically. No visible signs of deformation were observed during the test up to the peak load. After attaining the peak load of 435 kips, the load began to drop gradually. At the load level of 413 kips, the axial load suddenly dropped to 79 kips due to flange local buckling followed by global lateral deformation of the pile. Figure 4.12(a) and (b) show the global deformation and flange local buckling of the tested pile, respectively. Longitudinal strain contours at peak load within the corroded flange, as shown in Figure 4.12(c), suggest the initiation of flange local buckling at the locations of with strain concentration, although at this stage no sign of deformation was observed. Strain contours at the ultimate loading stage indicate strain relief on edge of the corroded flange where the local buckling was observed.

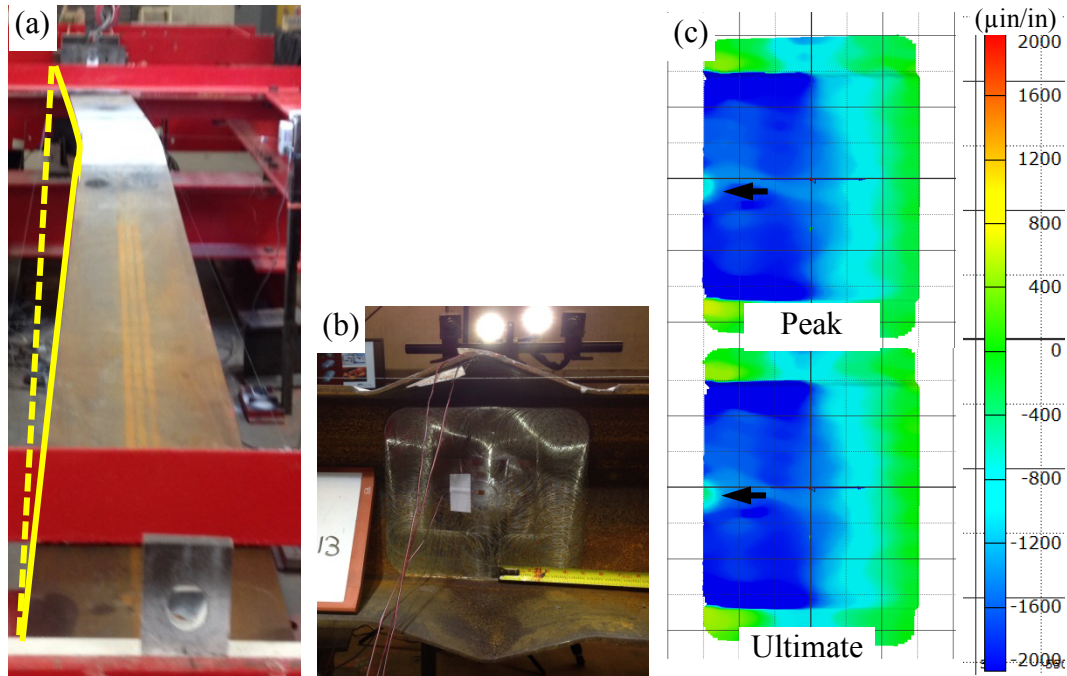


Figure 4.12: Global deformation, local deformation, and strain contours of pile 40/20

Figure 4.13 shows the reduced section before and after failure. Two strain gauges were installed on the top and bottom surfaces of one flange tip as shown in Figure 4.13(a), to detect the occurrence of local buckling. Figure 4.13(b) shows the measured strains during the test. The vertical axis shows the applied axial load, and the horizontal axis illustrates the measured strains on the top and bottom surfaces of the flange tip. The solid line indicates the strain gauge on the bottom surface, marked as 'Bottom SG', and the dashed line indicates the strain gauge on the top surface, marked as 'Top SG'. The three horizontal dashed lines refer to three load levels at the time of testing. The tips of the reduced flange started to buckle locally at a load level of 366 kips, when bifurcation occurred between the top and bottom strain gauges as shown in Figure 4.13(b). After the section deformation caused excessive yielding, at a load level of 412 kips, the measured strains were not reliable due to partial detachment of the strain gauges. The measured peak load was 435 kips.

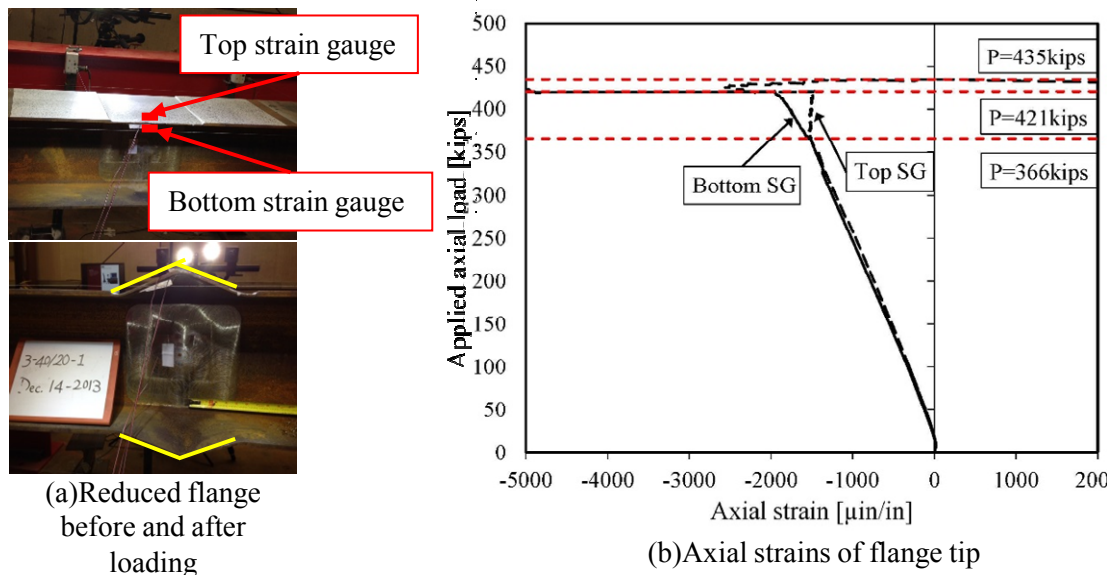


Figure 4.13: Buckled flange of pile 40/20

- **Pile 40/60**

Pile 40/60 had a 40% reduction of the flange thickness and a 60% reduction of the web thickness along a 1 ft. length of the pile. The axial load-shortening response of the pile is shown in Figure 4.14. The axial capacity of the tested pile, $P_{n,c}$, is about 42% lower than the nominal axial capacity of the un-corroded pile, $P_{n,u}$.

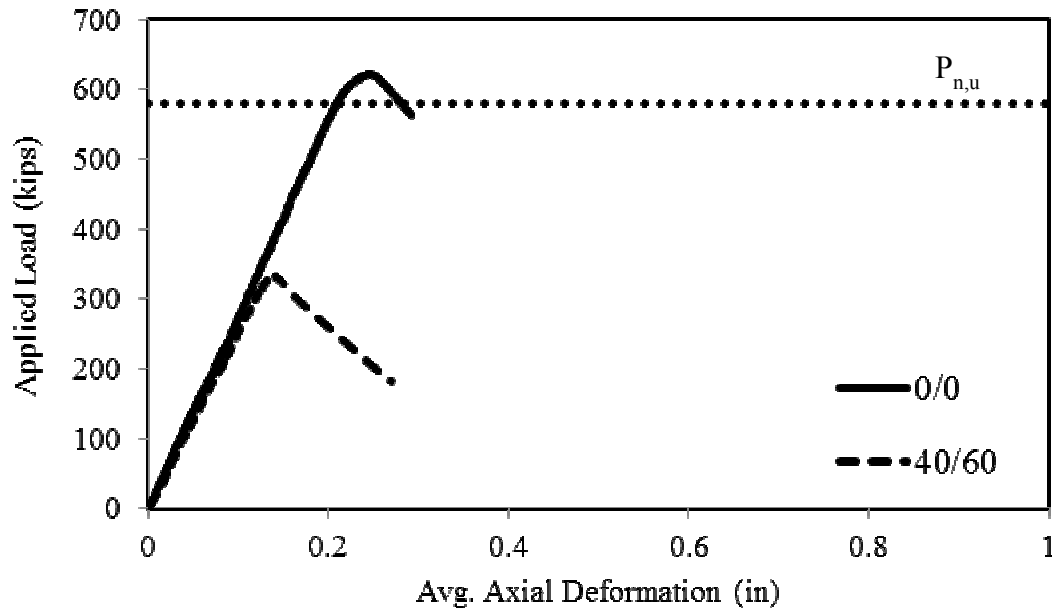


Figure 4.14: Axial load-shortening response of pile 40/60

After applying one loading cycle up to 49 kips to seat the specimen, pile 40/60 was loaded up to the peak load monotonically. No visible signs of deformation were observed during the test up to the peak load. After attaining the peak load of 333 kips, the load began to decrease gradually. At the load level of 327 kips, the axial load suddenly dropped to 182 kips due to flange and web local buckling followed by global lateral deformation. Figure 4.15(a) and (b) show the global deformation and flange and web local buckling of the tested pile, respectively. Longitudinal strain contours at peak load from the top surface of the top flange within the corroded region, shown in Figure 4.15(c), indicate initiation of flange local buckling at the locations of measured strain concentrations, although at this stage no sign of deformation was observed. The gradient of the strain contours at the ultimate loading stage indicate strain relief on edge of the corroded flange where the local buckling was observed.

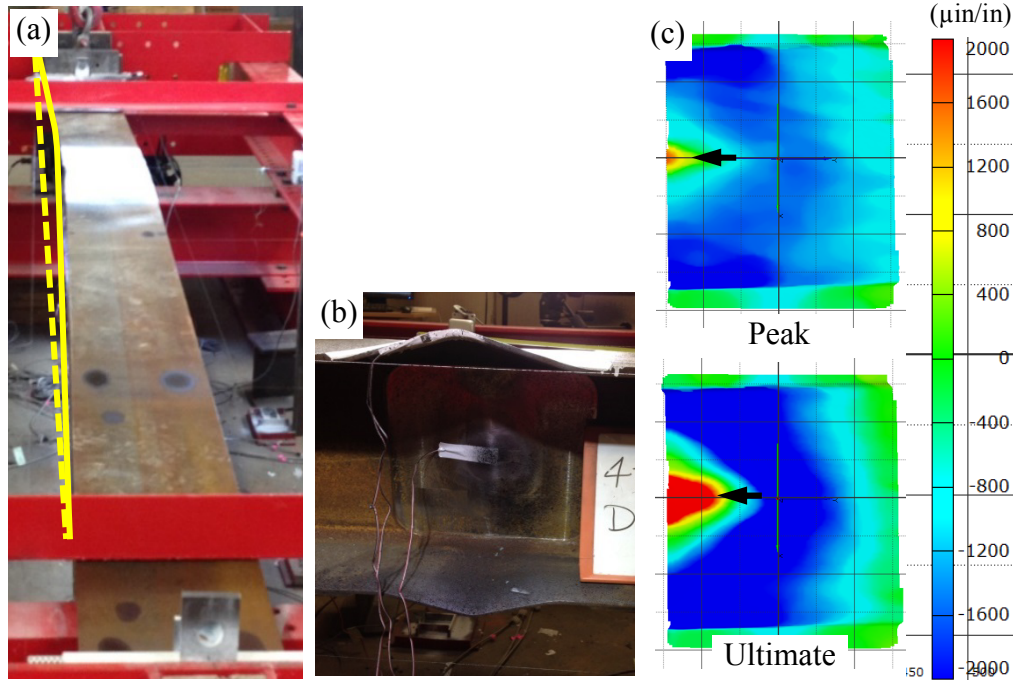


Figure 4.15: Global deformation, local deformation, and strain contours of pile 40/60

As shown in Figure 4.16(c) two strain gauges were installed on the top and bottom surfaces of one flange tip, referred to as ‘Flange top’ and ‘Flange bottom’ and two strain gauges were attached on the two faces at the center of the reduced section of the web, marked as ‘Web north’ and ‘Web south’, to indicate the occurrence of local buckling.

Figure 4.16(c) shows the measured strains during the test. The vertical axis shows the applied axial load, and the horizontal axis illustrates the magnitudes of the strain gauges on flange and web. The blue solid line and dashed line indicate the strains on the top and bottom surfaces of the flange tip, respectively. The black solid and dashed lines indicate the strain gauges on the south and north side of the web, respectively. The two horizontal dashed lines refer to two load levels during testing. At the load level of 313 kips, bifurcation of the flange and web strain measurements was observed as shown in Figure 4.16(c). The measured peak load was 333 kips.

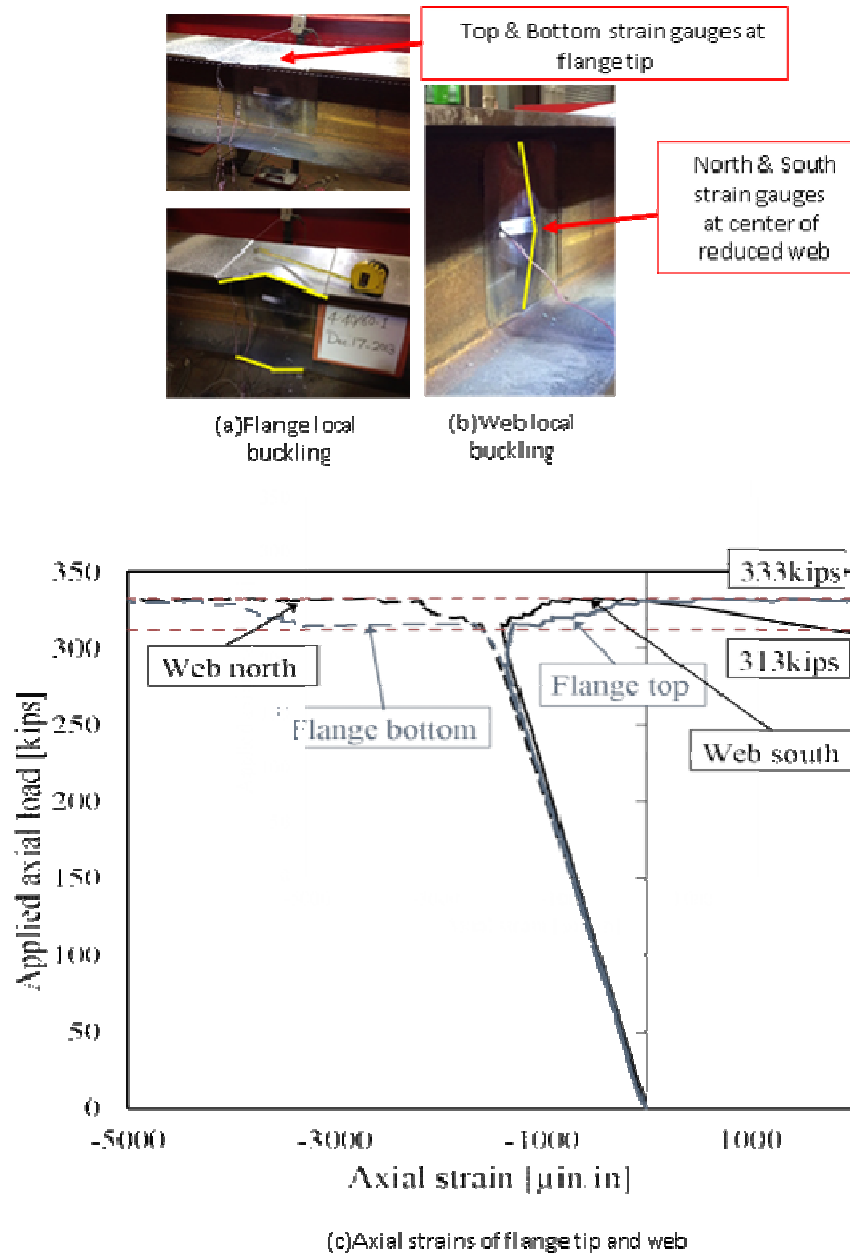


Figure 4.16: Flange and web local buckling of pile 40/60

- Pile 80/60**

Pile 80/60 had an 80% reduction of the flange thickness and a 60% reduction of the web thickness along a 1 ft. length of the pile. The axial load-shortening response of the pile is shown in Figure 4.17. The axial capacity of the tested pile, $P_{n,c}$, is 68% lower than the nominal axial capacity of the un-corroded pile, $P_{n,u}$.

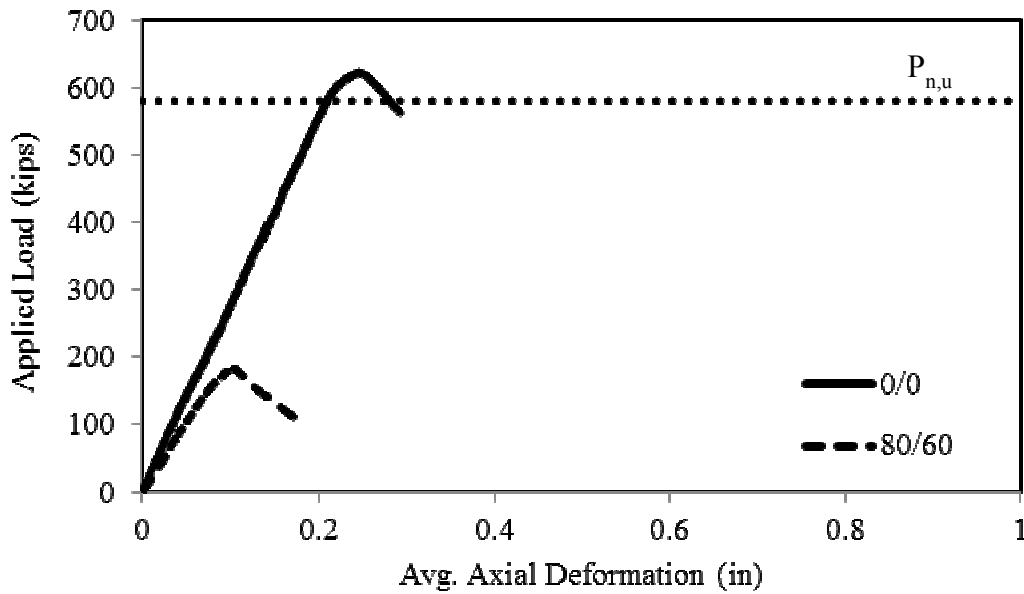


Figure 4.17: Axial load-shortening response of pile 80/60

The pile 80/60 was subjected to a seating load of 45 kips. Then, it was loaded up the peak load monotonically. No visible signs any deformation were observed during the test up to the peak load. After attaining the peak load of 182 kips, the load began to drop gradually. At the load level of 164 kips, the axial load suddenly dropped to 102 kips due to flange and web local buckling followed by global deformation. Figure 4.18(a) and (b) show the global deformation and flange and web local buckling of the tested pile, respectively. Longitudinal strain contours at measured at the peak load on the top surface of the top flange within the corroded region, shown in Figure 4.18(c), indicate initiation of flange local buckling at the locations of strain concentrations, although at this stage no sign of deformation was observed. Strain contours at the ultimate loading stage indicate strain relief on edge of the corroded flange where the local buckling occurred.

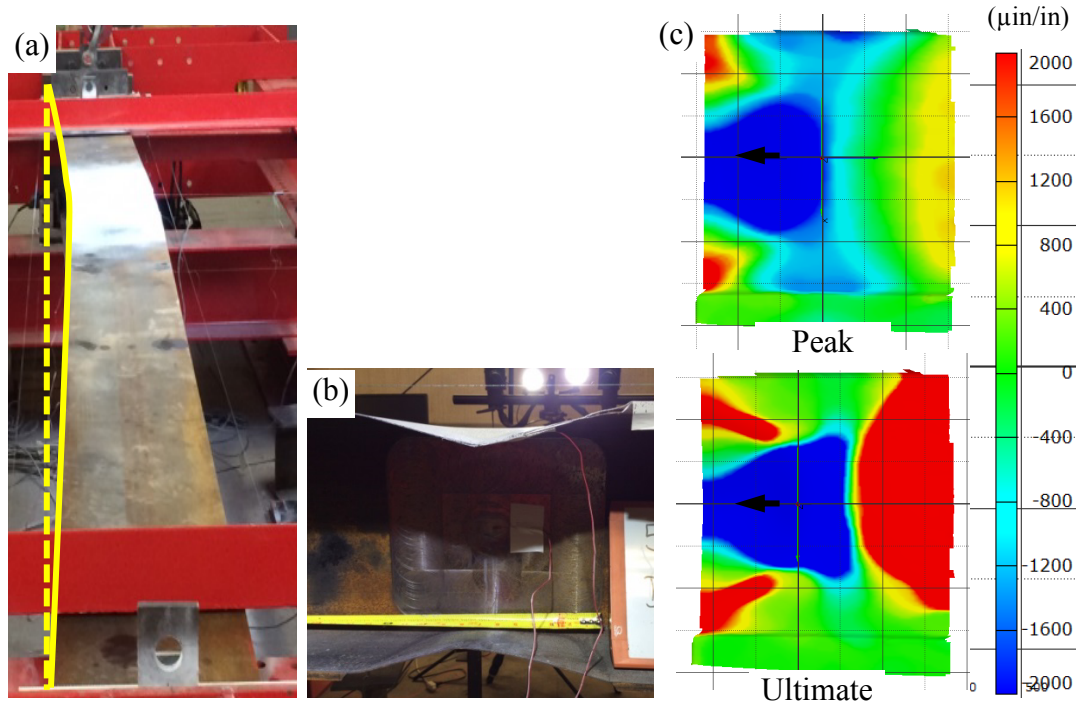
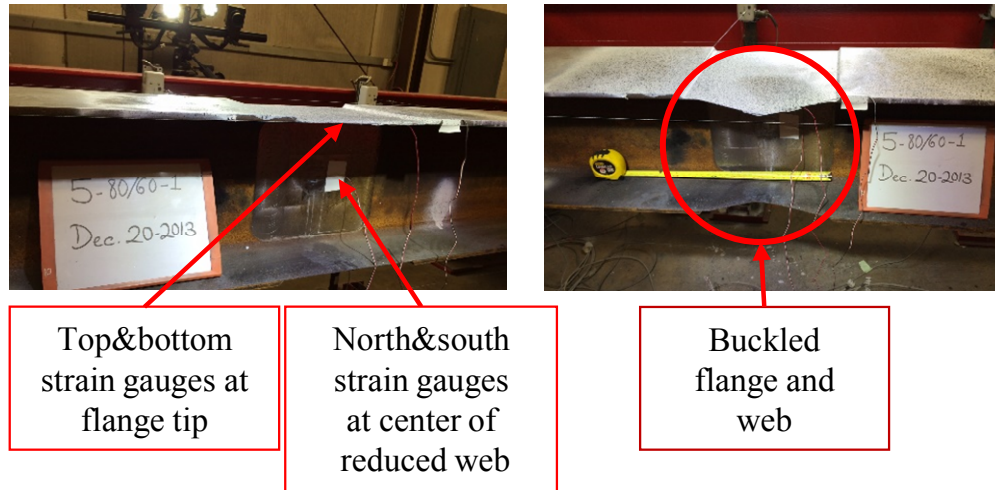
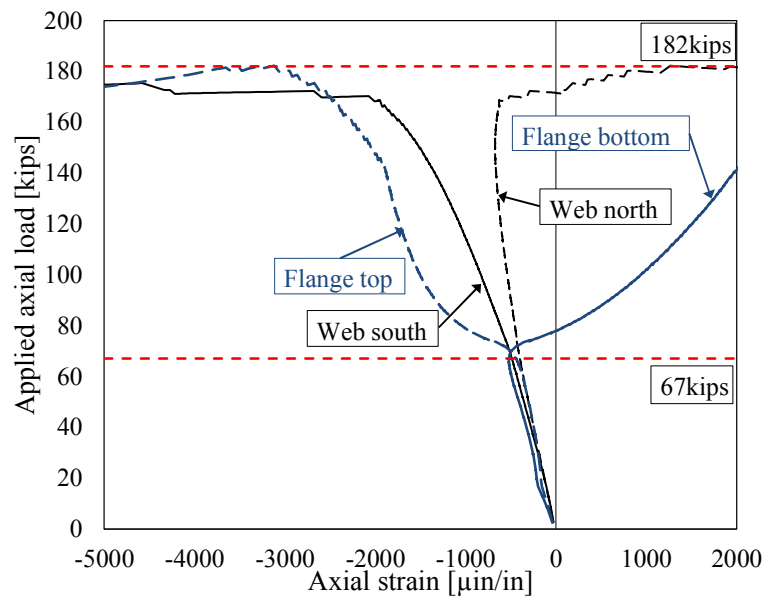


Figure 4.18: Global deformation, local deformation, and strain contours of pile 80/60

The measured strains plotted in Figure 4.19(b), further indicate the occurrence of local buckling. At the load level of 67 kips sudden bifurcation of the measured strains at the flange tip was observed which was accompanied by a gradual deviation of the measured strains on either side of the web. Thus suggests the onset of flange local buckling which induced out-of-plane bending of the web. Sudden bifurcation of the measured strains in the web was observed at a load level of 170 kips suggesting sudden buckling of the web as well.



(a) Reduced region before and after loading



(b) Axial strains of flange tip and web

Figure 4.19: Flange and web local buckling of pile 80/60

- **Pile 80/60/V**

Pile 80/60/V had an 80% reduction of the flange thickness and a 60% reduction of the web thickness along a 1 ft. length of the pile. Additionally, a 2 in. void along the entire depth of the web was milled at the center of the corroded region. The axial load-shortening response

of the pile is shown in Figure 4.20. The axial capacity of the tested pile, $P_{n,c}$, is 78% lower than the nominal axial capacity of the un-corroded pile, $P_{n,u}$.

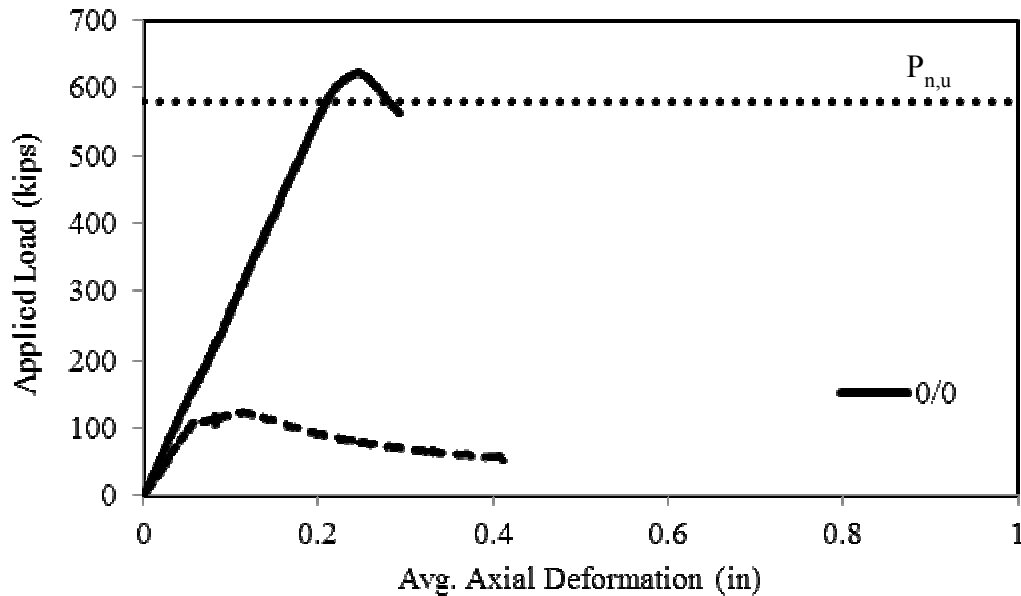


Figure 4.20: Axial load-shortening response of pile 80/60/V

After applying one loading cycle up to 25 kips to seat the specimen, pile 80/60/V was loaded up to the peak load monotonically. The axial load-deflection response of the pile exhibits a notable reduction in stiffness at a load level of 109 kips. This was attributed to the initiation of localized bending of the bottom flange which was confirmed by strain gauge measurements as discussed below. After attaining the peak load of 125 kips, the load began to drop gradually to 52 kips at which point the test was terminated due to excessive axial deformation of the pile. The pile failed due to localized one-way bending of the flanges on either side of the void rather than in the two-way plate bending mode that is commonly associated with local buckling. Figure 4.21(a) and (b) show the global deformation and flange localized bending of the tested pile, respectively. Longitudinal strain contours at peak

load within the corroded flange, as shown in Figure 4.21(c), indicate initiation of flange localized bending at the spots with strain concentration, although at this stage no sign of deformation was observed.

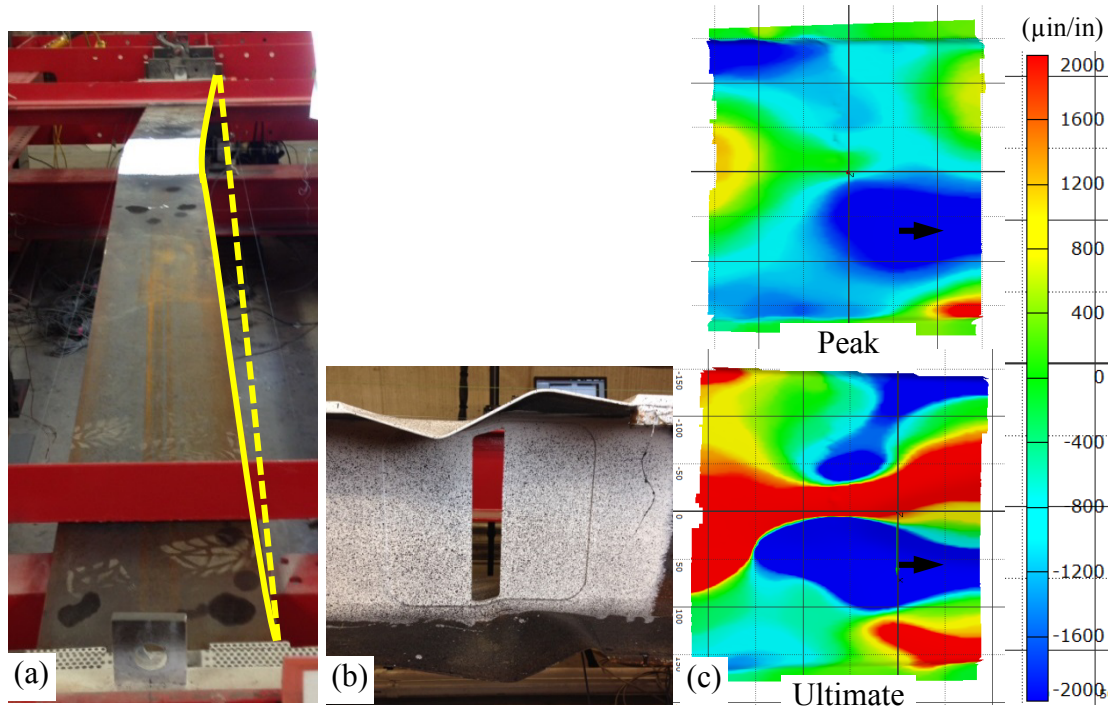


Figure 4.21: Global deformation, local deformation, and strain contours of pile 80/60/V

Figure 4.22(a)-(d) illustrates the progression of the flange failure at the corroded section at different load levels, and Figure 4.22(e) presents the axial strains obtained from the strain gauges attached on the flanges. As shown in Figure 4.22(a), two strain gauges were attached at the center of the reduced flanges on the top and bottom surfaces, referred to as ‘Flange top center’ and ‘Flange bottom center’ in Figure 4.22(e). Inspection of the measured strains indicates that the strains in the bottom flange began to increase dramatically at a load level of 109 kips suggesting the onset of failure of that flange. Failure of the top flange initiated at 125 kips which was accompanied by a drop in the applied load and global lateral deformation of the pile.

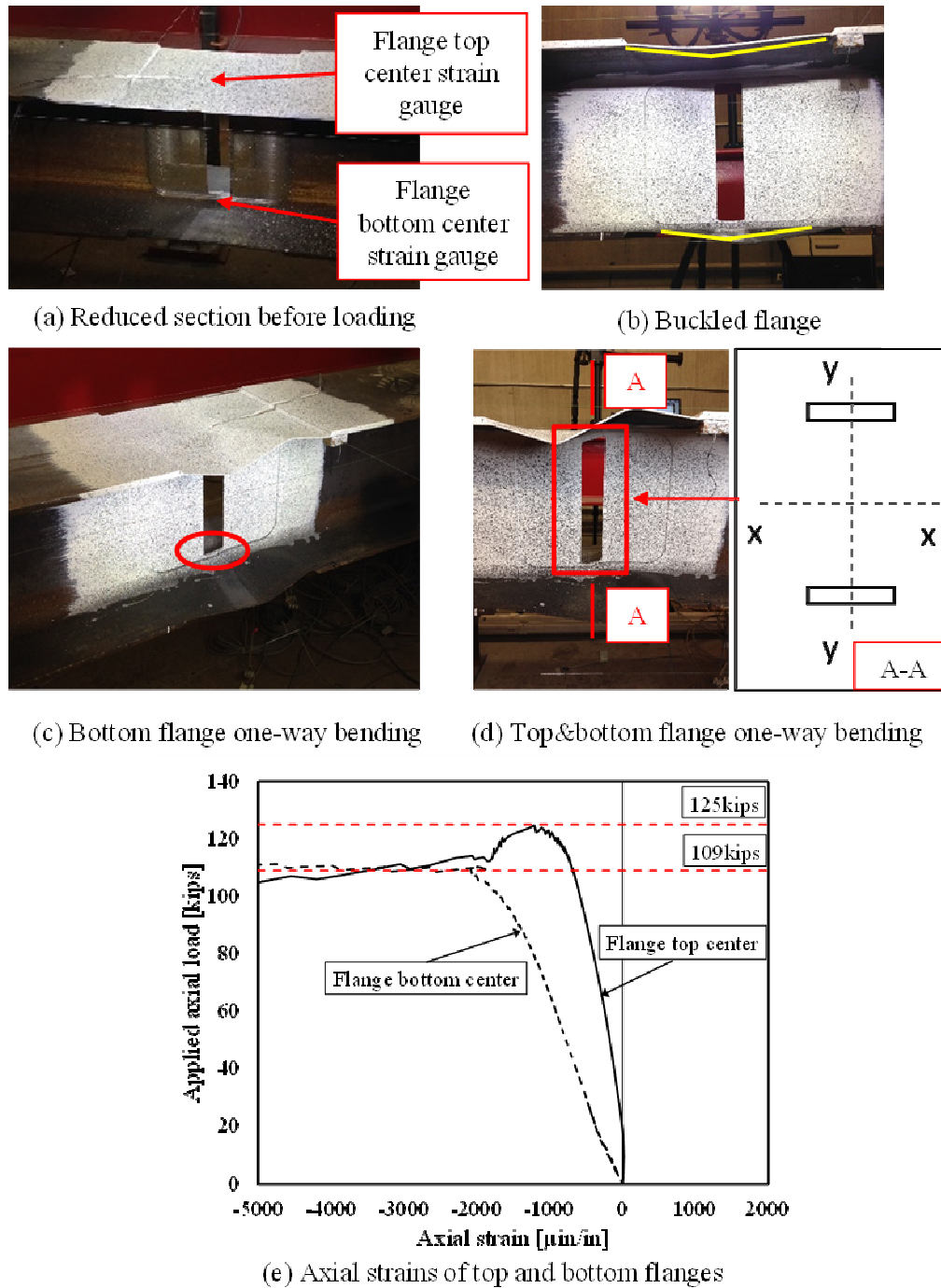


Figure 4.22: Flange and web local buckling of pile 80/60/V

- **Pile 80/60/3**

Pile 80/60/3 had an 80% reduction of the flange thickness and a 60% reduction of the web thickness along a 3ft. length of the pile. The axial load-shortening response of the pile is shown in Figure 4.23. The axial capacity of the tested pile, $P_{n,c}$, is 72% lower than the nominal axial capacity of the un-corroded pile, $P_{n,u}$.

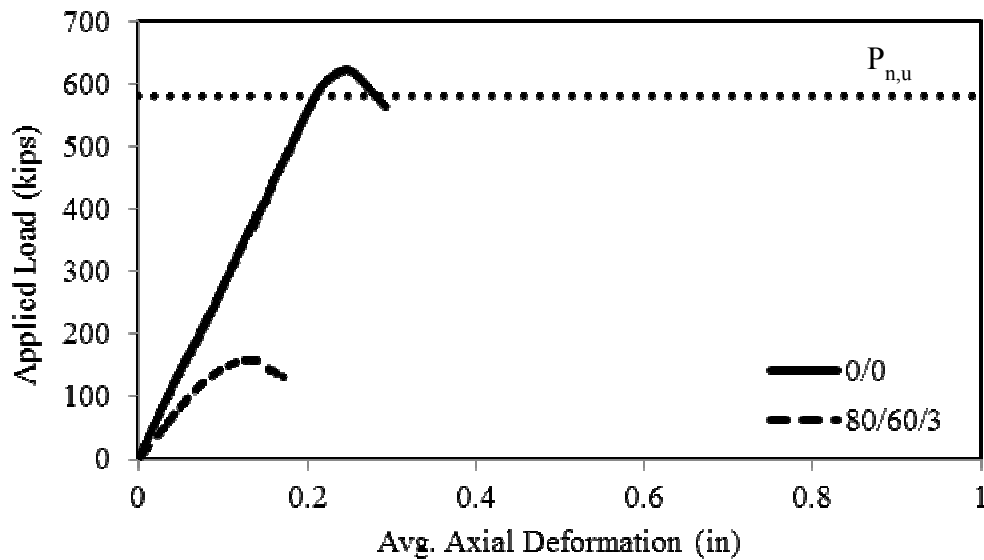


Figure 4.23: Axial load-shortening response of pile 80/60/3

The pile 80/60/3 was loaded up to the peak load monotonically. No visible signs of any deformation were observed during the test up to the peak load. After attaining the peak load at 159 kips, the load began to drop gradually to 132 kips at which point the test was terminated. The pile failed by flange and web local buckling followed by global lateral deformation. Figure 4.24(a) and (b) show the global deformation and flange and web local buckling of the tested pile, respectively. Longitudinal strain contours at the peak load on the top surface of the top flange within the corroded region, shown in Figure 4.24(c), indicate initiation of flange local buckling at the locations with strain concentrations, although at this

stage no sign of deformation was observed. Strain contours at the ultimate loading stage indicate strain relief on edge of the corroded flange where the local buckling happened.

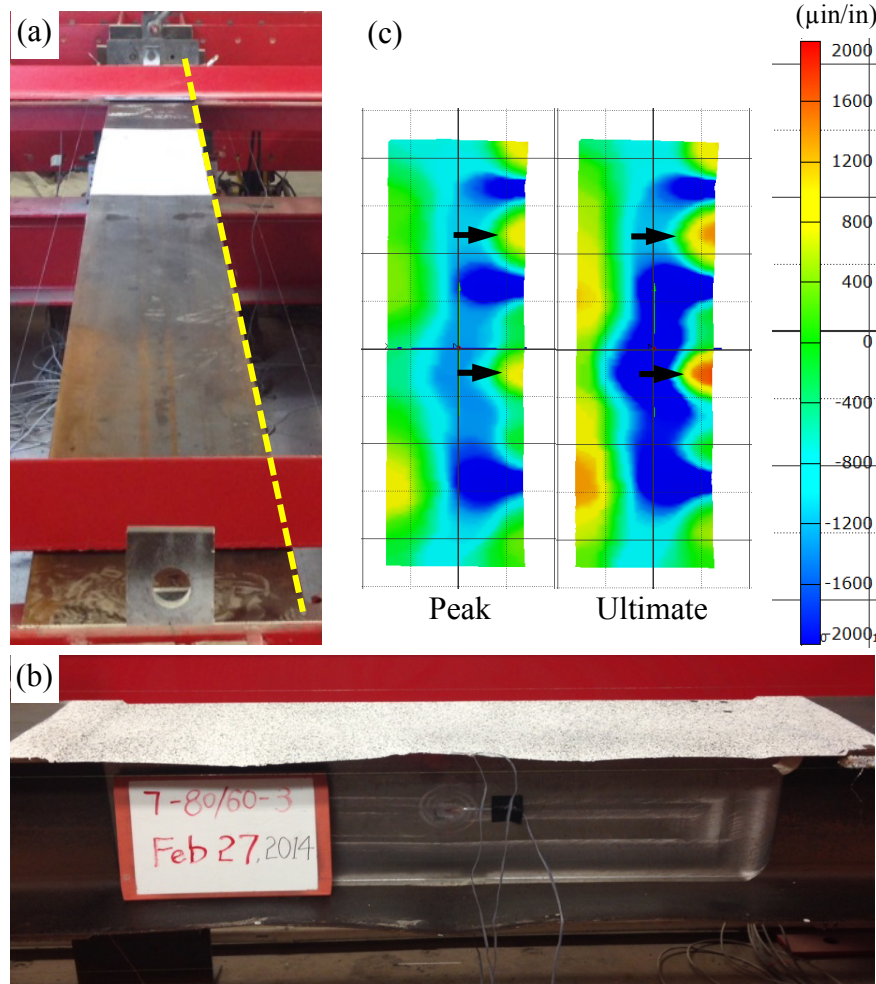


Figure 4.24: Global deformation, local deformation, and strain contours of pile 80/60/3

4.7. Discussion of the results

Table 4.4 summarizes the measured peak load and failure mode of the tested piles. It also presents the peak load and cross-sectional area of each pile normalized with respect to the peak load and cross-sectional area of the control pile. The effect of deterioration on the failure mode and axial capacity of the tested full-scale piles are discussed in the following sections.

Table 4.4: Degradation of the Specifications of the Tested Piles due to Corrosion

Pile Designation	Peak Load (kips)	Corroded/ Control Peak Load	Corroded/ Control Cross-Sectional Area	Failure Mode
0/0	623	1.00	1.00	Global buckling
0/20	604	0.970	0.959	Global buckling
40/20	435	0.699	0.673	Flange local buckling
40/60	333	0.534	0.494	Flange and web local buckling
80/60	182	0.293	0.292	Flange and web local buckling
80/60/V	124	0.199	0.180	Flange local bending
80/60/3	159	0.255	0.348	Flange and web local buckling

4.7.1. Failure Mode

As the level of deterioration increased, and the cross sectional elements (flanges and webs) became more slender, the failure mode switched from global buckling to flange and web local buckling. The un-corroded control pile, 0/0, and pile 0/20 failed by global buckling. The piles with simulated corrosion of the flanges, with the exception of pile 80/60/V, failed by flange local buckling. For those piles with 60% reduction of the web thickness the failure was accompanied by out of plane buckling of the web. In the case of severe corrosion with a through-web void, pile 80/60/V, the dominant failure mode was localized flange bending. In the absence of the support provided by the web the two ligaments of the flanges that were adjacent to the void demonstrated one-way bending, as opposed to two-way plate buckling. This change in the failure mode should be considered when provisions of existing design specifications are used to predict the axial capacity of the deteriorated piles.

Extending the length of the corroded region resulted in a higher mode of flange local buckling. Comparing piles 80/60 to 80/60/3 shows that when the length of the corroded

region was extended from 12 in. to 36 in., the failure mode shifted from first-mode flange local buckling (with the flange deforming into a single half-sine wave) to third-mode flange local buckling (with the flange deforming into three half-sine waves).

4.7.2. Axial Capacity

Figure 4.25 shows the correlation between the normalized peak load and cross-sectional area with respect to the peak load and cross-sectional area of the control pile. Reduction of the cross-sectional area demonstrates a linear relationship with reduction in the axial capacity with a coefficient of determination, R^2 , of 0.983. This relationship is similar to the one observed for the small-scale piles.

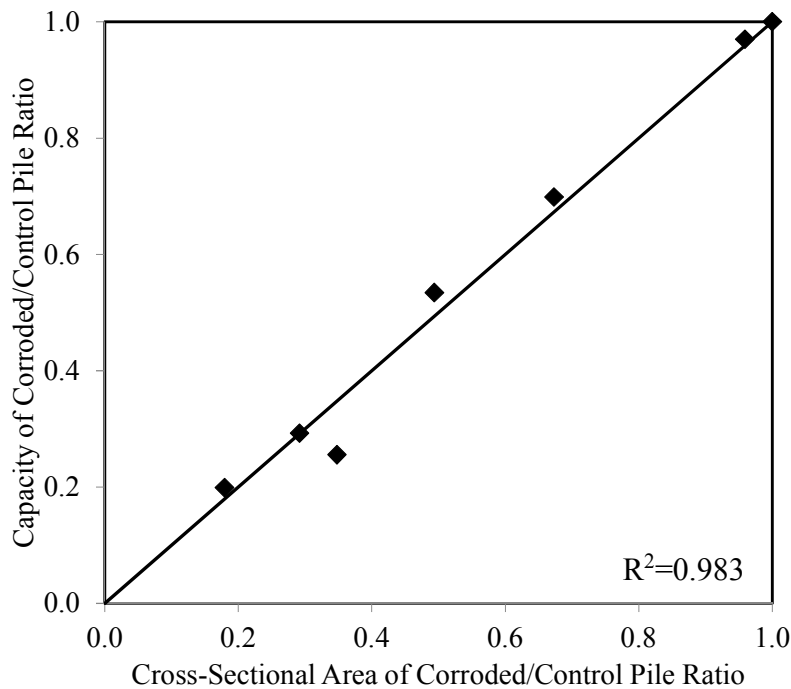


Figure 4.25: Correlation between the loss of axial capacity and loss of cross section

As presented in Table 4.4, axial capacity reduces by increasing the level of deterioration. However, the effect of reduction of the flange thickness is more significant than reduction

of the web thickness since the flanges have a greater contribution to the weak-axis moment of inertia and cross-sectional area of the section. Comparing the axial capacity of piles 40/20 to 40/60 shows that decreasing the web thickness by 40% to a 23% reduction in the axial capacity. On the other hand, comparing 40/60 to 80/60, revealed decreasing the flange thickness by 40% resulted in 45% loss of axial capacity. The same conclusion can be drawn by comparing pile 0/0 to 0/20 and pile 0/20 to 40/20.

Extending the length of the corroded region increased the flange aspect ratio. This, in turn, led to reduction of the flange buckling coefficient and critical flange buckling load. Consequently, the axial capacity of pile 80/60/3 was lower than that of pile 80/60, although the cross-sectional area of the reduced section of pile 80/60/3 was slightly greater than that of pile 80/60.

Chapter 5. Comparison to Existing Design Specifications

This chapter compares the measured capacities of the tested small-scale and full-scale piles with different corrosion patterns to the predicted capacities obtained using three different design approaches that are found in the US design specifications: AISC and AASHTO, the AISI effective width method, and the AISI direct strength method. The details of the three methods are presented in Chapter 2. This chapter summarizes the assumptions that were made to predict the capacities of piles with localized corrosion using the provisions of existing specifications which are formulated for prismatic members with constant cross-sections. Recommendations regarding how to implement these methods to corroded steel piles are also presented.

5.1. Comparison with Existing Design Specifications

The provisions of AASHTO (2012) (which are the same as those of AISC (2011)), the AISI-EWM, and the AISI-DSM (AISI, 2012) were used to predict the remaining axial capacity of the tested piles. The calculated capacities of the corroded piles using these design approaches required several assumptions, some of which were inherent to the development of the design models and others which were implemented to represent as closely as possible the physical reality of the tested columns:

- The columns were assumed to be prismatic with uniform section loss caused by corrosion along the entire length. This is an inherent assumption in all of the design models investigated and represents the most significant deviation from the physical reality of columns with localized, severe corrosion.

- For the small-scale piles, the effective length factors, k , about the weak and strong axes for global buckling were assumed to be 1.0 and 0.8, respectively, based on the boundary conditions provided in the test.
- For the full-scale piles, effective length factors, k , about the weak and strong axes for global buckling were assumed to be 1.0 and 0.65, respectively, based on the boundary conditions provided in the test.
- For local buckling calculations the unloaded edges of the web and flanges were considered as fixed-fixed and fixed-free, respectively, and loaded edges were assumed to be simply supported. Consequently, plate buckling coefficient for web, k_w , and flanges, k_f , were taken as 6.97 and 1.28, respectively.
- To calculate the capacity of the columns with through-web voids only the global buckling of the two flange ligaments adjacent to the void with the length of $L=2$ in was considered. The critical buckling stress was calculated for one single flange ligament, and then to obtain the nominal capacity, the critical stress was multiplied by the cross-sectional area of the two flange ligaments.
- Based on the experimental observation (see Figure 5.1), the effective length factor for one single flange ligament, k , about its weak and strong axes for global buckling were assumed to be 1.2 and 0.65, respectively.

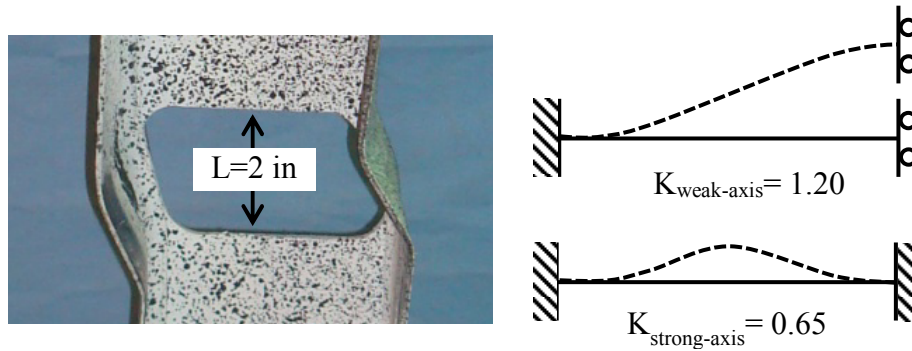


Figure 5.1: Strong and weak-axis effective length factor

- The maximum slenderness ratio, $(KL/r)_{\max}$, for the columns with a through-web void was calculated with $L=2$ in. The cross-sectional properties for the columns with through-web voids were calculated for a single flange ligament.
- The material properties obtained from stub column test were used for global and local buckling calculations. Poisson's ratio of $\nu=0.3$ was assumed for the calculations.

5.1.1. AASHTO Method

Calculations of the axial capacities of the tested columns in accordance with AASHTO (2012) are summarized in Table 5.1 and Table 5.2, for small-scale and full-scale columns, respectively. Measured-to-predicted axial capacity ratios with their mean values, standard deviations (STDV), and coefficients of variation (COV) are also presented in the tables. A Test/AASHTO Capacity ratio greater than 1.0 indicates that the prediction is conservative.

Table 5.1: Prediction of the Axial Capacity of Small-Scale Columns using AASHTO

Column Designation	$(KL/r)_{\max}$	F_e	Q_s	Q_a	$Q=Q_sQ_a$	F_{cr}	$P_{n,c}$	Test/AASHTO Capacity
		(ksi)				(ksi)	(kip)	
Phase I								
0/0	30.9	312	1	1	1	53	215	1.00
0/30	29.7	338	1	1	1	53	195	1.03
0/60	28.4	370	1	1	1	53	180	0.989
50/0	34.7	247	1	1	1	53	127	0.918
50/30	27.2	404	1	1	1	53	120	1.08
75/0	42.3	167	0.531	1	0.531	28	46	1.99
75/60	31.6	299	0.814	1	0.814	43	55	1.27
Phase II								
75/60/NV/US	32.8	277	0.573	1	0.573	30	31	1.5
75/60/NV/US/WR	44	154	0.837	1	0.837	44	47	1.32
75/60/V/S	85.7	41	N/A ^a	N/A ^a	N/A ^a	31	25	1.56
75/60/V/S/WR	84	42	N/A ^a	N/A ^a	N/A ^a	31	13	2.68
75/60/V/US	85.7	41	N/A ^a	N/A ^a	N/A ^a	31	25	1.6
75/60/V/US/WR	79.2	48	N/A ^a	N/A ^a	N/A ^a	33	29	1.33
Mean								1.45
STDV								0.485
COV								0.335

^a flange and web slenderness ratios were not applicable to the columns with through-web void since only flexural buckling of a single flange ligament was considered

Table 5.2: Prediction of the Axial Capacity of Full-Scale Columns using AASHTO

Pile Designation	F_e	Q_s	Q_a	$Q=Q_sQ_a$	F_{cr}	$P_{n,c}$	Test/AASHTO Capacity
	(ksi)				(ksi)	(kip)	
0/0	73	0.996	1	0.98	38	591	1.06
0/20	76	0.998	1	0.98	39	573	1.06
40/20	71	0.751	1	0.751	31	324	1.34
40/60	81	0.6	0.68	0.408	19	146	2.29
80/60	57	0.104	0.806	0.0839	4	19	9.52
80/60/V	54	N/A ^a	N/A ^a	N/A ^a	35	96	1.29
80/60/3	67	0.205	0.751	0.154	8	41	3.86
Mean							2.92
STDV							2.85
COV							0.978

^a flange and web slenderness ratios were not applicable to the pile with through-web void since only flexural buckling of a single flange ligament was considered

5.1.2. AISI-EWM

Table 5.3 presents the local buckling stresses, F_{cr} , and the effective widths, h_e and b_{fe} , of the corroded web and flange elements the small-scale columns calculated according to (AISI, 2012). Table 5.4 presents these results for the full-scale columns.

Table 5.3: Effective Width of the Corroded Web and Flange – Small-Scale

Column Designation	Effective Width of the Corroded Web					Effective Width of the Corroded Flange				
	k	F_{cr}	λ	ρ	h_e	k	F_{cr}	λ	ρ	b_{fe}
		(ksi)			(in)		(ksi)			(in)
Phase I										
0/0	6.97	1931	0.161	1	3.48	1.28	1041	0.219	1	4.17
0/30	6.97	974	0.233	1	3.46	1.28	1000	0.23	1	4.17
0/60	6.97	315	0.41	1	3.45	1.28	1023	0.228	1	4.17
50/0	6.97	1666	0.178	1	3.53	1.28	229	0.48	1	4.17
50/30	6.97	896	0.243	1	3.49	1.28	279	0.436	1	4.17
75/0	6.97	1666	0.177	1	3.52	1.28	48	1.05	0.752	3.14
75/60	6.97	233	0.476	1	3.52	1.28	93	0.753	0.94	3.93
Phase II										
75/60/NV/US	6.97	198	0.516	1	3.54	1.28	51	1.02	0.771	3.22
75/60/NV/US/WR	6.97	212	0.497	1	3.53	1.28	101	0.719	0.965	4.02
75/60/V/S	N/A ^a	N/A ^a	N/A ^a	N/A ^a	N/A ^a	N/A ^a	N/A ^a	N/A ^a	N/A ^a	N/A ^a
75/60/V/S/WR	N/A ^a	N/A ^a	N/A ^a	N/A ^a	N/A ^a	N/A ^a	N/A ^a	N/A ^a	N/A ^a	N/A ^a
75/60/V/US	N/A ^a	N/A ^a	N/A ^a	N/A ^a	N/A ^a	N/A ^a	N/A ^a	N/A ^a	N/A ^a	N/A ^a
75/60/V/US/WR	N/A ^a	N/A ^a	N/A ^a	N/A ^a	N/A ^a	N/A ^a	N/A ^a	N/A ^a	N/A ^a	N/A ^a

^a flange and web slenderness ratios were not applicable to the columns with through-web void since only flexural buckling of a single flange ligament was considered

Table 5.4: Effective Width of the Corroded Web and Flange – Full-Scale

Pile Designation	Effective Width of the Corroded Web					Effective Width of the Corroded Flange				
	k	F _{cr}	λ	ρ	h _e	k	F _{cr}	λ	ρ	b _{fe}
	(ksi)				(in)	(ksi)				(in)
0/0	6.97	307	0.355	1	11.10	1.28	174	0.471	1	12.09
0/20	6.97	231	0.412	1	11.10	1.28	174	0.474	1	12.09
40/20	6.97	157	0.496	1	11.10	1.28	75	0.716	0.967	11.69
40/60	6.97	43	0.967	0.799	8.86	1.28	52	0.872	0.857	10.35
80/60	6.97	58	0.786	0.916	10.16	1.28	9	1.98	0.449	5.43
80/60/V	N/A ^a	N/A ^a	N/A ^a	N/A ^a	N/A ^a	N/A ^a	N/A ^a	N/A ^a	N/A ^a	N/A ^a
80/60/3	6.97	51	0.858	0.866	9.61	1.28	18	1.45	0.585	7.09

^a flange and web slenderness ratios were not applicable to the pile with through-web void since only flexural buckling of a single flange ligament was considered

Table 5.5 and Table 5.6 summarize the calculation of axial capacity of the small-scale and full-scale columns, respectively, according to AISI-EWM (AISI, 2012). The nominal axial capacity, $P_{n,c}$, was obtained by multiplying the nominal stress, F_n , by the effective cross-sectional area, A_e . The effective cross-sectional area was calculated using the effective web depth and flange width. The critical buckling stress using AISI-EWM is much less sensitive to the element slenderness since this method introduces a reduction in the area of the section to account for the effect of local buckling on the loss of capacity. Measured-to-predicted axial capacity ratios with their mean values, standard deviations (STDV), and coefficients of variation (COV) are also computed. A Test/EWM Capacity ratio greater than 1.0 indicates that the prediction is conservative.

Table 5.5: Prediction of the Axial Capacity of Small-Scale Columns using AISI-EWM

Column Designation	F_e (ksi)	λ_c	F_n (ksi)	A_e (in ²)	$P_{n,c}$ (kip)	Test/EWM Capacity
Phase I						
0/0	312	0.414	50	4.05	202	1.06
0/30	338	0.152	53	3.68	195	1.03
0/60	370	0.145	53	3.39	180	0.989
50/0	247	0.177	53	2.41	127	0.918
50/30	404	0.139	53	2.27	120	1.08
75/0	167	0.216	52	1.48	78	1.18
75/60	299	0.161	53	1.22	64	1.08
Phase II						
75/60/NV/US	277	0.167	53	0.87	46	1.25
75/60/NV/US/WR	154	0.224	52	1.04	55	1.28
75/60/V/S	41	1.15	31	0.81	25	1.56
75/60/V/S/WR	42	1.12	31	0.43	13	2.68
75/60/V/US	41	1.15	31	0.81	25	1.6
75/60/V/US/WR	48	1.06	33	0.87	29	1.33
					Mean	1.31
					STDV	0.443
					COV	0.338

Table 5.6: Prediction of the Axial Capacity of Full-Scale Columns using AISI-EWM

Pile Designation	F_e (ksi)	λ_c	F_n (ksi)	A_e (in ²)	$P_{n,c}$ (kip)	Test/EWM Capacity
0/0	73	0.846	39	15.47	598	1.04
0/20	76	0.828	39	14.83	580	1.04
40/20	71	0.857	38	10.18	391	1.11
40/60	81	0.803	40	6.45	256	1.30
80/60	57	0.956	36	2.99	107	1.71
80/60/V	54	0.988	35	2.77	96	1.29
80/60/3	67	0.881	38	3.70	140	1.14
					Mean	1.23
					STDV	0.217
					COV	0.176

5.1.3. AISI-DSM

Table 5.7 and Table 5.8 summarize the calculation of the axial capacity of the small-scale and full-scale columns, respectively, according to AISI-DSM, (AISI, 2012). The AISI-

DSM includes predictions of the overall and local buckling capacities. Prediction of distortional buckling requires the use of finite strip method for prismatic members. For the tested columns, which are non-prismatic, the experimental results and the results of finite element analysis (discussed later) showed that distortional buckling mode was not a predominant failure mode. As such, calculation of the distortional buckling capacity was not considered in calculation of the axial capacity of the corroded columns. Measured-to-predicted axial capacity ratios with their mean values, standard deviations (STDV), and coefficients of variation (COV) are also presented. A Test/DSM Capacity ratio greater than 1.0 indicates that the prediction is conservative.

Table 5.7: Prediction of the Axial Capacity of the Small-Scale Columns using AISI-DSM

Column Designation	Overall Buckling Load			Local Buckling Load			P _{n,c} (kip)	Test/DSM Capacity	
	P _y	P _{cre}	λ _c	P _{ne}	P _{crl}	λ _l			P _{nl}
	(kip)	(kip)		(kip)	(kN)				(kip)
Phase I									
0/0	217	1267	0.414	202	4221	0.219	202	202	1.06
0/30	197	1243	0.398	184	3585	0.227	184	184	1.09
0/60	182	1255	0.38	171	1068	0.4	171	171	1.04
50/0	129	596	0.465	118	553	0.462	118	118	0.992
50/30	121	915	0.364	115	632	0.426	115	115	1.13
75/0	88	273	0.566	77	78	0.992	66	66	1.4
75/60	68	381	0.423	63	119	0.729	63	63	1.11
Phase II									
75/60/NV/US	54	282	0.439	50	52	0.981	43	43	1.32
75/60/NV/US/WR	57	163	0.589	49	107	0.676	49	49	1.43
75/60/V/S	43	33	1.148	25	N/A ^a	N/A ^a	N/A ^a	25	1.56
75/60/V/S/WR	23	18	1.125	13	N/A ^a	N/A ^a	N/A ^a	13	2.68
75/60/V/US	43	33	1.148	25	N/A ^a	N/A ^a	N/A ^a	25	1.6
75/60/V/US/WR	47	42	1.06	29	N/A ^a	N/A ^a	N/A ^a	29	1.33
								Mean	1.37
								STDV	0.427
								COV	0.313
^a flange and web slenderness ratios were not applicable to the columns with through-web void since only flexural buckling of a single flange ligament was considered									

^a flange and web slenderness ratios were not applicable to the columns with through-web void since only flexural buckling of a single flange ligament was considered

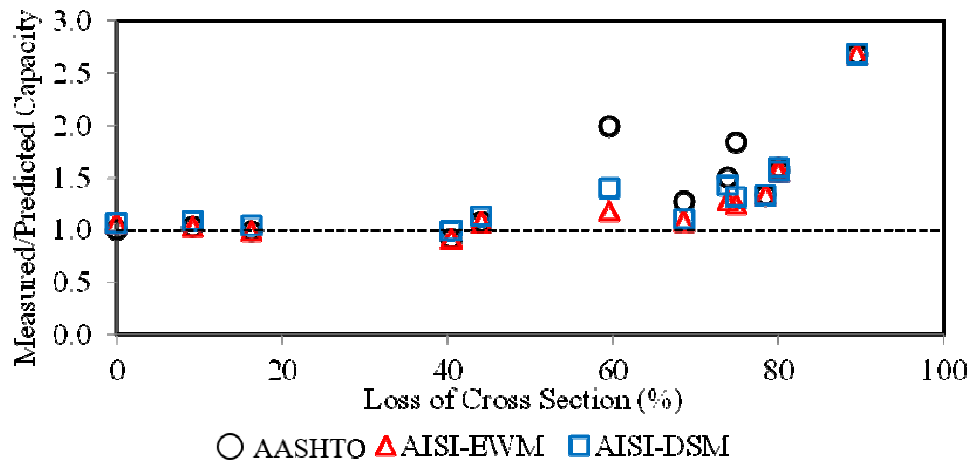
Table 5.8: Prediction of the Axial Capacity of the Small-Scale Columns using AISI-DSM

Pile Designation	Overall Buckling Load				Local Buckling Load			$P_{n,c}$ (kip)	Test/DSM Capacity
	P_y	P_{cre}	λ_c	P_{ne}	P_{cr1}	λ_l	P_{nl}		
	(kip)	(kip)		(kip)	(kip)		(kip)		
0/0	807	1128	0.846	598	2694	0.471	598	598	1.04
0/20	773	1128	0.828	580	2584	0.474	580	580	1.04
40/20	544	739	0.857	400	780	0.716	400	400	1.09
40/60	398	618	0.803	303	326	0.967	265	265	1.26
80/60	236	258	0.956	161	41	1.98	85	85	2.14
80/60/V	145	148	0.988	96	N/A ^a	N/A ^a	N/A ^a	96	1.29
80/60/3	281	362	0.881	203	96	1.45	134	134	1.19
								Mean	1.29
								STDV	0.360
								COV	0.278

^a flange and web slenderness ratios were not applicable to the pile with through-web void since only flexural buckling of a single flange ligament was considered

5.1.4. Comparison

Figure 5.2 shows the comparison of the tested-to-predicted axial capacity ratios for small-scale columns. Figure 5.3 presents this information for the full-scale specimens. The predicted capacities were calculated in accordance with AASHTO, AISI-EWM, and AISI-DSM. The data points above the dashed line indicate conservative predictions.

**Figure 5.2: Comparison of the measured and predicted axial capacities for small-scale piles**

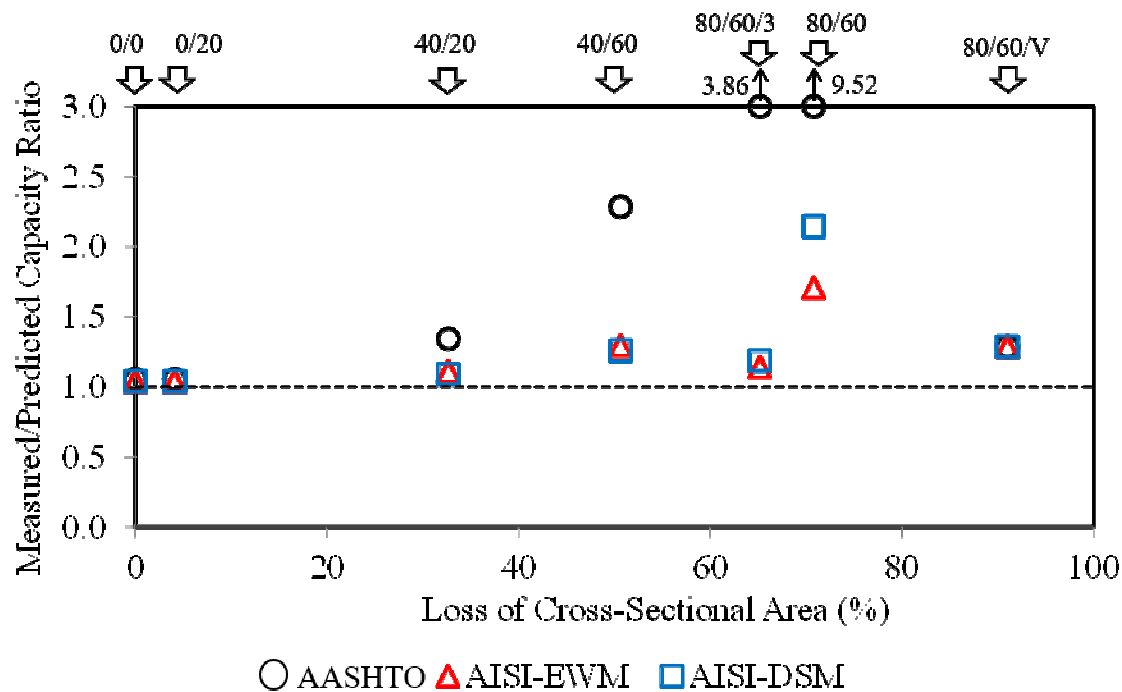


Figure 5.3: Comparison of the measured and predicted axial capacities for full-scale piles

As shown in Figure 5.2 and Figure 5.3 for cases with less than 50% loss of the cross-sectional area the predicted capacities are relatively accurate using all three methods; Figure 5.3 shows that in this case the predicted capacities are up to 1.3 times the measured capacity using all three methods. However, when the loss of the cross-sectional area is greater than 50%, the prediction by AISC becomes overly conservative compared to the predictions from the two AISI methods, for both small-scale and full-scale columns. This is due to the fact that AASHTO does not fully account for the post-buckling strength of slender elements. In addition, the AASHTO model was developed based on results from compression members with only slightly slender elements. The other two models, AISI-EWM and AISI-DSM, are applicable to thin-walled members with highly slender elements. The AISI-EWM, while still being quite conservative, gives the most accurate prediction of the capacity among the methods considered with a mean

ratio of 1.31 and a coefficient of variation of 0.338 for small-scale piles, and a mean ratio of 1.20 and a coefficient of variation of 0.18 for full-scale piles. These results are consistent with the findings of others for prismatic members (Seif and Schafer, 2010).

Chapter 6. Finite Element Simulations

This chapter presents the details of a numerical modeling approach that was established to predict the response of steel piles with localized severe corrosion. The details of the model are presented. The model is validated by comparison of the predicted response to the measured response that was obtained for small-scale (Chapter 3) and full-scale (Chapter 4) piles. The validated model is used to conduct a parametric study to investigate the effect of different parameters, including degree and extent of flange and web reduction, pile slenderness, magnitude of residual stresses, and the location of the corroded region on the pile capacity

6.1. Description of the Finite Element Model

A non-linear, 3D finite element model was developed using the commercial finite element package ABAQUS v6.12 (SIMULIA, 2012). Two consecutive steps were performed in the FEA: 1) eigenvalue analysis to obtain the elastic buckling modes; 2) with elastic buckling modes imposed as the initial imperfections shapes, an inelastic buckling analysis was conducted incorporating the effect of residual stresses and large deformations. Boundary conditions were modeled to represent the test set-up at the supports. The piles were loaded by imposing an axial displacement at one end to simulate the action of the hydraulic jack used in the experimental program. The modified Riks method (Riks, 1979) was employed to solve the model which incorporated both geometric and material nonlinearity.

6.1.1. Element Types and Mesh Size

To evaluate different types of elements and mesh sizes, a sensitivity study of inelastic buckling analysis was performed on two piles, 0/0 and 80/60 from the full-scale

experimental program. The pile 0/0 refers to the un-corroded control specimen with 0% reduction on flange and web thicknesses, and 80/60 refers to the pile with 80% and 60% reduction flange and web thickness, respectively. These two representative piles were chosen for the sensitivity analysis because they encompass failure modes of flexural buckling, flange local buckling, and web local buckling. Also, the two cases represent the extreme cases of corrosion that were considered in this research. The FE model adopted the measured dimensions of flange and web thicknesses and material properties from tension coupon tests of the large scale pile materials. The thicknesses of the cross-sectional elements are relatively small compared to their lengths and widths. The aspect ratio is less than 1/15. Therefore, three commonly used shell element types were compared and evaluated to select an efficient element type for the numerical framework. The first element type was a four-node element, with six degrees of freedom per node, linear shape functions, fully integrated, finite-membrane-strain shell element, S4. It is a general-purpose shell element, which uses thick shell theory (Mindlin-Reissner plate theory) (Mindlin, 1951) when the shell thickness is over 1/15 of a characteristic length and becomes discrete Kirchhoff thin shell element, in which transverse shear flexibility is neglected, as the thickness decreases. The second element type is S4R, which is similar to S4 but uses reduced integration to form the element stiffness matrix. The third element type is an eight-node element, with six degrees of freedom per node, thick shell element, with non-linear shape functions, and reduced integration, S8R. The elementary mesh size to start the investigation was 2 in.×2 in. The mesh was subdivided twice, into 1 in.×1 in. and 0.5 in.×0.5., to evaluate the convergence of the results.

Figure 6.1(a) and (b) present the axial capacities for pile 0/0 and 80/60, respectively, predicted by FEA using S4, S4R, and S8R elements. The horizontal axis refers to the three values of mesh size, and the vertical axis refers to the predicted axial capacity. The dashed line indicates the converged load level as the mesh size is refined. The predicted inelastic buckling loads for pile 0/0 using the three element types showed comparable results when the mesh size was 2 in.×2 in. However, regarding 80/60 with substantial reduction of the flange and web thicknesses, only the model with S8R elements showed converged results when the mesh size was 2 in.×2 in. Predictions using element S4 and S4R converged when the mesh size was refined to 1 in.×1 in. This is because flexural buckling of pile 0/0 resulted in smoother element deformations, and both first-order (S4 and S4R) and second-order (S8R) elements were able to provide satisfactory predictions with the same mesh size. In contrast, for the pile that failed by local buckling, 80/60, the local buckling induced larger element curvatures and the elements with linear shape functions (S4 and S4R) could not smoothly capture the corresponding deformations. Reduction of the mesh size (from 2 in.×2 in. to 1 in.×1 in.) or increasing the degree of the element shape functions (doubly curved shell S8R instead of elements with linear shape function) provided better predictions.

The results of the sensitivity study indicate that S4 and S4R elements with 1 in×1 in mesh size, and S8R element with 2 in.×2 in. mesh size can be used for the current study. When reduced integration is used for linear elements, such as for element S4R, hourglass effects need to be checked and controlled (Flanagan and Belytschko, 1981). Element S8R was capable to provide reliable predictions of the behavior for corroded piles. However, in problems involving contact, such as for piles repaired using the clamped steel-based

system (described in detail in the subsequent chapters), the S8R element automatically transfers to element S9R5 (SIMULIA, 2012). To maintain consistency of the modeling approach between corroded piles and repaired piles, element S4 with a mesh size as 1 in. \times 1 in. was selected.

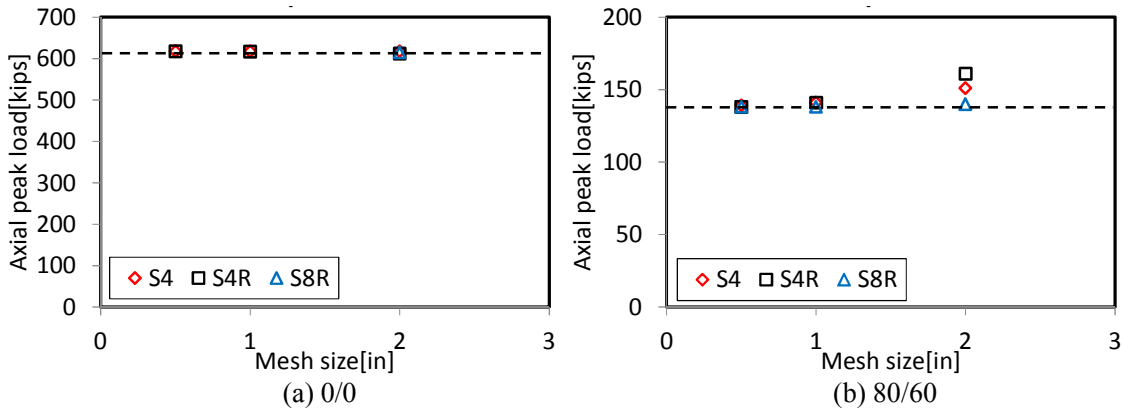


Figure 6.1: Sensitivity study for element type and mesh size

6.1.2. Initial Out-of-Straightness

The first modes of flexural and local buckling, shown in Figure 6.2, were used as the initial global and local imperfection shapes for all of the simulated piles. According to the AISC specifications (2011), the permissible fabrication sweeps for axial members with flange width less than or greater than 6 in. are $L/480$ and $L/960$, respectively; while the maximum value of out-of-straightness of a compression member considered in the design formulations is $L/1000$, where L is the length of the member. In contrast, AASHTO (2012) allows a maximum out-of-straightness of $L/1500$. Figure 6.3(a) and (b) shows the effects of the amplitude of the initial global imperfection, Δ_G , on two representative piles that failed by flexural and local buckling, respectively. Figure 6.3(a) shows the axial load-deformation responses of small-scale piles 0/0 (un-corroded control pile) and 75/60 (pile with 75% and 60% reduction of the flange and web thicknesses, respectively) with

three different magnitudes of global imperfections. Figure 6.3(b) shows the axial load-deformation curves of full-scale piles 0/0 and 80/60 with different values of global imperfections. Inspection of Figure 6.3 indicates that the amplitude of the initial global imperfection has a minor influence on the axial capacity of the piles. The differences of axial capacities caused by varying values of global imperfection are less than 5% for piles with no damage and with major cross-section loss, regardless of the section size. In practical applications it is difficult to measure the actual magnitude of global imperfections. Therefore, the initial global imperfection was taken conservatively as the maximum of the three values in AISC (2011) and AASHTO (2012), which were $L/480$ and $L/960$ for W4×13 and HP12×53 sections, respectively. The peak magnitude of the local imperfections, Δ^L , was taken as the fabrication tolerance defined in AISC, which was 0.06 in. The global and local initial imperfections were implemented by scaling the first mode of flexural and local buckling to the values determined above.

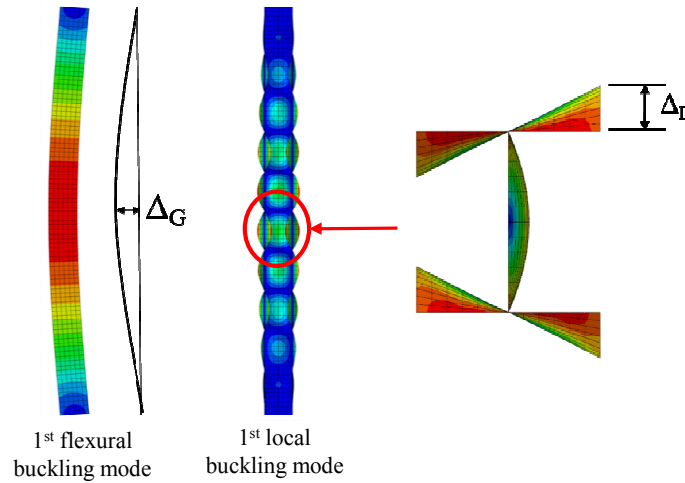


Figure 6.2: Shapes initial global and local imperfections from elastic buckling analysis

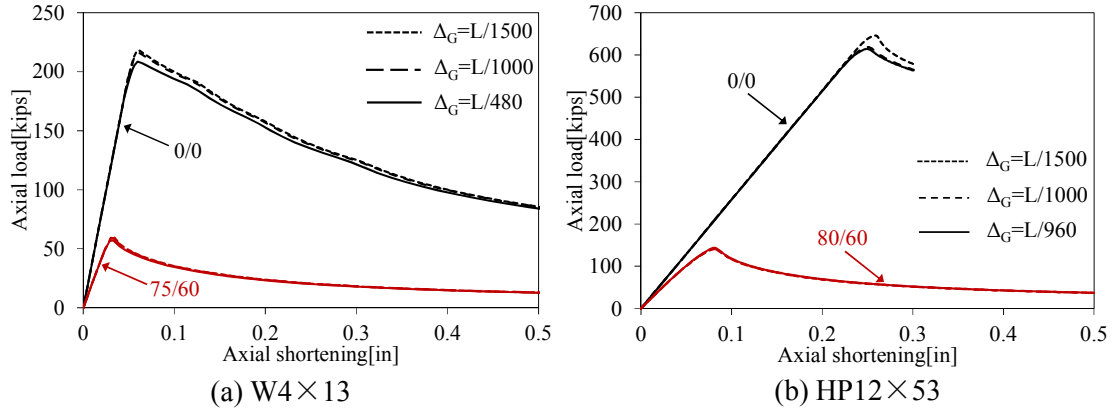


Figure 6.3: Effects of initial global imperfection on pile axial capacity

6.1.3. Material Properties

The material model that was used in the simulations adopts a classical plasticity formulation with von Mises yield criterion, an associated flow rule, and isotropic hardening. The uniaxial stress-strain relationship uses a bilinear curve as shown in Figure 6.4, where F_y and F_u refer to yield and ultimate stresses, respectively. As two types of piles, small-scale W4×13 section and full-scale HP12×53 section, were used to validate the numerical framework, the material properties from tension coupon tests and stub column tests of both piles were used. Table 6.1 summarizes the material properties for the two sizes of piles that were adopted in the validation. For small-scale W4×13 piles, the moduli of elasticity and yield strengths of the flanges and web were adopted values from the stub column test results. The ultimate strengths were taken from the results of the tension coupon tests. For full-scale HP12×53 piles, the elastic moduli, yield and ultimate strengths of the flanges and web were taken as the mean values obtained from tension coupon tests.

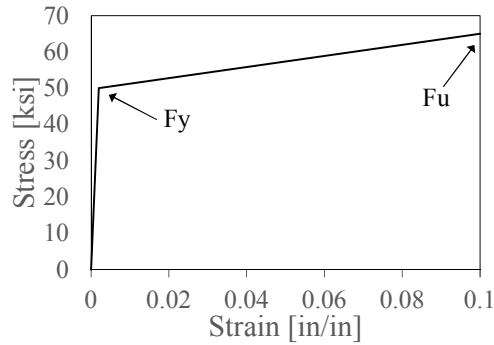


Figure 6.4: Stress-strain relationship of steel used in FEA

Table 6.1: Material Properties of W4×13 and HP12×53

Pile	Element	Yield strength [ksi]	Ultimate strength [ksi]	Elastic modulus [ksi]
W4×13	Flange	56.0	69.5	26900
	Web	63.5	77.0	26100
	Stub column	53.5	--	30200
HP12×53	Flange	52.5	66.5	28400
	Web	60.5	71.0	32000

6.1.4. Effect of residual stresses

Figure 6.5 presents the distribution of residual stresses, which was suggested by Ziemian (2010) with maximum compression stresses, σ_c , at the flange tips and uniform tension, σ_t , in the web. The residual stresses were implemented as predefined stresses on selected elements before applying the axial load. The maximum magnitude of residual stresses was assumed as 30% of the yield stress of the material in AISC (2011). However, a sensitivity analysis was conducted on the small-scale and full-scale control specimens, 0/0, to identify a magnitude of residual stress that provides the most accurate axial capacity. Peak residual stresses of 10%, 20%, and 30% of the nominal yield stress (5 ksi, 10 ksi, and 15 ksi, respectively) were considered. Figure 6.6 presents the axial capacities of small-scale and full-scale piles with three values of maximum residual stress. The figure shows the axial load-deformation responses and the horizontal dashed line indicates the measured axial peak load of the un-corroded control pile. The predicted

axial capacities of the HP12×53 control specimen were 652 kips, 618 kips and 579 kips in the three cases, while the capacity obtained from test was 623 kips. The predicted capacity with peak residual stresses of 10 ksi matched the axial capacity of the control pile most closely. Therefore, the residual stresses were taken as 10 ksi in compression at the tips of flanges and 10 ksi in tension along the depth of the web for the full-scale piles. For the W4×13 section, the obtained axial capacities for piles with 5 ksi, 10 ksi, 15 ksi maximum residual stresses were 209 kips, 208 kips, and 208 kips, respectively. The maximum magnitude of residual stresses for small-scale piles was taken as 5 ksi, because the stress-strain relationship obtained from the stub column test indicated minor residual stresses on the section.

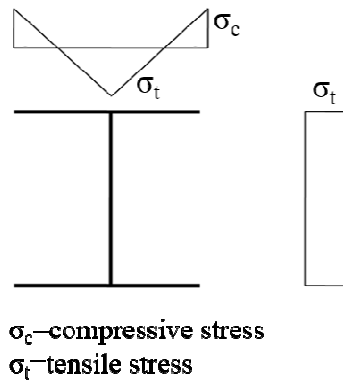


Figure 6.5: Distribution of residual stresses on the flange and web

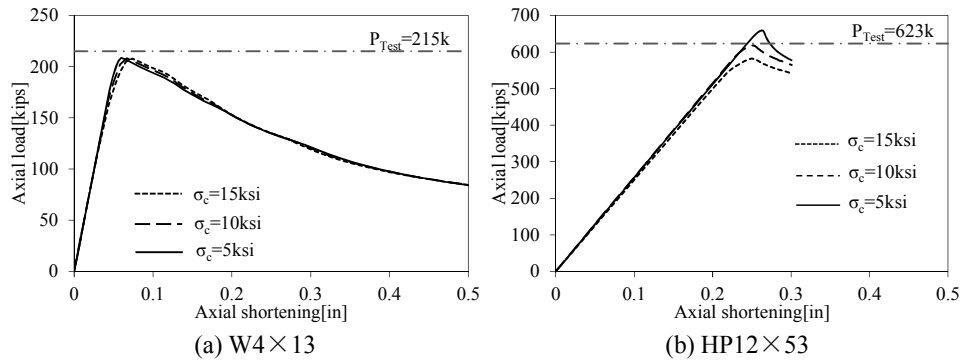


Figure 6.6: Effects of residual stresses on axial capacity

6.2. Validation of the Finite Element Model

This section presents the comparison of the experimental results and the FEA predictions for small-scale and full-scale piles. The results were compared on the basis of axial capacity, stiffness, axial load-deformation response, and failure mode.

6.2.1. Small-scale piles

Table 6.2 presents the measured and predicted axial peak loads and failure modes for the tested small-scale piles. For piles with flange thickness reduction less than 50%, the differences between measured and predicted capacities were generally less than 10%. For piles with flange thickness reductions up to 75%, the discrepancy between measured and predicted capacities was up to 50%. For severely corroded sections the percentage error was relatively large, but the absolute value of the error in kips was a small percentage of the design capacity of the pile. For pile 70/60/V/S/WR, the difference between the measured and predicted capacities was 12 kips. For an un-corroded pile with a nominal capacity of 200 kips, the error was only 6% of the nominal capacity, which is within an acceptable tolerance when considering the design of the repair system. Moreover, the FEA predictions generally under-predicted the pile capacity.

Table 6.2: Axial Peak Loads and Failure Modes of W4×13 from FEA and tests

Pile designation	Axial peak load [kips]		$P_{\text{test}}/P_{\text{FEA}}$	Failure mode	
	P_{test}	P_{FEA}		Test	FEA
0/0	215	209	1.03	FB ^a	FB
0/30	201	185	1.09	FB	FB
0/60	178	170	1.05	FB	FB
50/0	117	124	0.94	FLB ^b	FLB
75/0	92	73	1.26	FLB	FLB
50/30	130	116	1.12	FLB/WLB ^c	FLB/WLB
75/60	70	58	1.21	FLB/WLB	FLB/WLB
75/60/V/S	39	34	1.15	FOWB ^d	FOWB
75/60/NV/US	57	43	1.33	FLB/WLB	FLB/WLB
75/60/V/US	40	36	1.11	FOWB	FOWB
75/60/NV/US/WR	70	52	1.35	FLB/WLB	FLB/WLB
75/60/V/S/WR	36	24	1.50	FOWB	FOWB
75/60/V/US/WR	39	34	1.15	FOWB	FOWB

^aFlexural Buckling; ^bFlange Local Buckling; ^cWeb Local Buckling; ^dFlange One-way Bending

Figure 6.7 shows the typical failure modes that were observed experimentally and the corresponding predicted deformed shapes. The deformed shapes predicted by FEA matched the experimental observations.

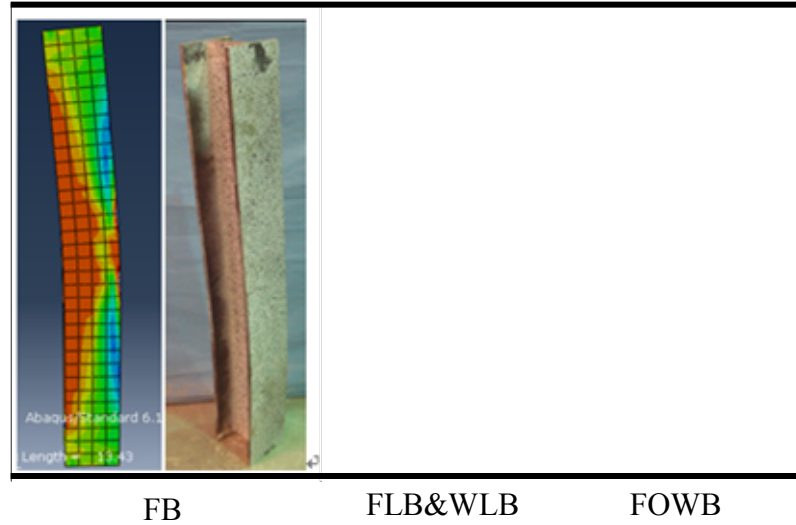
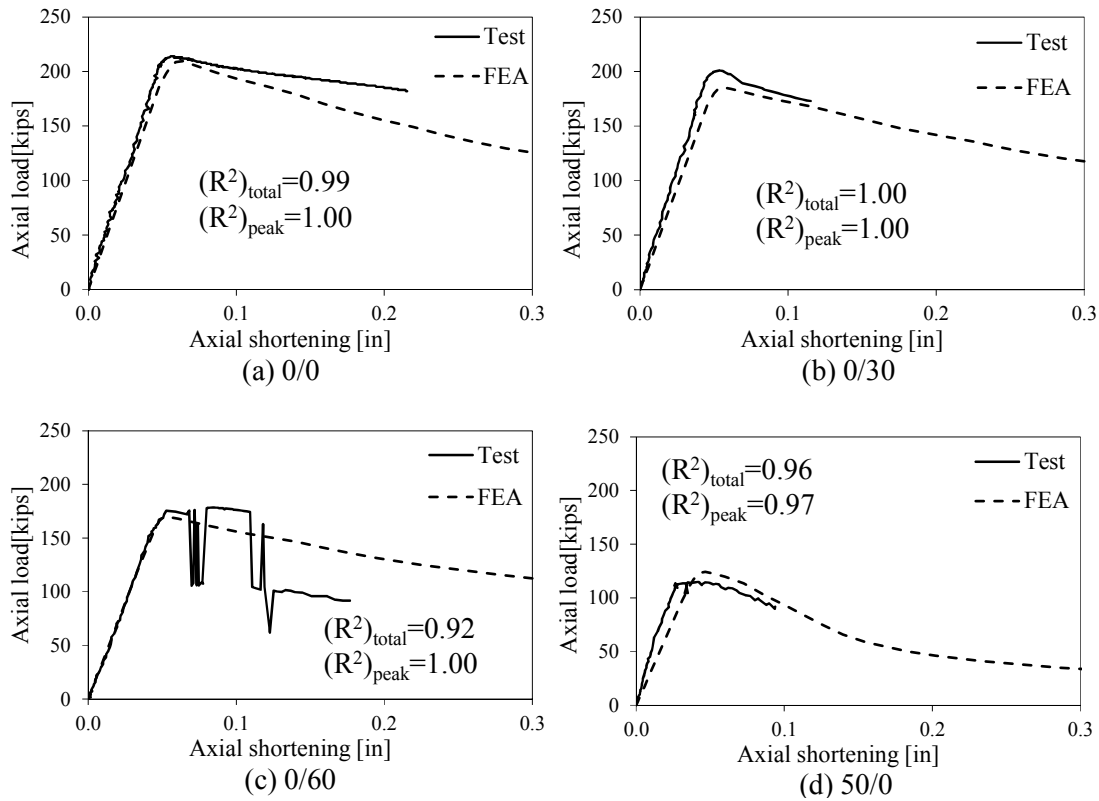
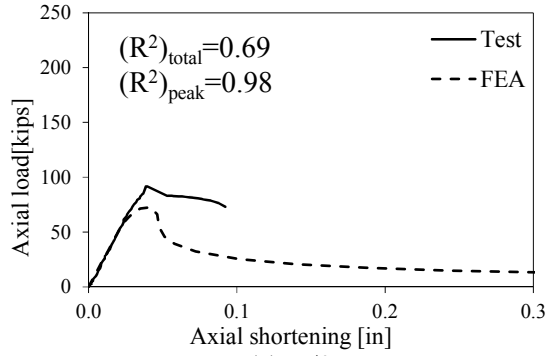


Figure 6.7: Deformation of small-scale piles from FEA and tests

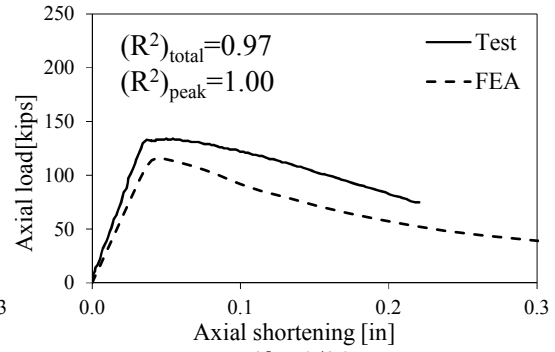
Figure 6.8 compares the measured and predicted axial load-shortening relationships. The figure also presents the coefficients of determination, R^2 , between experimental and numerical curves. $(R^2)_{\text{total}}$ was calculated from the total range of the curves from zero deformation to the maximum deformation of the test or FEA. The end of the range when calculating $(R^2)_{\text{total}}$ depended on the maximum deformation point obtained from tests. $(R^2)_{\text{peak}}$ was calculated within a range from zero load/deformation to the peak load of the curves, to quantify the correlation of FEA and experimental results regardless of the post-peak behavior. Inspection of Figure 6.8 indicates excellent correlation between the experimental and FEA results before peak load. The values of $(R^2)_{\text{peak}}$ are no less than 0.97 for all of the tested small-scale piles. The post-peak portions of the load-displacement curves exhibit good correlation when the failure mode of the pile is flexural buckling. In these cases, values of $(R^2)_{\text{total}}$ are not less than 0.82 except for pile 0/60. However, the discrepancy increases as the flange becomes slender. The abnormal post-buckling behavior of 0/60 was attributed to a noisy load signal from electro-magnetic interference during testing. The discrepancies between the measured and predicted axial

load-displacement relationships were attributed to four reasons: (1) unintentional eccentricity of the applied load during testing; (2) uncertainty of the magnitude and pattern of the residual stresses, especially for degraded piles with, which may have experienced relief of the residual stresses during milling of the flange and web; (3) conservativeness of the assumed magnitude and pattern of initial imperfections; (4) effect of the fillet at the junction of flange and web, which was not modeled in the FE simulation but partly existed in tested specimens.

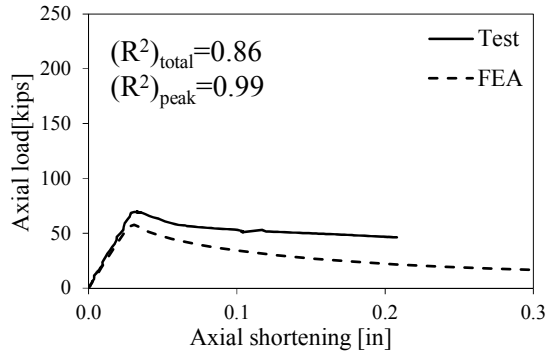




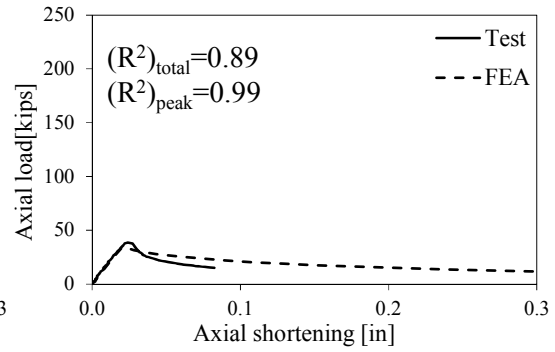
(e) 75/0



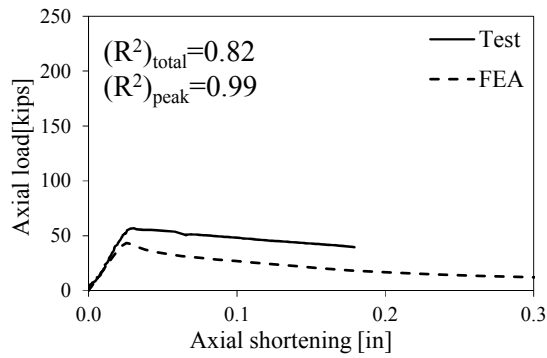
(f) 50/30



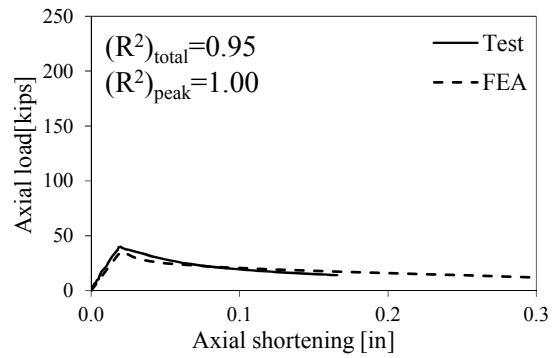
(g) 75/60



(h) 75/60/V/S



(i) 75/60/NV/US



(j) 75/60/V/US

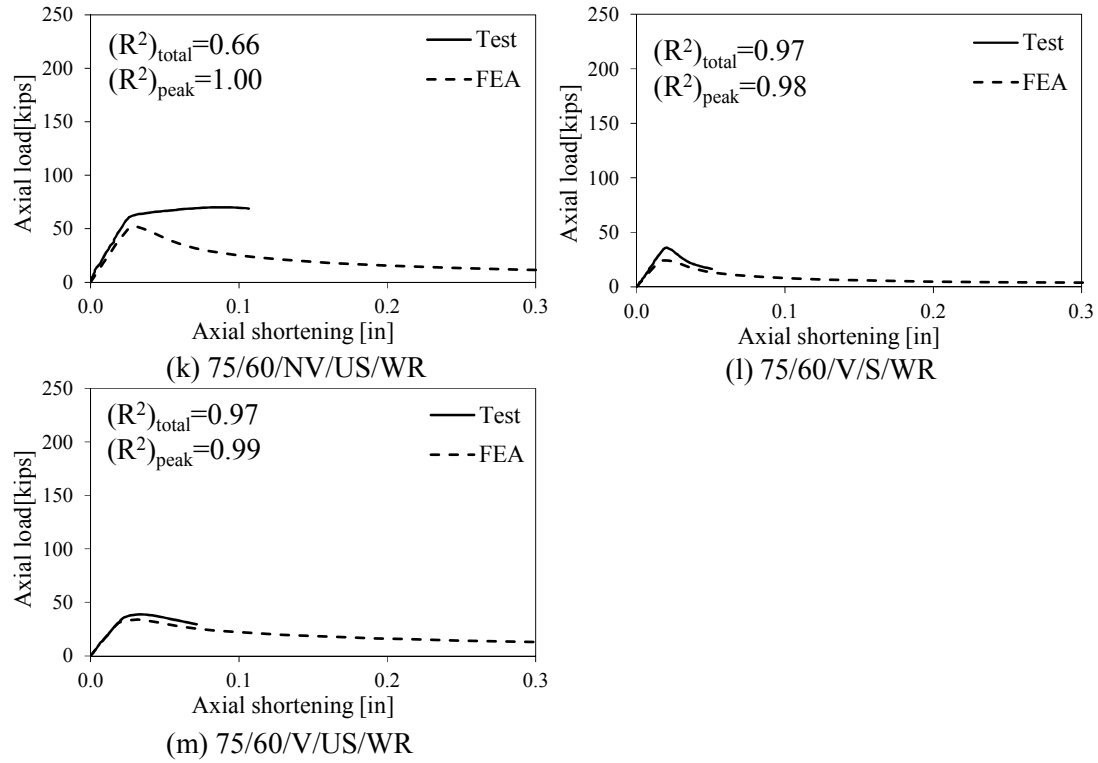


Figure 6.8: Comparison of axial load-shortening responses from tests and FEA of W4×13

6.2.2. Full-scale piles

Similar to small-scale piles, the experimental results from full-scale H-piles were also used to validate the FE model. Table 6.3 presents the measured and predicted axial peak loads and failure modes of the full-scale HP12×53 piles. The predicted axial peak loads are slightly conservative except for pile 0/20 and 40/20 for which the capacities were over-predicted by 3% and 8%, respectively. This is attributed to a higher unintentional load eccentricity during testing. This was identified from the test data of four string potentiometers which showed a slightly larger discrepancy than for the other pile tests. Similarly to the small-scale piles, for severely corroded piles, 80/60 and 80/60/V, the discrepancy between measured and predicted capacities was slightly larger since the capacities of these piles were relatively small. The absolute differences between the

measured and predicted capacities are 41 kips and 28 kips, respectively. These correspond to only 7% and 5% of the nominal capacity of the un-corroded pile of 580 kips.

Table 6.3: Axial peak loads and failure modes of HP12×53 from FEA and tests

Pile designation	Axial peak load [kips]		$P_{\text{test}}/P_{\text{FEA}}$	Failure mode	
	P_{test}	P_{FEA}		Test	FEA
0/0	623	618	1.01	FB ^a	FB
0/20	604	621	0.97	FB	FB
40/20	435	472	0.92	FLB ^b	FLB
40/60	333	303	1.10	FLB/WLB ^c	FLB/WLB
80/60	182	141	1.29	FLB/WLB	FLB/WLB
80/60/V	124	96	1.29	FOWB ^d	FOWB
80/60/3	159	160	1.00	FLB/WLB	FLB/WLB

^aFlexural Buckling; ^bFlange Local Buckling; ^cWeb Local Buckling; ^dFlange One-way Bending.

The numerical model accurately predicted the failure mode of all of the tested piles. The characteristic failure modes that were observed experimentally are illustrated in Figure 6.9 and compared to the predicted deformed shapes. The deformed shapes predicted by the FEA closely matched the experimental observations.

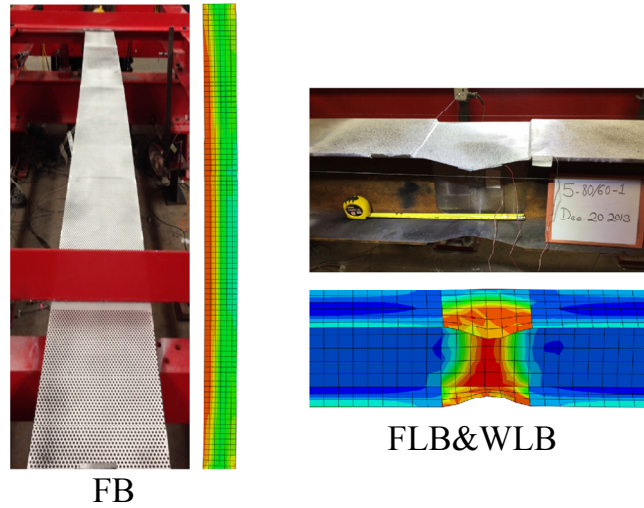
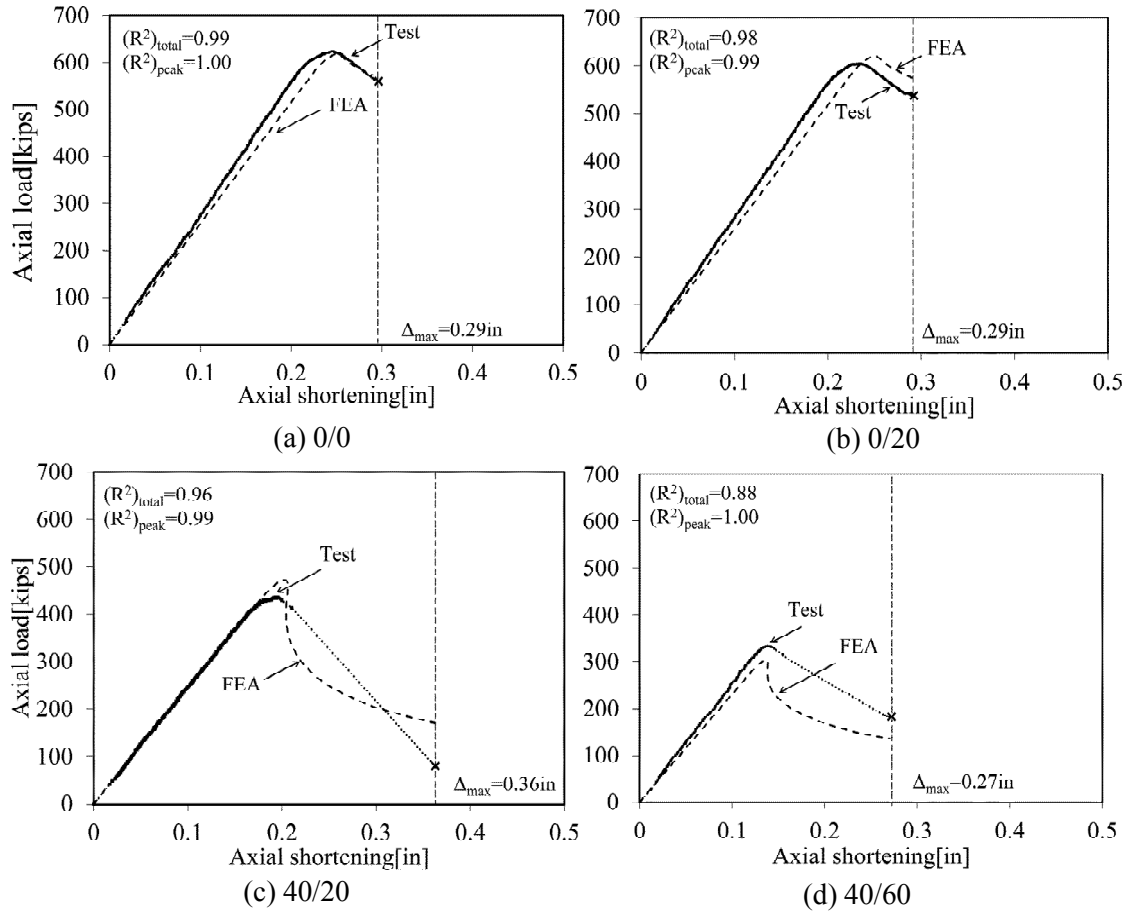


Figure 6.9: Deformation of full-scale piles from FEA and test

Figure 6.10 compares the predicted axial load-deformation relationships from FEA to the measured response. The figure also presents the coefficients of determination, R^2 , between experimental and numerical curves. Inspection of Figure 6.10 shows $(R^2)_{\text{peak}}$ ranges between 0.98 to 1.00. Comparing the coefficients of determination, $(R^2)_{\text{total}}$, of 0/0 and 0/20 indicates that FEA accurately predicted the full axial load-deformation responses for these piles. For piles 40/20 and 40/60, the post-peak measured response exhibited a sudden drop of capacity. Consequently, there are very few measured data points in the post peak range for these piles and the trend does not closely match the predicted response. The FEA under-predicted the post-buckling capacity of pile 80/60, 80/60/V, and 80/60/3 compared to the measured response. The discrepancies between the measured and predicted axial load-displacement relationships was attributed to four possible causes: (1) unintentional eccentricity of the applied load during testing; (2) uncertainty of the magnitude and pattern of the residual stresses; (3) conservativeness of the assumed magnitude and pattern of initial imperfections; (4) effect of the fillet at the junction of flange and web.



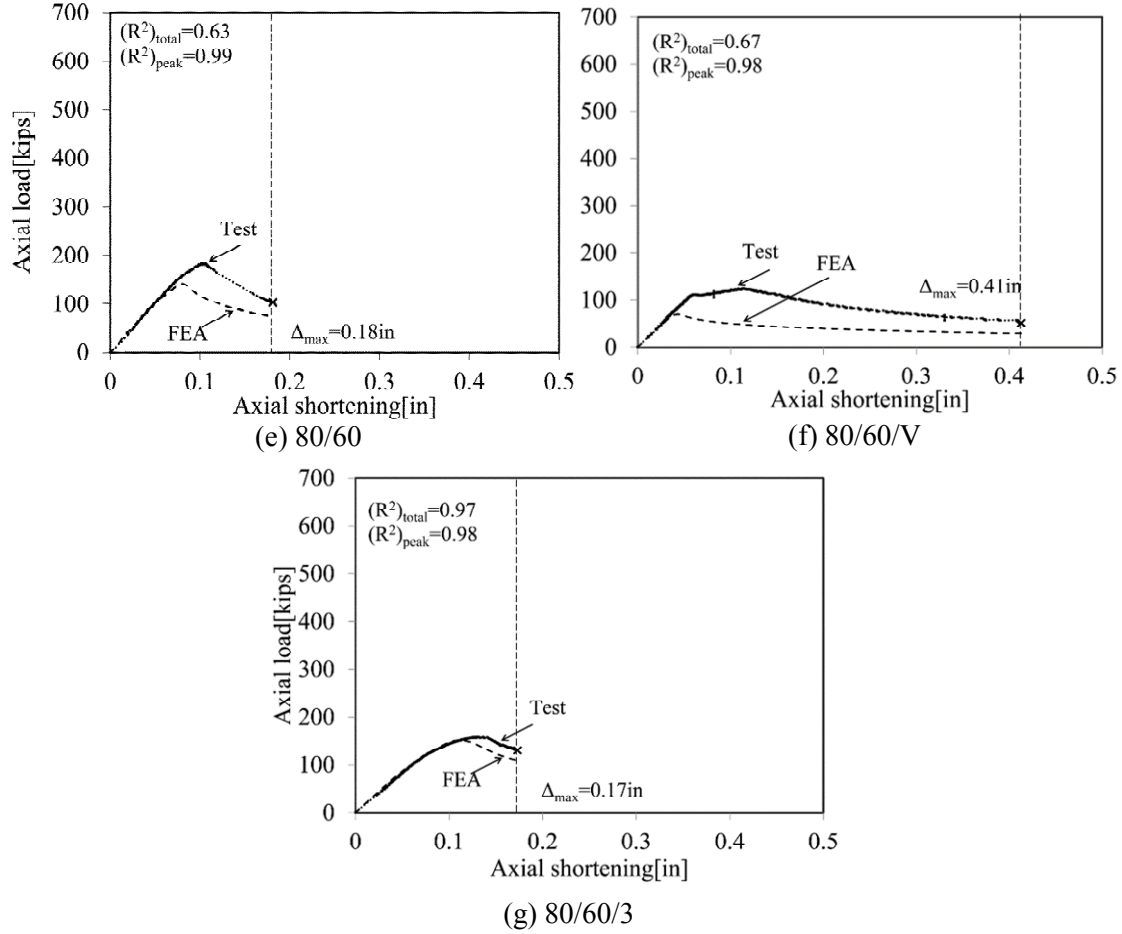


Figure 6.10: Comparison of axial load-deformation responses from test and FEA of HP12×53

6.3. Parametric Study

Parametric studies on both small-scale and full-scale piles were performed using the validated FE model, to investigate the influence of factors that might affect the axial behavior of partially corroded H-piles. The parameters considered include the degree of the reduction of the flange and web thicknesses, slenderness of the piles, location and extent of the degraded regions, and magnitude of the residual stresses.

Each pile that was considered in the parametric study was assigned a unique identifier following a similar naming convention to that used in the experimental study. The nominal values of the material properties of Grade 50 steel and dimensions of the piles, as specified

by AISC (2011) were used in the parametric study. The magnitudes of initial global imperfections were taken as $L/480$ and $L/960$ for $W4 \times 13$ and $HP12 \times 53$, respectively. The initial local imperfection was taken as the maximum fabrication tolerance of the out-of-square for the section, 0.06 in. The base configurations of the piles were 32 in long $W4 \times 13$ pile and 15 ft long $HP12 \times 53$ pile, with yield and ultimate strengths of 50 ksi and 65 ksi, respectively, an elastic modulus of 29,000 ksi, and a peak magnitude of residual stresses of 15 ksi (30% of the yield stress). The corroded region was 1 ft long, centered at the mid-height of the pile.

6.3.1. Effect of Degree of Flange Corrosion, Web Corrosion, and Pile Slenderness

Figure 6.11 shows the effects of flange and web corrosion on the predicted axial capacities of corroded $W4 \times 13$ and $HP12 \times 53$ piles with different slenderness ratios, kL/r , where k is the effective length factor, L is the clear length of the member, and r is the radius of gyration of the cross section about the axis of bending. The horizontal and vertical axes illustrate the degree of the reduction of the web thickness and the normalized axial capacity, respectively. For $W4 \times 13$ shown in Figure 6.11(a), the axial load was normalized with respect to the capacity of the un-corroded pile, 0/0, with a slenderness ratio of 32. For $HP12 \times 53$ shown in Figure 6.11(b), the axial load was normalized with respect to the capacity of the un-corroded pile, 0/0, with a slenderness ratio of 42. The points in the figure indicate the predicted peak loads of the simulated piles, and they are connected by lines for visual convenience. The marker styles indicate the degrees of flange thickness reduction. The line styles indicate pile slenderness ratios of 32, 48, and 64 for $W4 \times 13$ (Figure 6.11(a)), 42, 63, and 84 for $HP12 \times 53$ (Figure 6.11(b)).

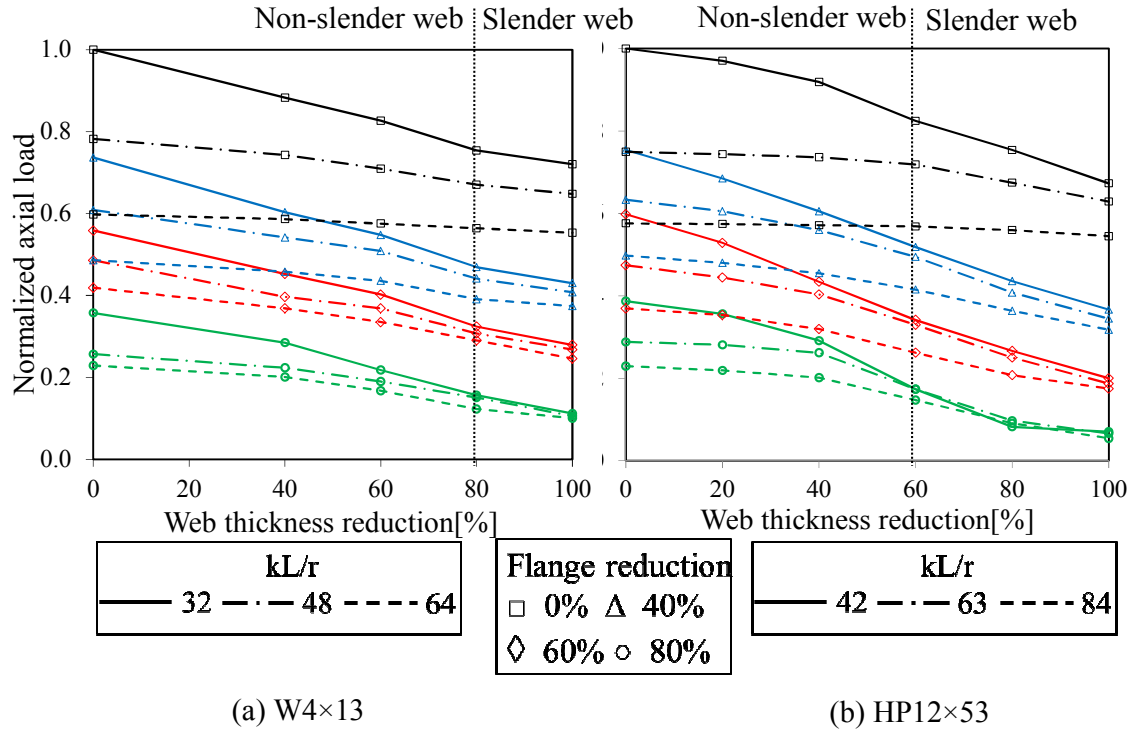


Figure 6.11: Axial peak loads for piles with different reduction on flange and web

Inspection of Figure 6.11 indicates that flange thickness reduction has a greater effect on the remaining axial capacity of corroded piles than web thickness reduction. With the same loss of cross-sectional area, piles with moderate loss of flange thickness and minor loss of web thickness exhibit lower capacities than piles with significant loss of web thickness and minor loss of flange thickness. This can be illustrated by considering two HP12×53 piles with slenderness (kL/r) of 84 and 53% reduction of cross-sectional area. The pile with 80% reduction of flange thickness, 80/0, has a remaining capacity of 171 kips while the pile with 40% reduction of flange thickness and 80% reduction of web thickness, 40/80, has a remaining capacity of 282 kips, which is 65% higher than the capacity of pile 80/0. This is due to the following: (1) the flanges contribute more to the weak-axis moment of inertia of the section, (2) reducing the flange thickness causes the flanges to become slender resulting in a local buckling failure mode while reducing the

thickness of the web does not since the web is a stiffened element while the flange is an unstiffened element.

Figure 6.11 also shows the influence of pile slenderness on the axial capacity of corroded piles. The slenderness of the pile has a significant effect for piles failing by flexural buckling. For un-corroded HP12×53 piles decreasing the slenderness from 84 to 42 increases the axial capacity of the piles by 74%. A similar trend was observed for the small-scale piles as well. By decreasing the pile slenderness from 64 to 32 for un-corroded W4×13 piles, the axial capacity increased by 67%. However, the effect of pile slenderness becomes negligible when the dominant failure mode of the pile is local buckling of the flange or web. Observation of Figure 6.11 indicates that for severely corroded piles with both slender flanges and webs (the cases at the bottom right corners of the two figures), the slenderness of the piles does not have any influence on their axial capacities as local buckling in the deteriorated region controls the failure. Therefore, bracing a pile to reduce its effective length may only be an effective repair strategy if the pile corrosion is relatively minor with no slender flange or web.

6.3.2. Effect of the Location of the Corroded Region

To investigate the effect of the location of the corrosion, the corroded region was moved to the third-height of the 64 in W4×13 pile and 15 ft HP12×53 pile from mid-height. Five representative cases with different failure modes including flexural buckling, flange and/or web local buckling, were modeled for each section. Inspection of the capacities that are summarized in Table 6.4 demonstrates that the location of corrosion has a

negligible effect on the axial capacities of the piles regardless of the failure mode and section scale.

Table 6.4: Comparison of Axial Capacities for Different Locations of Reduction

Pile designation		Axial peak load [kips]		Difference [%]
		Third-height	Mid-height	
W4×13	20/0	100	99	1
	20/40	97	96	1
	60/40	65	66	1
	60/80	50	52	2
	80/80	23	22	1
HP12×53	0/20	506	505	0
	40/20	406	414	2
	40/60	320	330	3
	80/60	120	127	6
	80/100	44	45	2

6.3.3. Effect of the Extent of the Corroded Region

The effect of the extent of the corroded region was studied by considering three different extents of the corroded region. For W4×13 piles, 0.5 ft., 1 ft., and 2 ft. extents were considered for a 5ft.-4in. long pile. For HP12×53 piles, 1 ft., 3 ft., and 5 ft. extents were considered for a 15 ft. long pile. These values represent 1.5, 3, and 6 times the nominal section depth of the W4×13 pile, and 1, 3, and 5 times the nominal section depth of the HP12×53. Figure 6.12 presents the axial peak loads of W4×13 (Figure 6.12(a)) and HP12×53 (Figure 6.12(b)) piles with three different extents of corrosion on each section. The three types of bars in the figures refer to the axial capacities of piles with three different extents of corrosion. Each group of three extents of corrosion indicates piles with flange and web thickness reductions varied from 0% to 80%.

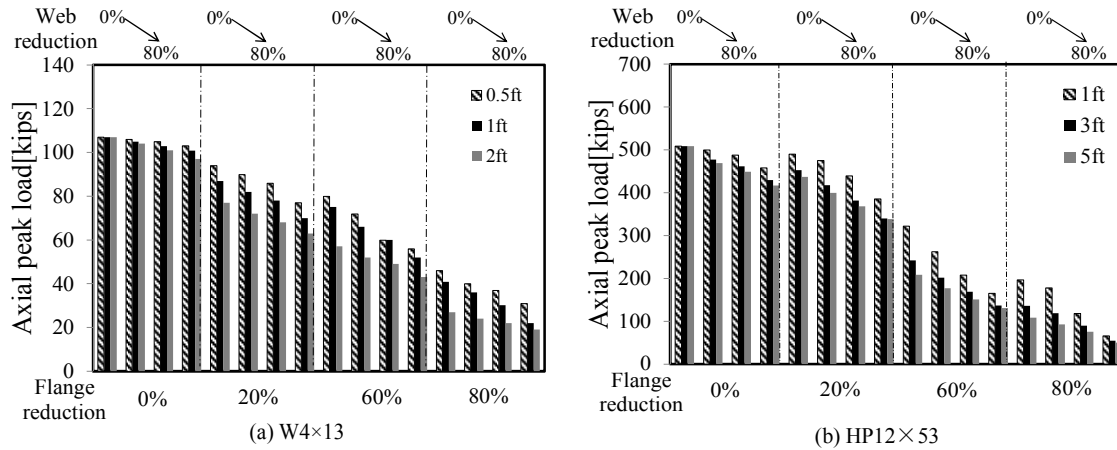


Figure 6.12: Axial peak loads of piles with different corroded extents

Inspection of Figure 6.12 indicates that the small-scale piles and the full-scale piles exhibited similar trends of behavior. Inspection of Figure 6.12 indicates that the extent of corrosion has minor effect on the capacity of piles with non-slender elements which failed by flexural buckling. In these cases, increasing the extent of corrosion by three times changed the pile capacity by 4% and 6% for the W4×13 and HP12×53 piles, respectively. In contrast, when the flange and web were more severely corroded and became slender, the effect of the extent of corrosion on the pile capacity became significant. In extreme cases, increasing the extent of corrosion by three times reduced the axial capacity of small-scale and full-scale piles by 41% and 33%, respectively. The reason for this phenomenon is that the aspect ratio of the corroded region of the flange (length of corroded region divided by half of the flange width) significantly affects the plate buckling strength of the corroded flange. The observed result is consistent with the classic plate buckling equations which predict a comparable reduction of strength for higher mode flange buckling (Lundquist and Stowell, 1942; Timoshenko, 1961).

The current design codes are formulated for prismatic members. To apply these design equations directly to corroded piles one must inherently assume that the loss of thickness

is uniform along the entire length of the pile. This results in very high aspect ratios of the buckling plates, and the predictions are thus conservative. The results shown in Figure 6.12 indicate that in extreme cases of corrosion, when flange reduction differs substantially from web reduction (i.e. 80/0), this assumption could lead to overly conservative predictions of capacity. Seif and Schafer (2013) presented relevant findings that when the slenderness of flange and web differed substantially, current design codes provided conservative predictions. The presumption that the local buckling of the slender element initiates similar buckling in the other element did not happen. However, based on field observations, it is uncommon for the degree of flange and web corrosion to differ dramatically.

6.3.4. Effect of Residual Stresses

To investigate the effect of the magnitude of residual stresses on the remaining axial capacity of the corroded piles, two different maximum magnitudes of residual stresses were considered: 10% F_y (5 ksi) and 30% F_y (15 ksi). Figure 6.13 presents the axial peak loads of piles with different residual stresses. The different bar styles refer to axial capacities of piles with different values of maximum residual stresses. For each value of flange reduction, five sets of bars indicate five degrees of web thickness reduction, including 0%, 40%, 60%, 80%, and 100% (2 in. void in the web).

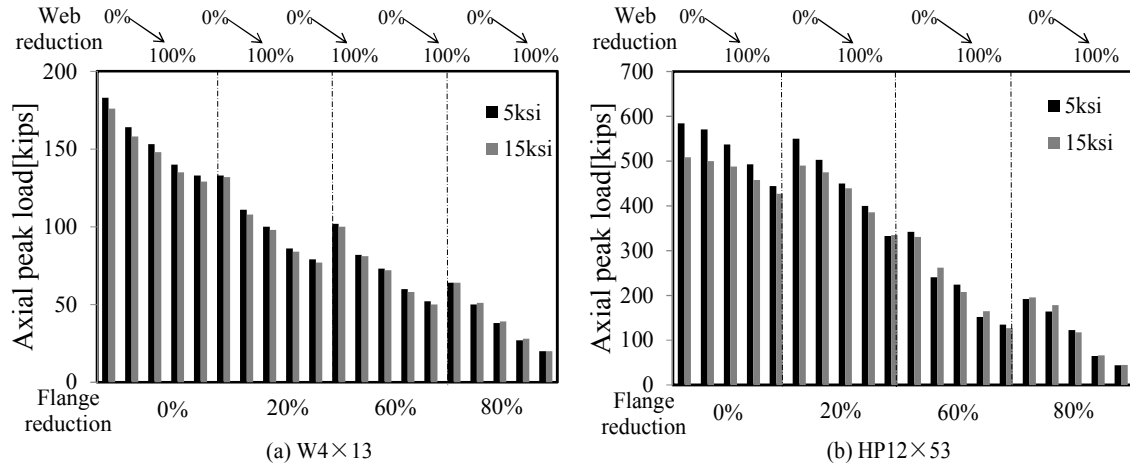


Figure 6.13: Axial peak loads of piles with different residual stresses

Inspection of Figure 6.13(a) indicates that the magnitude of residual stresses does not have much effect on the axial capacity of the small-scale piles. The differences of the axial peak loads from piles with 5 ksi and 15 ksi maximum residual stresses does not exceed 4%. In contrast, Figure 6.13(b) indicates a decrease of capacity as the residual stresses increase for piles with minor section loss and with flexural buckling as the dominant failure mode. In these cases, the differences of axial capacities of piles with residual stresses of 5 ksi and 15 ksi vary by as much as 10 to 15%. As the degree of corrosion increases the piles fail by local buckling and the influence of the magnitude of the residual stresses on the pile capacities decreased. For small-scale piles with flange thickness reduction greater than 80%, the pile capacities exhibited a slight increase as the residual stresses increased from 5 ksi to 15 ksi, as shown in Figure 6.13(a). This was also observed for some of the full-scale piles with flange thickness reductions of greater than 60%. This was due to the increase of the uniformly distributed tensile residual stresses in the web, σ_t , which increased the predicted compression capacity of the piles. However, in practical applications this slight increase of capacity should not be considered since

residual stresses are highly variable and some relaxation may occur with the severe loss of section caused by corrosion.

Chapter 7. Design of FRP-based and Steel-Based Repair Systems for Corroded Steel H-Piles

In this chapter, the design approaches for the FRP-based and steel-based repair systems are described and explained.

7.1. Design Approach for FRP-Confined Grout Repair System

The FRP-confined grout system has two functions; (1) stabilizing slender cross-sectional elements and (2) directly resisting a portion of the applied load. The design approach is illustrated schematically in Figure 7.1 for a corroded HP12×53 pile with a 60% reduction of the web thickness. The axial capacity of the corroded pile with different degrees of reduction of the flange thickness was calculated using the AISI-EWM and is shown by the solid diagonal line in Figure 7.1. The solid horizontal line indicates the nominal capacity of the un-corroded pile. This is the retrofitting target. The dotted diagonal line shows the yield capacity of the corroded section, $P_{y,c}$, which can be achieved if local buckling and global buckling are prevented. Regions ① and ② in Figure 7.1 indicate the increase of the nominal axial capacity of the corroded pile that can be achieved by preventing local buckling of the slender flanges and web. To fully realize this level of capacity increase, global buckling of the pile must be prevented as well. Region ② in the figure indicates that for piles with 60% reduction of the web thickness and less than 20% reduction of the flange thickness, restraining local and global buckling of the pile is sufficient to restore the capacity to the retrofitting target (the nominal strength of the un-corroded pile). Region ③ indicates that for piles with more than 20% corrosion of the flanges the yield capacity of the corroded section is inadequate to reach the retrofitting target. For these piles, load must be transferred out of the pile and into the

repair system above the corroded region and reintroduced into the pile below the corroded region. This may be achieved by the bond between the grout and the steel, by friction, or by mechanical anchorage.

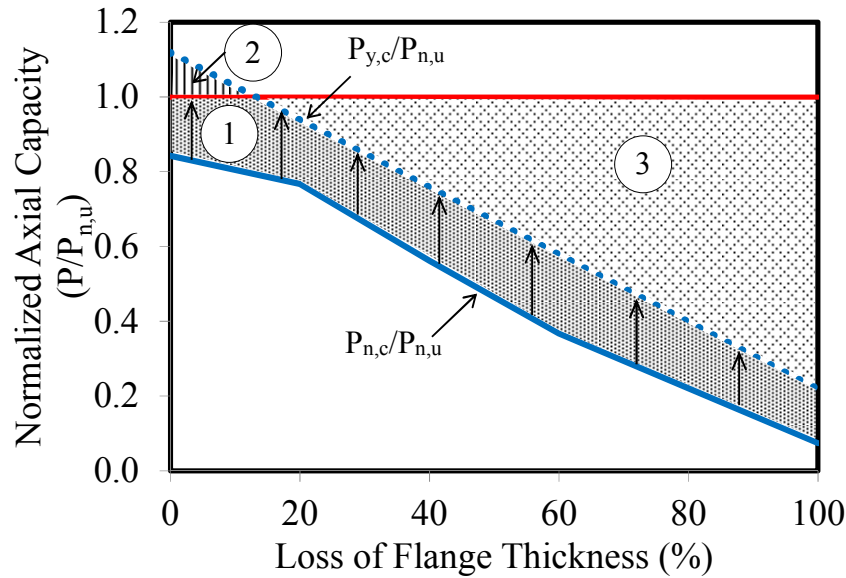


Figure 7.1: Design approach to repair corroded HP12×53 with 60% loss of web thickness

According to Figure 7.1, as the level of deterioration increases, the repair system is required to carry a greater portion of the axial load transferred from the steel pile. This is due to the fact that the yield capacity of the corroded section is not adequate to compensate the loss of axial capacity. The various components of the grouted FRP jacket repair system are designed to achieve these required functions based on the extent and degree of the corrosion.

Three classes of repair system are defined, namely minor, moderate, and major. Figure 7.2 illustrates the key components of the three classes of repair. The repair system consists of an FRP jacket, expansive grout, longitudinal steel reinforcing bars, and headed stud anchors. In the minor repair configuration, local buckling of the slender flanges and web is restrained by the expansive grout. The FRP jacket provides confinement, restrains the dilation of the grout core and prevents separation of the grout core from the steel pile. Minor loss of the weak-axis

bending stiffness of the corroded pile is assumed to be compensated by the additional bending stiffness provided by the grout and FRP jacket. As the degree of corrosion increases, localized deterioration and cracking may compromise the integrity of the grout core. Consequently, in the moderate repair configuration, longitudinal steel reinforcing bars are embedded in the grout as shown in Figure 7.2(b) to reinforce the grout and restore the weak-axis moment of inertia of the corroded section of the pile. In this case, the more substantial loss of the cross-section of the pile could decrease the yield capacity of the section such that it is no longer sufficient to transmit the required load. In this case, simply stabilizing the slender elements and delaying global buckling is insufficient to restore the capacity. Rather, a fraction of the applied load must be transferred from the steel pile to the repair system. In the moderate repair configuration the bond at the steel-grout interface is assumed to be adequate to transmit this additional load. In cases of severe corrosion, the amount of the load that must be transferred to the repair system may exceed the bond strength of the steel-grout interface. As illustrated in Figure 7.2(c), headed-stud anchors attached to the web are engaged to provide mechanical anchorage and transfer the excess load in these cases. The anchors are installed in the load introduction regions above and below the corroded region.

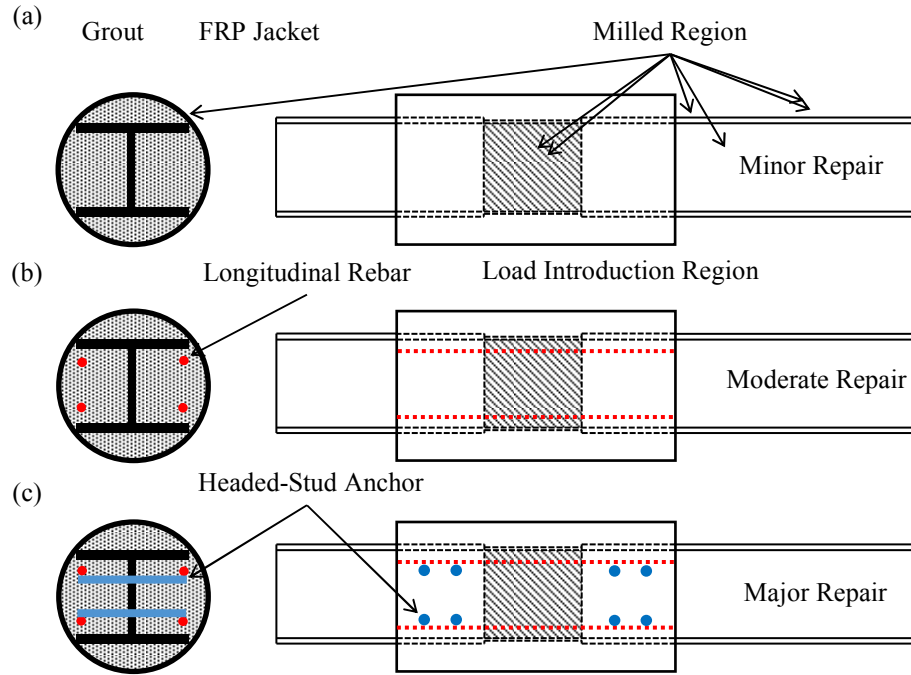


Figure 7.2: Classification of the repair systems

7.1.1. Failure Modes

Considering the FRP-confined grout system described above and using the design approach explained earlier, six possible strength-based failure modes for the repaired piles are considered.

- **Yielding of the Steel Pile at the Un-Corroded Section**

The nominal axial capacity of un-corroded pile, $P_{n,u}$, is limited to yield capacity of the un-corroded section, $P_{y,u}$.

- **Yielding of the Steel Pile at the Corroded Section**

By restraining the corroded region, the corroded section is able to attain its yield capacity. If the yield capacity of the corroded section, $P_{y,c}$, is less than the nominal

axial capacity of un-corroded pile, $P_{n,u}$, the load must be transferred to the repair system through bond at the steel-grout interface or through mechanical anchorage.

- **Debonding at the Steel-Grout Interface**

The excess load that must be transmitted from the pile to the repair system can be transmitted across the steel-grout interface by bond or mechanical anchorage. If the amount of the axial load transferred from the pile to the grout exceeds the bond strength of the interface debonding may occur. In this case, mechanical anchors can be designed to transmit the excess load across the interface.

- **Crushing of the Grout**

The crushing capacity of the grout cylinder should be sufficient to resist the additional force that must be transmitted by the repair system.

- **Rupture of the FRP Jacket**

Lateral dilation of the grout core induces hoop stresses in the FRP jacket due to confinement. If this hoop stress exceeds the strength of the FRP material, rupture of the jacket may occur.

- **Global Buckling of the Pile**

Global buckling of the pile should be evaluated by considering the strong- and weak-axis moments of inertia at the repaired section and considering the corresponding effective lengths of the pile.

7.1.2. Design Considerations and Calculations

The objective of designing the repair system is to restore the axial capacity of corroded piles, $P_{n,c}$, to the axial capacity of the un-corroded pile, $P_{n,u}$. The amount of the load that must be restored, P_f , is defined as:

$$P_f = P_{n,u} - P_{n,c} \quad (\text{Eq. 7-1})$$

Therefore, each of the components of the system must be designed to ensure that the repair system can transmit this additional load. The recommended design provisions for each component of the system are summarized in the following sections.

7.1.2.1. FRP Jacket

The FRP jackets in the repair system primarily serve three functions: (i) act as a stay-in-place form to simplify casting of the grout core, (ii) provide confinement to prevent premature splitting of the grout core, and (iii) prevent moisture ingress which could lead to further deterioration in the repaired region. Two commercially-available FRP-based repair systems, referred to as F1 and F2, were used in this study. The number of layers, diameter, and length of the FRP jackets were determined based on the following considerations.

- Number of Layers and Diameter of the Jacket

Figure 7.3 shows the configuration of the F1 and F2 FRP jackets. As shown in Figure 7.3(a), the F1 jacket consisted of a 2-ply prefabricated flexible CFRP laminate with an un-balanced bidirectional fiber lay-up. The primary direction of the fibers was oriented in the hoop direction of the jacket. The pre-cut laminate was wrapped around the pile in a continuous spiral and bonded to itself using an underwater curing

adhesive to form a continuous thin-walled cylinder. The F2 jacket consisted of 2 FRP laminates as illustrated in Figure 7.3(b). The interior laminate was a prefabricated GFRP laminate with the fibers oriented in the hoop direction. It was fabricated as an open cylinder that was wrapped around the pile and fastened by applying an adhesive to the overlap region and fastening the overlap with self-tapping screws. The exterior laminate was a two-ply, unidirectional CFRP laminate that was installed by hand using a wet lay-up technique and an under-water curing resin.

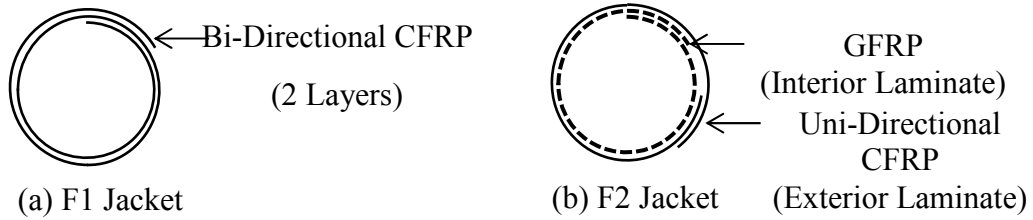


Figure 7.3: F1 and F2 jacket configurations

The minimum diameter of the FRP jacket is governed by the diagonal dimension of the cross-section of the pile. The confinement pressure, f_l , provided by an FRP jacket with a diameter of D is given by (ACI440.2R, 2008):

$$f_l = 2 \sum_{i=1}^n \frac{t_{fi} (E_{fi} \epsilon_{fe, \min})}{D} \quad (\text{Eq. 7-2})$$

where t_{fi} is the thickness and E_{fi} is the tensile modulus of the i^{th} FRP layer, $\epsilon_{fe, \min}$ is the minimum effective rupture strain at failure of all of the FRP layers, and n is the total number of FRP layers. For FRP laminates that are wrapped into a circular cylinder, the effective rupture strain can be taken as 55% of the ultimate strain of a flat laminate, ϵ_{fu} (ACI440.2R, 2008). Therefore, the confinement pressure can be written as:

$$f_l = 2 \sum_{i=1}^n \frac{t_{fi} (0.55 E_{fi} \epsilon_{fu, \min})}{D} \quad (\text{Eq. 7-3})$$

where $\epsilon_{fu, \min}$ is the minimum rupture strain of all of the FRP layers. For confining circular concrete columns, ACI committee 440 recommends a minimum confinement ratio, f_l/f_c' of 0.08 (where f_c' is the 28-day strength of the unconfined concrete) to ensure that the confined concrete exhibits a hardening behavior (ACI440.2R, 2008).

- **Length of the Jacket**

In the case of minor repairs, the grouted FRP jacket should completely encase the corroded region of the pile to restrain the slender flanges and web and to prevent local buckling. While in theory, little to no overlap onto the un-corroded portion of the pile should be necessary, for practical purposes an extension of 18 in. from each end of the corroded region is recommended to provide a moderate degree of anchorage and stress transfer in the development region. In the case of moderate repairs, the additional force, P_f , must be transferred from the steel pile to the repair system through bond at the steel-grout interface. This load transfer is provided in two load introduction regions with the length of L_d , one above and one below the corroded region as illustrated in Figure 7.4. So, the total length of the FRP jacket, L_{FRP} , is:

$$L_{FRP} = L_c + 2L_d \quad (\text{Eq. 7-4})$$

where L_c is the length of the corroded region.

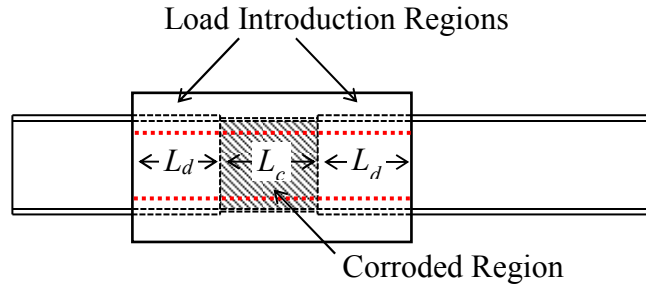


Figure 7.4: Length of the FRP jacket

Assuming a uniform distribution of shear stress at the steel-grout interface along the entire load introduction region, the length of the load introduction region, L_d can be calculated as:

$$L_d = \frac{P_f}{\tau_{\max} L_p} \quad (\text{Eq. 7-5})$$

where P_f is the force that must be transferred from the pile to the repair system, τ_{\max} , is maximum average shear stress that can be developed along the steel-grout interface, and L_p is the perimeter length of the cross section of the steel pile. The bond-slip relationships proposed by Frauenberger et al. (2003) and Liu et al. (2005) result in maximum bond strengths, of 0.49 and 0.52 ksi, respectively. For the purpose of preliminary design the maximum average shear stress that can be developed along the steel-grout interface, τ_{\max} , was taken as 0.30 ksi.

7.1.2.2. Grout

The function of the grout in the system is to (i) restrain local buckling of the corroded flanges and web, and (ii) carry part of the axial load which transferred from the pile to the repair system through the load introduction region. The axial capacity of the grout core, P_g , can be calculated as:

$$P_g = 0.85 f'_g A_g \quad (\text{Eq. 7-6})$$

where A_g is the cross-sectional area of the grout core and f'_g is the ultimate compressive strength of the unconfined grout. This capacity should exceed the force, P_f , which is required to be transferred to the repair system. Even for a moderate strength grout (3.6 ksi), the axial capacity of the grout core considering the dimensions of the piles tested in this study is 700 kip. This is 1.1 times greater than the capacity of the undamaged control pile which suggests that crushing of the grout core will not be a predominant failure mode.

7.1.2.3. Headed-Stud Anchors

If the bond at the steel-grout interface is insufficient to transfer the necessary force within an acceptable development length, mechanical anchorage can be provided to increase the force transfer in the development region. Figure 7.5 shows the configuration of the headed-stud anchors installed for the major repair configuration. The anchors were designed according to provisions for steel headed stud anchors in composite components (AISC, 2011) to transfer the load P_f from the steel pile to the repair system as:

$$Q_{nv} = F_u A_{sa} \quad (\text{Eq. 7-7})$$

where Q_{nv} is the nominal shear strength of a single stud anchor, F_u is the specified tensile strength of the anchor, and A_{sa} is the cross-sectional area of the steel headed stud anchor. For a threaded anchor rod the cross-sectional area can be calculated as (ACI318, 2014):

$$A_{sa} = \frac{\pi}{4} \left(d_a - \frac{2.4747}{n_t} \right)^2 \quad (\text{Eq. 7-8})$$

Where n_t is the number of threads per inch, and d_a is the major diameter of the threaded anchor rod. In addition, the detailing requirement for normal weight concrete should comply with the following:

$$h_a \geq 5 d_a \quad (\text{Eq. 7-9})$$

$$4d_a \leq s_1 \quad (\text{Eq. 7-10})$$

$$s_2 \leq 32d_a \quad (\text{Eq. 7-11})$$

where h_a is steel headed stud anchor shank length to the top of the stud head, s_1 and s_2 are the center-to-center spacing of steel headed stud anchors in longitudinal and transverse directions respectively (as shown in Figure 7.5). Also steel anchors should have at least 1 in. of lateral clear grout cover.

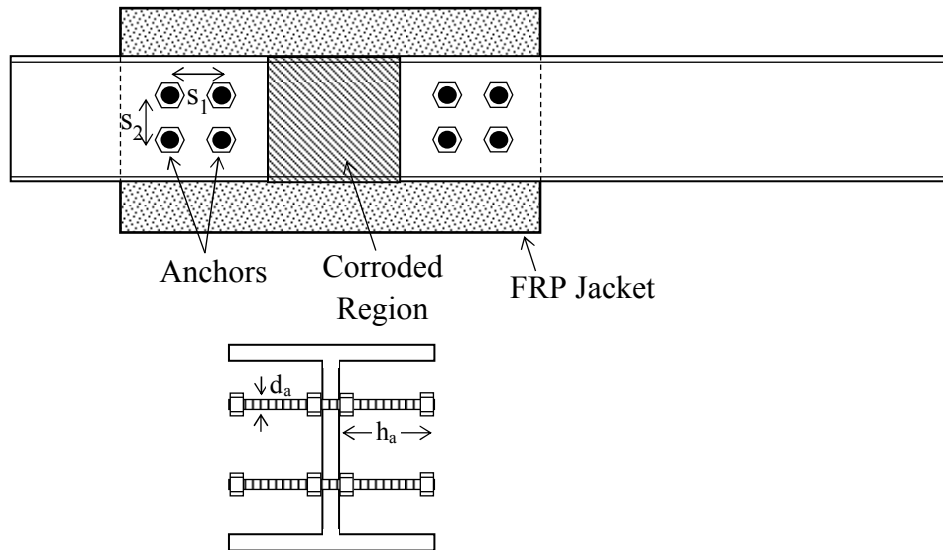


Figure 7.5: Headed-stud anchor configuration

7.1.2.4. Longitudinal Reinforcing Bars

Corrosion reduces the weak-axis bending stiffness of the pile and thus the global buckling capacity. Longitudinal reinforcing bars are provided inside the FRP jacket as shown in Figure 7.6 to compensate the loss of the weak-axis bending stiffness in case of moderate to severe corrosion.

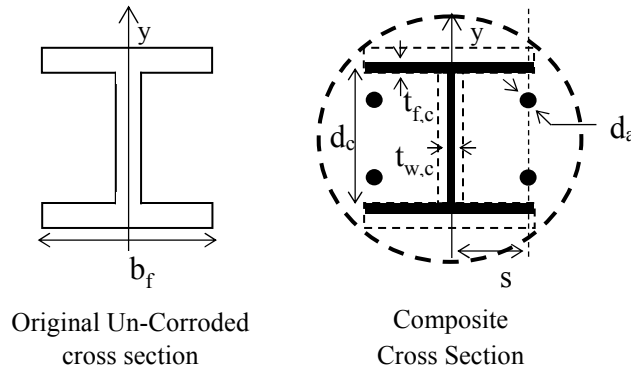


Figure 7.6. Configuration of the longitudinal reinforcing bars in the repaired pile

The diameter and locations of the longitudinal reinforcing bars should be calculated such that the weak-axis moment of inertia of the repaired cross section is greater than or equal to that of the original un-corroded steel pile. Conservatively in this calculation only the contributions of the corroded steel section and the steel reinforcing bars are considered. That is, the contribution of the grout core and the FRP jacket to the flexural stiffness of the system are neglected for the purpose of calculating the weak axis global buckling strength of the section. The bending stiffness of the repaired cross section was calculated as:

$$(E_s I_y)_{uncorroded\ pile} \leq (E_s I_y)_{corroded\ pile} + (E_s I_y)_{rebars} \quad (\text{Eq. 7-12})$$

$$(I_y)_{corroded\ pile} = 2 \frac{t_{f,c} b_f^3}{12} + \frac{d_c t_{w,c}^3}{12} \cong \frac{t_{f,c} b_f^3}{6} \quad (\text{Eq. 7-13})$$

$$(I_y)_{rebars} = 4 \left(\frac{\pi d_a^4}{64} + \frac{\pi d_a^2}{4} s^2 \right) \cong \pi d_a^2 s^2 \quad (\text{Eq. 7-14})$$

where I_y is the weak axis moment of inertia. The other geometric variables are defined as illustrated in Figure 7.6.

7.2. Design Approach for Steel-based Repair System

From the studies on corroded piles, flange reduction was found to be one of most critical factors in decreasing the remaining axial capacity of a deteriorated H-pile. This is due to the facts that (1) the flanges contribute more to the weak-axis moment of inertia of the section, (2) the flanges contribute more to the total cross-sectional area of the piles, and (3) the webs can remain non-slender even with a more significant reduction of thickness since they are stiffened by the flanges along two edges. Therefore, the repair system was designed to focus on strengthening the flanges, with no additional material attached to the web. Strengthen the flange can increase its plate buckling strength. Also, the strengthened flange contributes to the increment of the rotational fixity of the flange and web junction, which is beneficial to the plate buckling strength of the web. This section illustrates the configuration and working concept of the proposed repair system, and the design procedure of the detailed parameters of the system.

Figure 7.7 shows the configuration of the repair system. On each side of the flange, one main steel plate and two clamping plates are bolted to clamp the flange, as shown in Figure 7.7(a). Axial load is transferred to the main plates of the repair system through friction over a development length, L_d , on either end of the corroded region, as shown in Figure 7.7(b). The repair system has two contributions to the strengthening of a corroded pile. First, it stiffens the flange to enhance its plate buckling capacity. Second, the

pretension in the bolts creates friction between the main plates of the repair system and the flanges of the deteriorated pile to transfer the axial load from the pile to the steel plates. The main plates are coated with coatings that (1) can be used underwater to protect the plates from corrosion and (2) provide adequate slip resistance.

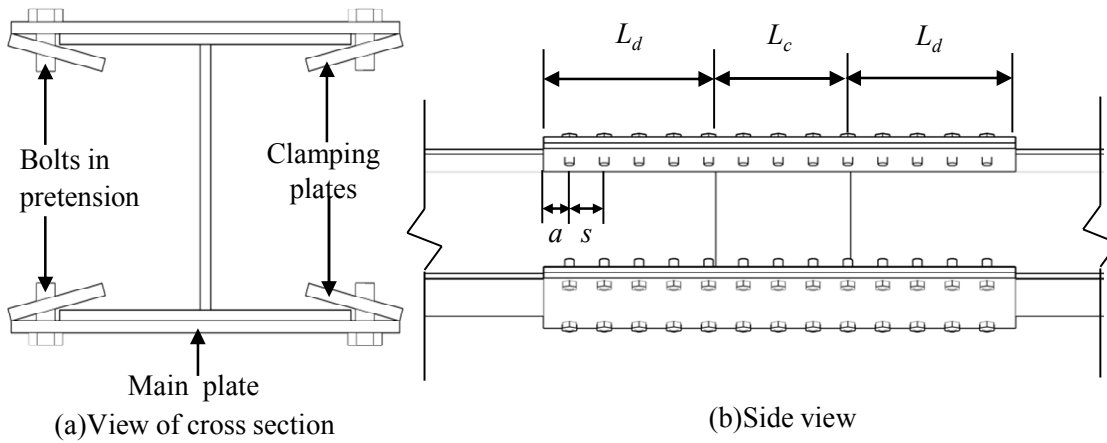


Figure 7.7: Friction-type bolted plate-based repair system

7.2.1. Failure Modes

For this repair system, the following failure modes have been identified:

- **Yielding of the Steel Pile at the Un-Corroded Section**

The nominal axial capacity of un-corroded pile, $P_{n,u}$, is limited to yield capacity of the un-corroded section, $P_{y,u}$.

- **Yielding of the Steel Pile at the Corroded Section**

By restraining the corroded region, the corroded section is able to attain its yield capacity. If the yield capacity of the corroded section, $P_{y,c}$, is less than the nominal axial capacity of un-corroded pile, $P_{n,u}$, the load must be transferred to the repair system through bond at the steel-grout interface or through mechanical anchorage.

- **Compression Yielding of the Steel Plates**

The steel strengthening plates should have a sufficient cross-sectional area so as not to yield prior to achieving the target capacity of the pile.

- **Flexural Yielding of the Steel Plates**

The thickness of the steel plates should be sufficient to prevent flexural yielding of the over-hanging portion of the repair plates due to the bending moments induced in the plates during the pretensioning of the bolts.

- **Buckling of Steel Plates**

The portion of the steel repair plates between the two parallel bolt lines is a stiffened element subjected to axial compression. Consequently, the thickness of the plate should be designed to ensure that the plates are non-slender to prevent local buckling of the repair plates.

- **Interfacial Slip**

Load is transferred between the corroded pile and the repair plates through friction at the interface between the two components. The friction force at the interface should be sufficient, in wet conditions, to prevent interfacial slip prior to achieving the retrofitting target.

7.2.2. Design Considerations

The nominal strength of the un-corroded pile, $P_{n,u}$, is the target capacity of the repaired pile, although a lower value may be considered if the demand on the structure safely permits this. The following design consideration are adopted to facilitate the design of the steel-based repair system to achieve the design target and considering the failure modes discussed above.

7.2.2.1. Determination of required friction provided by the repair system

The load that is required to be transferred to the repair system through friction, $P_{n,r}$, can be calculated as:

$$P_{n,r} = P_{n,u} - P_{n,c} \quad (\text{Eq. 7-15})$$

Conservatively, this does not take into account the enhancement of the plate buckling capacity of flanges within the repaired region.

7.2.2.2. Determination of size, number, and spacing of the bolts

Based on the required friction force, $P_{n,r}$, the size and number of bolts can be calculated according to the strength of slip-critical connection specified in AASHTO (2012). The required number of bolts, $N_{b,d}$, over each load introduction region is determined according to:

$$N_{b,d} = P_{n,r} / R_n \quad (\text{Eq. 7-16})$$

$$R_n = K_h K_s N_s P_t \quad (\text{Eq. 7-17})$$

where

R_n = Friction force provided by one bolt in a slip-critical connection;

K_h = Hole size factor (summarized in AASHTO (2012) for different hole types;

K_s = Surface condition factor;

N_s = Number of slip planes per bolt, (conservatively neglecting the contribution of the clamping plates)

P_t = Minimum required bolt pretension (summarized in AASHTO (2012) for different types and diameters of bolts)

The surface condition factor, K_s , between the new coated steel plates and the corroded pile flanges, should be determined by a coefficient of friction test. The practical surface conditions should be considered, such as the presence of corrosion product or moisture on the steel surface.

According to the minimum spacing and clear distance specified in AASHTO (2012) for each diameter of bolt, to ensure sufficient space for installation, the following should be satisfied:

$$s \geq 3d \text{ for standard holes} \quad (\text{Eq. 7-18})$$

$$s \geq 2d + d_h \text{ for oversize or slotted holes} \quad (\text{Eq. 7-19})$$

where

s = Bolt spacing

d = Bolt diameter

d_h = Hole diameter

For built-up members comprised by tightened bolts, the pitch of stitch bolts should not exceed $12t$ to ensure that the parts act as a unit and to prevent buckling in compression members:

$$s \leq 12t \quad (\text{Eq. 7-20})$$

where

t = Thickness of the thinner outside plate or shape

Because the shear distribution in bolts is not uniform and the ends of the connection take higher stress, at the ends of the repair system, the bolts spacing should satisfy:

$$s \leq 4d \text{ within a length of } 1.5b_{pl} \quad (\text{Eq. 7-21})$$

where

b_{pl} = Width of the plates

For practical purposes, the minimum edge distance, a , should satisfy the values specified in AASHTO (2012) for bolts of different diameters. Furthermore, maximum edge distances should be satisfied to prevent corrosion from accumulating on connecting members and forcing them to separate (AISC, 2011):

$$a \leq \min\{8t, 5\text{in}\} \quad (\text{Eq. 7-22})$$

7.2.2.3. Determination of width and thickness of the plates

The width and thickness of the plates are designed to ensure that the weak axis flexural rigidity of the repaired pile is greater than or equal to that of the un-corroded piles:

$$(EI_y)_c + (EI_y)_{pl} \geq (EI_y)_u \quad (\text{Eq. 7-23})$$

where

E =Elastic modulus of steel, and

$$(I_y)_c = \frac{1}{12} [2b_f t_{w,c}^3 + (h_w - 2t_{f,c}) t_{w,c}^3] \quad (\text{Eq. 7-24})$$

$$(I_y)_{pl} = \frac{1}{6} t_{pl} b_{pl}^3 \quad (\text{Eq. 7-25})$$

$$(I_y)_u = \frac{1}{12} [2b_f t_w^3 + (h_w - 2t_f) t_w^3] \quad (\text{Eq. 7-26})$$

The minimum width of the main plates should satisfy:

$$b_{pl, \min} = b_f + 2a + d_h \quad (\text{Eq. 7-27})$$

where the geometric parameters are defined in Figure 7.8.

The thickness of the plates, t_{pl} , is designed to ensure that the plate satisfied the non-slender element requirements in AASHTO (2012):

$$t_{pl} \geq 0.714(b_{pl} - 2a)\sqrt{\frac{F_y}{E}} \quad (\text{Eq. 7-28})$$

Further, to ensure that the plate does not yield in flexure due to tightening of the bolts, the minimum plate thickness can be calculated according to:

$$t_{pl,min} = 1.442 \times \sqrt[3]{\frac{P_t(b_{pl} - b_f - 2a - d_h)}{F_y s}} \quad (\text{Eq. 7-29})$$

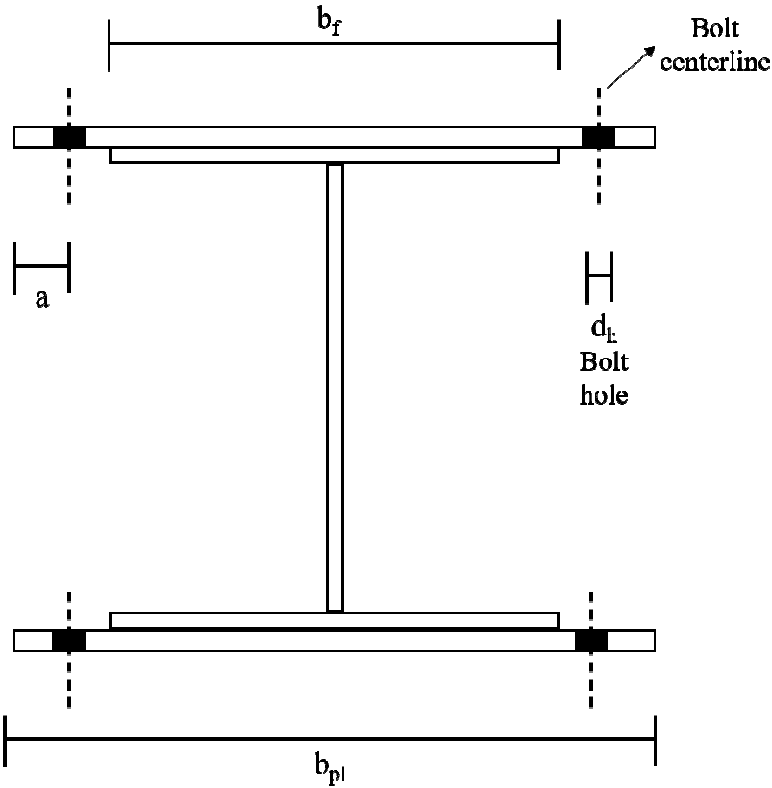


Figure 7.8. Cross section of repaired pile (clamping plates not shown for clarity)

7.2.2.4. Determination of length of the plates

The development length of the plates, L_d , at one end of the corroded region can be calculated based on the required number and spacing of the bolts, as shown in Figure 7.7.

$$L_d = (P_{n,r} / R_n - 1) \times s + a \quad (\text{Eq. 7-30})$$

The total length of the plates is determined by:

$$L_{pl} = 2 L_d + L_c \quad (\text{Eq. 7-31})$$

Chapter 8. Experimental Evaluation of Repaired Full-scale Steel H-Piles

This chapter presents the details of an experimental program that was conducted to evaluate the behavior of corroded steel piles that are repaired with FRP-based and steel-based repair systems. The details of the experimental program are summarized. The experimental results are presented, compared and discussed. The repair systems were designed according to the guidelines that were presented in the previous chapter.

8.1. Grouted FRP-Jacket Repair System

The following sections summarize the details of the experimental program that was conducted to evaluate the behavior of corroded steel piles that were repaired with grouted FRP jackets. The materials used, fabrication of the test piles, fabrication and installation of the repair system, test setup, and instrumentation are presented.

8.1.1. Materials

The following sections summarize the mechanical properties of the FRP jackets, grout, headed stud anchors, longitudinal reinforcing bars, and steel piles that were used in this portion of the experimental program.

8.1.1.1. FRP Jackets

Two types of FRP jackets were considered in the experimental program, F1 and F2. Table 8.1 summarizes the nominal material properties of the F1 and F2 jacket as reported by the manufacturers. F1-CFRP is a bidirectional laminate with the 0-deg direction installed in hoop direction of the jacket. F2-CFRP and F2-GFRP are

unidirectional laminae with the main fibers installed in hoop direction of the jacket. According to (ACI440.2R, 2008), the minimum confinement ratio is defined as:

$$f_l/f_g' \geq 0.08 \quad (\text{Eq. 8-1})$$

where f_l and f_g' are FRP confinement pressure and ultimate compressive strength of the unconfined grout, respectively. Using the properties as reported by manufacturers, an average grout compressive strength, f_g' , of 6 ksi, and a jacket diameter, D , of 17 in., the confinement ratio for F1 and F2 jackets are 0.060 and 0.088, respectively. This indicates that F1 jacketing system does not satisfy the minimum confinement ratio, which could be addressed by providing one additional layer of CFRP.

Table 8.1: Properties of the FRP Material used for F1 (PileMedic LLC) and F2 (Fyfe Co. LLC) Repair Systems as Reported by the Manufacturers

FRP System	Fiber Type	Thickness	Fiber Direction	E_f	f_{fu}	ϵ_{fu}	Fiber Volume Fraction	Fiber Density	Aerial Weight of Fabrics
		(in)		(ksi)	(ksi)	(in/in)	(%)	(lb/in ³)	(lb/in ²)
F1	Carbon	0.028	0-deg	7149	101	0.0085	N/A ^a	N/A ^a	N/A ^a
			90-deg	2944	64	0.0142			
F2	Carbon (exterior layer)	0.039	0-deg	12340	142	0.012	N/A ^a	0.063	9.016
	Glass (interior layer)	0.051	0-deg	3785	83	0.022	33	0.092	12.810

^a Not reported; E_f : tensile elastic modulus, f_{fu} : ultimate tensile strength, ϵ_{fu} : strain at ultimate strength

Table 8.2 shows the properties of the underwater-curing epoxies that were used for the F1 and F2 repair systems as reported by the manufacturers. Both epoxies had two components, resin and hardener.

Table 8.2: Properties of the Adhesive used for F1 (QuakeWrap LLC) and F2 (Fyfe Co. LLC) Repair Systems as Reported by the Manufacturers

FRP System	Underwater Adhesive	Curing Time (hour)	Compressive Strength (ksi)	Tensile Strength (ksi)
F1	QuakeBond UR220	12	11.70	5.60
F2	Tyfo SW-1	8-10	7-8	N/A ^a

^aNot reported

8.1.1.2. Grout

Table 8.3 summarizes the compressive strength and elastic modulus obtained from testing 4 in.×8 in. grout cylinders after 28 days according to (ASTM C39 and C469, 2014). The shortening of the cylinders was measured using a 5-in averaging extensometer.

Table 8.3: Properties of the Grout used for the Repair Systems

Repair System	Un-Repaired Pile Designation	Compressive Modulus (E_g) (ksi)	Ultimate Strength (f_g') (ksi)
F1	0/20	3625	6.13
	40/20	3480	6.34
	40/60	3915	6.44
	80/60	3915	4.81
	80/60*	3480	5.39
	80/60/V	4060	5.10
	80/60/3	3625	4.81
F2	0/20	4060	6.71
	40/20	4495	7.26
	40/60	4205	7.06
	80/60	4205	7.25
	80/60*	4060	5.16
	80/60/V	4640	7.38
	80/60/3	4205	5.76

8.1.1.3. Headed-Stud Anchors

The headed-stud anchors were made using 1 in. diameter threaded rods with a nominal tensile strength of $F_u = 125$ ksi and heavy duty nuts that were bonded to the threaded rods using a fast setting epoxy (thread lock).

8.1.1.4. Longitudinal Reinforcing Bars

Table 8.4 presents the properties of the longitudinal reinforcing bars that were used for the retrofitting systems. The average, standard deviation, and coefficient of variation of the measured values are also presented in Table 8.4. The reinforcing bars were tested according to (ASTM706-14, 2014). Both #6 and #8 reinforcing bars were used in the research and tested

Table 8.4: Properties of the longitudinal reinforcing bars used for the repair systems

Reinforcing Bar	Nominal Diameter	Tensile Modulus (E_s)	Yield Stress (f_{sy})	Ultimate Stress (f_{su})	Strain at Ultimate Stress (ϵ_{su})
	(in)	(ksi)	(ksi)	(ksi)	(in/in)
#6-1	0.75	28700	69.5	105	0.123
#6-2	0.75	31300	70.5	109	N/A ^a
#6-3	0.75	29400	69.5	104	N/A ^a
#6-4	0.75	30300	67.5	105	N/A ^a
#6-5	0.75	29900	66.6	104	0.121
Mean	0.75	29900	68.7	105.50	0.122
STDV		873	1.45	1.71	0.001
COV		0.03	0.02	0.02	0.008
#8-1	1.00	34400	61.5	90.0	0.125
#8-2	1.00	29700	61.0	90.2	0.13
#8-3	1.00	33500	62.9	94.0	0.117
Mean	1.00	32500	61.8	91.4	0.124
STDV		2010	0.81	1.81	0.005
COV		0.06	0.01	0.02	0.043

^a Test was terminated before rupture of the bar.

8.1.1.5. Steel Piles

The steel piles that were tested in this stage of the research were taken from the same batch as those used for the full-scale corroded pile tests (Chapter 4). The material properties of the piles were reported in detail previously and are summarized in Table 8.5.

Table 8.5: Material properties of steel piles

Location of Coupons	Tensile Modulus (E_s) (ksi)	Yield Stress (f_{sy}) (ksi)	Ultimate Stress (f_{su}) (ksi)	Strain at Ultimate Stress (ϵ_{su}) (in/in)
Flange	28420	52.2	66.6	0.1742
Web	32045	60.6	71.2	0.0797

nominal material properties of the steel pile: $E_s=29000$ ksi, $f_{sy}=50$ ksi, $f_{su}=65$ ksi

8.1.2. Details and Construction of the Retrofitted Piles

A total of fourteen deteriorated HP12×53 piles were tested under axial compression. The piles were tested in two groups of seven, each group being repaired using a different FRP-based repair system denoted F1 and F2. The deterioration patterns were selected to be the same as those used for the un-repaired, corroded control piles.

8.1.2.1. Deteriorated Steel Piles

The corrosion patterns for the tested piles were created by milling the thickness of flanges and web to a certain level to increase the slenderness of these elements and make them susceptible to local buckling. Figure 8.1 presents a schematic of the corroded regions for the tested piles. The length of the piles was 15 ft., and the centroid of the corroded region was located at 5 ft. from one end of the piles. Three levels of nominal reduction of the flange thickness were considered: 0%, 40%, and

80%. The thickness of the web was reduced symmetrically by either 20% or 60%. One pile in each group had a 2 in. through-web void as illustrated in Figure 8.1. The extent of the corroded region, L_c , was 12 in. for six of the piles while one pile in each group had a 36 in. extent of the corroded region, L_c .

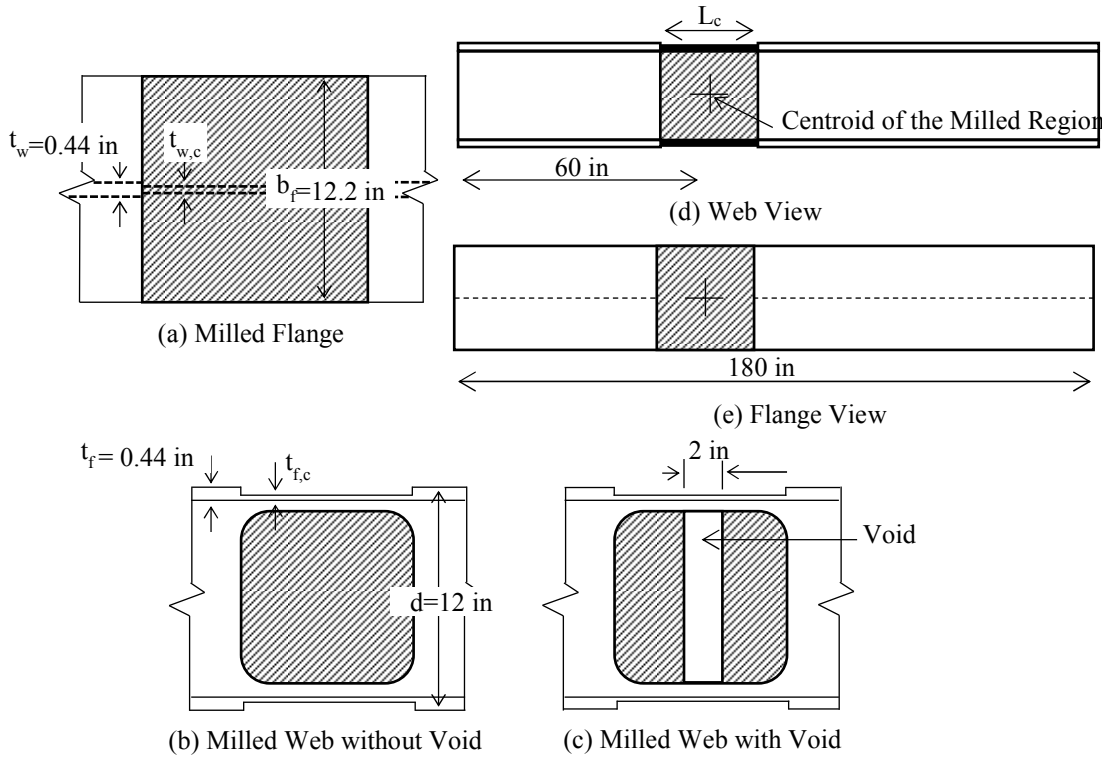


Figure 8.1: Schematic drawing of the location and geometry of the milled region

Table 8.6 summarizes the measured flange and web thickness, $t_{f,c}$ and $t_{w,c}$, within the milled region of the corroded piles that were repaired with the F1 and F2 systems. The table also presents the calculated area, $A_{s,c}$, and weak-axis moment of inertia, $I_{y,c}$, of the milled section for each pile. The same specimen designation method was used to identify the piles as was used for the corroded, un-repaired control piles. A two or three-part identifier was used. The first two parts represent nominal percentage reduction of the flange and web thickness, respectively. The third part, if present, shows either the

existence of 2 in. void in the web, “V”, or a 36 in. extent of the milled region, “3”. There were two piles of the 80/60 configuration tested in each group which are identified by a serial number in parentheses in the identifier. The details of the repair system are add to the designations subsequently in this chapter.

Table 8.6: Measured Geometry and Designations of the Repaired H-piles at Milled Section

Repair System	Un-Repaired Pile Designation	$t_{f,c}$	$t_{w,c}$	$A_{s,c}$	$I_{y,c}$	L_c
		(in)	(in)	(in ²)	(in ⁴)	(in)
F1	0/20	0.44	0.33	14.32	130.46	12
	40/20	0.30	0.35	10.97	87.38	12
	40/60	0.29	0.19	9.18	86.75	12
	80/60(1)	0.12	0.20	5.11	34.76	12
	80/60(2)	0.12	0.18	4.95	36.25	12
	80/60/V	0.12	0.18	4.98	36.25	12
	80/60/3	0.13	0.17	4.94	37.74	36
F2	0/20	0.44	0.35	14.50	130.36	12
	40/20	0.29	0.35	10.93	86.13	12
	40/60	0.30	0.22	9.53	87.48	12
	80/60(1)	0.13	0.20	5.44	39.93	12
	80/60(2)	0.13	0.18	5.00	36.88	12
	80/60/V	0.12	0.21	5.37	36.85	12
	80/60/3	0.14	0.22	5.87	41.85	36

The remaining axial capacities of the corroded piles before installation of the repair systems were calculated using two different methods, the AISI-EWM and a non-linear finite element analysis. Using the AISI-EWM the capacity was calculated once using measured geometry and nominal material properties and another time using measured geometry and measured material properties. The approach using nominal material

properties was adopted as being representative of the case when the design engineer does not have more detailed information about the in-situ material properties, such as a material testing report, which may not be available for older in-service structures. The finite element model presented in Chapter 5 was adopted for the FEA predictions. Table 8.7 summarizes the predicted capacities of the corroded piles, $P_{n,c}$.

Table 8.7: Prediction of the Remaining Nominal Axial Capacity, $P_{n,c}$, of the Deteriorated Piles

Repair System	Un-repaired Pile Designation	Nominal Axial Capacity of Corroded Piles ($P_{n,c}$)		
		FEA	AISI-EWM ^a	AISI-EWM ^b
			(nominal)	(actual)
			(kip)	(kip)
F1	0/20	575	552	567
	40/20	477	407	414
	40/60	382	349	355
	80/60(1)	177	136	137
	80/60(2)	159	128	129
	80/60/V	75	117	120
	80/60/3	132	126	127
F2	0/20	577	557	571
	40/20	462	400	410
	40/60	422	362	371
	80/60(1)	186	147	151
	80/60(2)	160	129	131
	80/60/V	78	120	123
	80/60/3	177	162	168
^a using measured geometry and nominal material properties,				
^b using measured geometry and measured material properties				

8.1.2.2. Fabrication and Installation of the Repair Systems

The installation of the repair system was implemented in a 5ft.-7 in. deep steel tank to simulate as closely as possible an on-site repair application. The repairs were conducted in five steps as summarized below: (i) preparation and installation of the end-caps, (ii) preparation and installation of the reinforcing bars and anchors, (iii) submerging the corroded piles in water, (iv) installation of the FRP jackets, and (v) casting grout.

- **Preparation and Installation of End-Caps**

Figure 8.2 shows the installation of the end caps at the base of the piles. The end-caps were made of 20in. \times 10 in. plywood boards. The thicknesses of the plywood boards were 0.75 and 1.5 in. for the piles with 12 and 36 in. long corroded regions, respectively. The shape of the H-pile cross section was cut out of the end caps to ensure a tight fit between the piles and the end caps. The plywood end caps were reinforced with light gauge steel angles that were screwed to one side of the boards as shown in Figure 8.2(a). The boards were subsequently mounted to the piles and care was taken to ensure that the end caps were installed perpendicular to the pile's longitudinal axis (see Figure 8.2(b)). Finally, the end-caps were clamped to the piles using four heavy-duty C-clamps as shown in Figure 8.2(a). Figure 8.2(c) shows the silicone rubber sealant that was used to fill the voids between the end-cap and the steel pile.

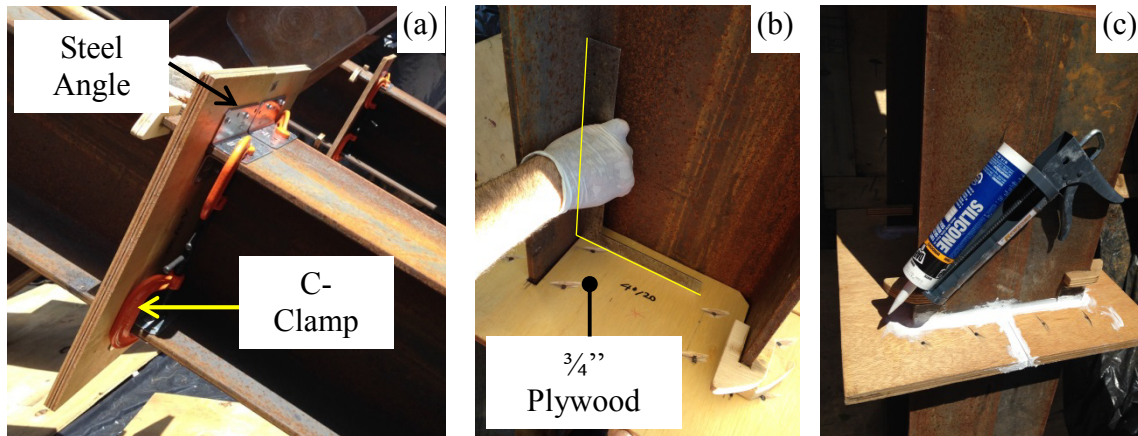


Figure 8.2: Installation of end-caps

- **Preparation and Installation of Reinforcing Bars and Anchors**

Figure 8.3 shows the installed reinforcing bars on the piles with and without anchors. Longitudinal reinforcing bars were installed for the piles with 40 or 80% reduction of the flange thickness. The #6 and #8 reinforcing bars were held in place using tie wires that were wrapped around the reinforcing bars, piles, and anchors as indicated by the arrows in Figure 8.3(a) and (b).

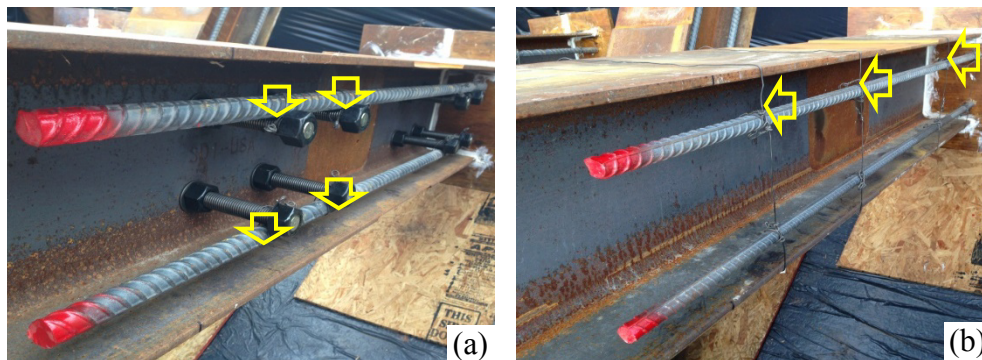


Figure 8.3: Installation of reinforcing bars

The anchors consisted of 12 in. long, 1 in. diameter threaded rods (UNC thread) with double heavy nuts that were used to snug tighten the anchors to the web of the piles and to provide a head similar to that of a headed anchor. Figure 8.4(a) shows the partially

assembled anchors. Anchors were installed on the three piles with the most severe loss of section in each group, 80/60(2), 80/60/V, and 80/60/3. Eight 1-1/16 in. diameter holes were drilled in the web of each pile using a magnetic drill as shown in Figure 8.4(b), four above and four below the milled region. In an underwater application this can be achieved using a pneumatic drill. Figure 8.4(c) shows the installed anchors.

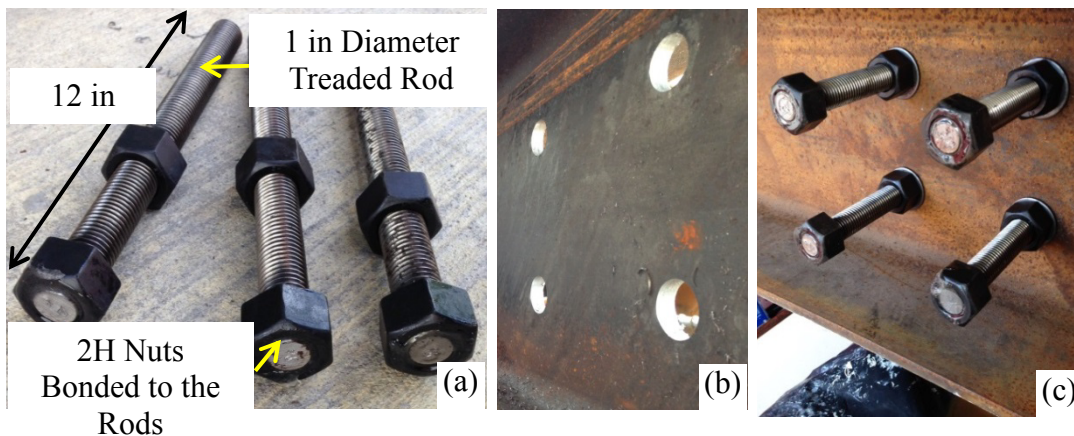


Figure 8.4: Installation of headed-stud anchor

- **Submerging the Corroded Piles**

Figure 8.5: shows the 22 ft. \times 8 ft. \times 5 ft.-7 in. tank that was used to simulate the underwater repair process. All seven piles in each group were placed into the tank at one time. The piles rested on the edge of the tank in an inclined configuration to ensure that the milled region was submerged in water after filling the tank as shown in Figure 8.5:(a). The tanks were filled with potable municipal water after installing the end-caps, reinforcing bars, and anchors but before the jacket installation as shown in Figure 8.5:(b). The end-caps, reinforcing bars, and anchors were installed prior to filling the tank with water to simplify the lab installation process. Installing these components in a dry condition is not expected to influence the structural performance of the system.

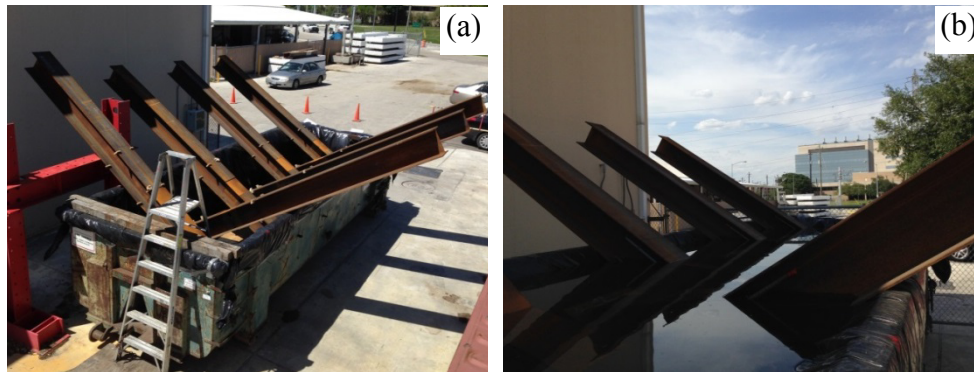


Figure 8.5: Tank used to simulate underwater repair process

- **Installation of FRP Jackets**

Before installing the FRP jackets, the repair tank was filled with water to submerge the milled region of the piles. Each group of seven piles was repaired with a different type of FRP jacket. That is, all of the piles that were repaired with the F1 jackets were submerged and repaired together and all of the piles that were repaired with the F2 jackets were submerged and repaired together.

- **Installation of F1-Type FRP Jacket**

Figure 8.6 shows the process of installing the F1-type FRP jackets. The FRP laminate for the F1 repair system was pre-cut to the desired length and shipped to the laboratory by the manufacturer. As shown in Figure 8.6(a), the laminate was hand sanded with 60 grit sand paper to roughen the surface and wiped clean with a piece cotton cloth. Figure 8.6(b) shows the application of an underwater-curing epoxy to the surface of the laminate. After applying the epoxy the laminate was immediately transferred to the tank, wrapped around the pile, and pressed against the end-cap as shown in Figure 8.6(c). A 10 ft. long laminate was wrapped completely around each pile twice (providing a jacket with two layers of CFRP) with a minimum of 8-in of overlap length at the end of the

wrap. For the piles with degradation along 12 in., of the pile in the longitudinal direction, a 48 in. long repair was implemented resulting in load introduction lengths of 18 in. above and below the corroded regions. For the pile with a 36 in. long corroded region, two 48 in. wide laminates were provided with an 18 in. overlap located at the center of the milled region resulting in a total repair length of 78 in. (see Figure 8.6(d)). The installation of the jackets on the seven piles required one day of labor by one experienced representative from the manufacturer and two graduate student assistants. The jacket installations were achieved using hand tools and minimal power tools and did not require any heavy equipment. The epoxy cured for a week before casting the grout. The jacket installation was done in May 2014 when the average temperature and relative humidity were 75°F and 65%, respectively.

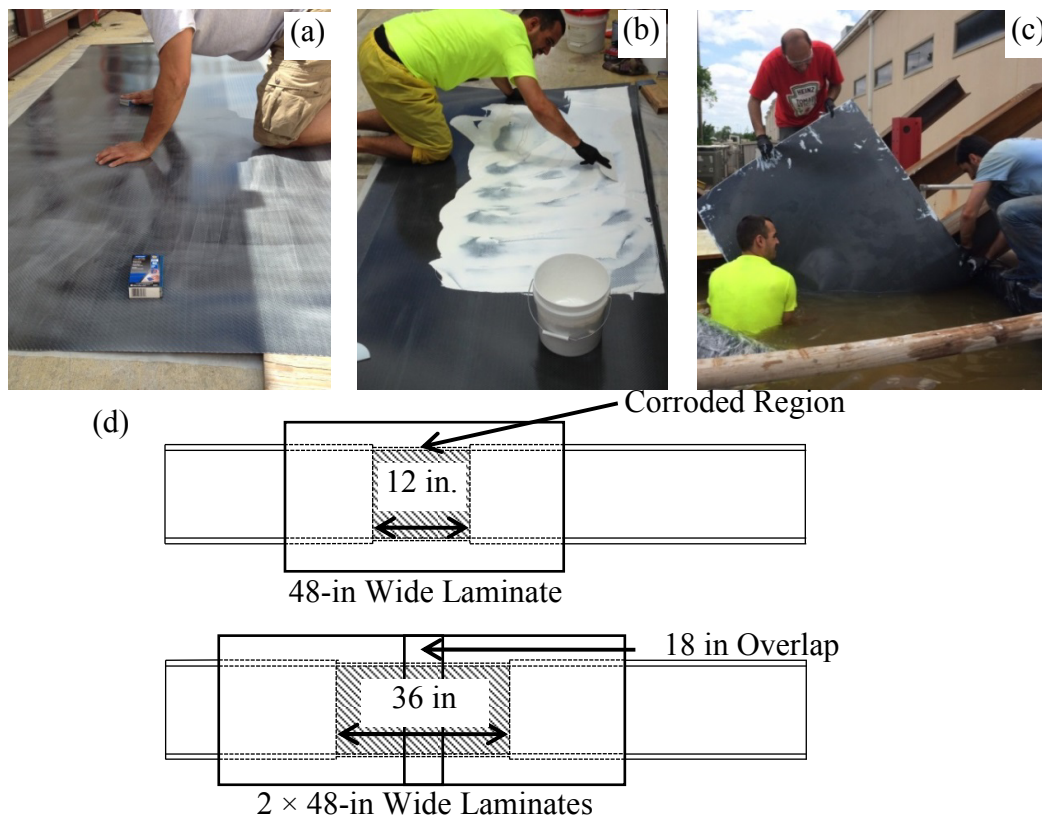


Figure 8.6: Installing FRP jacket for F1 FRP-based repair system

- **Installation of F2-Type FRP Jacket**

Figure 8.7 shows the installation of the F2-type FRP jackets. The F2 FRP jackets consisted of 2 laminates. The interior laminate was a pre-fabricated laminate that consisted of two layers of glass fiber reinforced polymers (an inner unidirectional layer with fibers oriented in the longitudinal direction of the jacket and an outer unidirectional layer with fibers oriented in the hoop direction of the jacket). The jacket, which had a nominal diameter of 18 in., had an un-bonded vertical seam that ran the entire length of the jacket which allowed it to be easily installed around the pile. As shown in Figure 8.7(a), (b), and (c), the 12 in. wide overlapping seam was sealed using self-tapping screws spaced at 6 in. on-center and an underwater curing epoxy adhesive. The exterior laminate was a wet lay-up unidirectional CFRP that was installed with the structural fibers oriented in the hoop direction. The lengths of the jackets in the longitudinal direction of the pile were 48 and 78 in. for the piles with 12 in. and 36 in. long corroded regions, respectively. As shown in Figure 8.7(d), the carbon fiber was shipped to the site in 24 in. wide rolls, and cut into 68 in. long pieces which provided one complete wrap around the pile with a 12 in. overlap. Figure 8.7(e) shows the fibers that are being impregnated with an underwater-curing epoxy. Finally, the impregnated carbon fabric was transferred to the pile and installed on the GFRP jacket as shown in Figure 8.7(f). Two layers of carbon fiber fabric were wrapped around the piles. Installation of the jackets on all seven piles was completed in three days by three experienced representatives who were sent by the manufacturer. The jacket installation was completed using basic hand and power tools and did not require any heavy equipment. The epoxy

cured for a week before casting the grout. The jacket installation was done in July 2014 when the average temperature and relative humidity were 86°F and 71%, respectively.

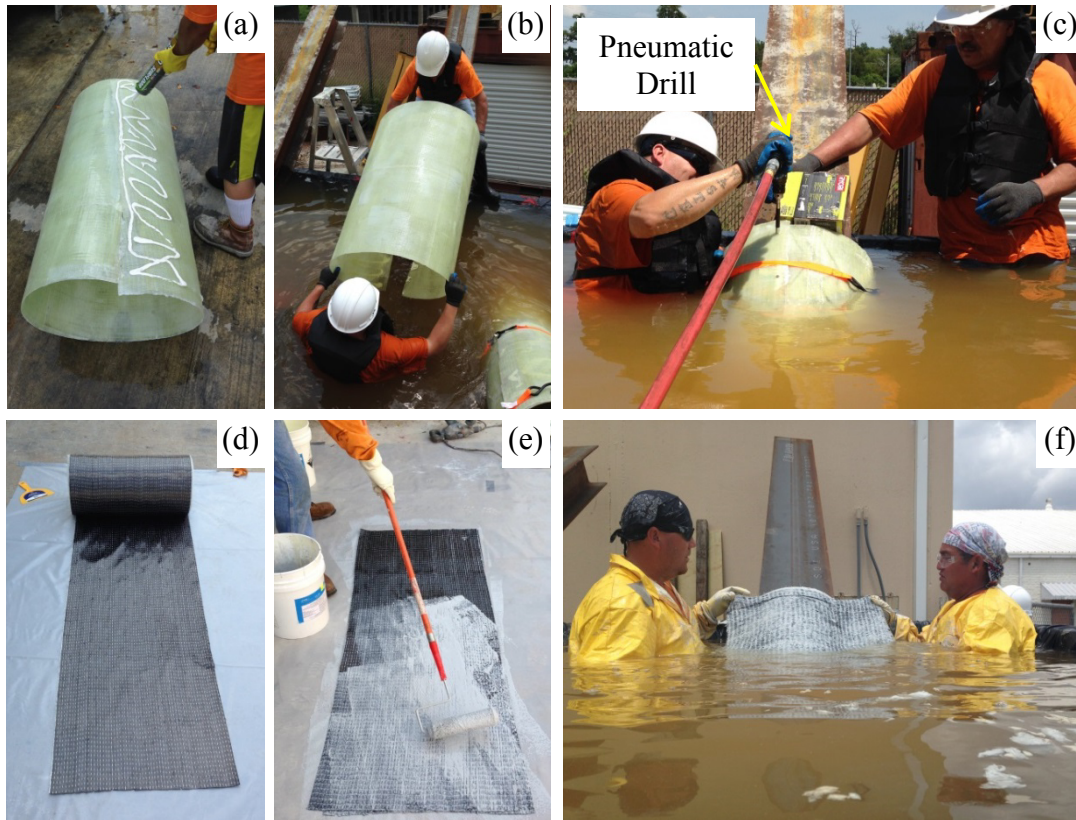


Figure 8.7: Installing FRP jacket for F2 FRP-based repair system

- **Casting Grout**

Two types of grout were used to fill the FRP jackets. The grout was cast by an independent contractor with previous experience in concrete repair and field installation of FRP. The F1 jackets were filled using an underwater curing hydraulic cement-based grout that was supplied by the jacket manufacturer as part of the repair system. The F2 jackets were filled using an expansive grout that was provided by the manufacturer but supplied by a third party. Both manufacturers indicated that any underwater curing expansive, hydraulic cement based grout could be used. Casting grout for the F1 and F2

jackets was completed in June and August 2014, respectively. The average temperature during casting grout for the F1 and F2 repair systems were 86°F and 90°F, respectively. Casting of F1 and F2 systems were achieved when the relative humidities were 73% and 70%, respectively.

Figure 8.8 shows the casting process. Grout was mixed in a bucket using a hand mixer and then poured into a grout pump as shown in Figure 8.8(a) and (b). As illustrated in Figure 8.8(c), the grout was cast using a tremie approach in which the grout hose was lowered into the bottom of the jacket and gradually extracted as the grout was cast. This was done to the extent possible within the constraints of the laboratory environment. The piles were left submerged in the repair tank for one month after casting to represent field conditions during curing of the grout in an underwater application. Testing of the first pile started at least two weeks after removing the piles from the tank and testing of the piles lasted for four months.

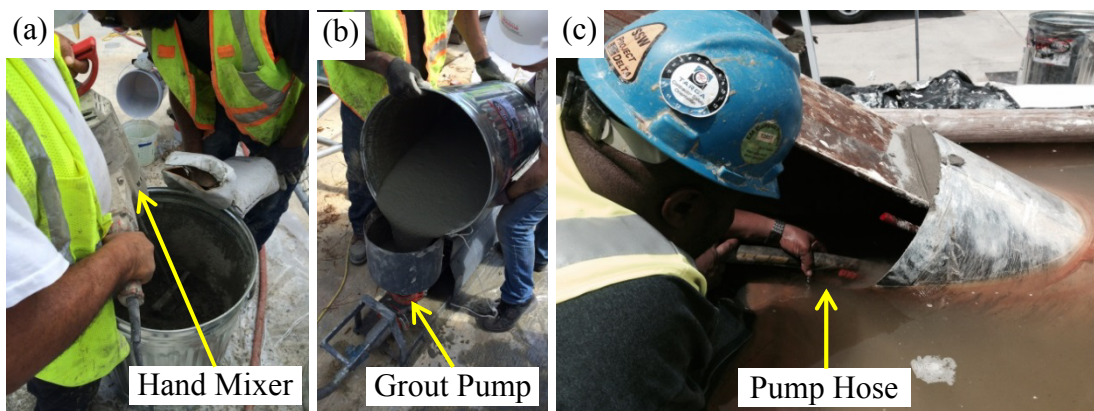


Figure 8.8: Grout casting

When grouting the F1 jackets, the available grouting hoses were too short to achieve a complete tremie installation for all of the piles. Consequently, voids were observed after removing the piles from the tanks and removing the end-caps of piles the 0/20 and 40/20

piles that were repaired with the F1 system. The presence of the voids could also be audibly detected by lightly knocking on the jackets using a blunt tapping tool. The voids were subsequently filled with the same type of grout in dry conditions after removing the piles from the water tanks. Figure 8.9(a) and (b) shows the two piles before and after filling the voids with grout. Longer pump hoses were used to cast the grout for the piles with the F2 jackets to ensure that the nozzle could be fully inserted into the jackets.

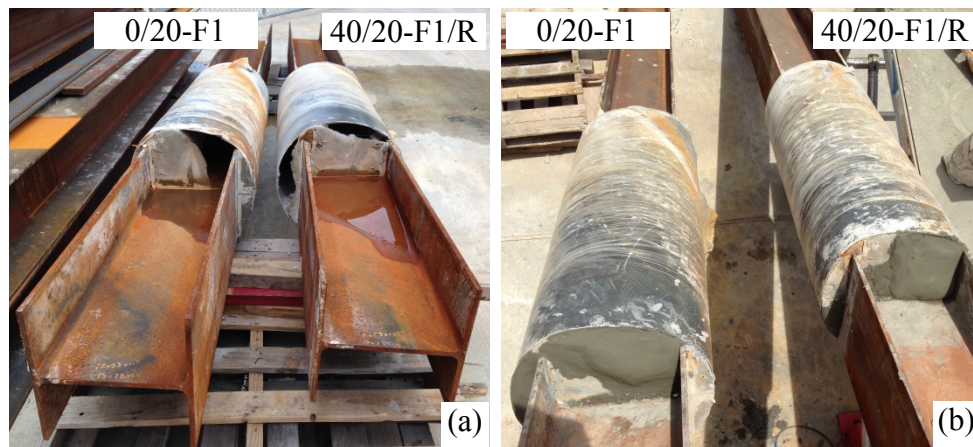


Figure 8.9: Filling the two piles with end-void

The grouting operation of the piles that were repaired using the F2 jackets required an excessive amount of grout. The process was halted after filling five of the seven jackets to inspect the seal at the bottom of the jackets. The cause of the excessive use of grout was attributed to an incomplete seal at the bottom of two of the jackets. Figure 8.10 shows the end cap of two of the piles that were repaired with F2 jackets. The photos were taken after draining the repair tank for the inspection. The inspection indicated that the jacket at the base of the 80/60/3 pile that was repaired with the F2 jacket was larger than the plywood seal allowing grout to leak out of the base as shown in Figure 8.10(a). This was due to a taper of the jacket in the as installed condition which resulted in the diameter of the jacket at the base being 1.9 in. larger than the diameter of the jacket at the

top. The pile was sealed using tape and shrink wrap before re-filling the tank and casting as shown in Figure 8.10 (b). Figure 8.10(c) shows the bottom of the 80/60(1) pile that was repaired with the F2 jacket which also exhibited an incomplete seal between the jacket and the end-cap. Careful inspection of the seals at the base of the piles prior to grouting is recommended. If possible, the base of the repair should be monitored during the grouting operation to detect leaking grout as soon as possible. In addition the volume of grout being pumped into the jacket should be monitored and compared to theoretical values to indicate if any excessive or unexpected use of grout.

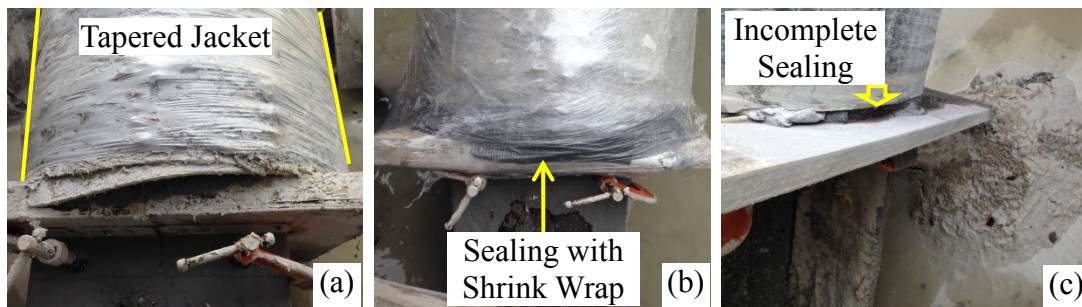


Figure 8.10: Sealing condition of the piles repaired with F2 repair system

8.1.2.3. Details of the Repair Systems as Installed

Each of the repaired piles was assigned a multi-part identifier as summarized in Figure 8.11. The first section of the identifier, before the hyphen, indicates the designation of the un-repaired pile. In this section the first two parts indicate the percentage loss of flange and web thicknesses, respectively. The presence of a through-web void, or an elongated milled region (three times longer than the basic case), is indicated by a V or a 3, respectively in the third part (if present) of the designation as shown in Figure 8.11. Multiple repetitions of the same corroded pile configuration are indicated by a serial number in parentheses before the hyphen. The

second section of the identifier is used to present the details of the repair system. It consists of three sections identifying the type of the FRP jacket (F1 or F2), presence of the longitudinal reinforcing bar (R), and presence of the headed-stud anchors (A), respectively.

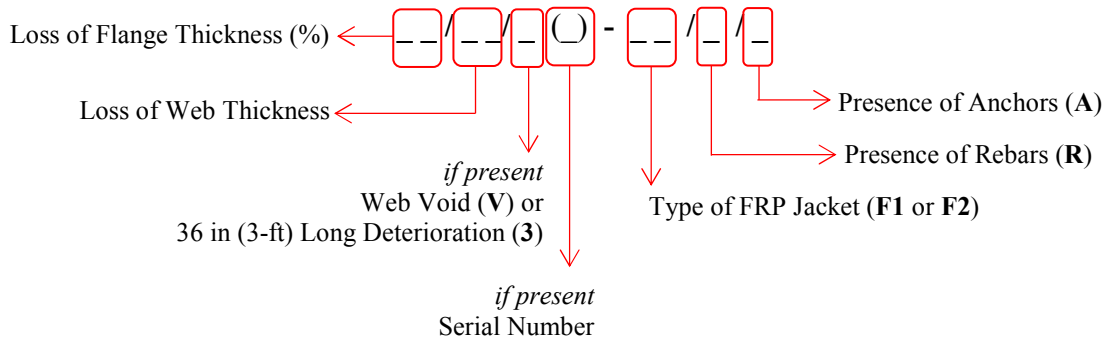


Figure 8.11: Designation of the repaired piles

Table 8.8 summarizes the geometric specifications of the F1 and F2 repair systems. As mentioned earlier, there were two piles in each group with 80% loss of the flange thickness and 60% loss of the web thickness (80/60 pile configurations). One of these in each group included headed anchors in the repair while the other in each group was repaired without anchors to investigate the effect of mechanical anchorage on the behavior of the repaired piles. Due to the fabrication process, the diameter of the bottom of the FRP jacket of the 80/60/3-F2/RA pile was 1.9 in larger than the diameter at the top of the jacket.

Table 8.8: Geometric Specification of the F1 and F2 Repair Systems

Repaired Pile Designation	Longitudinal Reinforcing bars		Headed-Stud Anchors		FRP Jacket	
	Nominal Diameter	Length	Nominal Diameter	Length	Average Diameter	Length
	(in)	(in)	(in)	(in)	(in)	(in)
0/20-F1	N/A	N/A	N/A	N/A	17.09	49
40/20-F1/R	0.75	48	N/A	N/A	17.83	49
40/60-F1/R	0.75	48	N/A	N/A	17.60	49
80/60(1)-F1/R	1	48	N/A	N/A	17.13	49
80/60(2)-F1/RA	1	48	1	12	17.64	49
80/60/V-F1/RA	1	48	1	12	16.89	49
80/60/3-F1/RA	1	78	1	12	17.28	77
0/20-F2	N/A	N/A	N/A	N/A	17.76	48
40/20-F2/R	0.75	48.0	N/A	N/A	17.76	48
40/60-F2/R	0.75	48.0	N/A	N/A	17.76	48
80/60(1)-F2/R	1	48.0	N/A	N/A	17.83	48
80/60(2)-F2/RA	1	48.0	1	12	17.80	48
80/60/V-F2/RA	1	48.0	1	12	17.68	48
80/60/3-F2/RA	1	78.0	1	12	18/19.9 ^a	80

^a tapered jacket, 18 in at the end at the top of the repair region and 19.9 in at the bottom of the repair region

8.1.3. Test Setup

The repaired piles were tested using the 600-kip self-reacting test frame that was used to test the full-scale corroded control piles. Both ends of the piles were free to rotate about their weak axes and fixed about their strong axes. The piles were loaded in a horizontal configuration at a rate of 20 kip/min up to the peak load.

8.1.4. Instrumentation

A similar instrumentation scheme was adopted for measurement of the repaired piles as that used in the measurements of the un-repaired, corroded control piles. The axial load was measured using three load cells, each with a capacity of 200 kips. The load cells were installed in a triangular configuration located behind the jack as shown in Figure 8.12(a). The axial shortening of the piles were measured by taking the average of the four linear string potentiometers that were mounted symmetrically at the four corners of the tested piles between the two end plates as shown in Figure 8.12(a) and (b). Four linear potentiometers were mounted on both ends of the grout cylinder, as shown in Figure 8.12(c), to measure the slip between the steel pile and grout cylinder. Two electrical resistance strain gauges were installed to measure the hoop strains in the FRP jacket at the center of the repair system. The gauges were installed on either side of the web as illustrated in Figure 8.12(a).

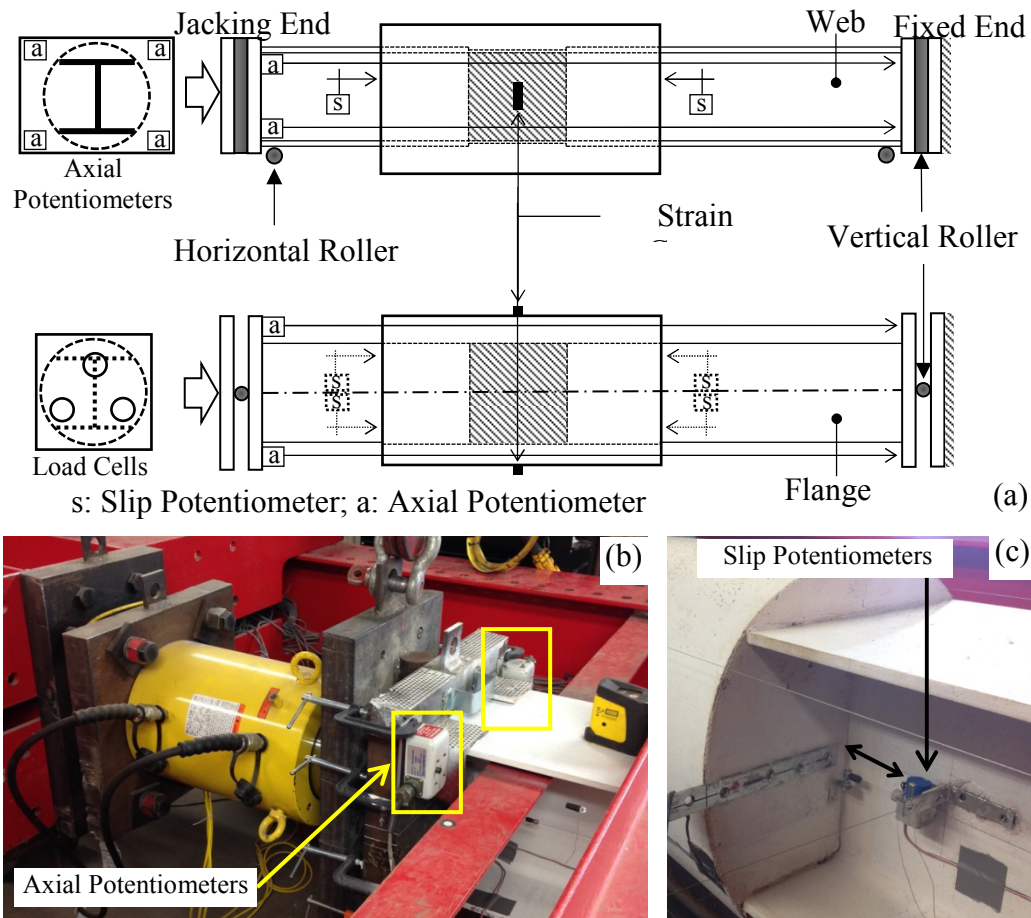


Figure 8.12: Instrumentation of repaired corroded piles

8.2. Steel Plate Based Repair System

Table 8.9 illustrates the test matrix of the repaired piles. The pile designation is defined as described previously for the un-repaired piles. The first and second numbers indicate the percentages of reduction of flange and web thickness, respectively. The third part, when included, indicate the presence of a 2 in. void in the web (V0 or corrosion along a 3 ft. extent of the pile (3) rather than along 1 ft. which was used for the other piles in the test matrix. The ‘S’ at the end of each specimen designation indicates that the piles were repaired using the steel-based repair system. Two piles, 80/60-S(1) and 80/60-S(2), were degraded and retrofitted identically to evaluate the repeatability of the tests. The remaining axial capacities

of the seven corroded piles were predicted by the numerical framework that was proposed in Chapter 6. The designed length of the steel repair plates and the number of bolts for each specimen are listed in Table 8.9. The widths of the main plates and clamping plates were designed as 16 in. and 4 in, respectively. The thickness of the plates was 0.5 in. ASTM A325 structural bolts with $\frac{3}{4}$ in. diameter were used.

Table 8.9: Test Matrix of Repaired H-piles

Pile Designation	Predicted Nominal Strength	Corroded Section		Length of Plates	Number of Bolts per line
		Flange Thickness	Web Thickness		
	$P_{n,c}$ [kips]	$t_{f,c}$ [in]	$t_{w,c}$ [in]	L_{pl} [ft]	N_b
0/20-S	587	0.431	0.362	2	7
40/20-S	475	0.289	0.318	2	7
40/60-S	418	0.289	0.207	3.5	13
80/60-S(1)	181	0.133	0.199	6.5	25
80/60-S(2)	176	0.142	0.181	6.5	25
80/60/V-S	100	0.140	0.213	7.5	29
80/60/3-S	153	0.134	0.196	7.5	29

8.2.1. Materials

The following sections present the mechanical properties of the materials that were used in this portion of the research. These sections include the properties of the steel piles and steel repair plates, and the interfacial friction of the coated steel repair plates.

8.2.1.1. Steel piles and steel repair plates

The piles from corroded control group and retrofitted group were made from the same batch, so the material properties of H-piles were determined from tension coupon tests presented in Chapter 3 and summarized previously in this chapter.

Three tension coupons were cut from the steel plates of the repair system, and tested in a 110-kip MTS machine to determine the mechanical properties of the steel that was used in the repair system. The loading rates were 0.01 in/min and 0.2 in/min in the elastic and inelastic ranges of the tests, respectively. An extensometer with a 2 in. gauge length was used to measure the axial strain. Table 8.10 presents the elastic moduli, yield strengths, ultimate strengths, and ultimate strains of the steel repair plates. The mean, STDEV, and COV of the properties are also presented.

Table 8.10: Material Properties of the Steel Repair Plates

Coupon location	Elastic modulus [ksi]	Yielding stress [ksi]	Ultimate stress [ksi]	Ultimate strain [in/in]
Plate	28,200	33.3	49.0	0.18
Plate	29,200	32.4	48.4	0.19
Plate	28,300	33.7	49.1	0.20
Mean	28,800	33.1	48.8	0.19
STDEV	640	0.66	0.37	0.01
COV	2%	2%	1%	5%

8.2.1.2. Coatings for surface of repair plates and corroded piles

The steel repair plates were sandblasted and coated with two layers of coatings to resist corrosion and to obtain adequate slip resistance. The first layer, directly applied on the steel surface, was a solvent-based, inorganic ethyl silicate, zinc-rich coating (Zinc Clad II Ethyl Silicate Product Information, 2012). The zinc in the coating was designed to serve as a sacrificial anode to protect the steel from corrosion. The second layer, which was applied on top of the first layer after it cured, was a non-zinc containing, Class B-rated, polyamide epoxy coating (Steel Spec Epoxy Primer Product Information, 2012). This coating protected the first layer of coating and provided higher slip resistance. To investigate the underwater behavior of the coatings, coefficient of friction tests were conducted.

Table 8.11 summarizes the details of the coefficient of friction tests. The double-lap type test specimens, shown schematically in the last column of the table, consisted of two main steel plates and two splice plates.

Four groups of tests were conducted. Each group had five replicate specimens. Group A was a control group with both contact surfaces abrasive blasted and tested in dry condition. Since the bolting pattern was different from the standard configuration for slip-critical connections, Group A was tested as a reference group to investigate the effects of bolting configuration. In Group B, the main plates were corroded by submerging in hydrochloric acid for several days to form a layer of surface rust on the steel plates. This was intended to simulate the condition of a steel pile which has been cleaned using hand tools and mechanical means to remove extensive pack rust, dirt,

and possible marine growth from the surface while leaving surface rust intact. The splice plates were sandblasted to simulate the surface preparation of new steel plates without any coating. All plates were wetted with water before tightening the bolts to simulate the underwater application. The splice plates in Group C were coated with two layers of coatings described above to evaluate the effect of the coatings on the coefficient of friction of the contacting surfaces. The contact surfaces were also wetted. Group D had the same configuration as Group C but had an additional epoxy-based coating applied on the main plate that can cure underwater (Armor Plate 360 Date Sheet, 2009).

Table 8.11: Test matrix of coefficient of friction

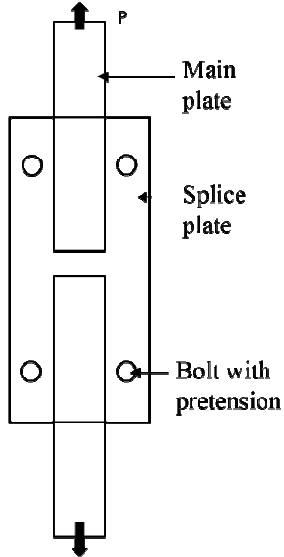
Group	Main Plate (2 in×0.5 in)	Splice Plate (6 in×0.5 in)	Surface Condition	
A	Sand blasted	Sand blasted	Dry	
B	Corroded Steel	Sand blasted	Wet	
C	Corroded Steel	Steel-Spec epoxy+ Zinc Clad II Ethyl silicate	Wet	
D	Corroded Steel+ Armor Plate 360	Steel-Spec epoxy+ Zinc Clad II Ethyl silicate	Wet	

Figure 8.13 shows the details of the tested specimens. The main plates were butted against each other with a small gap between their ends. The splice plates were centered on the main plates and clamped in place using $\frac{3}{4}$ in. diameter steel bolts that were tightened to achieve 28 kips pretension, as shown in Figure 8.13(a). The bolts were installed on either side of the main plates to simulate the clamping effect of the

repair system. A 400-kip capacity Tinius-Olsen universal testing machine was used to apply tensile load on the top main plate and the bottom main plate was fixed by clamping force from the machine. The axial tension load and the displacement of the top crosshead of the machine were recorded continuously during testing. A plateau in the load-displacement curve reflected the first slip between the faying surfaces. Figure 8.13 also shows the corroded surface of the main plates and the coated surface of the splice plates.

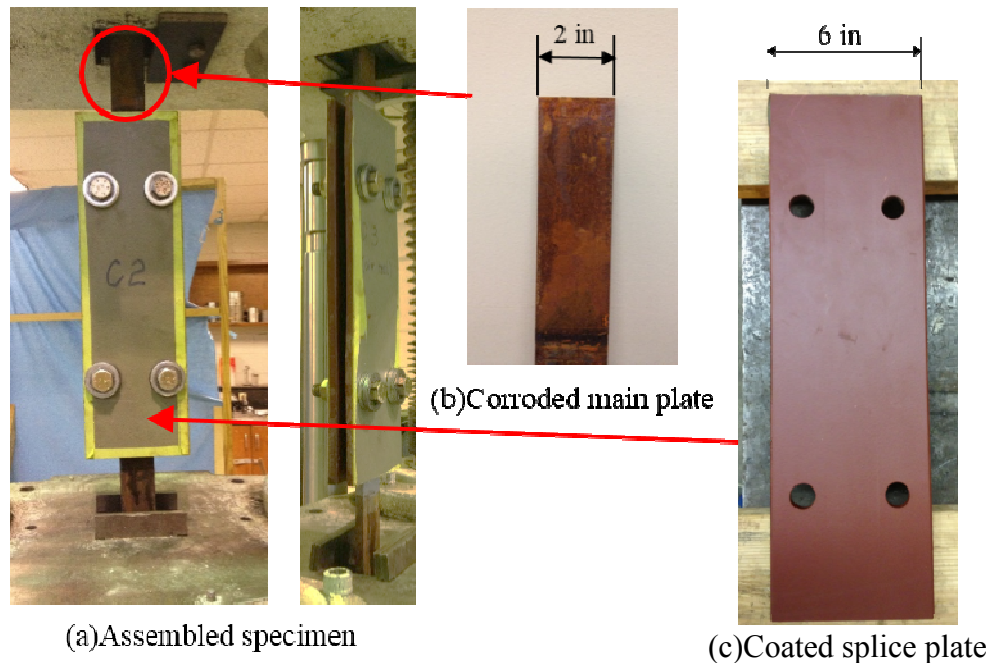


Figure 8.13: Specimen of slip resistance tests

Figure 8.14 shows the measured load-displacement relationships from each group. The figure indicates that Group A, B, and C exhibited similar behavior with a constant load plateau after the initiation of slipping as expected. However, specimens in Group D exhibited softening behavior with softening behavior after reaching the peak load. This this was attributed to the failure of the Armor plate 360 coating, as shown in the bottom right portion of Figure 8.14.

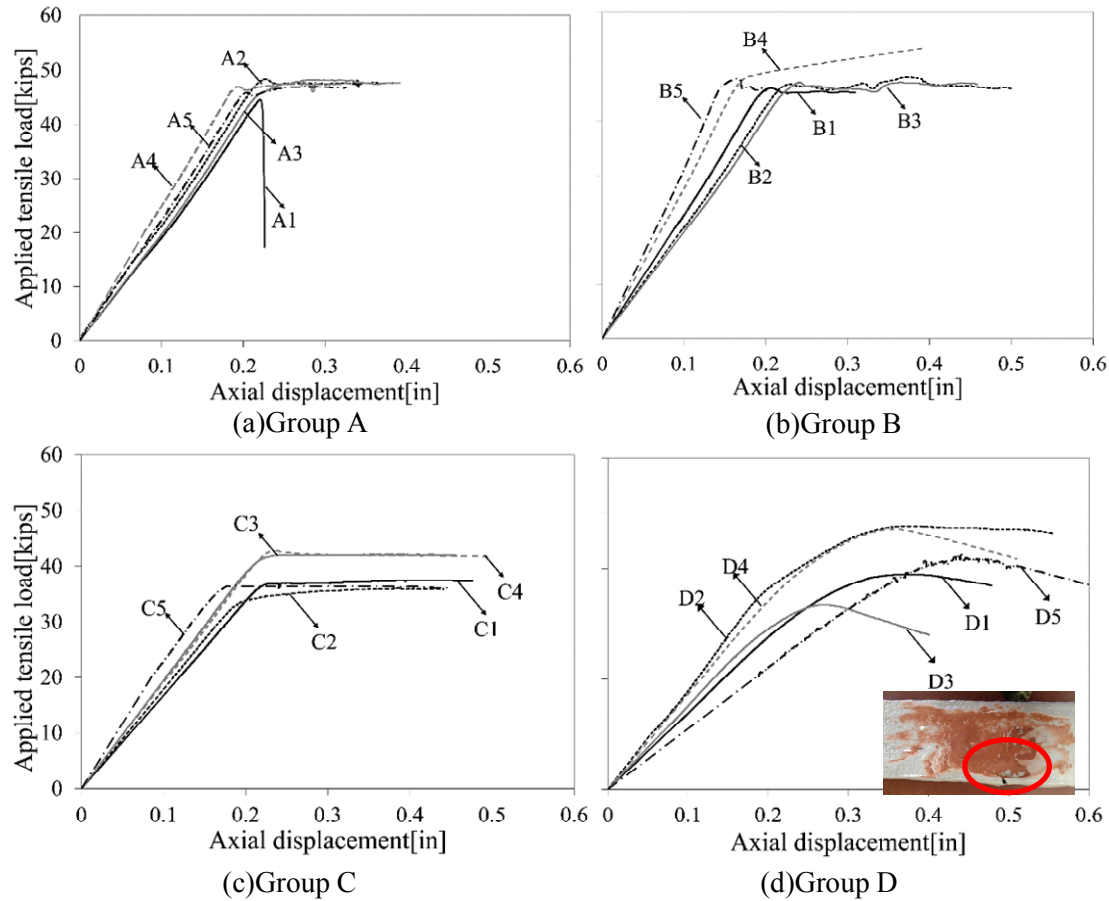


Figure 8.14: Load-slip relationships from slip resistance tests

Table 8.12 summarizes the obtained friction loads and calculated coefficient of friction of each group of specimens. The obtained friction coefficient of Group A was 0.42, which was lower than the standard value 0.5 specified in AASHTO (2012) for Class B coatings. The reason is the different bolting pattern from the standard configuration for slip-critical connections. Comparison between Group B and Group A shows the effect of surface corrosion and wet surface was negligible. The slip resistant coefficient obtained from Group C was 0.34, which was lower than the specified value in the coating data sheet. The possible reasons include the wet surfaces, surface corrosion, and the pattern of bolting. Inspection of Table 8.12 also indicates that the use of coatings increased the variability of the measured friction

force. Consequently, the mean value of coefficient of friction obtained from Group C, 0.34, was adopted for the design of the repair system of the experimental program.

Table 8.12: Experimental results of coefficient of friction test

Test Group	Friction load R_n [kips]								K_s
	1	2	3	4	5	Mean	STDEV	COV	
A	44.6	48.4	48.3	47.9	47.0	47.2	0.63	3%	0.42
B	47.5	45.5	48.2	47.2	48.0	47.3	0.96	2%	0.42
C	36.8	33.9	42.1	42.7	36.5	38.4	3.42	10%	0.34
D	38.9	47.7	33.4	47.1	42.5	41.9	5.33	14%	0.37

8.2.2. Details and Construction of the Retrofitted Piles

Figure 8.15 illustrates the sequence used in the fabrication of the repair system. First, a CNC mill was used to reduce the thickness of the flanges and webs, to simulate the corrosion effects as shown in Figure 8.15(a). The measured reduced thicknesses of the flanges and webs are summarized in Table 8.9. The steel repair plates (main plates and clamping plates) were grit blasted and coated with the two coatings by the manufacturer and allowed to cure. Water was sprayed on the original pile before placing the steel repair plates to simulate fabrication “in-the-wet”, as shown in Figure 8.15(b). All bolts were tightened using a calibrated torque wrench, as shown in Figure 8.15(d), to reach the minimum pretension for a slip-critical connection specified in AASHTO (2012), which is 28 kips for $\frac{3}{4}$ in A325 bolts. In all specimens except 40/60-S, bevel washers were used to balance the angle between the main plate and the clamping plate to keep the bolts straight, as shown in Figure 8.15(c).

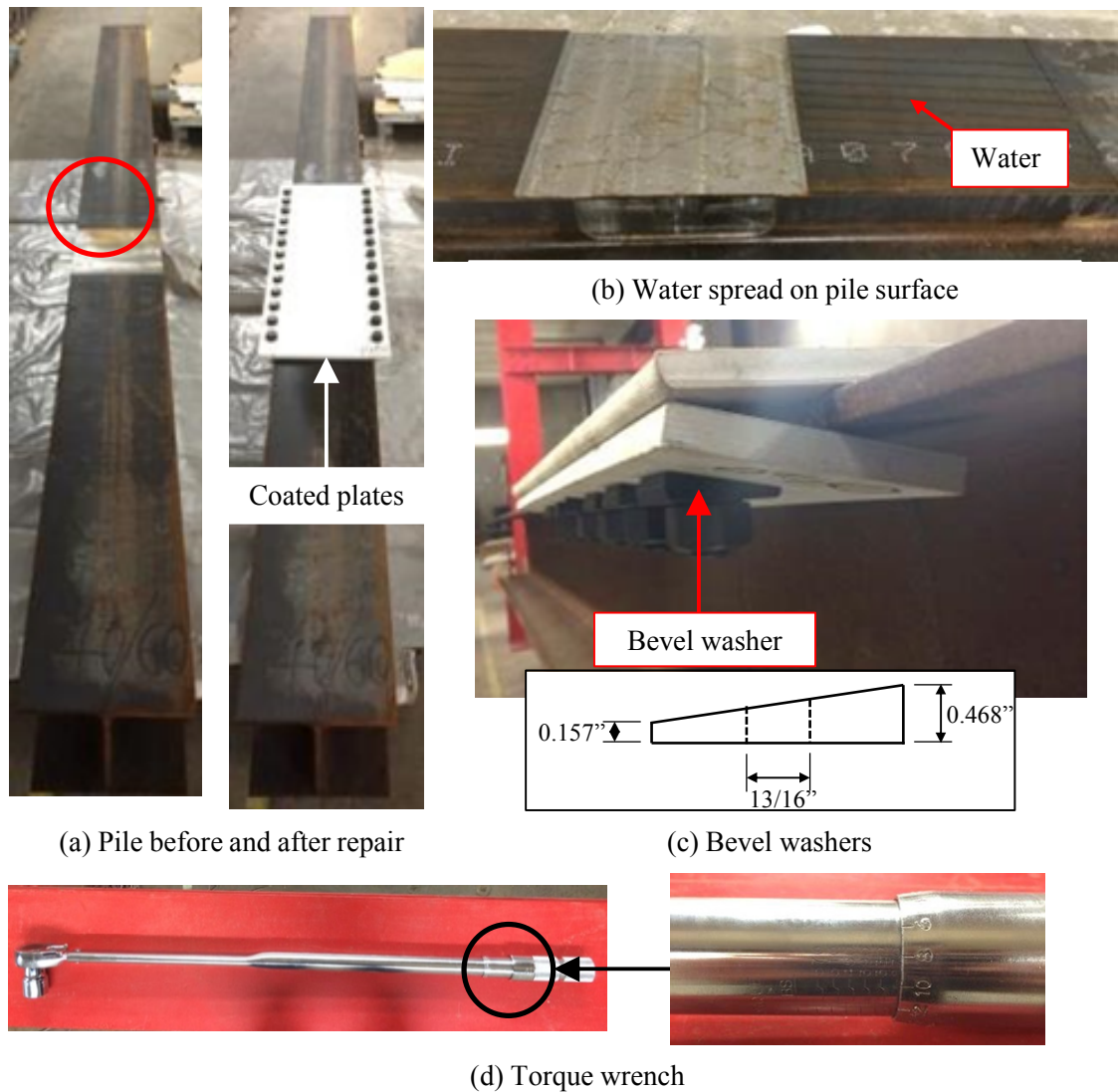


Figure 8.15: Fabrication of the repair system

8.2.3. Test setup

The 600 kip capacity self-reacting test frame that was used to test the corroded piles, was also used to test the retrofitted piles. The same boundary conditions were applied to the repaired piles: the piles were free to rotate along their weak axes, while the strong axes of the piles were restrained from rotation. The specimens were loaded manually at a rate of 20 kip/min until the peak load was achieved and the descending portion of the load-deformation curve was identified.

8.2.4. Instrumentation

Four string potentiometers were installed at the four corners of the base plate to measure axial deformation of the piles, as shown in Figure 8.16(b). Additional string potentiometers were mounted at both ends of the steel repair plates to capture the slip between the pile flanges and the steel repair plates, as shown in Figure 8.16(c). Two strain gauges were attached at the center of the top main plate and the flange of the original pile at the center of the reduced region as shown in Figure 8.16(c). The values obtained from strain gauges indicated the axial load distribution between the original pile and the repair system.

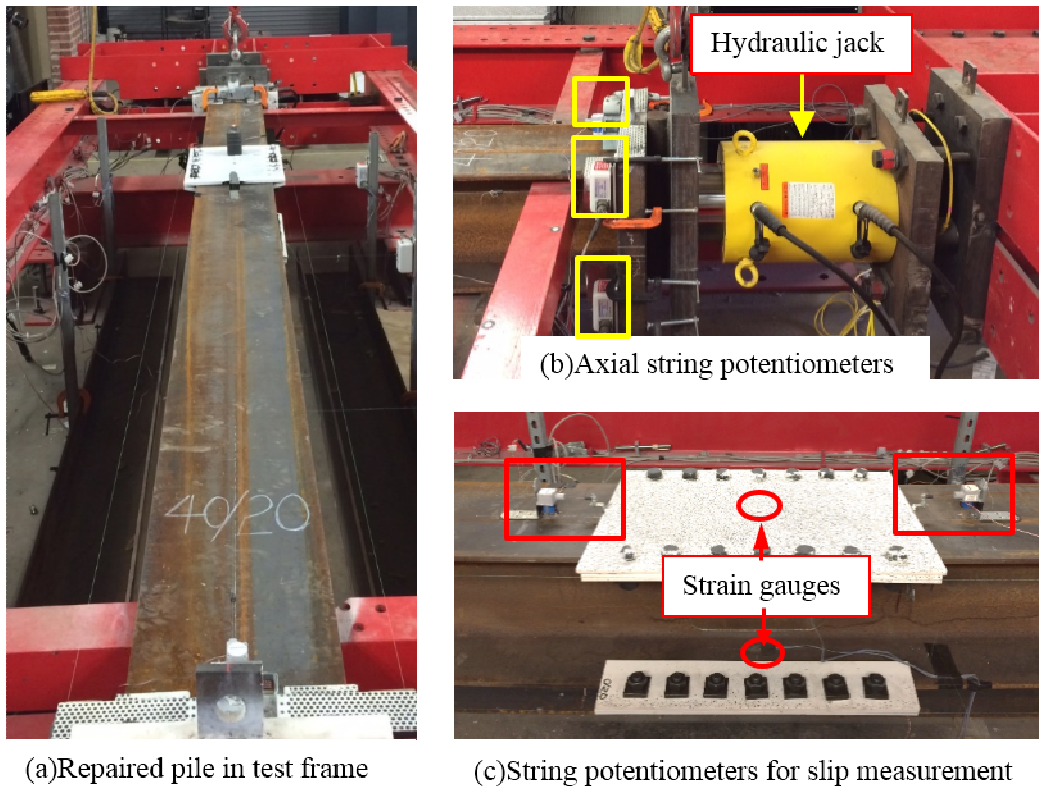


Figure 8.16: Test instrumentation used in the of the test of the repaired piles

8.3. Results for Grout-filled FRP Jacket Repair System

Two groups of seven repaired piles were tested under axial compression. The two groups of piles were repaired with two different grout-filled FRP jacket systems. In the following sections the behavior of the piles that were repaired with the two FRP repair systems are presented, discussed and compared to the corresponding corroded control piles for each of the damage levels considered in this study. The yield capacities of the corroded sections, $P_{y,c}$, that are plotted on each of the load-shortening responses for each pile group were the average values of the capacities for all of the repaired and un-repaired corroded sections in that pile group. The yield capacities were calculated based on the measured dimensions and measured material properties. The nominal axial capacity of a 15 ft. long, un-corroded HP12×53 pile, $P_{n,u}$, which is also plotted on the axial load-shortening responses, was calculated in accordance with AISC (2011) using nominal geometry and nominal material properties. The nominal axial capacity, $P_{n,u}$, is the retrofitting target.

8.3.1. Pile Group 0/20

All of the piles that were tested in this group had no simulated flange corrosion and 20% reduction of the web thickness along a 12 in. length. The piles were repaired with grout-filled FRP jackets with no reinforcing bars or anchors. Figure 8.17 compares the axial load-shortening responses of the piles in the 0/20 group. The response of the un-corroded control pile, 0/0, is also shown in the figure for comparison purposes. The figure indicates that the average yield capacity of the corroded section is higher than the measured axial capacity of the un-corroded control pile. The axial capacities of the two piles that were repaired using the two different FRP-based repair systems, $P_{n,r}$, were

greater than the axial capacity of the un-corroded control pile and approached the yield capacity of the corroded section indicating that the onset of non-linearity was imminent.

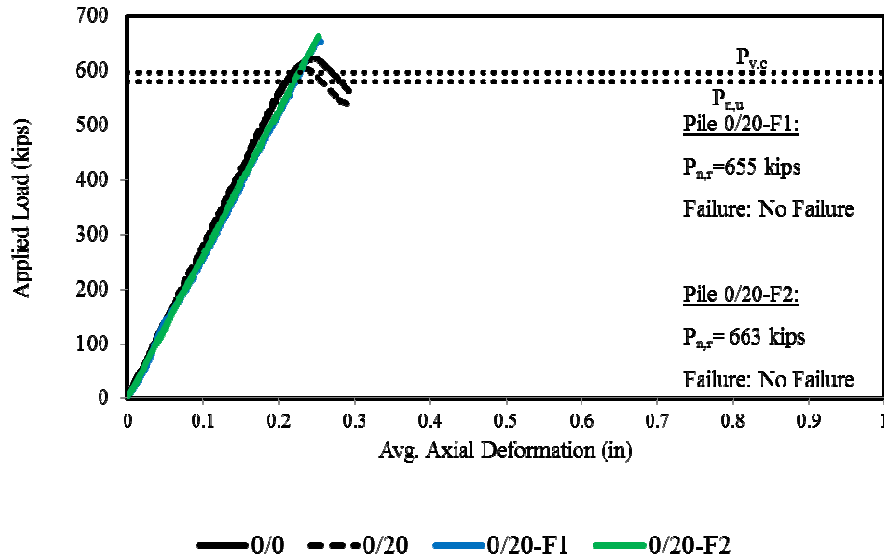


Figure 8.17: Axial load-shortening behavior of 0/20 pile group

The repaired piles were loaded up to the peak load monotonically. The axial load-shortening response of the repaired piles, shown in Figure 8.17, remained linear up to the peak load. The recorded peak axial loads for the 0/20-F1 and 0/20-F2 piles were 655 kips and 663 kips respectively. The tests were terminated when the capacity of the hydraulic loading system was reached. No non-linearity or visible sign of lateral deformation was observed. Figure 8.18 shows the repaired piles after testing. As shown Figure 8.18, no failure was observed for 0/20-F1 and 0/20-F2 piles. Before the test, the piles were examined by tapping the FRP jacket, and no air voids were identified.

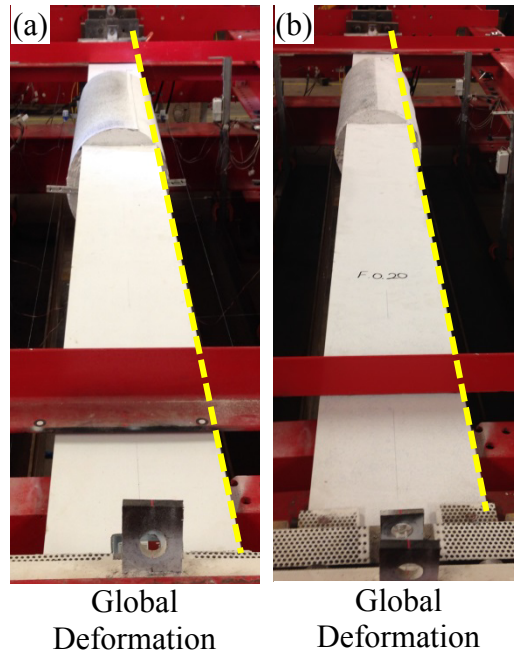


Figure 8.18: Piles 0/20 repaired with the F1 and F2 repair systems after testing

Figure 8.19 shows the axial load-slip relationship of the 0/20-F1 and 0/20-F2 piles. There are two curves for each pile, each corresponding to a slip measurement at one end of the repaired region. The dashed line indicates the measured steel-grout slip at the end of the repair that is closest to the fixed side of the pile (fixed end). The solid line shows the measured slip at the end of the repair that is closest to the loaded end of the pile (jacking end). Positive values indicate that the steel surface slipped into the grout cylinder. Both piles demonstrated comparable amounts of slip at the two ends.

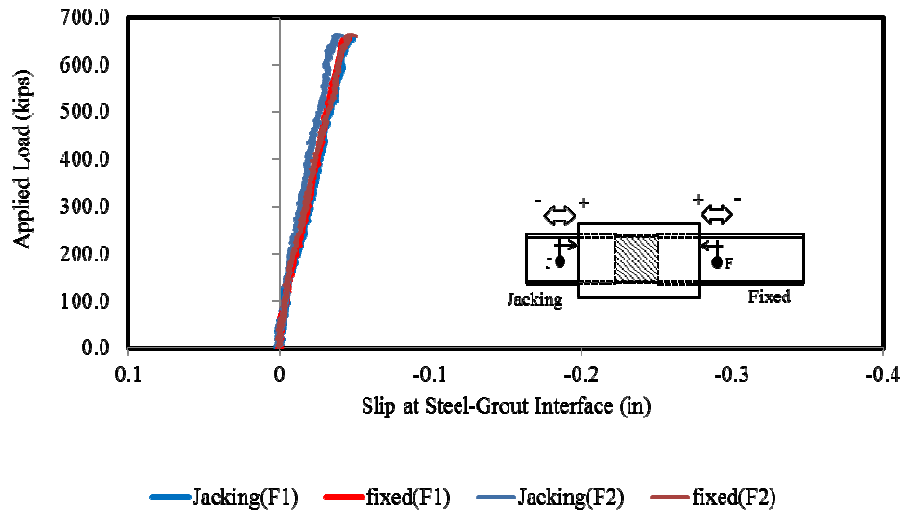


Figure 8.19: Comparing the slip at steel-grout interface of 0/20 repaired piles

Figure 8.20 shows the relationship between the axial load and the measured hoop strain in the FRP jackets for piles 0/20-F1 and 0/20-F2. For a given load level the hoop strain in the F1 jacket is slightly higher than F2 jacket. This is attributed to the lower stiffness of the F1 jacket compared to the F2 jacket. The low measured strains suggest that the grout cores remained intact throughout the test and did not exhibit significant lateral dilations that would have engaged the confinement effect of the FRP jackets.

Both FRP repair systems described in this study are patented by Professor Mo Ehsani; U.S. Patent #8,650,831 and #9,376,782

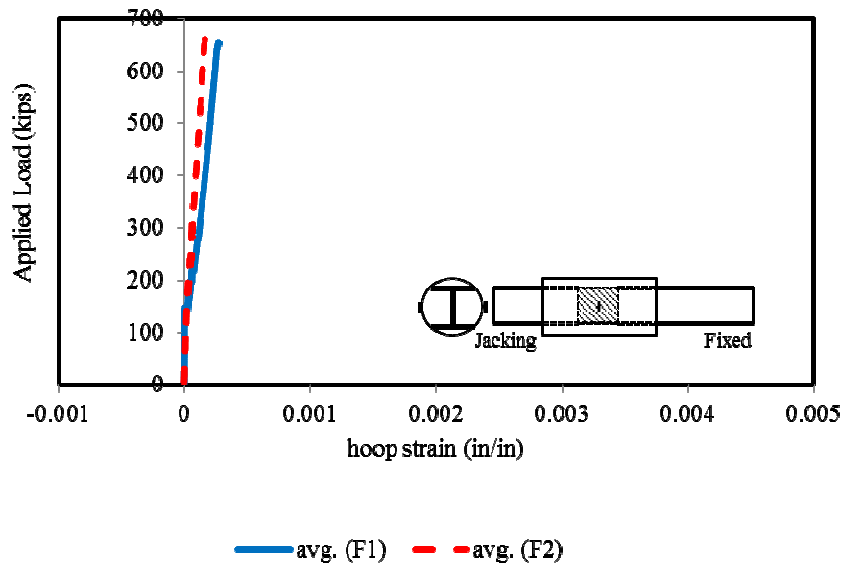


Figure 8.20: Comparing FRP hoop strain of 0/20 repaired piles

8.3.2. Pile Group 40/20

All of the piles that were tested in this group had 40% reduction of the flange thickness and 20% reduction of the web thickness along a 12 in. length. The piles were repaired with grout-filled FRP jacket with four #6 longitudinal reinforcing bars embedded in the grout. Figure 8.21 compares the axial load-shortening responses of the piles in the 40/20 pile group. The response of the un-corroded control pile, 0/0, is also shown in the figure for comparison purposes. The yield capacity of corroded section, $P_{y,c}$, is less than the axial capacity of un-corroded pile, $P_{n,u}$, as shown in Figure 8.21. The axial capacity of both repaired piles, $P_{n,r}$, increased beyond the yield capacity of the corroded section indicating that the corroded section attained the yield stress and that load was transmitted to the repair systems.

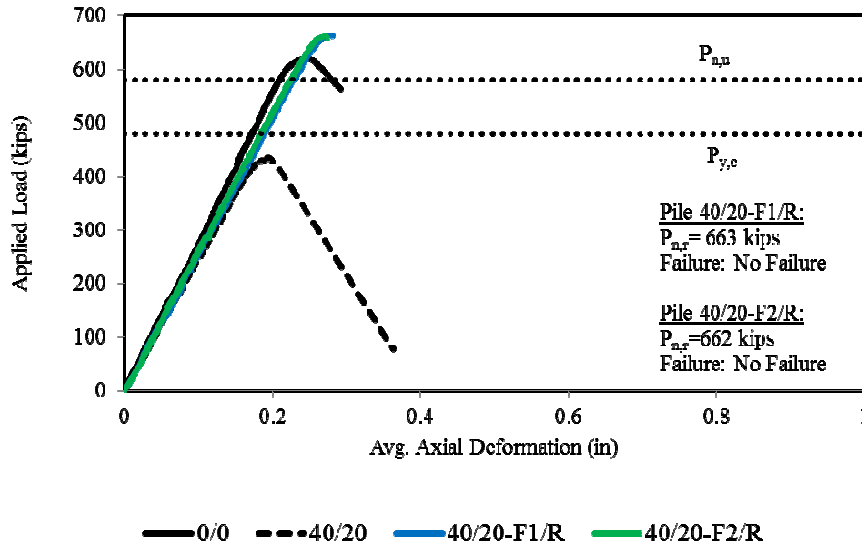


Figure 8.21: Axial load-shortening behavior of 40/20 pile group

The repaired piles were loaded up to the peak load monotonically. The axial load-shortening response of the repaired piles, shown in Figure 8.21, remained linear up to the peak load. The recorded peak axial loads for the 40/20-F1/R and 40/20-F2/R piles were 663 kips and 662 kips, respectively. The tests were terminated when the capacity of the hydraulic loading system was reached. No non-linearity or visible sign of lateral deformation was observed. Figure 8.22 shows the repaired piles after testing. As shown Figure 8.22, no failure was observed for 40/20-F1/R and 40/20-F2/R piles. Before the test, the piles were examined by tapping the FRP jacket, and no air voids were identified.

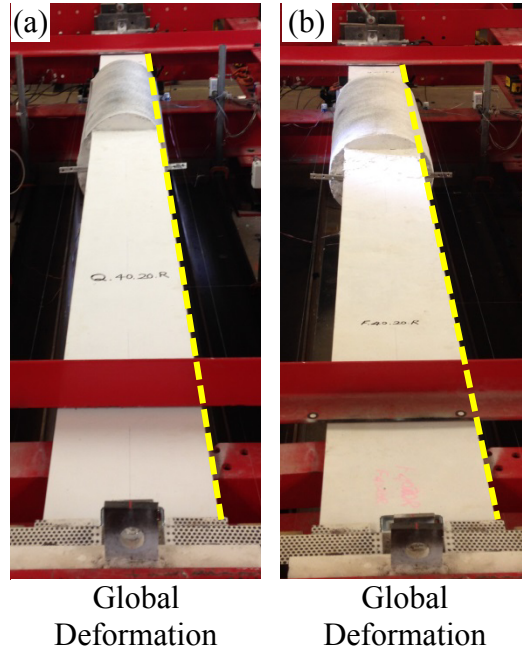


Figure 8.22: Piles 40/20 repaired with the F1 and F2 repair systems after testing

Figure 8.23 shows the axial load-slip relationship of 40/20-F1/R and 40/20-F2/R. There are two curves for each pile, each corresponding to a slip measurement at one end of the repaired region. The dashed line indicates the measured steel-grout slip at the end of the repair that is closest to the fixed side of the pile (fixed end). The solid line shows the measured slip at the end of the repair that is closest to the loaded end of the pile (jacking end). Positive values indicate that the steel surface slipped into the grout cylinder. Both piles demonstrated comparable amounts of slip at the two ends.

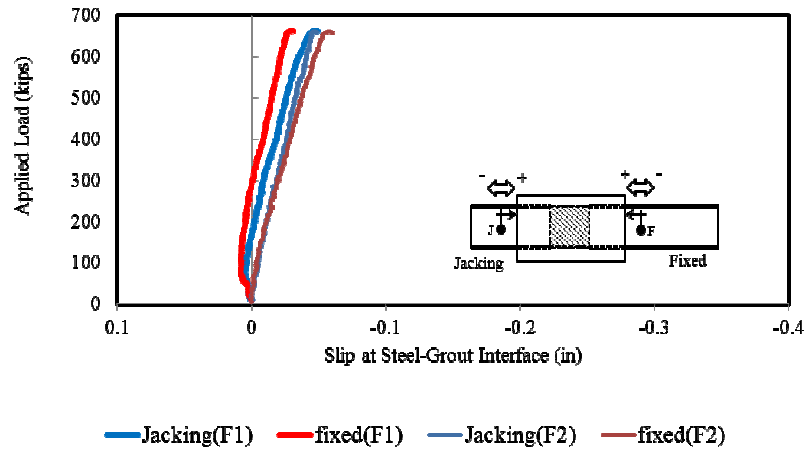


Figure 8.23: Comparing the slip at steel-grout interface of 40/20 repaired piles

Figure 8.24 shows the relationship between the axial load and the measured hoop strain in FRP jacket for the piles 40/20-F1/R and 40/20-F2/R. For a given load level the hoop strain in the F1 jacket is slightly higher than F2 jacket. This is attributed to the lower stiffness of the F1 jacket compared to the F2 jacket. The slight jump in hoop strain of 40/20-F1/R is an indication of localized cracking of the grout inside the jacket in the vicinity of the strain gauge.

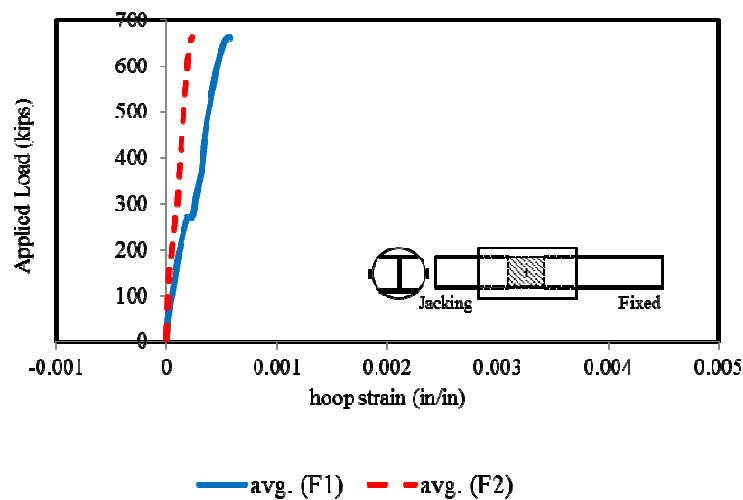


Figure 8.24: Comparing FRP hoop strain of 40/20 repaired piles

8.3.3. Pile Group 40/60

All of the piles that were tested in this group had 40% reduction of the flange thickness and 60% reduction of the web thickness along a 12 in. length. The piles were repaired with grout-filled FRP jackets with four #6 longitudinal reinforcing bars embedded in the grout. Figure 8.25 compares the axial load-shortening responses of the piles in the 40/60 pile group. The yield capacity of the corroded section, $P_{y,c}$, is less than the axial capacity of the un-corroded pile, $P_{n,u}$, as shown in Figure 8.25. The axial capacity of both repaired piles, $P_{n,r}$, increased beyond the yield capacity indicating that the repair system effectively restrained the slender flanges and webs and transmit some of the axial load in the piles. The repair system was able to completely restore the axial capacities of these corroded piles to the axial capacity of the un-corroded pile as shown in Figure 8.25.

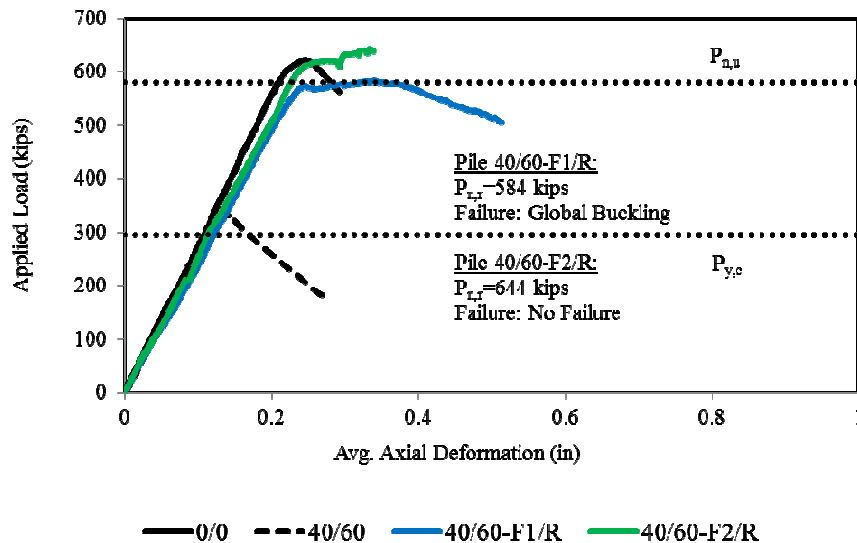


Figure 8.25: Axial load-shortening behavior of 40/60 pile group

The axial load-shortening response of the repaired piles remained linear up to 562 kips and 607 kips for the 40/60-F1/R and 40/60-F2/R piles, respectively. Testing of the pile 40/60-F1/R was terminated when the load decreased to 504 kips after a short plateau and

visible lateral deformation as shown in Figure 8.26(a). However, no post peak response was obtained for the pile 40/60-F2/R due to limitation of capacity of the hydraulic loading system. Figure 8.26(a) shows pile 40/60-F1/R which failed by global buckling. However, no failure was observed for the pile 40/60-F2/R as shown in Figure 8.26(b).

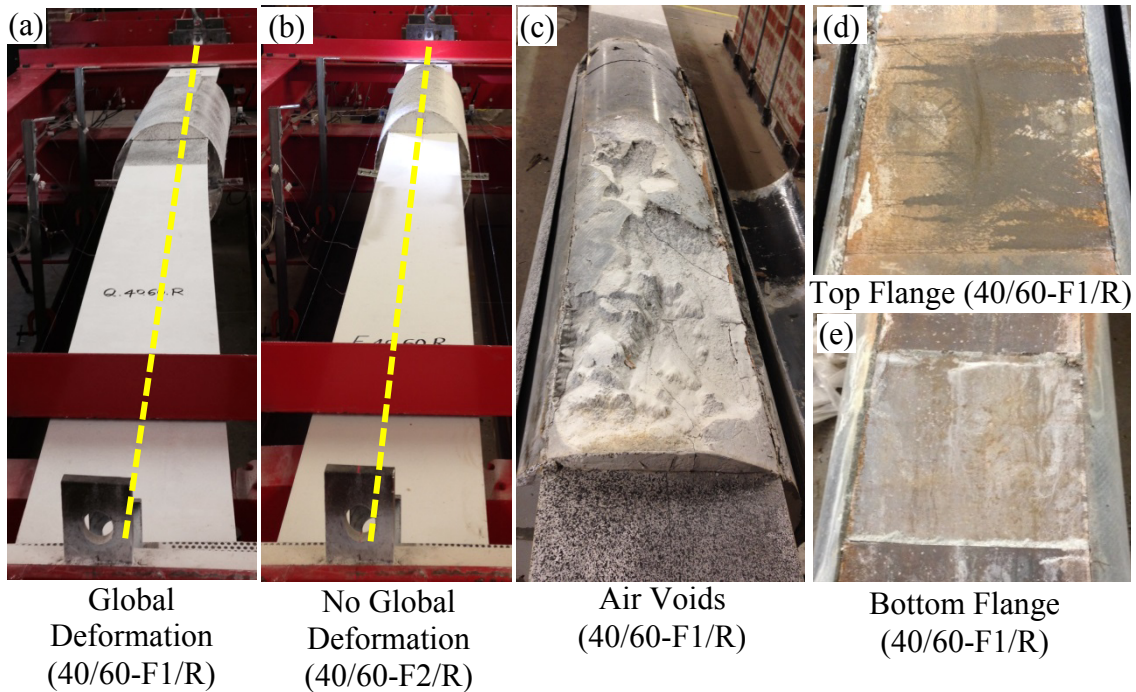


Figure 8.26: Piles 40/60 repaired with the F1 and F2 repair systems after testing

After the test, the FRP jacket was removed from pile 40/60-F1/R. Removal of the jacket indicated the presence of significant air voids in the grout on top of one of the flanges as shown in Figure 8.26(c). The grout was removed to inspect the condition of the flange in the area with the reduced flange thickness. No localized deformation was observed in either flange within the corroded region as shown in Figure 8.26(d) and (e).

Figure 8.27 shows the axial load-slip relationship of 40/60-F1/R and 40/60-F2/R. There are two curves for each pile corresponding to slip measurement at each end of the repair region. Noting the sign of the slip values, the steel surface slipped into the grout cylinder.

The pile repaired with the F1 jacket demonstrated slightly more slip compared to the one repaired with F2 jacket. This is attributed to the higher stiffness of F2 jacket relative to the F1 jacket which provided more confinement and resulted in less slip.

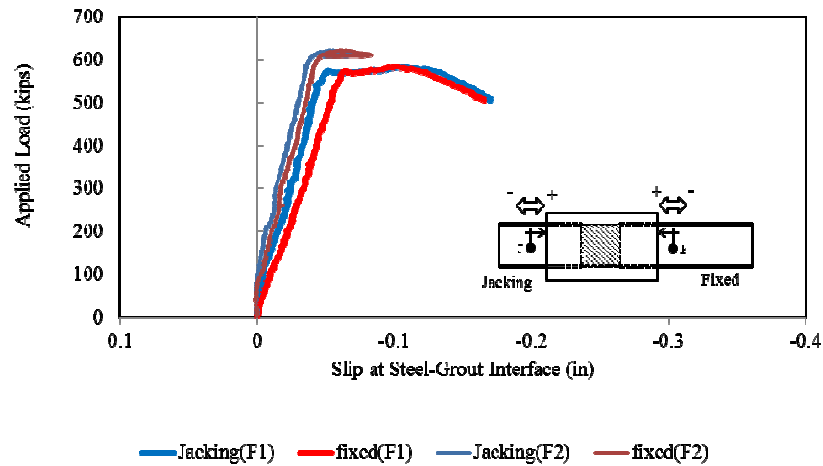


Figure 8.27: Comparing the slip at steel-grout interface of 40/60 repaired piles

Figure 8.28 shows the relationship between the axial load and hoop strain in FRP jacket of the piles 40/60-F1/R and 40/60-F2/R. The increases of the hoop strains near the peak loads suggest that dilation of the grout core engaged the confinement action of the FRP jackets. The maximum measured strains in the stiffer F2 jacket were lower than those in the less stiff F1 jacket.

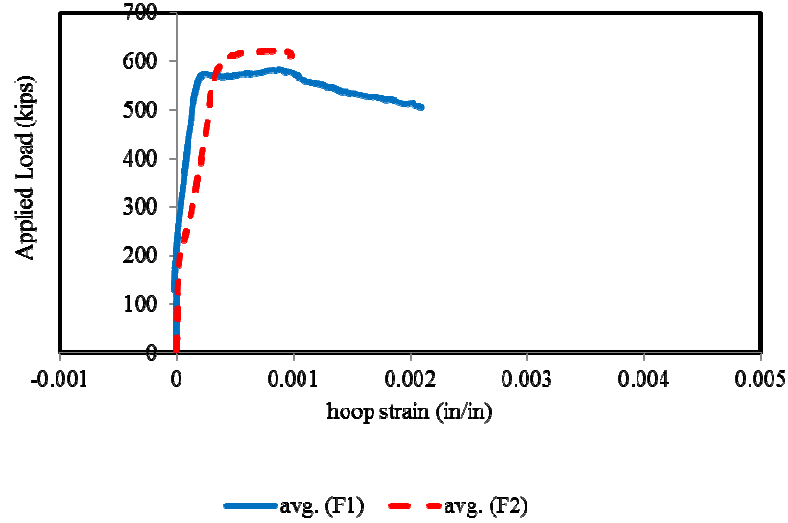


Figure 8.28: Comparing FRP hoop strain of 40/60 repaired piles

8.3.4. Pile Group 80/60

All of the piles that were tested in this group had 80% reduction of the flange thickness and 60% reduction of the web thickness along a 12 in. length. The piles were repaired with grout-filled FRP jacket with four #8 longitudinal reinforcing bars embedded in the grout. In two of the piles, 80/60(2)-F1/RA and 80/60(2)-F2/RA, four headed-stud anchors were attached to the web above and below the corroded region. The other two piles, 80/60(1)-F1/R and 80/60(1)-F2/R, had no anchors. Figure 8.29 compares the axial load-shortening responses of the piles in the 80/60 group. The axial capacity of the repaired piles, $P_{n,r}$, increased beyond the yield capacity of the corroded section, $P_{y,c}$, as shown in Figure 8.29, indicating effective restraint of the slender flanges and webs by the repair system and transfer of load from the piles to the repair system. The repairs were able to successfully restore the axial capacity of all of the repaired piles in this group except 80/60(1)-F1/R to the axial capacity of the un-corroded pile. The piles 80/60(1)-F1/R and

80/60(1)-F2/R were intentionally repaired without using the headed-stud anchors (although the design indicated that the anchors were necessary) for comparison purposes.

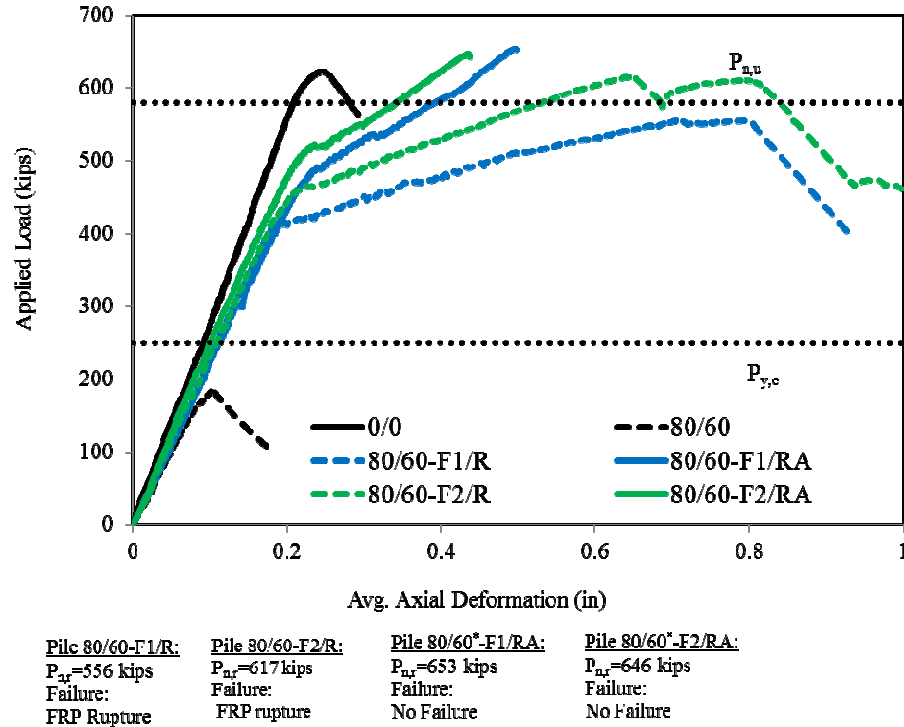


Figure 8.29: Axial load-shortening behavior of 80/60 pile group

The responses of piles 80/60(1)-F1/R and 80/60(1)-F2/R were linear up to loads of 404 kips and 449 kips, respectively at which point the axial stiffness demonstrated a degradation. Afterwards, the loading continued to increase until the FRP jackets of the piles ruptured at peak loads of 556 kips and 617 kips, respectively, as indicated in Figure 8.29 by black dots. After rupture of the jackets the load dropped to about 70% of the peak load. For the piles 80/60(2)-F1/RA and 80/60(2)-F2/RA, the axial load-shortening responses of the repaired piles remained linear up to load levels of 449 kips and 494 kips, respectively, where the axial stiffness degraded. The loading continued to increase up to the peaks of 653 kips and 646 kips for the piles 80/60(2)-F1/RA and 80/60(2)-F2/RA,

respectively. Testing of these two piles was terminated at these stages, due to limitations of the capacity of the hydraulic loading system.

Figure 8.30 shows the axial load-slip relationships of the repaired piles in the 80/60 group. There are two curves for each pile corresponding to slip measurement at each end of the repair region. Comparing Figure 8.30(a) and (b) reveals that slip at the steel-grout interface of the piles that were repaired with headed-stud anchors is less than their counterparts without mechanical anchorage. Noting the sign of the slip values, the steel surface slipped into the grout cylinder. The piles repaired with the F1 jackets demonstrated slightly more slip compared to the ones repaired with the F2 jackets. This was attributed to the lower stiffness of the F1 jacket which provided less confinement of the grout core. This can be addressed by increasing the number of layers in the F1 jacket to match the hoop stiffness of the F2 jacket.

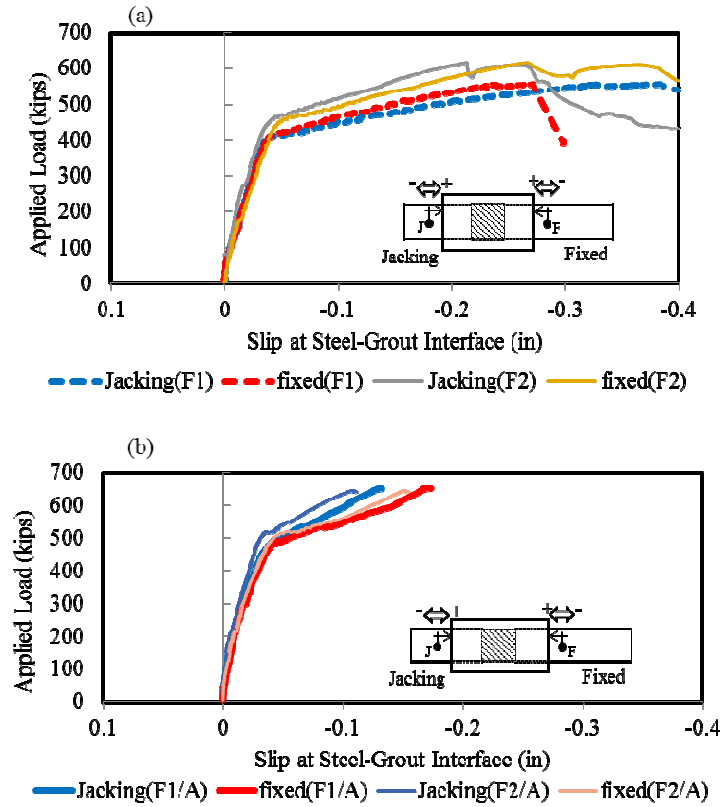


Figure 8.30: Comparing the slip at steel-grout interface of 80/60 repaired piles (a) piles without mechanical anchors, and (b) piles with mechanical anchors.

Figure 8.31 shows the relationship between the axial load and hoop strain in FRP jacket of the 80/60 repaired pile group. The hoop strain in the F1 jacket is higher than that in the F2 jacket at the same load due to lower stiffness of the F1 jacket relative to the F2 jacket. Further, comparing Figure 8.31 (a) and (b) indicates that the presence of the mechanical anchors in the load introduction region helped to reduce the hoop strains in the FRP jackets at a given load for both types of jacket.

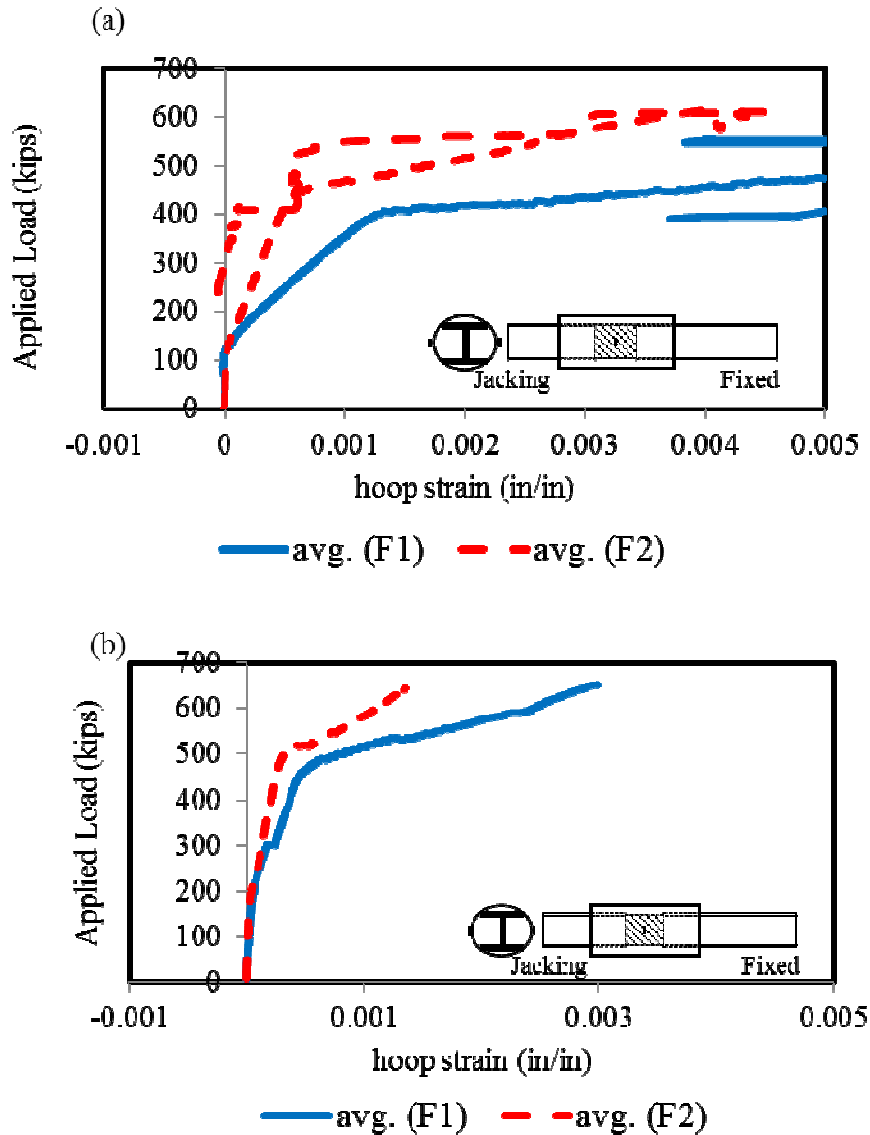


Figure 8.31: Comparing FRP hoop strain of 80/60 repaired piles

8.3.4.1. Pile 80/60(1)-F1/R

Figure 8.32(a) shows the failure of the tested pile 80/60(1)-F1/R. The pile failed with a sudden drop of load accompanied by a loud sound and partial delamination of the FRP jacket as shown in Figure 8.32(b), although no sign of lateral deformation was observed. Removal of the jacket after testing indicated rupture of the interior layer of the FRP jacket as shown in Figure 8.32(c). Removal of the jacket also indicated the

presence of air voids in the grout above the top flange as shown in Figure 8.32(d). The grout was removed using a jack hammer to observe the web and flanges in the corroded regions. The flanges and web exhibited localized crumpling deformation within the corroded region as shown in Figure 8.32(e) - (g). Crumpling deformation was low amplitude but higher mode consisting of multiple complete sine waves of deformation. This mode is distinguished from local buckling primarily based on the restraining effect of the repair system.

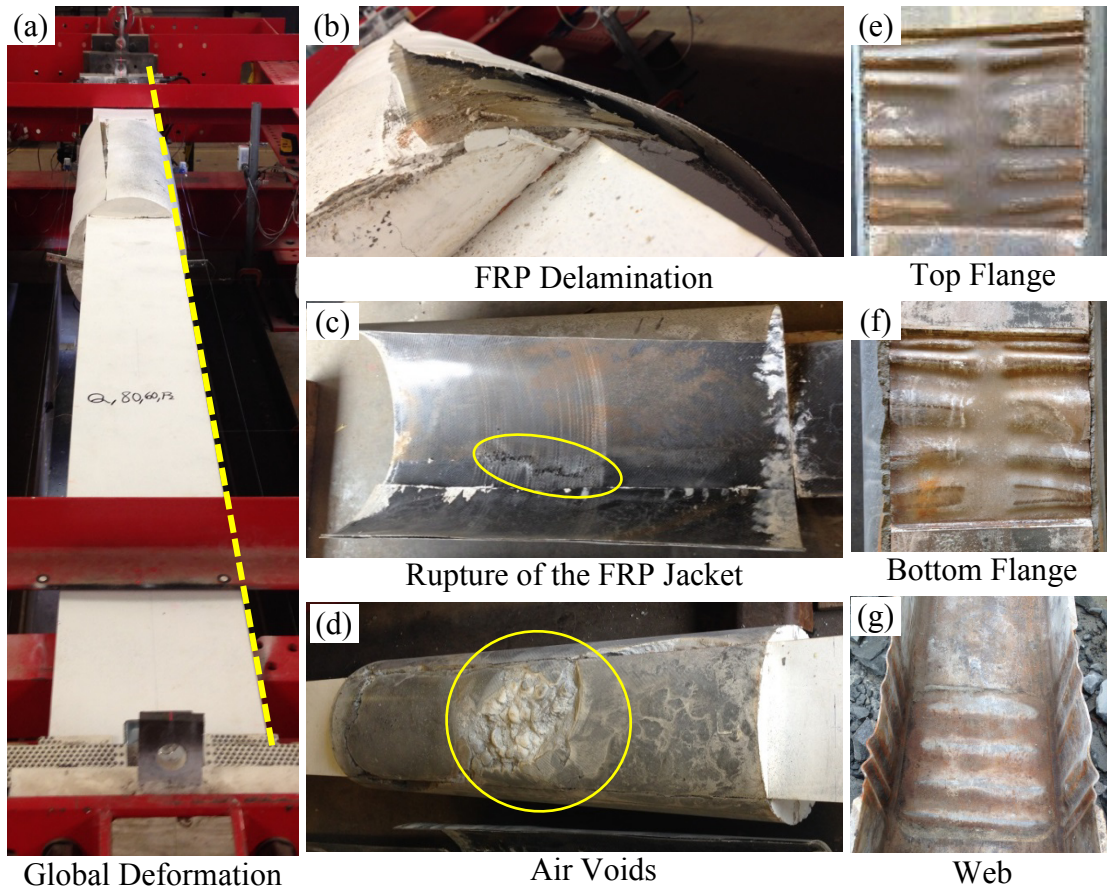


Figure 8.32: Pile 80/60(1)-F1/R after testing

8.3.4.2. Pile 80/60(1)-F2/R

Figure 8.33(a) shows the failure mode of the tested 80/60(1)-F2/R pile. The pile failed by rupture of FRP jacket which first occurred partially near the top corroded flange (see Figure 8.33(b)). Subsequently, another FRP rupture was initiated and propagated near the bottom flange which was followed by separation of the grout from the steel pile as shown in Figure 8.33(c) and (g). After the test, the repair materials were removed from the pile. It was observed that the flanges and web demonstrated localized crumpling deformation within the corroded region as shown in Figure 8.33(d) - (f).

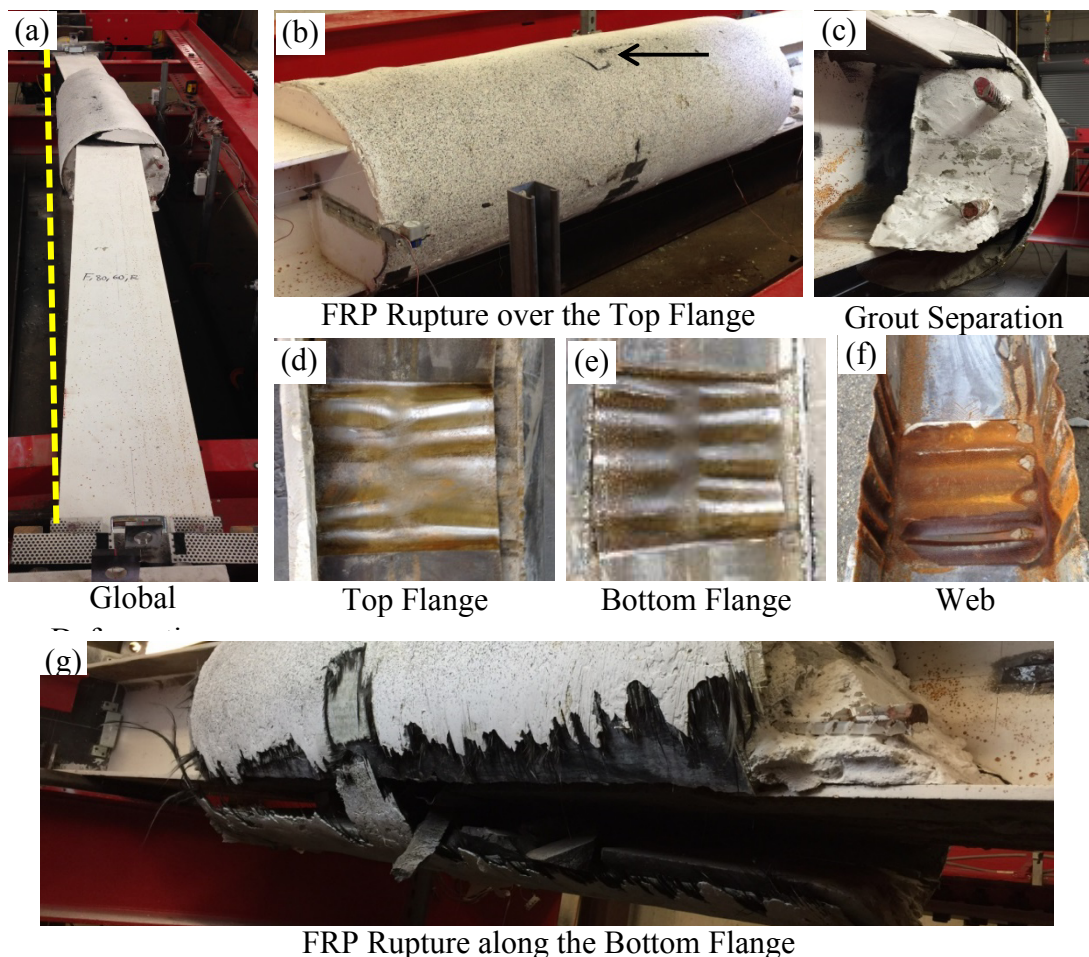


Figure 8.33: Pile 80/60(1)-F2/R after testing

8.3.4.3. Pile 80/60(2)-F1/RA

This pile is similar to pile 80/60(1)-F1/R, except it also included anchors attached to the web. Figure 8.34(a) shows pile 80/60(2)-F1/RA pile after testing. The test was terminated when the capacity of the hydraulic loading system was reached before any failure was observed. After the test, the repair materials were removed for more detailed investigation. As shown in Figure 8.34(b), air voids were observed in the grout, but they were not located within the corroded region. Both flanges demonstrated localized crumpling deformation as shown in Figure 8.34(c) and (d). However, the amplitude of the localized deformations was smaller than for the counterpart pile, 80/60(1)-F1/R, which was attributed to the effect of adding the anchors to the repair system. Adding mechanical anchors to the repair system enhanced the composite action between the steel pile and the repair system by preventing the grout from separating from the pile after the corroded region began to crumple.

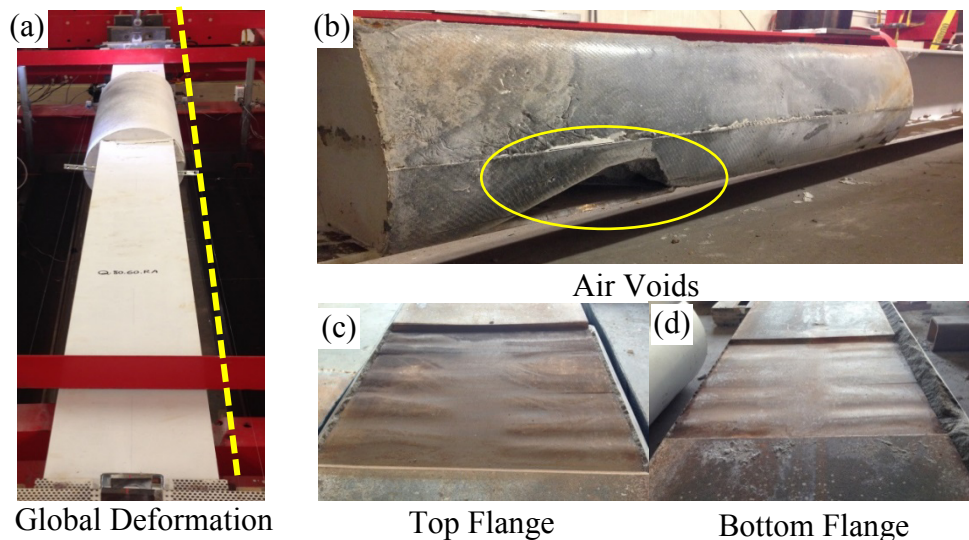


Figure 8.34: Pile 80/60*-F1/RA after testing

8.3.4.4. 80/60(2)-F2/RA

This pile is similar to pile 80/60(1)-F2/R, but it also included anchors attached to the web. Figure 8.35(a) shows pile 80/60(2)-F2/RA after testing. The test was terminated when the capacity of the hydraulic loading system was reached before any failure was observed. After the test, the repair materials were removed for a more detailed investigation of the grout core. As shown in Figure 8.35(b), air voids were observed in the grout adjacent to the top flange at the end of the region with simulated corrosion. The top flange demonstrated localized deformation at the section adjacent to the void. However, no localized deformation was observed in the bottom flange or web as shown in Figure 8.35(c) and (d). Figure 8.35(e) shows the headed-stud anchors after removing the grout using an electric jack hammer. No visible sign of damage was observed in the anchors.

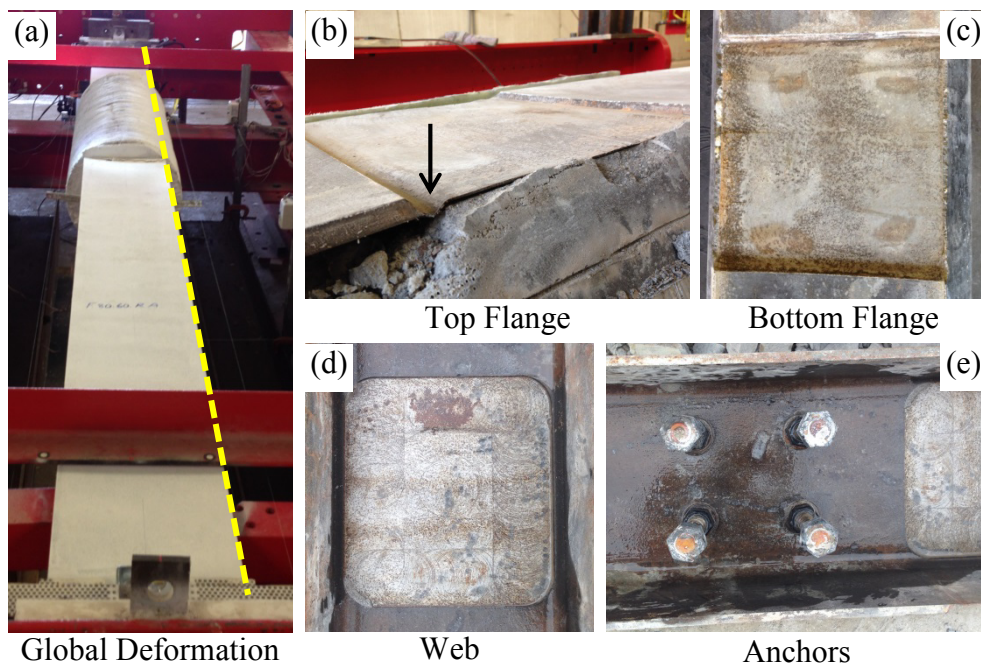


Figure 8.35: Pile 80/60(2)-F2/RA after testing

8.3.5. Pile Group 80/60/V

All of the piles that were tested in this group had 80% reduction of the flange thickness and 60% reduction of the web thickness along a 12 in. length. A 2 in. through-web void was also created to simulate severe corrosion. The piles were repaired with grout-filled FRP jackets with four #8 longitudinal reinforcing bars embedded in the grout. Four headed-stud anchors were also attached to the web above and below the corroded region. Figure 8.36 compares the axial load-shortening responses of 80/60/V pile group. The axial capacity of both repaired piles, $P_{n,r}$, increased beyond the yield capacity and the axial capacity of the un-corroded pile. This indicates that the repair system restored the axial capacity of the corroded piles beyond the retrofitting target by restraining the slender flanges within the corroded region, delaying global buckling, and transferring some of the load out of the pile and into the repair system.

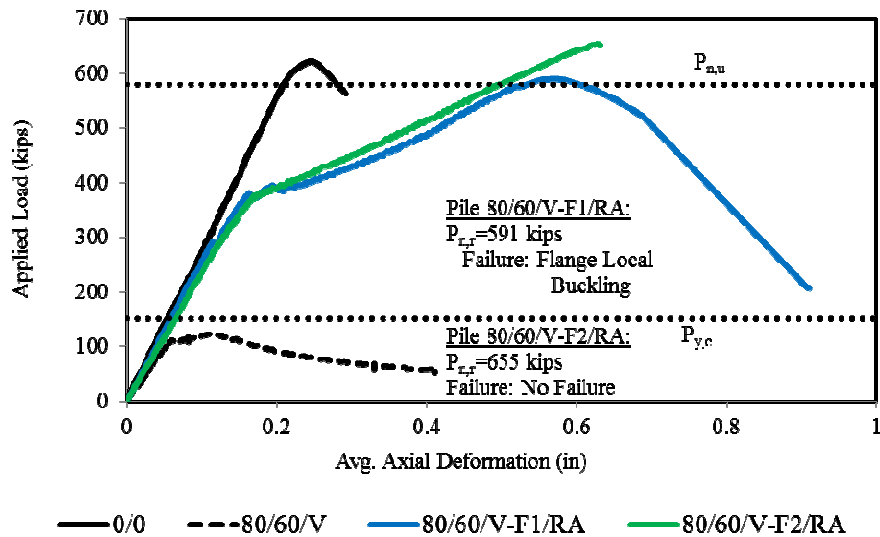


Figure 8.36: Axial load-shortening behavior of 80/60/V pile group

The axial load-shortening response of the repaired piles, shown in Figure 8.36, remained linear up to 360 kips for both repaired piles. Subsequently, as the load continued to

increase, the behavior became non-linear and the axial stiffness degraded. After attaining a peak load of 591 kips, the flanges of the pile 80/60/V-F1/RA buckled locally outside of the repaired region and caused an abrupt reduction of the load to 207 kips as shown in Figure 8.36. Testing of the pile 80/60/V-F2/RA was terminated prior to failure when the load reached to 655 kips due to limitation of capacity of the hydraulic loading system.

Figure 8.37 shows the axial load-slip relationship of 80/60/V repaired pile group. There are two curves for each pile corresponding to slip measurement at each end of the repair cylinder. Noting the sign of the slip values, the steel surface slipped into the grout cylinder. The pile repaired with the F1 jacket demonstrated slightly more slip compared to the one repaired with F2 jacket due to the lower stiffness of the jacket. The large slips are consistent with yielding and crumpling of the corroded region.

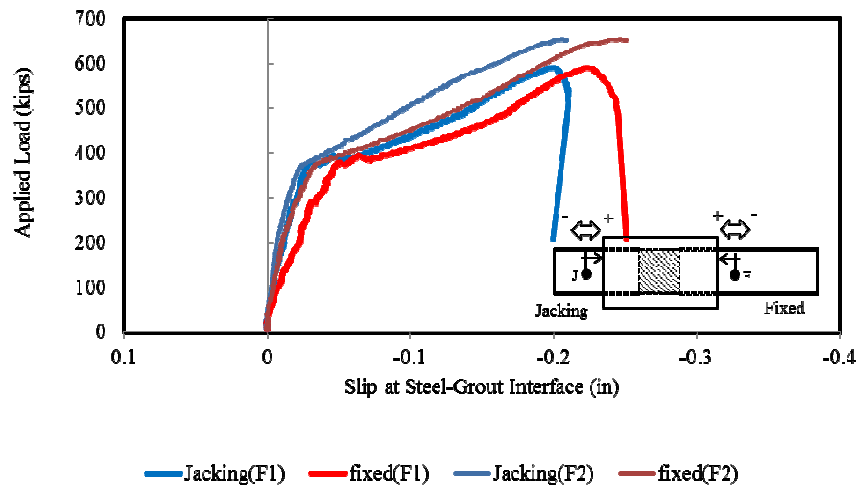


Figure 8.37: Comparing the slip at steel-grout interface of 80/60/V repaired piles

Figure 8.38 shows the relationship between the axial load and hoop strain in FRP jacket of the 80/60/V repaired pile group. The hoop strains in both FRP jackets are comparable although the strains in the F2 jacket continued to increase after failure of the F1 jacket.

The large strains in the FRP indicate that the confinement action of the jackets was engaged, likely due to deterioration of the grout or crumpling of the corroded region.

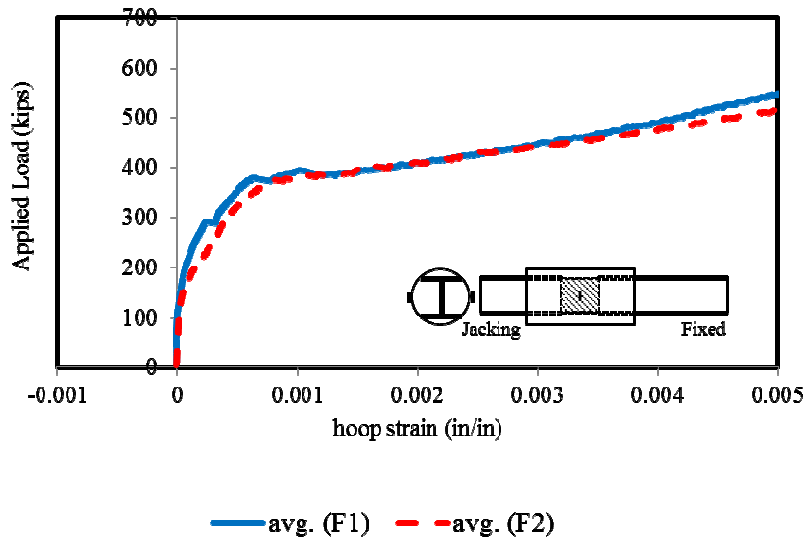


Figure 8.38: Comparing FRP hoop strain of 80/60/V repaired piles

8.3.5.1. 80/60/V-F1/RA

Figure 8.39(a) shows the tested 80/60/V-F1/RA pile which failed by local buckling of the flanges just beyond one end of the repaired region as shown in Figure 8.39(b). Figure 8.39(c) shows air voids in the grout adjacent to the top flange that were observed after removing the FRP jacket. These caused the top flange to demonstrate a different pattern of local deformation from the bottom flange as shown in Figure 8.39(e) and (f). No visible sign of damage was observed in the headed-stud anchors as indicated in Figure 8.39(d).

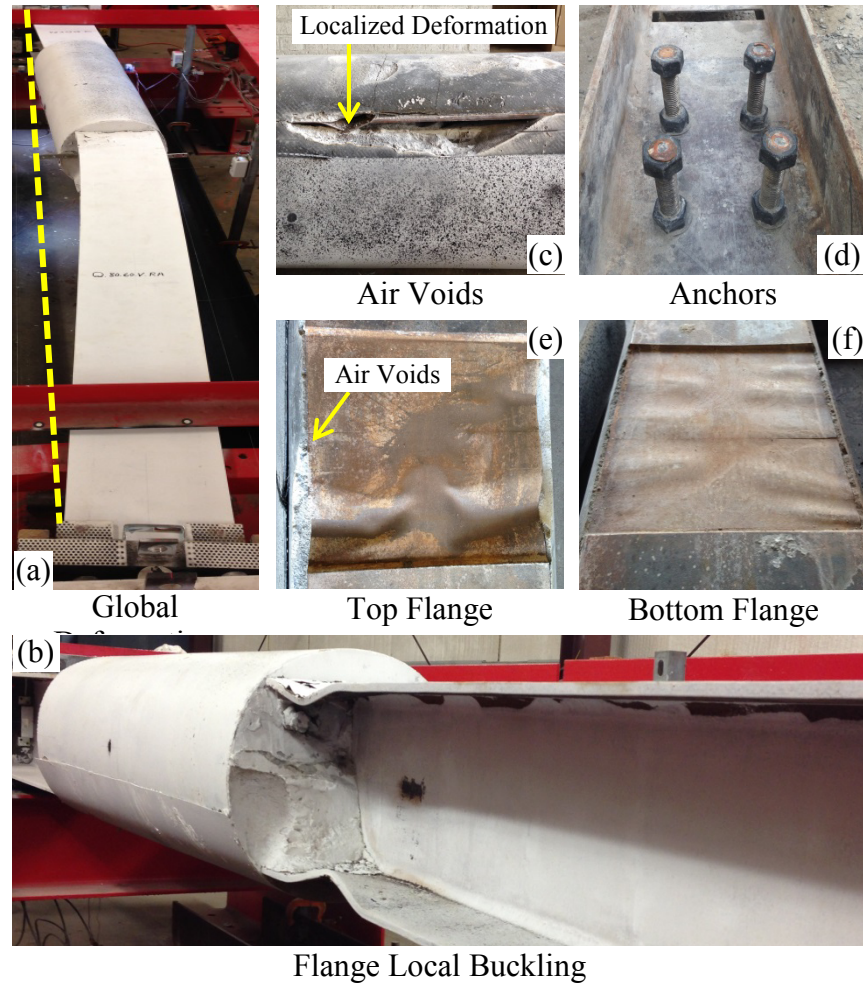


Figure 8.39: Pile 80/60/V-F1/RA after testing

8.3.5.2. 80/60/V-F2/RA

Figure 8.40(a) shows the tested 80/60/V-F2/RA pile which demonstrated no failure. The test was terminated when the capacity of the hydraulic loading system was reached. After removing the FRP jacket, air voids were observed in the grout as shown in Figure 8.40(b), but they were not within the corroded region. Both flanges exhibited crumpling deformations within the corroded region as shown in Figure 8.40(c) and (d).

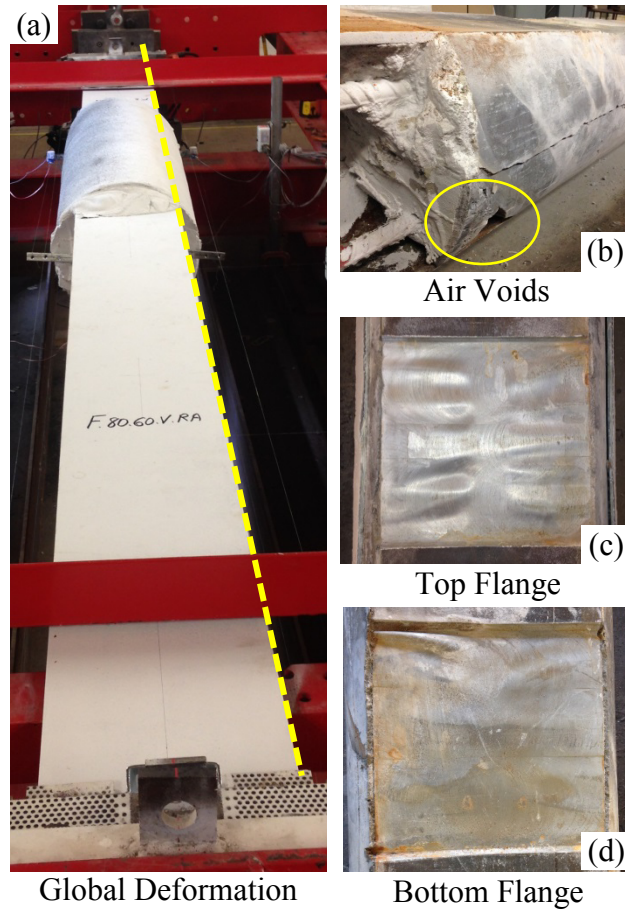


Figure 8.40: Pile 80/60/V-F2/RA after testing

8.3.6. Pile Group 80/60/3

All of the piles that were tested in this group had 80% reduction of the flange thickness and 60% reduction of the web thickness along a 36 in. length. The piles were repaired with grout-filled FRP jackets with four #8 longitudinal reinforcing bars embedded in the grout. Four headed-stud anchors were also attached to the web above and below the corroded region. Figure 8.41 compares the axial load-shortening responses of the piles in the 80/60/3 pile group. The axial capacity of both repaired piles, $P_{n,r}$, increase beyond the yield capacity and the axial capacity of un-corroded pile. This indicates that the repair system completely restored the axial capacity of the corroded piles by restraining the

slender flanges and web within the corroded region, delaying global buckling, and transferring some of the load in the piles.

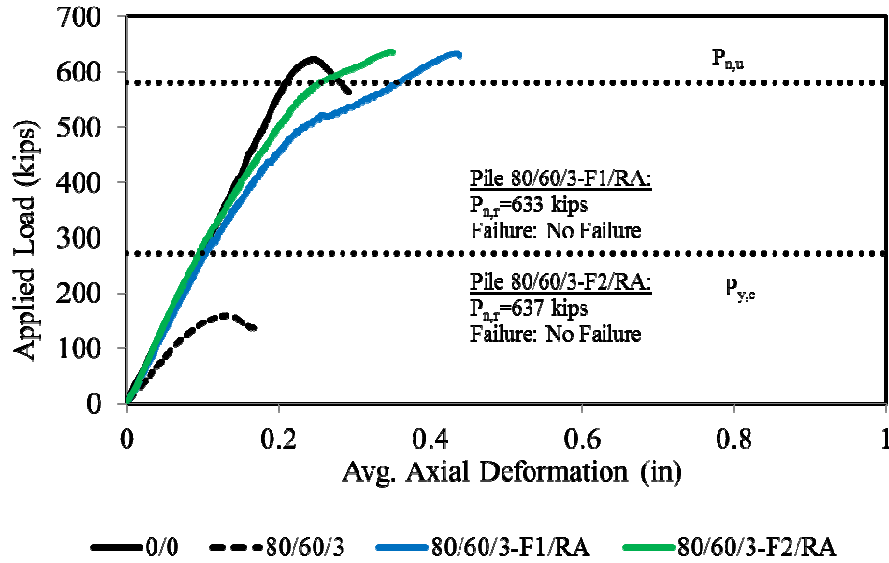


Figure 8.41: Axial load-shortening behavior of 80/60/3 pile group

The axial load-shortening response of the repaired piles, shown in Figure 8.41, remained linear up to 427 kips and 517 kips for 80/60/3-F1/RA and 80/60/3-F2/RA, respectively. Subsequently, as the load continued to increase, the behavior became non-linear and the axial stiffness degraded. Testing of the piles was terminated prior to failure when the hydraulic loading system reached its capacity at peak loads of 633 kips and 637 kips for the piles 80/60/3-F1/RA and 80/60/3-F2/RA, respectively.

Figure 8.42 shows the axial load-slip relationship of 80/60/3 repaired pile group. There are two curves for each pile corresponding to slip measurement at each end of the repair cylinder. Noting the sign of the slip values, the steel surface slipped into the grout cylinder. The pile repaired with F1 jacket demonstrated slightly more slip compared to the one repaired with F2 jacket due to the lower stiffness of the F1 jacket compared to the F2 jacket.

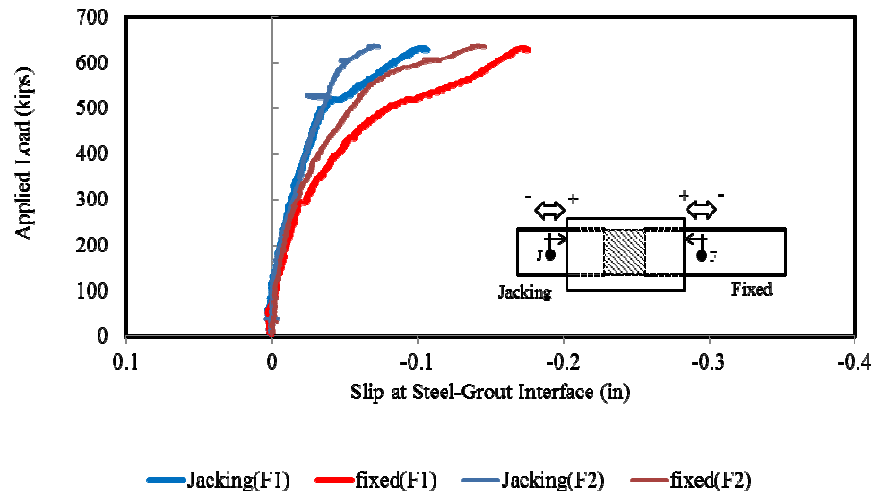


Figure 8.42: Comparing the slip at steel-grout interface of 80/60/3 repaired piles

Figure 8.43 shows the relationship between the axial load and hoop strain in FRP jacket of the 80/60/3 repaired pile group. The hoop strains in the F1 jacket are higher than the strains in the F2 jacket at the same load level due to the lower stiffness of the F1 jacket compared to the F2 jacket. The strains in both jackets were relatively low suggesting that the confinement effect of the jackets was not fully engaged.

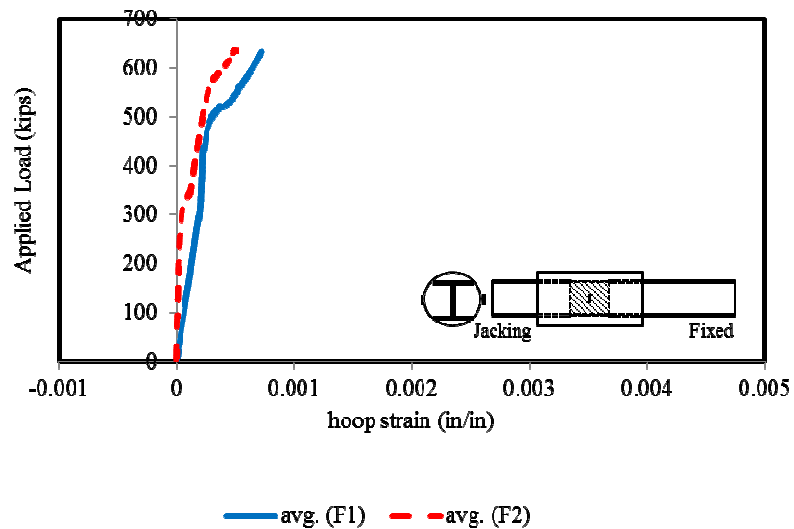


Figure 8.43: Comparing FRP hoop strain of 80/60/3 repaired piles

8.3.6.1. Pile 80/60/3-F1/RA

Figure 8.44(a) shows the tested 80/60/3-F1/RA pile which demonstrated no failure. After removing the FRP jacket, air voids were observed in the grout which caused localized deformation in the adjacent slender flange as indicated in Figure 8.44(b) and (g). The bottom flange and headed-stud anchors demonstrated no visible deformation as shown in Figure 8.44(c) and (f). Figure 8.44(d) shows localized deformation in the web which occurred adjacent to the air voids in the grout. Figure 8.44(e) shows a longitudinal cut mark on the internal layer of the FRP jacket due to abrasion from the edge of the corroded flange. This highlights the importance of proper placement of protective spacers between the FRP jacket and the corroded pile during construction.

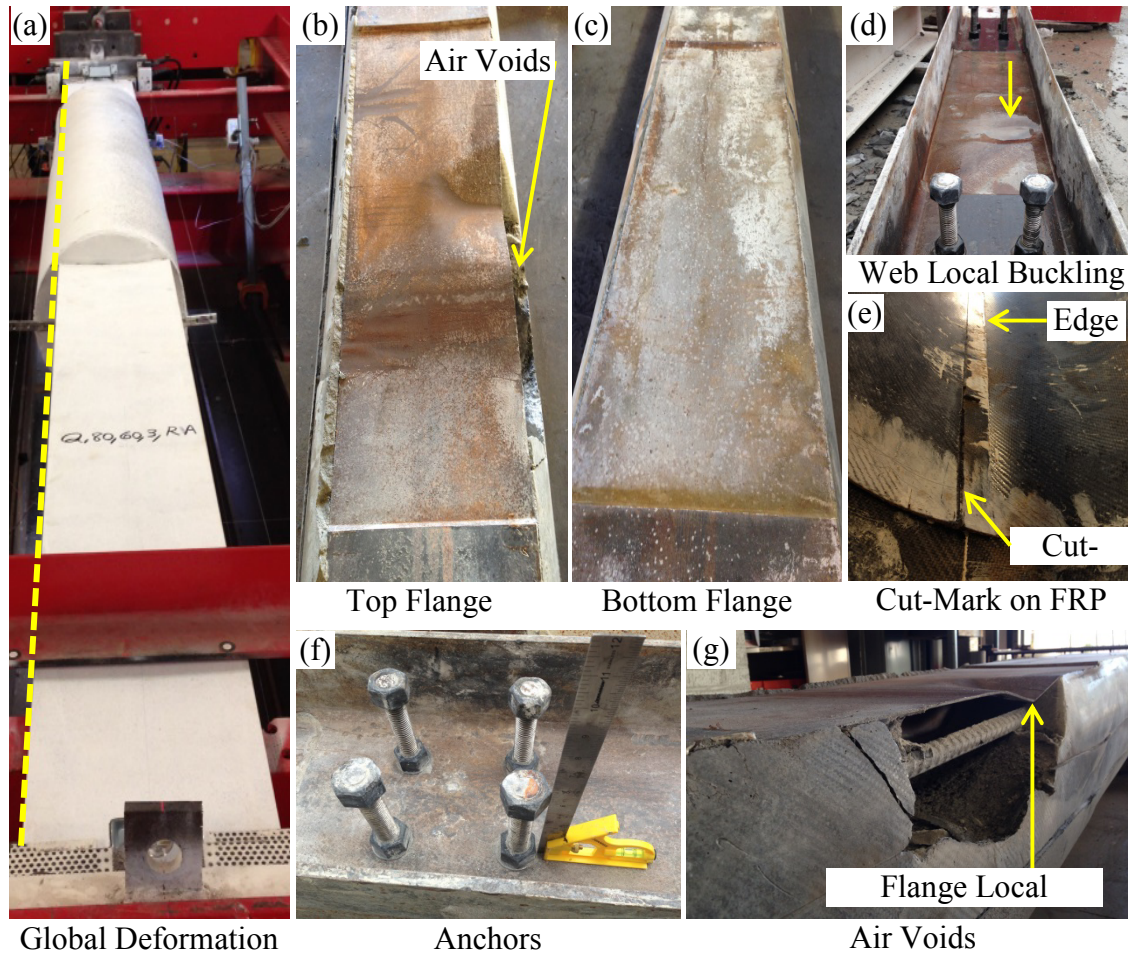


Figure 8.44: Pile 80/60/3-F1/RA after testing

8.3.6.2. Pile 80/60/3-F2/RA

Figure 8.45(a) shows the tested 80/60/3-F2/RA pile which demonstrated no failure. The repair system was removed after the test for more detailed investigation. As shown in Figure 8.45(f), there were air voids in the grout located outside of the corroded region. No sign of deformation was observed in the flanges or web as can be seen in Figure 8.45(b) - (d). Also, no deformation was observed in the headed-stud anchors (see Figure 8.45(e)). Figure 8.45(g) shows that the jacket diameter was 1.9 in. larger at one end compared to the other end

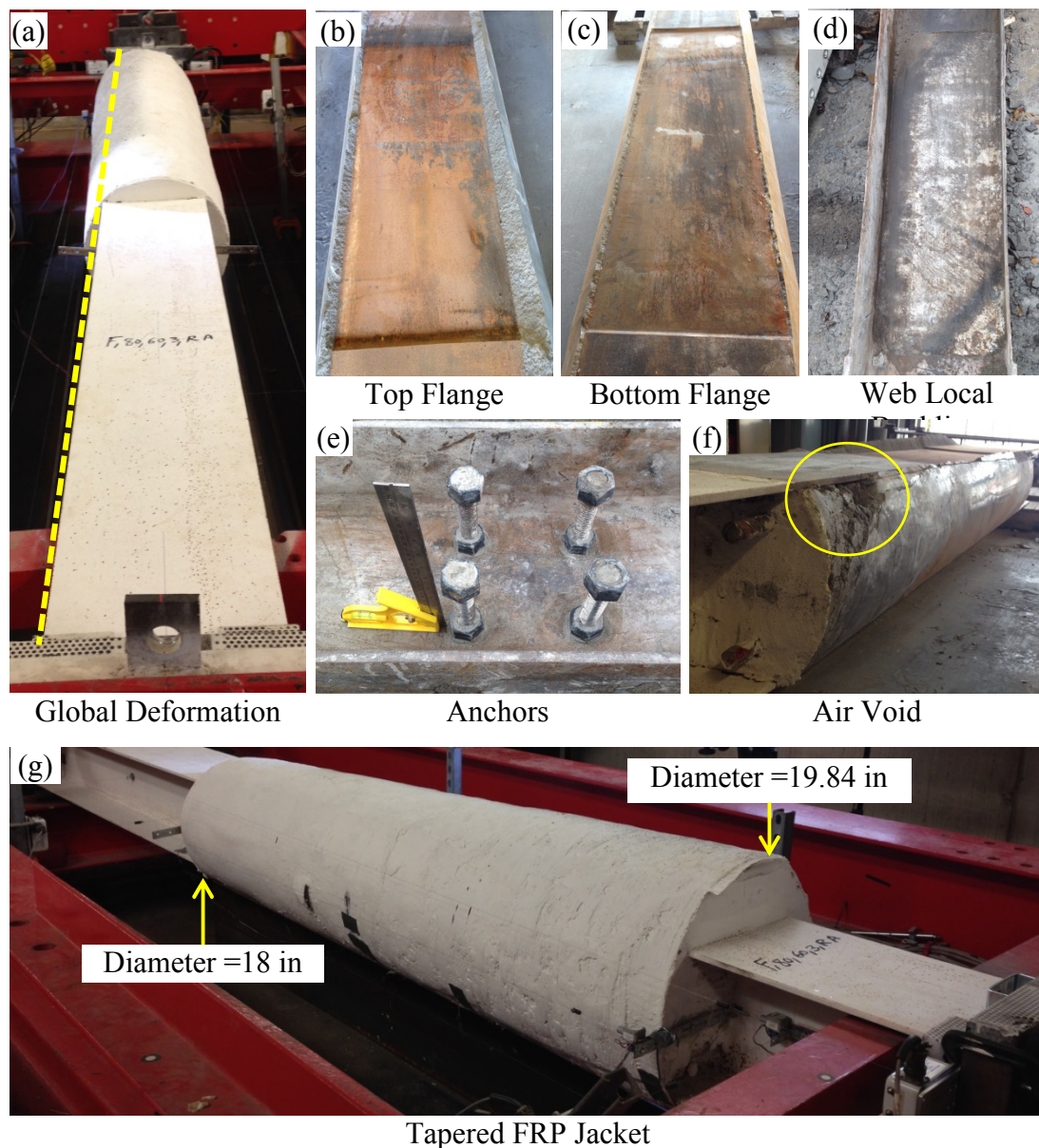


Figure 8.45: Pile 80/60/3-F2/RA after testing

8.3.7. Comparison and Discussion

Table 8.13 summarizes the axial capacities and failure modes of the tested repaired and un-repaired piles. Also, the presence of air voids adjacent to the corroded region is indicated for each of repaired piles. Comparison and discussion of the results are presented in the following sections.

Table 8.13: Axial Capacities and Failure Modes of the Tested Repaired and Un-Repaired Piles

Pile Designation	Measured Capacity (kip)	Failure Mode	Air Void Adjacent to Corroded Region
0/0	623	Global buckling	N/A ^a
0/20	604	Global buckling	N/A ^a
0/20-F1	655	No failure	N/A ^b
0/20-F2	663	No failure	N/A ^b
40/20	435	Flange local buckling	N/A ^a
40/20-F1/R	663	No failure	N/A ^b
40/20-F2/R	662	No failure	N/A ^b
40/60	333	Flange and web local buckling	N/A ^a
40/60-F1/R	584	Global buckling	Yes
40/60-F2/R	644	No failure	No
80/60	182	Flange and web local buckling	N/A ^a
80/60(1)-F1/R	556	FRP rupture	Yes
80/60(1)-F2/R	617	FRP rupture	No
80/60(2)-F1/RA	653	No failure	No
80/60(2)-F2/RA	646	No failure	Yes
80/60/V	124	Flange local bending	N/A ^a
80/60/V-F1/RA	556	Flange local buckling	Yes
80/60/V-F2/RA	617	No failure	No
80/60/3	159	Flange and web local buckling	N/A ^a
80/60/3-F1/RA	633	No failure	Yes
80/60/3-F2/RA	637	No failure	No

^a Not applicable to un-repaired piles

^b The FRP jacket was not removed and so the presence or absence of voids in the grout could not be observed.

8.3.7.1. Axial Capacity

Figure 8.46 plots the ratios of the axial capacity of the repaired piles to the nominal axial capacity of the un-corroded control pile (retrofitting target), $P_{n,r}/P_{n,u}$, as a function of the reduced cross-sectional area of the corroded section of the pile. The dashed line represents the retrofitting target which is the nominal axial capacity of the un-corroded pile, calculated according to AISC (2011) for a 15 ft. long HP12×53 pile.

The data points above the dashed line indicate that the repair system completely restored the axial capacity of the corroded piles. The axial capacity ratio for the piles repaired with F1 and F2 FRP jacket are shown by solid and hollow markers, respectively.

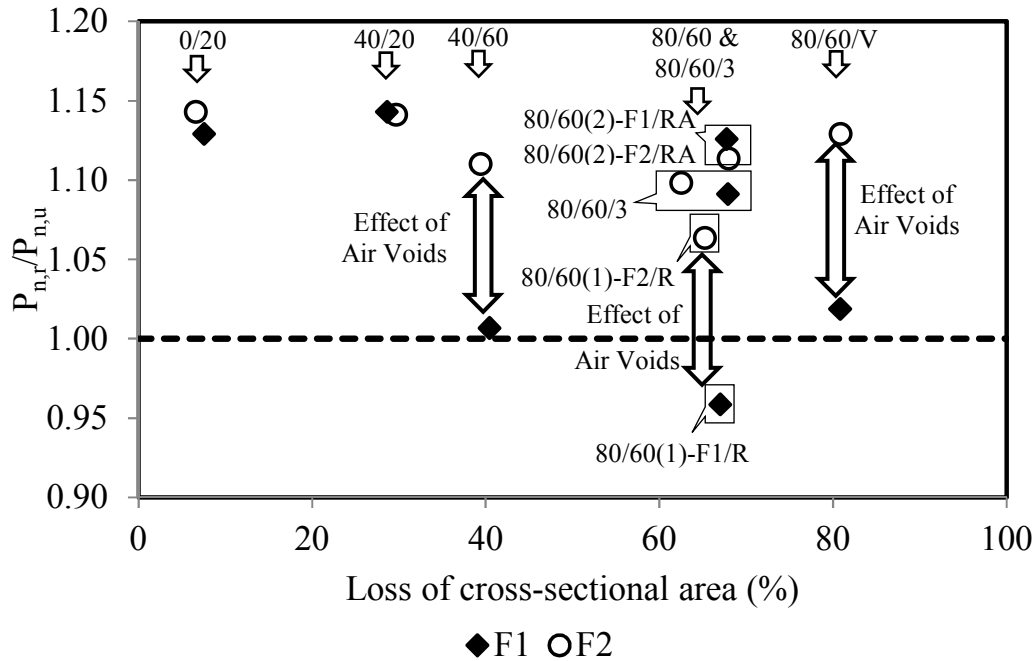


Figure 8.46: Ratio of the axial capacity of the repaired piles to the control un-corroded pile

As shown in Figure 8.46, the tested FRP-confined grout repair system was able to effectively restore the axial capacity of the corroded piles to the nominal axial capacity of the un-corroded pile. The only exception was pile 80/60(1)-F1/R. While the design calculations indicated that this pile would require mechanical anchors, anchors were not provided for comparison with pile 80/60(2)-F1/RA to investigate the effect of anchorage. The axial capacity of the pile 80/60(2)-F1/RA was fully restored to the nominal axial capacity of the un-corroded pile. Comparison of the capacity of pile 80/60(1)-F1/R with that of 80/60(2)-F2/R suggests that a similar

effect could have been achieved increasing the number of layers of the F1 jacket and eliminating air voids in the grout.

Comparing the corresponding piles repaired with the F1 and F2 FRP jackets indicates that gains in axial capacity using both FRP systems were comparable. Noting that the presence of air voids in the grout especially adjacent to the slender flange or web caused major reduction in the axial capacity. This is concluded by comparing 40/60-F1/R to 40/60-F2/R, 80/60-F1/R to 80/60-F2/R, and 80/60/V-F1/RA to 80/60/V-F2/RA.

8.3.7.2. Failure Modes

Table 8.14 compares the failure mode of the steel piles tested with and without the repair system. This comparison shows the repair system changed the failure mode of the repaired piles, most commonly from a local buckling failure mode to a crumpling failure mode (when failure of the repaired piles was observed).

Table 8.14: Comparing the Failure Mode of the Steel Piles Tested with and without the Repair

Pile Designation	Failure Mode of the Steel Pile	Air Void Adjacent to Corroded Region
0/0	Global buckling	N/A ^b
0/20	Global buckling	N/A ^b
0/20-F1	No failure ^a	N/A ^c
0/20-F2	No failure ^a	N/A ^c
40/20	Flange local buckling	N/A ^b
40/20-F1/R	No failure ^a	N/A ^c
40/20-F2/R	No failure ^a	N/A ^c
40/60	Flange and web local buckling	N/A ^b
40/60-F1/R	Global Buckling	Yes
40/60-F2/R	No Failure ^a	No
80/60	Flange and web local buckling	N/A ^b
80/60(1)-F1/R	Flange and Web Crumpling	Yes
80/60(1)-F2/R	Flange and Web Crumpling	No
80/60(2)-F1/RA	Flange and Web Crumpling	No
80/60(2)-F2/RA	Flange and Web Crumpling/ Premature Flange Local Deformation	Yes
80/60/V	Flange local bending	N/A ^b
80/60/V-F1/RA	Flange Local Buckling Outside the Repair System Flange and Web Crumpling/ Premature Flange Local Deformation	Yes
80/60/V-F2/RA	Flange and Web Crumpling	No
80/60/3	Flange and web local buckling	N/A ^b
80/60/3-F1/RA	Premature Flange Local Deformation	Yes
80/60/3-F2/RA	No Failure ^a	No

^a The test was terminated when the capacity of the hydraulic loading system was reached before any significant damage of the repaired pile was observed

^b Not applicable to the un-repaired piles

^c The FRP jacket was not removed and so the presence or absence of voids in the grout could not be observed.

Based on the experimental observations and comparing the failure modes of the repaired and un-repaired piles with 40% or less reduction in the flange thickness, the failure mechanism is explained as follows: confining the corroded region with the repair system prevented the slender flanges and web from local buckling. The shear force transferred across the grout/steel interface at the peak load was smaller than the bond strength at the interface because the cross-sectional loss was not severe and the demand on the bond was low. Consequently, global buckling occurred prior to failure

of the grout/steel bond and the flanges and webs inside the repair system did not exhibit significant local deformations or crumpling.

For the piles with 80% reduction in the flange thickness and 60% reduction in the web thickness, the repair system changed the failure mode of the slender cross sectional elements from flange and web local buckling to crumpling deformation. The corroded control pile 80/60 failed by flange and web local buckling in the first mode. The repaired piles 80/60(1)-F1/R, 80/60(1)-F2/R, 80/60(2)-F1/RA, and 80/60(2)-F2/RA demonstrated flange and web crumpling deformation along the corroded region. Piles 80/60-F1/R and 80/60-F2/R demonstrated rupture of the FRP jackets at the peak load. The 80/60/V corroded control pile which had a 2 in. through-web void failed by localized flange bending adjacent to the void. By restraining the corroded region, crumpling deformations were observed within the corroded region of the repaired piles 80/60/V-F1/RA and 80/60/V-F2/RA.

Based on these observations the failure mechanism of the repaired piles with 80% reduction of the flange thickness can be summarized as follows: as the load increased the shear load that was transferred to the repair system through the grout/steel interface increased beyond the bond capacity of the interface. Subsequently, the axial load demand on the corroded section increased after the bond failure, and the flanges and web in the corroded region began to yield and buckle or crumple locally within the repair system. The out-of-plane deformations of the flanges pushed the grout outward which, in turn, induced hoop strains in the FRP jacket. Further increasing the axial load eventually resulted in rupture of the FRP jacket.

Using headed-stud anchors attached to the web within the load introduction region reduced the axial deformation of the steel pile and reduced the amplitude of the localized flange crumpling deformations within the corroded region. This suggests that the out-of-plane deformations of the flanges and web pushed the grout outward which mobilized hoop strains in the FRP jacket but this was restrained by the presence of the headed mechanical anchors thereby reducing the demand for confinement by the FRP jackets.

The presence of air voids in the grout adjacent to the corroded region caused premature localized deformation of the corroded elements. Comparing 80/60(2)-F1/RA to 80/60(2)-F2/RA, 80/60/V-F1/RA to 80/60/V-F2/RA, and 80/60/3-F1/RA to 80/60/3-F2/RA shows premature localized deformation within the corroded region due to lack of restraint of the flanges by the grout core when voids were present in the grout near the corroded region.

8.3.7.3. FRP Confinement and Slip at Grout/Steel Interface

The trend of the measured strains in the FRP jackets indicated that increase the degree of deterioration of the piles increased the hoop strains in the corresponding FRP jackets of the repair system at peak load. This is attributed to the increase of the localized flange and web deformations within the corroded region as the level of deterioration increased. As a result, the surrounding grout was pushed outward to a greater degree to accommodate the localized deformation thereby inducing larger hoop strain in the FRP jacket.

The results further indicate that the measured slip at peak load also increased as the degree of deterioration of the piles increased. This is because increasing the degree of deterioration increased the axial shortening of the corroded portion of the pile. The mismatch between the axial shortening of the corroded steel pile and the repair system increased the shearing stresses and slip at the grout/steel interface.

Comparing the piles repaired with F1 jacket to those repaired with F2 jacket, e.g. 40/20-F1/R to 40/20-F2/R or 80/60(1)-F1/R to 80/60(1)-F2/R, shows that generally hoop strains in the FRP and slip at the grout/steel interface in the piles repaired with the F1 FRP jacket were larger than those for the piles repaired with the F2 jacket. This was attributed to the lower stiffness of the F1 jackets. Using nominal material properties, the elastic stiffness of the F1 and F2 jackets, $\Sigma E_{fi}t_{fi}$, were calculated as 394 kip/in and 679.5 kip/in, respectively, where E_{fi} and t_{fi} are the elastic moduli and thicknesses, respectively of the i^{th} FRP layer in the jackets. This indicates that the F2 jacket provided more confinement pressure and reduced the slip and separation at the steel-grout interface.

Comparing pile 80/60(1)-F1/R to 80/60(2)-F1/RA and 80/60(1)-F2/R to 80/60(2)-F2/RA demonstrated that added the headed stud anchors to the repair systems reduced the hoop strains in the FRP jackets and the slip at the grout/steel interface. This is consistent with the previously described failure mechanisms. The piles without anchors demonstrated more localized deformation within the corroded region which, in turn, induced larger hoop strains in the FRP jackets.

8.4. Results for Steel Plate Based Repair System

Seven steel piles were repaired using the clamped steel-based repair system and were tested under axial compression. The following sections describe the behavior of the repaired piles. The results are discussed and compared to the corresponding corroded control piles for each of the damage levels considered in this study. The nominal axial capacity of the 15 ft. long, un-corroded HP12×53 pile, $P_{n,u}$, which is also plotted on the axial load-shortening responses, was calculated in accordance with AISC (2011) using nominal geometry and nominal material properties. The nominal axial capacity, $P_{n,u}$, is the retrofitting target.

8.4.1. Pile 0/20-S

The pile was loaded up to 629 kips and failed by flexural buckling. The maximum lateral deformation was observed at mid-height of the column, which was the same as the corroded control pile, 0/20, as shown in Figure 8.47(a). Figure 8.47(b) shows the axial load-deformation responses of the un-corroded control pile, corroded control pile, and the repaired pile. The red line refers to the repaired pile, while the black solid and dashed lines refer to the corroded control pile and the un-corroded control pile, respectively. The horizontal dashed line indicates the target capacity of repaired pile. Similar figures were prepared for each pile in this section. Inspection of Figure 8.47(b) indicates that the repair method restored the capacity of the corroded pile back to the level of the un-corroded pile. After testing, the repair plates were removed and the pile was inspected. No flange or web local buckling was observed after removing the plates, since both flange and web were non-slender. The length of the repair system for 0/20-S was 2 ft., which provided

only limited enhancement to resist flexural buckling. Therefore, the pile failed by flexural buckling similarly to the un-corroded pile.

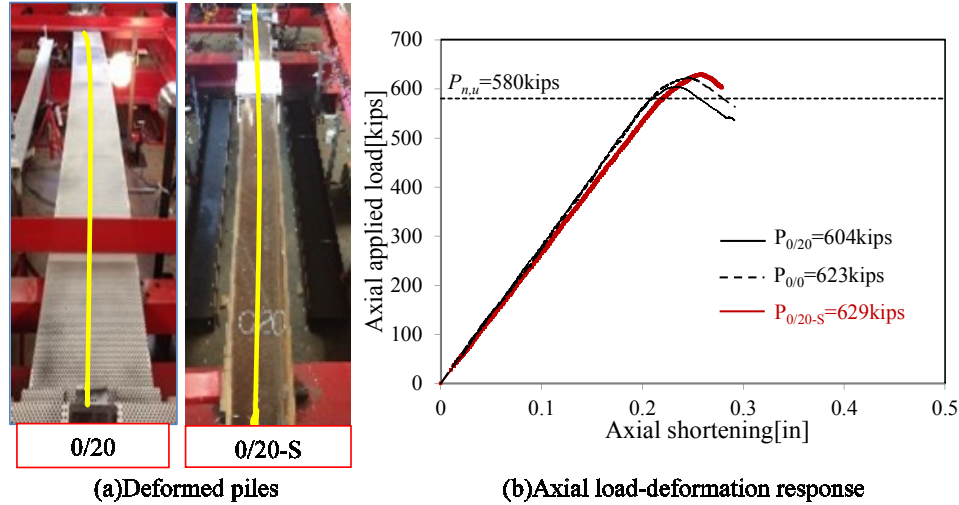


Figure 8.47: Comparison of Pile 0/20 and Pile 0/20-S

8.4.2. Pile 40/20-S

The pile was loaded monotonically up to a peak load of 665 kips at which point it failed by flange local buckling. The failure of the pile progressed according to the following sequence: (1) at the load level of 615 kips, the bottom flange buckled; (2) at the load level of 665 kips the top flange buckled, and the bottom plate slipped as the axial deformation of the reduced section of the pile increased after which the load began to decrease as indicated in Figure 8.48(b); (3) at the load level of 599 kips, the slip of top plate occurred, the reduced section deformed dramatically, which led to a lateral deformation of the pile as shown in Figure 8.48(a).

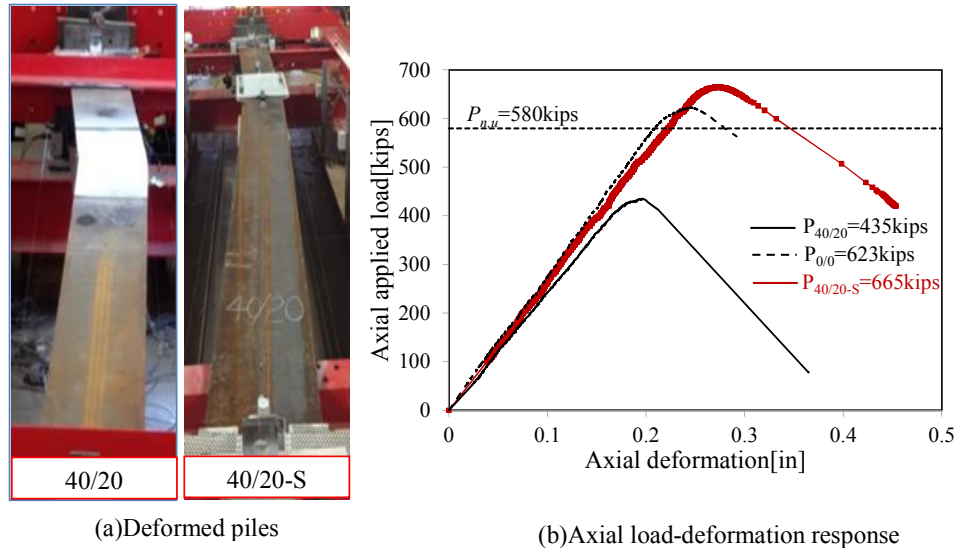


Figure 8.48: Comparison of Pile 40/20 and Pile 40/20-S

Inspection of the pile after failure indicated the presence of a localized buckle in the web as shown in Figure 8.49(a). After completing the test, the strengthening plates were removed to observe the flanges. The inspection indicated a minor local buckle in the flange as shown in Figure 8.49(b). The visual inspection also revealed localized damage and flaking of the protective coating on the main steel repair plate as shown in Figure 8.49(c). This did not appear to have an effect on the strength of the piles. However, it may affect the long-term durability of the system.

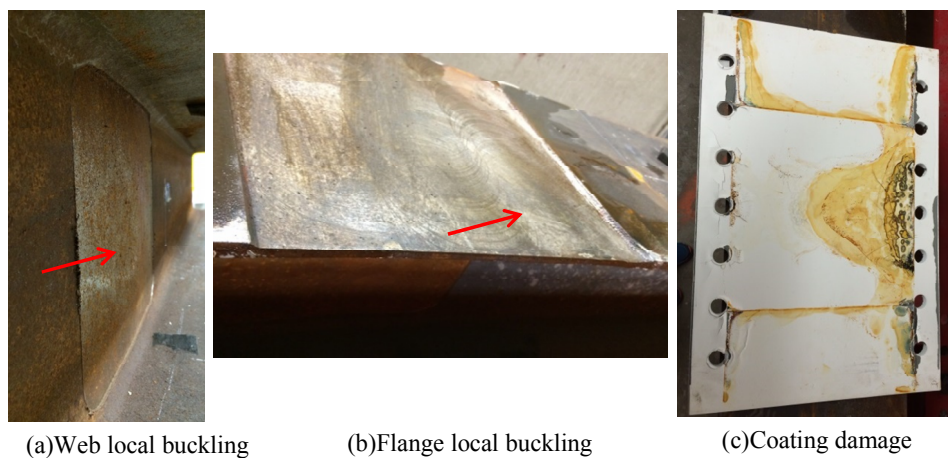


Figure 8.49: Observed local failure on Pile 40/20-S

Figure 8.50 presents the axial strain values obtained from the two strain gauges that were mounted to the repair plate and the pile. One gauge was attached to the steel repair plate and the other was attached to the pile on the reduced flange close to the flange/web junction. Two horizontal dashed lines indicate two load levels: 615 kips when bottom the flange reached the yield strain, and 665 kips when peak load was achieved. The strain of the top plate remained negligible during the test, which indicates that very little axial load was transmitted from the pile to the plate through friction. This indicates that the primary contribution of the repair system was to restrain the slender flanges enabling the deteriorated section to resist higher axial loads than the corroded control pile.

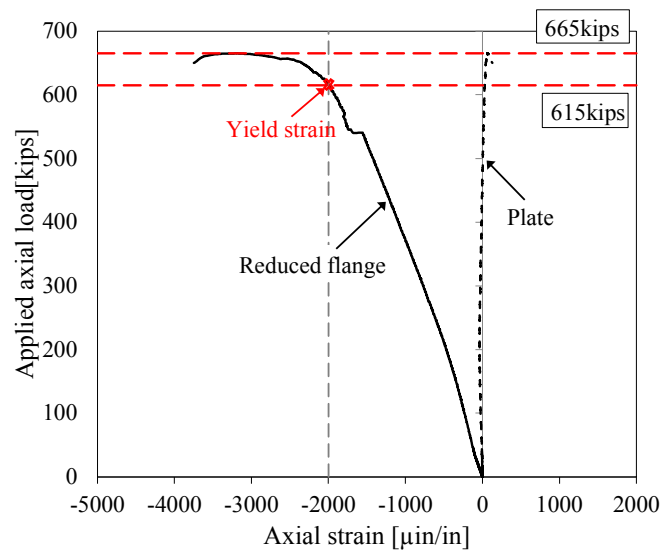


Figure 8.50: Axial strains of the plate and the reduced flange of Pile 40/20-S

Figure 8.51 shows the relative slip displacements between the steel repair plates and the flanges of the pile at the end of test frame away from the jack. The black and grey lines represent the top and bottom plate, respectively. The two horizontal dashed lines indicate the peak load level of 665 kips and the load level when axial deformation exhibited a sudden increase, which was 599 kips after the peak load. Inspection of Figure 8.51

reveals that the bottom plate slipped substantially at the peak load, and the top plate slipped substantially when the load decreased to 599 kips as seen by the horizontal plateaus in the figure. The difference between the top and bottom sides of the pile was attributed to unintentional eccentricity of the test set-up.

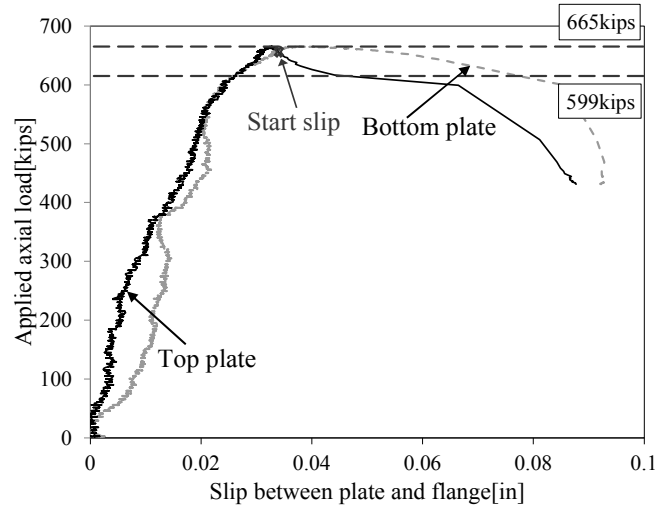


Figure 8.51: Slip of the steel repair plates of Pile 40/20-S

8.4.3. Pile 40/60-S

The pile was loaded monotonically up to a peak load of 618 kips at which point it failed by flange and web local buckling. Lateral displacement of the pile was observed after the peak load, as shown in Figure 8.52(a). After the peak load, the load dropped to 575 kips and increased slightly to 593 kips followed by a gradual decrease, as shown in Figure 8.52(b). This was attributed to progressive slip of the top and bottom repair plates.

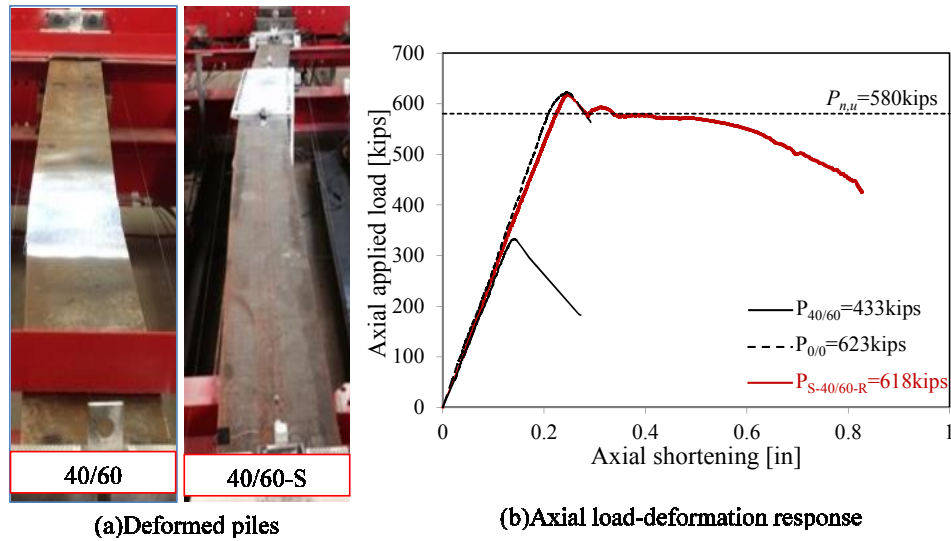


Figure 8.52: Comparison of Pile 40/60 and Pile 40/60-S

Web buckling was observed during testing before the peak load as shown in Figure 8.53(a). After completing the test, the strengthening plates were removed to observe the flanges. A higher order plate buckling (or crumpling) of the flanges was observed as shown in Figure 8.53(b). Additionally, all of the bolts were bent and one of them ruptured as shown in Figure 8.53(c). Pile 40/60-S was the only pile for which bevel washers were not used. The bending of the washers was believed to have occurred during installation of the repair system and may have been worsened during testing. The bolts in the remaining repaired piles, for which bevel washers were used, were straight after testing.

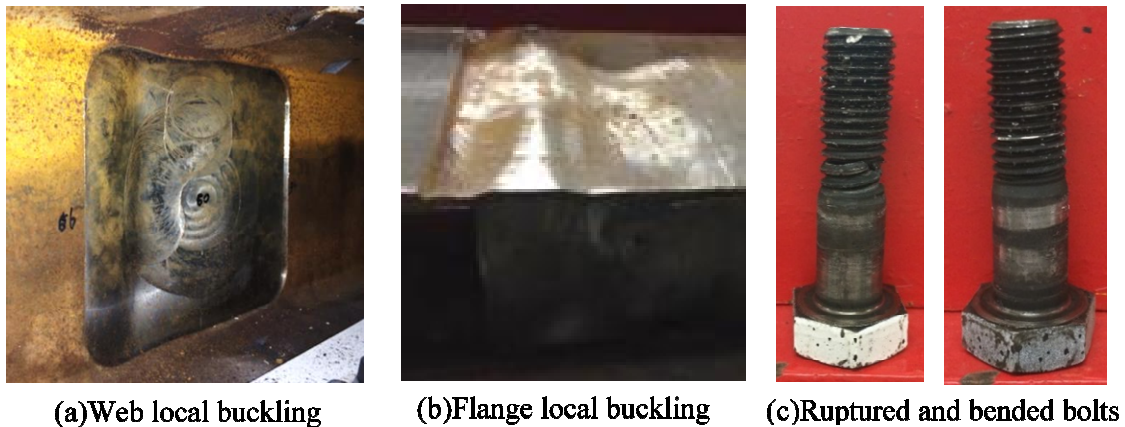


Figure 8.53: Buckled flange and web and damaged bolts of Pile 40/60-S

Figure 8.54(a) presents the axial strain values obtained from the two strain gauges, one attached on the steel repair plate and the other attached at the reduced flange close to the flange-to-web junction. The two horizontal dashed lines refer to two load levels, the first peak load of 618 kips, and the second smaller peak load of 593 kips. Inspection of Figure 8.54 indicates that the bottom flange buckled at the peak load. The strain in the repair plate was negligible throughout the loading history suggesting that very little load was transmitted to the repair system and the repair plates primarily served to delay buckling of the flanges.

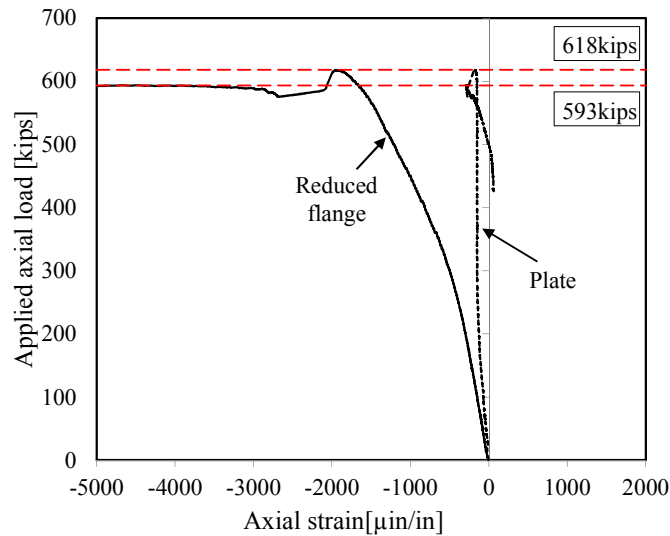


Figure 8.54: Axial strains of the plate and the reduced flange of Pile 40/60-S

Figure 8.55 shows the relative slip deformation between the steel repair plates and the pile flanges. The two horizontal dashed lines indicate the two peak loads of 618 and 593 kips. Inspection of Figure 8.55 reveals that the top plate slipped at the peak load, and the bottom plate slipped at the second peak load of 593 kips. This explains the load drop after the first peak load. Slip of the plates was followed by global lateral displacement of the pile. The difference between top and bottom sides of the pile was due to unintentional

eccentricity of the test set-up. The inspection also revealed localized damage and flaking of the protective coating on the main steel repair plate similarly to pile 40/20-S.

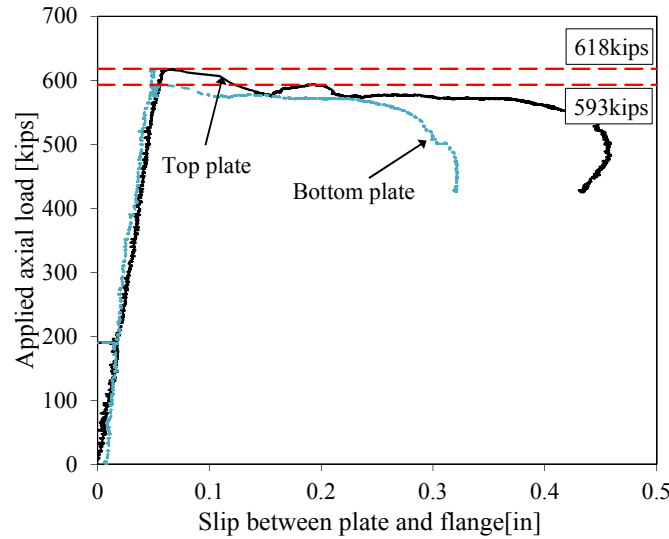
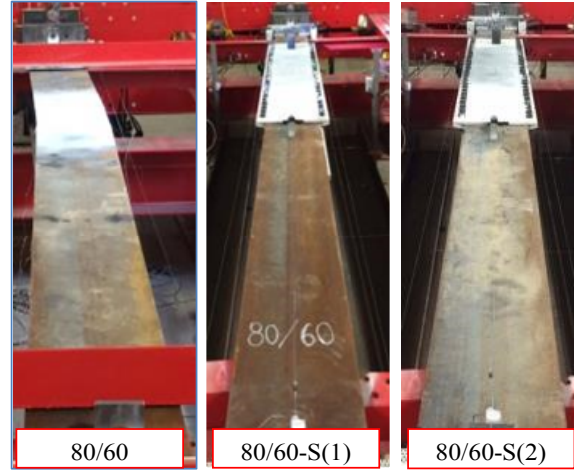


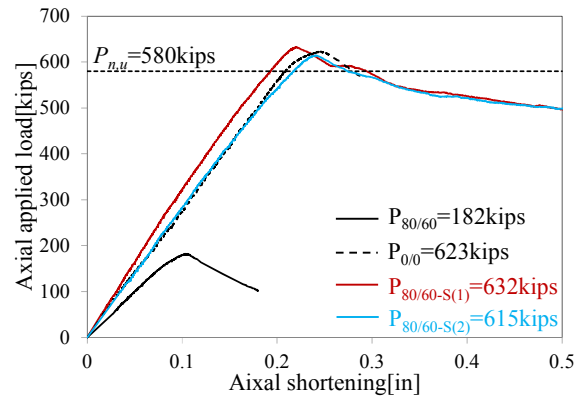
Figure 8.55: Slip of the steel repair plates of Pile 40/60-S

8.4.4. Piles 80/60-S(1) and 80/60-S(2)

Two piles were milled and repaired in nominally the same manner to evaluate the repeatability of the results. The piles were loaded monotonically to failure. Both piles exhibited the same failure, a crumpling deformation of flanges and web in the corroded region, and their peak loads were comparable. The comparable behaviors of these two piles indicate the repeatability of the steel-based repair system. Piles 80/60-S(1) and 80/60-S(2) failed at load levels of 632 kips and 615 kips, respectively. No lateral displacement was observed for the two piles, as shown in Figure 8.56(a). The onset of non-linearity was observed at a load level of 600 kips and 580 kips for piles 80/60-S(1) and 80/60-S(2), respectively, as shown in Figure 8.56(b). At this stage, web local buckling was observed, accompanied by sounds of the coating cracking.



(a) Deformed piles



(b) Axial load-deformation response

Figure 8.56: Comparison of Pile 80/60 and Piles 80/60-S(1) and 80/60-S(2)

After the test, the steel plates were removed to inspect the failure of the corroded region, as shown in Figure 8.57(a). The flanges and web within the corroded region exhibited crumpling deformations. The deformation indicated that the flanges were too slender to stiffen the web at the junction; meanwhile, the destabilization of the web caused the excessive deformation of the flanges. The outer layer of the coatings cracked and peeled near the edges of the flanges while both layers of coatings were damaged at the locations of the largest flange deformations, as shown in Figure 8.57(b).

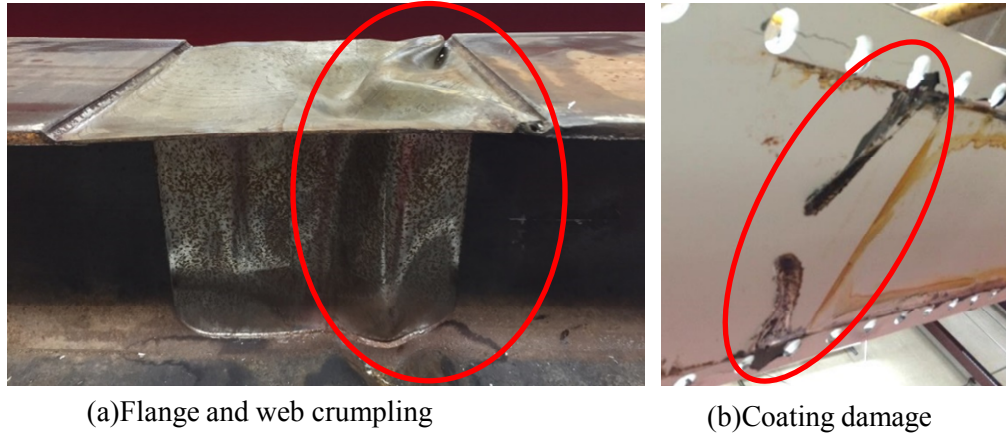


Figure 8.57: Buckled flange and web and coating damage of Pile 80/60-S(1) and 80/60-S(2)

Figure 8.58 shows the slip between steel repair plates and the pile flanges during testing. The top plate exhibited an increase of slip before the peak load was achieved and a sudden slip at the peak load, as shown in Figure 8.58. This indicated that the load demand at the interface between the pile and the repair plate exceeded the friction capacity of the interface. This caused the crumpling deformation of the corroded section and an increase in the axial deformation of the pile.

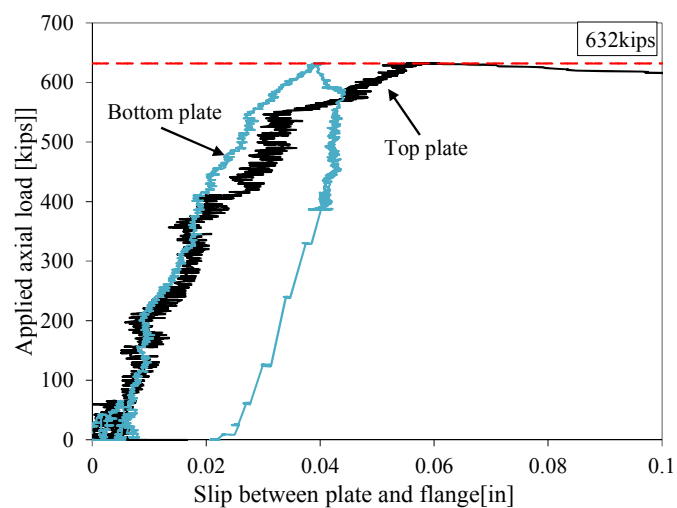


Figure 8.58 Slip of the steel repair plates of Pile 80/60-S(1)

8.4.5. Pile 80/60/V-S

Pile 80/60/V-S was loaded up to 630 kips, however, no lateral deformation was observed as illustrated in Figure 8.59. The axial load-shortening response of the pile closely matched that of the un-corroded control pile as shown in Figure 8.59.

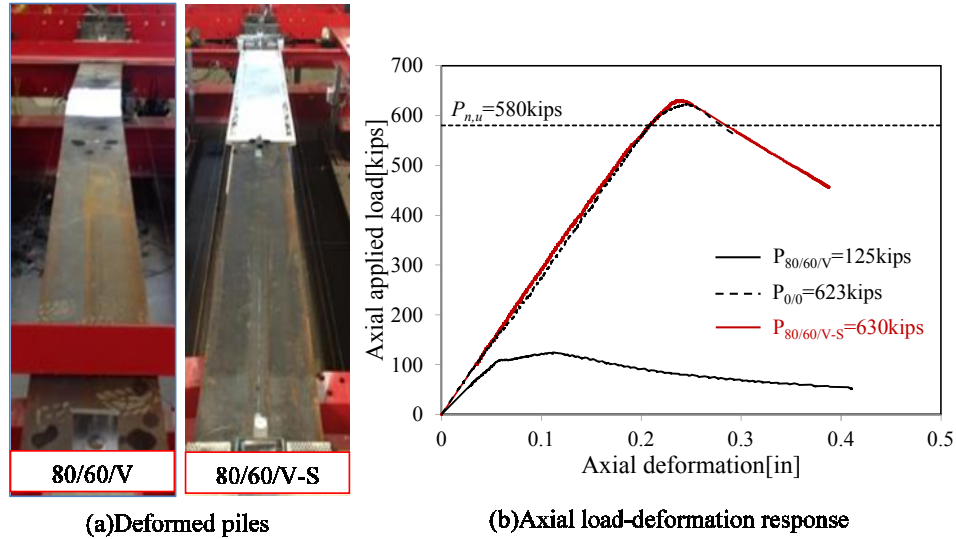


Figure 8.59: Comparison of Pile 80/60/V and Pile 80/60/V-S

The failure mode of the flange was similar to that of the corroded control pile as shown in Figure 8.60(a). Both piles exhibited flange one-way bending failures. However, removing the repair plates after testing indicated that the deformation patterns of the flanges of the corroded pile and the repaired pile were slightly different as shown in Figure 8.60(b). This was due to the restraint provided by the repair plates which prevented outward buckling of the flanges.

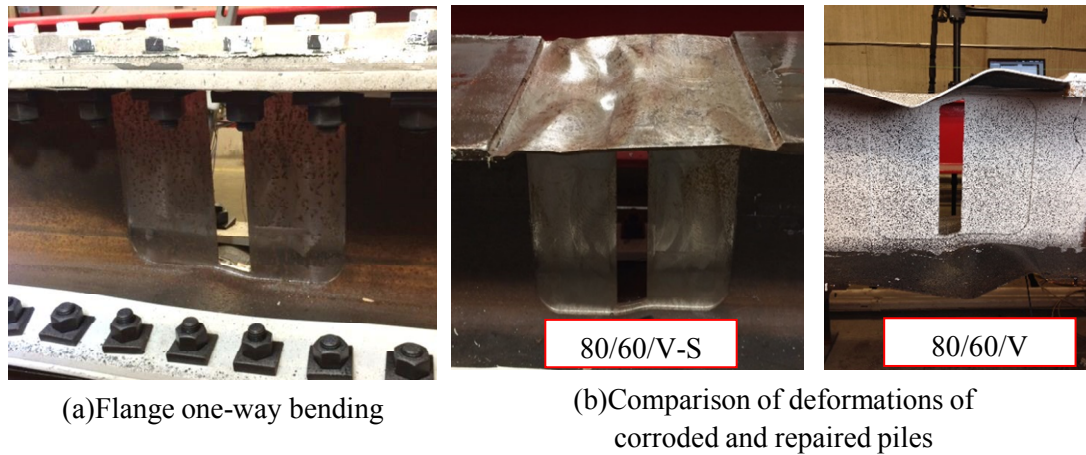


Figure 8.60: Observed failure on Pile 80/60/V-S and Pile 80/60/V

Figure 8.61 shows the slip between the steel repair plates and the flanges of the piles. Inspection of Figure 8.61 indicates that slip between the top flange of the pile and the repair plate increased dramatically after the peak load.

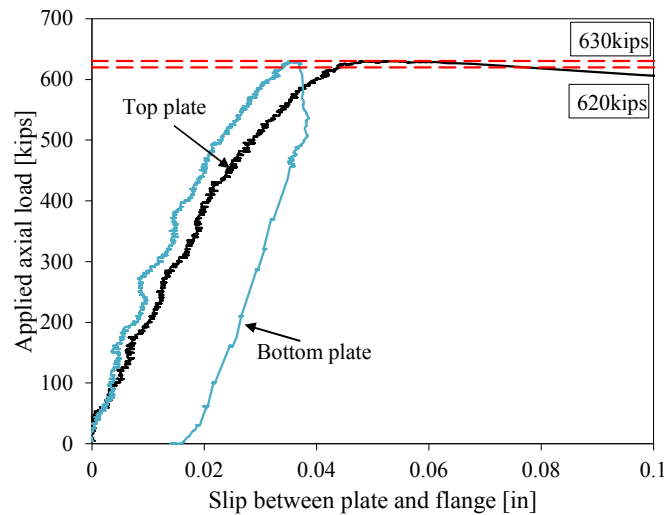


Figure 8.61: Slip of the steel repair plates of Pile 80/60/V-S

8.4.6. Pile 80/60/3-S

Pile 80/60/3-S had an 80% reduction of the flange thickness and 60% reduction of the web thickness along a 3 ft. long section of the pile. It was loaded up to 532 kips and failed by crumpling deformation of the flanges and web within the corroded region, with

no visible lateral displacement as shown in Figure 8.62(a). The load dropped substantially after reaching the peak, as illustrated in Figure 8.62(b).

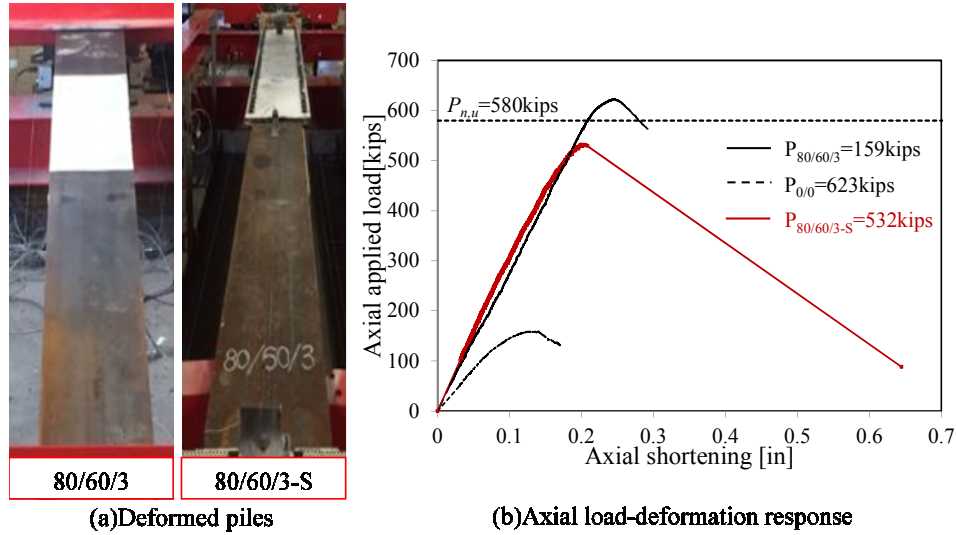


Figure 8.62: Comparison of Pile 80/60/3 and Pile 80/60/3-S

The measured capacity of the repaired pile was lower than the nominal capacity of the un-corroded control pile (the retrofitting target). This was because the location of the rollers of the test frame limited the length of the repair system, as shown in Figure 8.63(a). According to the design guidelines presented in the previous chapter the required length of the repair system to achieve the nominal capacity of the pile was 8.5 ft. However, the location of the roller on the test frame limited the length of repair system to 7.5 ft. Considering the reduced length of the repair system, the predicted pile capacity based on the design procedure described in the previous chapter is 496 kips which is 7% lower than the experimental result. This suggests that, although the repaired pile did not achieve the retrofitting target, the proposed design guidelines still conservatively predicted the reduced capacity of the repaired pile based on the modified repair configuration. Removing the steel repair plates after test demonstrated that the flanges

and web exhibited crumpling deformations similarly to piles 80/60-S(1) and 80/60-S(2), as shown in Figure 8.63(b).

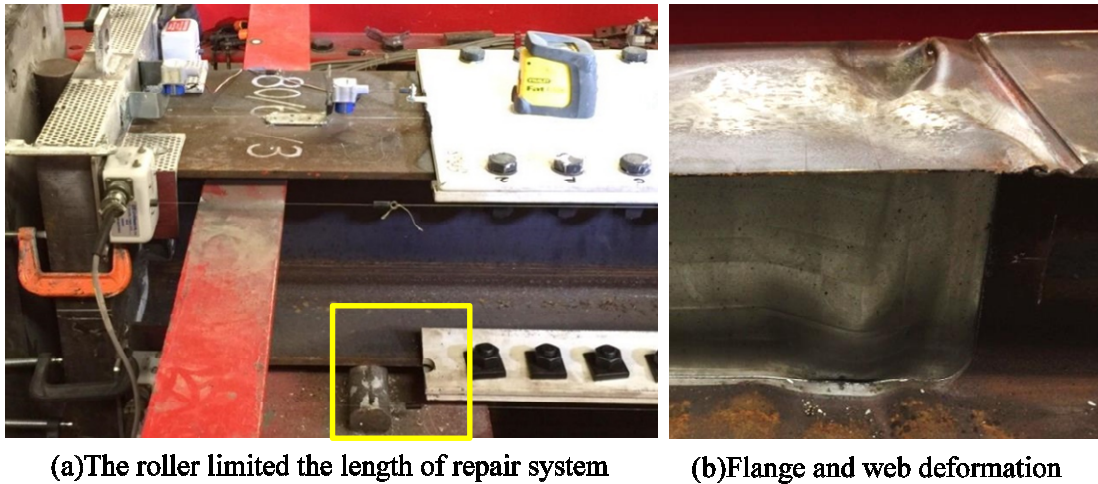


Figure 8.63: Observed failure on Pile 80/60/3-S

Figure 8.64 plots the relative slip deformations between the top repair plate and the top flange throughout the test. The top plate slipped dramatically after the peak load was achieved as shown in Figure 8.64. This was accompanied by the substantial axial deformation of the pile which resulted from the crumpling of the flanges and the web within the corroded region.

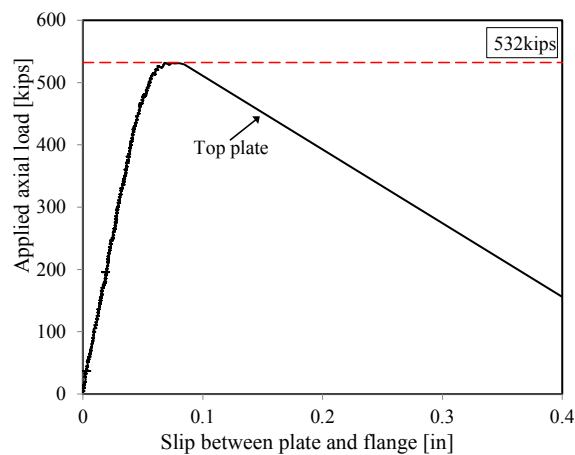


Figure 8.64: Slip of the steel repair plates of Pile 80/60/3-S

8.4.7. Comparison and Discussion

This section compares the experimental results of the full-scale corroded piles that were retrofitted using the friction-type bolted steel plate-based repair system. Comparisons of axial capacity and stiffness between corroded control piles and repaired piles are summarized to evaluate the effectiveness of the repair system.

Table 8.15 summarizes the axial capacity, axial stiffness, and failure mode of all of the corroded control piles and the piles that were repaired using the steel-based system. The target axial capacity of the repaired piles was taken as the nominal axial load of an uncorroded pile, $P_{n,u}$, calculated using the design method adopted in AASHTO (2012), which is 580 kips for 15-ft-long HP12×53 pile. Inspection of **Error! Reference source not found.** indicates that the repair system generally changed the failure mode of the piles from flange and web local buckling to a crumpling failure mode. This was attributed to the restraint of the flanges that was provided by the repair plates. The observed failures generally indicated that the flanges were too slender to stiffen the web at the junction; meanwhile, the destabilization of the web caused the excessive deformation of the flanges. Pile 80/60/V-S exhibited a similar failure mode to the corroded control pile 80/60/V, which was flange one-way bending near the web void.

Table 8.15: Experimental results of full-scale corroded and repaired piles

Pile Designation	Axial Peak Load [kips]	Stiffness [kip/in]	Failure Mode
$P_{n,u}$ or $k_{n,u}$	580	2,497	
0/0	623	2,776	FB ^a
0/20	604	2,816	FB
0/20-S	629	2,647	FB
40/20	435	2,448	FLB ^b
40/20-S	665	2,650	FLB
40/60	333	2,520	FLB/WLB ^c
40/60-S	618	2,750	Crumpling
80/60	182	2,001	FLB/WLB
80/60-S(1)	632	3,271	Crumpling
80/60-S(2)	615	2,798	Crumpling
80/60/V	124	1,930	FOWB ^d
80/60/V-S	630	2,907	FOWB
80/60/3	159	1,645	FLB/WLB
80/60/3-S	532	3,180	Crumpling

^aFlexural Buckling (FB); ^b Flange Local Buckling (FLB); ^c Web Local Buckling (WLB); ^dFlange One-way Bending (FOWB).

Figure 8.65 shows the comparison of the axial capacity between corroded and retrofitted piles. The horizontal axis represents the loss of the cross-sectional area, and the vertical axis refers to the axial capacity obtained from tested piles normalized by the nominal capacity of the un-corroded pile. The horizontal solid line indicates the nominal capacity of the un-corroded pile, the retrofitting target. The round dots indicate the corroded control piles, while the square dots represent the repaired piles. Inspection of **Error! Reference source not found.** and Figure 8.65 demonstrates the effectiveness of the steel-based repair system. Six out of seven of the repaired piles were effectively strengthened to the target capacity. The exception was due to the limitations of testing frame. Pile 80/60/3-S was knowingly designed to have a lower capacity. The predicted capacity of pile 80/60/3-S was 496 kips, which was 7% lower than the measured capacity. Figure

8.65 indicates that even with the most severe loss of the axial capacity, as in the case of pile 80/60/V, which had a remaining capacity of only 20% of the nominal capacity of uncorroded pile, the repair system effectively restored its capacity back to the nominal value.

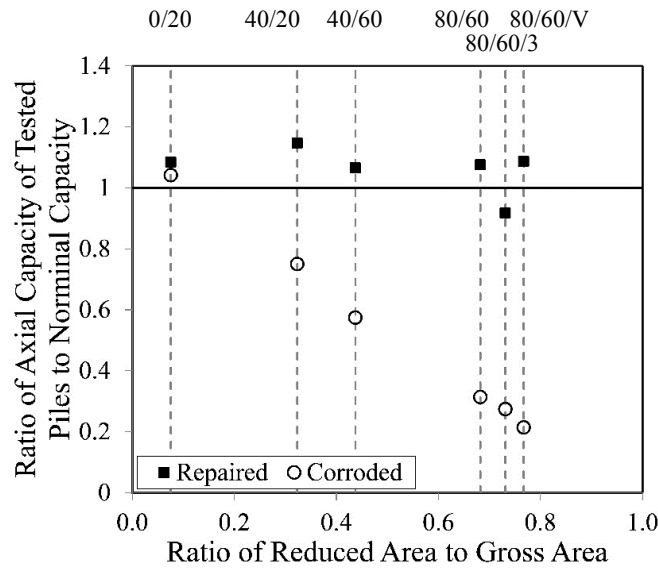


Figure 8.65: Comparison of axial load capacities between corroded and retrofitted piles

Figure 8.66 compares the axial stiffness of the corroded piles to those of the retrofitted piles. The horizontal axis represents the loss of cross-sectional area, and the vertical axis presents the experimentally determined axial stiffness of the piles normalized with respect to the nominal value of a 15 ft. HP12×53 section. The horizontal solid line indicates that the axial stiffness of tested piles equals the nominal stiffness of the uncorroded pile. The round dots refer to the corroded control piles, while the square dots refer to the repaired piles. Observation of **Error! Reference source not found.** and Figure 8.66 demonstrates that the axial stiffness of the corroded piles did not decrease as severely as their capacities. This was because the degraded region was only 1/15 of the total length of the piles (for pile 80/60/3 this value was 1/5). The greatest reduction of

axial stiffness was found for the pile with severe section loss along the longest section of the pile, namely 80/60/3. The stiffness was reduced by 34% compared to the stiffness of the un-corroded pile. The repair system increased the stiffness of that pile by 51%. Pile 0/20-S exhibited lower axial stiffness than Pile 0/20 due to its slightly smaller cross-sectional area. Therefore, the repair system efficiently enhanced the axial stiffness of the piles by compensating the cross-sectional area with the addition of the steel repair plates within the deteriorated region. This is beneficial to the serviceability of the piles, to prevent excessive deformation or differential settlement.

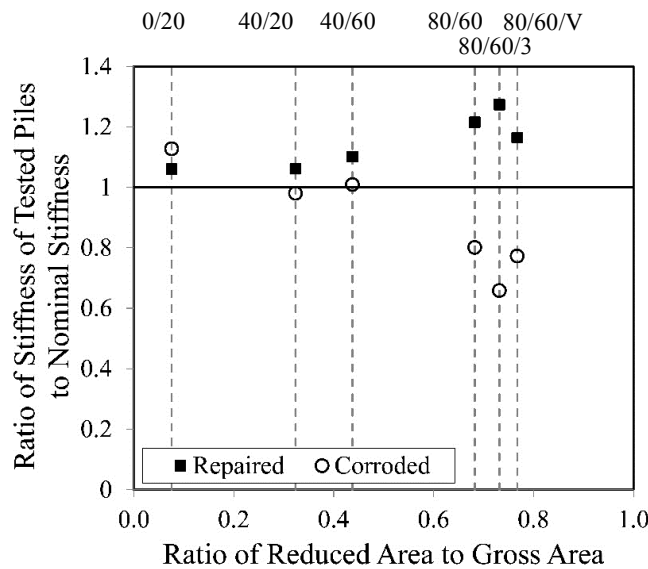


Figure 8.66: Comparison of axial stiffness between corroded and retrofitted piles

Chapter 9. Finite Element Analysis of Repaired Piles

A numerical study was conducted to simulate the behavior of corroded steel piles that are repaired with grouted FRP jackets and clamped steel plates and to complement the experimental investigation. A major component of this numerical investigation was to examine the assumed bond characteristics between the steel pile and the confined grout and to quantify the parameters of bond-slip characteristics that were used to represent the grout/steel interface. The numerical framework was used to predict the response of the 14 repaired full-scale piles that were tested in the corresponding experimental program. The numerical platform that was presented in Chapter 6 to predict the capacity of corroded steel piles was also extended to incorporate the steel plate-based repair system. The model was validated by comparing the predictions to the results of the seven tested piles that were presented in the previous chapter. The validated model was used to conduct a parametric study. The parameters considered included the coefficient of friction between the faying surfaces, magnitude of bolt pretension, and length of steel plates.

9.1. Finite Element Modeling of Grouted FRP Jacket Repairs

The following sections describe the finite element model that was developed to study corroded steel H-piles that are repaired using grout filled FRP jackets. The element types, mesh size, boundary conditions and material properties are presented. The influence of the interface law used at the grout/steel interface is discussed in detail. The model is used to predict the response of the 14 repaired piles that were discussed in the previous chapter and the predicted response is compared to the measured values.

9.1.1. Description of the Finite Element Model

Finite element modeling was implemented using the commercial finite element package ABAQUS v. 6.12 (SIMULIA, 2012). General static solution method, which uses full Newton approach, was selected as the solution technique. The model accounted for material and geometric non-linearity, residual stresses, initial imperfections, and imperfect bond at the grout/steel interface.

9.1.1.1. Element Types and Mesh Size

Figure 9.1 illustrates the components of a modeled repaired pile with a through-web void. The FRP jacket and steel piles were modeled with four-noded shell elements with six degrees of freedom at each node and linear shape functions (S4). The grout was modeled using eight-noded, 3D continuum brick elements with three degrees of freedom at each node and linear shape functions (C3D8). Truss elements were employed to model reinforcing bars and anchors. The truss elements were two-noded three dimensional truss element with three degrees of freedom at each node and linear shape function (T3D2). Steel end plates were modeled at the ends of the pile to restrain warping and to represent the thick loading plates that were used in the experimental program. In bridge applications one end of the steel pile is embedded in the ground while the other is typically embedded in a concrete bent cap. This embedment would have a similar restraining effect as the steel plates used in this analysis. Since nodal degrees of freedom of solid and shell elements are not compatible, ABAQUS uses a coupling formulation at the shell-solid interface to address this lack of compatibility. The displacement of the shell node constrains the

displacement of the corresponding solid node. In addition, the rotation of the shell node at the interface constrains to the rotation of the corresponding line of the nodes in the adjacent solid component (SIMULIA, 2012).

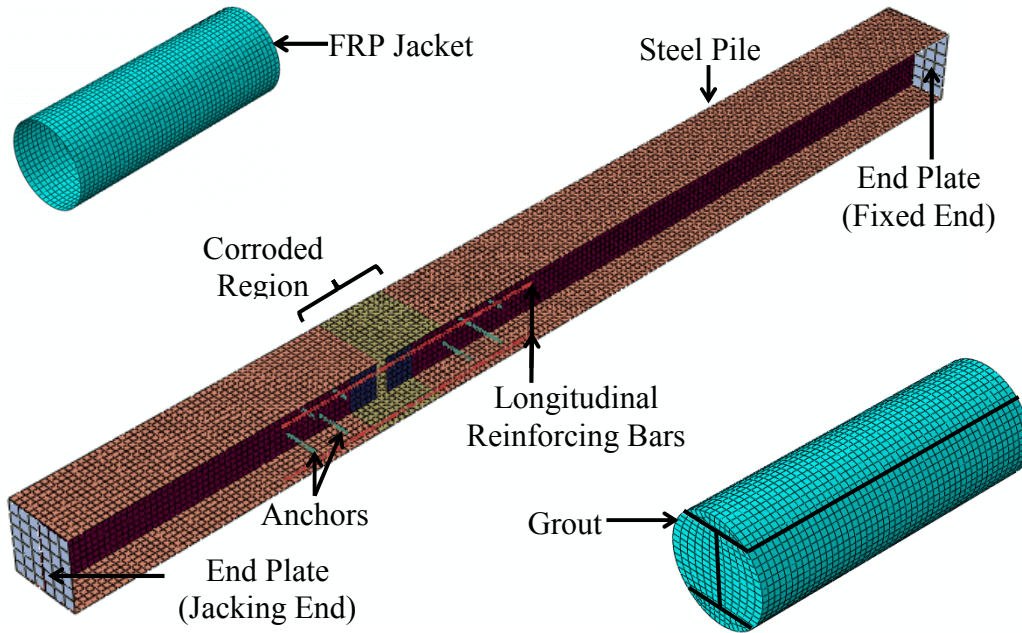


Figure 9.1: Components of modeled repaired piles

In previous studies, both linear and quadratic shell elements were used to model thin-walled steel columns (Schafer et al., 2010) or steel tubes in contact with concrete (Ellobody and Young, 2006). To investigate the sensitivity of the response to mesh size and element type, pile 40/60-F2/R was modeled with different mesh sizes and element types. Three different mesh sizes, 2 in., 1 in., and 0.5 in., were selected to conduct the sensitivity analysis. In addition, the results of the analysis with linear and quadratic shape functions with 2-in. mesh size were compared. The mesh size (h-refinement) and element type (p-refinement) for all of the components of the model were refined simultaneously. That is, uniform element types (linear or quadratic) and mesh sizes were used throughout the entire model. Table 9.1 summarizes the element

types considered in the sensitivity analysis along with the corresponding designations used in ABAQUS.

Table 9.1: Type of elements used to model each part in sensitivity study

Part	Shape Function	Element Designation	
Pile	Linear	S4	4-node linear general shell, finite membrane strain
Grout		C3D8	8-node linear 3D continuum (brick)
FRP		S4	4-node linear general shell, finite membrane strain
Reinforcing bars		T3D2	2-node linear 3D truss
Pile	Quadratic	S8R	8-node quadratic thick shell, reduced integration
Grout		C3D20R	20-node quadratic 3D continuum (brick), reduced integration
FRP		S8R	8-node quadratic thick shell, reduced integration
Reinforcing bars		T3D3	3-node quadratic 3D truss

Table 9.2 summarizes the number of nodes and elements associated with the different mesh sizes. The models ran on the Maxwell cluster at the University of Houston using 8 processor cores. The table also shows the computation time in seconds per processor core. The FE model with the mesh size of 2 in. was analyzed with both linear and quadratic elements. The analysis for the other two mesh sizes was conducted using only linear elements.

Table 9.2: Comparison of the number of nodes, elements, and computational time for different mesh sizes and element types

Component	Mesh Size						
	2 in.		Quadratic Shape Functions	1 in.		0.5 in.	
	Linear Shape Functions			Linear Shape Functions		Linear Shape Functions	
	# of Elements	# of Nodes	# of Nodes	# of Elements	# of Nodes	# of Elements	# of Nodes
Pile	1620	6920	10268	6480	11888	25920	31544
Grout	1776	2800	10038	10656	14210	78336	91762
FRP	648	675	1998	2592	2646	10272	10379
Reinforcing bar	100	96	196	192	196	384	388
Total	10495	4140	22500	19920	28940	114912	134073
Computational Time (sec./core)	260		574	394		4303	

Figure 9.2 shows the effect of the element size and shape functions on the predicted axial load-shortening relationship of the 40/60-F2/R pile as compared to the measured response. The figure indicates that the predicted response is not sensitive to the mesh size or element type up to the peak load. However, the model with 2 in. linear elements predicts a slightly higher post peak capacity than the other models. Considering the computational time and axial load-shortening response 1 in. linear elements were selected for the modeling of the rest of the repaired piles.

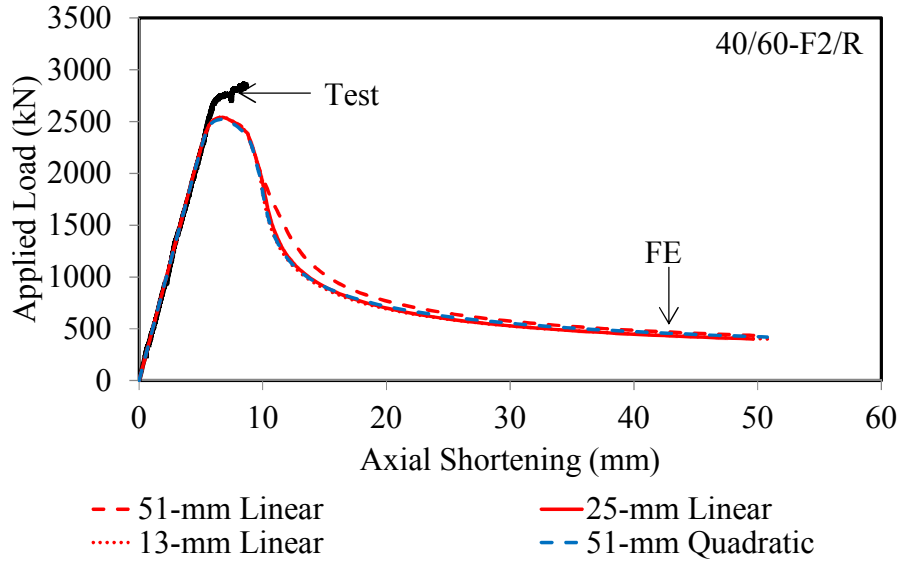


Figure 9.2: Sensitivity of load-shortening response to different mesh size and type

Table 9.3 shows the element type and size selected for FE modeling of the tested repaired piles. Since the pile considered in the sensitivity study did not include anchors element type and mesh size of the anchor elements were selected to be consistent with those of the reinforcing bar elements.

Table 9.3: Selected element type and mesh size for FE modeling

Part	Element Type	Element Size (in)
Pile	S4	1×1
Grout	C3D8	1×1×1
FRP	S4	1×1
Reinforcing bars	T3D2	1
Anchors	T3D2	1

9.1.1.2. Boundary Conditions

Figure 9.3 shows the modeled pile with the un-restrained degrees of freedom, in a global sense. The repaired piles were modeled with both ends fixed against rotation about the strong axis and free to rotate about the weak axis to represent the boundary conditions used during testing. At the fixed end of the pile translation was restrained

in three perpendicular directions. At the jacking end translation was restrained in the global X and Y directions but the pile was free to translate in the axial, global Z, direction as shown in Figure 9.3. The pile was loaded in displacement control by increasing the Z-direction displacement at the jacking end.

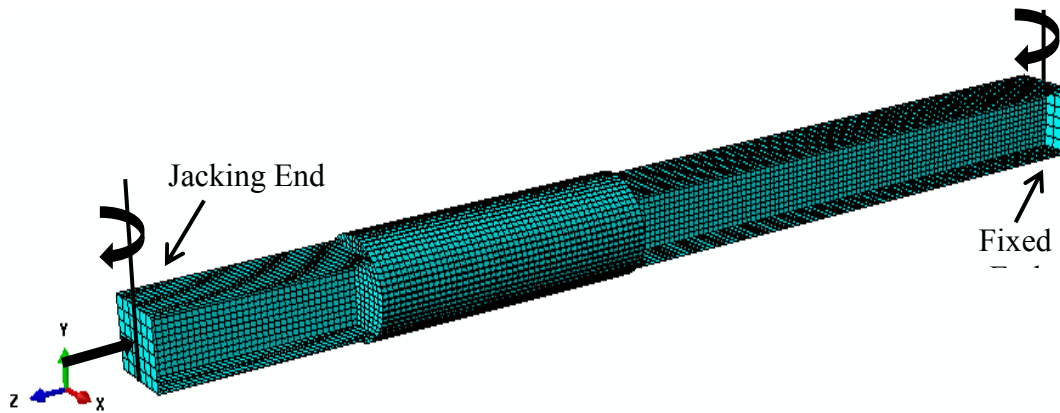


Figure 9.3: Applied boundary conditions to FE model

9.1.1.3. Initial Out-of-Straightness

Initial out-of-straightness of columns was considered as a half-sine lateral deformation (Ziemian, 2010; AISC, 2010; Seif and Schafer, 2010a; Shi et al., 2014). Figure 9.4 shows the global initial imperfection which was applied after installation of the repair system on the pile. The initial global imperfections were applied after the repair system was implemented in the model to avoid an error due to the distance between the adjacent nodes of the steel pile and grout core being beyond the acceptable tolerances to model contact. To apply the initial imperfection, prior to analyzing the pile under axial deformation the repaired pile was analyzed under a half-sine lateral displacement until the maximum magnitude of deflection at mid-span reached the pre-defined target value. A sensitivity analysis to assess the impact of the magnitude of the initial imperfection was conducted by considering pile 40/60-F2/R.

The pile was analyzed under two maximum magnitudes of the lateral deformations at mid-span, $L/1000=0.18$ in and $L/1500=0.12$ in.

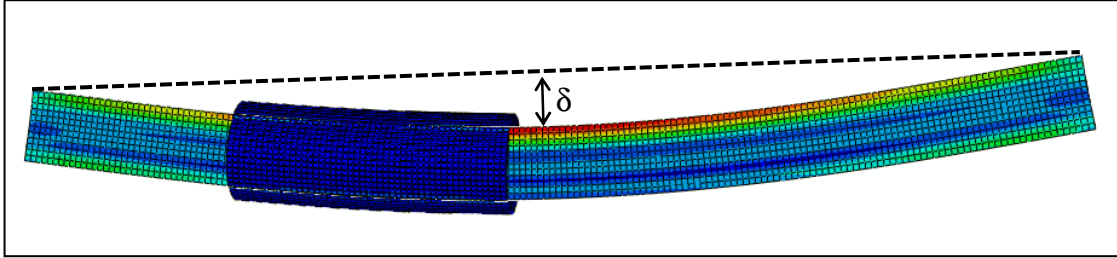


Figure 9.4: Applied initial global imperfection to FE models

Figure 9.5 compares the axial load-shortening responses of the pile 40/60-F2/R analyzed with two different maximum magnitudes of lateral deformation at mid-span. Increasing the maximum initial imperfection by 50% resulted in a 5% decrease in the peak load. The amplitude of the initial global imperfection was taken as $L/1000$ since this is the maximum value used to develop the column curves in the existing AASHTO and AISC design specifications (Ziemian, 2010)

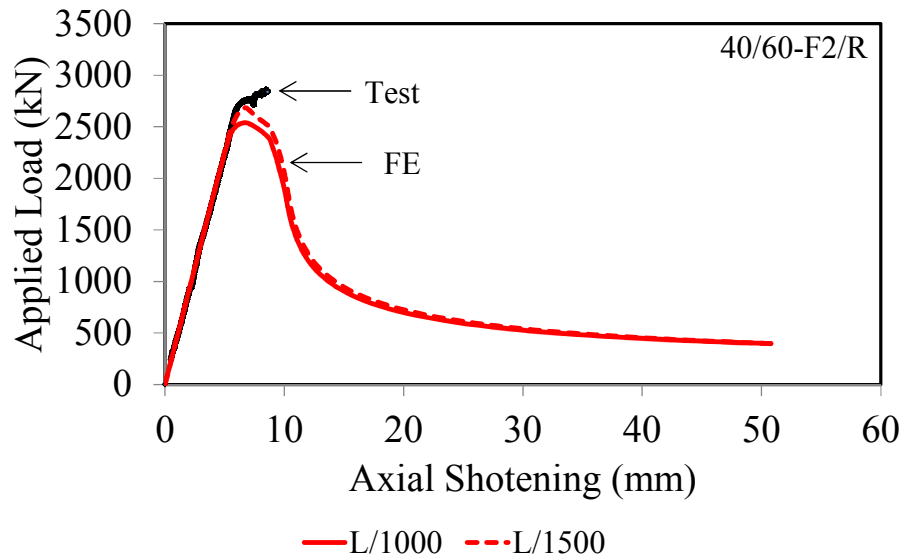


Figure 9.5: Effect of initial imperfection on axial load-shortening response

9.1.1.4. Material Properties

The following sections describe the material models that were adopted for the steel piles, steel reinforcing bars, steel anchors, grout, and FRP jackets in the finite element analyses.

- **Steel Piles**

A bilinear elasto-plastic material model was used for the steel piles. In the elastic region an isotropic model was defined using the measured elastic modulus and Poisson's ratio of the steel as obtained from the tension coupon tests reported in Chapter 4. The von Mises yield surface with associated plastic flow and isotropic hardening were considered with yield stress, ultimate stress, and corresponding plastic strains determined from material level tests. Table 9.4 summarizes the properties assigned to the flange and web elements. The tensile modulus, yield stress, ultimate stress, and ultimate plastic strain were measured while the Poisson's ratio was assumed.

Table 9.4: Assigned properties to steel flange and web elements

Part	Tensile Modulus	Yield Stress	Ultimate Stress	Ultimate Plastic Strain	Poisson's Ratio
	[ksi]	[ksi]	[ksi]	[in/in]	
Flange	28420	52.2	66.6	0.1724	0.3
Web	32045	60.6	71.2	0.0778	0.3

The magnitude and distribution of residual stresses as defined by Seif and Schafer (2010a) were adopted in this study as shown in Figure 9.6. The maximum compressive and tensile residual stresses were calculated as:

$$\sigma_c = 0.3 f_y = -15.0 \text{ ksi} \quad (\text{Eq. 9-1})$$

$$\sigma_t = \sigma_c \left(\frac{b_f t_f}{b_f t_f + t_w (d - 2t_f)} \right) = +7.83 \text{ ksi} \quad (\text{Eq. 9-2})$$

Figure 9.6(a) shows the idealized distribution of residual stresses while Figure 9.6(b) shows the discretized form that was adopted in this study based on the selected 1 in element size and considering equilibrium of forces in the axial direction.

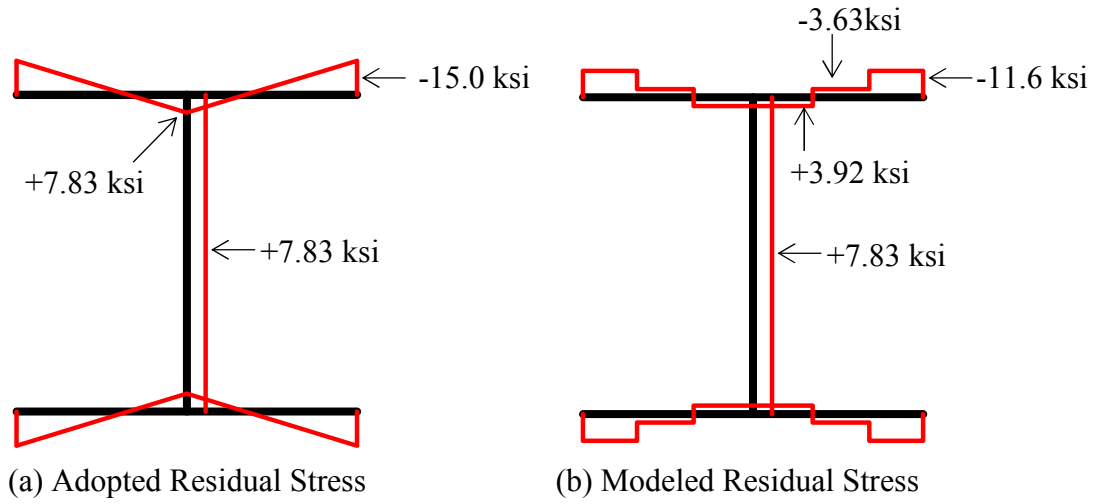


Figure 9.6: Residual stress magnitude and distribution

Figure 9.7 compares the axial load-shortening response of the tested pile to the FE prediction. As illustrated in this figure, incorporating the residual stresses in the model led to a 13% reduction of the peak load as compared to a similar model without residual stresses while the residual stresses had no influence on the post-peak response. The adopted residual stress distribution and magnitude were applied to all the modeled piles throughout this numerical analysis.

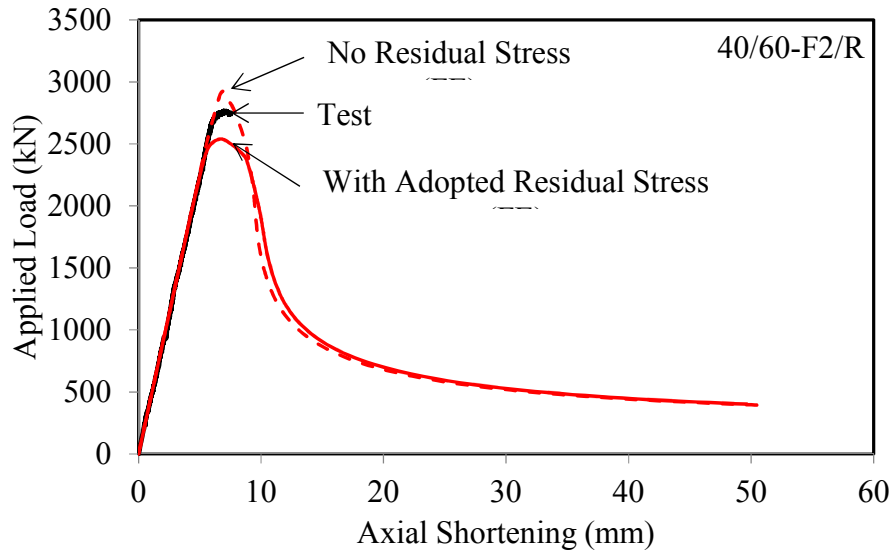


Figure 9.7: Effect of residual stress on axial load-shortening response

- **Steel Reinforcing Bars**

Similarly to the steel piles a bi-linear elasto-plastic material model was used to model the steel reinforcing bars. Table 9.5 presents the material properties that were adopted for the rebar elements. Measured values were adopted for the tensile modulus, yield stress, ultimate stress, and corresponding ultimate plastic strain. While nominal values were adopted for the diameter and Poisson's ratio.

Table 9.5: Assigned properties to reinforcing bar elements

Part	Diameter	Tensile modulus	Yield stress	Ultimate stress	Ultimate plastic strain	Poisson's ratio
	(in)	(ksi)	(ksi)	(ksi)	(in/in)	
Rebar #6	0.75	29870	68.7	104.5	0.1195	0.3
Rebar #8	1.0	32480	61.8	91.5	0.122	0.3

- **Steel Anchors**

A linear-elastic isotropic model was used for the steel anchors. Table 9.6 shows the properties of the anchor elements. The tensile modulus and Poisson's ratio are nominal values. The effective diameter was calculated by considering the effect of threads in reducing the cross-sectional area.

Table 9.6: Assigned properties to anchor elements

Part	Effective diameter (in)	Tensile modulus (ksi)	Poisson's ratio
Anchor	0.87	29000	0.3

- **Grout**

Since crushing of the grout was not observed in the experimental study an isotropic elastic stress-strain model was assigned to the grout using the measured initial elastic modulus. No failure was defined for the grout material. Table 9.7 summarizes the measured compressive modulus assigned to the grout elements of the modeled piles.

Table 9.7: Assigned properties to grout elements

Pile	Compressive modulus (ksi)	Pile	Compressive modulus (ksi)
0/20-F1	3625	0/20-F2	4060
40/20-F1/R	3480	40/20-F2/R	4495
40/60-F1/R	3915	40/60-F2/R	4205
80/60(1)-F1/R	3915	80/60(1)-F2/R	4205
80/60(2)-F1/RA	3480	80/60(2)-F2/RA	4060
80/60/V-F1/RA	4060	80/60/V-F2/RA	4640
80/60/3-F1/RA	3625	80/60/3-F2/RA	4205

- **FRP Jackets**

The FRP jackets were modeled as orthotropic, layered, elastic materials as summarized in Table 9.8. The F1 system consisted of one type of CFRP while the F2 system consisted of two types of FRP, one GFRP and one CFRP.

Table 9.8: Assigned properties to FRP elements

FRP Laminate	Thickness per layer (in)	E ₁ (ksi)	E ₂ (ksi)	G ₁₂ (ksi)	G ₁₃ (ksi)	G ₂₃ (ksi)	ε _{fu} (in/in)
F1-CFRP	0.028	7105	2900	2755	2755	0	0.3
F2-CFRP	0.039	12325	435	435	435	0	0.3
F2-GFRP	0.051	3770	435	435	435	0	0.3

9.1.1.5. Grout/Steel Pile Interface Properties

This FE models include several interfaces as summarized in Table 9.9. Tie constraints were employed at all of the interfaces except the grout/steel pile interface. In the tie model, all of the degrees of freedom at the nodes on the slave surface were constrained to the corresponding degrees of freedom of the adjacent nodes on the master surface which represents a perfect bond condition.

Table 9.9: Existing interfaces in FE model

Interface	Interaction Type	Master Surface	Slave Surface
Grout/Steel Pile	Surface-to-surface contact	Steel pile	Grout
Grout-FRP	Tie constraint	Grout	FRP
Grout-Rebar	Tie constraint	Grout	Rebar
Grout-Anchor	Tie constraint	Grout	Anchor

For the surface-to-surface contact model the bond characteristics, i.e. bond stiffness and strength in tangential and normal directions, were utilized to correlate the movement of the node on the slave nodes to the adjacent nodes on the master surface

based on a bond stress-slip relationship as shown in Figure 9.8 for the tangential direction (SIMULIA, 2012). Contact properties are defined using cohesive and friction properties at the interface. The cohesive properties include the bond stiffnesses in the normal and tangential directions, K_n and K_s , bond strengths in the normal and tangential directions, τ_n and τ_s , and fracture energy, G as shown in Figure 9.8(a). Friction is defined by the coefficient of friction, μ (see Figure 9.8(b)). To investigate the influence of bond characteristics at the grout/steel pile interface on the behavior of the repaired piles, a sensitivity analysis was conducted. Pile 80/60-F2/R was used for the sensitivity analysis since this was the only pile which exhibited complete separation between the grout and the steel pile during the failure process (after rupture of the FRP jacket at the end of the test).

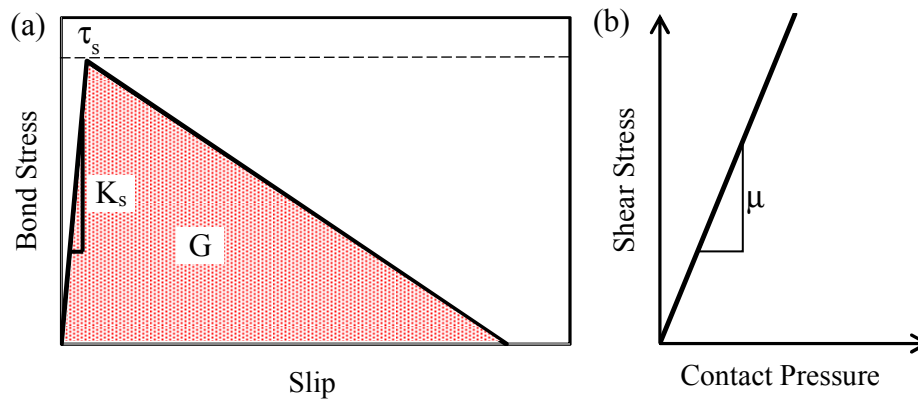


Figure 9.8: Cohesive and friction properties in tangential direction

9.1.1.6. Bond-Slip Model

Figure 9.9 shows the bond-slip relationship proposed by Liu et al. (2005) for the interface between FRP-confined expansive concrete and steel. The dashed line in the figure represents a simplified bi-linear bond-slip model from the proposed model which was used in the numerical modeling.

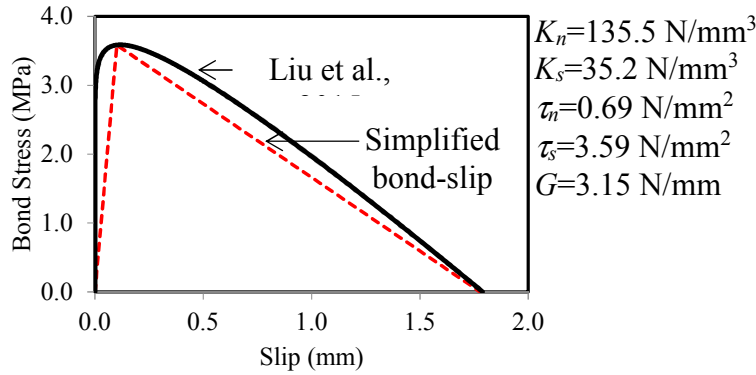


Figure 9.9: Comparing of the proposed model (Liu et al., 2005) and simplified model

In addition, the pile was analyzed under two other extreme cases, full bond and negligible bond interaction at the grout/steel pile interface. Full-bond interaction was defined by using a tie model at the interface. A friction type contact with a coefficient of friction, μ , of 0.1 was used to define the negligible bond interaction. Table 9.10 summarizes the characteristics of the defined interface models.

Table 9.10: Bond characteristics of the existing models

Model	Interaction Type	Coefficient of friction (μ)	Normal Stiffness (K_n) lb/in ³	Normal Stress (τ_n) lb/in ²	Tangential Stiffness ($K_s=K_t$) lb/in ³	Tangential Stress ($\tau_s=\tau_t$) lb/in ²	Fracture energy (G) lb/in
Full-bond	Tie constraint	N/A ^a	N/A ^a	N/A ^a	N/A ^a	N/A ^a	N/A ^a
Low friction	Surface-to-surface contact	0.1	N/A ^a	N/A ^a	N/A ^a	N/A ^a	N/A ^a
Liu et al., 2005	Surface-to-surface contact	N/A ^a	499000	100	130,000	520	18.0

^a This parameter did not apply to the model

Figure 9.10 compares the measured axial load-shortening responses of the tested pile to the predicted response using the different bond characteristics described above. Modeling the bond at the grout/steel interface using the relationship proposed by Liu et al. (2005) resulted in a response that was closer to the full-bond model than to the

negligible bond model. The responses of the full bond model and the model by Liu et al. (2005) were linear up to the peak load with axial stiffnesses that were 30% and 15% higher, respectively, than the measured values. This suggests that the full-bond and Liu et al. (2005) models are not representative of the actual bond behavior of the tested piles. Consequently, a series of sensitivity analyses were conducted to investigate the influence of different bond characteristics on the axial load-shortening response.

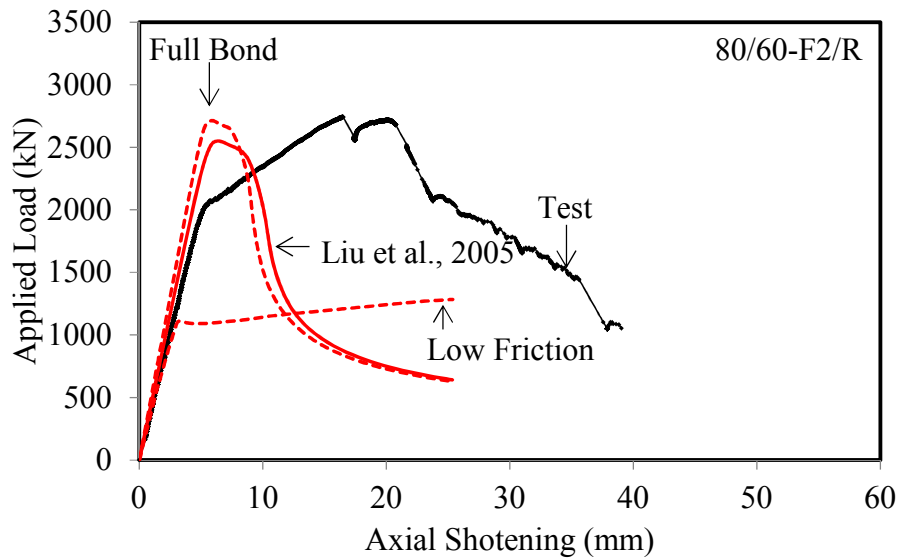


Figure 9.10: Comparison of full-bond, low friction, and Liu et al. bond-slip relationship

9.1.1.7. Effect of Tangential Bond Stiffness

Figure 9.11 compares the load-shortening responses of the tested pile and responses obtained by changing the tangential stiffness, K_s , of the grout/steel interface. As shown in Figure 9.11, modeling the pile with tangential stiffnesses of 130,000, 50,100, and 9,940 lb/in³ at the interface resulted in 16%, 13% and 5% errors, respectively, in the calculated axial stiffnesses of the modeled pile compared to the

measured value. All of the modeled piles failed by global buckling. A tangential stiffness, K_s , of 9,940 lb/in³ was selected for modeling the rest of the piles.

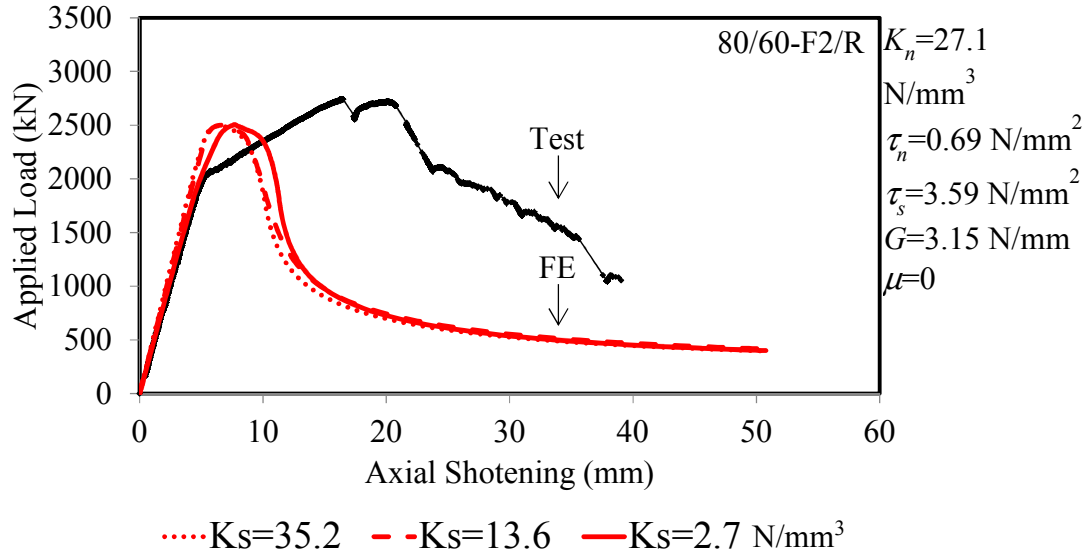


Figure 9.11: Effect of tangential bond stiffness on axial load-shortening response

9.1.1.8. Effect of Tangential Bond Strength, τ_s

Three different tangential bond strengths 0.52, 0.30, and 0.20 ksi were considered, and the results showed that the dominant failure mode changed by reducing the bond strength. Figure 9.12(a) shows the failure mode of the pile with a bond strength of 0.52 ksi at the grout/steel interface. In the figure the FRP-confined grout repair system has been removed for clarity. Using a tangential bond strength of 0.52 ksi the modeled pile demonstrated global lateral deformation accompanied by local buckling of the flange in the un-corroded region, just outside the repair system. Reducing the bond strength to 0.30 or 0.20 ksi led to localized crumpling deformation within the corroded region as shown in Figure 9.12(b).

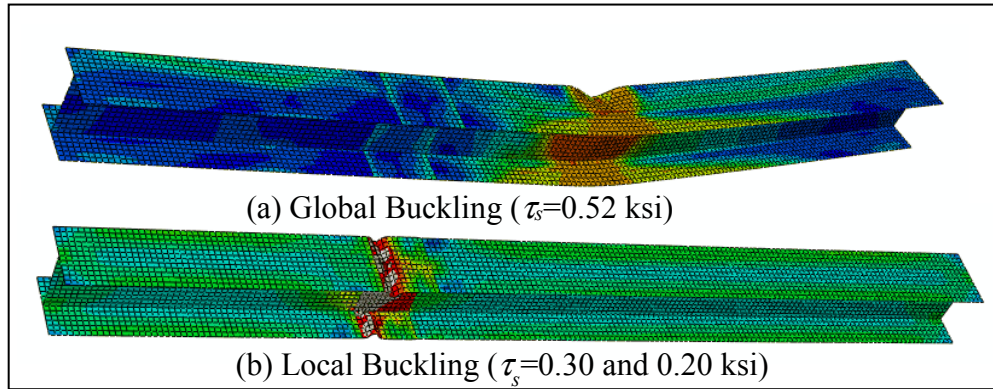


Figure 9.12: Changing the pile deformation by decreasing the bond strength

Figure 9.13 compares the load-shortening responses of the tested pile to the predicted responses obtained by changing the tangential bond strength of the grout/steel interface in the FEM. Point 1 and 2 are associated with changes in the axial stiffness of the piles with 0.20 and 0.30 ksi bond strengths, respectively. Point 3 corresponds to the peak load of the pile with bond strength of 0.52 ksi.

The response of the pile with bond strength of 0.52 ksi showed a descending branch after the peak load, point 3 in Figure 9.13, due to the local and global buckling of the pile. The responses of the other piles with lower bond strengths demonstrated hardening responses after a change in the axial stiffness at points 1 and 2 in Figure 9.13. The analysis of the piles modeled with shearing bond stress of 0.20 ksi and 0.30 ksi terminated prior to observing any drop in the axial load.

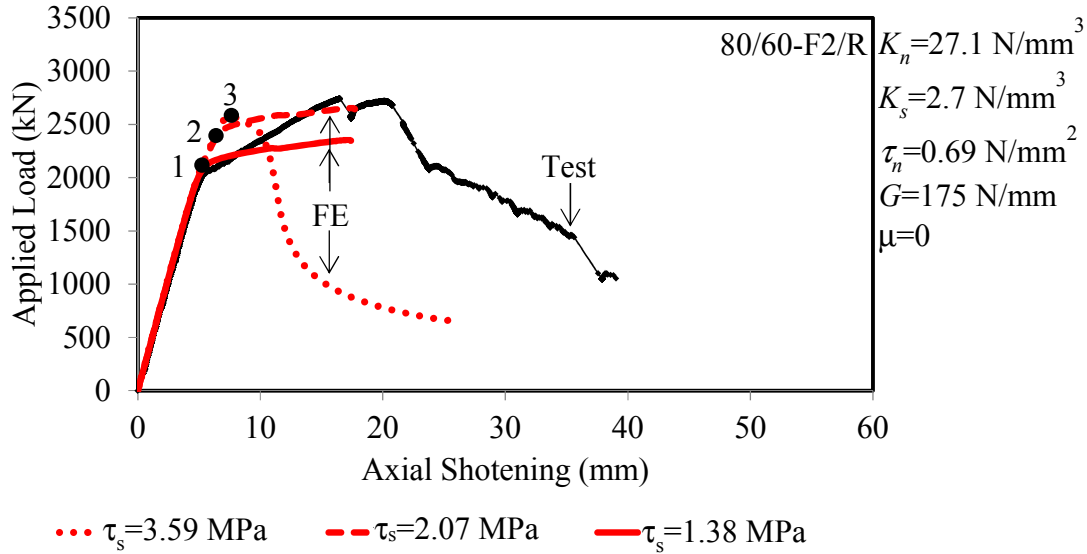


Figure 9.13: Effect of tangential bond strength on axial load-shortening response

Considering the axial load-shortening response and failure mode of the steel pile observed in the test, the bond strength of $\tau_s=0.20$ ksi was selected to model rest of the tested piles.

9.1.1.9. Effect of Fracture Energy

Figure 9.14 compares the response obtained from the test to the calculated axial load-shortening response of the repaired pile 80/60-F2/R with different magnitudes of fracture energy at the grout/steel interface. Increasing the magnitude of the fracture energy increased the axial deformation at the peak load. The pile modeled with the lowest value of fracture energy, $G=18.0$ lb/in, showed a softening response immediately after the onset of non-linearity at an axial shortening of 0.27 in. However, the piles analyzed with the fracture energy values of 100 and 1000 lb/in did not exhibit a softening response after the bond failure and attained 37% and 71% higher values of axial shortening at their peak loads compared to the pile with fracture

energy of 18.0 lb/in. All three modeled piles demonstrated localized flange and web crumpling deformations. The analysis of the pile modeled with G of 100 lb/in terminated prior to observing any drop in the axial load. The fracture energy value, G of 1000 lb/in was selected for analyzing the rest of the piles since it provided the closest prediction of the trend of the axial load-shortening response to that obtained experimentally.

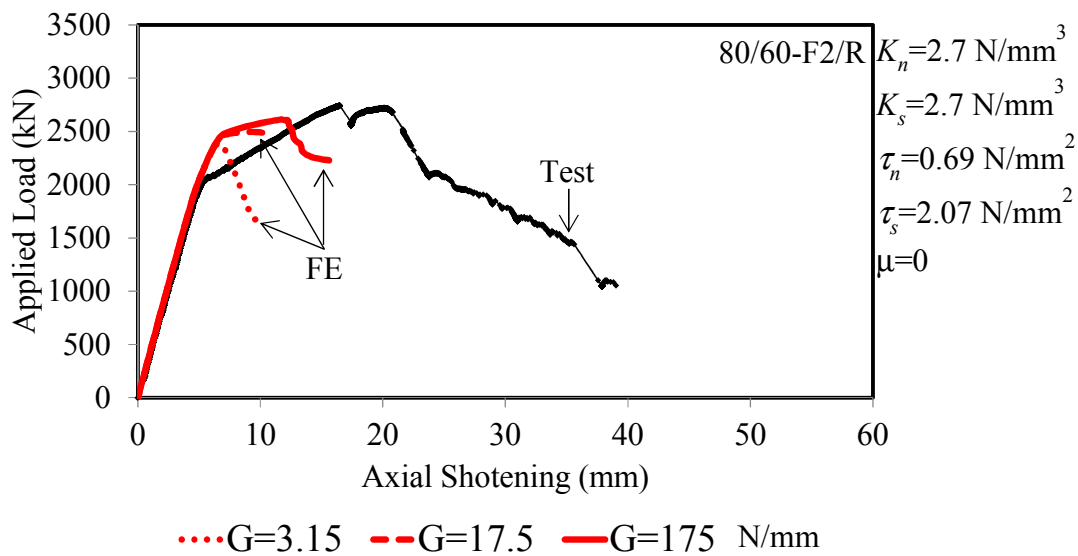


Figure 9.14: Effect of fracture energy on axial load-shortening response

9.1.1.10. Effect of Coefficient of Friction

Figure 9.15 compares the response obtained from the test to the predicted axial load-shortening responses obtained from FE models with different values of the coefficients of friction at the grout/steel interface. In previous studies in which numerical modeling of concrete filled tube (CFT) columns was conducted, coefficients of friction ranged from 0.05 to 0.55 (Hu et al., 2005; Ellobody and Young, 2006; Hu and Su, 2011; Gupta et al., 2014; Lai and Varma, 2015). Two values of the coefficient of friction, 0 and 0.55, were used to examine the sensitivity

of the FE model. Increasing the value of the coefficient of friction from 0 to 0.55 increased the second-slope stiffness of the axial load-shortening response by 63%. This is because friction is not engaged in the model until after a cohesive failure occurs. Localized crumpling deformation of the steel pile within the corroded region was observed for both of the analyzed piles with different values of the coefficient of friction. The analysis of the modeled piles terminated prior to observing any drop in the axial load. A coefficient of friction of 0.55 was selected to analyze the rest of the piles since the corresponding second-slope stiffness was comparable to the measured response.

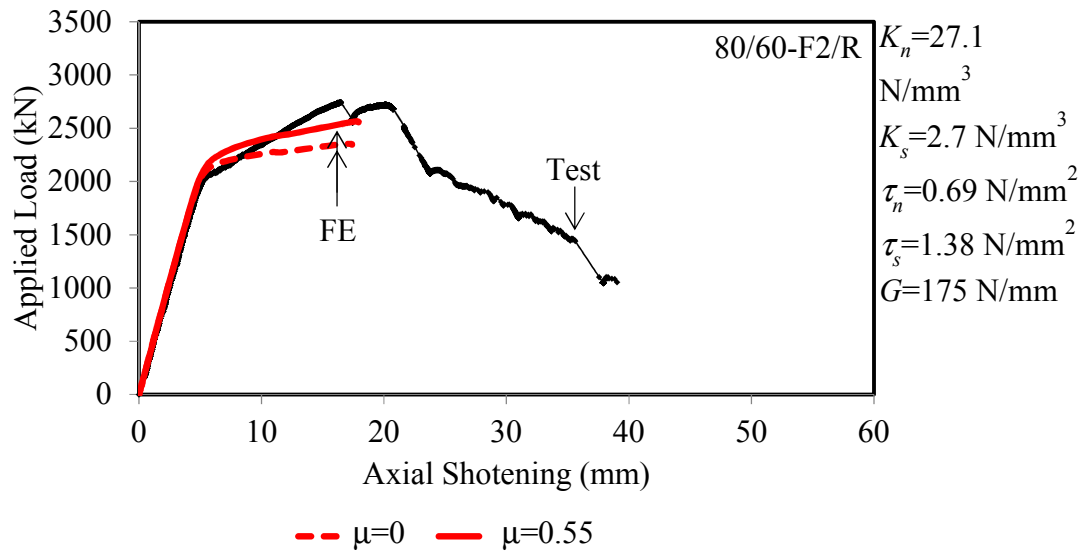


Figure 9.15: Effect of coefficient of friction on axial load-shortening response

9.1.1.11. Effect of Normal Bond Stiffness and Strength

Figure 9.16(a) and (b) compare the axial load-shortening response of the tested pile to the predicted response from FE models with different normal bond stiffnesses and strengths, respectively. No significant influence on the axial load-shortening response or the predicted failure mode was observed by changing the normal stiffness or

strength. The analysis of the modeled piles terminated prior to observing any drop in the axial load. However, the analysis of the modeled piles with lower normal bond stiffness and strength terminated at a lower axial shortening than their counterparts that were modeled with higher values of normal bond stiffness and strength. As a result, the normal bond strength, τ_n , and stiffness, K_n , were taken as 1000 lb/in² and 100,000 lb/in³ respectively.

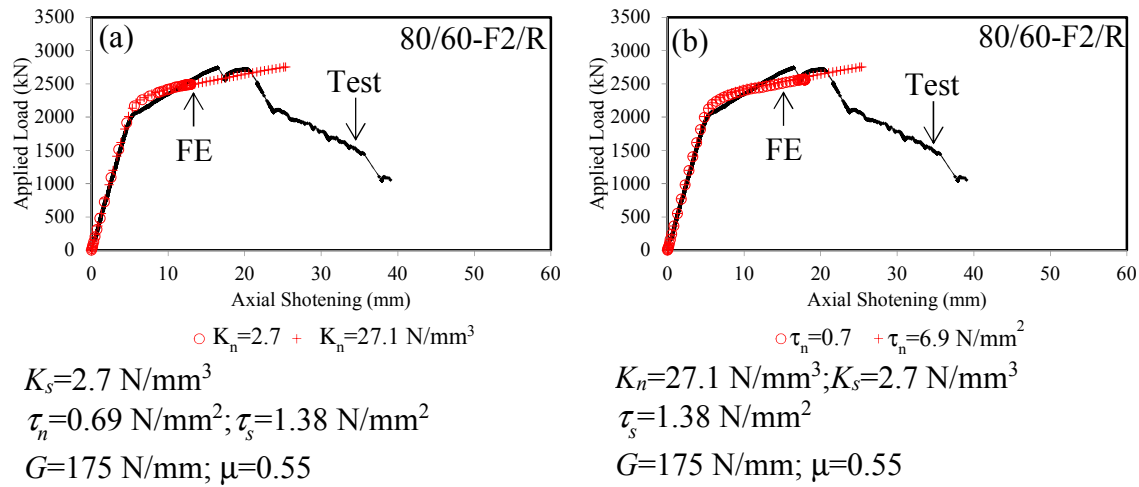


Figure 9.16: Effect of normal bond stiffness and strength on axial load-shortening response

9.1.1.12. Adopted Bond Characteristics for FE Modeling

Based on the results of the sensitivity analysis and comparison of the axial load-shortening response of the tested pile 80/60-F2/R with the FE predictions, the bond characteristics summarized in Table 9.11 were used to define the grout/steel interface.

Table 9.11: Assumed bond characteristic for FE modeling

Normal bond stiffness (K_n)	100,000 lb/in ³
Tangential bond stiffness (K_s)	9,940 lb/in ³
Normal bond strength (τ_n)	1000 lb/in ²
Tangential bond strength (τ_s)	200 lb/in ²
Bond fracture energy (G)	10,000 lb/in
Coefficient of friction (μ)	0.55

9.1.2. Results Comparison and Discussion: FRP-Confined Grout Repair System

Using the measured geometry, the developed FE model was used to analyze the tested piles, and the results were compared to the experimental results to validate the model. The following sections compare the axial capacity, load-shortening response, failure mode, and load-slip relationship obtained from numerical analyses with the experimental results of the corresponding piles.

9.1.2.1. Axial Capacity

Table 9.12 and Table 9.13 compare the measured and predicted axial capacities for the piles that were repaired using the F1 and F2 systems, respectively. They also show the ratio of the measured peak load to the predicted peak load with calculated means, standard deviations and coefficients of variation. Inspection of the tables indicates that for all but one of the tested piles (80/60-F1/R) the finite element model under-predicted the axial capacity. The conservativeness of the predictions is attributed to using the maximum suggested residual stresses and initial geometric imperfection. For the unconservative case, the model only over-predicted the capacity by 4% which was likely due to the presence of significant air voids in the grout of the tested pile. With the exception of two piles, both of which had voids in the webs (80/60/V-F1/RA and 80/60/V-F2/RA), the predicted capacities were within 20% of the measured values.

Table 9.12: Comparison of the Test and FE peak load for piles repaired with F1 jacket

Pile Designation	Peak Load (Measured) (kip)	Peak Load (Predicted) (kip)	Peak Load Ratio (Measured/Predicted)
0/20-F1	655 ^a	562	1.16
40/20-F1/R	663 ^a	556	1.19
40/60-F1/R	584	558	1.05
80/60(1)-F1/R	556	576	0.966
80/60(2)-F1/RA	653 ^a	558	1.17
80/60/V-F1/RA	591	359	1.64
80/60/3-F1/RA	633 ^a	562	1.13
		Mean	1.19
		STDV	0.201
		C.O.V.	0.169

^a The test was terminated when the capacity of the hydraulic loading system was reached prior to failure of the pile.

Table 9.13: Comparison of the Test and FE peak load for piles repaired with F2 jacket

Pile Designation	Peak Load (Measured) (kip)	Peak Load (Predicted) (kip)	Peak Load Ratio (Measured/Predicted)
0/20-F2	663 ^a	565	1.17
40/20-F2/R	662 ^a	565	1.17
40/60-F2/R	644 ^a	571	1.13
80/60(1)-F2/R	617	602	1.03
80/60(2)-F2/RA	646 ^a	565	1.14
80/60/V-F2/RA	655 ^a	362	1.81
80/60/3-F2/RA	637 ^a	575	1.11
		Mean	1.22
		STDV	0.243
		C.O.V.	0.199

^a The test was terminated when the capacity of the hydraulic loading system was reached prior to failure of the pile.

9.1.2.2. Axial Load-Shortening Response

Figure 9.17 and Figure 9.18 compare the axial load-shortening responses of the tested piles that were repaired with the F1 and F2 FRP systems, respectively, with those obtained from the FE models. The repaired piles with 0% and 40% reduction of the flange thickness, with the exception of 40/60-F1/R, did not demonstrate any failure

during the test due to limitations of the hydraulic loading system. The pile 40/60-F1/R demonstrated a global buckling failure mode. However, the FE model was able to predict the complete axial-load shortening response and post-peak behavior for the piles that did not fail. Comparison of the measured and predicted responses and peak loads for these piles suggests that failure was imminent. For the piles with 80% reduction in the thickness of the flanges, the onset of non-linearity of the repaired piles was predicted accurately. However, the predicted second-slope stiffnesses were 65% and 75% lower than the measured values for piles 80/60-F1/R and 80/60-F2/R, respectively. Comparing the predicted to measured inelastic stiffness after cohesive bond failure for the piles with mechanical anchors, piles 80/60(2)-F1/RA, 80/60(2)-F2/RA, 80/60/V-F1/RA, 80/60/V-F2/RA, 80/60/3-F1/RA, and 80/60/3-F2/RA, shows that the errors are even higher. This may have been due to the fact that the anchors were modeled using truss elements that were only effective in their axial directions and did not have any shear or flexural stiffness.

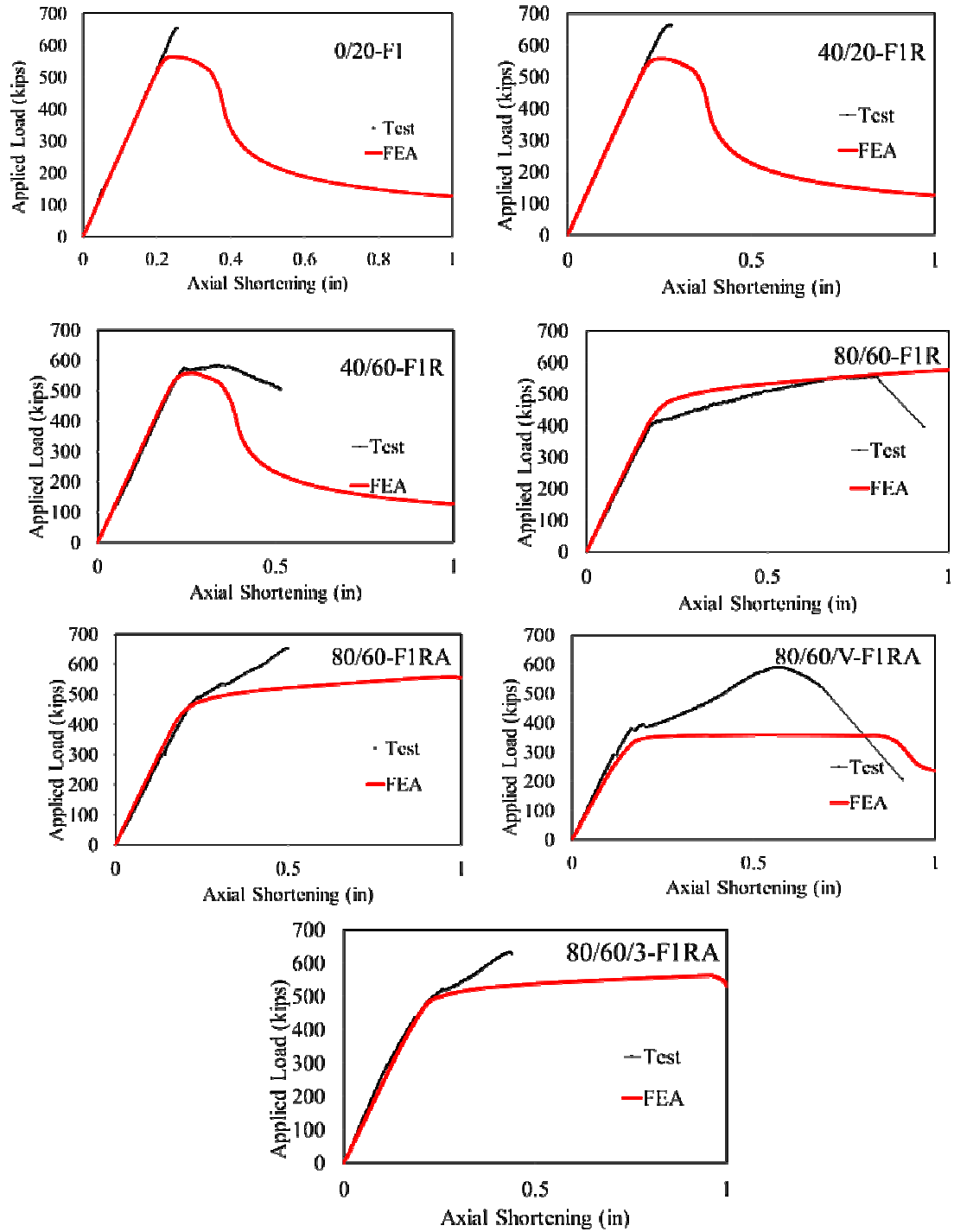


Figure 9.17: Comparison of the test and FE load-shortening response for the piles repaired with F1 jacket

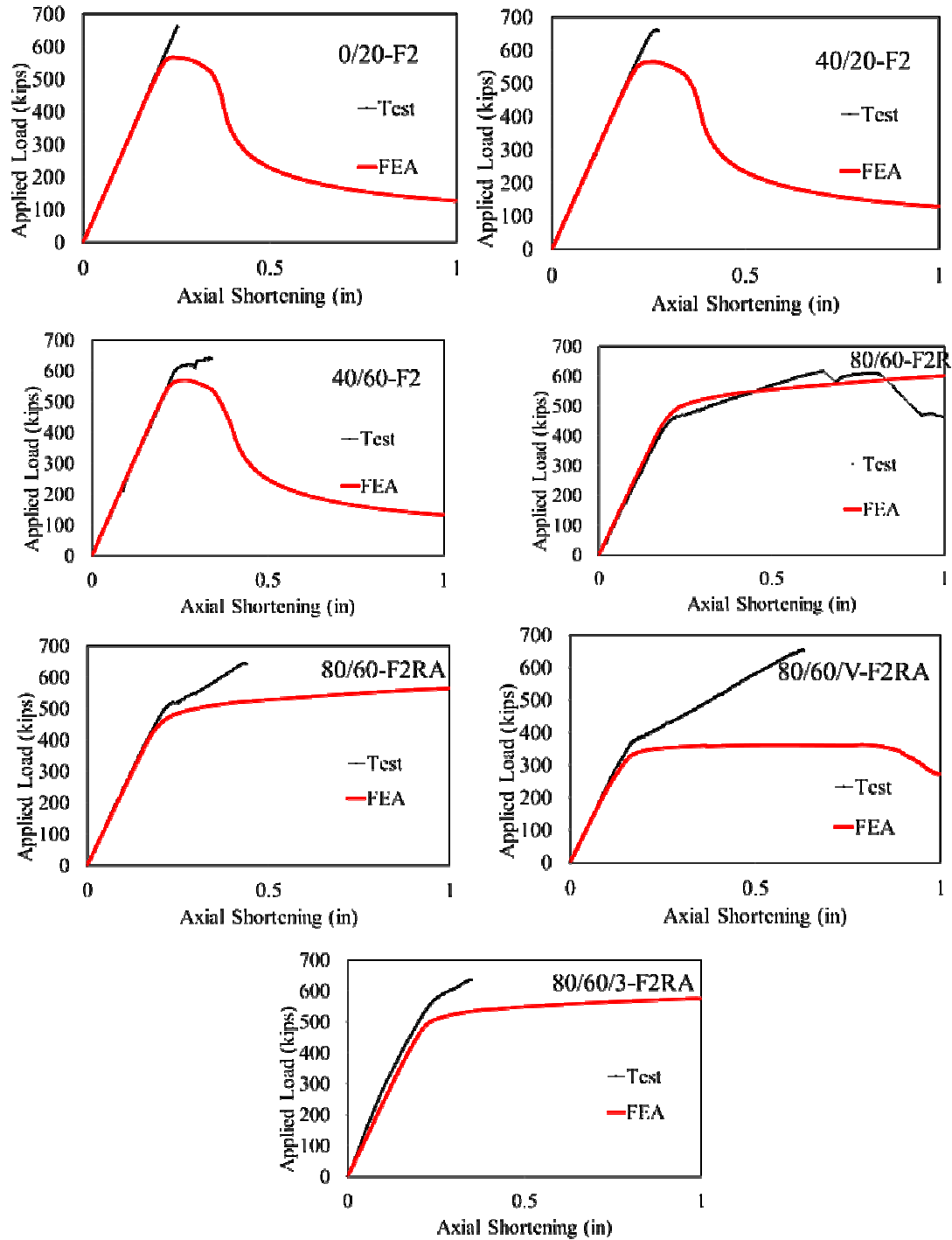


Figure 9.18: Comparison of the test and FE load-shortening response for the piles repaired with F2 jacket

9.1.2.3. Failure Modes

The predicted failure modes of all the piles with 0% and 40% reduction in the flange thickness was flange local buckling outside of the repaired region followed by global lateral deformation. Figure 9.20(a) shows the predicted failure mode of the 40/60-F1/R pile after applying 2 in. of axial shortening. According to the experimental observations, only the pile 40/60-F1/R demonstrated a global buckling failure mode while the remaining repaired piles with 0% or 40% reduction of flange thickness did not fail due to the limitation of the hydraulic loading system. Figure 9.20(b) shows the global deformation of the pile 40/60-F1/R after 0.5 in axial shortening. HP 12×53 piles are very close to having slender flanges. As such, the slight increase of the measured flange thickness of the tested pile may have precluded local buckling from occurring outside of the repair region.

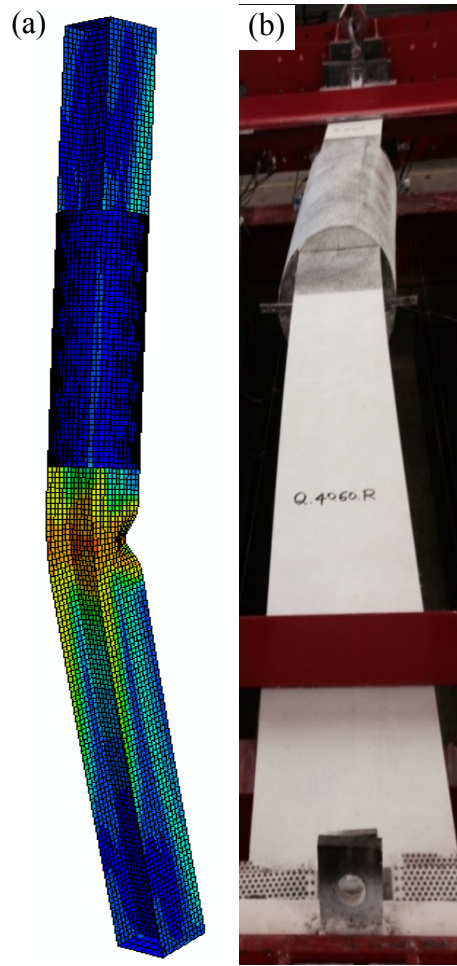


Figure 9.19: Comparison of the deformation of the tested and modeled pile 40/60-F1/R

The predicted failure mode of the piles with 80% reduction of the flange thickness was flange local crumpling within the corroded region. Figure 9.20 illustrates the localized deformation of piles 80/60(1)-F1/R, 80/60/V-F1/RA, and 80/60/3-F1/RA in the corroded regions. The corroded flanges of the corresponding piles after the test are also shown in Figure 9.20. Comparing Figure 9.20(a) - (c) and Figure 9.20(d) - (f) indicates that the patterns of flange localized deformations are similar but not identical.

Pile 80/60/V-F1/RA demonstrated flange local buckling followed by global lateral deformation during the test as shown in Figure 9.20(g), while the modeled 80/60/V-

F1/RA failed by flange local buckling within the corroded region. HP 12×53 piles are very close to having slender flanges and a minor reduction of the flange thickness for the tested pile may have induced local buckling of the pile outside of the repair region, modified the predicted failure mode, and reduced the predicted capacity slightly. Due to the limitation of the loading system, no localized deformation or failure was observed in the pile 80/60/3-F1/RA as shown in Figure 9.20(f):

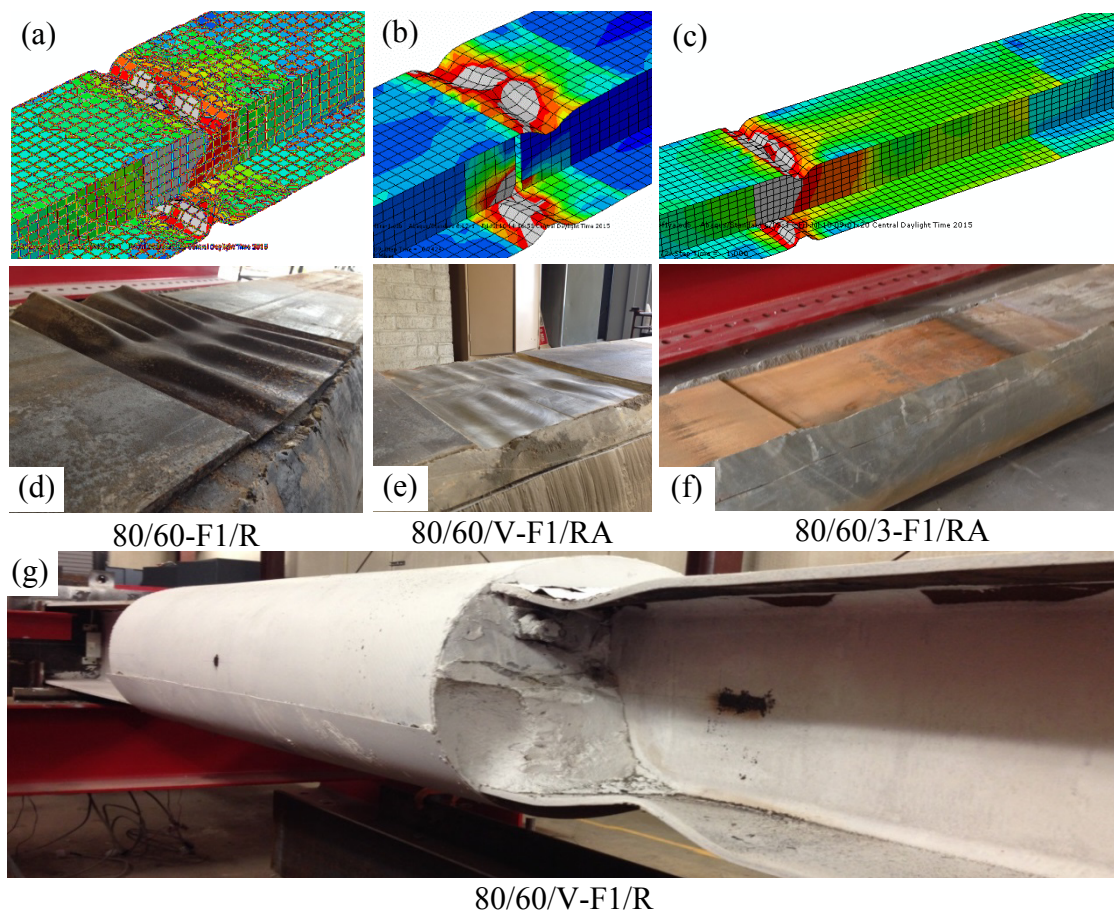


Figure 9.20: Comparison of the deformation of the tested and modeled piles with 80% reduction of the flange thickness

Error! Reference source not found. and

present the maximum predicted in-plane principal stresses in the FRP jackets and the maximum and minimum predicted principal stresses in the grout cylinders for the

modeled piles that were repaired with the F1 and F2 systems, respectively. The maximum predicted stresses in the hoop direction in the FRP jackets did not reach the FRP ultimate stress in any of the modeled piles. As shown in Table 9.14 and Table 9.15 the maximum stress-to-nominal strength ratio was 0.728 corresponding to pile 80/60(1)-F1/R. However, the FRP jackets for the tested piles 80/60(1)-F1/R and 80/60(2)-F2/R did exhibit rupture.

Comparing the maximum hoop stresses in the F1 and F2 FRP jackets in **Error! Reference source not found.** and Table 9.15 indicates that the stresses in the F1 jacket are higher than those in the F2 jackets since F1 jackets are thinner and less stiff in the hoop direction relative to the F2 jackets resulting in a lower degree of confinement of the grout core at a given strain level. Consequently, since the F1 jackets are thinner than the F2 jackets, they must achieve a higher hoop stress to provide a similar confining pressure to the F2 jackets. This is consistent with the experimental observations where hoop strains in F1 jacket were higher than F2 jacket.

Table 9.14: Maximum and Minimum Principal Stresses Observed in FRP jacket in FE Model for the Pile Repaired with F1 System

Pile Designation	Max. Stress in Hoop Direction	Nominal Strength in Hoop Direction	Max Stress/ Nominal Strength Ratio
	(ksi)	(ksi)	
0/20-F1	19	101	0.192
40/20-F1/R	18	101	0.181
40/60-F1/R	18	101	0.182
80/60(1)-F1/R	74	101	0.728
80/60(2)-F1/RA	65	101	0.639
80/60/V-F1/RA	26	101	0.254
80/60/3-F1/RA	40	101	0.396

Table 9.15: Maximum and Minimum Principal Stresses Observed in FRP jacket in FE Model for the Pile Repaired with F2 System

Pile Designation	Max. Stress in Hoop Direction	Nominal Strength in Hoop Direction	Max Stress/ Nominal Strength Ratio
	(ksi)	(ksi)	
0/20-F2	10	83	0.115
40/20-F2/R	9	83	0.113
40/60-F2/R	10	83	0.114
80/60(1)-F2/R	28	83	0.333
80/60(2)-F2/RA	25	83	0.301
80/60/V-F2/RA	14	83	0.163
80/60/3-F2/RA	17	83	0.209

Figure 9.21 indicates stress concentrations at the tips of the flanges in the FRP jacket at the ultimate loading stage for the pile 80/60(1)-F2/R. This pile demonstrated rupture of the FRP jacket which occurred along the tips of the bottom flange of the tested pile.

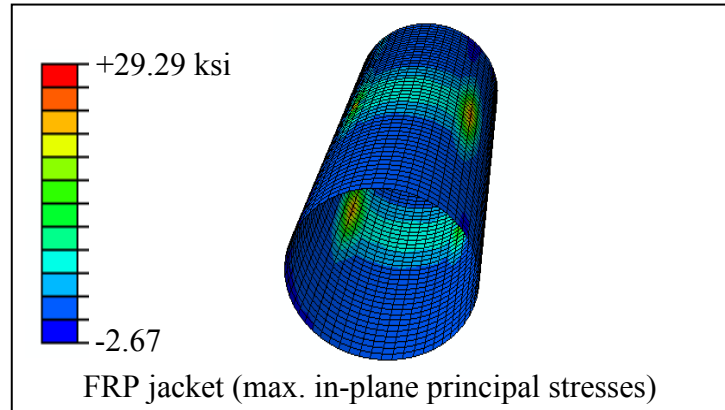


Figure 9.21: Stress contours in FRP jacket and grout cylinder

9.1.2.4. Slip at Grout/Steel Interface

Figure 9.22 and Figure 9.23 compare the measured and predicted axial load-slip responses of the piles at the jacking and fixed ends. The good agreement between the initial slope in the linear region and the point where the onset of non-linearity occurred indicates that the assumed values for the tangential bond stiffness and strength, K_s and τ_s , were suitable to accurately predict the bond behavior up to the bond failure. However, the differences between the slopes of the responses after bond failure for the piles with anchorage suggest that the anchors were not effective in the modeled piles. This may have been due to the fact that in the FE models the anchors were defined as truss elements without any shear or flexural stiffnesses as discussed previously.

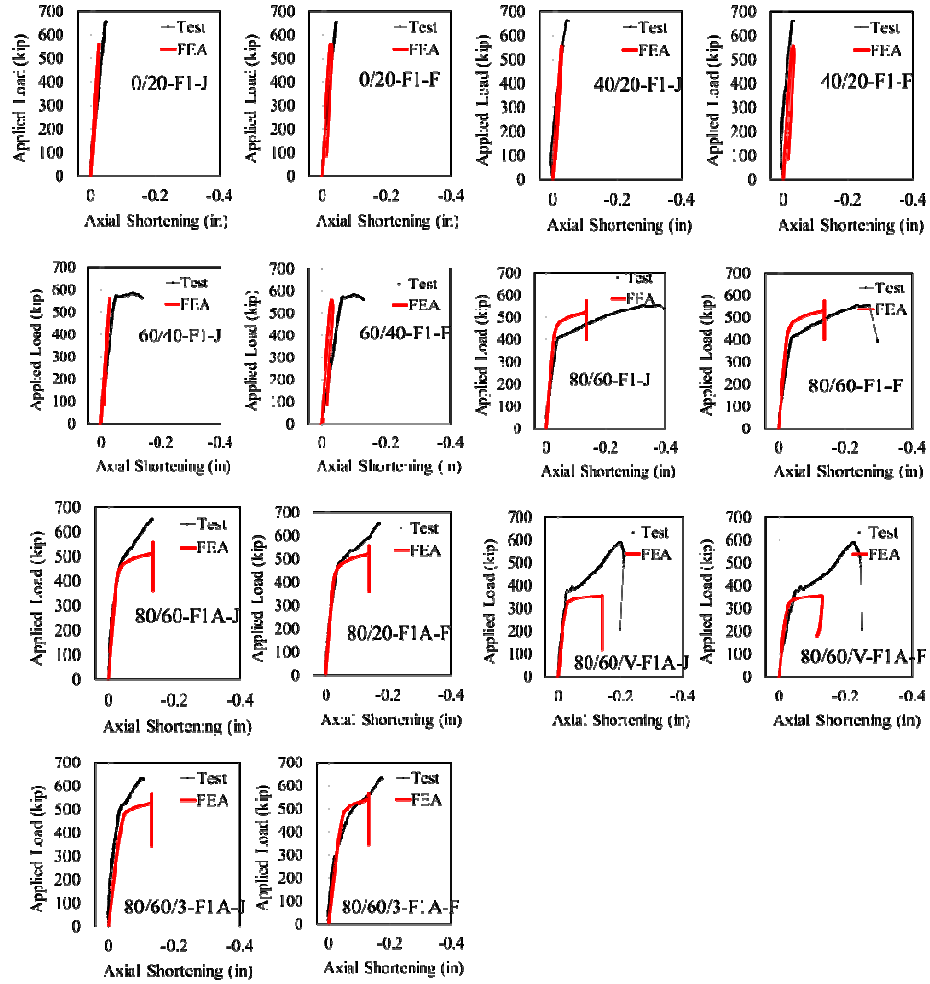


Figure 9.22: Comparison of measured and predicted slip at grout/steel interface for the piles repaired with F1 jacket

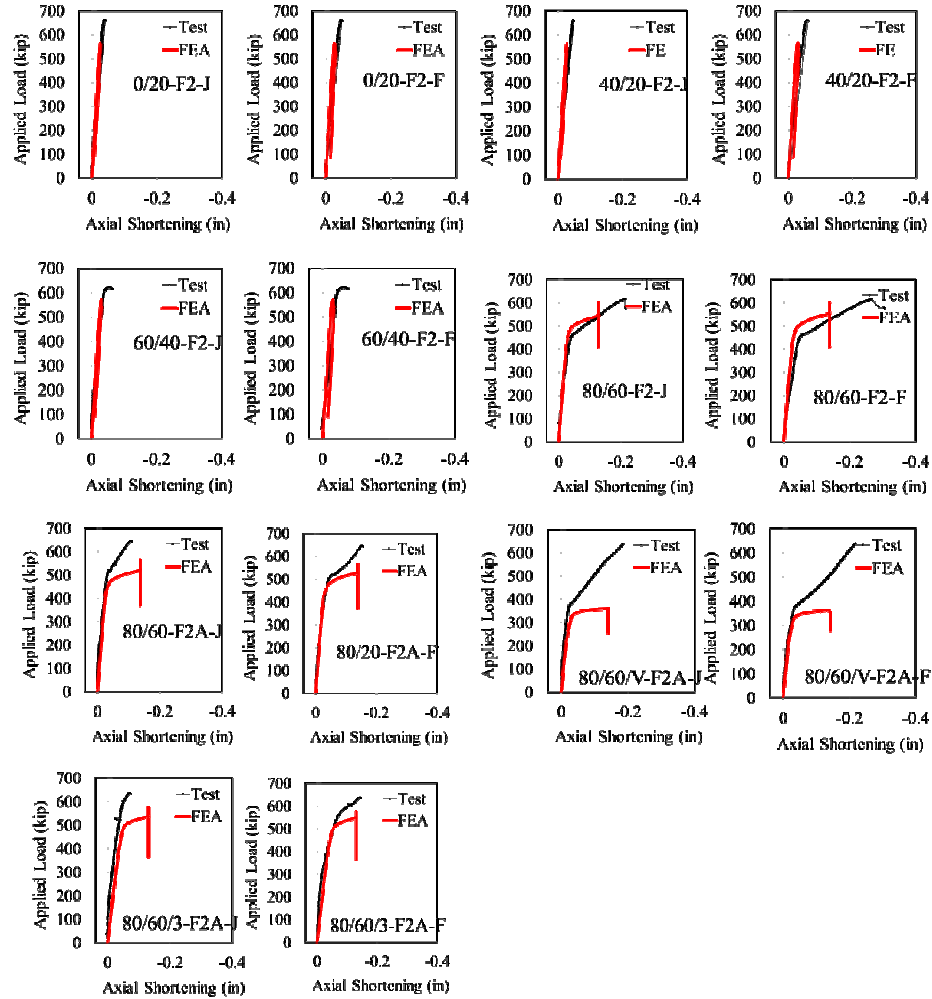


Figure 9.23: Comparison of measured and predicted slip at grout/steel interface for the piles repaired with F2 jacket

9.2. Finite Element Modeling of Steel-based Repair System

This section presents the details of a numerical analysis of partially corroded H-piles that are repaired using a friction-type bolted steel plate-based repair system. The objective of the numerical analysis was to evaluate factors that might affect the axial behavior of retrofitted piles and to optimize the design of the proposed repair system. A FE model was developed to simulate the repaired piles. The model was validated using the full-scale experimental results of seven piles that were repaired with the same system. Then a parametric study was conducted using the validated model to further investigate different factors that might affect

the strengthened axial capacity of the pile. The studied factors included the coefficient of friction between the faying surfaces, magnitude of the bolt pretension, and length of steel plates.

9.2.1. Simulation of Corroded Piles

The FE model that was developed for corroded H-piles (Chapter 6) was adapted to model the repaired piles. The element type, mesh size, material properties, initial global and local imperfections, and distribution of residual stresses were implemented as described in Chapter 6. The four-node fully integrated finite-membrane-strain shell element with linear shape function, S4, was used and the pile was discretized into 1 in.×1 in. elements. The material model follows classic plasticity with von-Mises yield criteria, associated flow, and isotropic hardening. The yield strengths of the flanges and webs were 52.5 ksi and 60.5 ksi, respectively, with elastic moduli of 28,400 ksi and 32,000 ksi for the flanges and web, respectively. The ultimate strengths of the flanges and web were taken as 66.5 ksi and 71.0 ksi, respectively. The magnitudes of the initial global and local geometric imperfections were taken as 0.18 in and 0.06 in, respectively. The distribution of residual stresses was assumed to have maximum compression stresses at the flange tips and uniform tension stress in the web. The maximum value of residual compressive and tensile stresses was assumed as 10 ksi. Boundary conditions were modeled to represent the test set-up at the supports with only rotation about the weak axis permitted while the other degrees of freedom were restrained. The piles were loaded by imposing an axial displacement at one end to simulate the action of the hydraulic jack in the experimental program. The modified Riks method, was employed to solve the nonlinear model.

9.2.2. Simulation of Steel Plates

The steel plates of the repair system were modeled using the same element type as the H-piles. The FEA results of corroded H-piles demonstrated that this element type provided accurate predictions for members loaded in compression and failing by plate buckling. The mesh size was determined as 0.5 in.×0.5 in. according to a preliminary sensitivity study, in which coarser mesh sizes did not converge. The difficulty of convergence was caused by the large stress concentration in the steel plates around the bolts due to bolt pretension. The mechanical properties of the steel plates were determined experimentally. The yield and ultimate strengths of the plates were taken as 33.1 ksi and 48.8 ksi, respectively. The elastic modulus was taken as 28,600 ksi.

Figure 9.24(a) shows the assembly of the plates and the pile in FEA: the two main steel plates were assembled on the outside surfaces of each flange, and the four clamping plates were positioned inside the surfaces of the flanges. After tightening the bolts, the clamping plates rotated by an angle θ along the edges of the flanges until the outer edges of the clamping plates were contacting the edges of the main plates, as shown in Figure 9.24(b). For stabilization purpose, the main plates and the clamping plates were restrained along their transverse edges from translational movements while applying the bolt pretension. The constraint was released before applying axial load.

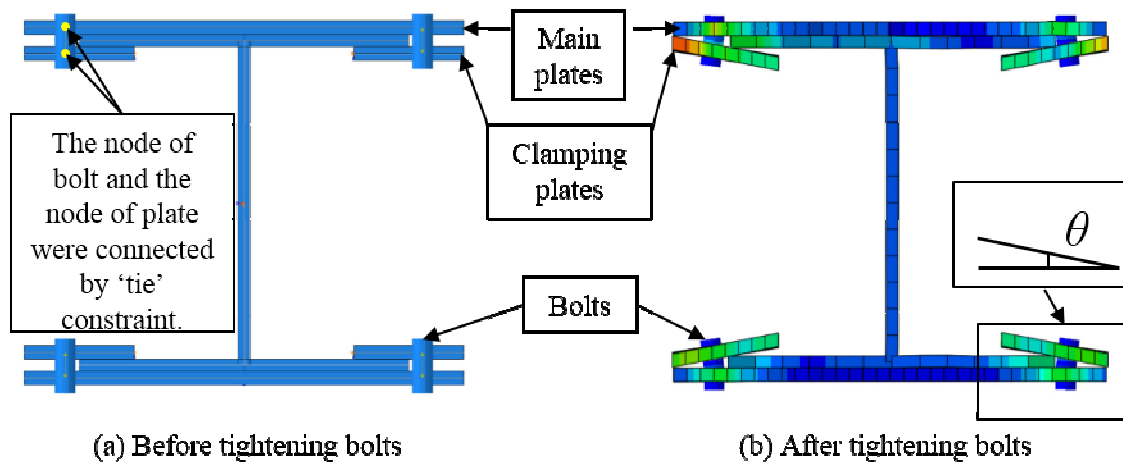


Figure 9.24: Cross sectional views of the repaired piles simulated in FEA

9.2.3. Simulation of High-Strength Bolts

The bolts were simulated using a two-node linear beam element, B31, which is a Timoshenko beam that allows for transverse shear deformation. According to ASTM A325 (2014), the minimum yield strength and tensile strength for A325 bolts are 92 ksi and 120 ksi, respectively, which were adopted for the bolts in FEA. The head of the bolts, flat washers, bevel washers, and nuts were not modeled for two reasons: (1) the detailed behavior of the bolts (i.e. the magnitudes and distributions of stress and strain within each bolt across its section) was not the focus of this study, and (2) for the efficiency of calculation. Instead, the bolts were simulated to be connected to the main plates and clamping plates using 'tie' constraint, as shown in Figure 9.24(a). This indicated that the node of the bolt and the node of the plate displaced together in all degrees of freedom. The pretension was applied on each bolt as a bolt load between the main plates and the clamping plates. The bolts bent after full pretension was applied, as shown in Figure 9.24(b), since the bevel washers were not included in the model. This caused a force from

the clamping plates acting on the bolts in the direction perpendicular to the bolt axis. However, the bolts had adequate shear strength to resist the transverse load. As long as the bolts provided the required pretension in the model the effect of bent bolts on the axial capacity of the repaired pile was negligible to the investigation of the behavior of repaired piles. This was supported by the test results of Pile 40/60-S, which did not have bevel washers but was still effectively repaired.

9.2.4. Simulation of the Interface Properties

The normal and tangential properties of the interfaces between the pile and the repair plates were defined independently. The normal direction behavior was defined as ‘hard contact’ allowing separation between contacting surfaces. This type of contact prevents the penetration between contacting surfaces and does not allow tensile stress across the interface but allows only compression. The tangential direction behavior was defined using an isotropic penalty friction formulation with friction coefficient K_s , as shown in Figure 9.25. Figure 9.25 shows the relationship between the friction force versus the normal force between the contact surfaces. In Figure 9.25, the coefficient of friction is shown as 0.34. However, two values of K_s were considered in FEA: the mean value (0.34) and the minimum value (0.30) of the slip resistance factor obtained from the coefficient of friction tests.

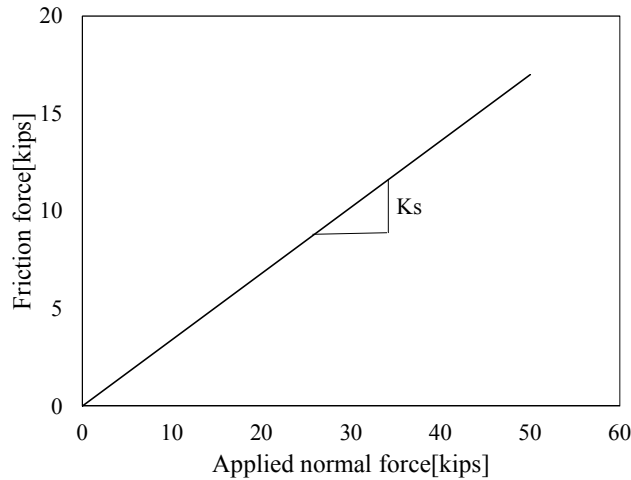


Figure 9.25: Relationship of friction force and normal force defined in FEA

9.2.5. Comparison to Experimental Results and Discussion

The predicted response of the repaired piles was compared to the measured response on the basis of several factors including axial capacity, axial load-shortening response, and failure mode. The results of this comparison are discussed in the following sections.

9.2.5.1. Axial Capacity

Table 9.16 presents the measured and predicted axial capacities of the repaired piles. The pile designations were adopted from the experimental program. Pile 80/60-S refers to Pile 80/60-S(1) as Pile 80/60-S(2) was a duplicate specimen of 80/60-S(1), with only slight differences of flange and web thicknesses.

The ratios of the axial capacities obtained from tests and FEA indicate that the FEA with slip resistance of 0.34 and 0.3 showed comparable predictions for piles with less than 80% reduction of flange thickness. However, for piles with 80% reduction of flange thickness, the FEA overestimated the slip resistance when a coefficient of

friction of 0.34 was adopted; while the FEA showed more accurate though slightly conservative predictions using a coefficient of friction of 0.30. Moreover, the predicted failure modes of piles with 80% reduction of flange thickness indicated that 0.3 provided better match between the FEA and experiments.

Table 9.16: Axial peak loads and failure modes of repaired piles from FEA and tests

Pile designation	Axial peak load [kips]			$P_{\text{test}}/ P_{\text{FEA}}$	
	P_{test}	P_{FEA}			
		$K_s=0.34$	$K_s=0.30$	$K_s=0.34$	$K_s=0.30$
0/20-S	629	603	603	1.04	1.04
40/20-S	665	569	567	1.17	1.17
40/60-S	618	600	587	1.03	1.05
80/60-S	632	639	600	0.99	1.05
80/60/V-S	630	677	632	0.93	1.00
80/60/3-S	532	584	525	0.91	1.01

According to the experimental observation of Pile 80/60-S, the failure occurred only at the corroded section with no lateral displacement or damage outside of the repair system. A similar trend was observed for Pile 80/60/3-S. This fact suggests that the obtained friction force in the full-scale experiments may have been lower than the expected value. The friction force that can be achieved may decrease in full-scale applications for several reasons: (1) the larger contact area increases the likelihood of defects in the coating that could potentially reduce the coefficient of friction, (2) the increased number of bolts increases the likelihood that some of the bolts may not be fully tightened due to the statistical variability of the bolt tightness, (3) the edge of the strengthening plate being in contact with the edge of the clamping plate may cause

some of the bolt pretension force to be transferred through that interface rather than at the interface between the strengthening plate and the pile, and (4) localized out-of-straightness of the flanges may influence the frictional force that can be achieved at the interface. To accurately predict the capacities of the retrofitted piles, the results of the FEA using a coefficient of friction of 0.30 were used for comparison and validation in the following sections.

The differences of the FEA predicted capacities and tested capacities were less than 5% except for Pile 40/20-S. The unexpectedly high measured capacity of Pile 40/20-S was attributed to a lower magnitude of the unintentional eccentricity for that pile, which was demonstrated by the difference of the values of the four axial string potentiometers that were used in the test.

9.2.5.2. Axial Load-Shortening Response

Figure 9.26 compares the predicted axial load-deformation relationships from the FEA to the measured response. The solid curves show the measured responses while the dashed curves show the predicted response with a coefficient of friction, K_s , of 0.3. The figure also presents the coefficients of determination, R^2 , between experimental and numerical curves. $(R^2)_{\text{total}}$ was calculated from the total range of the curves from zero deformation to the maximum deformation of the test or FEA, whichever ended first. The maximum deformation obtained from tests was determined as the last data point before the sudden drop of axial load. The maximum deformation of FEA predictions was defined as the end of the analysis. $(R^2)_{\text{peak}}$ was calculated within a range from zero load and deformation to the peak load of the

curves, to quantify the correlation between the FEA and experimental results in the elastic range.

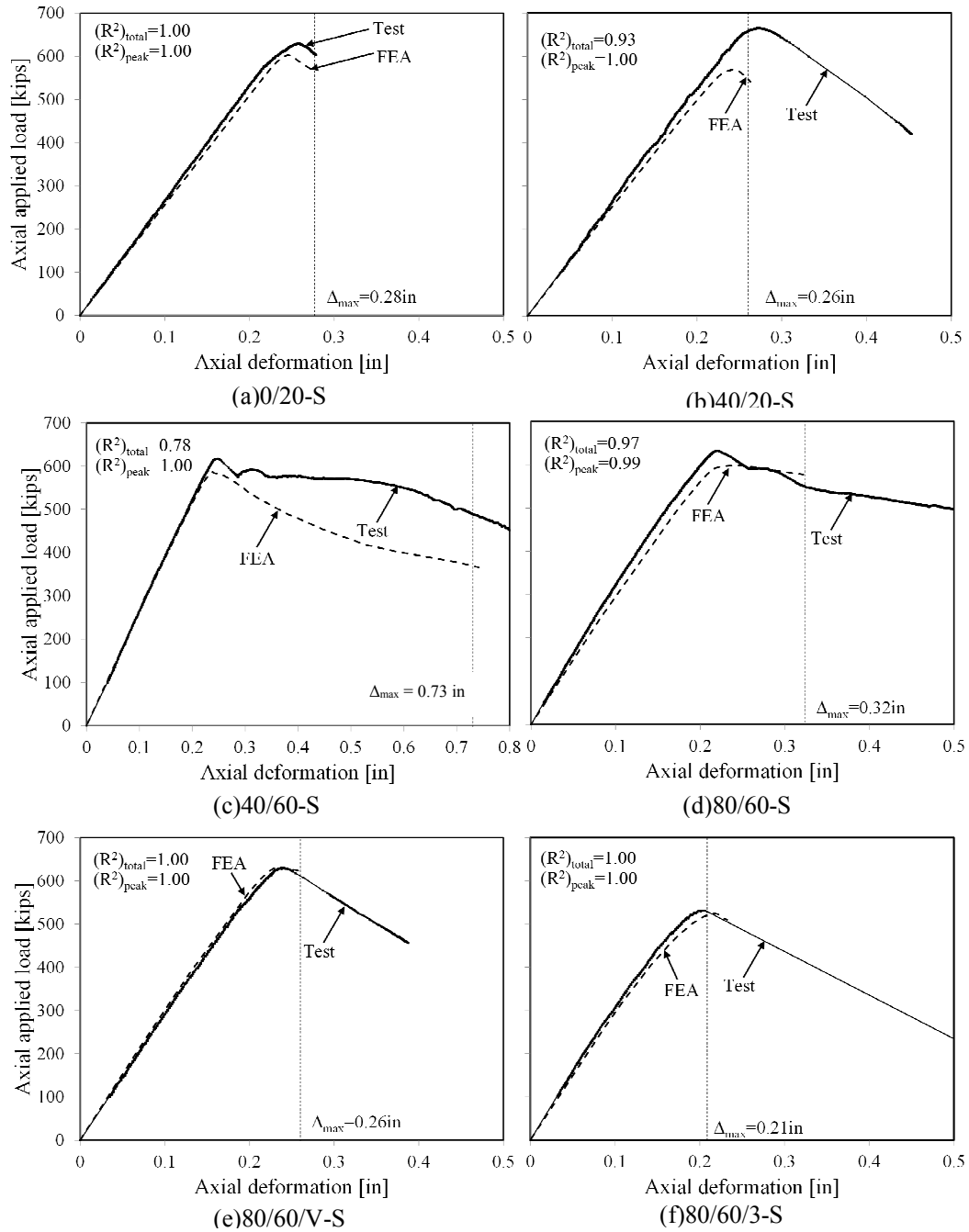


Figure 9.26: Axial load-deformation responses of repaired piles from tests and FEA

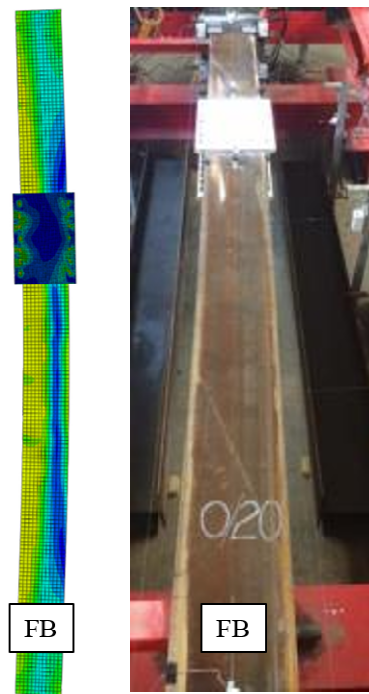
Inspection of Figure 9.26 indicates that $(R^2)_{\text{total}}$ for all of the piles presents satisfactory correlation ranging from 0.93 to 1.00, except for pile 40/60. The measured post-peak response for that pile exhibits a higher capacity than the FEA prediction. The discrepancies were attributed to five possible reasons: (1) reduced magnitude of the unintentional eccentricity of the applied load during testing; (2) uncertainty of the magnitude and pattern of the residual stresses; (3) conservativeness of the assumed magnitude and pattern of initial imperfections; (4) effect of the fillet at the junction of flange and web, which was not modeled in the FE simulation but partly existed in tested specimens; (5) the difference of the actual slip resistance obtained from the tests and the value used in FEA. The predicted capacities of the piles that failed within the corroded region are sensitive to the friction force between steel plates and pile flanges (this is illustrated and discussed in the parametric study in the following section).

For piles with 80% reduction of the flange thickness, the FEA did not capture the post-peak response well, because the excessive deformation of the thin and slender flanges led to lack of convergence of the FE model. The values of $(R^2)_{\text{peak}}$ range between 0.99 to 1.00 for all of the examined cases and indicate that the FE model accurately predicted the elastic response.

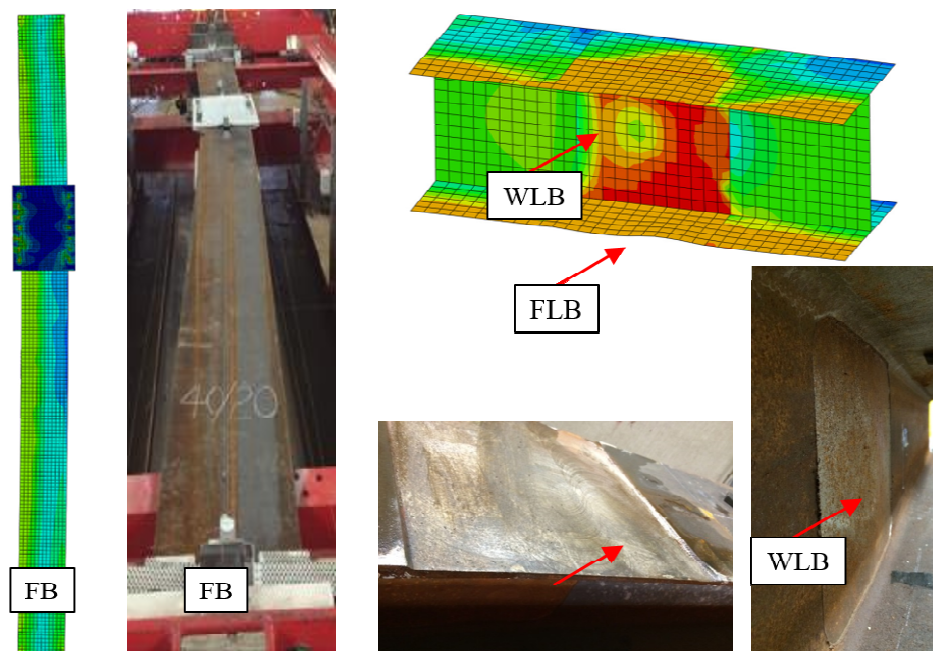
9.2.5.3. Failure Mode

Figure 9.27 compares the predicted and observed failure modes of the deformed piles. The figure shows a close agreement between the measured and predicted deformations. Detailed global and local deformations include (1) the flexural buckling failure of pile 0/20-S, as shown in Figure 9.27(a), (2) the minor buckling of

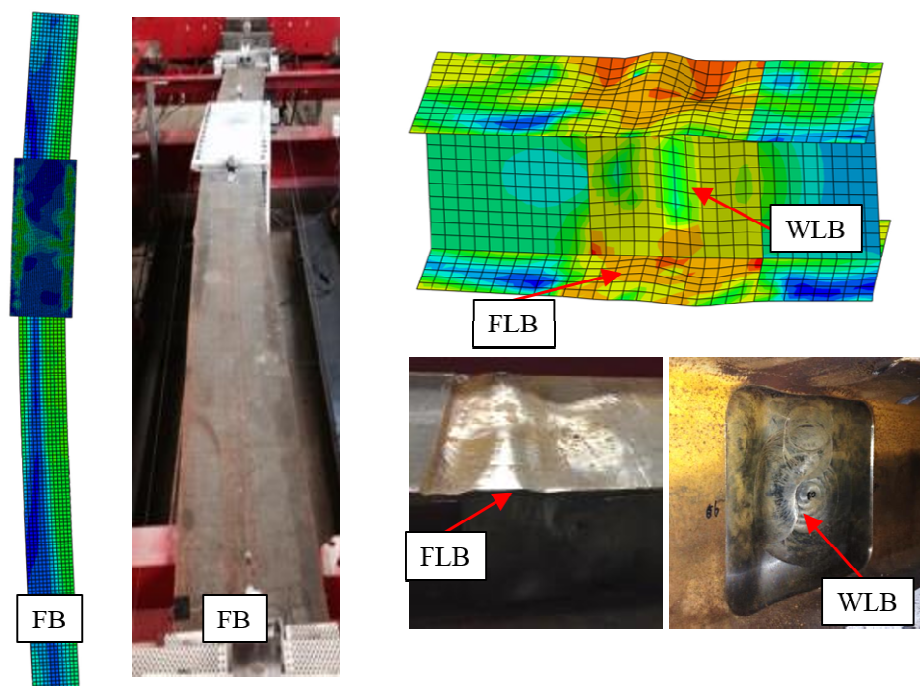
the flanges of pile 40/20-S, as shown in Figure 9.27(b), (3) the crumpling deformations of the flanges of pile 40/60-S (Figure 9.27(c)) and pile 80/60-S (Figure 9.27(d)) (pile 80/60/3-S, not shown, exhibited a similar failure), and (4) the one-way flange bending mode of pile 80/60/V-S, (Figure 9.27(e)). The flexural buckling shape of pile 40/60-S shown in Figure 9.27(c) was observed after the peak load in both the FEA and the test.



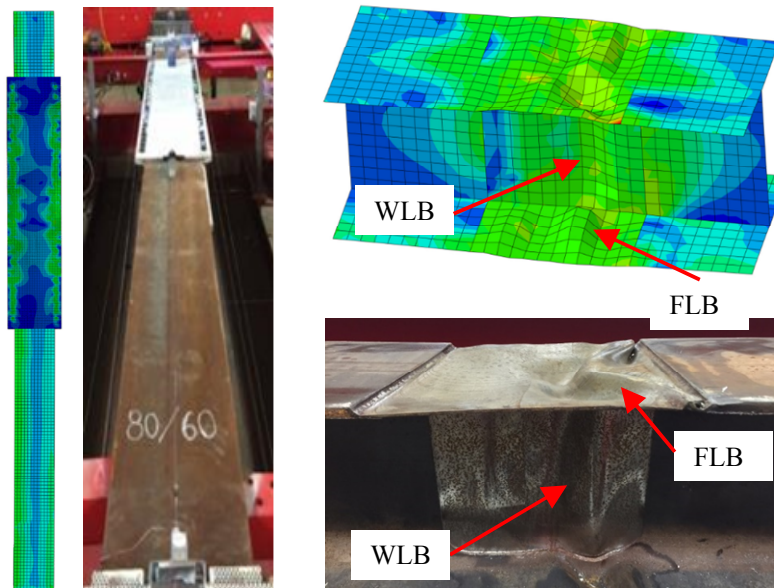
(a) 0/20-S
(FB=Flexural buckling)



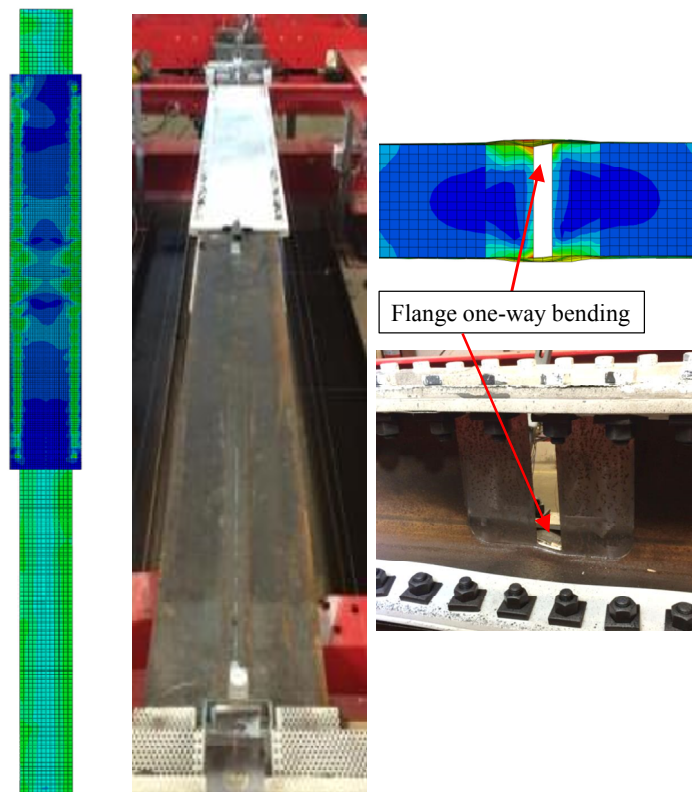
(b) 40/20-S (FLB=Flange local buckling; WLB=Web local buckling)



(c) 40/60-S



(d) 80/60-S



(e) 80/60/V-S

Figure 9.27: Comparison of deformations of FEA and experiments for repaired piles

9.2.6. Parametric Study

After validating the numerical model using the experimental results of the repaired piles, a parametric study of the retrofitted piles was performed to investigate the factors that affect the capacity of the repaired, partially corroded H-piles. The parameters considered include the coefficient of friction between steel main plates and pile flanges, the pretension in the bolts, and the length of steel plates. The parametric study was carried out using the FE model of pile 40/60-S and changing one parameter at a time while keeping the other two constant.

Pile 40/60-S was selected as a base configuration for several reasons. That pile exhibited the largest axial deformation prior to failure in the FE simulations of all of the piles considered in the validation study. Also its degree of deterioration was so severe that the pile failed by crumpling deformations, which was representative of several of the piles that require rehabilitation. Finally, to investigate the effect of different lengths of the steel repair plates, Pile 40/60-S provide sufficient length between the corroded region and the end of the pile to effectively change the repair length. For a 15-ft-long pile with corroded region centered at its third-height, the maximum length of the repair system could be up to 10 ft. Based on the established design guidelines, which were validated experimentally) pile 40/60-S required a 3.5 ft. long repair system to achieve the retrofitting target. This provided a significant range through which to investigate the effect of the length of the repair system on the response of the pile.

9.2.6.1. Effect of Coefficient of Friction

Figure 9.28 shows the effect of the coefficient of friction on the axial capacity of the repaired piles. The bolt pretension was kept constant at 28 kips for each case. The horizontal and vertical axes in the figure present the values of the friction coefficients and the axial capacities, respectively. The dots in the figure indicate the predicted peak load of each pile. The three marker styles indicate three different lengths of the steel plates: the circular dots refer to 3.5 ft. long steel plates, the square dots refer to 5 ft long steel plates, and the triangular dots refer to 6.5 ft. long steel plates. The four cases that are circled are piles which failed by crumpling within the corroded region, as shown in Figure 9.29; otherwise the piles failed by flange local buckling outside of the repaired region followed by flexural buckling, as shown in Figure 9.30. Five values of coefficient of friction were investigated, 0.1, 0.2, 0.34, 0.5, and 0.75. The value 0.34 is the mean value of slip resistance factors obtained from coefficient of friction test, which is very close to the Class A slip coefficient of 0.33 defined in AASHTO (2012). The value of 0.5 is the Class B slip coefficient specified in AASHTO (2012). The other three values were selected to form a trend with uniform increments.

Figure 9.28 indicates that increasing the slip resistance enhanced the strengthened axial capacity of the pile when the failure occurred within the corroded region. However, as soon as the failure moved from the corroded region to the un-corroded portion of the pile outside of the repair system, increasing the coefficient of friction did not increase the pile capacity. At this stage, the capacity was dominated by the axial capacity of the un-corroded pile. For HP12×53 piles, the dominant failure mode

is flexural buckling and flange local buckling since the flange slenderness ratio is just at the limit of slender elements as defined in AASHTO (2012) and AISC (2011).

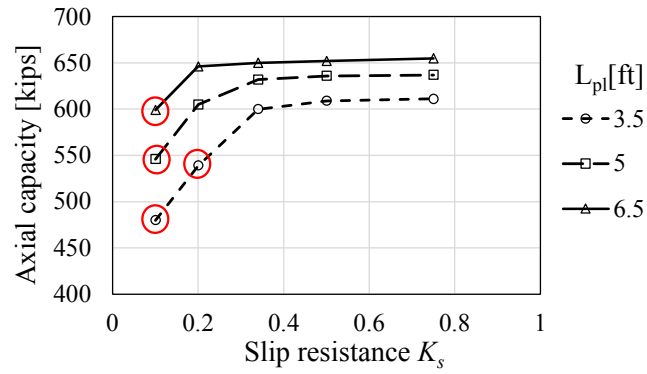


Figure 9.28: Axial peak loads of repaired piles as function of different slip resistances

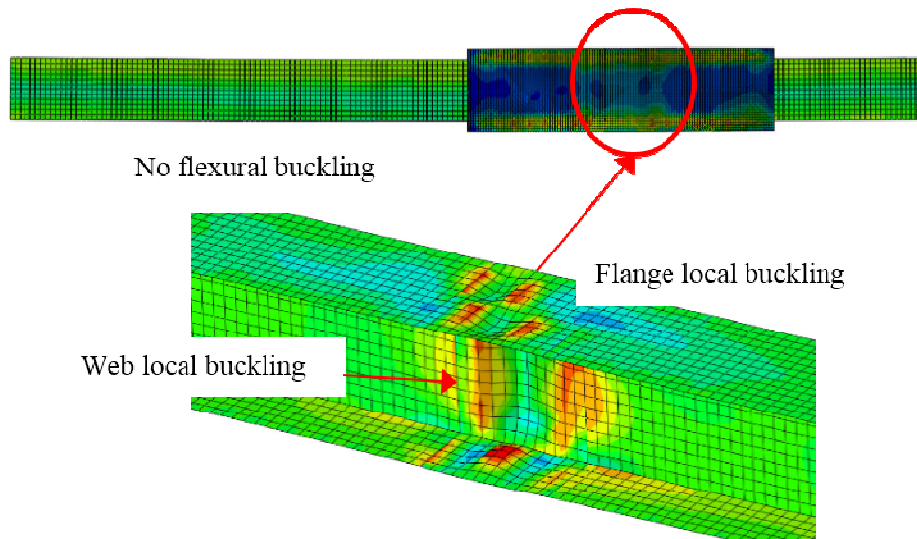


Figure 9.29 Failure within the corroded region

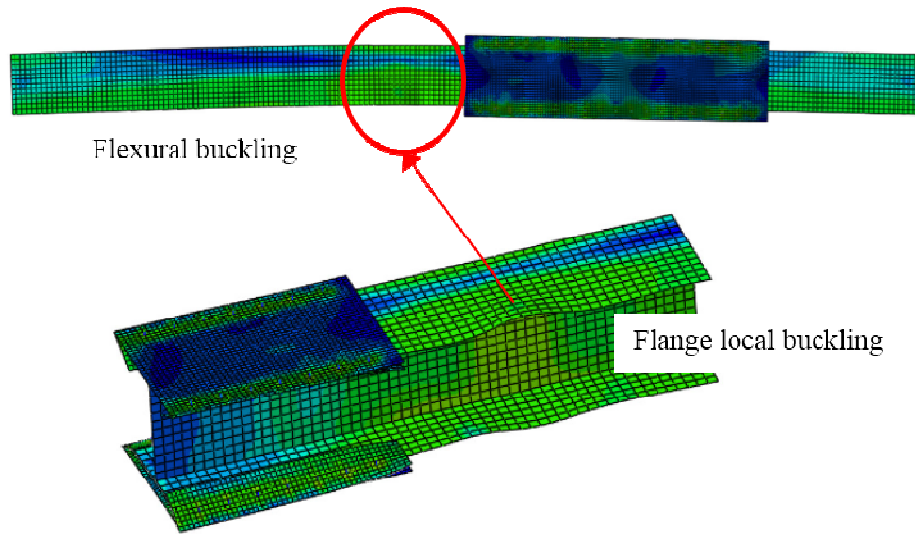


Figure 9.30 Failure outside the repair system

9.2.6.2. Effect of Bolt Pretension

Figure 9.31 presents the influence of bolt pretension on the axial capacity of retrofitted piles. The marker styles indicate various lengths of repair system. Three magnitudes of bolt pretension were evaluated, 12 kips, 19 kips, and 28 kips, which corresponded to the minimum pretension for slip-critical connection using A325 bolts with diameters of 1/2 in, 5/8 in, and 3/4 in, respectively (AASHTO, 2012). The circled points indicate the piles that failed by crumpling within the corroded region, while in other cases the failures occurred outside of the repaired region. The results demonstrate that the axial capacity increases as the bolt pretension increases for configurations in which the pile fails by crumpling within the corroded region. However, once the friction force from the repair system was adequate to transfer the necessary load across the interface, the failure shifted to the un-corroded part of the pile and increasing the bolt pretension did not increase the capacity of the repaired piles. This is reflected in Figure 9.31 by comparing axial capacities of piles with 5 ft.

and 6.5 ft. long repair systems. The three values of axial capacities were almost the same despite the three different levels of bolt pretension that were applied to the repaired piles.

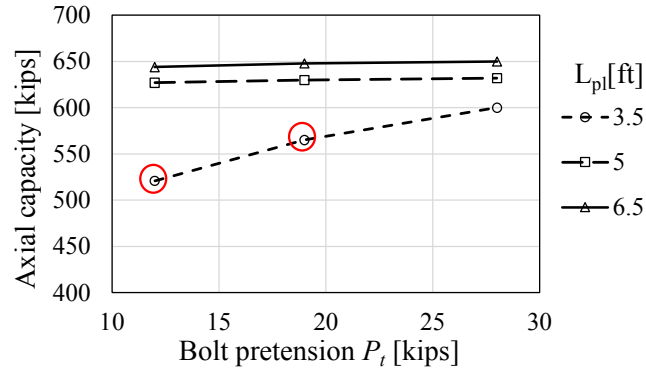


Figure 9.31 Axial peak loads of repaired piles as function of varying bolt pretension

9.2.6.3. Effect of length of steel plates

Three different lengths of the steel repair plates were investigated, namely: 3.5 ft, 5 ft, and 6.5 ft. In order to illustrate the effect of the plate length, the results are reorganized and plot in Figure 9.32. Different styles of markers indicate different values of coefficient of friction. The bolt pretension was 28 kips for all cases. The circled points indicate piles that failed by crumpling within the corroded region, while the other piles failed by flange local buckling and flexural buckling outside of the repaired region. Inspection of the circled cases indicates that increasing the length of steel plates increased the axial capacity of these piles. This was attributed to the increase of the plate length leading to the use of more bolts thereby increasing the total clamping force and the friction force at the pile/repair plate interface. Inspection of the un-circled cases indicates a slight increase of the axial capacity although these piles failed within the un-corroded region. This is because increasing the length of the repair plate, even along the un-corroded portion of the pile, resulted in the plates

bracing more the flange that was susceptible to local buckling, thereby reducing the aspect ratio of the buckling plate and also increasing the resistance of the pile to global flexural buckling. However, the resulting increase of strength is relatively small and typically less than 5%.

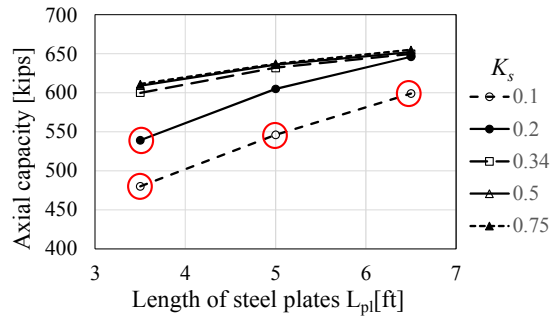


Figure 9.32 Axial peak loads of repaired piles with different lengths of plates

The results of the parametric study demonstrated that the optimized design of the friction-type bolted plates repair system is when the sum of the remaining capacity of the corroded pile, and the friction between the pile flanges and the plates of the repair system, equals the nominal design capacity of the un-corroded pile. In this case, the failure shifts from the corroded region to the un-corroded region beyond the repair system. Increasing the coefficient of friction, bolt pretension, or length of the steel plates beyond this point does not result in a significant increase of the capacity of the repaired pile.

Chapter 10. Experimental Evaluation of Durability of the Proposed Repair Systems

In the previous chapters, the effectiveness of the three proposed repair methods for corrosion-damaged steel piles was evaluated through various analytical and experimental works primarily on the full-scale steel piles that were carefully designed to simulate the field conditions observed in Texas. This chapter presents the experimental work conducted to evaluate the long-term durability of the proposed repair systems using small-scale piles.

10.1. Design of Small-Scale Test Piles

The objective was to design the small-scale test piles that could behave in the same fashion that was observed in the full-scale test piles, using the same materials and design approaches adopted in the full-scale tests. The following sections summarize the details of the small-scale piles used to evaluate the durability of the proposed repair systems.

10.1.1. Size of the Small-Scale Test Piles

The size of the small-scale piles was determined considering:

- Length: the size of the small-scale piles should be appropriate to be placed inside the environmental chamber.
- Slenderness ratio: the slenderness of the small-scale piles should be similar to that of the full-scale piles so that the small-scale piles would fail in a similar manner that was observed in the full-scale pile tests.

- Loading capacity: the ultimate capacity of the piles should be less than the loading capacity of the test set-up available at the Texas Tech Structures Laboratory.

As a result, it was determined that W4×13 Sections with 5-ft length fabricated from ASTM A992 steel should be used. Table 10.1 compares the key dimensional properties of the small-scale test piles to those of the full-scale test piles. As shown in Table 10.1, the length of the small-scale test piles was one-third of that of the full-scale test piles and the area of the small-scale test piles was one-fourth of that of the full-scale test piles. The slenderness ratio of the small-scale test piles was 60.5 while the slenderness ratio of the full-scale test piles was 62.9.

Table 10.1: Comparison of Small-Scale Test Piles and Full-Scale Test Piles

Pile Type	Area (in ²)	Length (ft)	Slenderness Ratio
W4X13	3.83	5	60.5
HP12X53	15.50	15	62.9
Scaling	1:4	1:3	1:1.04

10.1.2. Damage Levels and Locations of the Test Piles

To simulate the corrosion damage in the steel piles, two different cases were considered: (i) minor repair case and (ii) major repair case. As shown in Figure 10.1, the minor repair case considered 75% loss of flange thickness and 60% loss of web thickness within the 4-in. long damage region located at the mid-height of the test piles. As shown in Figure 10.2, the major repair case considered 75% loss of flange thickness and 60% loss of web

thickness within the 12-in. long damage region located at the mid-height of the test piles. In addition to the thickness reduction in the damage region, a void of 2 in. by 3.47 in. was created in the web to simulate the complete loss of web due to corrosion in the major repair case, as shown in Figure 10.2.

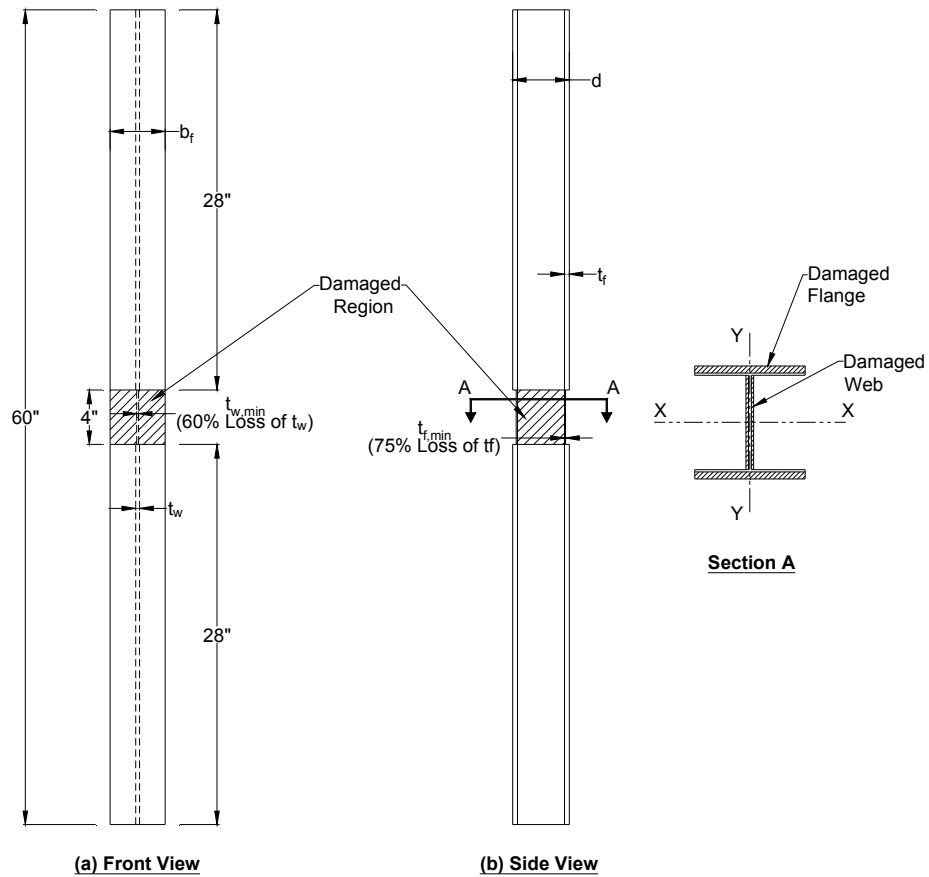


Figure 10.1: Damage level for minor repair case

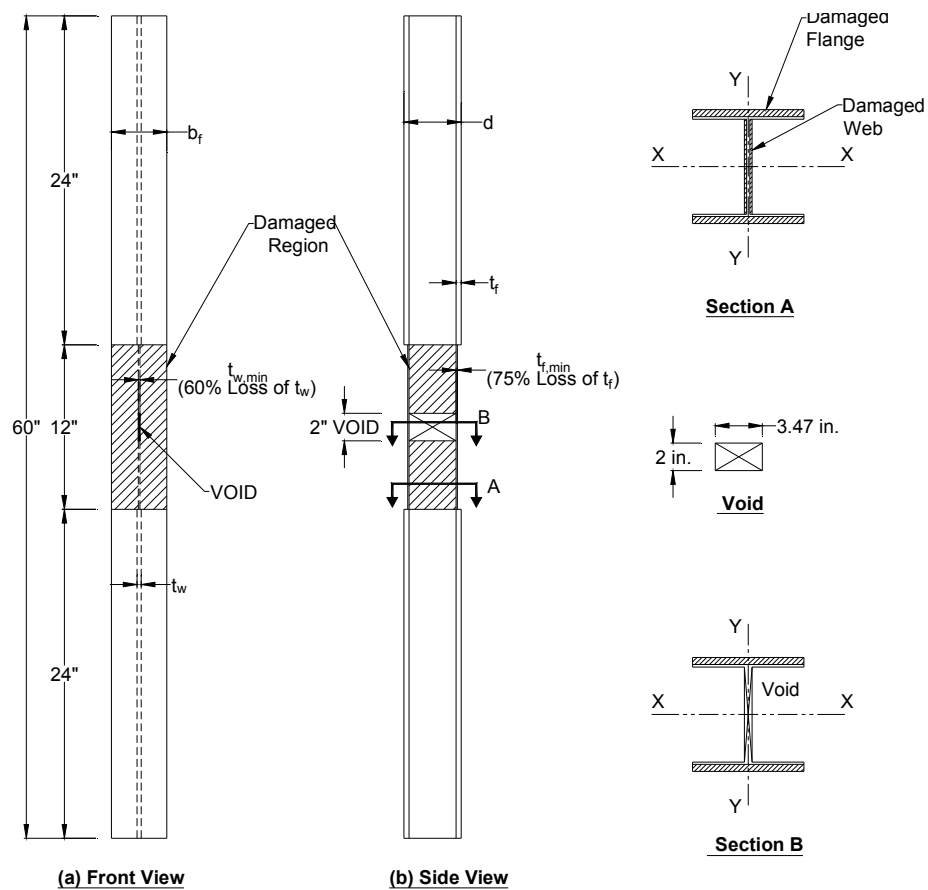
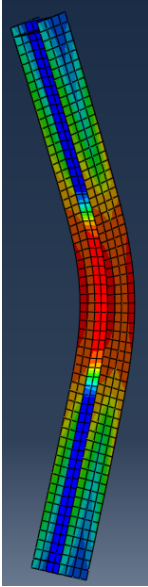
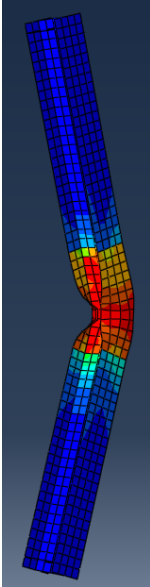
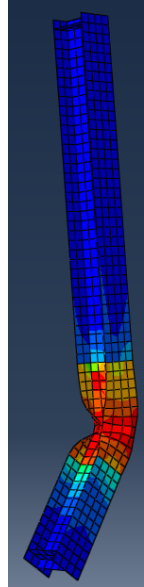
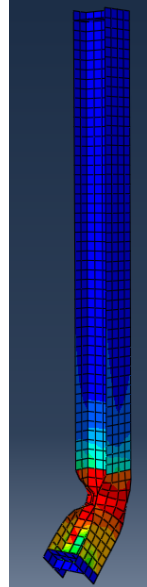


Figure 10.2: Damage level for major repair case

The location of the damage region was determined based on multiple finite element (FE) model analyses. The FE model analyses were performed according to the procedures described in Chapter 6 and the key results of four different FE models are summarized in Table 10.2.

Table 10.2: Summary of the FE Model Analysis to Determine the Effects of Damage Locations

FE Model ID	Control	75/60	75/60	75/60
Damage Location	-	Mid-Height	At 1/4 Height	At Bottom
Failure Modes				
	GB	FLB/WLB	FLB/WLB	FLB/WLB
Peak Load, P_{cr} (kips)	176.6	40.5	41.5	42.6
$\frac{P_{cr}}{P_{cr,control}} \times 100$ (%)	100%	29%	29%	29%
GB = Global Buckling, FLB = Flange Local Buckling, WLB = Web Local Buckling				

The control model simulated the test piles without corrosion damage. The other three models simulated the test piles with corrosion damage (75 % loss of flange thickness and 60% loss of web thickness) in the 12-in. damage region at different locations. As shown in Table 10.2, the remaining capacity of all FE models, simulating the test piles with corrosion damage, was 29% of that of the control model regardless of the damage

location considered. Therefore, a single location of the proposed damage region for both the minor repair case and the major repair case was used in this experimental work (i.e., at the mid-height of the test piles) as it was concluded that the damage location would not significantly influence the test results.

10.1.3. Design of FRP-Confined Grout Repair Systems

The design of the FRP-based repair systems were conducted as described in Chapter 7.

10.1.3.1. Design of Repair System 1

Number of Jacket Layers and Diameter

Figure 10.3 shows the configuration of the FRP jackets used for Repair System 1. As shown in Figure 10.3, the FRP jacket consisted of a 2-ply pre-cured CFRP laminate with an un-balanced bidirectional fiber lay-up. The primary direction of the fibers was oriented in the circumferential direction of the jacket system.

The diameter of the FRP jackets was governed by the diagonal dimension of the cross-section of the test pile (W4x13) and constructability of the pre-cured CFRP laminates used. The diameter selected for the fabrication of Repair System 1 was 6.5 in.

Length of the FRP Jacket

The transfer length of 12-in. was used for both the minor and major repair cases. As a result, the length of the FRP jackets was determined to be 28 in. and 36 in. for the minor repair case and the major repair case, respectively, as shown in Figure 10.4.

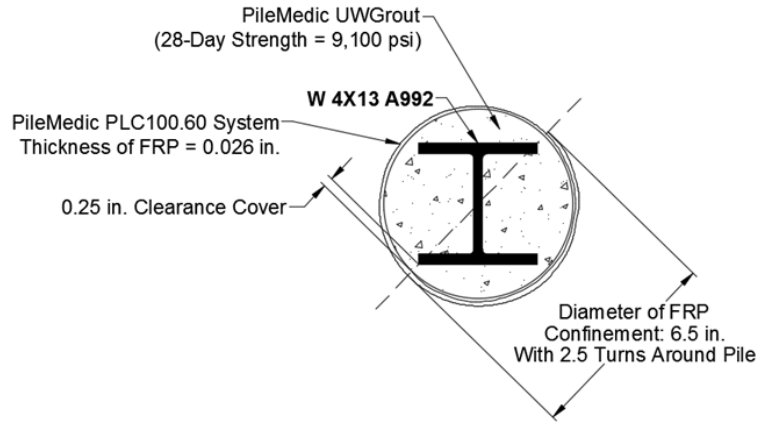


Figure 10.3: FRP jacket configuration for Repair System 1

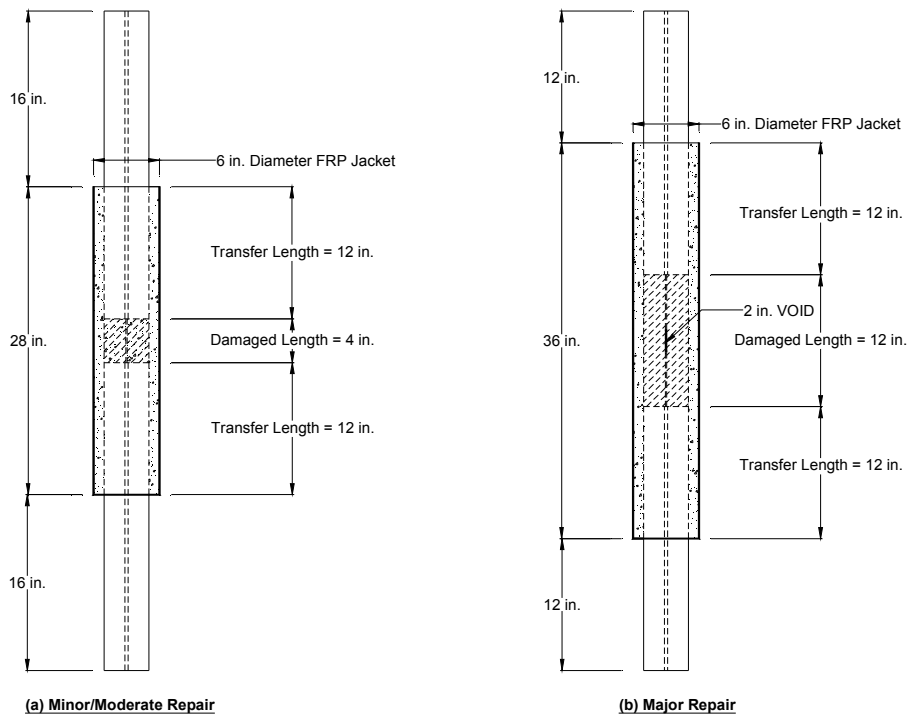


Figure 10.4: Length of the FRP jackets used for the minor repair case and the minor repair case

10.1.3.2. Design of Repair System 2

Figure 10.5 shows the configuration of the FRP jackets used for Repair System 2. As shown in Figure 10.5, the FRP jacket consisted of two different types of FRP layers. The inner layer was a prefabricated GFRP laminate with the fibers oriented in the circumferential direction of the FRP system. The outer layer was a one-ply unidirectional CFRP sheet that was applied manually using the wet lay-up technique. The diameter selected for the fabrication of Repair System 1 was 6.875 in. The length of the FRP jackets was identical to that used for Repair System 1 as shown in Figure 10.4.

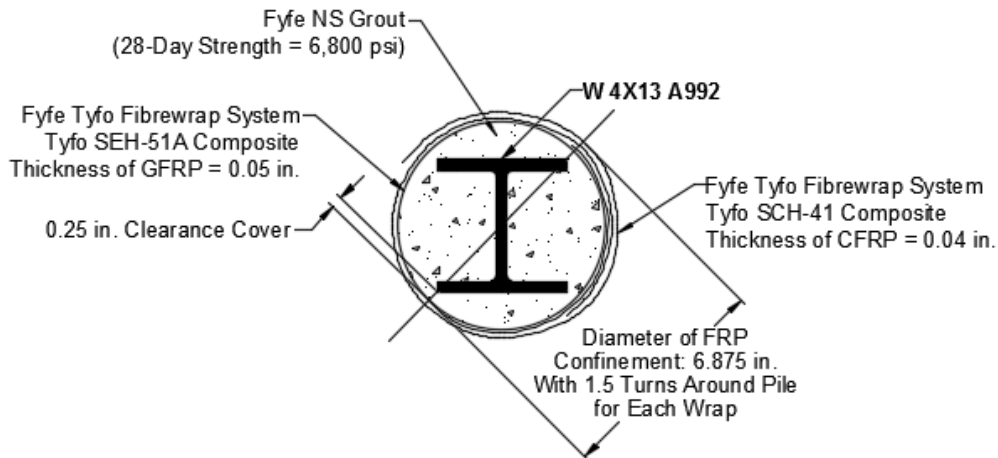


Figure 10.5: FRP jacket configuration for Repair System 2

10.1.4. Design of Steel-Based Repair Systems - Repair System 3

The design of the FRP-based repair systems was conducted as described in Chapter 7. The design was done to strengthen the flanges with no materials attached to the web. To strengthen the flanges, one main steel plate and two clamping steel plates were bolted to clamp the flange on each side of the flange as shown in Figures 10.6 through 10.8.

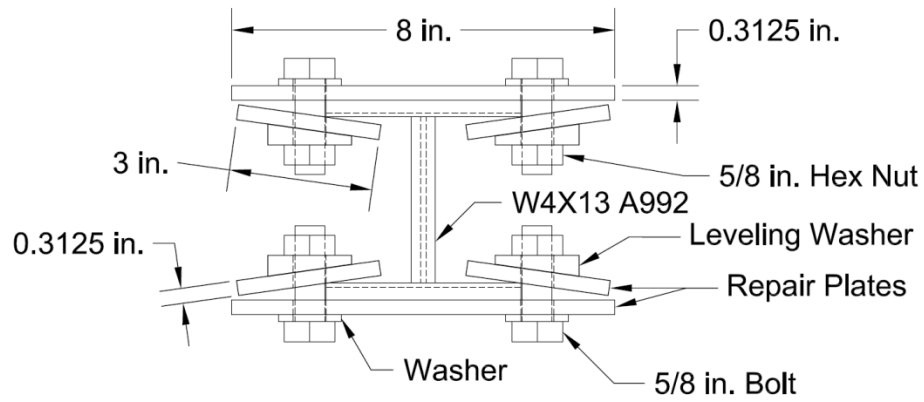


Figure 10.6: Configuration the Repair System

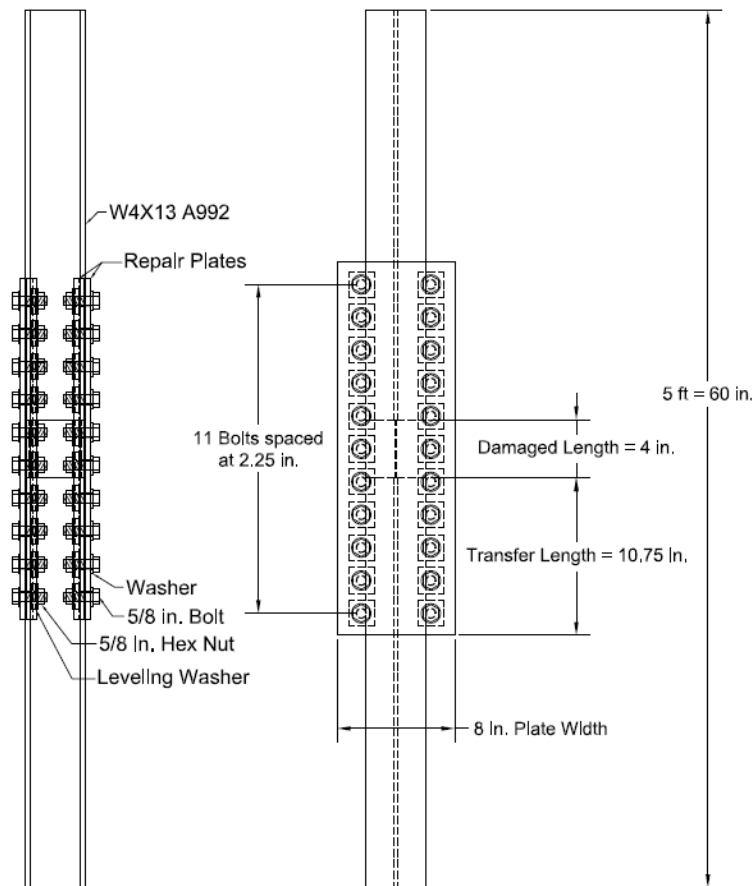


Figure 10.7: Design of Repair System 3 for the minor repair case

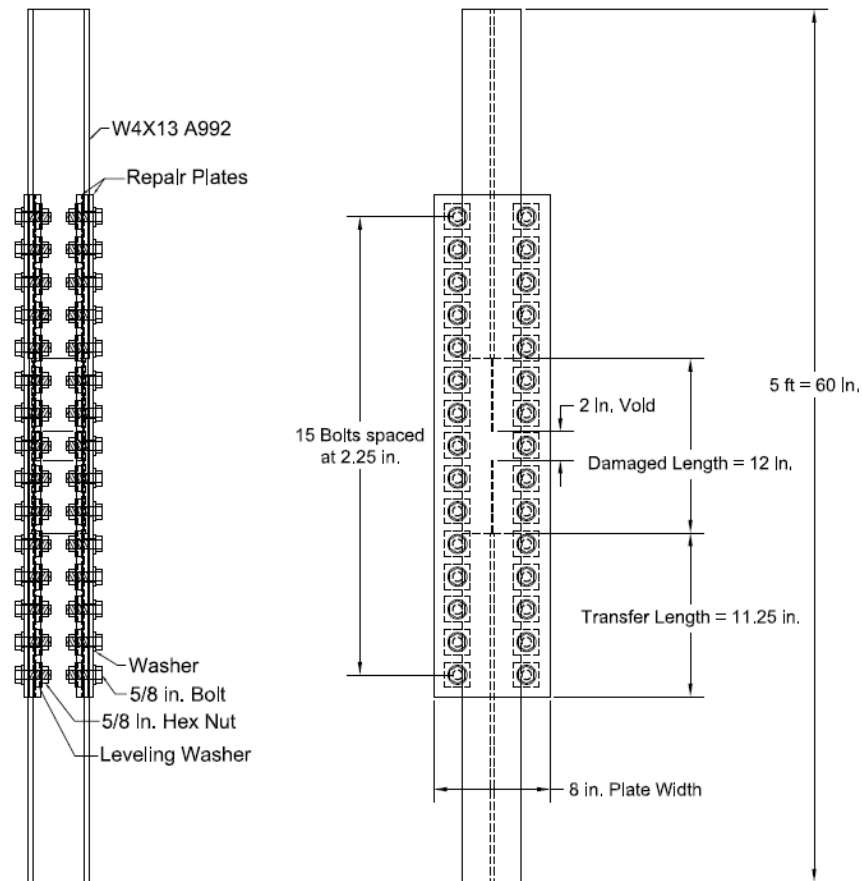


Figure 10.8: Design of Repair System 3 for the major repair

The bolt connection was done with a bevel washer using a torque wrench to provide pretension force in the bolt. The pretension created friction between the main plate and the flange. In addition, the main plates and clamping plates were coated with two different coating materials to increase the slip resistance and corrosion resistance.

10.2. Fabrication of Test Piles

10.2.1. Simulation of Corrosion Damage

The corrosion damage was simulated by milling off the surface of flange and web of W4x13 sections. Figure 10.9 shows the small-scale test piles with the minor damage (4-

in. damage region at the mid-height) and the major damage (12-in. damage region with a void in the web at the mid-height).

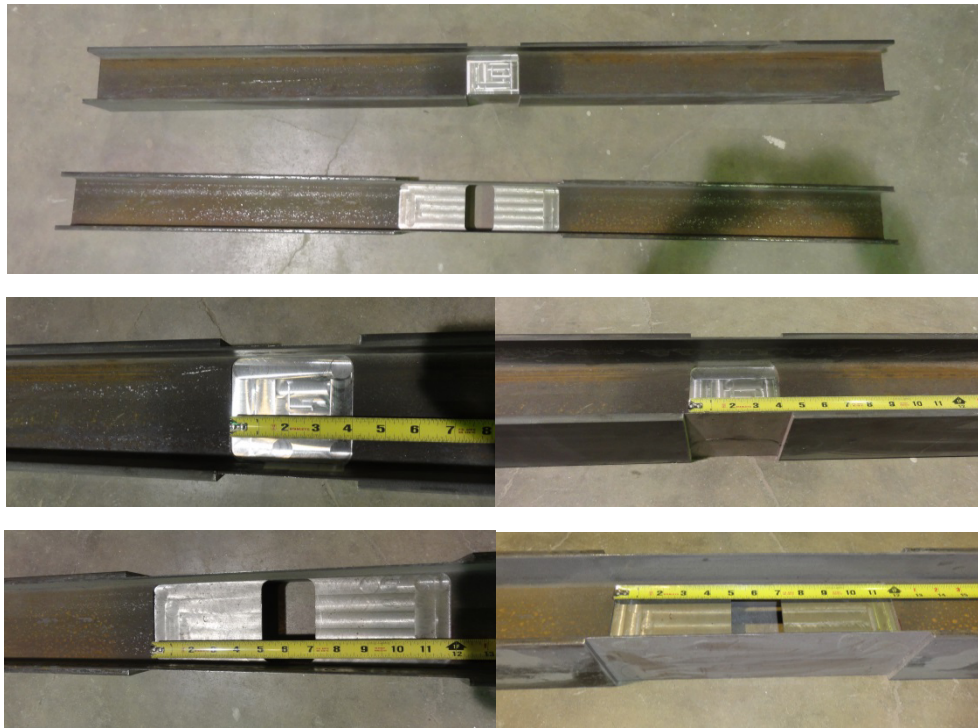


Figure 10.9: Small-scale test piles with minor/moderate corrosion damage and major corrosion damage.

10.2.2. Repair System 1

Repair System 1 used the materials provided by PileMedic LLC and is basically identical to F1-System of the two Grout-filled FRP Jacket Repair Systems considered in the full-scale tests presented in Chapter 8. The properties of the materials for Repair System 1 (or F1- System) can be found in Tables 8.1 through 8.3.

The CFRP sheets used for System 1 were cut from a roll of CFRP. The design diameter of the FRP jacket for the piles was 6.5 in. and the design called for 2.5 turns around the piles at the design diameter. This gave a required minimum length of CFRP of 41 in.

In the full-scale tests, the CFRP sheets were wrapped around the piles manually without use of any device as described in Chapter 8. For the small-scale test piles, however, it was not practically possible to wrap the CFRP sheets around the piles manually.

The CFRP sheet used for both the full-scale and small-scale tests was a precured laminate with a thickness of 0.026 in. and it was not as flexible as sheet-type dry fibers. The CFRP sheet can easily be rolled to form a cylindrical shape with a relatively large diameter. The manufacturer informed that they were able to use the CFRP sheet to fabricate 10-in. diameter easily by hand. The desired diameter of the FRP jackets for the small-scale test piles, however, was 6.5 in. and it was almost impossible to apply the CFRP sheet manually to form a 6.5 in. diameter cylindrical FRP jacket for the small-scale piles placed in a water tank that was used to simulate the actual on-site application cases. As a result, it was determined to fabricate the cylindrical FRP jackets on the dry land and slide into the small-scale piles.

To assist with rolling the CFRP to the desired diameter, a specially designed rolling device was used as shown in Figure 10.10. The device was made using a steel tube that was cut lengthwise in half and an expansion system was made at both ends of the tube. Two guiding clamps were used to ensure that the tube was expanded to 6.5 in.-diameter before rolling the CFRP sheet. Upon finishing the rolling process, the expansion system was compressed slightly to allow the CFRP to be slid off of the steel tube. Figure 10.11 shows the fabricated CFRP jackets used for Repair System 1.

End-caps were installed before placing the piles in the plastic water tank as shown in Figure 10.11. The end-caps were made out of plywood boards. The shape of the cross-section of the small-scale test piles was cut out of the end-caps to ensure tight fit.

Once a small-scale test pile with the installed end-cap was placed inside a plastic water tank, tap water was poured into the water tank. Then, the pre-fabricated FRP jacket was placed in the desired position by sliding them from the top of the pile. The interface of the FRP jacket and the end-cap was sealed with the rubber type silicone as shown in Figure 10.12.

After waiting at least 24 hours of application of the silicone to ensure that the applied silicone was fully cured, underwater grout was applied using a hand-operated grout pump to fill the voids between the FRP jacket and the piles.



Figure 10.10: Fabrication of FRP jackets for Repair System 1



Figure 10.11: Fabricated FRP jackets for Repair System 1

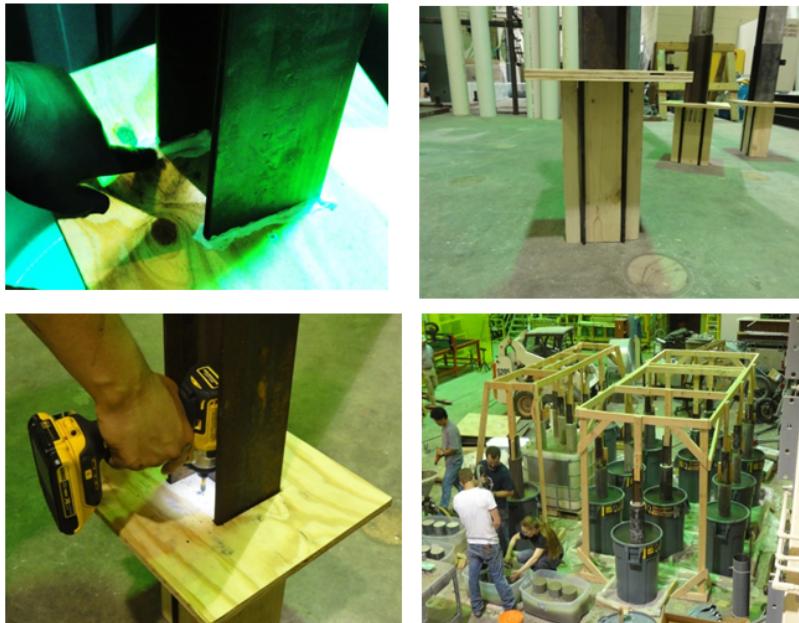


Figure 10.12: Fabrication of Repair System 1

10.2.3. Repair System 2

Repair System 2 used the materials provided by Fyfe Co., LLC, and is basically identical to F2- System of the two Grout-filled FRP Jacket Repair Systems considered in the full-scale tests presented in Chapter 8. The properties of the materials for Repair System 2 (or F2- System) can be found in Tables 8.1 through 8.3.

Repair System 2 consisted of two layers. The inner layer was a pre-fabricated cylindrical GFRP shell, while the outer layer was flexible CFRP dry sheet that was applied using wet lay-up technique.

In the full-scale tests, the pre-fabricate GFRP shells used as the inner layer were fabricated by the manufacturer and delivered to the laboratory. However, the manufacturer terminated the production of the GFRP shells when the small-scale test piles were fabricated. Therefore, the pre-fabricated GFRP shells had to be fabricated in the Structures Laboratory at Texas Tech University according to the guidelines provided by the manufacturer.

Figure 10.13 and 10.14 show the fabrication procedure of the GFRP shells. The GFRP sheets used for Repair System 2 were cut from a single roll of dry GFRP sheets. The GFRP sheets were then impregnated with the epoxy resin. Then, the molding stations for the GFRP wraps were constructed using PVC pipes with an outer diameter of 6.625 in. which were secured to saw horses on each end. These PVC pipes were then wrapped in plastic wrap to protect the GFRP sheets from adhering to the PVC pipe during the epoxy curing process. The GFRP sheets were then gently wrapped around the PVC pipes and a ribbed epoxy roller was gently used to ensure the saturation of sheets with epoxy resin. A plastic sheet was used to separate the GFRP sheet from itself where there was overlap in the mold.



Figure 10.13: Fabrication of cylindrical GFRP shells

The GFRP sheets were then wrapped with plastic wrap to keep the GFRP sheets clean during curing as well as to help ensure the shape of the GFRP sheets remained as desired. The GFRP sheets were allowed to cure for 72 hours before the plastic wrap was removed and the molded sheets were taken off the PVC pipes. Any plastic wrap that adhered to the GFRP molds was removed prior to their use. Then, the cured GFRP sheets were cut using a band saw to the desired length. PVC piping was used as a guide for cutting off the non-straight edges of the GFRP wraps. The PVC piping was slid inside of the GFRP wrap to hold the shape of the wrap to the proper diameter during the cutting process. The

pre-fabricated GFRP shells were then placed in the inside the plastic water tank and prepared for grouting, as shown in Figure 10.14. The underwater grout was injected into the gaps using a plastic nozzle that was designed to have enough length to reach the bottom of the GFRP shells, as shown in Figure 10.15.

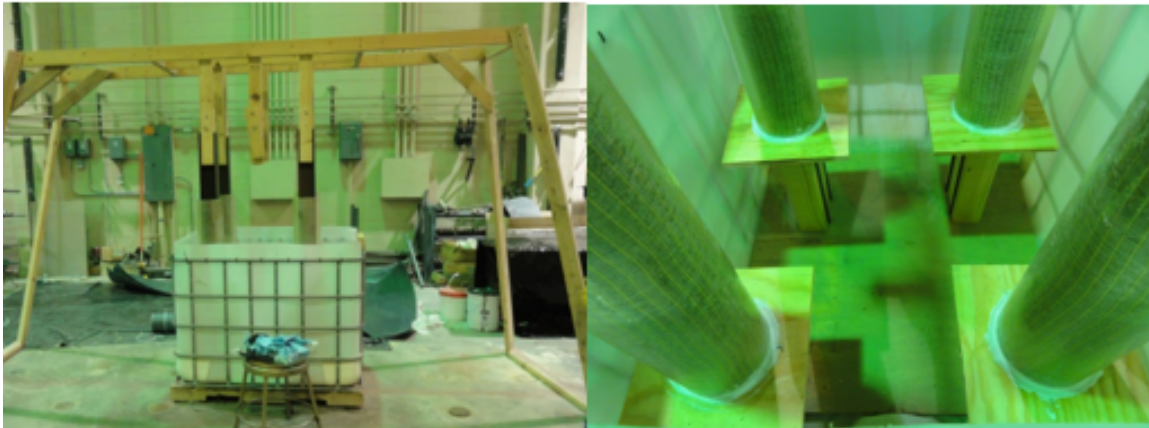


Figure 10.14: Installed Pre-Fabricated Cylindrical GFRP shells



Figure 10.15: Grout injection into the voids between the GFRP shell and the pile

Once the grout was cured for at least 24 hours, the outer layer CFRP sheets were applied.

Figure 10.16 shows the application process for the outer layer. The CFRP sheets used for the outer layer came in rolls measuring 24 in. in width; therefore, two sheets were cut and

used per pile to cover the entire length of the GFRP shells. The first sheet of CFRP was 24 in. in width, and the second sheet varied in width depending on the length of the GFRP shells. A 2-in. overlap length was assumed to give adequate coverage for the breakpoint between the two CFRP sheets according to ACI 440.2R-08; therefore, the second sheet of CFRP measured 14 in. and 6 in. for the major repair case and minor repair case, respectively.

The CFRP sheets were pre-impregnated with the epoxy resin before the application. In addition, the epoxy resin was applied to the surface of the GFRP shells. Then, the pre-impregnated CFRP sheets were wrapped around the GFRP shells, as shown in Figure 10.16. Then, additional epoxy resin was applied on the surface of the wrapped CFRP sheets and a piece of clear plastic sheet and multiple ratchet straps were used to wrap around the CFRP sheets to hold the applied CFRP sheets in the desired shape during the curing time, as shown in Figure 10.16.

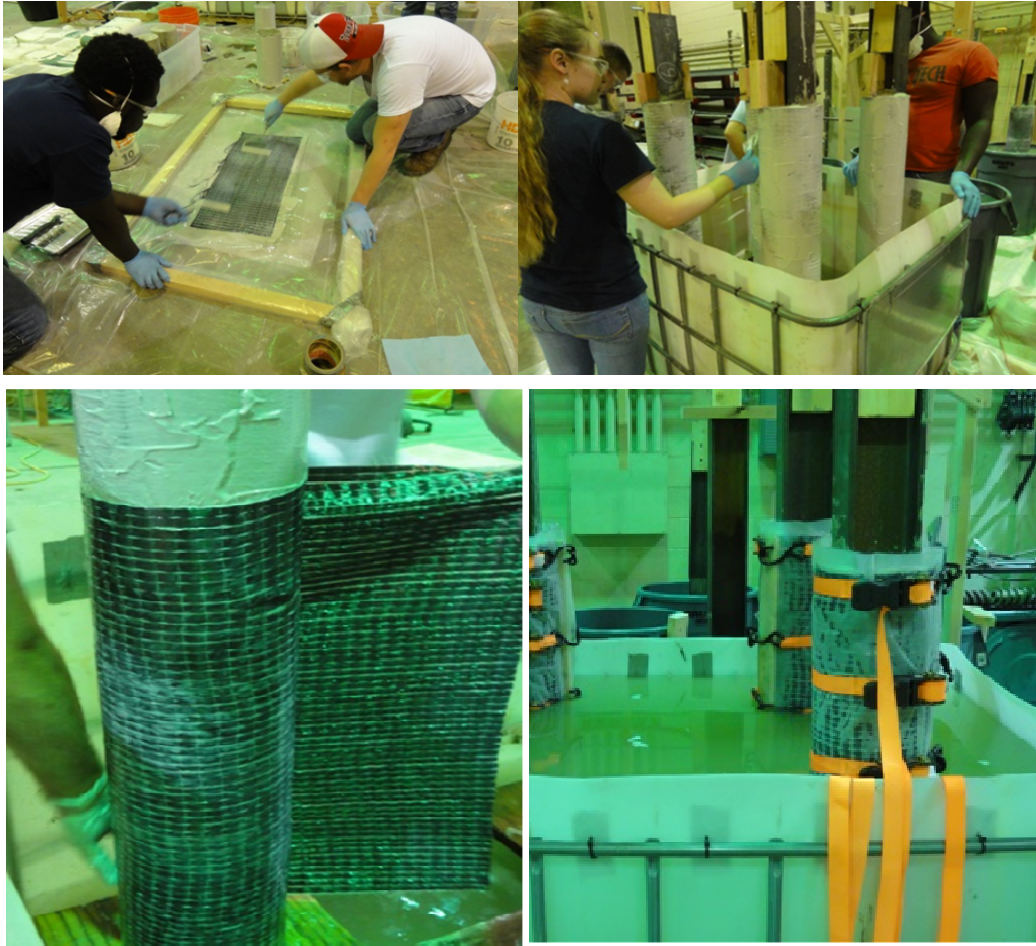


Figure 10.16: Application of CFRP Sheets using wet lay-up technique

10.2.4. Repair System 3

Repair System 3 consisted of steel plates secured with bolts on both sides of the flanges of the test piles. The steel plates used in Repair System 3 were milled from a local steel mill and sent off to a contractor to be coated for corrosion and slip resistance as would be done in the actual field application.

Figure 10.17 shows the fabrication procedure of Repair System 3. The test piles to be repaired were wiped with a saturated cloth to simulate the underwater application in the field. The same was done for each of the steel plates that were to be used on each pile. Bolts and washers were inserted into the main repair plates and then laid down. The pile

was then placed on top of the main repair plate and centered longitudinally along the plate. The clamping plate was then set in place and secured with leveling washers and nuts. The nuts were then hand tightened using wrenches to hold the plates in place when being moved. The plates were wiped between each step with the saturated cloth to ensure that there was moisture present during the entire procedure.

Once the plates were secured on both sides of the pile, the pile was then laid on the floor and weighted while a torque wrench was used to tighten the bolts to 19 kips in tension. In order to ease the strength required to use the torque wrenches, a long steel pipe was placed around the handle of the torque wrench to extend the moment arm of the torque wrench. One person held a wrench in place to stop the nut from turning while another person used the torque wrench on the bolt head to tighten the connection. During this process, it was observed that the repair plates were bent in on the side closest to the web when the bolts were tightened over the area with the flange and web reduction.



Figure 10.17: Fabrication of Repair System 3

10.3. Environmental Cycles

A large-scale environmental chamber with the inside dimension of 9 ft and 8 in. long, 7 ft 9 in. wide and 7 ft 6 in. high, shown in Figure 10.18, was used to expose six tests piles (two from each repair systems) to the predetermined environmental cycles as shown in Figure 10.19. Several test runs were conducted to make sure the environmental chamber was capable of performing the predetermined environmental cycles.



Figure 10.18: Environmental chamber and the small-scale test piles placed inside

The environmental cycle shown in Figure 10.19 was designed to simulate the seasonal change throughout one year. For that purpose, ten freeze-thaw cycles were included in the combined environmental cycles in order to simulate the rapid temperature change during the winter season. Thirty high-temperature cycles were included in order to account for the rapid variation of temperature over the day and night in the summer season. Thirty high-humidity cycles are for the rapid variation of humidity during the change of season from spring to summer and from summer to fall. This one-year environmental cycle was repeated ten times to simulate at least 10 years of exposure.

The freeze-thaw cycles consisted of one-hour freeze at 0°F with 20% relative humidity and one-hour thaw at 50°F with 40% relative humidity, and 30 min. ramping up and down. The high temperature cycles consisted of one-hour low temperature of 80°F with 70% relative humidity, one-hour high temperature of 120°F with 90% relative humidity, and 20 min. ramping up and down. The high humidity cycle consisted of 20-min. 60% relative humidity at 60°F, 20-min. 95% relative humidity at 80°F, and 30 min. ramping up and down.

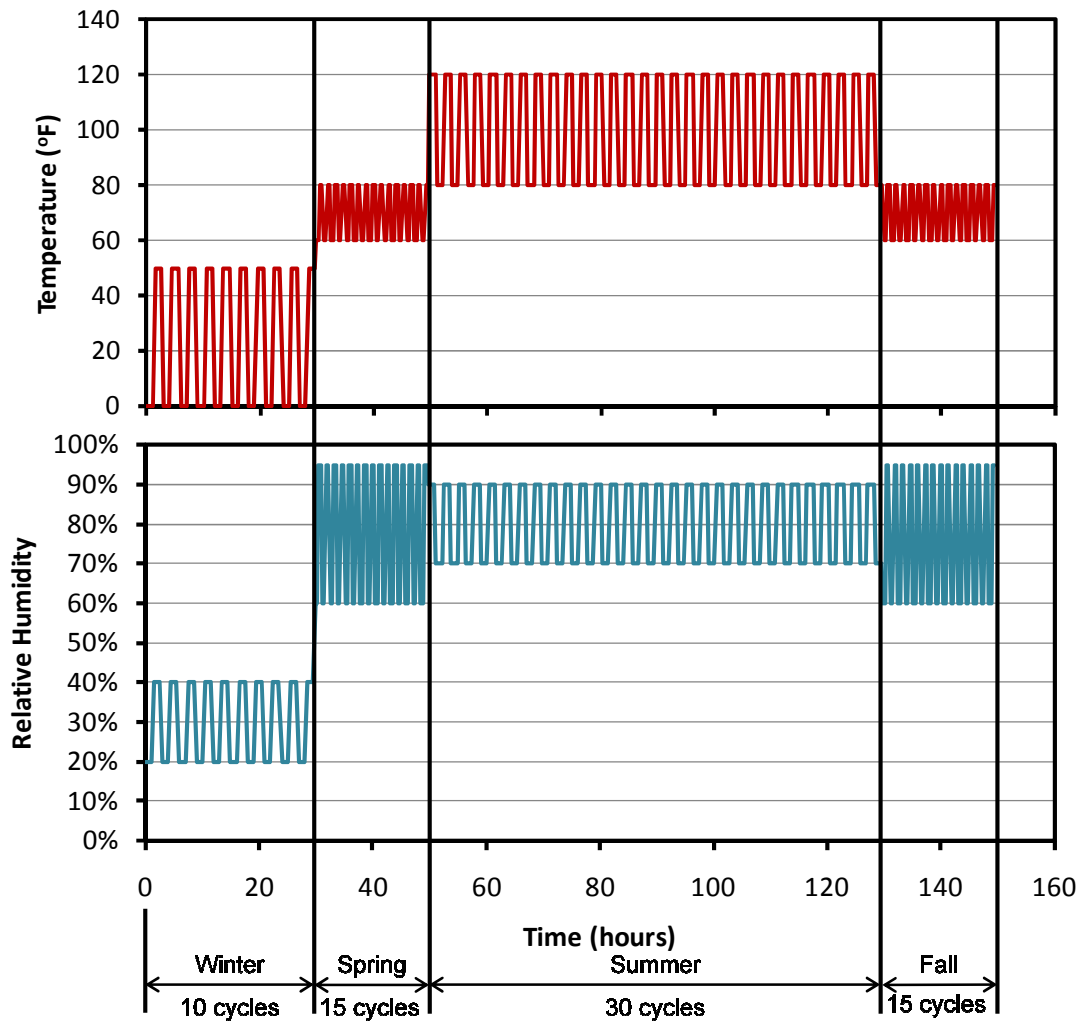


Figure 10.19: One year environmental cycle

10.4. Accelerated Corrosion Process

Since the corrosion of steel occurs over several years in the real world, it is necessary to establish an accelerated corrosion process to induce the corrosion of steel in a laboratory within a relatively short period. To this end, the concept of electrolyte cell was adapted, as shown in Figure 10.20.

The repaired test piles were placed in the water tank filled with a 5% saline solution in order to destroy the passive film of steel reinforcements and supply water and oxygen. In addition,

it was possible for the anode (steel pile) to lose a large amount of electrons by imposing fixed electric potential. The fixed electric potential was supplied by a DC power supply. The corrosion rate was monitored by means of checking the electric current between the anode (steel pile) and the cathode (wire mesh). The measured corrosion current, in turn, will be converted into steel loss using Faraday's Law, as shown in Equation (10-1):

$$\Delta w(g) = \frac{A_m \cdot I \cdot t}{z \cdot F} \quad (\text{Eq. 11-1})$$

where, $\Delta w(g)$ is incremental steel loss (grams), A_m is atomic mass (for iron 55.85 g), I is uniform current (Am) applied over time increment t (second), z is valency (assuming that most of rust product is $\text{Fe}(\text{OH})_2$, it is taken as 2), and F is Faraday's constant (96487 C/eq). In (Eq. 11-1), it was assumed that all of the current resulting from the accelerated corrosion process was used to produce rust.

Thus, the total accumulated steel loss over the period of the accelerated corrosion process will be determined from the area under the corrosion current vs. time curve by integration, as shown in Equation (10-2):

$$w = \frac{A_m}{z \cdot F} \sum \Delta t \cdot I_{ave} \quad (\text{Eq. 11-2})$$

With this accumulated steel loss, the cross-sectional area loss was indirectly calculated.

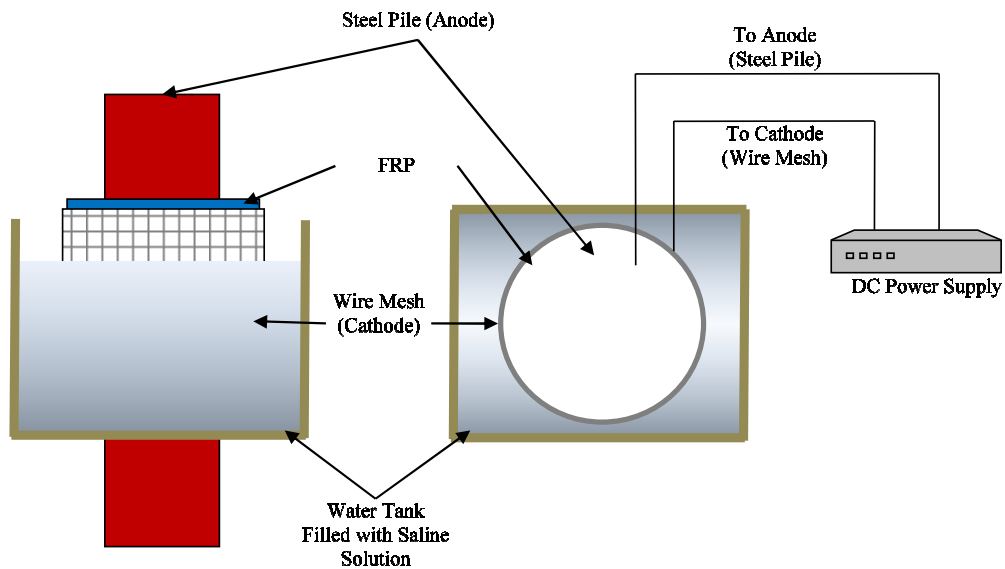


Figure 10.20: Schematic of accelerated corrosion process

Figure 10.21 shows the actual set-up for the accelerated corrosion process. For the undamaged, unrepaired piles and all piles repaired with Repair System 3, the pile was placed in a large container and filled with soil up to the edge of the damaged region near the mid-height. For the undamaged control pile, this was done to simulate the conditions that a column would experience in the field. For the piles repaired with Repair System 3, this was done to keep the saline solution near only the middle area of the pile. For the piles repaired with Repair System 3, a thin layer of non-shrink grout used in Repair System 2 was poured on top of the soil to create a waterproof seal. The grout was then coated in waterproofing paint to prevent transfer of the water through the grout. A 5-gallon container was then placed around the pile and sealed to the coated grout surface using epoxy. To prevent leaks from occurring around the bolts during the accelerated corrosion process, epoxy putty was used to seal the connections between the washers, nuts, and plate. The epoxy was also coated with waterproofing paint to slow the rusting of the bolts.

For the piles repaired with Repair System 1 and System 2, a wooden platform was used to hold a 5-gallon container around the mid-height of the pile. A thin layer of non-shrink grout used in Repair System 2 was poured on top of the wooden platform to prevent water from leaking through the wood or between the set-up and the pile. The grout was then coated in waterproofing paint to prevent the transfer of the water through the grout. A 5-gallon container was then placed around the pile and sealed to the coated grout surface using epoxy.

The 5-gallon containers and the undamaged, repaired pile container were then filled with the 5% saline solution. Air hoses were then submerged with bubble-producing aquarium stones suited for salt water to provide oxygen continuously to the containers. A bolt was welded to the top of each pile to connect the voltage system to the test specimen. Aluminum mesh caging was placed around each pile, but not touching the piles, and each pile was connected to a 1 Ohm resistor to measure the voltage drop across the system. The piles were subjected to 6 months of accelerated corrosion simulation. After a few months of accelerated corrosion process, the aquarium stones were clogged with corrosion residue and needed to be replaced or removed altogether.

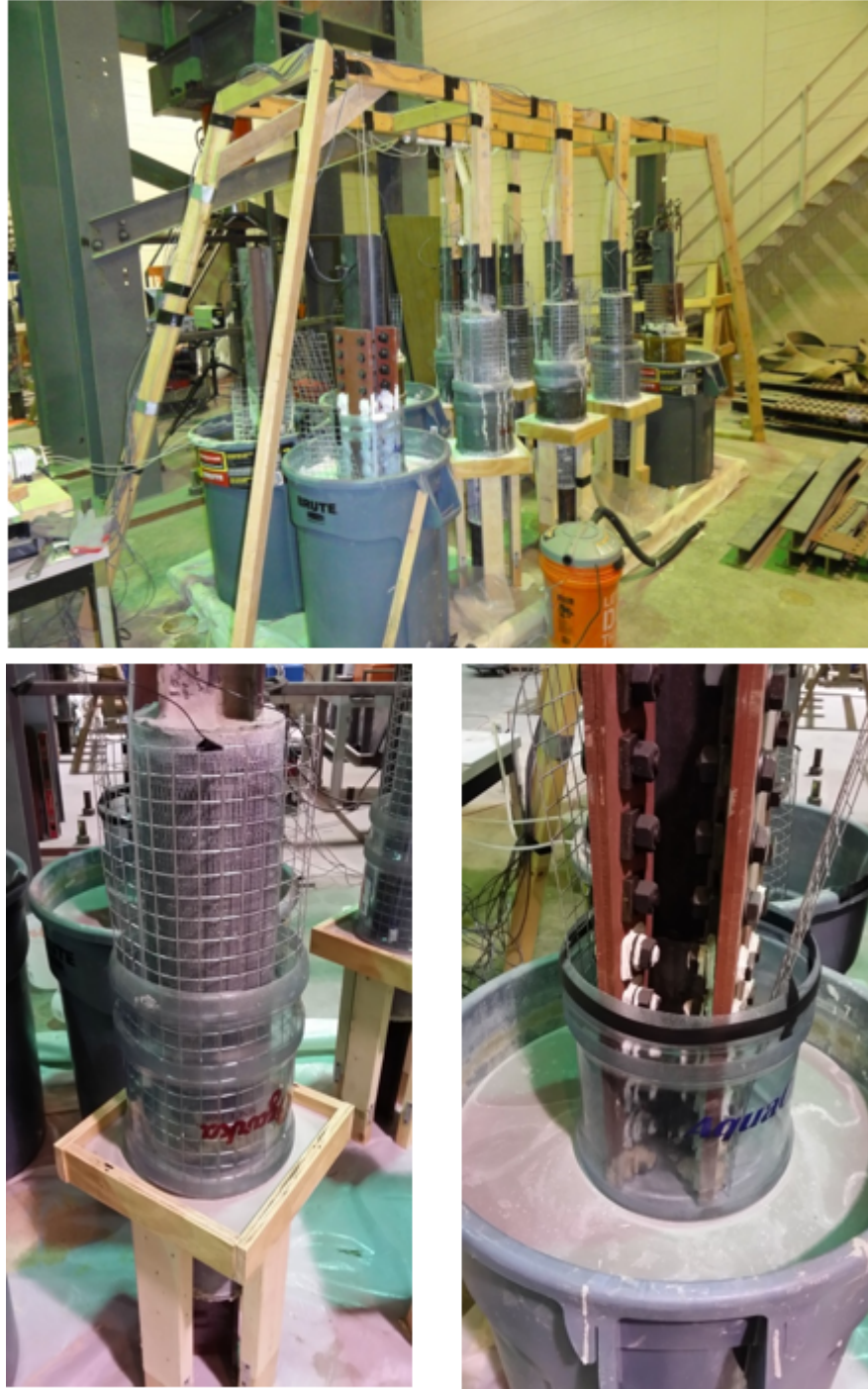


Figure 10.21: Actual set-up of accelerated corrosion process

10.5. Failure Test Set-Up and Instrumentation

A loading frame of 500-kip capacity shown in Figure 10.22 was used for failure testing of the test piles. A hydraulic jack (the maximum loading capacity of 500 kips and the maximum stroke of 12 in.) was used to apply axial force. The test piles were situated on top of a spherical support with a pin support holding the specimen in place at the top, as shown in Figure 10.23 and 10.24. A total of five linear variable displacement transducers (LVDTs) were used to measure axial and lateral displacement of the test piles. A laser extensometer was used to measure the axial strain of the test piles during testing at the mid-height of the test pile. A Vishay 7000 Data Acquisition System was used to collect the test data.



Figure 10.22: Loading frame for failure testing of the test piles

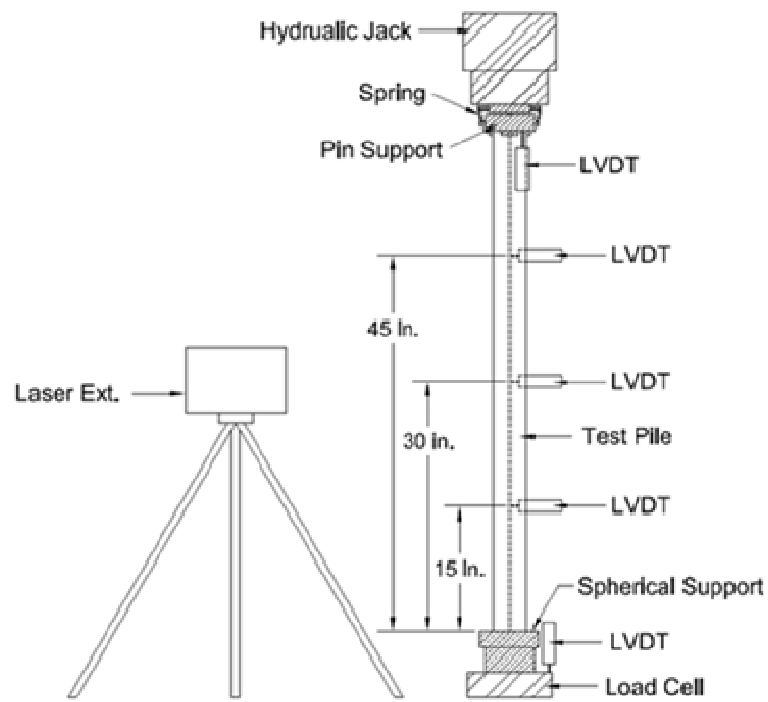


Figure 10.23: Schematic of the test set-up



Figure 10.24: Actual test set-up for failure testing

10.6. Test Matrix

A total of 32 test piles were fabricated in this experimental work. The test piles were categorized into three groups. Group 1 piles were the ones that did not undergo neither the environmental cycles nor the accelerated corrosion process. Group 2 piles were the ones that were subjected to the environmental cycles. Group 2 piles were used to evaluate the effects of the environmental effects on the performance of the proposed repair systems. The piles in Group 3 were subjected to the accelerated corrosion process. Group 3 piles were used to evaluate how the proposed repair systems were effective on preventing further corrosion activity after the repair was done.

10.6.1. Group 1 - Control Test Piles

A total of 13 piles were included in this group as shown in Table 10.3. The piles denoted as 'CONT' served as the control piles to evaluate the axial load capacity of undamaged and un-repaired piles. The piles denoted as 'DCONT' were used to measure the decrease in the axial load capacity due to corrosion damage. Pile DCONT-4 had the 4-in. damage region at the mid-height of the test pile, as shown in Figure 10.2(a) Pile DCONT-12 was fabricated with the 12-in. damage region (b). The piles with the capital letter S were repaired with one of the proposed repair methods, and they were used to evaluate the increase in axial load capacity of damaged piles after the repair was done. Piles S1-4-CONT and S1-12-CONT had the 4-in. and 12-in. damage regions, respectively, and they were repaired with Repair System 1. Piles S2-4-CONT and S2-12-CONT had the 4-in. and 12-in. damage regions, respectively, and they were repaired with Repair System 2.

Piles S3-4-CONT and S3-12-CONT had the 4-in. and 12-in. damage regions, respectively, and they were repaired with Repair System 3.

Table 10.3: Group 1 - Control Test Piles

Test Piles	Damage Levels	Repair Systems	Number of the Duplicates
CONT	None	None	4
DCONT-4	4-in.	None	2
DCONT-12	12 in.	None	1
S1-4-CONT	4-in.	System 1	1
S1-12-CONT	12 in	System 1	1
S2-4-CONT	4-in.	System 2	1
S2-12-CONT	12 in	System 2	1
S3-4-CONT	4-in.	System 3	1
S3-12-CONT	12 in	System 3	1

10.6.2. Group 2 - Test Piles Conditioned under the Environmental Cycles

All piles in Group 2 shown in Table 10.4 were subjected to the environmental cycles described previously. The test results of the Group 2 piles were compared with those of the corresponding control piles in Group 1 to evaluate the level of the performance degradation of the repair methods due to the environmental cycles. Piles S1-4-Env and S1-12-Env had 4-in. and 12-in. corrosion damage regions at the mid-height, respectively, and they were repaired with Repair System 1. Piles S2-4-Env and S2-12-Env had 4-in. and 12-in. corrosion damage regions at the mid-height, respectively, and they were repaired with Repair System 2. Piles S3-4-Env and S3-12-Env had 4-in. and 12-in. corrosion damage regions at the mid-height, respectively, and they were repaired with Repair System 3.

10.6.3. Group 3 - Test Piles for Evaluating Corrosion Rate

In Group 3, a total of thirteen piles were used to evaluate the effectiveness of the proposed repair systems in preventing further corrosion activity after the repair job was done, as shown in Table 10.5. A control pile (CONT-Cor) was used to monitor the corrosion rate of undamaged, unrepaired pile under the accelerated corrosion process. A total of six piles (marked with ‘Cor’ in the pile denomination) were fabricated to evaluate the corrosion rate of the damaged piles repaired with three different repair methods under the accelerated corrosion process. In the meantime, a total of six piles (marked with ‘N’ in the pile denomination) were placed in the natural condition without the accelerated corrosion process to evaluate the natural corrosion process.

Table 10.4: Test matrix for test piles subjected to environmental cycles

Test Piles	Damage Levels	Repair Systems	Number of Duplicates
S1-4-Env	4-in.	System 1	1
S1-12-Env	12 in	System 1	1
S2-4-Env	4-in.	System 2	1
S2-12-Env	12 in	System 2	1
S3-4-Env	4-in.	System 3	1
S3-12-Env	12 in	System 3	1

Table 10.5: Test matrix for test piles subjected to ~~environmental~~ ^{CORROSION} cycles

Test Piles	Damage Levels	Repair Systems	Applied Corrosion Test Methods	Number of Duplicates
CONT-Cor	None	None		1
S1-4-Cor	4-in.	System 1		1
S1-12-Cor	12 in	System 1		1
S2-4-Cor	4-in.	System 2	Accelerated Corrosion	1
S2-12-Cor	12 in	System 2		1
S3-4-Cor	4-in.	System 3		1
S3-12-Cor	12 in	System 3		1
S1-4-Cor-N	4-in.	System 1		1
S1-12-Cor-N	12 in	System 1		1
S2-4-Cor-N	4-in.	System 2	Natural Corrosion	1
S2-12-Cor-N	12 in	System 2		1
S3-4-Cor-N	4-in.	System 3		1
S3-12-Cor-N	12 in	System 3		1

10.7. Results and Discussion

The failure test results of Groups 1 and 2 were summarized in Table 10.6. The following sections discuss the test results in detail.

Table 10.6: Summary of the failure test results

Test Piles	Damage Levels	Repair Systems	P_u (kips)	Δ_u (in.)	Failure Mode
CONT(1)	None	None	109.1	0.160	Global Buckling
CONT(2)	None	None	102.8	0.220	Global Buckling
CONT(3)	None	None	98.9	0.177	Global Buckling
CONT(4)	None	None	105.2	0.156	Global Buckling
Average of CONT			104.0		
DCONT – 4(1)	4-in.	None	24.6	0.055	Flange Buckling
DCONT – 4(2)	4-in.	None	35.1	0.073	Flange Buckling
Average of DCONT-4			29.9		
DCONT-12	12 in.	None	8.2	0.035	Flange Buckling
S1-4-CONT	4-in.	System 1	106.4	0.585	Global Buckling
S1-4-Env	4-in.	System 1	108.9	0.599	Global Buckling
S1-12-CONT	12 in	System 1	93.9	0.581	Global Buckling
S1-12-Env	12 in	System 1	106.6	0.562	Global Buckling
S2-4-CONT	4-in.	System 2	97.3	0.460	Global Buckling
S2-4-Env	4-in.	System 2	103.6	0.372	Global Buckling
S2-12-CONT	12 in	System 2	115.6	0.402	Global Buckling
S2-12-Env	12 in	System 2	108.3	0.519	Global Buckling
S3-4-CONT	4-in.	System 3	75.3	0.121	Slip
S3-4-Env	4-in.	System 3	84.7	0.130	Slip
S3-12-CONT	12 in	System 3	68.8	0.130	Slip
S3-12-Env	12 in	System 3	76.7	0.122	Slip

10.7.1. Failure Mode

10.7.1.1. Undamaged Control Columns (CONT)

All of the undamaged control piles (CONTs) experienced global buckling about the weak axis with the largest deflection occurring between the upper quarter-point and mid-height of the column, as shown in Figure 10.25.



Figure 10.25: Failure of an undamaged control column (CONTs)

10.7.1.2. Damaged Control Columns (DCONT-4 and DCONT-12)

The damaged control piles with 4-in. damaged region (DCONT-4) exhibited flange local buckling in which the flanges buckled in a sinusoidal shape on one or both sides, as shown in Figure 10.26. The damaged control piles with 12-in. damaged region (DCONT-12) failed due to the buckling of the flange. At the same time, the

top half of the test pile shifted sideways out of alignment with the bottom half of the pile in the damaged region where there was no web, as shown in Figure 10.26.

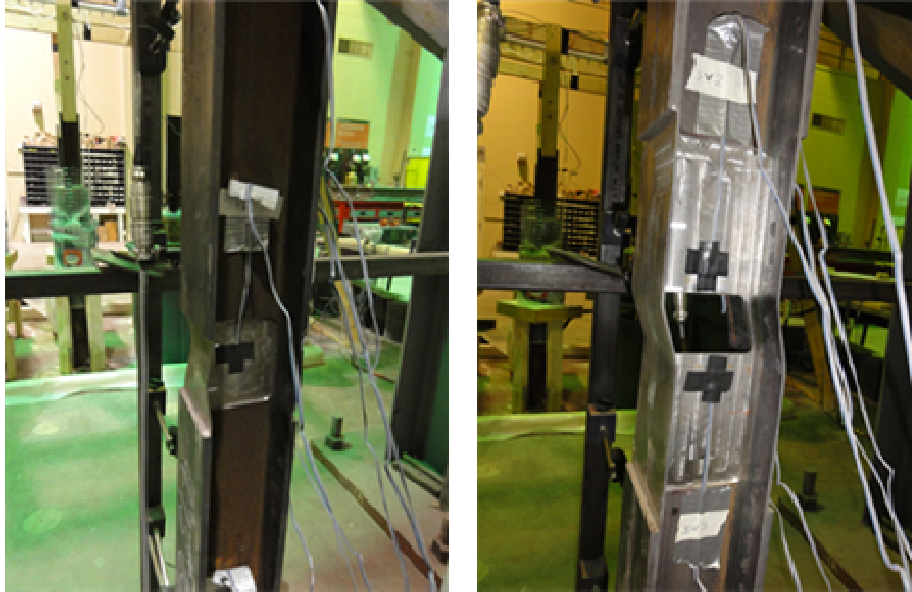


Figure 10.26: Failure of 4-in. damaged control piles (DCONT-4) and 12-in. damaged control piles (DCONT-12)

10.7.1.3. Repair System 1

4-in Damage (S1-4-CONT and S1-4-Env)

The test piles with 4-in. damage region repaired with Repair System 1 (S1-4-CONT and S1-4-Env) failed due to global buckling, as shown in Figure 10.27. Almost at the time of buckling of the test piles, it was observed that slight rupture of the FRP jacket occurred near the mid-height along the circumference of the pile (i.e., close to the end of 4-in. damage region), as shown in Figure 10.27; however, the largest lateral deflection was measured at the top interface between the pile and the jacket. The portion of the pile below the repair system stayed almost straight, and the pile buckled slightly above the start of the repair system, as shown in Figure 10.27.

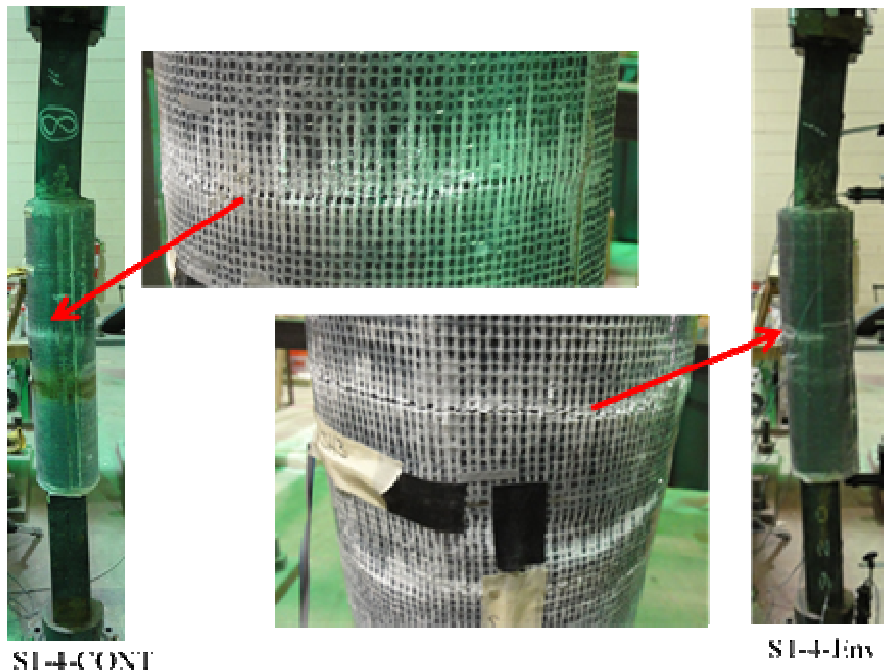


Figure 10.27: .Failure of 4-in damaged piles repaired with Repair System 1 (S1-4-CONT and S1-4-Env)

12-in Damage (S1-12-CONT and S1-12-Env)

The test pile with 12-in damage region repaired with System 1 (S1-12-CONT) failed due to global buckling, as shown in Figure 10.28. At buckling of the pile, the FRP jacket did rupture at the mid-height and 6-in. above the mid-height along the circumference of the pile, as shown in Figure 10.28. This location is also the start of the 12-in. long damaged section in the pile. In the region between the two circumferential FRP rupture lines, there was a large section of the FRP jacket that ruptured along the length of the column, as shown in Figure 10.28. The environmentally conditioned test pile (S1-12-Env) failed in a very similar fashion to that of the control pile (S1-12-CONT). However, unlike the control pile (S1-12-CONT), there was no rupture of the FRP jackets along the length of the pile in the environmentally conditioned pile (S1-12-Env). The environmentally conditioned pile

(S1-12-Env) experienced FRP jacket rupturing near the start and finish of the 12-in. damaged region and not at the mid-height of the column, as shown in Figure 10.28.

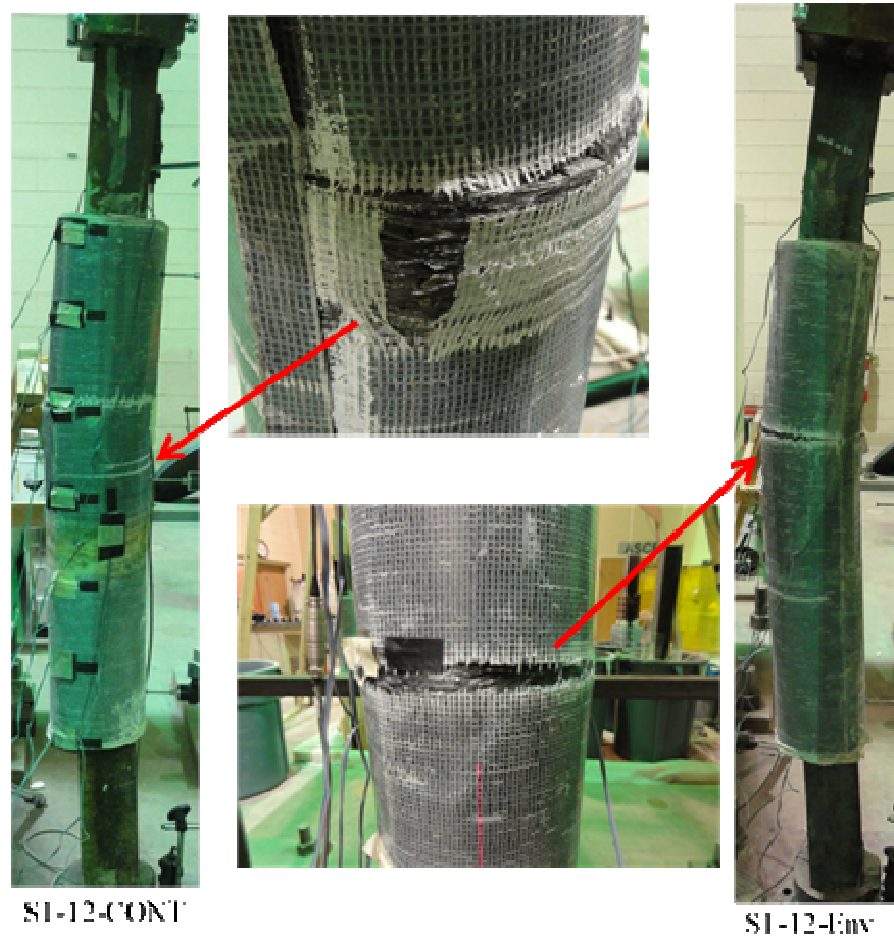


Figure 10.28: Failure of 12-in damaged piles repaired with Repair System 1 (S1-12-CONT and S1-12-Env)

10.7.1.4. Repair System 2

4-in Damage (S2-4-CONT and S2-4-Env)

The test piles with 4-in. damage region repaired with Repair System 2 (S2-4-CONT and S2-4-Env) failed due to global buckling, as shown in Figure 10.29. Almost at the time of buckling of the test piles, it was observed that slight rupture of the FRP jacket occurred in the circumferential direction near the start and end of where the damaged

region was located, as shown in Figure 10.29. The largest lateral deflection was measured near the mid-height of the piles. In the region between the two circumferential FRP rupture lines, there was a large section of the FRP jacket that ruptured along the length of the pile, in the case of S2-4-Env, as shown in Figure 10.29.

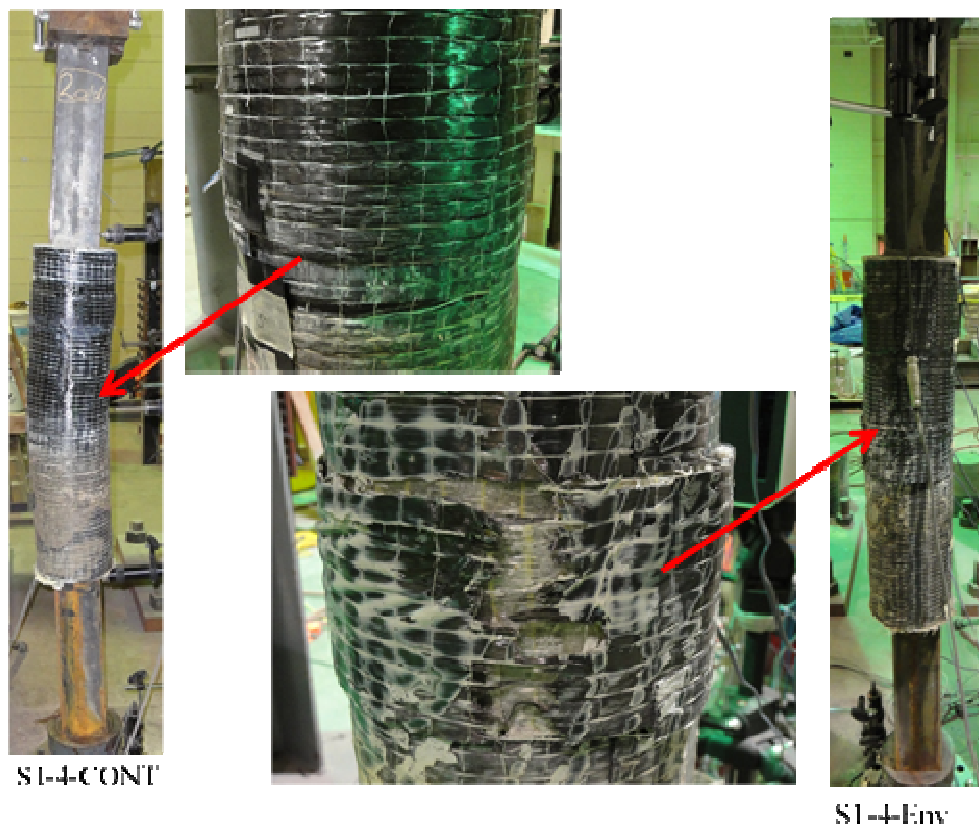


Figure 10.29: Failure of 4-in damaged piles repaired with Repair System 2 (S2-4-CONT and S2-4-Env)

12-in Damage (S2-12-CONT and S2-12-Env)

The failure mode of the test piles with 12-in. damage region repaired with Repair System 2 (S2-12-CONT and S2-12-Env) was global buckling as shown in Figure 10.30. The largest buckling of the pile was observed at the interface between the pile

and the top of the repair system, as shown in Figure 10.30. Below this interface, there was no buckling experienced by the pile at all. There was also no rupture of the FRP jacket either in the circumferential or longitudinal directions for both the S2-12-CONT and S2-12-Env piles.

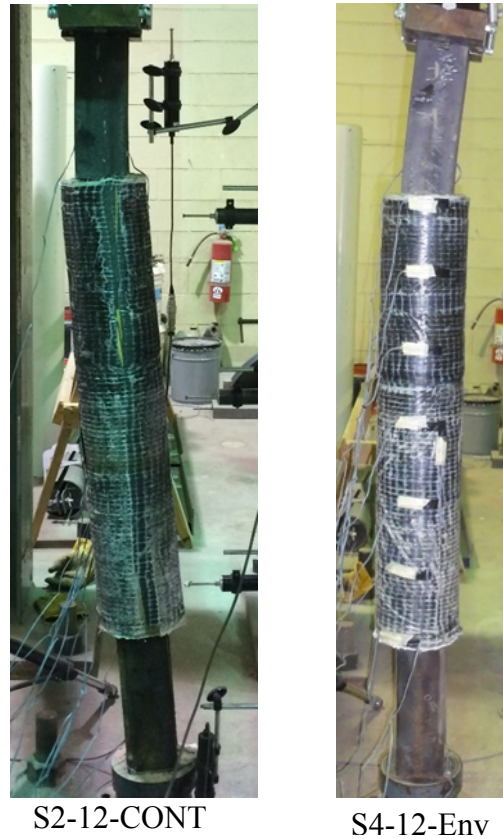


Figure 10.30: Failure of 4-in damaged piles repaired with Repair System 2 (S2-12-CONT and S2-12-Env)

10.7.1.5. Repair System 3 (S3-4-CONT, S3-4-Env, S3-12-CONT, and S3-12-Env)

All test piles repaired with Repair System 3 (S3-4-CONT, S3-4-Env, S3-12-CONT, and S3-12-Env) failed due to slip between the pile and the repair steel plate.

Although the slip-critical connection of the test piles was designed to restore the damaged piles to the strength of their corresponding undamaged, unrepaired control piles, the slip-critical connection started slipping at a lower axial load than the anticipated axial load capacity. Even after the slip occurred, the piles were continuously loaded until the damaged region at the mid-height was completely crushed as shown in Figures 10.31 and 10.32. Once the damaged region of the web was completely folded in on itself, the piles began buckling as shown in Figure 10.33. For the test pile S3-12-Env, the primer used to prevent corrosion and increase friction of the repair plate started to crack severely around the bolts in various locations near the mid-height of the pile, as shown in Figure 10.34.

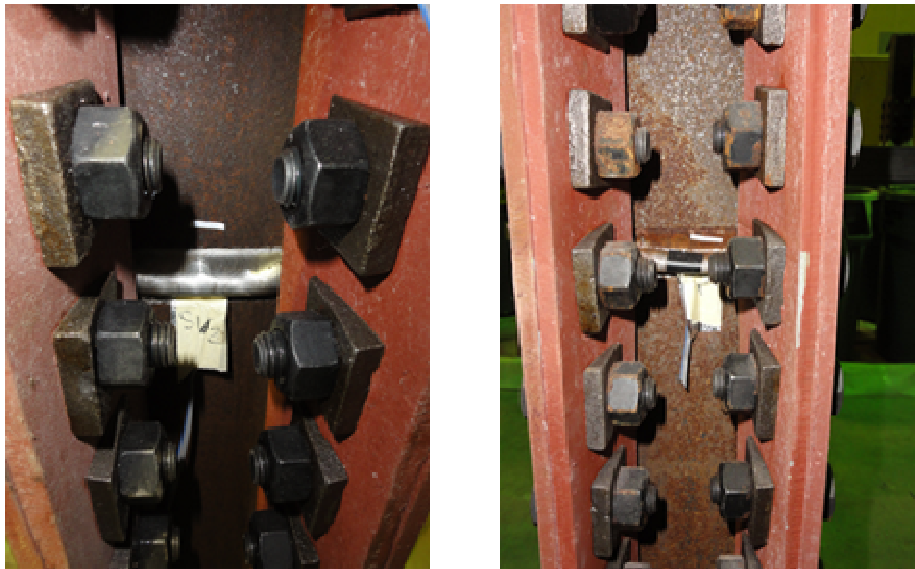


Figure 10.31: Crushing of 4-in. damaged region of the test piles repaired with Repair System 3

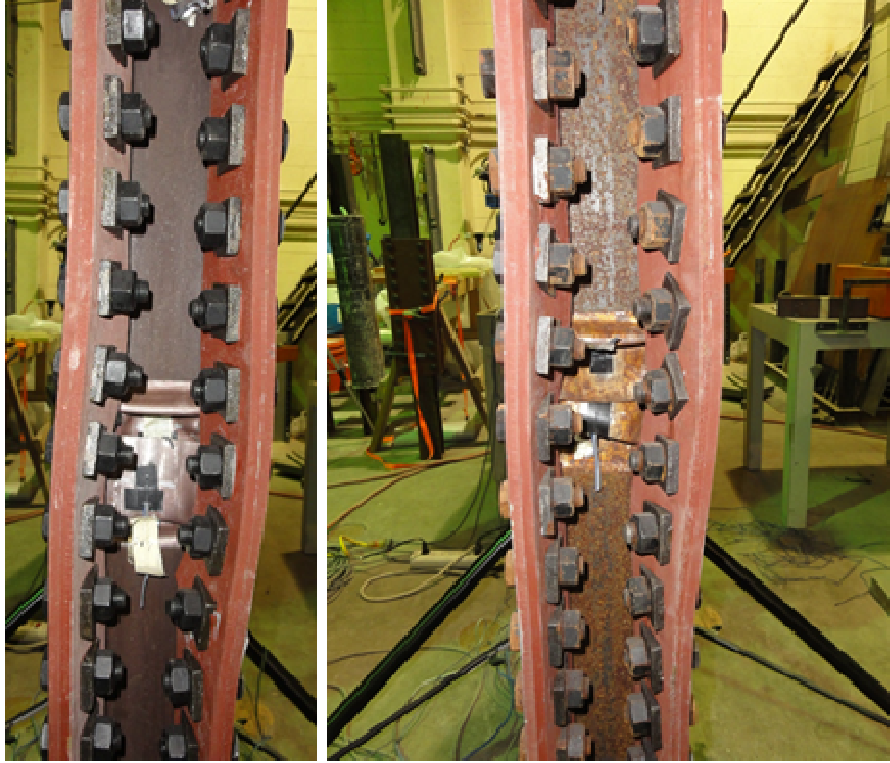


Figure 10.32: Crushing of 12-in. damaged region of the test piles repaired with Repair System 3

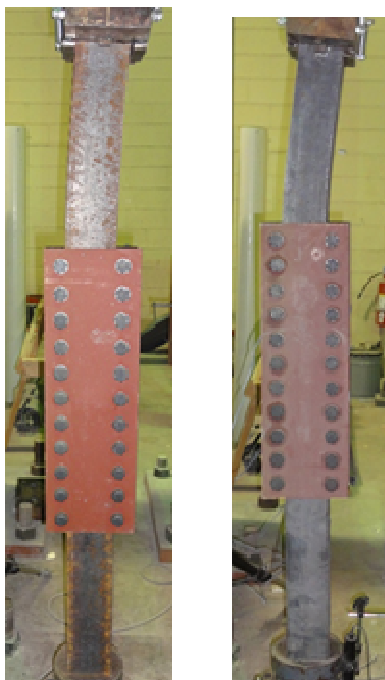


Figure 10.33: Global buckling of the piles repaired with Repair System 3



Figure 10.34: Global buckling of the piles repaired with Repair System 3

10.7.2. Axial Load Capacity of Undamaged Control Piles

Four undamaged, unrepaired control piles (CONTs) were tested to measure the axial load capacity of undamaged, unrepaired piles, as shown in Figure 10.35. As shown in Figure 10.35, the axial capacity of undamaged, unrepaired piles ranged from 98.9 kips to 109.1 kips with an average of 104.0 kips.

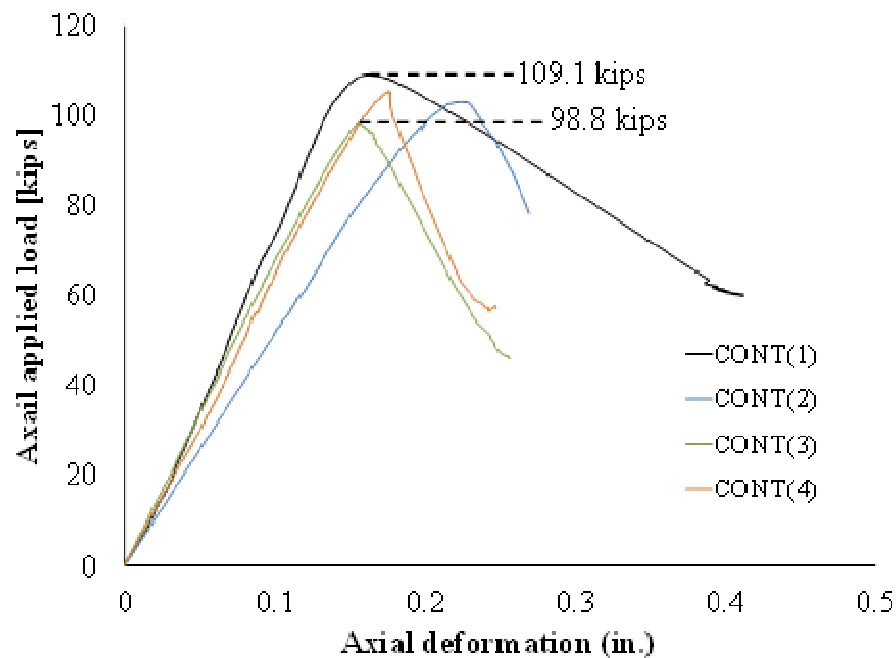


Figure 10.35: Axial load vs. axial deformation curves of the control piles (CONT)

10.7.3. Reduction in Axial Load Capacity Due to Simulated Corrosion-Damage

Figure 10.37 shows the axial load vs. axial deformation curves of damaged piles (DCONT-4 and DCONT-12). The piles with the 4-in. damage region (DCONT-4) failed at 24.6 kips and 35.1 kips, which was 76% and 66% reduction in the axial load capacity as compared to the average axial load capacity of the control piles (CONTs) of 104.0 kips. The piles with the 12-in. damage region (DCONT-12) failed at 8.2 kips which

corresponded to a 92% reduction in the axial load capacity when compared to the average axial load capacity of the control piles (CONTs) of 104.0 kips.

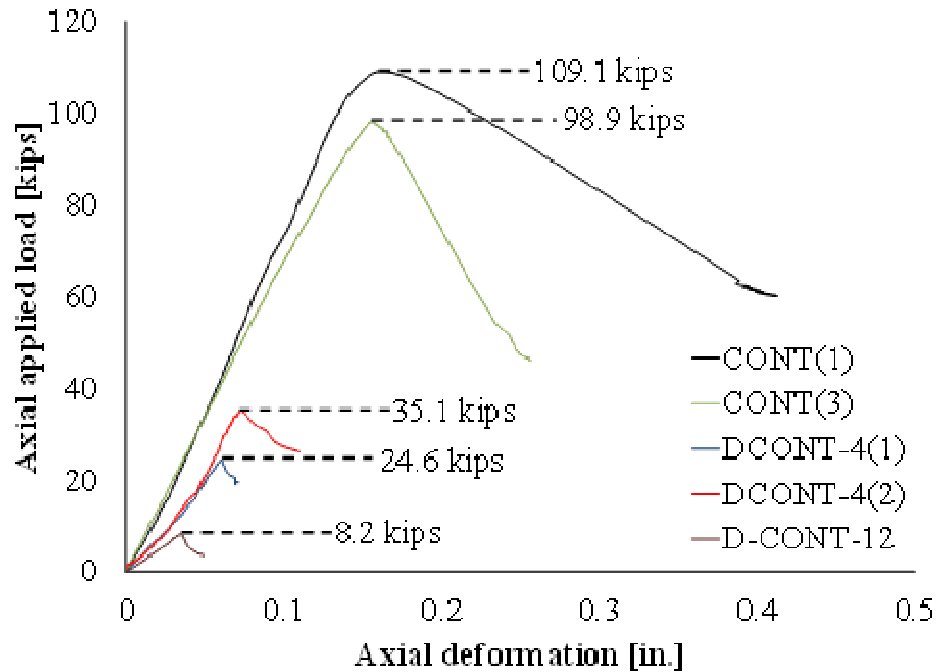


Figure 10.36: Axial load vs. axial deformation curves of the damaged control piles (DCONT-4 and DCONT-12)

10.7.4. Restoration of Axial Load Capacity by Repair System 1

Two piles repaired with Repair System 1 (S1-4-Cont and S1-12-Cont) were tested and the axial load vs. axial deformation curves of the two piles are presented with that of one of the undamaged, repaired control piles (CONT(1)), as shown in Figure 10.37(a). As shown in Figure 10.37(a), the axial load capacities of the damaged piles (S1-4-Cont and S1-12-CONT) were restored up to levels comparable to the axial load capacity of the undamaged, unrepaired control piles (CONT).

Figures 10.37(b) and 10.37(c) compare the behavior of the damaged piles (DCONT-4 and DCONT-12) with that of the damaged pile repaired with Repair System 1. As shown in

Figures 10.37(b) and 10.37(c), the axial load capacities of the damaged piles were restored to levels comparable to the average axial load capacity of the undamaged control piles (CONT) due to the repair.

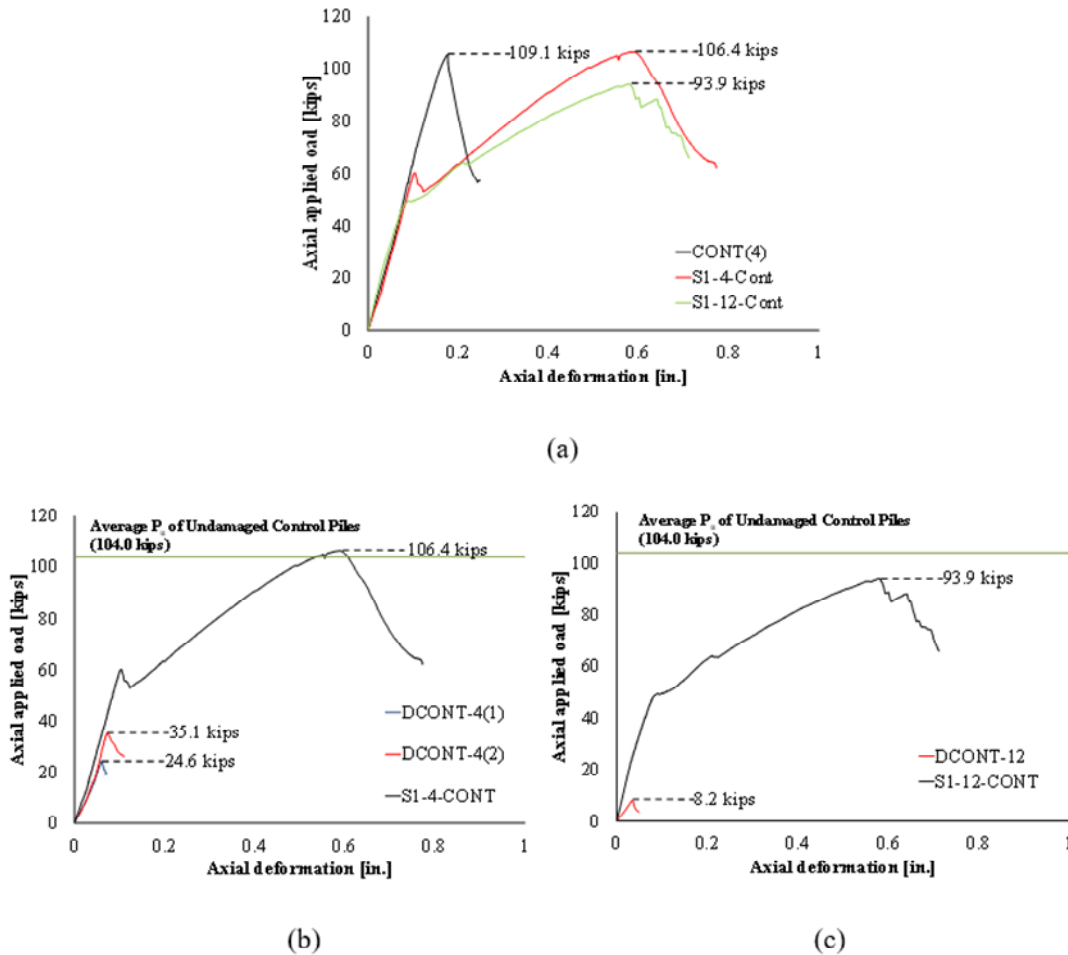


Figure 10.37: Axial load vs. axial deformation curves of the damaged piles repaired with Repair System 1

10.7.5. Restoration of Axial Load Capacity by Repair System 2

Two piles repaired with Repair System 2 (S2-4-Cont and S2-12-Cont) were tested and the axial load vs. axial deformation curves of the two piles are presented in Figure 10.38(a) with that of one of the undamaged, repaired control piles (CONT(1)). As shown

in Figure 10.38, the axial load capacity of the damaged piles (S2-4-Cont and S2-12-CONT) was restored up to levels comparable to the axial load capacity of the undamaged, unrepaired control piles (CONT).

Figures 10.38(b) and 10.38(c) compare the behavior of the damaged piles (DCONT-4 and DCONT-12) with that of the damaged pile repaired with Repair System 2. As shown in Figures 10.38(b) and 10.38(c), Repair System 2 was able to restore the axial load capacity of the damage piles to levels comparable to the average axial load capacity of the undamaged control piles (CONT).

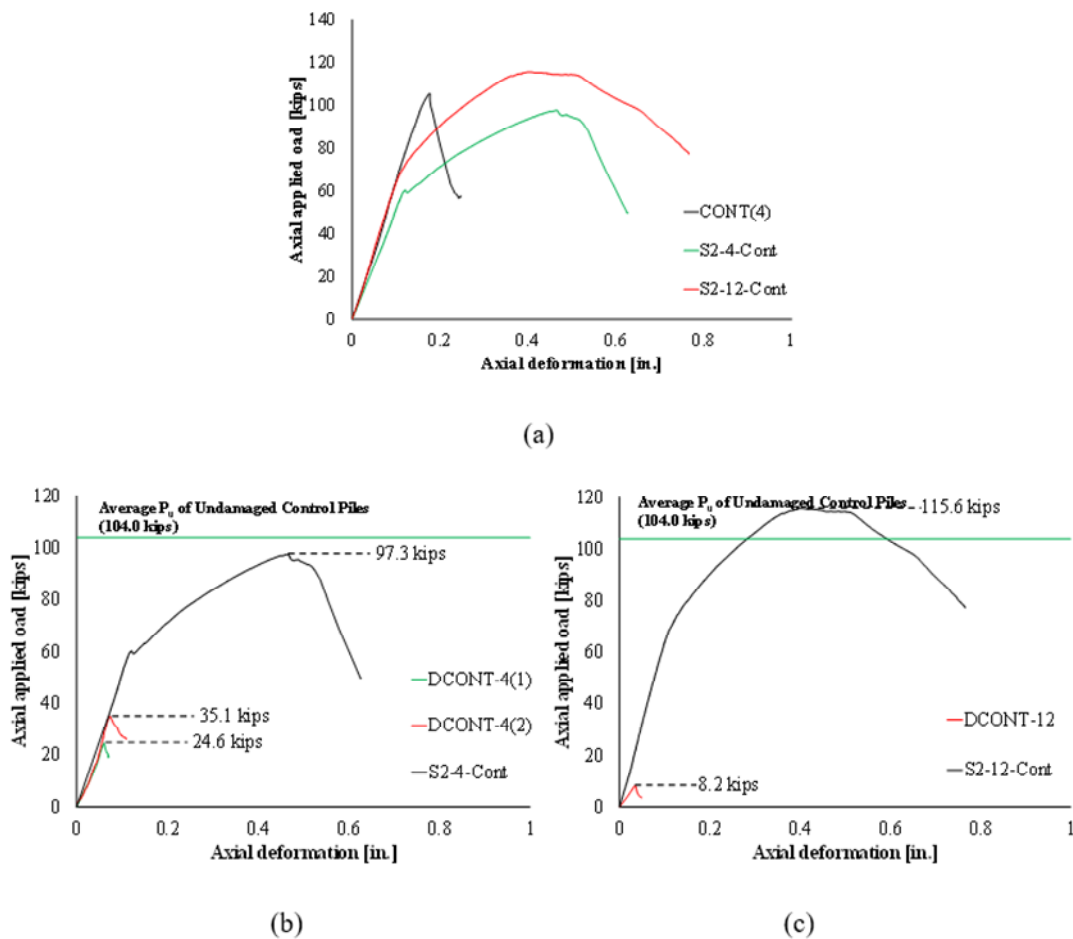


Figure 10.38: Axial load vs. axial deformation curves of the damaged piles repaired with Repair System 2

10.7.6. Restoration of Axial Load Capacity by Repair System 3

Two piles repaired with Repair System 3 (S3-4-Cont and S3-12-Cont) were tested and the axial load vs. axial deformation curves of the two piles are presented with that of one of the undamaged, repaired control piles (CONT(1)), as shown in Figure 10.39.

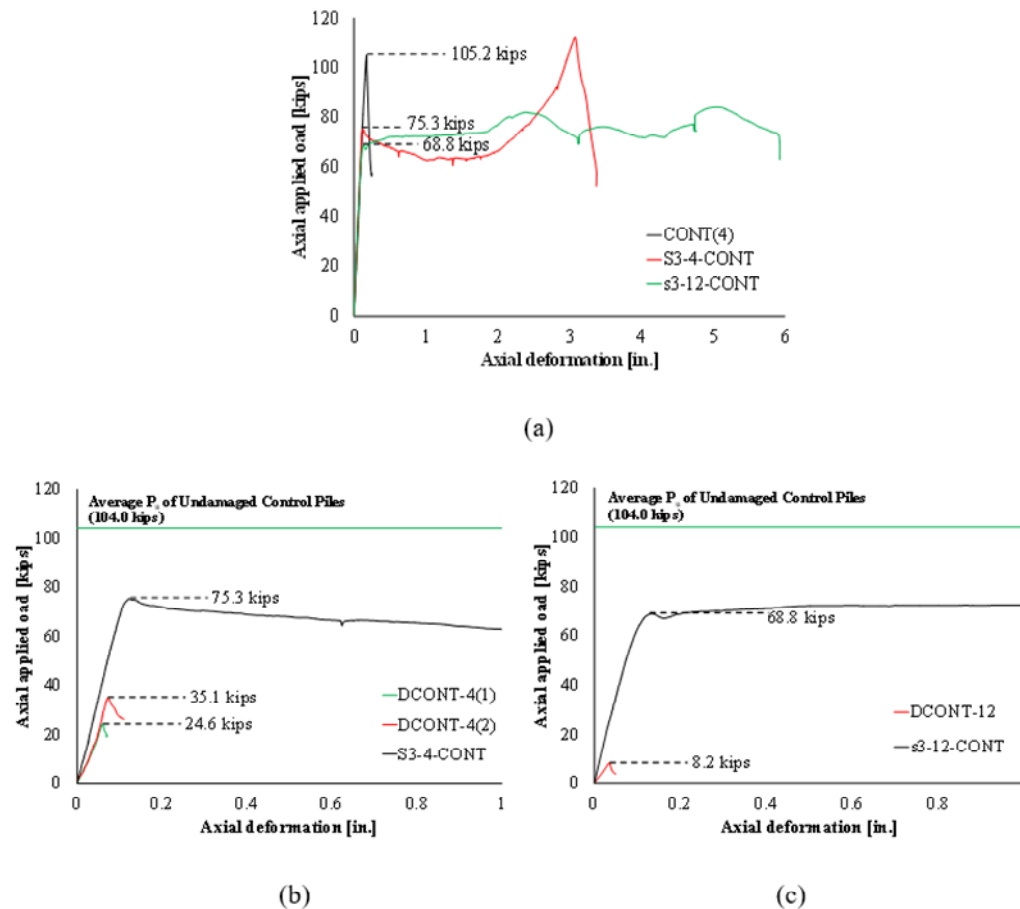


Figure 10.39: Axial load vs. axial deformation curves of the damaged piles repaired with Repair System 3

As shown in Figure 10.39, Repair System 3 was not able to restore the axial load capacity of the damaged piles up to the axial load capacity of the undamaged, unrepaired control piles (CONT). Pile S3-4-CONT reached the first peak load of 75.3 kips (75% of the average axial load capacity of the undamaged, repaired control piles) while Pile S3-12-

CONT reached the first peak load of 68.8 kips (66% of the average axial load capacity of the undamaged, repaired piles). After the first peak load, both piles underwent a significant amount of plastic axial-deformation. However, the objective of the small-scale pile tests was to evaluate the environmental durability of the repair systems. As such, the results will be analyzed more closely in terms of the relative performance of environmentally conditioned piles compared to un-conditioned piles while the effectiveness of the system was evaluated by considering full-scale piles which are not subject to some of the practical constraints associated with repairing the small-scale piles.

10.7.7. Effects of Environmental Cycles

Figure 10.40 compares the performance of the repaired piles with/without being subjected to the environmental cycles. As shown in Figure 10.40, the environmental cycles did not cause any significant reduction of the axial load capacity of the repaired piles. The smallest difference in axial load capacity between the piles with/without the environmental cycles was about +2% (see Figure 10.40(a)) while the biggest difference was about +13% (see Figure 10.30(b)). In all cases, the axial capacity of the piles that was subjected to the environmental cycles was slightly greater than that of their corresponding control piles that were not subjected to the environmental cycles as shown in Figures 10.40(a) through 10.40(f) except for one case (i.e., S2-12-CONT vs. S2-12-Env) in which the reduction in axial load capacity due to the environmental cycles was only 6%. This was comparable to the inter-specimen variability of the undamaged control piles (CONT) which varied by 9% between four nominally identical specimens.

10.7.8. Corrosion of the Test Piles

Corrosion of the undamaged, unrepaired pile (CONT-Cor) continuously occurred during the accelerated corrosion process as shown in Figure 10.41. The rust was built up mostly near the water level. The byproduct of the consumed salt for the corrosion process was deposited on the caging and around the waterline of the pile as shown in Figure 10.41.

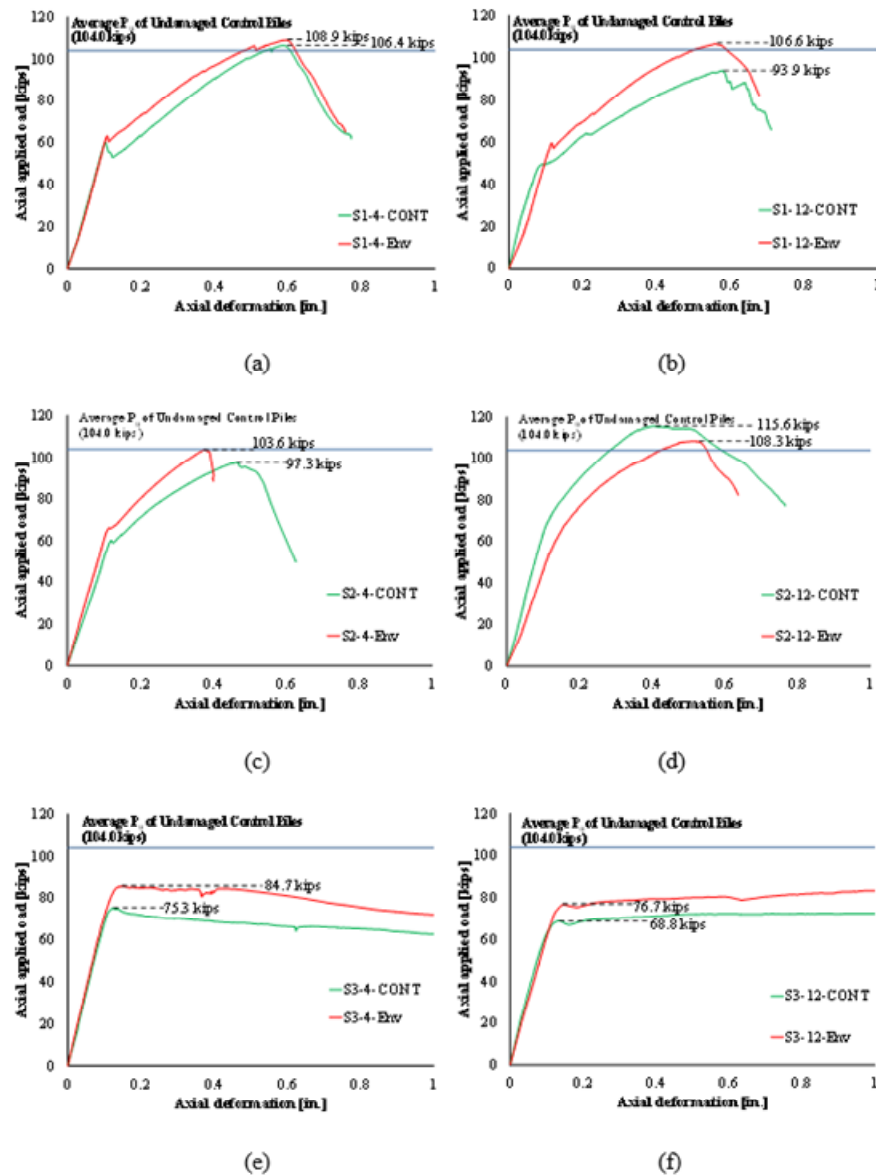


Figure 10.40: Comparisons of the performance of the repaired piles with/without being exposed to the environmental cycles

For the piles repaired with Repair Systems 1 and 2, corrosion was not detected. Figures 10.42 and 10.43 show the repaired piles subjected to the accelerated corrosion process in which no evidence of severe corrosion was observed. Figures 10.44 through 10.49 show the piles repaired with Repair System 3 subjected to the accelerated corrosion process. As shown in the figures, the bolts that were located near the water level during the accelerated corrosion process experienced a significant amount of corrosion as well as the exposed web of the piles.



Figure 10.41: Undamaged pile (CONT-Cor) showing the rust build-up



Figure 10.42: A damaged pile repaired with Repair System 1 (S1-4-Cor) showing no evidence of corrosion



Figure 10.43: A damaged pile repaired with Repair System 2 (S2-12-Cor) showing no evidence of corrosion

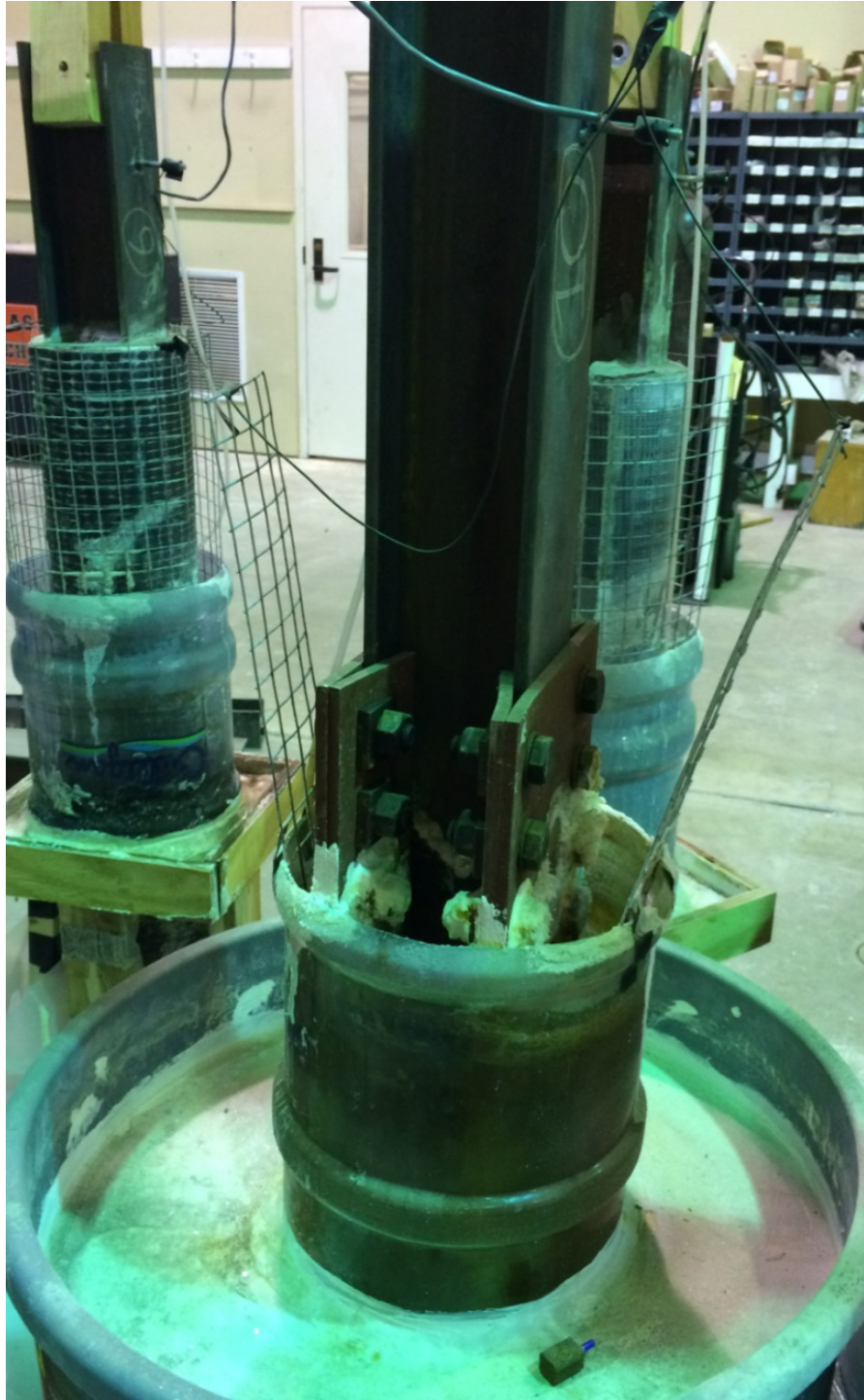


Figure 10.44: Accelerated corrosion test set-up for the piles repaired with System 3 (S3-4-Cor)



Figure 10.45: Bolt and web corrosion of Repair System 3 (S3-4-Cor)



Figure 10.46: Web corrosion of Repair System 3 (S3-4-Cor)



Figure 10.47: Accelerated corrosion test set up for Repair System 3 (S3-12-Cor)

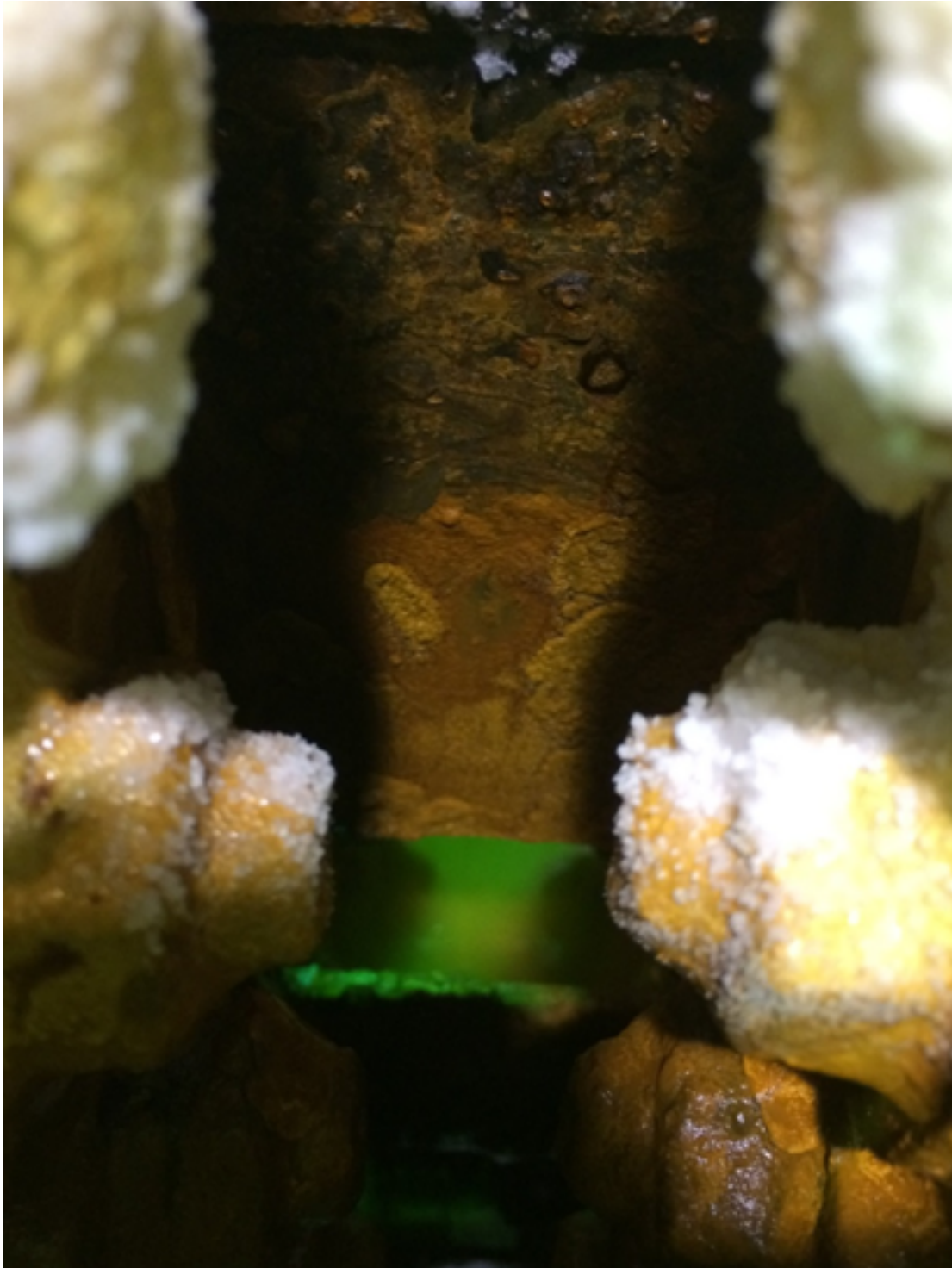


Figure 10.48: Web and bolt corrosion for Repair System 3 (S3-12-Cor)



Figure 10.49: Web and bolt corrosion of Repair System 3 (S3-12-Cor)

10.8. Concluding Remark

According to the experimental work presented in this chapter, it was found that the environmental cycles did not have adverse effects on the axial load capacity of the piles that were repaired with the proposed repair systems. It was also found that the FRP jackets used in Repair Systems 1 and 2 were effective in preventing further corrosion after the repair was implemented. However, a significant amount of corrosion on the web and bolts were observed on the piles repaired with Repair System 3.

Chapter 11. Life-Cycle Cost Analysis

This Chapter presents an evaluation of the anticipated life-cycle costs of the proposed pile repair systems and compares them to the costs of conventional repair methods which require dewatering. To achieve the objective of this task, it is necessary to evaluate currently available Life-Cycle Cost Analysis (LCCA) computer programs and investigate their feasibility and suitability with the application to bridge maintenance projects, since these software packages may not be explicitly developed to address the life-cycle costs of bridge pile repairs. Three existing federal-level LCCA computer programs have been selected and evaluated: BLCCA, BridgeLCC and RealCost. Various factors were considered in the evaluation of LCCA computer programs including implementation on a personal computer environment, integrated LCCA models that consist of direct and indirect cost models, inputting requirements, types of cost and analysis, limitations and strengths, and the suitability and adaptability to bridge pile repair projects. After a comprehensive evaluation of these programs, RealCost is recommended as the most suitable one for bridge pile repair projects.

11.1. Introduction

The Life-Cycle Cost Analysis (LCCA) is a cost-centered engineering economic analysis used to compare alternative courses of action over a specified time period (Kirk and Dell'Isola 1995). Life-cycle costs are the summations of cost estimates from inception to disposal for both equipment and projects as determined by an analytical study and the estimate of total costs experienced in annual time increments during the project life with consideration of the time value of money. The objective of LCCA is to choose the most cost effective approach from a series of alternatives to achieve the lowest long-term cost of ownership. Life-cycle

cost involves an economic model over the project life span. The best balance among cost elements is achieved when the total life-cycle cost is minimized (Landers 1996). Like most engineering tools, LCCA provides best results when both engineering and science are merged with good judgment to build a sound business case for action (Barringer 2003).

In designing civil engineering systems, the system performance must be considered as time-dependent. Therefore, a consistent design approach should comply with the desired performance not only at the initial stage when the system is supposed to be in the intact state, but also during its expected life-cycle (Biondini and Frangopol, 2008). So LCCA covers all major aspects of civil engineering and related topics. They may include: (1) life-cycle damage processes, (2) life-cycle assessment and design, (3) life-cycle monitoring, maintenance and rehabilitation, (4) life-cycle performance of special structures, and (5) life-cycle cost of structures and infrastructures.

Over the past two decades, LCCA has received increasing attention as a tool to assist Departments of Transportation (DOTs) in making investment decisions as well as in managing assets, mainly because the federal government recognized the importance of the economic analysis of whole life investment for civil infrastructures, and thus now legally requires applying LCCA to specified projects. For example, The National Highway System Designation Act of 1995 requires that states conduct an LCCA for each proposed National Highway System (NHS) project segment costing \$25 million or more. Federal Executive Order 12893 (Principles 1994), signed by President Clinton in January 1994, requires that all federal agencies use "systematic analysis of expected benefits and costs...appropriately discounted over the full life cycle of each project" in making major infrastructure investment decisions.

For transportation agencies, bridges compose a significant class of assets for which these agencies are responsible and are also usually regarded as a long-term, multi-year investment. The life-cycle costs of a bridges include all the costs associated with the various activities of planning, design, construction, operation, and maintenance during a whole service life. So the cost to an agency for managing a bridge is not a one-time expenditure. After finishing the stages of planning, design, and construction, a bridge still requires periodic routine maintenance and major repair or rehabilitation to maintain satisfactory structural conditions and public safety. From the life-cycle cost analysis, a more efficient alternative can be determined by transportation agencies based on a long-term strategy, which means that the alternative requiring higher initial cost expenditure may be more economical if it can reduce the anticipated frequency of future maintenance.

Therefore, the LCCA approach has been widely used for evaluating bridge projects. For example, Purvis et al. (1994) performed life-cycle cost analysis of bridge deck protection and rehabilitation. Mohammadi et al. (1995) introduced the concept of incorporating life-cycle costs into highway bridge planning and design. Hawk (2003) developed a bridge life-cycle cost analysis software tool for bridge project evaluation. The National Institute of Standards and Technology developed another bridge life-cycle cost analysis software in 2003 and the Federal Highway Administration (FHWA) produced the RealCost software in 2004. Berg et al. (2005) implemented life-cycle analysis to an FRP reinforced concrete bridge deck.

Before implementing a LCCA, several important components should be identified and defined clearly to produce meaningful and realistic results, such as agency costs and user costs:

(1) Agency cost includes all costs incurred by an agency responsible for bridge management and construction costs become the major input over the life of a project. These costs typically include initial construction expenditures such as cost of materials, labor, and equipment, preliminary engineering, contract administration, construction traffic control, construction supervision, and all future maintenance, routine and preventive, resurfacing, and rehabilitation (Demos, 2006).

(2) User cost is the cost incurred by highway users over a project analysis period, but is considered an important factor in performing the LCCA of pavement or bridge design alternatives. User cost components can be categorized as two:

Traveler time delay costs (Costs incurred while driving at slower speeds through work zones);

Vehicle Operating Costs (VOCs) (Increased operation costs, e.g. greater fuel consumption, caused by increased travel time);

Also, additional cost items, so-called external costs, such as vehicle emission, traffic accidents, and impact to local businesses can be considered. These costs are mostly intangible in nature and often very hard to measure in monetary units. Thus, they are not included in calculating a life-cycle cost in many cases (Wilde et al., 1999; Demos, 2006).

11.2. Evaluation Criteria

Three existing federal-level LCCA programs have been selected and compared: BLCCA, BridgeLCC, and RealCost, based on the following criteria:

- **Relevancy:** BLCCA and BridgeLCC were specifically developed by NCHRP and NIST as the LCCA programs for bridge projects: design, construction and maintenance. RealCost was originally developed by FHWA to perform the LCCA for pavement and bridge projects.
- **Reliability:** BLCCA, BridgeLCC and RealCost were developed by the federal-level agencies and widely accepted and implemented throughout the U.S. The LCCA results from them are reliable.
- **Accessibility:** BLCCA, BridgeLCC and RealCost can be easily downloaded from the websites of sponsor agencies.
- **Economy:** BLCCA, BridgeLCC and RealCost can be obtained from the sponsor federal agencies without any additional cost.
- **Versatility:** BLCCA, BridgeLCC and RealCost incorporate the general LCCA economic principles and have the specific capacity to evaluate agency costs and user costs with regard to bridge projects. And some of them can be tailored to meet the requirements of local agencies.

11.3. Introduction of Selected LCCA Programs

11.3.1. BLCCA

The Bridge Life-Cycle Cost Analysis (BLCCA) software was written as part of NCHRP Project 12-43, a study to develop a comprehensive methodology for life-cycle cost analysis of bridges implemented as a software package for a personal computer in 2003 (Hawk, 2003). It was developed by National Engineering Technology (NET) Corporation in Arlington Heights, IL, which conducted research on current life-cycle analysis

practices, availability and quality of data to support bridge life-cycle cost estimation, and computer-based facility management tools usable within government transportation agencies.

11.3.2. BridgeLCC

BridgeLCC is user-friendly life-cycle costing software developed by NIST to help bridge engineers assess the cost effectiveness of new, alternative construction materials (Ehlen 2003). The software uses a life-cycle costing methodology based on both ASTM standard E 917 and a cost classification developed at NIST. BridgeLCC is specifically tailored for comparing new and conventional bridge materials.

11.3.3. RealCost

RealCost was developed by FHWA to provide both an instructional tool for pavement design decision makers who want to learn about LCCA and an actual tool for pavement designers, which they can use to incorporate life-cycle costs into their pavement investment decisions (FHWA 2004). RealCost is based on a Microsoft Excel spreadsheet and has a detailed work-zone user costs computation. RealCost was developed for the pavement design originally, but it could be used for many other civil engineering fields, like bridge projects. It is considered the most versatile package compared to the other existing LCCA packages.

11.3.3.1. Background, Operation and Requirements of the Programs

This section describes the background of three programs and the life-cycle cost methodology, equations and models integrated into them, and provides general

analysis steps and operation procedures for each program, including starting the program, creating an analysis, inputting project parameters and alternatives' costs, running the analysis and simulation, and producing and visualizing the results.

11.3.4. BridgeLCC

11.3.4.1. Background

In 2003, in order to facilitate the use of cost-effective materials, designs, and processes for buildings, bridges, and other structures in built environments, the National Institute of Standards and Technology (NIST) developed BridgeLCC and provided it to the industry. Bridge LLC can be used to determine the cost effectiveness of building-related alternatives.

BridgeLCC is user-friendly, Windows® software specifically designed to help engineers, material specialists, and budget analysts determine the life-cycle cost effectiveness of their bridge designs and processes. The user defines a project, such as building a new bridge, or defines the alternatives, such as constructing the bridge with steel versus constructing the bridge with concrete, and then compiles the costs of building, maintaining, and then disposing of each of these alternatives. Cost components include project costs incurred by the agency responsible for the structure (agency costs), costs incurred by drivers on the highway that are inconvenienced by bridge construction and other bridge activity (user costs), and costs incurred by third parties who are not direct users of the structure but are impacted by construction and repair activity (third-party costs).

Once the cost components are compiled, the user compares the life-cycle costs of the alternative bridges or processes. The alternative with the lowest life-cycle cost, all other factors being equal, is the most cost effective alternative. The user utilizes the cost classification in BridgeLCC to compare the technical advantages and disadvantages of each alternative in life-cycle cost terms.

BridgeLCC uses a life-cycle costing methodology based on the ASTM practice for measuring the life-cycle costs of buildings and building systems (ASTM E917) and a NIST cost classification scheme for comparing life-cycle costs of alternatives. The ASTM practice ensures that the cost calculations follow accepted practice. The scheme helps the user account for all project costs, properly categorize them, and then compare breakdowns of the alternatives' life-cycle costs.

11.3.4.2. Life-Cycle Costing Formulas

Eq. 11-1 shows the formula used in BridgeLCC to convert future costs to present value and sum them into a single life-cycle cost number.

$$PVLCC = \sum_{t=0}^T \frac{C_t}{(1+d)^t} \quad (\text{Eq. 11-1})$$

Where:

$PVLCC$ = Present Value of Life-Cycle Costs

C_t = the sum of all costs incurred at time t , valued in base-year dollars

d = the real discount rate for converting time t costs to time 0

T = the number of time periods in the study period

Eq. 11-2 can be used to compute the cost to drivers of roadwork-related traffic delays.

$$\text{Driver Delay Costs} = \left(\frac{L}{S_a} - \frac{L}{S_n} \right) \times ADT \times N \times w \quad (\text{Eq. 11-2})$$

Where:

L is the length of affected roadway or which cars drive

S_a is the traffic speed during bridge work activity

S_n is the normal traffic speed

ADT is the average daily traffic, measured in number of cars per day

N is the number of days of road work

w is the dollar value of each hour of a driver's time

Eq. 11-3 can be used to compute Vehicle operating costs:

$$\text{Vehicle Operating Costs} = \left(\frac{L}{S_a} - \frac{L}{S_n} \right) \times ADT \times N \times r \quad (\text{Eq. 11-3})$$

Where:

r is a weighted-average vehicle cost

Eq. 11-4 can be used to compute Accident costs:

$$\text{Accident Costs} = L \times ADT \times N \times (A_a - A_n) \times C_a \quad (\text{Eq. 11-4})$$

Where:

C_a is the cost per accident, A_a and A_n are the during-construction and normal accident rates per vehicle-kilometer;

11.3.4.3. General Analysis Steps of BridgeLCC

- (1) Define the project objective and minimum performance requirements. The performance requirements of a project should be expressed in terms that do not preclude the use of a new technology material.
- (2) Identify the alternatives for achieving the objective. Each alternative must satisfy the minimum performance requirements of the project.
- (3) Establish the basic assumptions for the analysis. These assumptions include specification of the base year for the analysis, the life-cycle study period, and the real discount rate.
- (4) Identify, estimate, and determine the timing of all relevant costs. Relevant costs are those costs that will be different among alternatives. Use the classification to be sure all costs are screened for inclusion. Be sure to consider all costs to direct users of the project, and any spillover costs associated with the project.
- (5) Compute the life-cycle cost of each alternative using the common data assumptions identified in step 3.

(6) Perform sensitivity analysis by re-computing the life-cycle cost for each alternative using different assumptions about data inputs that are both relatively uncertain and significant in their impact on life-cycle cost. Sensitivity analysis shows how sensitive the technology's costs are to uncertain data used in the economic analysis.

(7) Compare the alternatives' life-cycle costs for each set of assumptions.

(8) Consider other project effects — quantifiable and non-quantifiable — that are not included in the life-cycle cost calculations. If other effects are not equal and are considered significant, then turn to techniques such as multi-attribute decision analysis to account for all types of benefits and costs.

(9) Select the best alternative. Where other things are equal (e.g., performance and non-quantifiable impacts) select the economically efficient alternative with the minimum lifecycle cost, i.e., the greatest net savings compared to the base-case alternative.

11.3.5. RealCost

11.3.5.1. Background

In 2003, the Federal Highway Administration (FHWA) initialized the development and kept continuously improving of RealCost in the following years to support the application of life-cycle cost analysis (LCCA) in the pavement project-level decision-making process. RealCost was created with two distinct purposes. The first is to provide an instructional tool for pavement design decision-makers who want to learn

about LCCA. The software allows the student of LCCA to investigate the effects of cost, service life, and economic inputs on life-cycle cost. For this purpose, a graphical user interface (GUI) was designed to make the software easy to use. The second purpose is to provide an actual tool for pavement designers, which they can use to incorporate life-cycle costs into their pavement investment decisions.

RealCost automates FHWA's LCCA methodology as it applies to pavements. The software calculates life-cycle values for both agency and user costs associated with construction and rehabilitation. The software can perform both deterministic and probabilistic modeling of pavement LCCA problems. Outputs are provided in tabular and graphic format. Additionally, RealCost supports deterministic sensitivity analyses and probabilistic risk analyses.

While RealCost compares two alternatives at a time, it has been designed to give the pavement engineer the ability to compare an unlimited number of alternatives. By saving the input files of all alternatives being considered, the analyst can compare any number of alternatives. Furthermore, the software has been designed so that a basic understanding of the LCCA process is sufficient to operate the software.

The software automates FHWA's work zone user cost calculation method. This method for calculating user costs compares traffic demand to roadway capacity on an hour-by-hour basis, revealing the resulting traffic conditions. The method is computation intensive and ideally suited to a spreadsheet application.

The software does not calculate agency costs or service lives for individual construction or rehabilitation activities. These values must be input by the analyst and should reflect the construction and rehabilitation practices of the agency.

While RealCost compares the agency and user life-cycle costs of alternatives, its analysis outputs alone do not identify which alternative is the best choice for implementing a project. The lowest life-cycle cost option may not be implemented when other considerations such as risk, available budgets, and political and environmental concerns are taken into account. As with any economic tool, LCCA provides critical information to the overall decision-making process, but not the answer itself.

11.3.5.2. Life-cycle cost analysis (LCCA) steps and forms

Table 11.1: FHWA LCCA Steps and corresponding RealCost Forms

FHWA LCCA Steps	Realcost Data Entry and Output Forms
1. Establish Design Alternatives	Project Details Analysis Options Traffic Data Traffic Hourly Distribution Value of User Time Added Vehicle Time and Cost
2. Determine Activity Timing	Alternative 1 and Alternative 2
3. Estimate Agency and User Cost	Alternative 1 and Alternative 2
4. Compute Life-Cycle Costs	Deterministic Results Simulation
5. Analyze the Results	Deterministic Results Probabilistic Results

11.3.6. Bridge Life-cycle Cost Analysis (BLCCA)

11.3.6.1. Background

The Bridge Life-cycle Cost Analysis (BLCCA) software was written as part of NCHRP Project 12-43, a study to develop a comprehensive methodology for life-cycle cost analysis of bridges implemented as a software package for a personal computer in 2003. The BLCCA system is designed for application to individual bridges. National Engineering Technology (NET) conducted research on current life-cycle analysis practices, availability and quality of data to support bridge life-cycle cost estimation, and computer-based facilities management tools usable within government transportation agencies. The results of this work are presented in a final report (NCHRP 483).

11.3.6.2. The General Analysis Steps

- (1) Characterize bridge and its elements: the Bridge to be analyzed is described in terms of the characteristics relevant to its life-cycle cost. National Bridge Inventory (NBI) and other inventory data, traffic information, inspection reports, and design information typically will be assembled.
- (2) Define planning horizon, analysis scenarios, and base case: The framework of the BLCCA next is laid out. Generally the planning horizon should be at least as long as the best-estimate service life of the element (under normal maintenance) that is the primary focus of analysis. The principal analysis scenario includes a description of what level of activity (and, at least implicitly, the annual cost) that will be defined as “normal maintenance”, the condition levels that will be

considered unacceptable or that will otherwise trigger maintenance or repair actions, hazard conditions that will influence vulnerability costs, forecast traffic and vehicle-load and climatic parameters that influence element deterioration, discount rate and aspects of agency policy that will influence action-timing or cost. The base case is then described. Typically, the base case includes simply normal maintenance and vulnerability costs. If the analyst chooses to compute costs of all alternatives relative to the base case, the base-case total life-cycle cost is, by definition, zero.

- (3) Define alternative bridge-management strategies: A management strategy will be described by the set of actions an agency plans to take to ensure the bridge remains in acceptable condition throughout the analysis period.
- (4) Specify/select appropriate deterioration models and parameters: The bridge elements and alternative management strategies will determine the deterioration models to be used in the BLCCA.
- (5) Estimate costs: Estimate agency and user costs based on how deterioration is modeled as well as on the details of the actions themselves and the analysis scenario.
- (6) Calculate net present values: The estimated costs of all actions are discounted to compute their equivalent present values.
- (7) Review results and modify management strategies.
- (8) Select preferred strategy: The primary purpose of the BLCCA is to identify a management strategy with least Total Life-Cycle Costs (TLCC). However, because of the uncertainty of estimating TLCC, there are several ways that the

several indicators identify a “best” alternative, e.g., least total present value of all costs, least agency cost, and others.

11.4. Analysis and Comparison of Three Programs

The emphasis will be placed on the comparison of suitability and adaptability of three programs, BridgeLCC, RealCost and BLCCA, to bridge repair projects. The first part will identify the requirements of input variables of each program and then examine the functions of each program, including the types of analysis and costs calculated. The third part will make the comparison of advantages and disadvantages of each program and recommend which program to be selected. Then the final part will study the previous related research work done by other DOTs.

11.4.1. Comparison of Inputs

The LCCA process requires two levels of information: 1) data pertaining to the proposed project and 2) data defining the project design alternatives that are being compared for accomplishing the project. The first class parameters are the project-level data, which are applied to all alternatives being considered for the project at hand. FHWA's best practice LCCA methodology requires that the analysis period, discount rate, normal operations traffic data, and normal operations roadway geometry are same for all alternatives. The second class parameters are alternative-level data, which define the differences between project alternatives, e.g. agency costs and work zone specifics for each alternative's component activities. Since alternative designs intend to similarly fulfill the performance requirements of a project, LCCA requires that each alternative carry the same amount of traffic during normal operations throughout the life of the project. In this way, the

benefits to road users provided by all alternatives are the same. The exception to this rule is during periods of work zone operations, when traffic flow may be restricted in some fashion (FHWA, 2004).

The following tables show the input variables required by three programs to perform a life-cycle cost analysis. Table 11.2 lists project-level inputs that are variables used to all alternatives in common. Table 11.3 lists alternative-level inputs that are variables each alternative has different values.

Table 11.2: The Comparison of Project-Level Inputs for Each Program

Project-Level Inputs			
	BLCCA	RealCost	BridgeLCC
Bridge Inventory Data (NBI)	Applicable <i>Note: NBI Data file contains bridge information tracked by State DOTs for the FHWA and needs to be uploaded by users.</i>	N/A	N/A
Project Details			
Project Name	Applicable	Applicable	Applicable
Project Description	Applicable	Applicable	Applicable
Project Location	Applicable	Applicable	Applicable
Analysis Options			
Analysis Units	English Units Only	English/Metric Units	English Units Only
Analysis Periods	Applicable	Applicable	Applicable
Discount Rate	Applicable	Applicable	Applicable
Beginning of Analysis Period	Applicable	Applicable	Applicable
Number of Alternatives	Unlimited	Up to 6 alternatives in an analysis	Up to 6 alternatives in an analysis

(Cont'd)

Include Agency Cost Remaining Value Option	N/A	Applicable <i>Note: The user can specify whether the remaining service life value will include a prorated share of agency costs if the service life of an improvement extends beyond the analysis period.</i>	N/A
Include User Costs In Analysis Option	N/A	Applicable <i>Note: The user can specify whether user costs will be included in the analysis and displayed in the results</i>	N/A
Traffic Direction Option	N/A	Applicable <i>Note: The user can direct RealCost to calculate user costs for the “inbound” lanes, the “outbound” lanes, or “both” inbound and outbound lanes.</i>	N/A

(Cont'd)

Traffic Profile			
AADT at Beginning of Analysis Period (total both directions)	Applicable	Applicable	Applicable
Single Unit Trucks as Percentage of AADT(%)	N/A	Applicable	N/A
Combination Trucks as Percentage of AADT(%)	N/A	Applicable	N/A
Annual Growth Rate of Traffic(%)	Applicable	Applicable	Applicable
Maximum ADT	N/A	Applicable	Applicable
Traffic Flow			
Normal Speed Limit	N/A	Applicable	Applicable
Lanes Open in Each Direction Under Normal Conditions	N/A	Applicable	N/A
Free Flow Capacity	N/A	Applicable <i>Note: The user can use the built-in "Free Flow Capacity Calculator" to calculate the free flow capacity.</i>	N/A

(Cont'd)

Queue Dissipation Capacity	N/A	Applicable <i>Note: The user can specify the capacity of each lane during queue dissipation operating conditions.</i>	N/A
Maximum Queue Length	N/A	Applicable <i>Note: The user can model the effects of self-imposed detours (traffic exiting from the work zone route yet still incurring some user costs.</i>	N/A
Traffic Hourly Distribution	N/A	Applicable	N/A
Added Time and Vehicle Stopping Costs	N/A	Applicable	N/A
Value of User Time			
Value of Time for Passenger Cars	N/A	Applicable	Applicable <i>Note: The user can only input the single category cost for the driver delay.</i>
Value of Time for Single Unit Trucks	N/A	Applicable	
Value of Time for Combination Trucks	N/A	Applicable	

Table 11.3: The Comparison of Alternative-Level Inputs for Each Program

Alternative-Level Inputs			
	BLCCA	RealCost	BridgeLCC
Alternative Details			
Alternative Name	Applicable	Applicable	Applicable
Alternative Description	Applicable	Applicable	Applicable
Number of Activities(Events)	Unlimited	Up to 24 Activities(Events)	Unlimited
Activity(or Events) Cost and Service Life Inputs			
Agency Construction Cost	Applicable	Applicable	Applicable
Activity Service Life	Applicable	Applicable	Applicable
Activity Structural Life	N/A	Applicable	Applicable
Maintenance Frequency	Applicable	Applicable	Applicable
Agency Maintenance Cost	Applicable	Applicable	Applicable
User Work Zone Costs	Applicable <i>Note: The user only can define the user costs based on his own calculation.</i>	Applicable <i>Note: The user can either specify the user costs based on his own calculation or use the user costs calculated by RealCost.</i>	N/A <i>Note: The user can not specify the user costs based on his own calculation.</i>

(Cont'd)

Activity Work Zone Inputs			
Work Zone Length	N/A	Applicable	Applicable
Work Zone Duration	N/A	Applicable	N/A
Work Zone Capacity	N/A	Applicable	N/A
Work Zone Speed Limit	N/A	Applicable	Applicable
Number of Lanes Open in Each Direction During Work Zone	N/A	Applicable	N/A
Work Zone Hours	N/A	Applicable	N/A
Crash Costs	N/A	Applicable	Applicable
Traffic Hourly Distribution Selection	N/A	Applicable <i>Note: The user can specify the type of Traffic Hourly Distribution (Rural or Urban; Weekday or Weekend) which are defined in the project-level inputs.</i>	N/A

11.4.2. Comparison of Outputs

The following tables make a comparison of three program main functions and outputs. Table 11.4 lists the outputs which can be calculated by the programs, i.e., agency costs, user costs, life-cycle costs, etc. Those costs can be shown either in a text report or in summary graphs. Most types of cost are common to three programs to calculate, while some type of costs are unique to some program, i.e., BLCCA can calculate vulnerability costs to natural disasters and BridgeLCC can calculate the third part costs. Table 11.5 shows the types of analysis which can be performed by the programs, i.e., life-cycle cost analysis that can be deterministic or probabilistic, or sensitivity analysis that can indicate the influence of each variable on the life-cycle costs and cost competitiveness of the alternative. Those results can also be shown either in a text report or graphically.

Table 11.4: The Comparison of Outputs for Each Program

Outputs	BLCCA	RealCost	BridgeLCC
Agency Costs	<p>Applicable</p> <p><i>Note: Calculates inspection and maintenance costs based on user-specified generic model.</i></p>	<p>Applicable</p> <p><i>Note: Agency costs are calculated based on activity inputting data.</i></p>	<p>Applicable</p> <p><i>Note: Agency costs are calculated by following the convention of most engineer's estimates and can be divided into three categories: Construction costs, OM&R costs and Disposal costs.</i></p>
User Costs	<p>Applicable</p> <p><i>Note: The program only shows user costs in total.</i></p>	<p>Applicable</p> <p><i>Note: The user cost can be calculated and show by components: WZ Speed Change VOC and Delay, WZ Reduced Speed Delay, Queue Stopping Delay and VOC, Queue Added Travel Time, Queue Idle Time.</i></p>	<p>Applicable</p> <p><i>Note: The program only shows user costs in total.</i></p>

(Cont'd)

Vulnerability Costs	Applicable <i>Note: Calculates agency and user cost components related to:</i> - Earthquakes - Scour - Structural damage due to fatigue - Structural damage due to overloads - Collision damage - Flooding	N/A	N/A
Third Party Costs	N/A	N/A	Applicable <i>Note: These costs could include revenues lost by adjacent businesses due to bridge construction, repair, and disposal, or environmental damage such as pollution of the stream under the bridge.</i>

(Cont'd)

Life-Cycle Costs	Applicable <i>Note: System calculates constant and discounted costs associated with a defined scenario and alternative.</i>	Applicable <i>Note: The life Cycle Costs can be deterministic and probabilistic results.</i>	Applicable <i>Note: The life Cycle Costs can be compared by bearer, timing and component. These costs can be viewed by 'Total' or 'Per Unit' and the net saving values can also be available to users.</i>
Graphic Reports	Applicable	Applicable	Applicable
Text Reports	Applicable	Applicable	Applicable

Table 11.5: The Comparison of the Analysis Performed by Each Program

Type of Analysis	BLCCA	RealCost	BridgeLCC
Life-cycle cost analysis	Applicable <i>Note: Calculates life cycle cost for different bridge management alternatives for an individual bridge.</i>	Applicable <i>Note: Calculates life cycle cost for different activities for an individual bridge project. The life-cycle cost analysis can be performed in deterministic and probabilistic mode.</i>	Applicable <i>Note: Calculates life cycle cost for different bridge management alternatives for an individual bridge project. The life-cycle cost analysis can be performed in basic mode (deterministic mode) and advanced mode (probabilistic mode).</i>

(Cont'd)

Probabilistic Analysis	Applicable <i>Note: Incorporates models to account for uncertainty in the magnitude and timing of costs.</i>	Applicable <i>Note: To conduct probabilistic analysis, RealCost uses Monte Carlo simulation, which allows modeling of uncertain quantities in the model with probabilistic inputs. The simulation procedure randomly samples these inputs and produces outputs that are described by both a range of potential values and a likelihood of occurrence of specific outputs.</i>	Applicable <i>Note: Incorporates advance models to account for uncertainty in the magnitude and timing of events. The Monte Carlo simulations are used.</i>
Sensitivity Analysis	Applicable	Applicable <i>Note: While the correlation coefficient graphics describe the sensitivity of outputs to individual inputs, the total cost probability distribution graphics provided by RealCost describe the sensitivity of outputs to combinations of inputs.</i>	Applicable <i>Note: In lieu of conducting a comprehensive analysis of uncertainties in the Advanced Mode, the user can analyze the effect of individual parameters on life-cycle costs.</i>

11.4.3. Assessment of the Three Programs

Based on the above comparisons in terms of inputs and outputs of three programs, RealCost has the following strengths to make it superior than the other two programs:

1) For bridge repair projects, the initial construction costs are not a significant factor, while the user costs become the main concerns of agencies and have an impact on the decision process of DOTs to choose the appropriate repair strategies. RealCost incorporates a detailed user cost analysis component and has a strong capacity to calculate user costs as one of its unique features. RealCost provides the user with detailed breakdown of user costs for each alternative for initial construction and every rehabilitation/reconstruction during the life cycle. The user cost components calculated include Work Zone (WZ) Speed Change Vehicle Operation Cost (VOC), WZ Speed Change Delay, WZ Reduced Speed Delay, Queue Stopping Delay, Queue Stopping VOC, Queue Added Travel Time, Queue Idle Time. RealCost can calculate these mentioned components of user cost for each state for each alternative.

2) RealCost is developed based on Microsoft Excel and is the most versatile software in the three programs. It can be relatively easily customized and enhanced for the local DOT's requirements. It is found that Indiana, Quebec, Maryland and Louisiana are using RealCost to perform their life-cycle cost analysis (Salem and Genaidy, 2008). RealCost is also easily tailored to bridge repair projects when needed.

3) RealCost has the simplest user interface and operations among three programs. The data can be input by either graphic user interface or spread sheet entry.

4) As for two other programs, BLCCA has the compatibility issues with current Windows systems and the user must specify every event and its impacts in detail. The good results of BLCCA depend on agencies' ability to research appropriate model parameters and other inputs. Although BridgeLCC has a good estimate of initial construction costs by following the convention of most engineers' estimates and input in terms of quantity, unit of measure, and unit cost, it does not include a powerful tool to calculate user costs, especially compared with RealCost.

5) RealCost was introduced by FHWA as a new life-cycle cost analysis software to support the application of LCCA in the project-level decision-making process in 2003. It has been updated since then and the current version is RealCost 2.5 that was released in March 2011. On the other hand, the other software is either not being updated since the first issuance (BLCCA) or not being updated for a long period (BridgeLCC). FHWA also provides a workshop on RealCost to assist state agencies to learn LCCA principals and gain hands-on experience with the RealCost software.

Based on the above comparisons and assessments, RealCost will be the most suitable and adaptable program for bridge repair projects among three programs studied in this report.

11.4.3.1. Previous Research Works on RealCost

Among LCCA tools, with the comprehensiveness in its treatment of different input parameters, the most powerful capability in the analysis and calculation of user costs, and the most adaptive customization for the requirements of different state agencies, RealCost was found to be widely used by the state agencies and was proposed as preferred software for use in their LCCA decision-making process. However,

currently the LCCA methods are mainly implemented to the highway pavement projects by DOTs, such as the pavement type selection, the pavement design, and the pavement maintenance and repair strategies. The following list presents previous research works performed by other DOTs regarding computer applications and a life-cycle cost analysis.

- In 2004, for its pavement selection process, the Colorado Department of Transportation (CDOT) formed a task force to investigate which probabilistic LCCA software to use and RealCost was unanimously selected. RealCost can calculate a probabilistic output for LCCA on roadways. (Demos, 2006).
- In 2004, Indiana Department of Transportation (INDOT) also conducted a LCCA research for INDOT pavement design procedures. In that study, the old LCCA-based pavement design and preservation practice in Indiana was further enhanced by due consideration of user costs. Also, the existing FHWA LCCA software RealCost was further enhanced for increased versatility, flexibility, and more specific applicability to the needs of Indiana, particularly with regard to treatment cost estimation and development of alternative feasible preservation strategies (rehabilitation and maintenance types and timings) (Lamprey et al., 2004).
- In 2007, with a growing awareness in the transportation community that the user costs may outweigh the initial construction and agency costs over the life of transportation facilities, Ohio Department of Transportation (ODOT) has conducted the research to improve models for user cost analysis. In the report prepared for ODOT, Salem and Genaidy provided a comprehensive review of literature and tools used to calculate user costs and also conducted a questionnaire

survey on the role played by user costs in payment type selection processes of various state and regional agencies in U.S. and Canada. Based on the findings from literature review and questionnaire survey, Salem and Genaidy recommended for including user delay costs quantitatively in ODOT's pavement type selection process. After review of the tools to calculate user costs, the report chose RealCost as the recommended tool for this study. Salem and Genaidy indicated that RealCost include a detailed and powerful user cost analysis component and the ability to conduct deterministic and probabilistic analysis life cycle costs. RealCost can calculate the user costs for each strategy for initial construction period and six rehabilitation/reconstruction cycles within the strategy. RealCost is also a Microsoft Excel based tool and hence it could be customized according to the user's needs. Those features make RealCost unique than other programs (Salem and Genaidy, 2008).

In 2008, the Michigan Department of Transportation (MDOT) also worked with University of Michigan and FHWA to evaluate its current LCCA Practices. MDOT has

- adopted LCCA in the pavement selection process since the mid-1980s, yet its application in actual projects has not been reviewed. This study analyzed MDOT's accuracy in projecting the actual costs over the pavement service life and choosing the lowest-cost pavement alternative and indicated that refinements to MDOT's pavement construction and maintenance cost estimating procedures would assist MDOT in realizing the full potential of LCCA in identifying the lowest cost pavement alternatives. The report also discussed RealCost as the

LCCA software and current level of application in the state agencies. (Chan et al., 2008).

- In 2008, the South Carolina Department of Transportation (SCDOT) also sponsored a LCCA research investigation to evaluate its pavement type selection process and propose a probabilistic LCCA approach for use. In addition to developing a protocol for a probabilistic LCCA approach, different LCCA software such as RealCost, DARWin and other customized software used by specific states were explored. Amongst these, RealCost software was found to be widely used by several state agencies and most comprehensive in its treatment of different input parameters. Further, FHWA has been instrumental in providing support to customize the RealCost to meet individual state's needs. Based on these findings, RealCost was proposed as preferred software for use with conducting LCCA for the pavement-type selection of SCDOT. (Rangaraju et al., 2008).
- Other than the DOTs mentioned above, there are still several state agencies are incorporating LCCA practices into their design and decision- making process and using RealCost as the analysis LCCA software. For example, Washington State Department of Transportation (WSDOT) follows a standard LCCA protocol when selecting pavement type for new facilities. This protocol is based on the FHWA's Life Cycle Cost Analysis in Pavement Design (Walls and Smith, 1998) and uses RealCost for calculations. California Department of Transportation (Caltrans) has developed a manual (Caltrans, 2007) that describes LCCA procedures for use in

Caltrans. The manual is based on RealCost and provides standard input values for a wide range of potential projects.

Although the use of LCCA software is at the discretion of each state, accordingly, states may apply LCCA at various levels and often use state-developed methods and tools, more and more state agencies choose RealCost as their preferred software for their LCCA practices. This tendency is even strengthened by the FHWA's instrumental help with state agencies to customize RealCost for their local requirements.

11.4.3.2. Example Case for Performance Evaluation

An example case is presented to make a performance evaluation for three programs. This example case was originally included in the user manual of BridgeLCC and then was adopted by the user guide of BLCCA to provide a comparison of results and procedures used by two programs for calculating the life-cycle cost of a same project. The results of this case by RealCost will be also provided herein and compared with those from BLCCA and BridgeLCC.

In this case, "...an engineer is making a preliminary design of a highway bridge and is considering two alternative types of concrete. The base case concrete is the conventional mix currently used by the engineer. The alternative concrete mix is high-performance concrete that the engineer has not used before. But, it should produce stronger and more durable bridge members. The engineer wants to determine which material is more life-cycle cost effective for this situation." The engineer is considering two alternatives for this case, as shown in Table 11.6.

Table 11.6: Description of Two Alternatives

Case	Description
Base Case: Conventional Mix	7 Beams Deck Repairs at years 25&50 Year 75 Demolition
Alternative Case: High-Performance Concrete Mix	5 Beams Deck Repairs at year 49 Year 75 Demolition

The base alternative, Conventional Concrete, involves four activities and each activity lasts one year (or less), while only three activities happen in the second alternative (High-Performance Concrete). The activities and their corresponding cost are shown in Table 11.7. After inputting all of the LCCA parameters and creating the alternatives by following appropriate procedures of each program, the results from all three programs are shown in

Table 11.8. Unlike the other two programs only providing the user cost in a total number, RealCost has the ability to present the user cost in a detailed breakdown components (see Table 11.9).

Table 11.7: Activities and Cost

Base Case: Conventional Concrete		
Activity	Description	Cost
Activity 1	Initial Construction	\$678,478
Activity 2	Deck Repair 1@YR 25	\$52,800
Activity 3	Deck Repair 2@YR 50	\$52,800
Activity 4	Demolition @YR 75	\$80,000
Alternative Case: High-Performance Concrete		
Activity 1	Initial Construction	\$652,478
Activity 2	Deck Repair @ YR 40	\$52,800
Activity 3	Demolition @YR 75	\$80,000

Table 11.8: LCCA Results in Present Value from Three Programs

(Present Value:\$)	Base Case	Alternative Case
	Agency Cost	Agency Cost
BLCCA	\$689,390	\$647,277
BridgeLCC	\$715,496	\$671,761
RealCost	\$709,248	\$666,188
	User Cost	User Cost
BLCCA	\$8,547	\$3,771
BridgeLCC	\$8,874	\$3,914
RealCost	\$8,468	\$3,598
	Total Cost	Total Cost
BLCCA	\$697,937	\$651,048
BridgeLCC	\$724,370	\$675,675
RealCost	\$717,716	\$669,786

Table 11.9: Detailed User Cost Component Results from RealCost (Base Case)

Cost Components	Cost	Percent
WZ Speed Change VOC	\$19.05	0%
WZ Speed Change Delay	\$6.36	0%
WZ Reduced Speed Delay	\$330.25	4%
Queue Stopping Delay	\$152.42	2%
Queue Stopping VOC	\$1,016.16	12%
Queue Added Travel Time	\$5,504.2	65%
Queue Idle Time	\$1,439.56	17%
Total Cost	\$8,468	100%

11.5. Summary of Evaluation

Life-Cycle Cost Analysis accounts for the effects on users by the agency's construction and maintenance activities, as well as the direct cost to the agency. Hence, LCCA provides a powerful economic tool for the agency in determining the lowest life-cycle cost way to accomplish the project from several alternatives.

Three federal-level LCCA computer programs (BLCCA, BridgeLCC and RealCost) have been selected in accordance with a set of criteria: (1) relevancy, (2) reliability, (3) accessibility, (4) economy and (5) versatility. A comprehensive evaluation and comparison was performed, with the emphasis on their adaptability and suitability to bridge pile repair projects. Based on the preceding evaluation of their integrated LCCA methodology, life-cycle cost types, and strengths and limitations of each program, RealCost was determined as the most suitable one to perform a LCCA for bridge pile repair projects, furnished with the following main features: (1) the powerful user cost computing capability, (2) the simple user

interface and operations, (3) the versatility to be tailored for local agencies' needs, and (4) the abundant supports, references and updates from FHWA.

Currently, RealCost has been widely accepted in the transportation field throughout the U.S. and Canada. It was found that state agencies of California, Indiana, Quebec, Maryland and Louisiana are using RealCost as a main tool to perform the LCCA of their major infrastructure projects. For state agencies, implementing RealCost to perform a LCCA for their bridge pile repair projects is at a minimal cost and without any need of developing a new LCCA program.

11.6. Implementation of LCCA for FRP-based and Steel-based Repair Systems for Corroded Steel H-Piles

To achieve this goal, a comprehensive survey was utilized to investigate various repair systems that are commercially available or currently in use in bridge pile repair projects in the first phase of the subtask. The survey questionnaires were distributed to five selected companies, including Quakewrap, Fyfe, Fox Industry, Five-Star and Pilecap. The first four companies are FRP-based repair systems and the last one is a conventional steel-based repair system. From the survey, the relevant information and cost data of these systems in two different water exposure conditions were collected as the basis for the LCCA in the next phase, such as service life, repair duration, material cost, labor cost, equipment cost, etc. In the second phase of the subtask, an LCCA was performed to identify alternative repair solutions requiring less life-cycle costs in a bridge pile repair project based on the survey cost data. Several major parameters such as discount rates, initial repair timing, and analysis periods, were examined in this study to test different scenarios and different combinations of variables. The LCCA results should be beneficial to TxDOT when they make decisions on

their bridge maintenance programs by reflecting uncertain factors. RealCost was also proved to be suitable for the cost analysis of bridge pile repair projects and even becomes more powerful in case a given situation involves the analysis of user costs.

11.6.1. Part I: Survey Questionnaire

11.6.1.1. Survey Methodology

The objective of the survey questionnaire was to investigate various repair systems that are commercially available or currently in use for repairing deteriorated steel bridge piles without the need of dewatering. The survey sought to ascertain the most commonly employed types of underwater repair techniques for steel structures, identify the most suitable underwater repair solutions for steel bridge piles, collect the relevant information and cost data of repair systems, and shed light on the LCCA of these repair systems in the follow-up research. Several resources were employed in this survey questionnaire to evaluate repair systems, including inputs from bridge engineers and project committee from TxDOT, direct communications with repair companies, and a review of existing technical literature.

Two types of repair techniques were determined as the most feasible underwater repair systems employed in the U.S.: Fiber Reinforced Polymer (FRP) bonded jacket system and bolted steel plate system. These two systems were mainly selected by considering various factors, e.g. sound underwater repair solutions, capacity of structural restoration, ease of installation, long-term durability, impact to natural environment, and traffic disruption. It should be noted that FRP jackets were primarily used to reduce corrosion rather than for structural purposes by DOTs in the

past projects. However, it is widely acknowledged that FRP jackets have the potential to restore the structural integrity of deteriorated bridge piles. In the end, five repair manufacturers were selected for further study, where four companies provide FRP-based repair techniques.

11.6.1.2. Survey Questionnaire Design

The survey questionnaire was designed to collect the relevant information and cost data of underwater repair systems for deteriorated steel bridge HP piles in different water exposure conditions. The reason to choose steel HP piles as the specimens in this survey is that steel HP piles are widely used in various states throughout the U.S. and many of these structures have been in service for 50 to 60 years. Extended exposure to the repeated cycles of wetting and drying commonly results in corrosion of these piles. While the corrosion is typically limited in some extent, it can create severe results like nearly total losses of cross section, which is in the urgent need to repair and restore the structural integrity of damaged piles. The HP 12x53 was designated as the specific type of HP pile in this survey since it is most commonly used in Texas. Various factors were considered to collect the relevant information and cost data in the survey questionnaire, including repair system information, repair duration, material cost, labor cost, equipment cost, service life of repair system, and traffic control plan.

Two case scenarios were created in this survey questionnaire to collect pile repair cost as specific as possible: shallow water condition case and deep water condition case. Typically, the corrosion introduced by the water exposure of HP steel piles is

localized within a zone a few feet above or below the water line. Field observations of the research team indicated that corrosion occurs in the form of severe reduction of the thickness of the flanges and web along the length of HP piles near the water line. As such, it is reasonable to design repair scenarios and the extent of corrosion according to the water depth and the location of water line. The first case was designed by assuming repairing deteriorated HP12x53 steel piles of a bridge with an at least 50% section loss in a shallow water condition. The second case was designed to have more serious extent of corrosion because of more exposure to the splashing zone in a deep water condition. The steel pile size, the typical extent of corrosion, and the water line location, the water depth of these two cases are shown in Figure 10.1. The 50% section loss is considered as the serious damage to the structural integrity of HP piles and requires major repair or even replacement of the piles. The surveyed companies were asked to develop a repair plan to restore the structural integrity of the piles, and make a cost estimate for repairing ten deteriorated steel piles in one bridge with their own repair techniques for both scenarios.

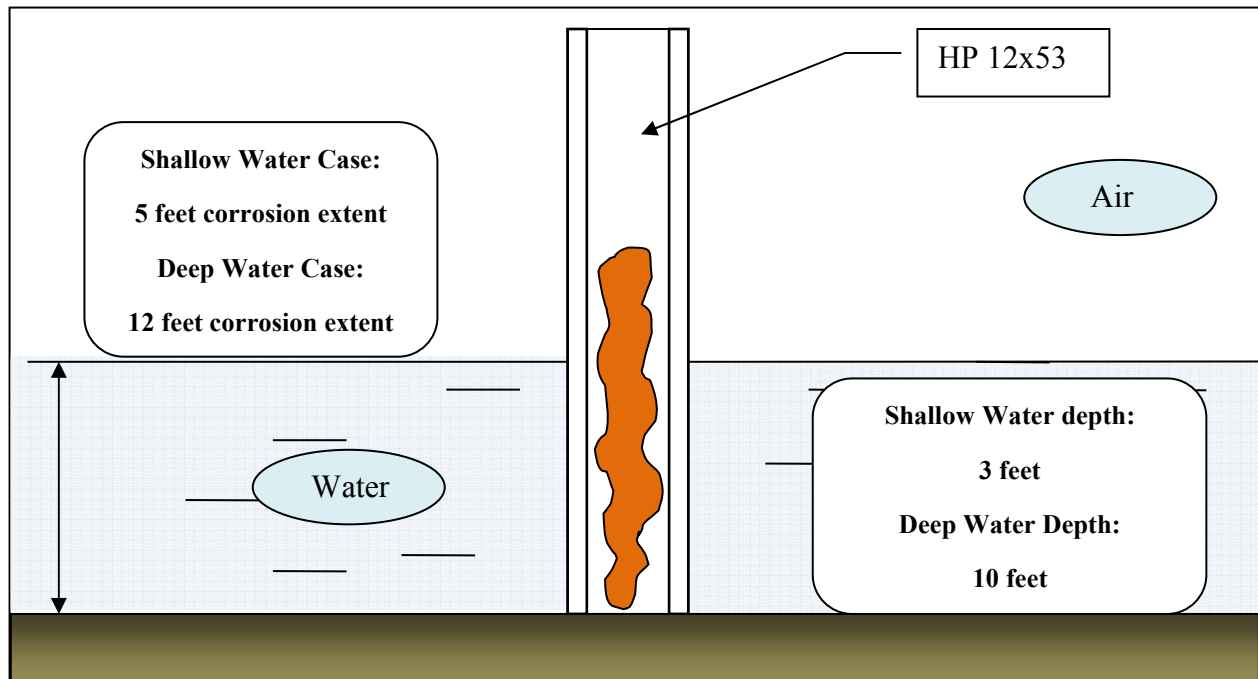


Figure 11.1: Corroded Steel Bridge Piles (Deep Water Case and Shallow Water Case)

The major part of the survey questionnaire is designed to collect relevant technical information and cost data of the repair systems proposed by repair companies. The survey consists of eight major categories that are described below in detail.

- *Information of repair products or systems:* This question investigates which repair product or system of each company is appropriate for two repair cases. The company needs to specify the model of their repair system.
- *The repair duration:* The repair duration starts from surface preparation of corroded steel piles, followed by installation of a new system, and ends up with painting or coating of the system. The repair companies were asked to estimate a construction period based on their previous project experiences or technical data and indicate it in hours. The repair duration is directly related with labor hours and labor cost.

- *Material cost:* The main material cost of FRP based system includes the cost of FPR jackets, epoxy, grouts and connectors. For the steel bolting system, the cost of steel plates, bolts, nuts and washers, and the coating was considered as the major material cost.
- *Labor cost:* The respondents were asked to estimate all related labor cost during the repair duration, including the number of labors in work crew, description of roles, hourly rates, total labor hours, and labor cost.
- *Equipment Cost:* Equipment requirements generally include minor equipment and heavy equipment. Minor equipment may include hand tools, small electric tools, or the like. And, heavy equipment may include boom truck, forklift, concrete pump, hydro blaster, or the like. In deep water case, a floating platform or boat may be needed to transport and install the repair system.
- *Service life:* In this part, repair companies were required to estimate the service life of their systems in underwater application in years. In case the service life is different for fresh water or sea water conditions, the companies need to specify it separately.
- *Traffic Control:* The repair companies were asked to explain a transportation control plan if a bridge needs to be closed during a repair period. The need of a traffic control plan greatly affects the user cost of bridge users.
- *Other cost items:* The repair companies may add some cost items that are specific to each repair system such as training fees or technical support fees.

11.6.1.3. Process of Survey Questionnaire

The questionnaire was initially targeted at company executives, i.e. presidents or vice presidents, of the repair companies. However, in case these people were not available for the survey or introduced other right people in a company, e.g. engineering-service directors or regional managers, new contacts were created to complete a survey questionnaire.

After securing survey contact points from five companies, survey distribution began on October 22, 2012 and the questionnaires were sent to the targets by e-mail. Considering the tight schedule of management executives or leading engineers, the questionnaire was designed as clearly as possible, while uncompromising the objective of the survey. Also, the amount of writing required to answer the questionnaire was kept as minimal as possible. In order to ensure responses in a timely manner, the questionnaire was designed to be taken within three to four hours. The collection period was set initially from October in 2012 to the end of February in 2013, but extended to the end of March in 2013 to ensure a 100% response rate.

11.6.1.4. Analysis of Survey Questionnaire Results

The information collected in this survey questionnaire is summarized in Table 11.10 for the case of shallow water and in Table 11.11 for the case of deep water. The survey questionnaire indicated that there is no need of traffic control plan for any proposed repair system during the repair. Although it may cause minor traffic control when delivering repair materials or transporting them between sites, this need was not considered in the life-cycle cost analysis. As per the requests of investigated

companies, the survey questionnaire only presented the company names in alphabetical order. The order of company names does not connect the cost data with any specific company, so as to protect commercial interests of the participants. The collected information and cost data such as repair duration, service life, total cost, and traffic control was compared comprehensively in the next part.

Table 11.10: Cost Comparison of Shallow Water Case

Questions	Company A	Company B	Company C	Company D	Company E
Repair Type	FRP-Based	FRP-Based	FRP-Based	FRP-Based	Structural Steel-Based
Repair duration to fix 10 steel bridge piles	3 to 4 days (24 to 32 hours)	13 days (100 hours)	10 days (80 hours)	10 days (80 hours)	5 days (40 hours)
Material cost (\$)	21,070 (Jacket, grout, rebars, & coating)	20,040 (Jacket, epoxy, & grout)	10,326.20 (Jacket, grout, epoxy, & steel screws)	13,104 (Jacket, rebars, & concrete)	85,790 (H-piles)
Labor cost (\$)	6,240	30,440	13,900	27,960	58,750
# of laborers on field	3	6	6	9	7
Equipment (\$, Heavy)	400 (Sandblasting)	17,587.50 (Hydro blaster, grout pump, & access equipment)	7,800 (Grout pump, High-pressure washer, forklift truck, & boat)	3,000 (Concrete pump)	Included in labor cost (Air package, boom truck or forklift)
Equipment (Minor)	None	Float, boat	Hand tools	Pressure washer	Rigging package, hydraulic package, & hydraulic impact wrench
Other cost items (\$)	2,000 (Engineering fee)	None	None	None	None
Total cost (\$, Estimate)	29,710	68,067.50	32,026.20	44,064	144,540
Service life (Estimate)	20 years	25 years	40 years	15 years	75 years
Transportation control	None	None	None	None	None

Table 11.11: Cost Comparison of Deep Water Case

Questions	Company A	Company B	Company C	Company D	Company E
Repair Type	FRP-Based	FRP-Based	FRP-Based	FRP-Based	Structural Steel-Based
Repair duration to fix 10 steel bridge piles	6 days (48 hours)	25 days (200 hours)	15 days (120 hours)	14 days (112 hours)	5 days (40 hours)
Material cost (\$)	42,140 (Jacket, grout, rebars, & coating)	42,350 (Jacket, epoxy, & grout)	21,232 (Jacket, grout, epoxy, & steel screws)	17,050 (Jacket, rebars, & concrete)	138,780 (H-piles)
Labor cost (\$)	9,360	60,880	34,100	43,880	58,750
# of laborers on field	3	6	6	11	7
Equipment (\$, Heavy)	720 (Sandblasting)	35,175 (Hydro blaster, grout pump, & access equipment)	16,980 (Grout pump, High-pressure washer, forklift truck, & boat)	3,500 (Concrete pump)	Included in labor cost (Air package, boom truck or forklift)
Equipment (Minor)	None	Float, boat	Hand tools	Pressure washer	Rigging package, hydraulic package, & hydraulic impact wrench
Other cost items (\$)	2,000 (Engineering fee)	None	None	None	None
Total cost (\$, Estimate)	54,220	138,405	72,312	64,430	197,530
Service life (Estimate)	20 years	25 years	40 years	15 years	75 years
Transportation control	None	None	None	None	None

11.6.1.5. Repair Duration

For FRP-based repair systems, the repair duration starts from surface preparation of steel pile, mixing of adhesives, positioning and installation of FRP jackets, curing time of epoxy and grout, and ends up with coating and painting of FRP system. The survey results (Figure 10.2) indicate that the repair duration has been extended in a considerable degree from the shallow water case to the deep water case. In the shallow water case, the repair duration of Company A, B, C and D are 32 hours, 100 hours, 80 hours, and 80 hours, respectively. While in the deep water case, the repair duration is extended by the rate of 50% for Company A (48 hours), 50% for Company C (120 hours), 40% for Company D (112 hours), and even 100% for Company B (200 hours).

For the structural steel-based system, steel plate jackets may be pre-fabricated with customized length in the factory and then delivered to the job site. There is neither the need of mixing adhesives nor curing epoxy or grout. As such, the repair duration for Company E is the same 40 hours in both shallow water and deep water cases. Also, the repair duration of Company E is shortest among five companies in the deep water case. The shortest repair duration should minimize the interruption of local traffic and user cost if any traffic control is needed during the repair.

Both FRP repair systems described in this study are patented by Professor Mo Ehsani; U.S. Patent #8,650,831 and #9,376,782

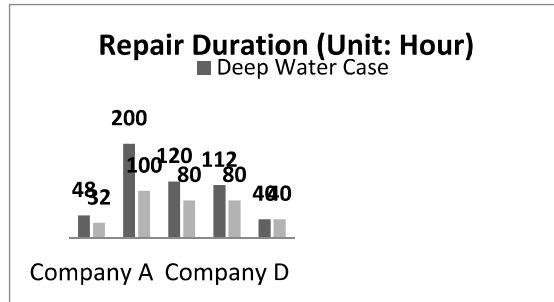


Figure 11.2: Repair Duration of Five Repair Systems

11.6.1.6. Service Life

Survey results show that Company E (the structural steel-based system) has the longest service life (75 years), which is much more durable than alternative FRP-based repair systems (Company A (20 years), B (25 years), C (40 years) and D (15 years)). Considering the bridge service life is normally 75 years, Company E is a maintenance-free system throughout the bridge life cycle, which minimizes potential user cost incurred by the future repair. On the contrary, the service lives of FRP-based systems are relatively short, which means more repair and rehabilitation activities during the bridge life-cycle, which may incur more user cost if any traffic interruption occurs during the repair. The service lives are shown in Figure 10.3.

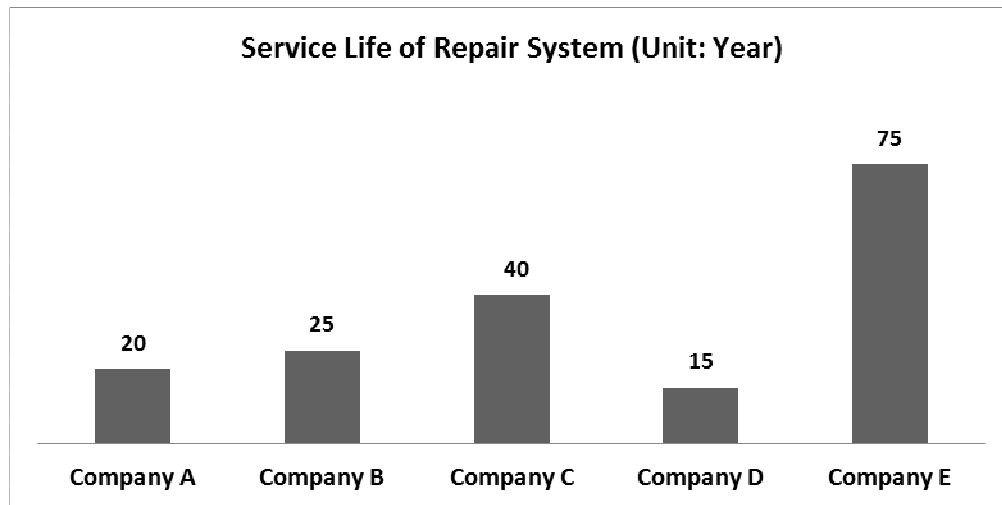


Figure 11.3: Repair System of Service Life for Shallow and Deep Water Cases

11.6.1.7. Cost Data

The collected cost data of five repair systems, as the main part of this survey questionnaire, includes three major components: material cost, labor cost and equipment cost (heavy or minor equipments). The cost data is illustrated in Figure 10.4 (the shallow water case) and Figure 10.5 (the deep water case). Noting Company E combines labor cost and equipment cost into a cost package, these two cost categories will be considered as one type of cost in the analysis of this survey, in order to make the cost data from all five companies comparable. The cost data is discussed in detail below.

(1) Total costs are estimated by repair companies based on two repair scenarios in which ten deteriorated piles of one bridge need to be repaired. The survey results indicate that Company E has the highest total cost, while Company A has the lowest one, in both shallow and deep water cases. The total costs of Company E are \$144,540 and \$197,530 for the shallow water case and the deep water case, respectively. In the contrary, the total costs of Company A are only \$29,710 and

\$54,220 for two cases. The costs of Company E are about 4.86 times of Company A for the shallow water case and 3.64 times for the deep water case.

The survey also indicates that total costs increase greatly from the shallow water case to the deep water case. In the shallow water case, total costs are \$29,710, \$68,068, \$32,026, \$44,064 and \$144,540 for Company A, B, C, D and E, respectively. However, in the deep water case, total costs have experienced large growth by the rates of 82.50%, 103.33%, 125.79%, 46.22% and 36.66% for Company A, B, C, D and E, respectively. It should be noted that Company E has the lowest increasing rate because its labor and equipment costs in shallow water case is the same with those in the deep water case. Total costs of both shallow water and deep water cases are shown in Figure 10.6.

(2) In the deep water case, a floating platform (or boat) and trained divers may be needed to install the repair system, which increases the labor cost and equipment cost greatly, compared with the shallow water case. Also, the more serious extent of corrosion of steel piles in the deep water condition is another critical concern of repair companies when they made the estimation of the labor and material cost.

(3) In the deep water case, the labor and equipment costs have experienced the large growth, compared with the costs of \$6,640, \$48,028, \$21,700 and \$30,960 for Company A, B, C and D in the shallow water case. The growth rates are 51.81%, 100%, 135.39%, and 53.04% for Company A, B, C, and D, respectively. However, this kind of cost for Company E is kept at the same level with its shallow water case. The survey results also show that this kind of cost for FRP-based repair systems is

usually lower than that of structural steel-based system, except for Company B in the deep water case.

(4) The material costs in the shallow water case are \$21,070, \$20,040, \$10,326, \$13,104 and \$85,790 for Company A, B, C, D and E, respectively. In the deep water case, the same tendency of substantial growth is observed for this cost, compared with the cost in the shallow water case. The increasing rates are 100%, 111.33%, 105.61%, 30.11%, 61.77%, for Company A, B, C, D and E, respectively. Company E has the highest material cost in both cases, while Company C has the lowest material cost in the shallow water case and Company D has the lowest cost in the deep water case. It is worthy of noting that Company D has the shortest service life, while Company E is the most durable one. Thence, the life-cycle cost of Company D is not necessarily lower than that of Company E in the whole service life. The cost-effectiveness of each repair system should be investigated in the later life-cycle cost analysis.

(5) Company A includes a special cost item (\$2,000 of engineering fee) other than the aforementioned costs, while other companies do not include any other costs.

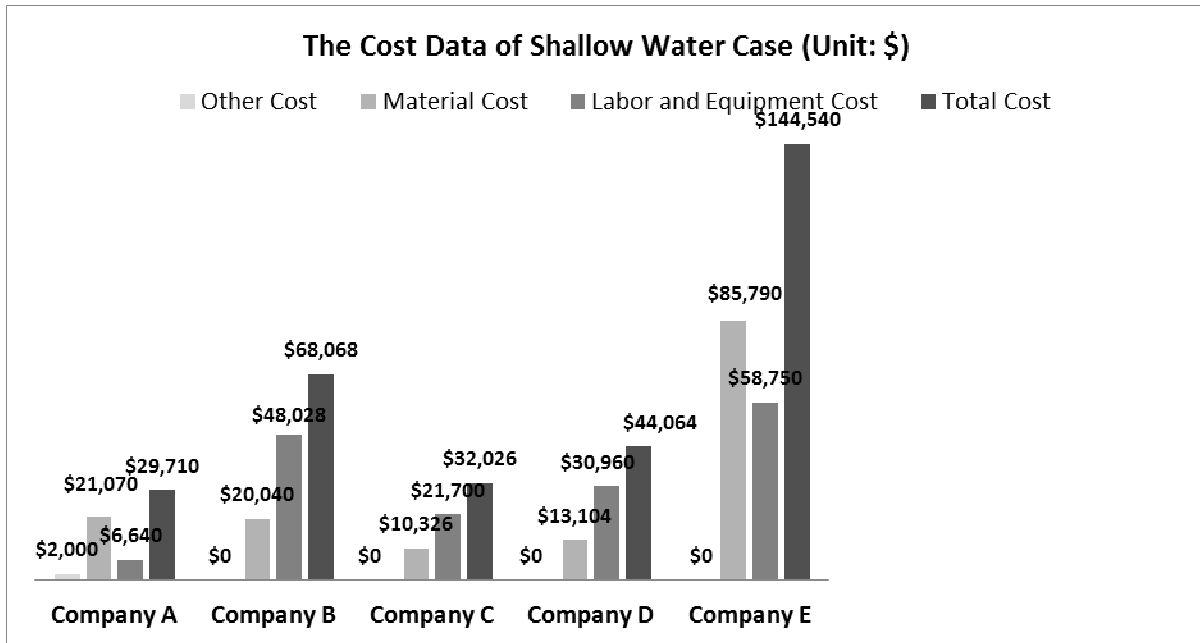


Figure 11.4: Cost Data of Repair Systems in Shallow Water Case

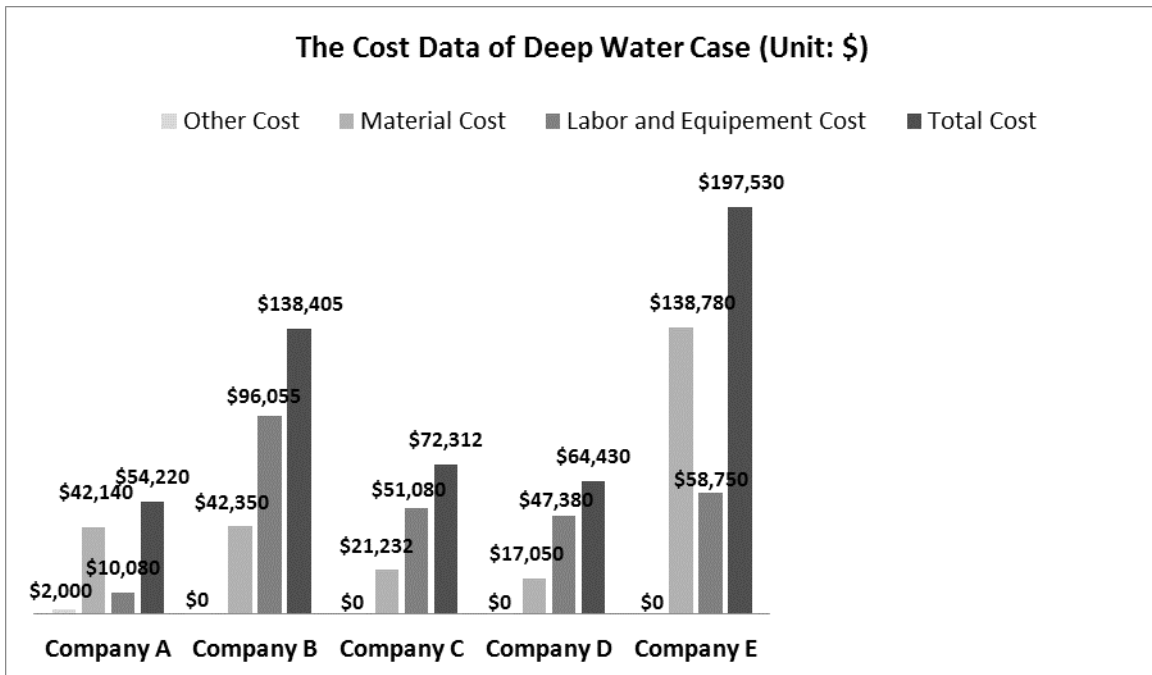


Figure 11.5: Cost Data of Repair Systems in Deep Water Case

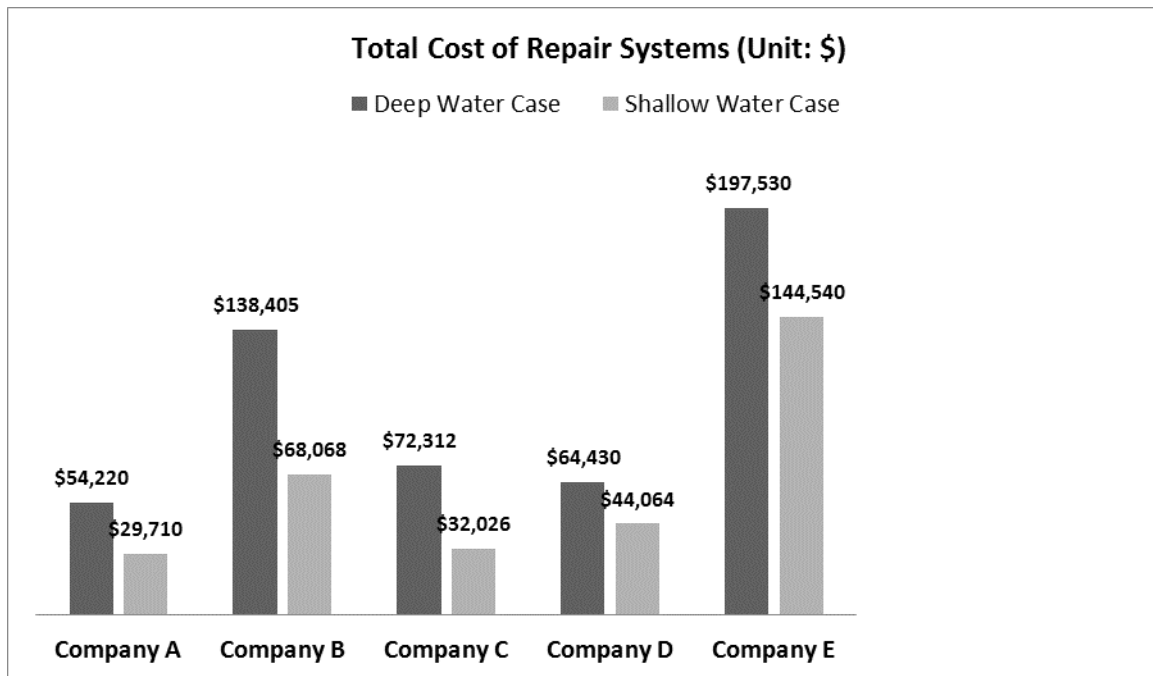


Figure 11.6: Total Cost of Repair Systems in Shallow and Deep Water Case

11.6.1.8. Traffic Control

The survey questionnaire indicates that there is no need of traffic control plan for any proposed repair system during the repair. Although it may cause minor traffic control when delivering the repair materials or transport them between sites of construction, this need will not be considered in the life-cycle cost analysis.

11.7. LCCA of Five Bridge Pile Repair Solutions

11.7.1. Introduction

Based on the survey data, an LCCA was performed to five feasible repair systems to identify repair solutions requiring less life-cycle costs in a bridge pile repair project. Repair plans were designed for each repair solution during the whole analysis period

according to different service lives and initial repair time. The LCCA results, expressed in terms of $LCC_{n,s,t,i}^m$, accounted for five main parameters. They were defined as below:

- Company Option: $m = A, B, C, D, E$ for five companies;
- Analysis Period (Years): $n = 35, 50, 75$;
- Service Life (Years): $s = 20, 25, 40, 15, 75$ for Company A, B, C, D and E;
- Initial Repair (Years): $t = 10, 20, 30$;
- Interest Rate (%): $i = 2.5, 3.5, 4.5$;

Generally, life-cycle costs comprise of agency costs and user costs, but the survey questionnaire indicated that none of five companies needed traffic control during their repair activities. It means that there is no disruption to traffic flow, and thus no user costs are borne by bridge users. Therefore, life-cycle costs in this study only considered agency costs incurred by repair activities. It should be noted that initial construction costs by agency were also dropped out since this project deals with a repair or rehabilitation project.

11.7.2. Implementation of RealCost

The *RealCost*, as a powerful LCCA tool, was originally developed by Federal Highway Administration (FHWA) in 2003 to support the application LCCA in the decision-making process for transportation projects. It was selected to perform the LCCA since the program was determined to be suitable for bridge repair projects. The application of the program involves several sequential steps that are also recommended by FHWA.

- *Establish alternative bridge pile repair strategies for the analysis period:* In this step, five repair solutions were determined to be suitable for this project. Among them,

Company A, B, C and D are FRP-based repair techniques, while Company E is steel-based.

- *Determine service life and repair activity timing:* The performance period and repair activity timing were determined according to the service lives from survey inputs and various initial repair times.
- *Estimate agency costs:* Agency costs of each repair activity for five companies were estimated based on the collected cost data from the survey.
- *Estimate user costs:* All repair companies indicated that their repair can be implemented without any traffic control plan. As such, user costs were not considered and dropped out from this LCCA. In *RealCost*, the work zone hours were set to be zero to reflect zero user costs of this study, as shown in Figure 10.7.

The screenshot displays the 'Alternative-Level Input' window in the RealCost software. At the top, 'Alternative' is set to 1, 'Alternative Description' is 'Company A', and 'Number of Activities' is 5. Below this, a tabbed interface shows 'Activity 1' through 'Activity 5', with 'Activity 1' selected. The 'Activity Description' is 'Repair @ Year 10'. The 'Activity Cost and Service Life Inputs' section contains fields for Agency Construction Cost (\$1000) (29.71), Activity Service Life (years) (20), User Work Zone Costs (\$1000) (empty), Activity Structural Life (years) (20), Maintenance Frequency (years) (1), and Agency Maintenance Cost (\$1000) (0). The 'Activity Work Zone Inputs' section includes Work Zone Length (miles) (3), Work Zone Duration (days) (5), Work Zone Capacity (vphpl) (1391), Work Zone Speed Limit (mph) (30), No of Lanes Open in Each Direction During Work Zone (2), and Traffic Hourly Distribution (Week Day 2). The 'Work Zone Hours' section at the bottom has a table for Inbound and Outbound lane closure periods, with the first period of lane closure set to 0 for both start and end times. Buttons for 'Open...', 'Save...', 'Ok', 'Cancel', 'Copy Activity', and 'Paste Activity' are visible at the bottom.

Figure 11.7: The Alternative-Level Input Example of RealCost (n = 75, i = 2.5%, Shallow Water)

- *Develop expenditure stream diagrams:* Expenditure stream diagrams are graphical representations of expenditures over time. They are generally developed for each

repair strategy to help visualize the amount and timing of expenditures. Figure 10.8, 10.9, and 10.10 represent expenditure stream diagrams for analysis periods of 35 years, 50 years and 75 years, respectively.

- *Compute life-cycles costs:* After inputting the required project and alternative-level data, *RealCost* can calculate the life-cycle costs of each alternative. Detailed results are presented in Net Present Value (NPV) and Equivalent Uniform Annual Cost (EUAC) forms. Table 11.12, Table 11.13, and Table 11.14 present the results for analysis periods of 35 years, 50 years and 75 years, respectively. Those results are also illustrated in Figure 10.11 through Figure 10.16.
- *Analyze results:* The analysis of LCCA results from *RealCost* was discussed in more detail in the next section.
- *Reevaluate design strategies:* Once life-cycle costs are generated for each alternative, the repair strategies can be modified by using the information acquired from the analysis, and the more cost-effective strategies may be developed.

Both FRP repair systems described in this study are patented by Professor Mo Ehsani; U.S. Patent #8,650,831 and #9,376,782

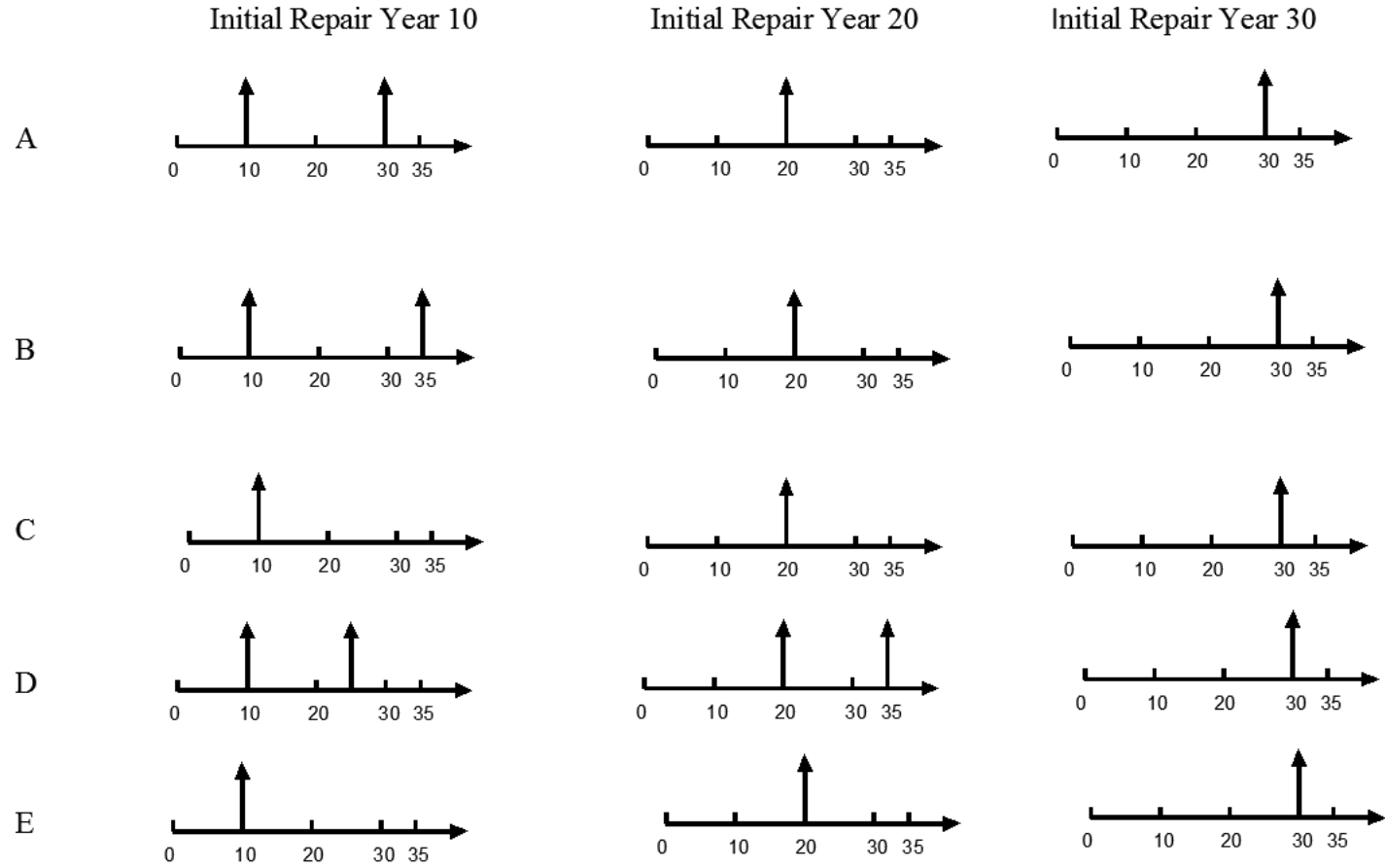


Figure 11.8: Repair Plans for Five repair alternatives ($t=10, 20$ and $30, n=35$)

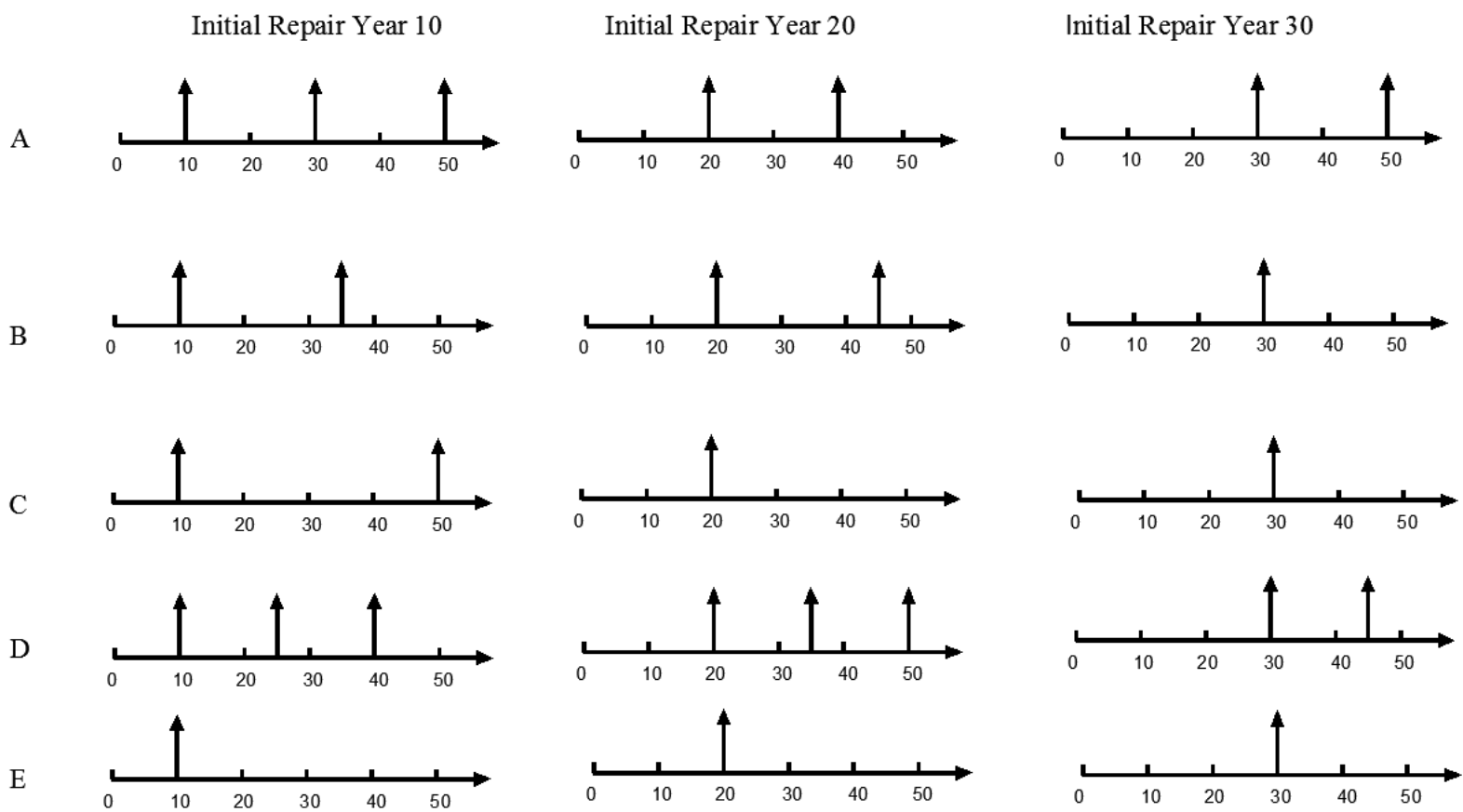


Figure 11.9: Repair Plans for Five repair alternatives ($t=10, 20$ and $30, n=50$)

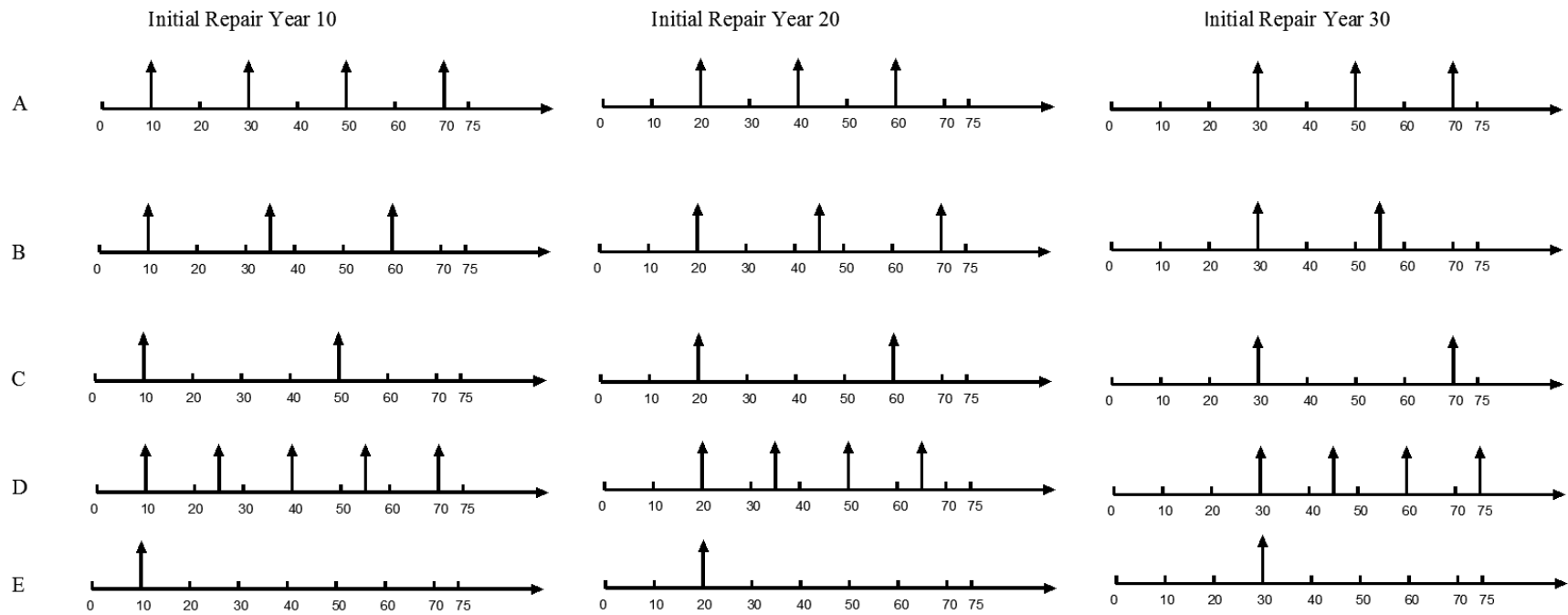


Figure 11.10: Repair Plans for Five repair alternatives ($t=10, 20$ and $30, n=75$)

Table 11.12: LCCA Results for Shallow Water Case and Deep Water Case (n=35)

LCC of Shallow Water Case ($n = 35$)											
		Company A		Company B		Company C		Company D		Company E	
s		20		25		40		15		75	
i		NPV	EUAC	NPV	EUAC	NPV	EUAC	NPV	EUAC	NPV	EUAC
$t=10$	2.5%	\$27,980	\$1,210	\$53,170	\$2,300	\$19,960	\$860	\$52,000	\$2,250	\$97,790	\$3,870
	3.5%	\$24,960	\$1,250	\$48,250	\$2,410	\$19,100	\$960	\$45,480	\$2,270	\$95,170	\$4,110
	4.5%	\$22,290	\$1,280	\$43,830	\$2,510	\$18,050	\$1,030	\$39,890	\$2,280	\$89,520	\$4,230
i		NPV	EUAC	NPV	EUAC	NPV	EUAC	NPV	EUAC	NPV	EUAC
$t=20$	2.5%	\$15,000	\$650	\$30,070	\$1,300	\$11,110	\$480	\$26,890	\$1,160	\$39,480	\$1,710
	3.5%	\$12,700	\$640	\$26,040	\$1,300	\$10,090	\$500	\$22,150	\$1,110	\$37,950	\$1,900
	4.5%	\$10,730	\$610	\$22,390	\$1,280	\$8,990	\$510	\$18,270	\$1,050	\$35,160	\$2,010
i		NPV	EUAC	NPV	EUAC	NPV	EUAC	NPV	EUAC	NPV	EUAC
$t=30$	2.5%	\$4,770	\$210	\$9,510	\$410	\$3,460	\$150	\$8,630	\$370	\$12,060	\$520
	3.5%	\$3,900	\$200	\$7,920	\$400	\$3,000	\$150	\$6,890	\$340	\$11,030	\$550
	4.5%	\$3,160	\$180	\$6,510	\$370	\$2,550	\$150	\$5,470	\$310	\$9,690	\$560

LCC of Deep Water Case ($n = 35$)											
		Company A		Company B		Company C		Company D		Company E	
s		20		25		40		15		75	
i		NPV	EUAC	NPV	EUAC	NPV	EUAC	NPV	EUAC	NPV	EUAC
$t=10$	2.5%	\$51,070	\$2,210	\$108,120	\$4,670	\$45,060	\$1,950	\$76,040	\$3,290	\$133,640	\$5,290
	3.5%	\$45,560	\$2,280	\$98,120	\$4,910	\$43,130	\$2,160	\$66,500	\$3,320	\$130,050	\$5,620

	4.5%	\$40,680	\$2,330	\$89,120	\$5,100	\$40,750	\$2,330	\$58,320	\$3,340	\$122,340	\$5,770
<i>i</i>		NPV	EUAC	NPV	EUAC	NPV	EUAC	NPV	EUAC	NPV	EUAC
<i>t=20</i>	2.5%	\$27,380	\$1,180	\$61,140	\$2,640	\$25,090	\$1,080	\$39,320	\$1,700	\$53,960	\$2,330
	3.5%	\$23,180	\$1,160	\$52,950	\$2,650	\$22,780	\$1,140	\$32,380	\$1,620	\$51,870	\$2,590
	4.5%	\$19,580	\$1,120	\$45,530	\$2,610	\$20,300	\$1,160	\$26,720	\$1,530	\$48,050	\$2,750
<i>i</i>		NPV	EUAC	NPV	EUAC	NPV	EUAC	NPV	EUAC	NPV	EUAC
<i>t=30</i>	2.5%	\$8,710	\$380	\$19,330	\$840	\$7,810	\$340	\$12,620	\$550	\$16,490	\$710
	3.5%	\$7,120	\$360	\$16,100	\$800	\$6,780	\$340	\$10,070	\$500	\$15,070	\$750
	4.5%	\$5,760	\$330	\$13,230	\$760	\$5,750	\$330	\$8,000	\$460	\$13,240	\$760

Table 11.13: LCCA Results for Shallow Water Case and Deep Water Case (n=50)

LCC of Shallow Water Case ($n = 50$)											
		Company A		Company B		Company C		Company D		Company E	
s		20		25		40		15		75	
i		NPV	EUAC	NPV	EUAC	NPV	EUAC	NPV	EUAC	NPV	EUAC
$t=10$	2.5%	\$37,370	\$1,320	\$73,930	\$2,610	\$25,020	\$880	\$70,330	\$2,480	\$93,290	\$3,290
	3.5%	\$31,650	\$1,350	\$63,800	\$2,720	\$22,700	\$970	\$58,380	\$2,490	\$90,390	\$3,850
	4.5%	\$27,060	\$1,370	\$55,400	\$2,800	\$20,620	\$1,040	\$48,990	\$2,480	\$85,610	\$4,330
i		NPV	EUAC	NPV	EUAC	NPV	EUAC	NPV	EUAC	NPV	EUAC
$t=20$	2.5%	\$24,870	\$880	\$48,100	\$1,700	\$17,220	\$610	\$45,460	\$1,600	\$62,980	\$2,220
	3.5%	\$19,780	\$840	\$38,930	\$1,660	\$14,660	\$630	\$35,360	\$1,510	\$57,110	\$2,430
	4.5%	\$15,780	\$800	\$31,690	\$1,600	\$12,390	\$630	\$27,710	\$1,400	\$50,330	\$2,550
i		NPV	EUAC	NPV	EUAC	NPV	EUAC	NPV	EUAC	NPV	EUAC
$t=30$	2.5%	\$14,160	\$500	\$28,490	\$1,000	\$10,610	\$370	\$26,970	\$950	\$38,070	\$1,340
	3.5%	\$10,590	\$450	\$21,810	\$930	\$8,540	\$360	\$19,810	\$840	\$32,520	\$1,390
	4.5%	\$7,930	\$400	\$16,670	\$840	\$6,780	\$340	\$14,590	\$740	\$26,860	\$1,360

LCC of Deep Water Case ($n = 50$)											
		Company A		Company B		Company C		Company D		Company E	
s		20		25		40		15		75	
i		NPV	EUAC	NPV	EUAC	NPV	EUAC	NPV	EUAC	NPV	EUAC
$t=10$	2.5%	\$68,210	\$2,400	\$150,330	\$5,300	\$56,490	\$1,990	\$102,830	\$3,630	\$127,490	\$4,500
	3.5%	\$57,750	\$2,460	\$129,720	\$5,530	\$51,260	\$2,190	\$85,370	\$3,640	\$123,530	\$5,270

	4.5%	\$49,390	\$2,500	\$112,650	\$5,700	\$46,560	\$2,360	\$71,630	\$3,620	\$116,990	\$5,920
<i>i</i>		NPV	EUAC	NPV	EUAC	NPV	EUAC	NPV	EUAC	NPV	EUAC
<i>t=20</i>	2.5%	\$45,390	\$1,600	\$97,810	\$3,450	\$38,870	\$1,370	\$66,470	\$2,340	\$86,060	\$3,030
	3.5%	\$36,090	\$1,540	\$79,170	\$3,380	\$33,100	\$1,410	\$51,710	\$2,200	\$78,050	\$3,330
	4.5%	\$28,800	\$1,460	\$64,230	\$3,250	\$27,980	\$1,420	\$40,520	\$2,050	\$68,780	\$3,480
<i>i</i>		NPV	EUAC	NPV	EUAC	NPV	EUAC	NPV	EUAC	NPV	EUAC
<i>t=30</i>	2.5%	\$25,850	\$910	\$57,930	\$2,040	\$23,950	\$840	\$39,430	\$1,390	\$52,030	\$1,830
	3.5%	\$19,320	\$820	\$44,350	\$1,890	\$19,290	\$820	\$28,970	\$1,230	\$44,440	\$1,890
	4.5%	\$14,480	\$730	\$33,890	\$1,710	\$15,300	\$770	\$21,340	\$1,080	\$36,700	\$1,860

Table 11.14: LCCA Results for Shallow Water Case and Deep Water Case (n=75)

LCC of Shallow Water Case ($n = 75$)											
		Company A		Company B		Company C		Company D		Company E	
s		20		25		40		15		75	
i		NPV	EUAC	NPV	EUAC	NPV	EUAC	NPV	EUAC	NPV	EUAC
$t=10$	2.5%	\$47,800	\$1,420	\$93,050	\$2,760	\$32,450	\$960	\$89,150	\$2,640	\$109,890	\$3,260
	3.5%	\$37,950	\$1,440	\$75,250	\$2,850	\$27,530	\$1,040	\$69,400	\$2,630	\$101,010	\$3,830
	4.5%	\$30,900	\$1,440	\$62,260	\$2,910	\$23,730	\$1,110	\$55,470	\$2,590	\$92,360	\$4,320
i		NPV	EUAC	NPV	EUAC	NPV	EUAC	NPV	EUAC	NPV	EUAC
$t=20$	2.5%	\$34,780	\$1,030	\$67,490	\$2,000	\$23,680	\$700	\$64,830	\$1,920	\$82,160	\$2,440
	3.5%	\$25,640	\$970	\$50,680	\$1,920	\$18,640	\$710	\$46,850	\$1,770	\$69,720	\$2,640
	4.5%	\$19,270	\$900	\$38,730	\$1,810	\$14,830	\$690	\$34,570	\$1,620	\$58,510	\$2,730
i		NPV	EUAC	NPV	EUAC	NPV	EUAC	NPV	EUAC	NPV	EUAC
$t=30$	2.5%	\$24,590	\$730	\$47,820	\$1,420	\$16,560	\$490	\$45,530	\$1,350	\$59,840	\$1,770
	3.5%	\$16,890	\$640	\$33,480	\$1,270	\$12,170	\$460	\$30,660	\$1,160	\$47,120	\$1,780
	4.5%	\$11,760	\$550	\$23,720	\$1,110	\$8,990	\$420	\$20,990	\$980	\$36,460	\$1,700

LCC of Deep Water Case ($n = 75$)											
		Company A		Company B		Company C		Company D		Company E	
s		20		25		40		15		75	
i		NPV	EUAC	NPV	EUAC	NPV	EUAC	NPV	EUAC	NPV	EUAC
$t=10$	2.5%	\$87,230	\$2,590	\$189,210	\$5,610	\$73,270	\$2,170	\$130,350	\$3,870	\$150,180	\$4,450
	3.5%	\$69,260	\$2,620	\$153,010	\$5,790	\$62,160	\$2,350	\$101,470	\$3,840	\$138,040	\$5,230

	4.5%	\$56,380	\$2,630	\$126,600	\$5,920	\$53,570	\$2,500	\$81,100	\$3,790	\$126,220	\$5,900
<i>i</i>		NPV	EUAC	NPV	EUAC	NPV	EUAC	NPV	EUAC	NPV	EUAC
<i>t=20</i>	2.5%	\$63,480	\$1,880	\$137,220	\$4,070	\$53,470	\$1,590	\$94,790	\$2,810	\$112,280	\$3,330
	3.5%	\$46,800	\$1,770	\$103,060	\$3,900	\$42,100	\$1,590	\$68,500	\$2,590	\$95,280	\$3,610
	4.5%	\$35,170	\$1,640	\$78,760	\$3,680	\$33,470	\$1,560	\$50,550	\$2,360	\$79,960	\$3,740
<i>i</i>		NPV	EUAC	NPV	EUAC	NPV	EUAC	NPV	EUAC	NPV	EUAC
<i>t=30</i>	2.5%	\$44,870	\$1,330	\$97,230	\$2,880	\$37,380	\$1,110	\$66,570	\$1,970	\$81,770	\$2,420
	3.5%	\$30,820	\$1,170	\$68,080	\$2,580	\$27,480	\$1,040	\$44,840	\$1,700	\$64,390	\$2,440
	4.5%	\$21,470	\$1,000	\$48,230	\$2,250	\$20,300	\$950	\$30,690	\$1,430	\$49,830	\$2,330

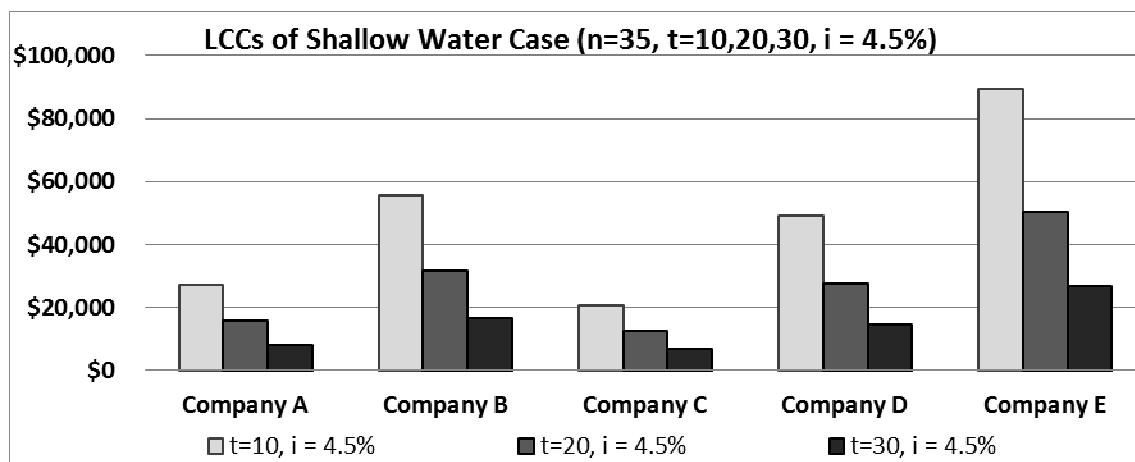
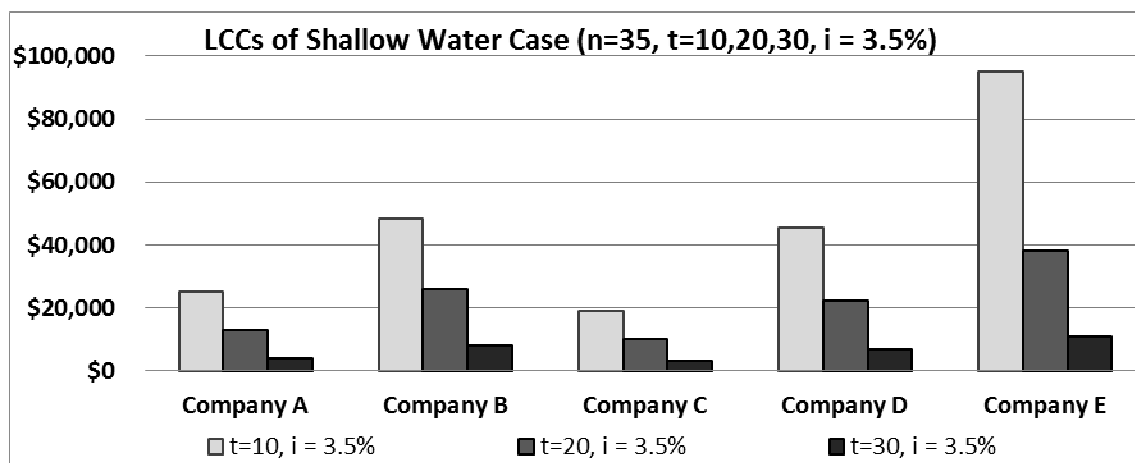
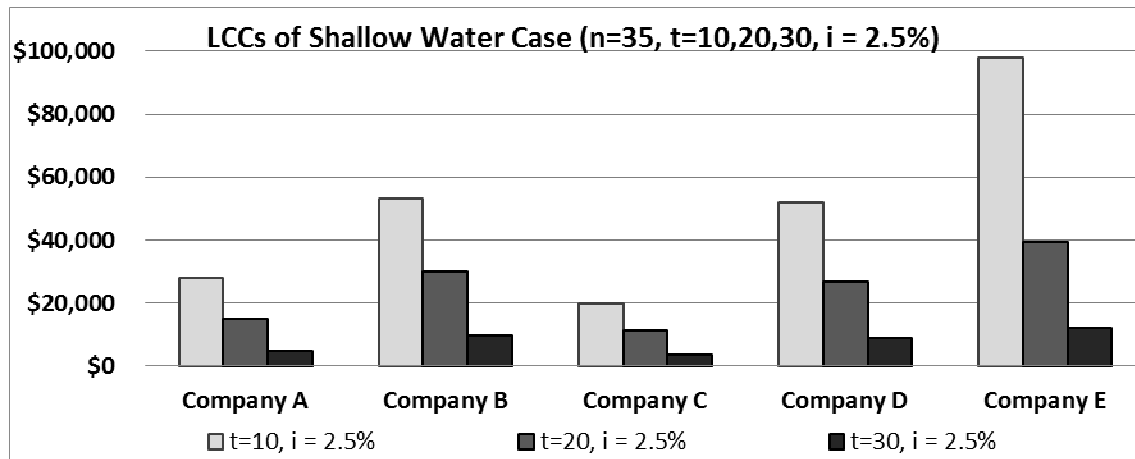


Figure 11.11: Life-Cycle Costs in NPV (Shallow Water Case, n =35)

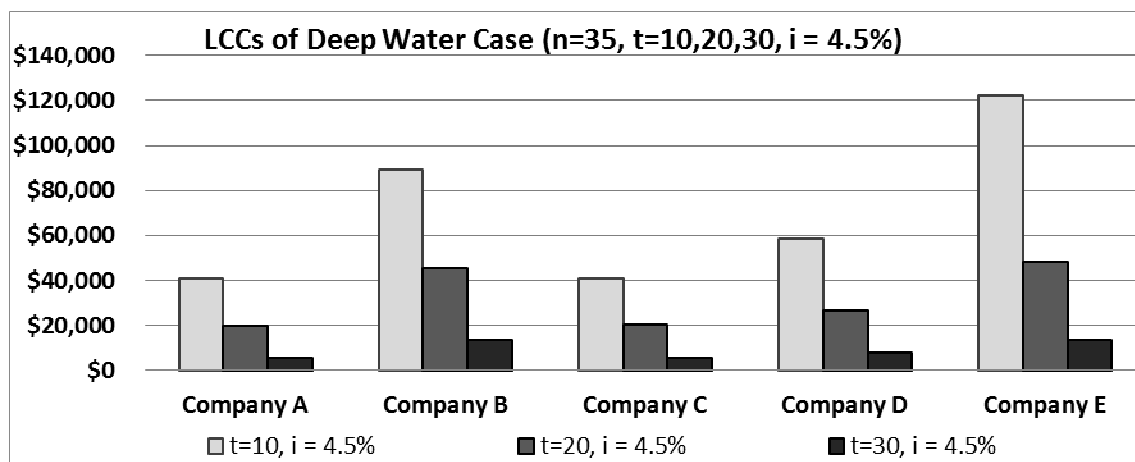
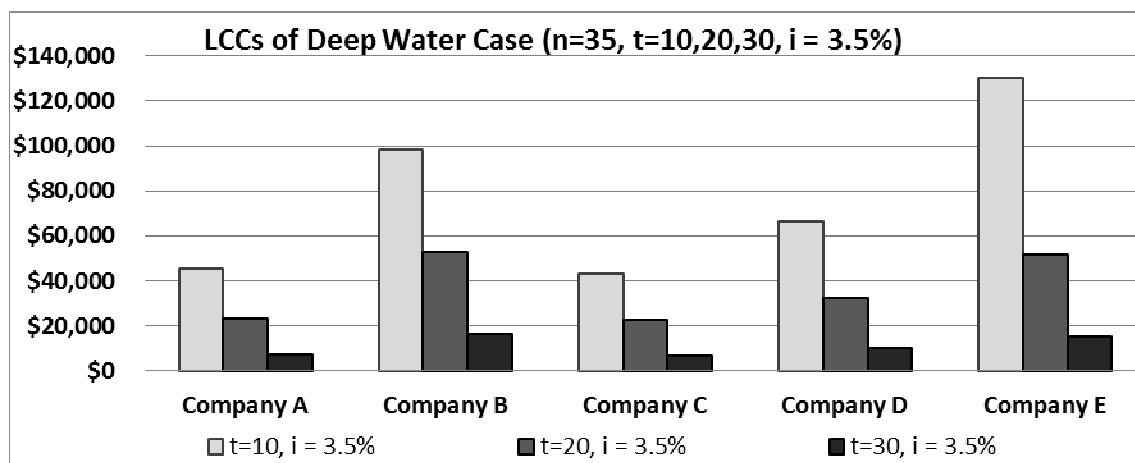
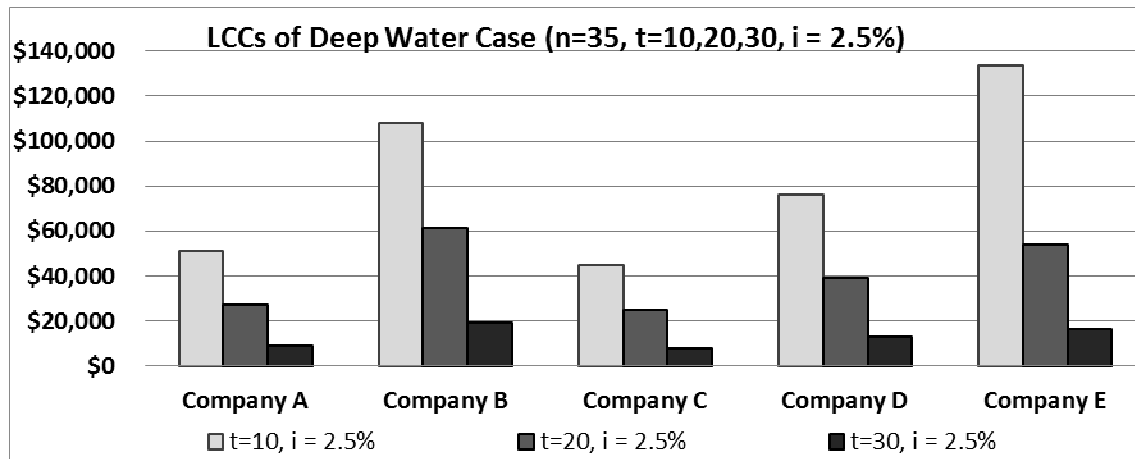


Figure 11.12: Life-Cycle Costs in NPV (Deep Water Case, n=35)

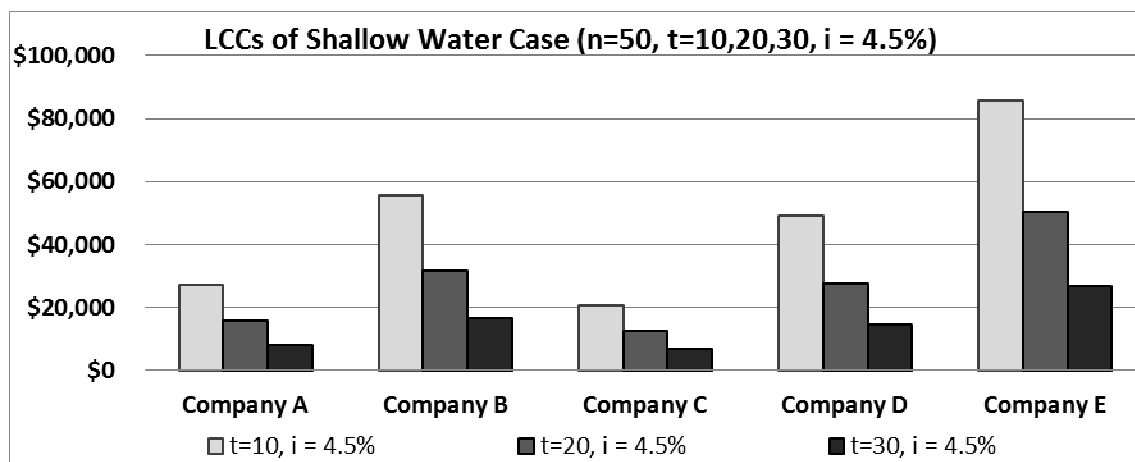
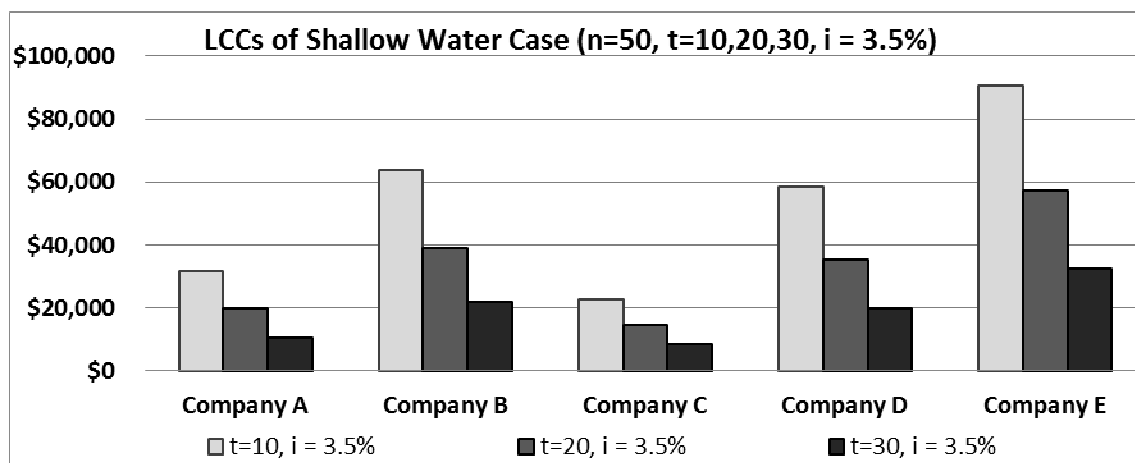
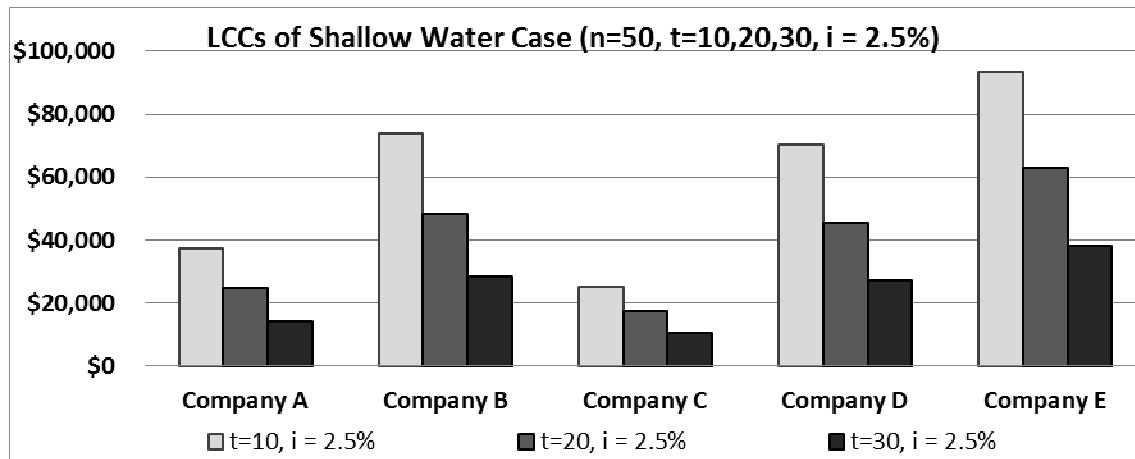


Figure 11.13: Life-Cycle Costs in NPV (Shallow Water Case, n=50)

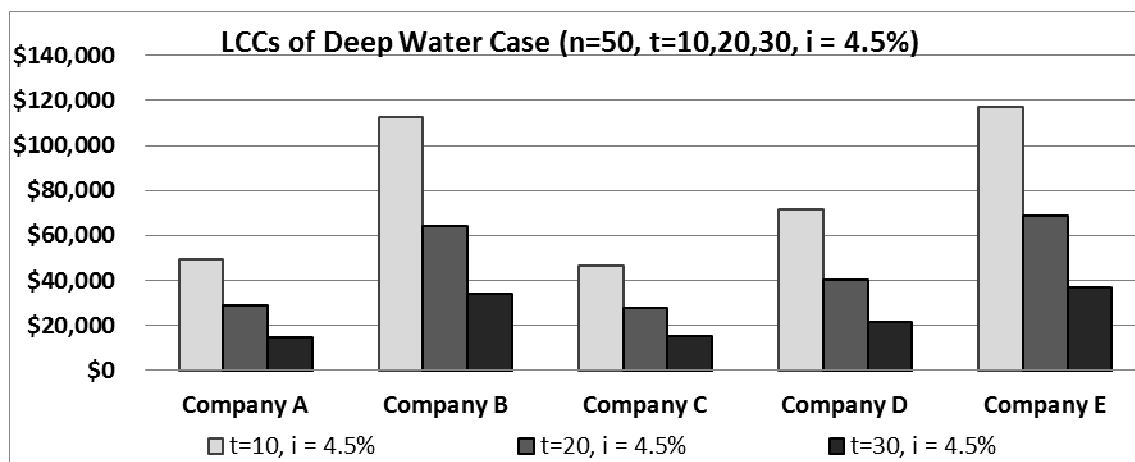
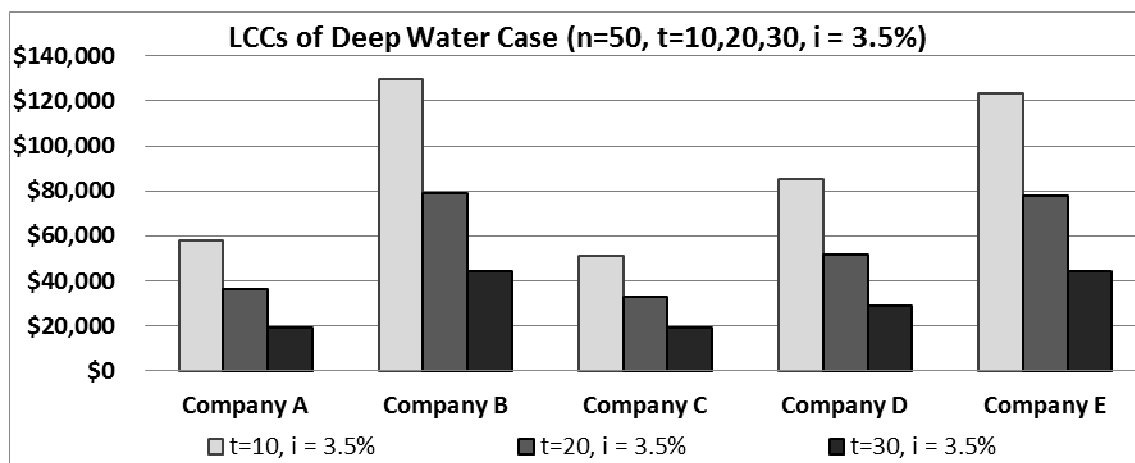
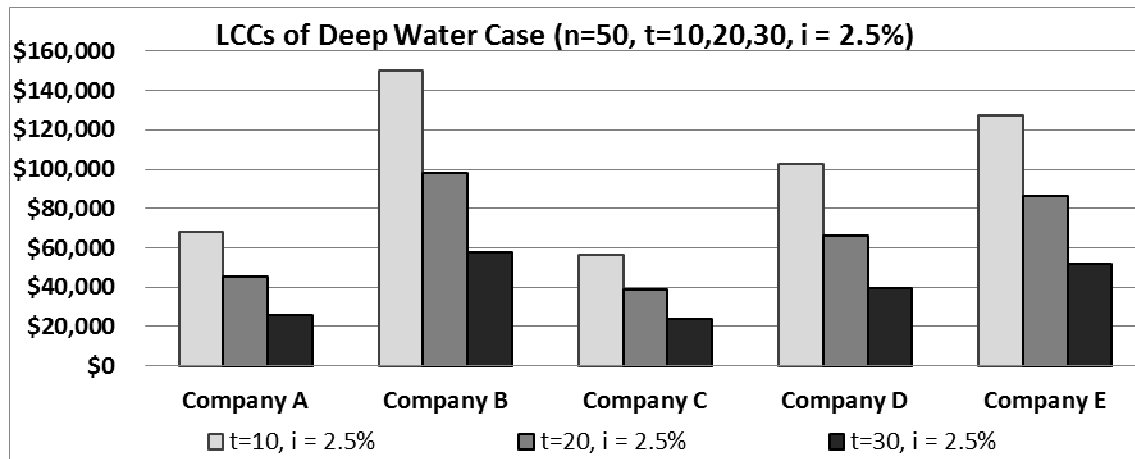


Figure 11.14: Life-Cycle Costs in NPV (Deep Water Case, n =50)

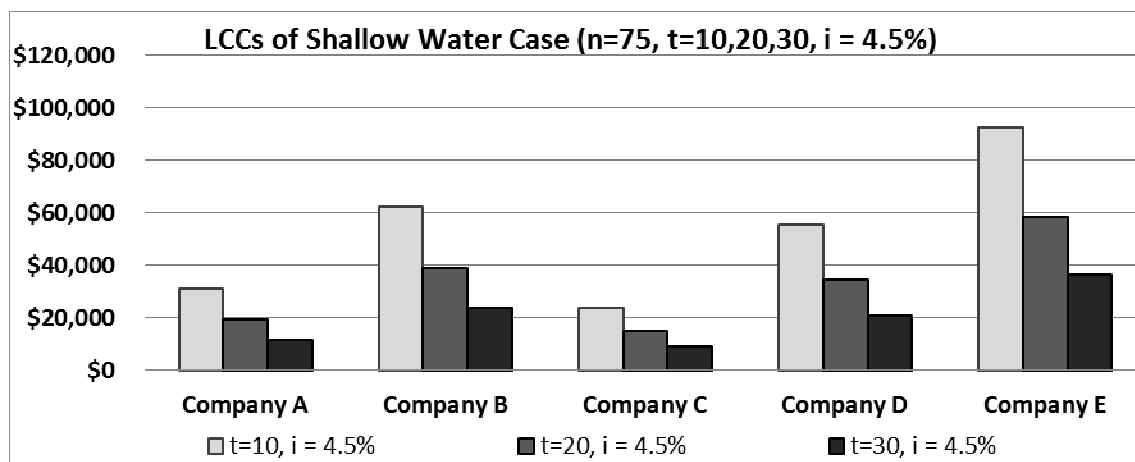
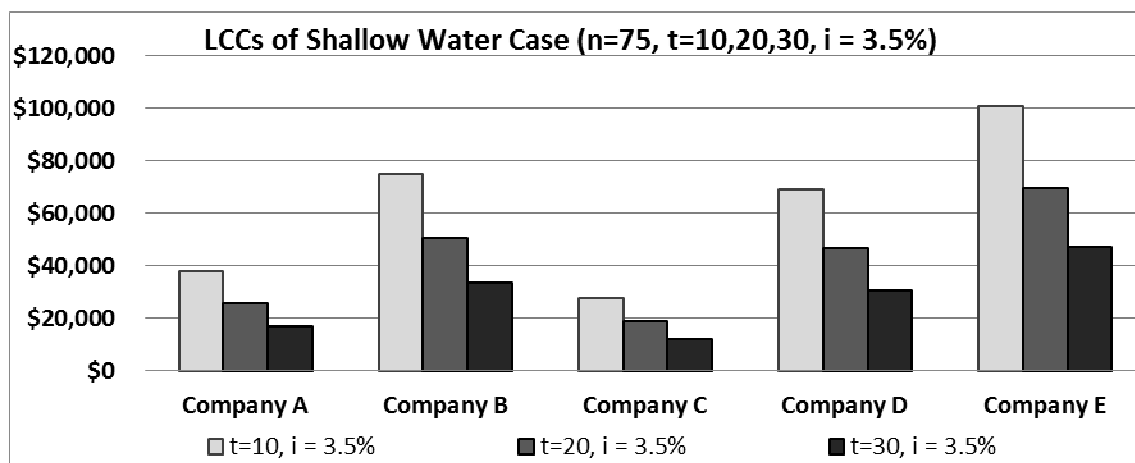
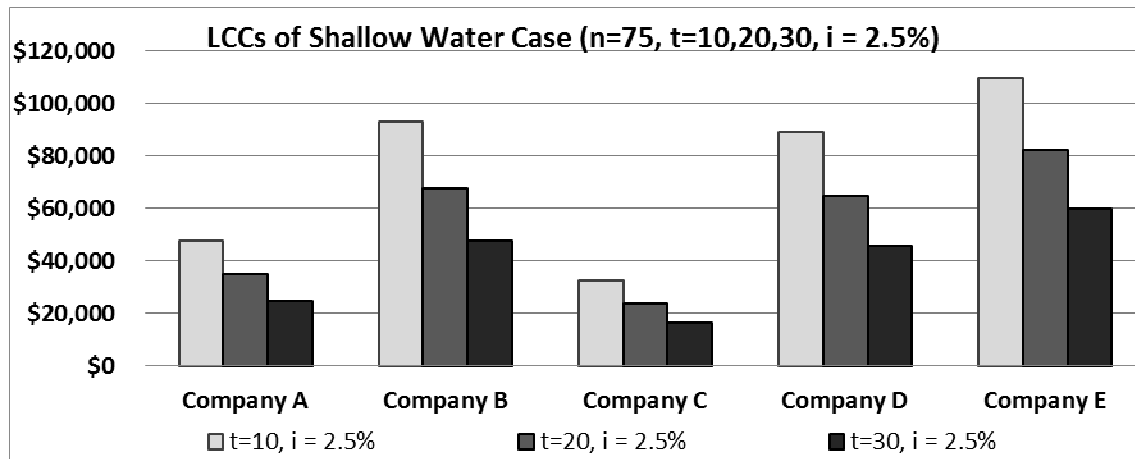


Figure 11.15: Life-Cycle Costs in NPV (Shallow Water Case, n =75)

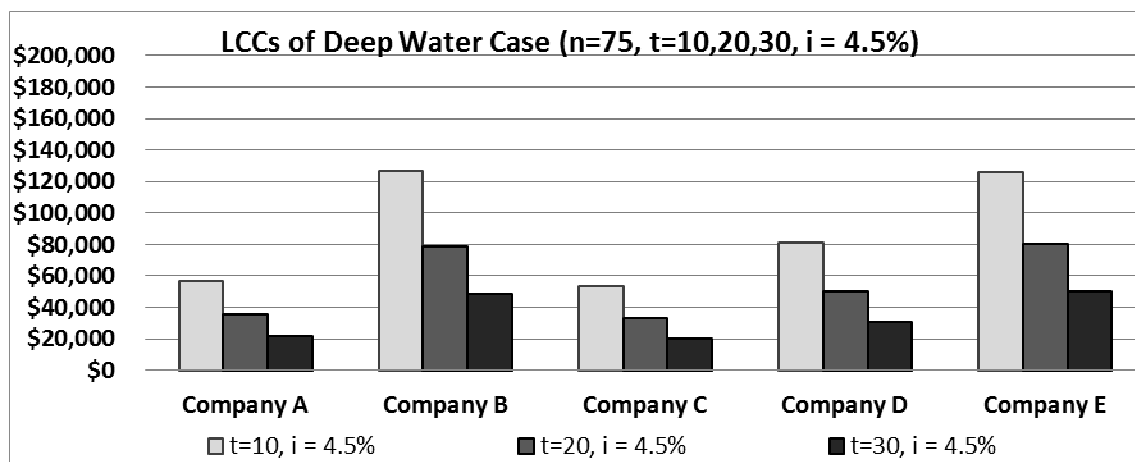
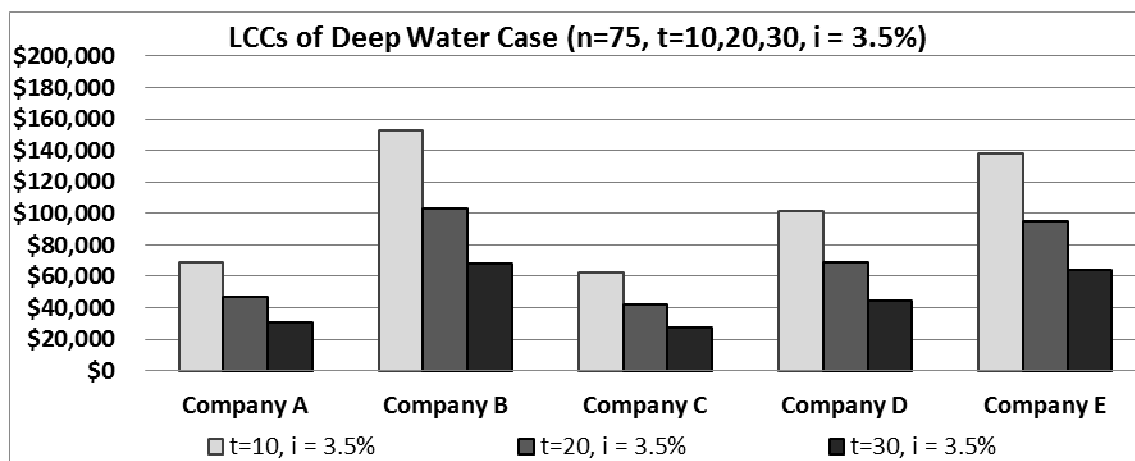
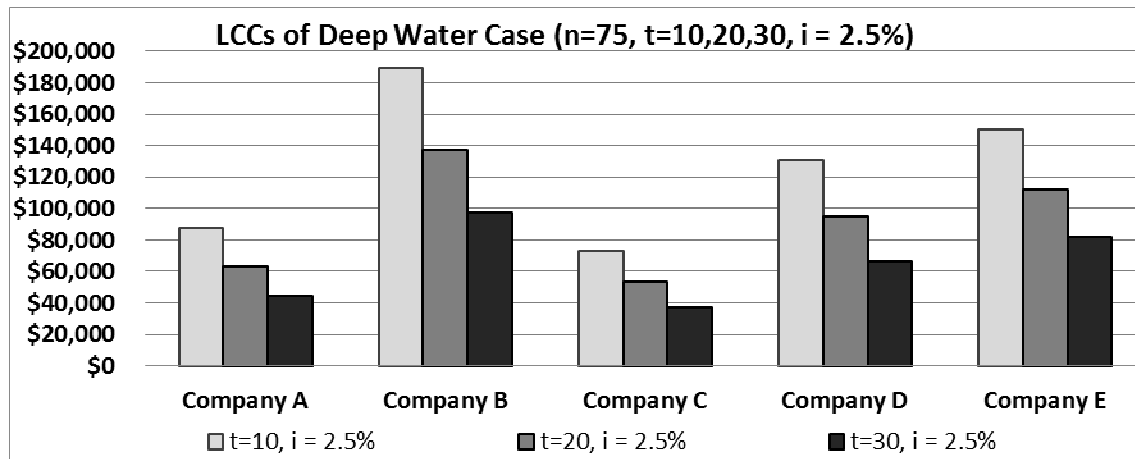


Figure 11.16: Life-Cycle Costs in NPV (Deep Water Case, n=75)

11.7.3. Analysis of Life-Cycle Costs

11.7.3.1. Shallow Water Repair Case

Based on Table 11.15, shallow water repair costs for the 35-Year analysis period were presented in Figure 10.11. As can be seen from the figure, Company E consistently shows the highest life-cycle cost (LCC), while Company C is the one with the lowest LCC under the combination of different discount rates and initial repair time. The order of repair cost from low to high is Company C, A, D, B, and E under different interest rates and initial repair time. Given the initial repair occurs at Year 10, the LCCs of Company C are \$19,960, \$19,100, and \$18,050 for the discount rates of 2.5%, 3.5% and 4.5%, respectively, which are only 27.60%, 25.97%, and 24.92% of those of Company E. If the initial repair is at Year 20, the LCCs of Company C are \$11,110, \$10,090, and \$8,990 for the discount rates of 2.5%, 3.5% and 4.5%, respectively, which are only 28.14%, 26.59%, and 25.57% of those of Company E. When the initial repair occurs at Year 30, the LCCs of company C are \$3,460, \$3,000, and \$2,550 for the discount rates of 2.5%, 3.5% and 4.5%, respectively, which are only 28.69%, 27.20% and 26.32% of those of Company E. The agency can save their repair funds substantially in the life-cycle term if they choose the repair solution from Company C.

The same trend was observed for the 50-year and 75-year analysis period cases and the order of repair cost from low to high is still Company C, A, D, B, and E. Based on Table 11.15, shallow water repair costs for the 50-Year

analysis period were presented in Figure 10.13. Given the initial repair occurs at Year 10, the LCCs of Company C are \$25,020, \$22,700, and \$20,620 for the discount rates of 2.5%, 3.5% and 4.5%, respectively, which is only 26.82%, 25.11%, and 24.09% of those of Company E. If the initial repair is at Year 20, the LCCs of Company C are \$17,220, \$14,660, and \$12,390 for the discount rates of 2.5%, 3.5% and 4.5%, respectively, which is only 27.34%, 25.67%, and 24.62% of those of Company E. When the initial repair occurs at Year 30, the LCCs of company C are \$10,610, \$8,540 and \$6,780 for the discount rates of 2.5%, 3.5% and 4.5%, respectively, which is only 27.87%, 26.26% and 25.24% of those of Company E.

Based on Table 11.16, shallow water repair costs for the 75-Year analysis period were presented in Figure 10.15. Given the initial repair occurs at Year 10, the LCCs of Company C are \$32,450, \$27,530, and \$23,730 for the discount rates of 2.5%, 3.5% and 4.5%, respectively, which is only 29.53%, 27.25%, and 25.69% of those of Company E. If the initial repair is at Year 20, the LCCs of Company C are \$23,680, \$18,640, and \$14,830 for the discount rates of 2.5%, 3.5% and 4.5%, respectively, which is only 28.82%, 26.74%, and 25.35% of those of Company E. When the initial repair occurs at Year 30, the LCCs of company C are \$16,650, \$12,170, and \$8,990 for the discount rates of 2.5%, 3.5% and 4.5%, respectively, which is only 27.67%, 25.83% and 24.66% of those of Company E.

It should be noted that, in the shallow water condition, all of FRP-based repair solutions show less LCC amounts than the steel-based repair solution by

Company E. This is attributed to advantages of FRP repair techniques such as shorter construction periods, simple repair processes, and relatively high durability.

11.7.3.2. Deep Water Repair Case

The results of LCCs for deep water case are shown as in Figures 10.12, 10.14 and 10.16 for the analysis periods of 35 years, 50 years and 75 years, respectively. At the analysis period of 35 years, Company E was not a repair technique with the highest LCC. The solution of Company B costs more than that of Company E in the deep water case. However, the solution of Company C still shows the lowest LCC among five companies. The order of repair cost from low to high is Company C, A, D, E, and B under different interest rates and initial repair timing. The main reason why a steel-based solution becomes more cost-effective than one FRP-based solution by Company B in the deep water case is in the repair durations and the durability. While FRP-based repair companies expected that repair durations would be increased by 1.5 to 2.0 times from shallow to deep, a steel-based repair company indicated no change in the repair duration. It also has the longest service life of 75 years among five companies. But in the life-cycle term, Company A, C and D still have less LCC amount than Company E with their relatively low repair cost of a single repair activity. When the initial repair occurs at Year 10, the LCCs of Company C are \$45,060, \$43,130, and \$40,750, for the discount rates of 2.5%, 3.5% and 4.5%, respectively, which is only 41.68%, 43.96%, and 45.72% of those of Company B. If the initial repair is at Year 20, the LCCs of

Company C are \$25,090, \$22,780, and \$20,300 for the discount rates of 2.5%, 3.5% and 4.5%, respectively, which is only 41.04%, 43.02%, and 44.59% of those of Company B. Given the initial repair occurs at Year 30, the LCCs of company C are \$7,810, \$6,780, and \$5,750 for the discount rates of 2.5%, 3.5% and 4.5%, respectively, which is only 40.40%, 42.11% and 43.46% of those of Company B. For other analysis periods of 50 and 75 years, this trend experienced little changes. Company B or E is the solution with highest LCC, while Company A or C has the lowest LCC on a case-by-case basis. The ranking orders for each scenario are summarized in Table 11.15 and Table 11.16 for shallow water case and deep water case, respectively.

In the case of deep water, a repair cost is increased significantly compared to the cost of shallow water case, due to increased water depth and requirements of special equipment or underwater diving. For example, in the case of Company C featuring the lowest LCC amount, the LCC amount in shallow water case is approximately 45% of the amount in deep water case under different discount rates when initial repair time is at Year 10. The case is also true for other initial repair time of Year 20 and Year 30, or for other companies.

Table 11.15: Ranking Orders of LCCs for Each Condition (Shallow Water)

Condition			Ranking Order (Most Cost-Effective to Least Cost-Effective)
n=35	<i>t=10</i>	<i>i=2.5%</i>	C(\$19,960)→A(\$27,980)→D(\$52,000)→B(\$53,170)→E(\$97,790)
		<i>i=3.5%</i>	C(\$19,100)→A(\$24,960)→D(\$45,480)→B(\$48,250)→E(\$95,170)
		<i>i=4.5%</i>	C(\$18,050)→A(\$22,290)→D(\$39,890)→B(\$43,830)→E(\$89,520)
	<i>t=20</i>	<i>i=2.5%</i>	C(\$11,110)→A(\$15,000)→D(\$26,890)→B(\$30,070)→E(\$39,480)
		<i>i=3.5%</i>	C(\$10,090)→A(\$12,700)→D(\$22,150)→B(\$26,040)→E(\$37,950)
		<i>i=4.5%</i>	C(\$8,990)→A(\$10,730)→D(\$18,270)→B(\$22,390)→E(\$35,160)
	<i>t=30</i>	<i>i=2.5%</i>	C(\$3,460)→A(\$4,770)→D(\$8,630)→B(\$9,510)→E(\$12,060)
		<i>i=3.5%</i>	C(\$3,000)→A(\$3,900)→D(\$6,890)→B(\$7,920)→E(\$11,030)
		<i>i=4.5%</i>	C(\$2,550)→A(\$3,160)→D(\$5,470)→B(\$6,510)→E(\$9,690)
n=50	<i>t=10</i>	<i>i=2.5%</i>	C(\$25,020)→A(\$37,370)→D(\$70,330)→B(\$73,930)→E(\$93,290)
		<i>i=3.5%</i>	C(\$22,700)→A(\$31,650)→D(\$58,380)→B(\$63,800)→E(\$90,390)
		<i>i=4.5%</i>	C(\$20,620)→A(\$27,060)→D(\$48,990)→B(\$55,400)→E(\$85,610)
	<i>t=20</i>	<i>i=2.5%</i>	C(\$17,220)→A(\$24,870)→D(\$45,460)→B(\$48,100)→E(\$62,980)
		<i>i=3.5%</i>	C(\$14,660)→A(\$19,780)→D(\$35,360)→B(\$38,930)→E(\$57,110)
		<i>i=4.5%</i>	C(\$12,390)→A(\$15,780)→D(\$27,710)→B(\$31,690)→E(\$50,330)
	<i>t=30</i>	<i>i=2.5%</i>	C(\$10,610)→A(\$14,160)→D(\$26,970)→B(\$28,490)→E(\$38,070)
		<i>i=3.5%</i>	C(\$8,540)→A(\$10,590)→D(\$19,810)→B(\$21,810)→E(\$32,520)
		<i>i=4.5%</i>	C(\$6,780)→A(\$7,930)→D(\$14,590)→B(\$16,670)→E(\$26,860)
n=75	<i>t=10</i>	<i>i=2.5%</i>	C(\$32,450)→A(\$47,800)→D(\$89,150)→B(\$93,050)→E(\$109,890)
		<i>i=3.5%</i>	C(\$27,530)→A(\$37,950)→D(\$69,400)→B(\$75,250)→E(\$101,010)
		<i>i=4.5%</i>	C(\$23,730)→A(\$30,900)→D(\$55,470)→B(\$62,260)→E(\$92,360)
	<i>t=20</i>	<i>i=2.5%</i>	C(\$23,680)→A(\$34,780)→D(\$64,830)→B(\$67,490)→E(\$82,160)
		<i>i=3.5%</i>	C(\$18,640)→A(\$25,640)→D(\$46,850)→B(\$50,680)→E(\$69,720)
		<i>i=4.5%</i>	C(\$14,830)→A(\$19,270)→D(\$34,570)→B(\$38,730)→E(\$58,510)
	<i>t=30</i>	<i>i=2.5%</i>	C(\$16,560)→A(\$24,590)→D(\$45,530)→B(\$47,820)→E(\$59,840)
		<i>i=3.5%</i>	C(\$12,170)→A(\$16,890)→D(\$30,660)→B(\$33,480)→E(\$47,120)
		<i>i=4.5%</i>	C(\$8,990)→A(\$11,760)→D(\$20,990)→B(\$23,720)→E(\$36,460)

Table 11.16: Ranking Orders of LCCs for Each Condition (Deep Water)

Condition			Ranking Order (Most Cost-Effective to Least Cost-Effective)
n=35	<i>t=10</i>	<i>i=2.5%</i>	C(\$45,060)→A(\$51,070)→D(\$76,040) →B(\$108,120) →E(\$133,640)
		<i>i=3.5%</i>	C(\$43,130)→A(\$45,560)→D(\$66,500)→B(\$98,120)→E(\$130,050)
		<i>i=4.5%</i>	A(\$40,680)→C(\$40,750)→D(\$58,320)→B(\$89,120)→E(\$122,340)
	<i>t=20</i>	<i>i=2.5%</i>	C(\$25,090)→A(\$27,380)→D(\$39,320)→E(\$53,960) → B(\$61,140)
		<i>i=3.5%</i>	C(\$22,780)→A(\$23,180)→D(\$32,380)→E(\$51,870)→B(\$52,950)
		<i>i=4.5%</i>	A(\$19,580)→C(\$20,300)→ D(\$26,720)→B(\$45,530)→E(\$48,050)
	<i>t=30</i>	<i>i=2.5%</i>	C(\$7,810)→A(\$8,710)→D(\$12,620)→E(\$16,490)→B(\$19,330)
		<i>i=3.5%</i>	C(\$6,780)→A(\$7,120)→D(\$10,070)→E(\$15,070)→B(\$16,100)
		<i>i=4.5%</i>	C(\$5,750)→ (\$5,760)→ D(\$8,000)→ B(\$13,230)→E(\$13,240)
n=50	<i>t=10</i>	<i>i=2.5%</i>	C(\$56,490)→A(\$68,210)→D(\$102,830)→E(\$127,490) →B(\$150,330)
		<i>i=3.5%</i>	C(\$51,260)→A(\$57,750)→D(\$85,370)→ E(\$123,530)→B(\$129,720)
		<i>i=4.5%</i>	C(\$46,560)→A(\$49,390)→D(\$71,630)→B(\$112,650)→E(\$116,990)
	<i>t=20</i>	<i>i=2.5%</i>	C(\$38,870)→A(\$45,390)→D(\$66,470)→E(\$86,060)→B(\$97,810)
		<i>i=3.5%</i>	C(\$33,100)→A(\$36,090)→D(\$51,710)→E(\$78,050)→ B(\$79,170)
		<i>i=4.5%</i>	C(\$27,980)→A(\$28,800)→D(\$40,520)→B(\$64,230)→E(\$68,780)
	<i>t=30</i>	<i>i=2.5%</i>	C(\$23,950)→A(\$25,850)→D(\$39,430)→E(\$52,030)→B(\$57,930)
		<i>i=3.5%</i>	C(\$19,290)→A(\$19,320)→D(\$28,970)→B(\$44,350)→E(\$44,440)
		<i>i=4.5%</i>	A(\$14,480)→C(\$15,300)→D(\$21,340)→B(\$33,890)→E(\$36,700)
n=75	<i>t=10</i>	<i>i=2.5%</i>	C(\$73,270)→A(\$87,230)→D(\$130,350)→E(\$150,180)→B(\$189,210)
		<i>i=3.5%</i>	C(\$62,160)→A(\$69,260)→D(\$101,470)→E(\$138,040)→B(\$153,010)
		<i>i=4.5%</i>	C(\$53,570)→A(\$56,380)→D(\$81,100)→E(\$126,220)→B(\$126,600)
	<i>t=20</i>	<i>i=2.5%</i>	C(\$53,470)→A(\$63,480)→D(\$94,790)→E(\$112,280)→B(\$137,220)
		<i>i=3.5%</i>	C(\$42,100)→A(\$46,800)→D(\$68,500)→E(\$95,280)→B(\$103,060)
		<i>i=4.5%</i>	C(\$33,470)→A(\$35,170)→D(\$50,550)→B(\$78,760)→E(\$79,960)
	<i>t=30</i>	<i>i=2.5%</i>	C(\$37,380)→A(\$44,870)→D(\$66,570)→E(\$81,770)→B(\$97,230)
		<i>i=3.5%</i>	C(\$27,480)→A(\$30,820)→D(\$44,840)→E(\$64,390)→B(\$68,080)
		<i>i=4.5%</i>	C(\$20,300)→A(\$21,470)→D(\$30,690)→B(\$48,230)→E(\$49,830)

11.7.4. Parametric Study

As discussed previously, there are many factors affecting the LCCA results. For example, repair costs may not remain constant as predicted, or a discount rate may fluctuate over time during the bridge service life, or traffic demand may not follow the projected path with a bridge service life shortened by heavy traffic. Furthermore, factors are also not

independent on each other. As such, the impact of primary factors on the LCCA results needs to be studied extensively.

11.7.4.1. Discount Rate

In the LCCA, future cost and benefit streams should be estimated in constant dollars and discounted to the present dollars using a real discount rate. As such, the discount rates employed in the LCCA are critical parameters and should reflect historical trends over long periods of time. The mathematical relationship between the discount rate (i_{dis}), the interest rate (i_{int}), and the inflation rate (i_{inf}) is as follows (Demos, 2006):

$$i_{dis} = \frac{(1+i_{int})}{(1+i_{inf})} - 1 \quad (\text{Eq. 11-5})$$

Since the discount rate has been quite stable historically, FHWA recommended standard discount rates of 2.5%, 3.5% and 4.5% for use in state/municipal projects, federal/long-term projects, and privately funded projects, respectively (Wilde et al., 1999). Therefore, the deterministic analysis was performed with these three recommended discount rates in this study as the sensitivity analysis.

The LCCs of initial repair Year 10 for the 35-year analysis period are presented in Figures 17 as examples to show the effects of discount rates on the life-cycle costs. In the two repair scenarios, the LCC amounts decrease as discount rates increase from 2.5% to 4.5%. For example, in the shallow water case, the LCC of Company E is \$27,980 in the discount rate of 2.5%. The LCC amounts decreased to \$24,960 and \$22,290 as the discount rate changed to 3.5% and 4.5%, respectively. This shows that

the change of discount rates may greatly affect the anticipated life-cycle costs. The findings are also true for the cases of initial repair at Year 20 and Year 30, or for other companies.

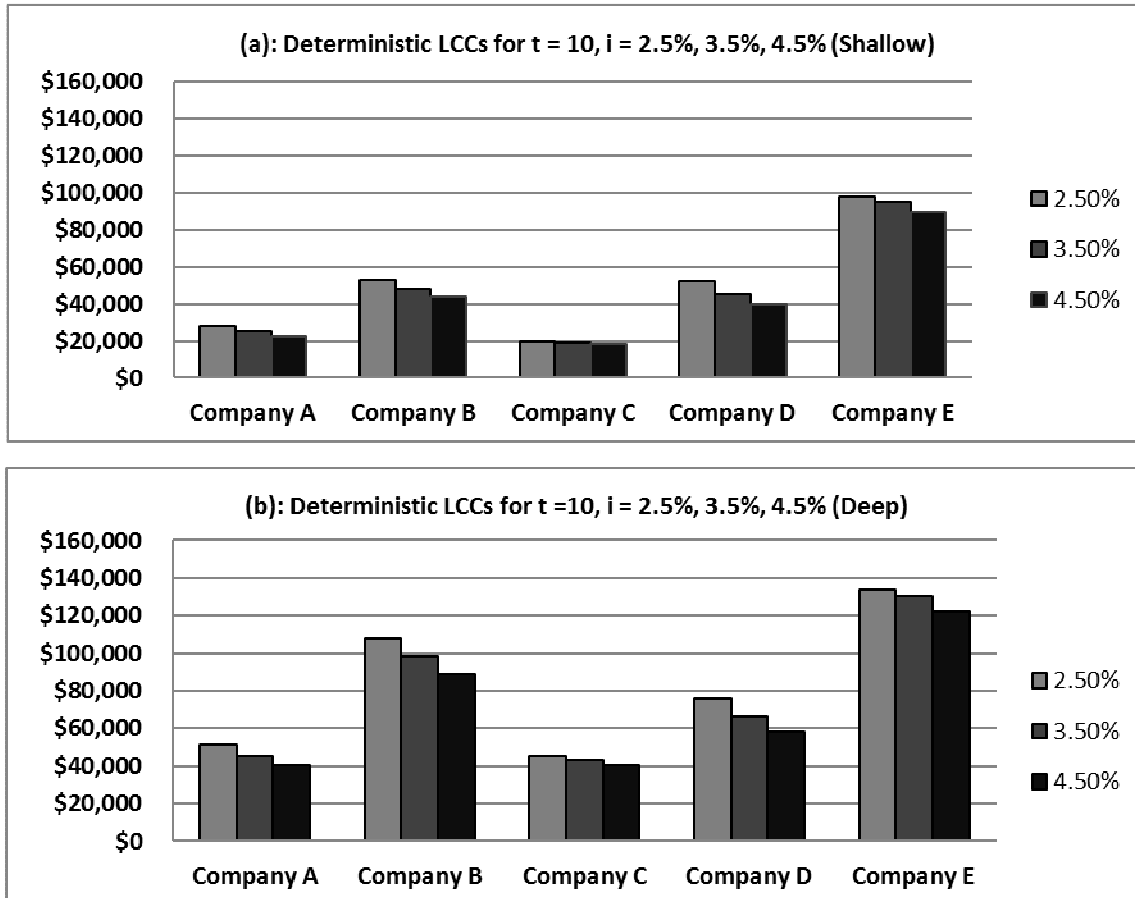


Figure 11.17: NPVs of Deterministic LCCA under Different Discount Rates ($n=35$)

The LCCs of initial repair Year 10 for the analysis periods of 50 years and 75 years are presented in Figure 10.18 and Figure 10.19, respectively. The same tendency has been observed in both analysis periods: the LCCs decreased when discount rates increased for all companies and initial repair time.

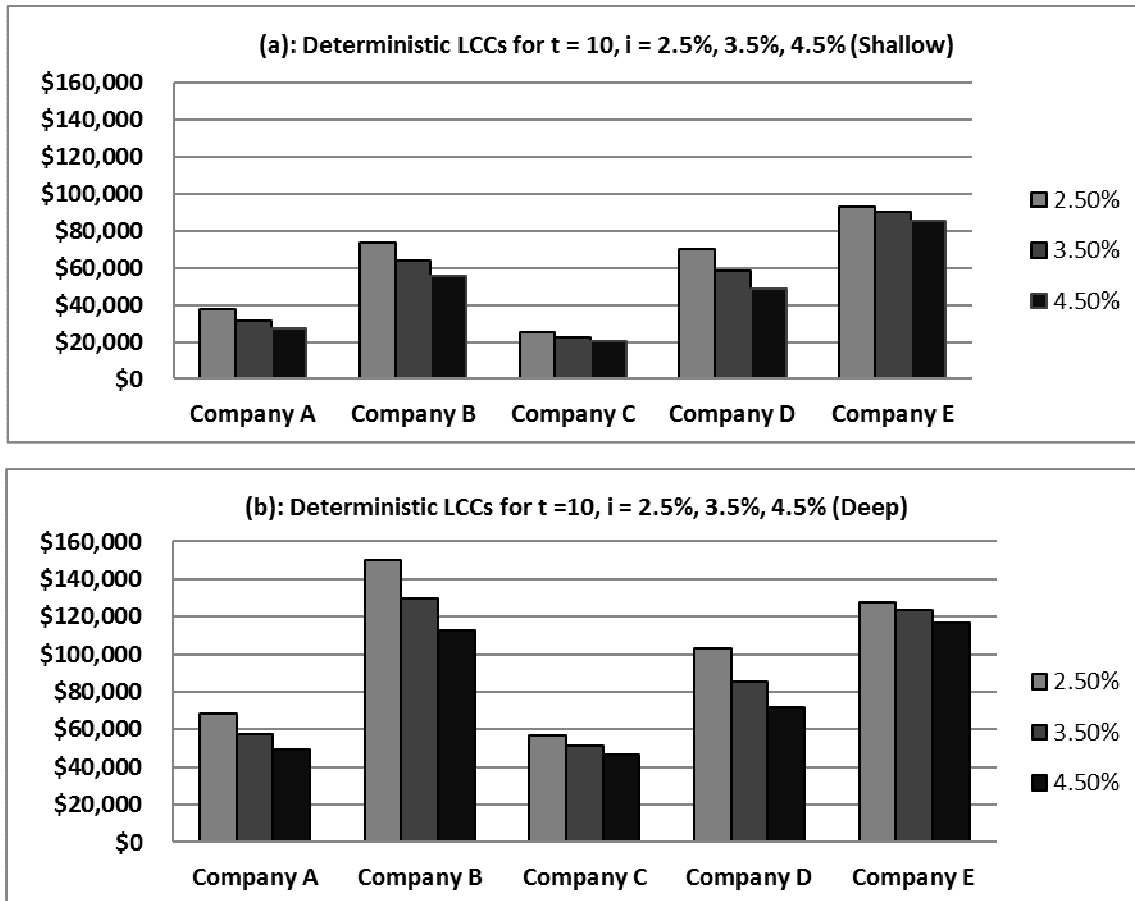


Figure 11.18: NPVs of Deterministic LCCA under Different Discount Rates (n=50)

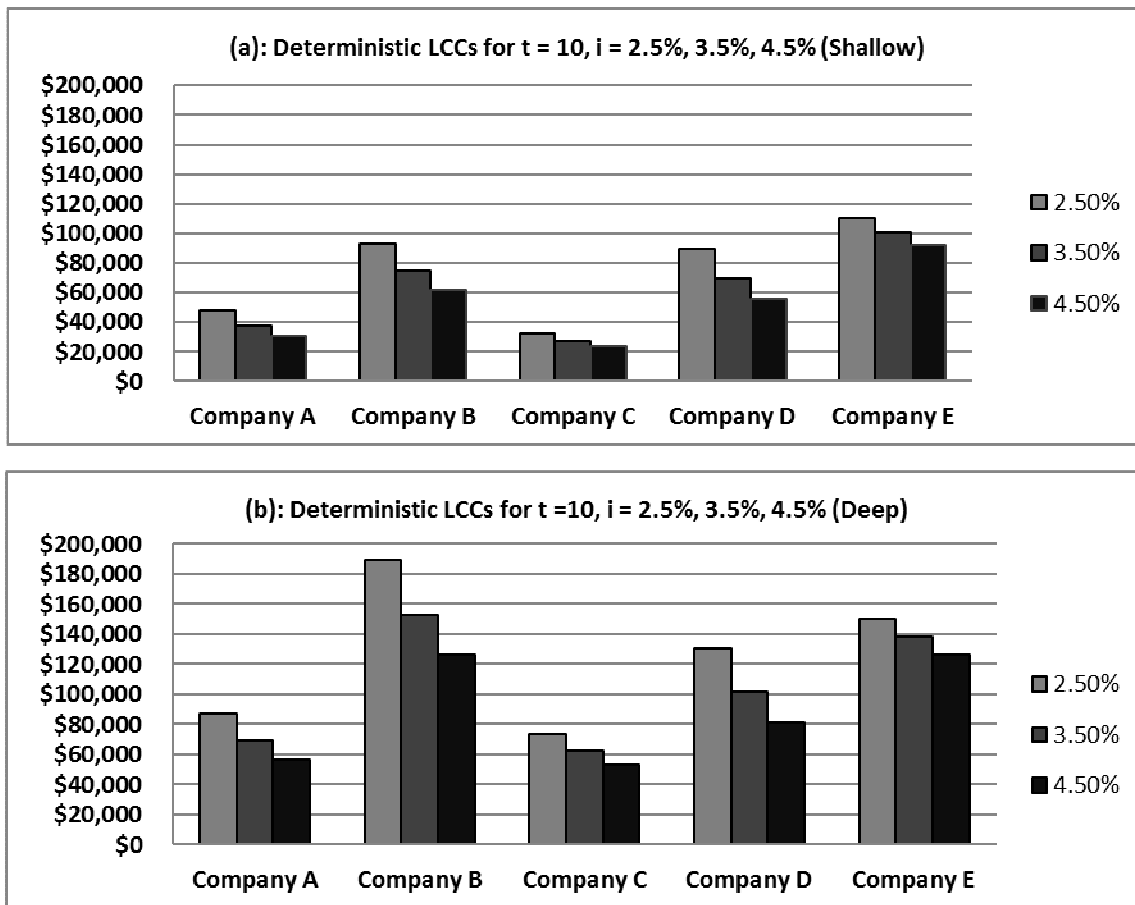


Figure 11.19: NPVs of Deterministic LCCA under Different Discount Rates ($n=75$)

Since discount rates may fluctuate over time during the facility service life-cycle, the deterministic analysis for three discrete discount rates may be insufficient for decision makers to reach a decision with adequate confidence. For example, suppose that the median estimate for the life-cycle cost of one repair alternative is less than other repair alternatives. But, if the probability distribution of the alternative spreads wider than other repair alternatives, it may have a larger chance that its actual costs exceed other choices. As such, the probabilistic analysis was performed to account for the uncertainty of discount rates in both shallow water case and deep water case. In this

analysis, a discount rate was assumed to have a triangle probability distribution with a minimum rate of 2.5%, the most likely rate of 3.5%, and a maximum rate of 4.5%.

The LCC distributions of five companies were presented in both relative and cumulative probability scales, shown as in Figure 10.20 and Figure 10.21 for shallow water case and deep water case, respectively. In a relative scale curve, the wider the curve is, the greater the variability is. As shown in the figure, Company C has the narrowest distribution curve, which means that the cost of the company has the least uncertainty. In a cumulative scale curve, the variability for the proposed alternative is inversely proportional to the slope of the cumulative scale curve. The slope of Company C is steepest, meaning that it has the least variability which is also consistent with its relative curve. Another observation from its cumulative curve is that about 90-percent chance of LCC from Company C will not exceed \$30,000. In short, Company C is the repair solution with the lowest LCC, while having the least chance of repair cost overrun.

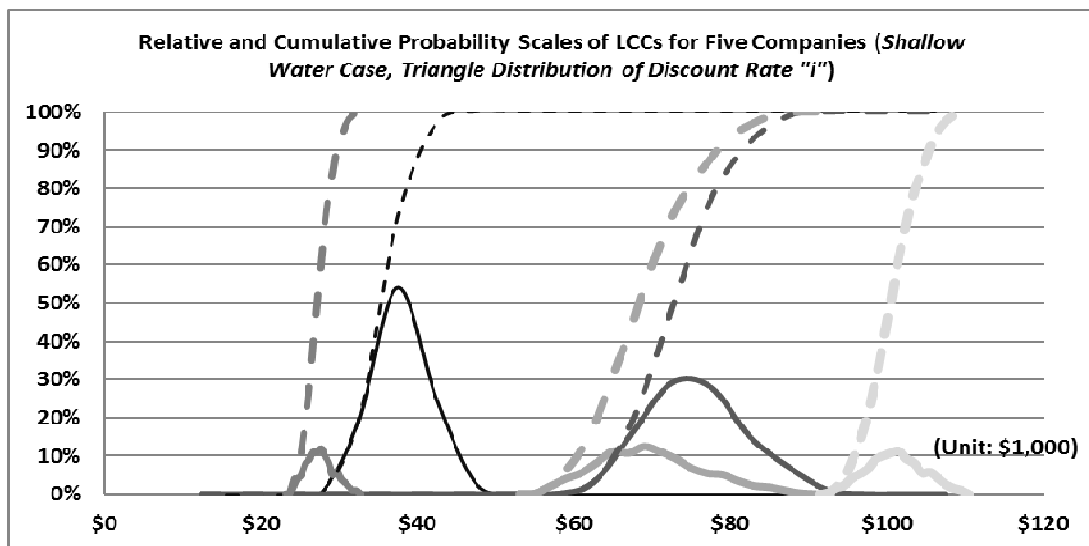


Figure 11.20: Probability Scales of LCCs for Five Companies under Probabilistic Interest Rates (Shallow Water, $n=75$)

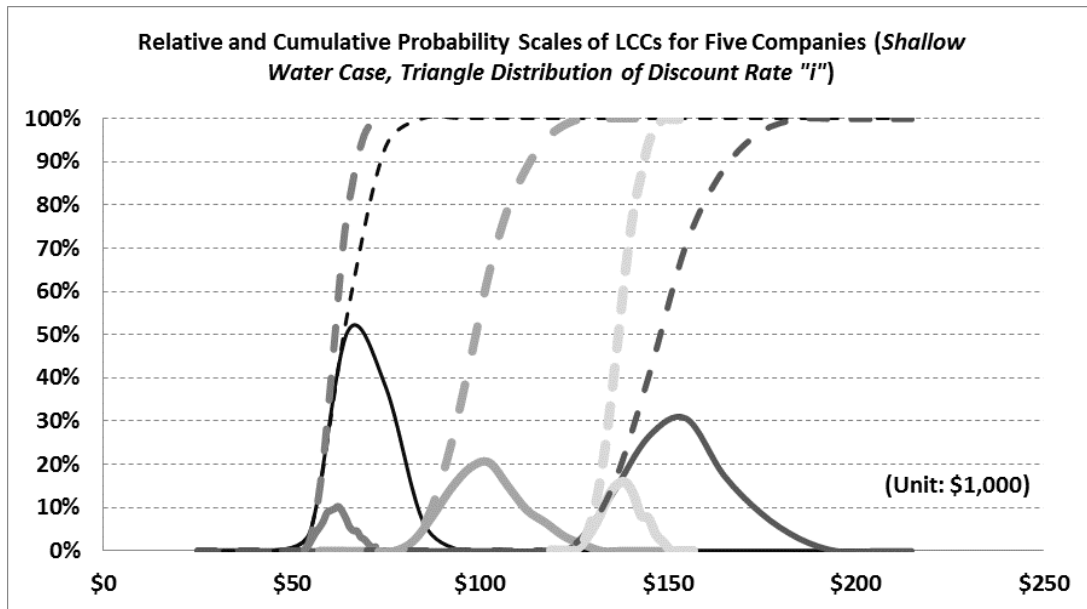


Figure 11.21: Probability Scales of LCCs for Five Companies under Probabilistic Interest Rates (Deep Water, $n=75$)

11.7.4.2. Initial Repair Time

The initial repair time is another important parameter. Different initial repair time usually leads to different repair strategies and net present values. The results of LCCA at different initial repair time are shown in Figures 22(a) and 22 (b), given the analysis period is 35 years and the discount rate is 2.5%. Taking Company E in shallow water case as the example, the LCC of Company E is \$97,790 when the initial repair occurs at Year 10. The repair amounts decreased to \$39,480 and \$12,060 as the first repair happens at Year 20 and 30, respectively. It means that the agency may save their repair funds greatly if they are able to build a more durable system and postpone their first repair of bridge piles. This is also true for the deep water repair case or for other companies.

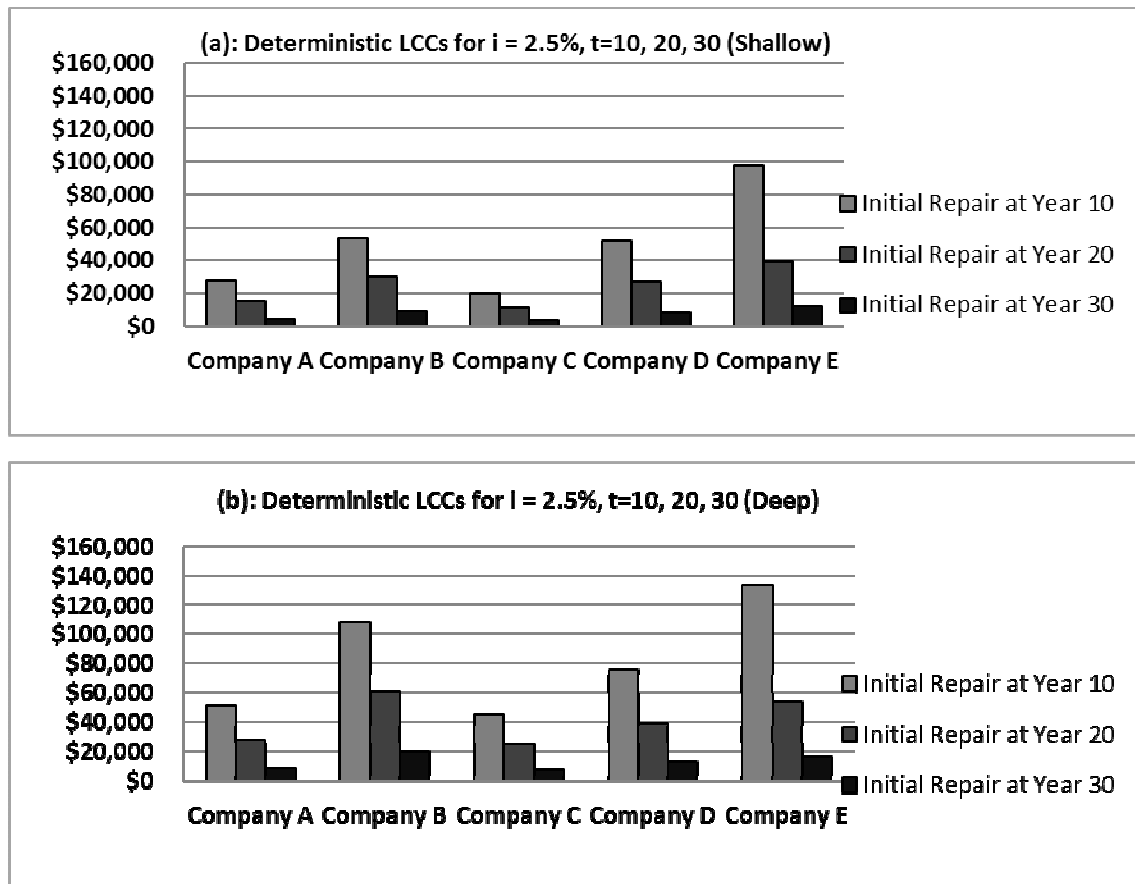
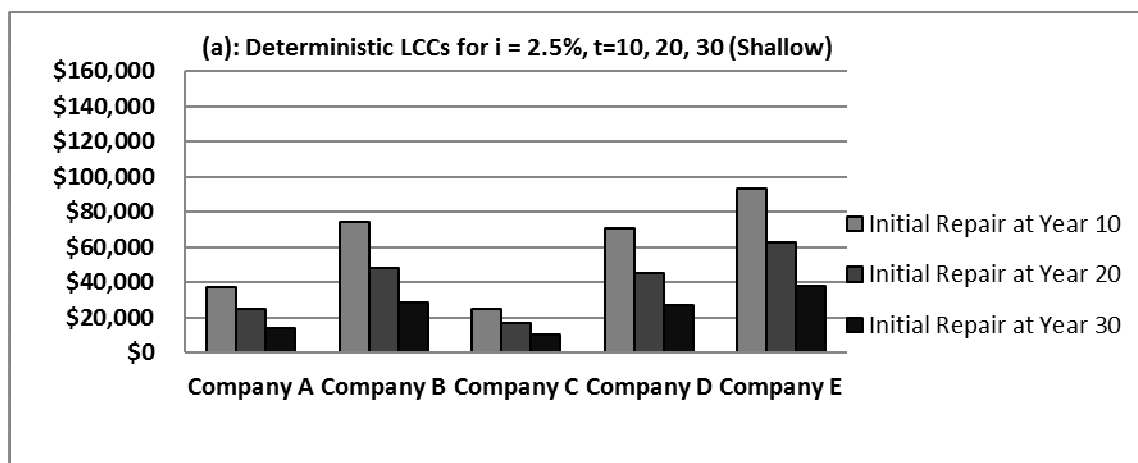


Figure 11.22: NPVs of Deterministic LCCA under Different Repair Time (n=35)

The results of LCCA at different initial repair time are shown in Figures 23 and 24 for analysis periods of 50-year and 75-year. The discount rate is still kept at the same rate of 2.5%. The same tendency of LCCs was also observed in these two cases.



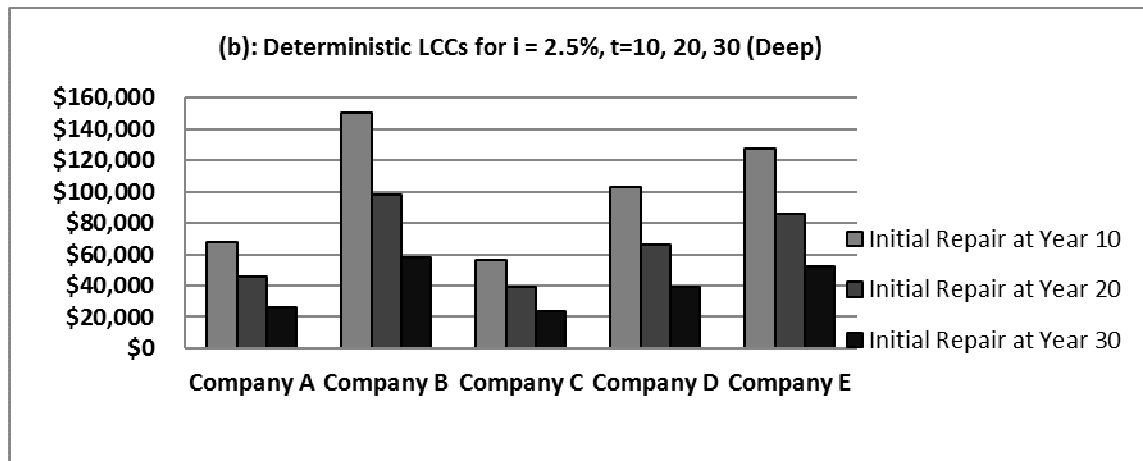


Figure 11.23: NPVs of Deterministic LCCA under Different Repair Time (n=50)

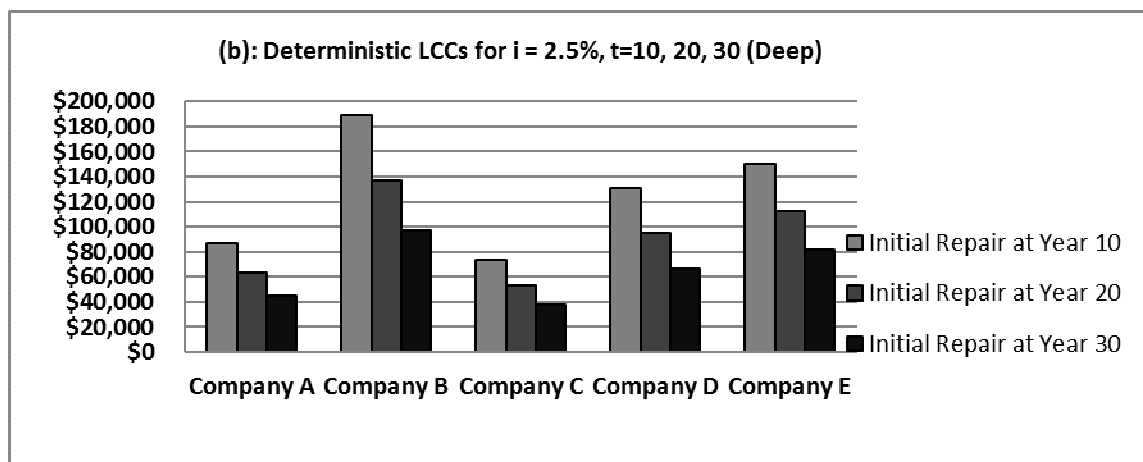
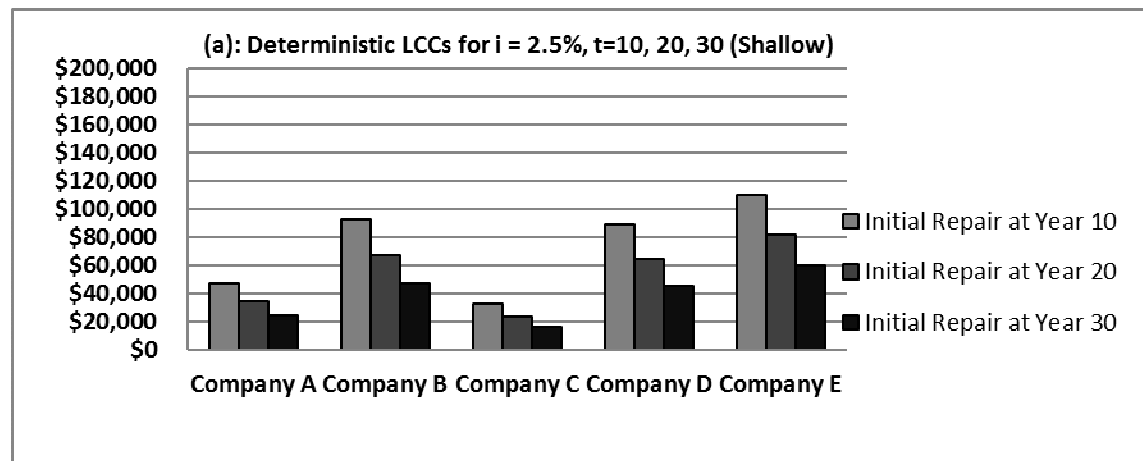


Figure 11.24: NPVs of Deterministic LCCA under Different Repair Time (n=75)

As stated previously, the deterministic analysis may not account for the uncertainty of changes in initial repair time caused by objective or subjective decisions. This

necessitated a probabilistic analysis by varying initial repair time. To do this, initial repair time was assumed to have a triangle probability distribution with a minimum time of 10 years, the most likely time of 20 years, and a maximum time of 30 years. The risk profiles of five companies were presented in Figure 10.25 and Figure 10.26, in both relative and cumulative probability scales. The figures indicated that Company C is still the best repair strategy with lowest LCC amount and least chance to overrun.

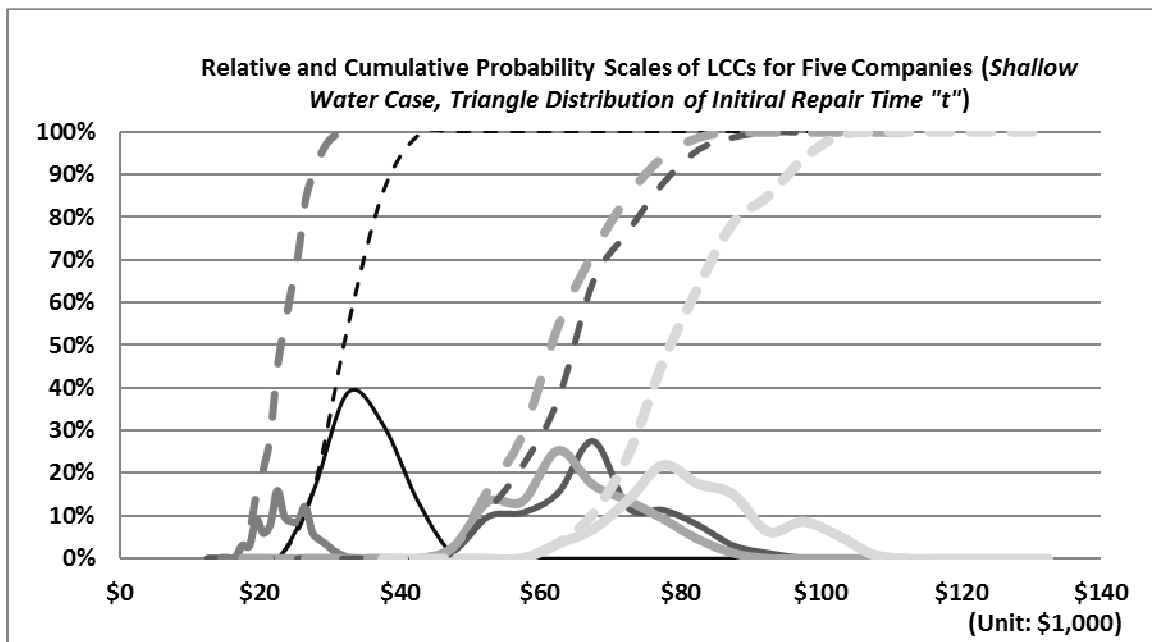


Figure 11.25: Probability Distributions of LCCs for Five Companies under Probabilistic Repair Time (Shallow Water, n=75)

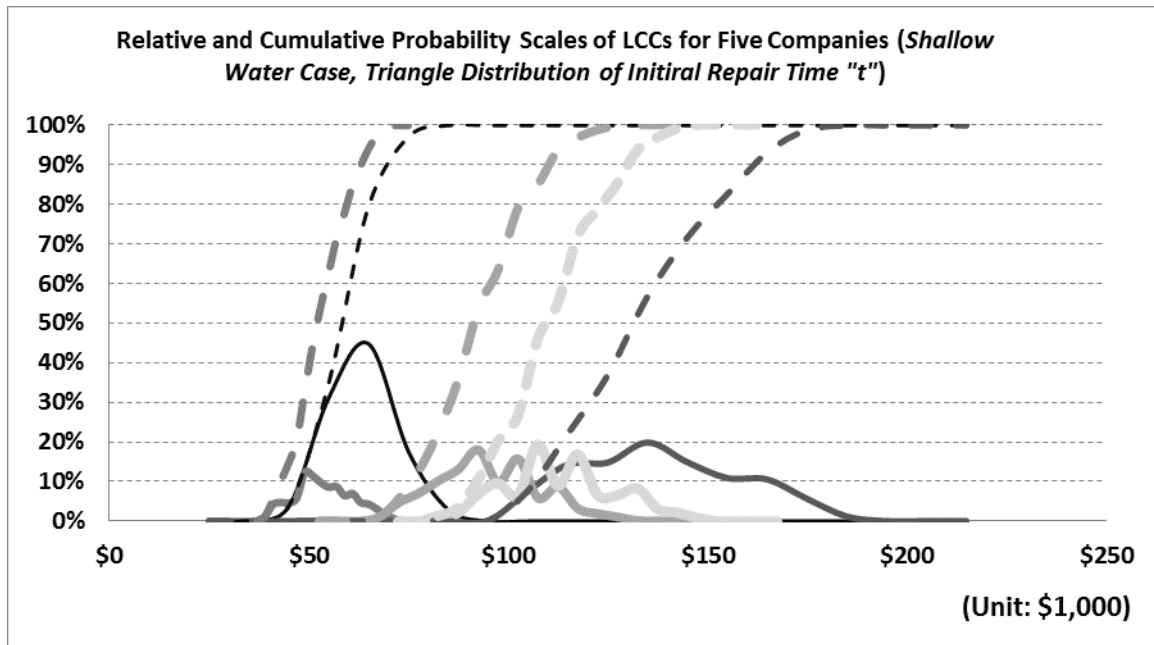


Figure 11.26: Probability Distributions of LCCs for Five Companies under Probabilistic Repair Time (Deep Water, $n=75$)

11.7.4.3. Analysis Period

Analysis period can be defined as the time period over which an initial construction cost and future maintenance costs are evaluated for different project alternatives. There is no clear-cut method to determine the period. The analysis period should be long enough to incorporate the cost of at least one rehabilitation activity for all alternatives, and can be determined by considering a reasonable service life (Demos, 2006). The service lives of highway bridges in North America are estimated from 35 to 50 years. However, the American Association of State Highway and Transportation Officials (AASHTO) specified that the service life of new bridges should be 75 years (Hawk, 2003).

In this study, analysis periods were chosen as 35, 50 and 75 years in a deterministic way. The results for different analysis periods were presented in Figure 10.27 and

Figure 10.28 for shallow water case and deep water case, respectively. Discount rates were kept at the same values of 2.5% for all of the scenarios. The figures indicated that the shorter the analysis period, the less repair activities and the associated life-cycle repair costs. Although the order of repair cost was on a case-by-case basis, Company E always shows the highest LCC amount, which means the steel-based solution is not so cost-effective, compared with the FRP-based solutions.

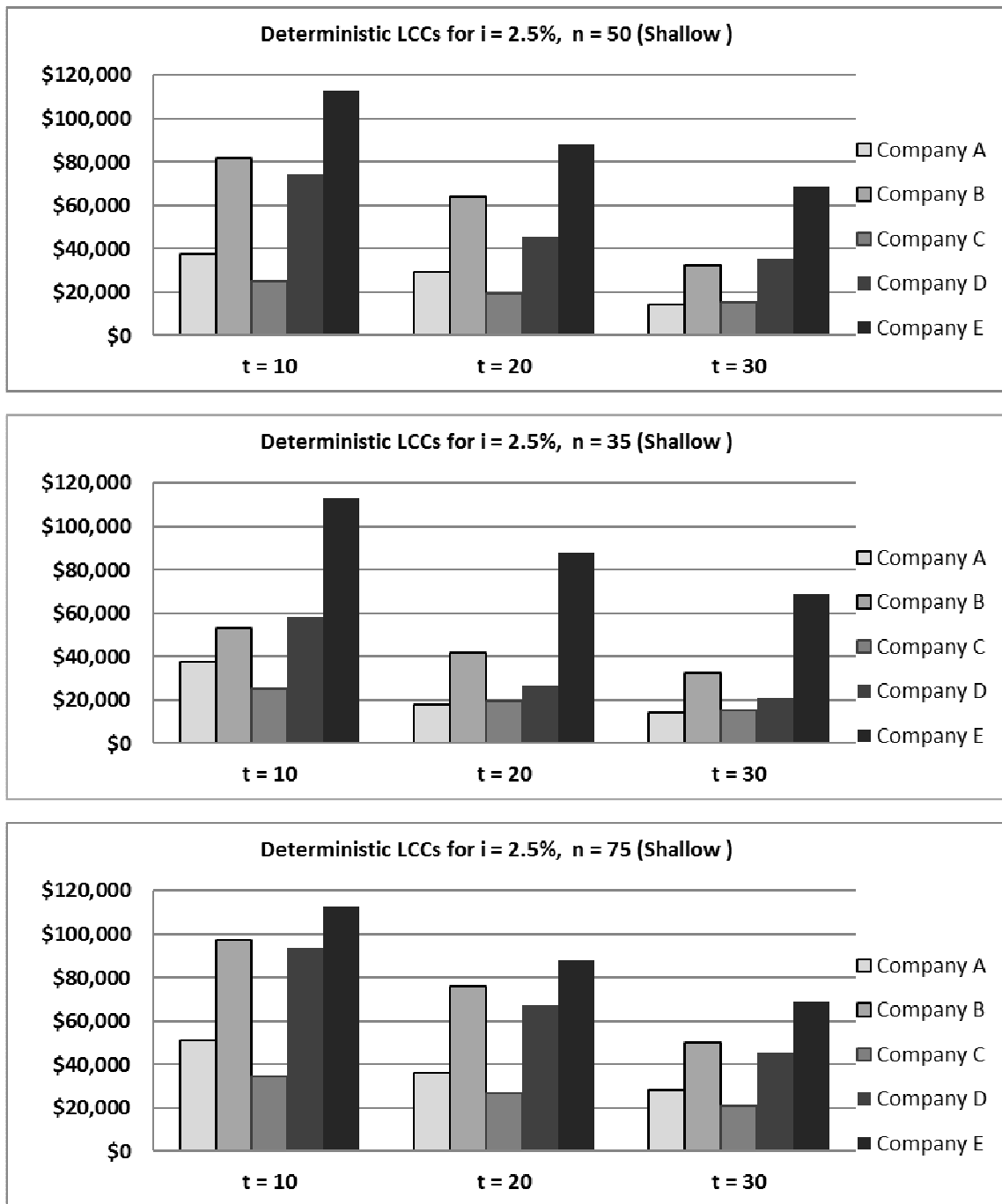


Figure 11.27: NPVs of Deterministic LCCA under Different Analysis Periods and Initial Repair Time (Shallow Water, i=2.5%)

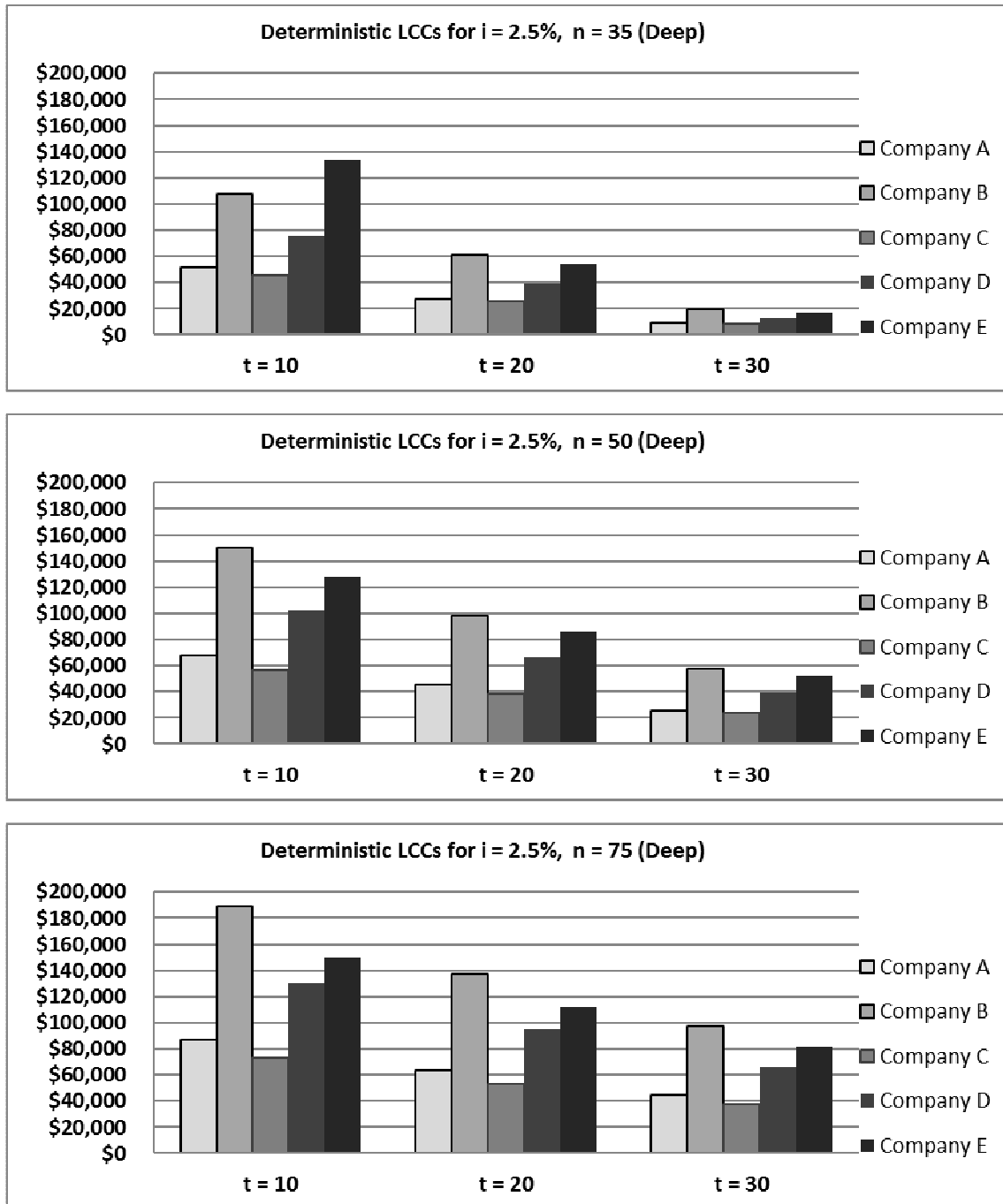


Figure 11.28: NPVs of Deterministic LCCA under Different Analysis Periods and Initial Repair Time (Deep Water, $i=2.5\%$)

Chapter 12. Field Implementation

This chapter summarizes the details of a field implementation that was conducted to evaluate practical challenges associated with installing the proposed repair systems in ‘real-world’ scenarios. The chapter summarizes the identification of the bridge site, evaluation of the existing conditions, design of the repair systems, and installation of the repairs.

12.1. Identification of Bridge Site

The research team worked with the members of the Texas Department of Transportation (TXDOT) project monitoring committee (PMC) to identify a suitable candidate bridge site for the field installation. The selected bridge is in district 15, county 07 (Atascosa), control section 0328-06, structure 07, maintenance section 14, on State Highway 97 over Chiltipin Creek. The bridge is located at 28°49'03.2"N, 98°44'38.7"W.

12.2. Evaluation of Existing Piles and Site Conditions

The bridge consists of five simple spans with concrete pan girders over concrete bent caps on steel H-piles. Records indicate that the bridge was built in 1955 and widened in 1963. Routine inspections have been conducted every two to three years since 1991, with the most recent inspection on record having been completed on 12/29/2014. The most recent inspection indicates that steel piles at bents 2, 3, and 4 from the northeast abutment exhibit corrosion and flaking of corrosion products near the ground line and water level with estimated section loss of 20 – 25% of the cross-sectional area of the piles. According to the plans, bent 1 is located at the northeast abutment and cannot be seen from underneath the structure.

In preparation for the field repair installation, the research team performed a preliminary site visit to inspect the site conditions, identify three candidate piles for the repair implementation and measure the as-found dimensions of the candidate piles. The field visit was conducted on Monday, July 6, 2015. The site visit was conducted by Dr. Mina Dawood, Hossein Karagah, and Cheng Shi from the University of Houston (UH) and Aaron Garza from the Texas Department of Transportation (TXDOT). The group identified three candidate piles, shown in Figure 9.1, at bent 2 from the north east abutment for implementation of the repairs. The three candidate piles are those labeled 3, 4, and 5 in the figure. The estimated high water level is shown by the dashed line in the figure based on the observed corrosion and the remaining paint on the surface of the piles.

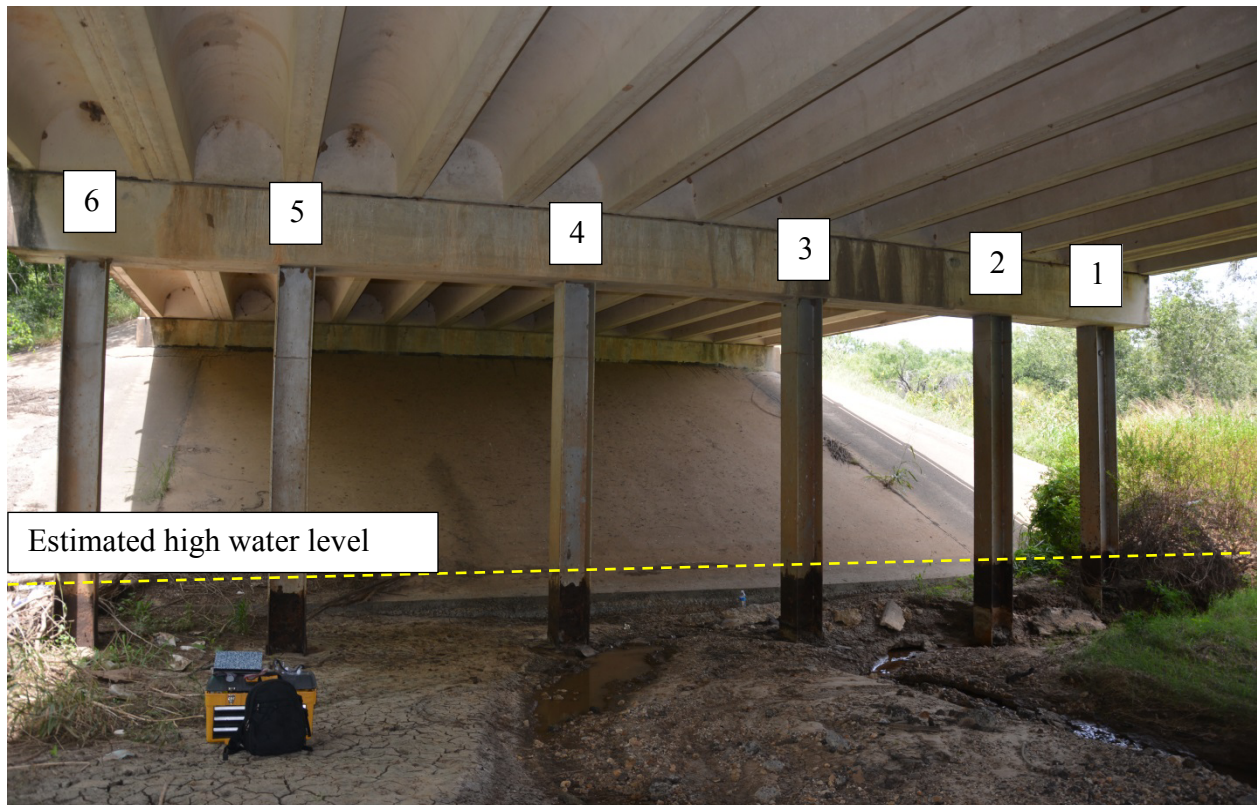
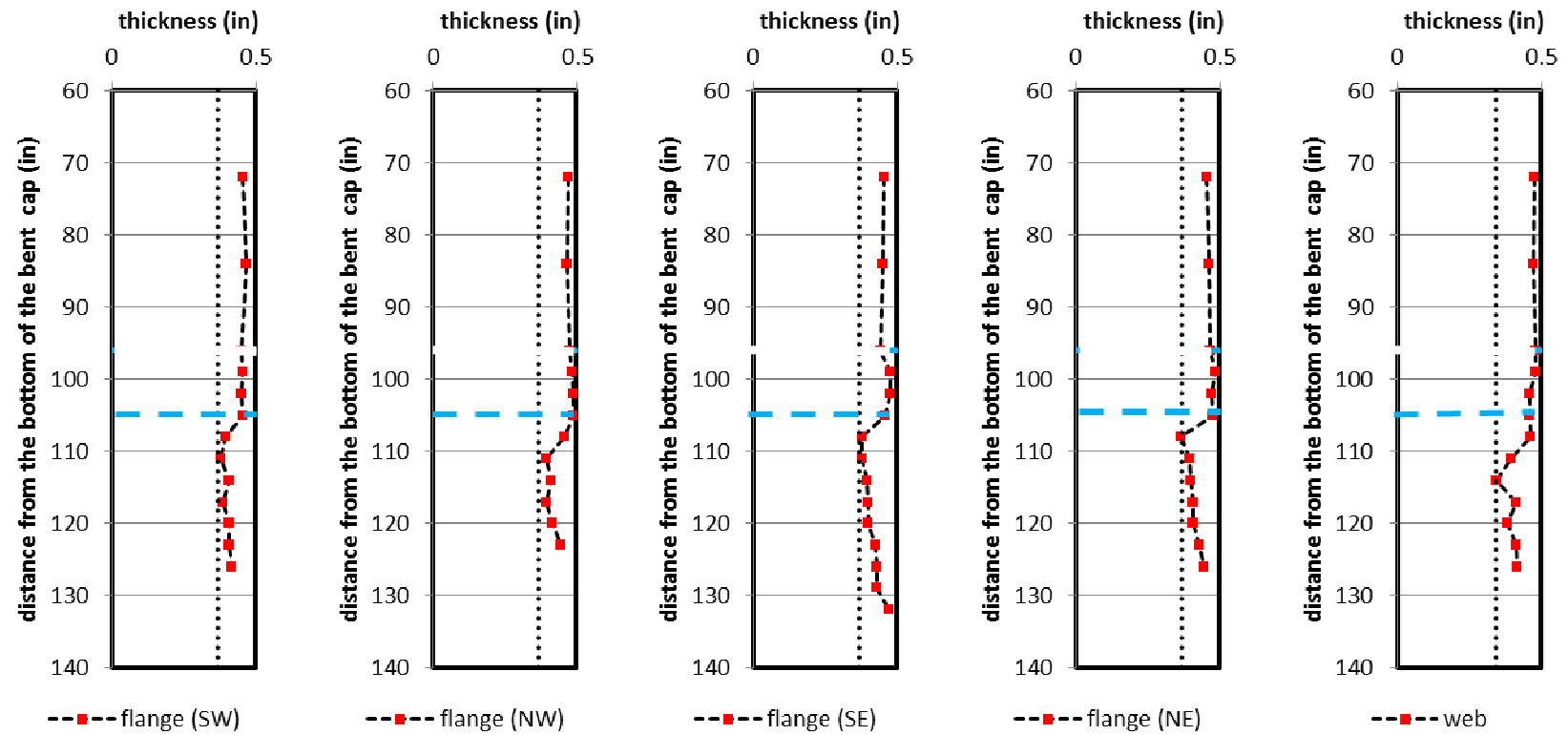


Figure 12.1: Candidate piles at bent 2 from northeast abutment, view towards northeast.

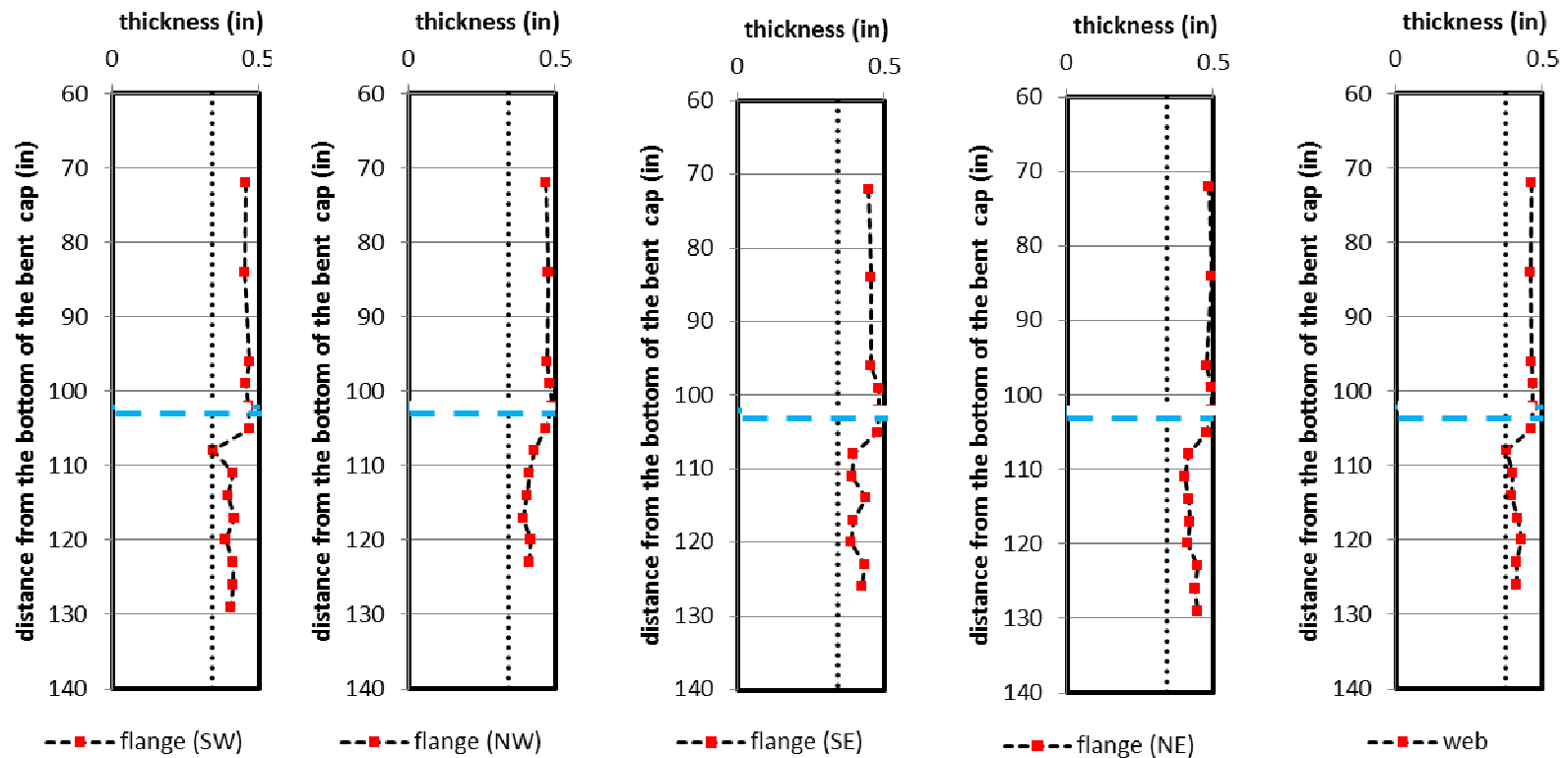
The exposed length of each pile was measured from the underside of the bent cap to the ground surface on the east and west of each pile. The piles were assumed to be embedded in soft clay and the effective length was calculated based on the AASHTO (2012) procedure. The widths of each flange and depth of the section were measured at one section above the estimated high water level on each pile. The thicknesses of the flanges and webs of the piles were measured at three locations 12 inches apart in the un-corroded region above the estimated high water level.

The research team excavated around the base of the piles to a depth of approximately 2 ft. below existing ground surface to measure the remaining thickness of in the corroded region of the piles. The piles were cleaned using hand tools to remove pack rust and debris on the pile surface. No reduction of flange width or web depth was observed by visual inspection of the corroded region. The thicknesses of the flanges and the web were measured in the corroded region every 3 in. until the measured thickness was within approximately 10% of the average measured un-corroded thickness of the element. The measured thickness profiles of the flanges and webs of the three candidate piles are plotted in Figure 12.2. In the figure the horizontal dashed line indicates the location of the estimated high water level while the vertical dotted line indicates the minimum measured thickness for each pile.

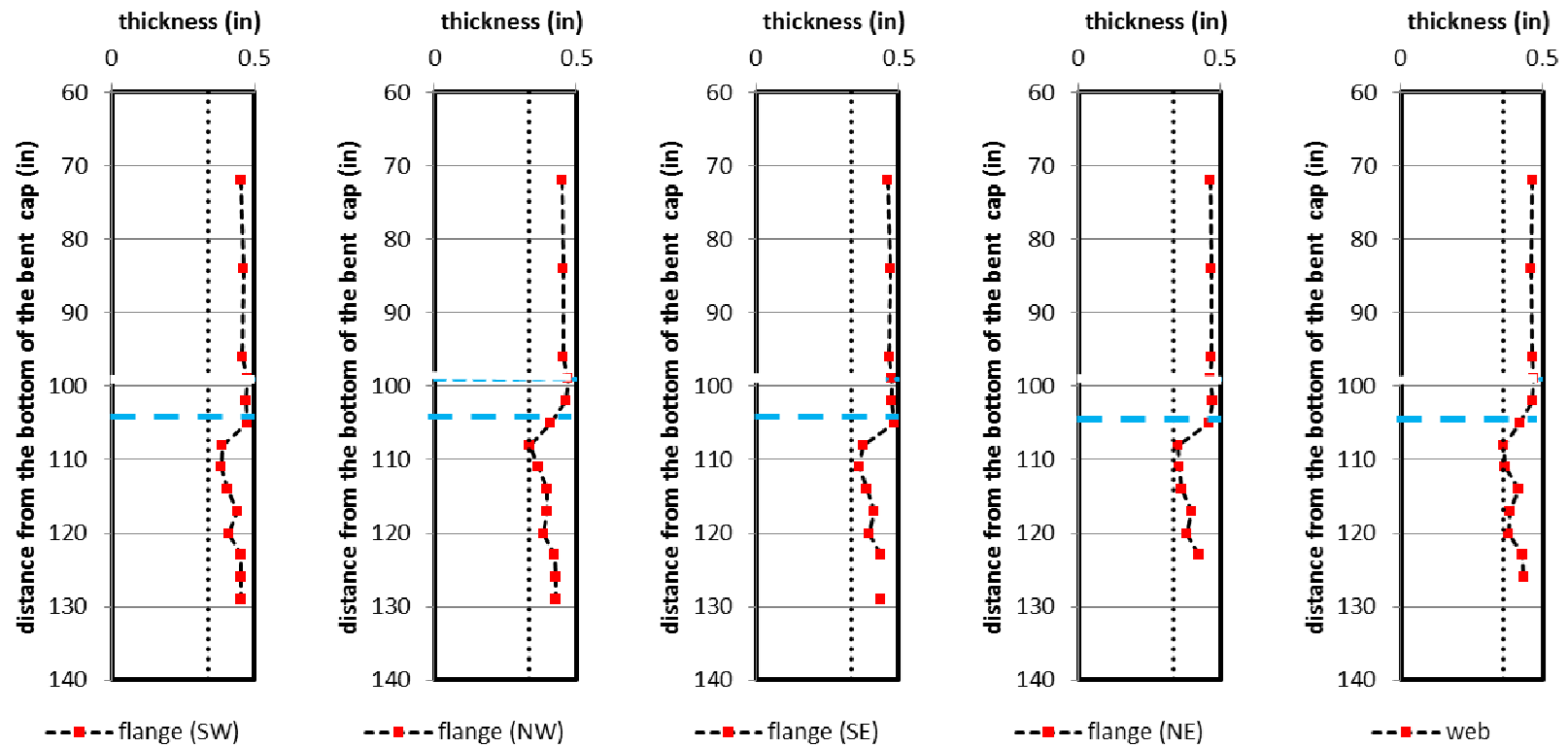
Both FRP repair systems described in this study are patented by Professor Mo Ehsani; U.S. Patent #8,650,831 and #9,376,782



(a) Measured thickness profile for elements of pile 3



(b) Measured thickness profile for elements of pile 4



(c) Measured thickness profile for elements of pile 5

Figure 12.2: Measured thickness profiles of flanges and webs of three candidate bridge piles for field installation of repairs

The measured dimensions of the piles are given in Table 12.1. The nominal axial capacities of the three piles were calculated according to the AASHTO guidelines (2012) using the nominal dimensions (according to AISC (2011) for an HP12×53 pile and an assumed steel yield strength of 33 ksi. The remaining capacities of the three piles were calculated according to the AISI (2012) EWM. To calculate the remaining capacity, the thickness of the flanges and webs were assumed to be constant within the corroded region and equal to the minimum measured value for each element. That is, for a given pile the flange thickness in the corroded region was assumed to be constant and equal to the minimum measured flange thickness for that candidate pile and similarly for the web. The calculated capacities and the intermediate parameters are summarized in Table 12.1 Inspection of the table indicates that piles exhibited losses of cross-sectional area of between 19 – 22% compared to the nominal sectional dimensions and 23 – 26% compared to the measured un-corroded sectional dimensions. The calculated remaining capacities of the piles were between 78 – 82% of the calculated nominal capacities. This corresponds to an average loss of capacity of 20%. Inspection of the table further indicates that the corrosion patterns and calculated remaining capacities were similar for all three piles.

Table 12.1: Measured Properties and Calculated Capacities of Candidate Piles

		Pile3	Pile4	Pile5
flange thickness	t_f [in]	0.459	0.467	0.462
web thickness	t_w [in]	0.474	0.462	0.462
corroded flange thickness	$t_{f,c}$ [in]	0.366	0.342	0.335
corroded web thickness	$t_{w,c}$ [in]	0.342	0.376	0.361
flange width	b_f [in]	12.125	12.125	12.188
depth of section	d [in]	11.781	11.844	11.781
depth of corroded section	d_c [in]	11.595	11.594	11.527
length of corroded region	L_c [in]	21	21	24
length of the entire pile	L [ft]	36	36	36
length of the pile above ground (clear length)	l [ft]	10.9	10.5	10.3
cross-sectional area (based on measured dimensions)	$A_{s,u}$ [in ²]	16.3	16.4	16.3
cross-sectional area (based on nominal dimensions)	A_s [in ²]	15.5	15.5	15.5
Corroded cross-sectional area	$A_{s,c}$ [in ²]	12.6	12.4	12.1
moment of inertia (strong axis)	I_x [in ⁴]	408	417	410
moment of inertia (weak axis)	I_y [in ⁴]	136	139	139
strong-axis radius of gyration	r_x [in]	5.00	5.05	5.02
weak-axis radius of gyration	r_y [in]	2.90	2.91	2.93
length of fixity (strong axis)	L_{fx} [ft]	9.85	9.90	9.87
length of fixity (weak axis)	L_{fy} [ft]	7.49	7.52	7.53
strong-axis effective length factor	K_x	1	1	1
weak-axis effective length factor	K_y	0.7	0.7	0.7
strong-axis effective length	$K_x(L_x+l)$ [ft]	20.8	20.4	20.1
weak-axis effective length	$K_y(L_y+l)$ [ft]	12.9	12.6	12.4
strong-axis pile slenderness	$K_x(L_x+l)/r_x$	49.8	48.5	48.1
weak-axis pile slenderness	$K_y(L_y+l)/r_y$	53.4	52.0	51.0
max. slenderness	$(KL/r)_{max}$	53.4	52.0	51.0
Nominal Axial Capacity (AASHTO)	(kips)	446	449	451
Remaining Axial Capacity (AISI-EWM)	(kips)	364	357	351

12.3. Repair Design

Since all three piles were similar, the resulting repair designs were similar. The details of the FRP-based and steel-based repair systems are summarized in Table 12.2 and Table 12.3, respectively. For the FRP-based repair, as an initial design trial, a similar jacket configuration to that used in the experimental program was considered. The design calculations indicate that the capacity of the system was adequate.

Table 12.2: Details of FRP-based Repair System^a

Number of GFRP Layers		2
GFRP Longitudinal Tensile Strength	[ksi]	83.4
Number of CFRP Layers		2
CFRP Longitudinal Tensile Strength	[ksi]	143
Diameter of FRP Jacket	[in]	18
Length of FRP Jacket	[ft]	4
Rebar Size		#4
Number of Rebars		4
Rebar Grade	[ksi]	60
Minimum Grout Compressive Strength	[ksi]	5
Threaded Anchor Size		None Needed

^aFRP jacket system to consist of Tyfo PR jacket and two layers of Tyfo SCH-41 carbon fiber saturated with Tyfo SW-1S epoxy or equivalent.

Table 12.3: Details of Steel-based Repair System

Bolt type		A325
Hole type		Standard
Bolt diameter	[in]	3/4
Bolt spacing	[in]	3
Bolt pretension	[kips]	28
Edge distance-longitudinal	[in]	1.5
Edge distance-transverse	[in]	1.5
Plate width	[in]	16
Plate length	[in]	39
Plate thickness	[in]	0.5
Total number of bolts ^a		52

^aBolts are to be installed in a slip-critical configuration. Faying surface to be prepared by coating the surface of the repair plates with a combination of Sherwin Williams Steel Spec Epoxy Primer and Zinc Clad II Ethyl Silicate or equivalent to achieve a coefficient of friction of 0.3 between the coated steel plates and the corroded pile in wet conditions.

12.4. Repair Installation

The field repair installation was conducted from Monday, November 30, 2015 to Tuesday, December 1, 2015 by Delta Structural LLC, under the supervision of Dr. Mina Dawood and Oswaldo Russian from the University of Houston, and Leon Flournoy, and Aaron Garza from the Texas Department of Transportation, Bridge Division.

The site conditions were assessed to confirm that there had been no material changes since the previous visit. As shown in Figure 12.3, site conditions were found to be generally consistent with those observed during the previous site visit.



Figure 12.3: Site conditions on November 30, 2015

The schematic positions of the repair systems are shown in Figure 12.4. The starting point for the FRP repair systems is 10 in. above the high water level, while for the steel based system it is 5.5 in. above the high water level. It was decided to implement the FRP based repairs on piles 3 and 5, while the steel based repair was installed on pile 4.

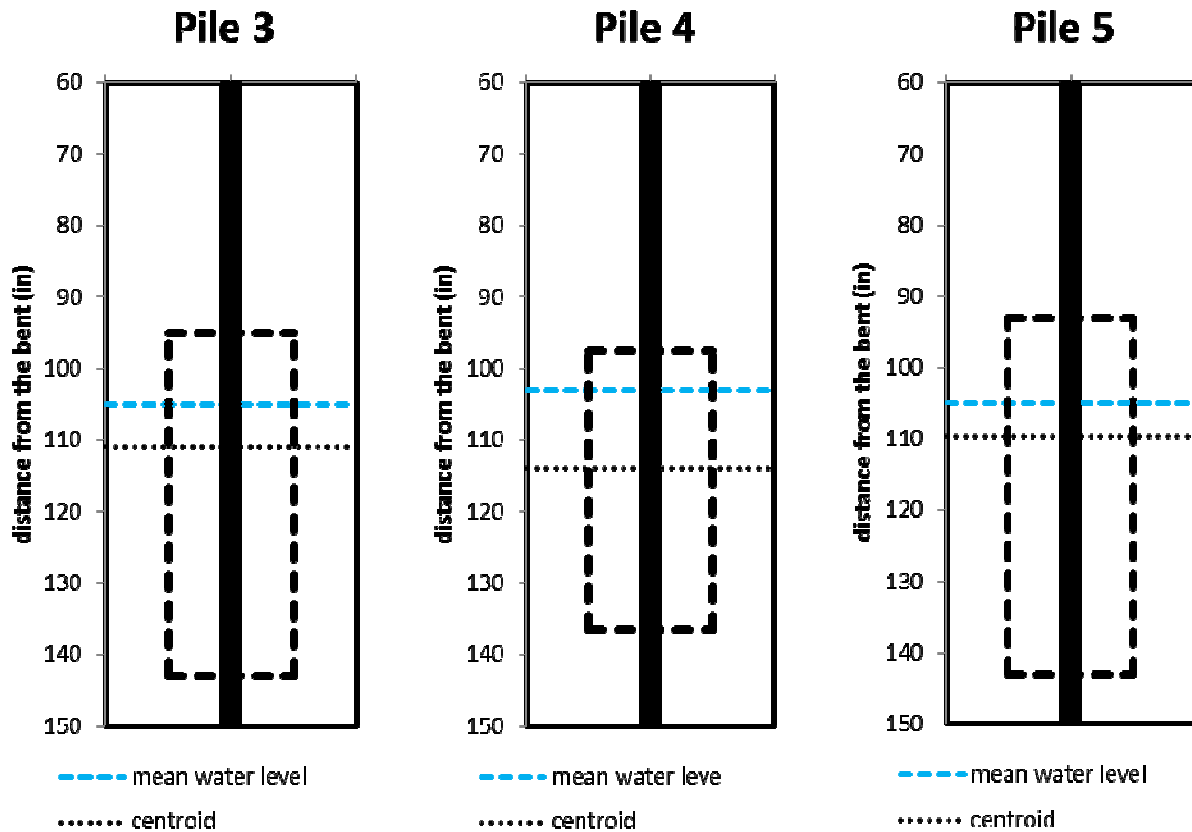


Figure 12.4: Updated high water levels and relative repair system positions

The contractor and research team proceeded to excavate around the base of the piles of interest up to an excavation depth of about 2 ft. in order to accommodate the repair systems and facilitate installation. The surfaces of the three piles were cleaned using hand tools and an electric wire brush.

12.4.1. Installation of the Grouted FRP Jacket Repair System

Following the previous stages, the contractor fabricated wooden supports in order to uphold the FRP jackets in position before the application of epoxy. Then, the two-layer, 18 in. diameter, GFRP Jackets were placed around piles 3 and 5 as shown in Figure 12.5. To facilitate installation, the jackets were installed and fabricated above the corroded

region and lowered around the corroded region after they were fully cured and subsequently grouted.



(a) Positioning of GFRP jacket on pile 5



(b) Positioning of GFRP jacket on pile 3

Figure 12.5: Positioning of GFRP jackets

The seam of the GFRP jackets were sealed with epoxy and self-tapping screws and two-layers, of CFRP were saturated with resin and installed around the GFRP, as shown in Figure 12.6 and Figure 12.7. The system was left to cure for at least 12 hours.



Figure 12.6: Coating the GFRP jacket with epoxy



Figure 12.7: Installation of the CFRP overwrap

After the curing period, the jacket system was lowered to its desired position and filled with grout as shown in Figure 12.8.



Figure 12.8: Completed installation of grouted FRP-jacket

12.4.2. Steel Plate Based Repair System

Wooden supports were placed in the excavation near the base of the pile to help maintain the position of the 16 in. x 39 in. main steel repair plates while installing the bolts to a snug-tight condition.

Two 4 in. wide clamping plates were positioned on the inside of the flange and several bolts were snug tightened to help hold the plates in position as shown in Figure 12.9. The bolts were installed with the bolt heads on the main-plate side of the repair (outside of the flange) and the nuts on the clamping plate side of the repair (inside of the flange). Flat washers were installed behind the bolt heads and bevel washers were installed behind the nuts. The bevel washers were oriented with the thicker end directed towards the flange tips and the thinner end oriented towards the pile web to compensate for the inclination of

the clamping plates. The bolts, were mechanically galvanized A325, $\frac{3}{4}$ in. bolts with corresponding mechanically galvanized flat washers and nuts. The bevel washers were black steel.



(a) Outside view



(b) Inside view

Figure 12.9: Initial positioning of steel plates

After all the bolts were installed to a snug-tight condition they were incrementally torqued up to the target pretension of 28 kips, according to the following stages:

- Stage 1: 8.4 kips (30% of target)
- Stage 2: 19.6 kips (70% of target)
- Stage 3: 28 kips (100% of target)
- Stage 4: 29.4 kips (105% of target)

For each stage, the 26 bolts were torqued up to the required pretension using a 650 lb-ft torque wrench, and according to the tightening sequence shown in Figure 12.10.

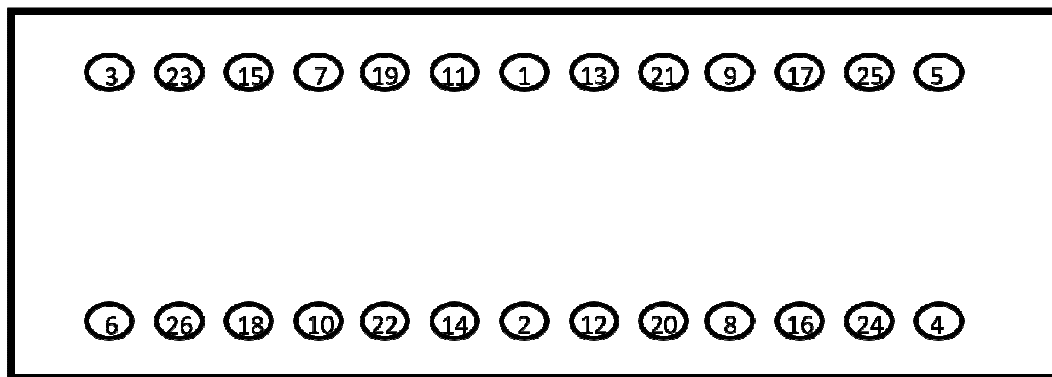


Figure 12.10: Bolt tightening sequence

The tension torque relationship of the galvanized bolts is presented in in Figure 12.11 up to a pretension level of 18 kips. Based on the linear trend line shown in the figure, tightening the bolts up to 105% of the target would require an applied torque of 590 ft-lbs.

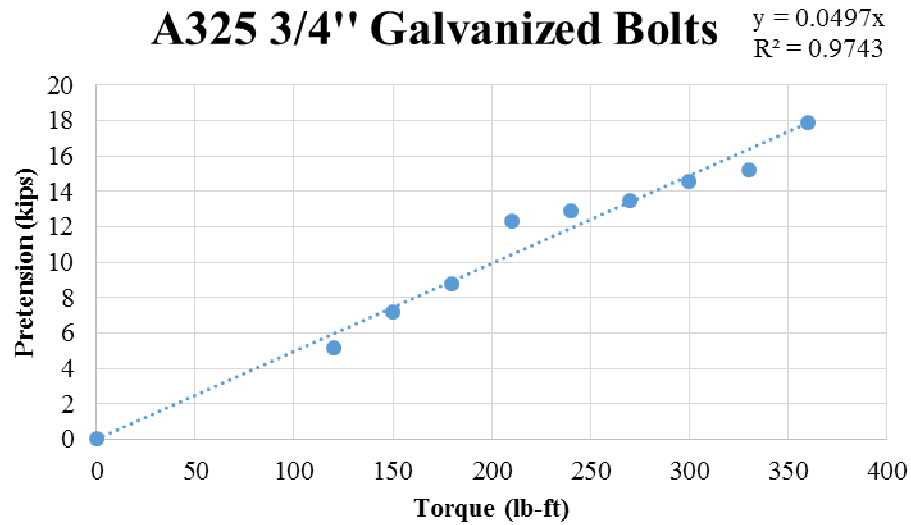


Figure 12.11: Torque wrench calibration curve

The bolts were tightened to 70% of the target value at which point it became evident to the team that the target torques would not be achievable. The team attempted to tighten one of the bolts to 105% of the target level. However, the bolt ruptured prior to reaching 100% of the required pretension. At this point, the required torque was 564 lb-ft. By comparison, to achieve this level of pretension with A325, $\frac{3}{4}$ in. diameter non-galvanized bolts, the required torque is only 350 lb-ft. This was attributed to the fact that mechanically galvanized bolts require substantially more torque to achieve the same pretension level as ungalvanized bolts. Further research is recommended to investigate the effect of lubrication on the tension-torque response of mechanically and hot-dip galvanized bolts as a possible means to improve the installation process of the steel-based repair system in practical applications. A sufficient number of bolts should be investigated to provide a statistically relevant data set and to provide confidence in the overall safety of the system.

The repair plates were installed on both sides of the flanges with the bolts torqued to achieve 70% of the target prestress level. Figure 12.12 illustrates the completed installation of the steel-based repair on one flange, prior to installation of the second repair plate.



Figure 12.12: Steel based repair system

Chapter 13. Summary, Conclusions and Recommendations for Future Work

This report summarizes the details of an experimental and numerical research project that was conducted to evaluate the remaining capacity of steel H-piles with severe but localized corrosion and to evaluate the performance of different FRP-based and steel-based repair alternatives that are suitable for underwater application, develop design guidelines for the repair systems and conduct a life-cycle cost analysis of the various alternatives. The research consisted of small-scale and full-scale testing of steel H-piles that were milled to represent the loss of cross-sectional area associated with corrosion. Different corrosion patterns were considered. The capacities of the corroded piles were predicted using three different existing design approaches: the approach used in AASHTO (2012) and AISC (2011), the effective width method, and the direct strength method (the latter two of which are used in the AISI (2012) specification for cold formed steel members). The experimental work was supplemented by a numerical study and a finite element modeling approach was developed and validated against the experimental results. The validated FEM was used to conduct a parametric study to investigate the influence of various parameters on the remaining capacity of corroded steel H-piles.

Subsequently, two different types of grout-filled FRP jackets, and a friction-based, clamped steel plate repair system were evaluated as potential repair alternatives for corroded steel piles. A total of 21 full-scale steel piles were milled to represent the loss of cross-section and subsequently repaired with one of the three repair systems. Seven piles were repaired with each of the F1 and F2 FRP-jacket systems while the remaining seven piles were repaired using the clamped steel plate system. A numerical framework was established to predict the response of the repaired piles (considering both types of repair systems) and to investigate various behaviors that could

not be readily observed or verified experimentally. Design methodologies were developed and summarized to facilitate the design of both the grouted FRP jacket type and friction-based steel plate type repair systems. A life cycle cost analysis was conducted based on cost data that were collected through a survey that was conducted by the researchers. The LCCA was implemented using the FHWA software RealCost.

Based on the successful completion of the experimental and numerical components of the research, a field implementation was conducted and was described, in which three piles of an existing bridge in Texas were repaired using the different types of repair systems that were considered in this study. The following sections present a more detailed summary and conclusions of the research and provide recommendations for future work.

13.1. Summary and Conclusions

The experimental and numerical study of corroded steel H-piles yielded the following conclusions:

- Increasing the degree of corrosion of the piles resulted in a greater reduction of the axial capacity. Removing 82% of the cross-sectional area, corresponding to the piles with through-web voids and severe loss of the flanges, resulted in 80% loss of the axial capacity relative to the axial capacity of a similar un-corroded control pile. The remaining capacity of the small-scale and full-scale corroded piles was proportional to the reduction of their cross-sectional areas. As the level of deterioration of the cross section increased the failure mode transitioned from global buckling to local buckling. In the presence of through-web corrosion failure occurred due to localized bending of the flanges on either side of the web void in a beam buckling mode rather than in a traditional two-way plate

Both FRP repair systems described in this study are patented by Professor Mo Ehsani; U.S. Patent #8,650,831 and #9,376,782

bending local buckling mode. Reduction of the axial capacity and changing the failure mode are attributed to reduction of the cross-sectional area and increasing the flange and web slenderness.

- Reduction of the flange thickness has a greater impact on the remaining axial capacity than the reduction of the web thickness. This is because reducing the flange thickness decreases the radius of gyration of the corroded section in addition to reducing the cross-sectional area. However, by reducing the web thickness only the cross-sectional area decreases.
- Extending the length of the corroded region increased the aspect ratio of the slender segments of the flanges and web. This in turn reduced the plate buckling coefficients, critical local buckling stresses, and axial capacity of piles with corrosion extending over a greater length of the pile.
- According to the test results, the reduction of the axial load carrying capacity correlates well with the reduction of the cross-sectional area in the corroded region with R^2 value of 0.985 and 0.983 in small-scale and full-scale tests respectively. This supports the rating approach of approximating the remaining axial capacity of corroded piles by assessment of the reduction of the cross-sectional area and proportionally reducing the initial design axial capacity for piles that exhibit inelastic buckling behavior.
- Test results revealed that localized reduction in the width of the flange and unsymmetric degradation of the flanges did not have a significant impact on the axial strength of the columns.
- Three existing design specifications, namely AASHTO (and AISC), AISI effective width method, and AISI direct strength method, were used to predict the remaining axial

capacity of the tested corroded piles. The AASHTO and AISI models were developed for prismatic hot-rolled and cold-formed thin-walled members, respectively. Comparison showed that when the loss of the cross-sectional area was less than 50% the maximum measured-to-predicted capacity ratios were 1.34, 1.11, and 1.09 using AASHTO, AISI-EWM, and AISI-DSM, respectively. However, for greater values of cross-sectional loss the prediction by the AASHTO method becomes overly conservative with a maximum measured-to-predicted capacity ratio of up to 9.52. This was attributed to the fact that AASHTO does not account for the post-buckling strength of the slender flanges. In contrast, AISI-EWM provided the most accurate prediction among all of the evaluated methods with the overall mean value and coefficient of variation of 1.23 and 0.176 of measured-to-predicted capacity ratio, respectively.

- The AASHTO design specification assumes a constant value of the plate buckling coefficient, k , which represents a specific level of fixity at the flange and web junction. This assumption is valid within the range of the flange and web slenderness of standard hot-rolled sections. However, corrosion can change the relative stiffness of the flanges and the web such that the assumed plate buckling coefficient may no longer be applicable for plate buckling strength calculations. This is a possible reason for the observed discrepancies between the prediction by these specifications and the experimental results.
- The design specifications considered in this study assume a large plate aspect ratio to calculate plate buckling coefficients. For a plate with large aspect ratios, the plate buckling coefficient converges to an asymptotic value, a lower bound that is adopted in the studied design specifications for prismatic members. However, based on the field

observations, corrosion of steel piles is limited in extent, and the assumption of large plate aspect ratio may result in conservative axial capacity predictions.

- The developed numerical framework provided accurate predictions of the remaining capacities and failure modes of corroded piles. The differences between FEA predictions and test results are no more than 19 kips and 41 kips for small-scale and full-scale specimens, respectively, which are 8.8% and 6.6% of the capacity of the un-corroded control piles.
- The numerical simulations confirmed that flange thickness reduction is the most critical parameter affecting the remaining axial capacity of an H-pile with localized corrosion. This is because the flanges contribute more to the weak-axis moment of inertia of the section. Additionally, the web can sustain a more severe degree of corrosion than the flange before becoming slender and being susceptible to local buckling. This is because the web is a stiffened element while the flange is an unstiffened element. Therefore, stabilizing the flanges of a corroded pile is a primary function of the repair system.
- Pile slenderness only has a substantial effect on the axial capacity of piles without slender elements that fail by flexural buckling. Reducing the effective length of a pile by bracing it will not be beneficial to increasing its capacity if the pile has corrosion so severe that the deteriorated flanges and web become slender.
- The magnitude of residual stresses and the extent of corrosion along the length of the pile are secondary factors affecting the axial capacity of the pile. The magnitude of residual stresses affects the axial capacity of corroded piles that fail by flexural buckling. But, a threefold increase in the magnitude of the residual stresses resulted in only a 15% reduction of the capacity. In contrast, varying the magnitude of residual stresses does not

have noticeable influence on piles with slender elements that fail by local buckling. Therefore, even without the measurements of residual stresses, which are difficult to obtain reliably from in service bridge piles, capacities of corroded piles can be predicted well using FEA techniques. The extent of the corroded region has noticeable effects only on piles that fail by local plate buckling in the corroded region. Increasing the extent of corrosion can decrease the axial capacity by up to 41% and 33% in the extreme cases that were considered for W4×13 and HP12×53 section piles, respectively, due to the reduction of plate buckling capacity of a larger aspect ratio element.

- The location of the corroded region does not have a significant effect on pile capacity regardless of the type of failure mode. Moving the corroded region from the mid-height to the third height of a pile only changed the capacity of the pile by within 5%.

With regards to the experimental and numerical study of the FRP-based repair system, the conclusions are as follows:

- All of the corroded piles that were repaired with FRP-confined grout repair systems, except 80/60-F1/R, were able to attain the retrofitting target which was to restore the nominal axial capacity of the un-corroded pile. The 80/60-F1/R pile was intentionally repaired without mechanical anchors (although the proposed design methodology indicated that anchors were required) to investigate the effect of the anchorage.
- Based on the experimental and numerical observations, a rational design methodology was proposed that can be used to design FRP-confined grout repair systems for steel piles with severe but localized corrosion. The proposed design methodology accounts for yielding of the section, global buckling of the repaired pile, confinement of the grout core

by the FRP jacket, debonding at the steel/grout interface, and mechanical anchorage of the grout core to the steel pile.

- The deformation of the steel piles that were repaired with grouted FRP jackets changed due to the restraint provided by the repair system compared to the corroded control piles. For the piles with 0% and 40% reduction of the flange thickness, the deformation of the steel piles changed from localized flange and web buckling to global buckling. For the piles with 80% reduction of the flange thickness, the piles failed by localized crumpling of the corroded flanges and web inside the repair system.
- The results of the experimental study and numerical analysis were used to explain the failure mechanism of the repaired piles. For the tested piles with 0% and 40% reduction of the flange thickness, restraining the corroded region by the repair system prevented the corroded flanges and web from local buckling. Consequently, global buckling of the pile occurred prior to bond failure. For the tested piles with 80% reduction of the flange thickness, the repair system provided lateral support to the corroded region. While the grout core remained bonded to the steel pile, stress was transferred to the grout core. Consequently, yielding of the corroded cross-section occurred at a larger load than predicted based on the yield capacity of the corroded steel section alone. The grout core debonded from the steel pile after yielding of the corroded section, but before global buckling of the pile. Consequently, the axial stiffness of the pile degraded after the bond failure. Due to loss of bond at the steel-grout interface, crumpling of the corroded region of the steel pile occurred which pushed the restraining grout outward and increased the hoop strain in the FRP jacket which was acting to confine the grout core. This eventually led to rupture of the FRP jacket. The presence of mechanical anchors contributed both to

the shear stress transfer at the steel-grout interface and prevented the outward motion of the grout after crumpling of the pile thereby reducing the demand on the FRP jacket.

- Comparison of numerical analysis to the experimental results revealed that the behavior of the repaired piles including axial capacity, axial load-shortening response, and failure mode are sensitive to the bond characteristics between the steel pile and the confined grout. Comparison showed that the initial axial stiffness of the load-shortening response of the repaired piles was affected by the tangential bond stiffness at the steel/grout interface. Reducing the tangential bond stiffness resulted in reduction in the axial stiffness of the repaired pile. In addition, comparing the measured and predicted axial load-shortening behaviors for the pile with 80% reduction of the flange thickness showed that the onset of non-linearity of the piles depends on the magnitude of the tangential bond strength at the steel/grout interface. Increasing the tangential bond strength can also change the failure mode of the repaired pile from localized crumpling of the corroded pile inside the repair to flange local buckling outside of the repair followed by global buckling.
- Comparing the corresponding piles repaired with F1 and F2 FRP jacketing systems indicated the gains in axial capacity using both FRP systems were comparable. However, hoop strains in the FRP laminate and slip at the steel/grout interfaces were slightly higher for the F1 jacket. This was attributed to the lower elastic stiffness of the F1 FRP jacket which was substantially thinner than the F2 jacket resulting in less confinement of the grout core. Additional confinement could be provided by adding one additional layer of FRP using the F1 system which is expected to result in a similar response to that of the F2 jacket.

- Using headed-stud anchors attached to the web within the development region reduced the amplitude of the pile localized deformations within the corroded region. The anchors also reduced the axial shortening of the piles and the slip at the steel-grout interface. The increased axial stiffness of the piles that were repaired with anchors compared to those that were repaired without anchors shows that after bond failure the anchors were able to transfer shearing force from the steel pile to the grout. The hoop strain in the FRP jackets of the piles that were repaired with headed-stud anchors was also lower than the hoop strain in the FRP jackets of those piles that were repaired without anchors. This shows that the anchors effectively prevented the grout from separating from the steel surface. The piles without anchors demonstrated more localized deformation within the corroded region which, in turn, induced more hoop strain in the FRP jacket.
- Based on the numerical analysis, maximum predicted in-plane stresses in the F1 FRP jacket were higher than F2 FRP jacket which was consistent with the experimental observations. According to the numerical results, the location of stress concentrations in the FRP jacket was observed along the tips of the flanges. This was consistent with the location where rupture of the FRP jacket initiated during testing. In addition, the location of stress concentrations in the grout core located on the top flange in the FE models indicate that localized deformation of the corroded flange pushed the grout outward and caused an increase in the confinement pressure induced by the FRP jacket.
- The discrepancies between the numerical and experimental results in terms of axial load-shortening responses and failure mode are attributed to (i) uncertainty in the values of bond fracture energy and coefficient of friction at the steel-grout interface, (ii) element type used to model the headed-stud anchors, (iii) material model used for confined grout

and (iv) complexities associated with the failure process and the interaction between components during this process.

The conclusions taken from the experimental and numerical study of the steel-plate-based repair system are:

- The proposed friction-type bolted plate-based repair system can effectively restore the capacity of a corroded pile to its nominal design capacity. For retrofitted piles that fail by local buckling within the corroded region, the increase of the capacity is directly proportional to the increase of the slip resistance (or coefficient of friction) and the bolt pretension level. Increasing the length of the steel plates also enhances the capacity since more friction force can be developed across the interface by increasing the number of bolts used to clamp the repair plates to the deteriorated pile. For retrofitted piles that fail by flexural buckling or local buckling at the un-corroded region beyond the repair system, the capacity is governed by the original strength of the un-corroded pile rather than the configuration of the repair system. Therefore, increasing the slip resistance or bolt pretension beyond the level that is required to force the failure into the un-corroded portion of the pile does not provide any additional capacity to the system. In this case, though the capacity can be enhanced by increasing the length of the steel plates due to the increased contribution of the plates to the lateral stiffness of the pile. However, the effect is nominal since doubling the plate length only increases the capacity by 7%.
- The repair system can increase the axial stiffness of the corroded piles. This may be beneficial to the serviceability control of the piles, to prevent excessive deformation or differential settlement.

- The piles with extremely thin flanges and webs such as pile 80/60-S(1), pile 80/60-S(2), and pile 80/60/3-S, showed a crumpling deformation at the corroded region. The deformation indicated that the flanges were too slender to stiffen the web at the junction; meanwhile, the destabilization of the web caused the excessive axial deformation of the flanges.
- The coatings applied on the steel plates of the repair system can provide the required friction resistance. However, numerical analysis suggests that the coefficient of friction achieved at the interface between the repair plates and the deteriorated pile may be up to 12% lower than the values obtained from small-scale double-lap tension coupon tests. This is attributed to the increased contact area of the piles which increases the probability of the existence of a flaw in the coating and also the increased number of bolts which increases the probability that some of the bolts may not be fully tightened to the target prestress level.
- The non-zinc containing, class B-rated, polyamide epoxy coating that was used in this system was brittle, cracked locally and peeled off of the repair plates during testing. Although the damage of the coatings did not appear to have any negative effects on the axial capacity, it may affect the durability of the repair system.
- Bevel washers are essential to be used in the proposed repair system, to prevent bolts from bending and rupture during tightening or during service of the piles.

The LCCA yielded the following conclusion:

- This survey questionnaire collected the information and cost data of five common bridge pile repair solutions. The cost data was estimated by repair companies based on two different repair scenarios designed by the research team. The repair companies use either

FRP-based repair technique or a structural steel-based repair solution (different from that considered in this research). The collected information included the type of repair system, the duration of repair, the required equipment (heavy and minor), material costs, labor costs, equipment costs, service life of repair system, and traffic control plans.

- Comparisons of the survey results indicates that Company B (FRP-based repair) has the lowest total cost for one repair activity while Company E (structural steel-based) is the most costly. However, the service life of Company E is about four times longer than that of Company B. As such, it is not necessarily the case that Company B has a lower life-cycle cost than that of Company E. A life-cycle cost analysis was performed to determine the most cost-effective approach according to the collected data in the survey questionnaire.
- The comprehensive life-cycle cost analysis revealed that FRP-based repair techniques proved to have greater economic advantages over a steel-based technique under different service lives and interest rates.
- Several major parameters such as discount rates, initial repair timing, and analysis periods, were examined in this study to test different scenarios and different combinations of variables. These approaches should be beneficial to state agencies when they make decisions on their bridge maintenance programs by reflecting uncertainty.
- A computer program, *RealCost*, seemed to be suitable for the cost analysis of bridge repair projects. This should be beneficial to state agencies since the program can be downloaded for free. The program becomes an even more valuable resource when a given situation involves the analysis of user costs.

The field installation of the two repair systems yielded the following conclusion:

- Both systems can be quickly and effectively installed using a trained labor force of three individuals with access to typical hand tools and small power tools.
- Installation of the steel-plate based repair system in-situ revealed a challenge associated with the installation of mechanically galvanized bolts. Namely, unlubricated mechanically galvanized bolts could not be tightened to the torque level required to achieve the necessary prestressing force in the system. The high friction of the unlubricated mechanically galvanized bolts caused premature rupture of one of the ¾” A325 bolts prior to achieving the target pretension level of 28 kips. Consequently, for the field demonstration, the bolts were only tightened to 70% of the target torque.

13.2. Recommendations for Future Work

The recommendations for future work stemming from the findings of this research project are as follows:

- This study only considered the corroded piles under uniaxial compression. However, battered piles, piles experiencing lateral loads from debris, or eccentrically loaded piles may behave as beam-columns transmitting both axial loads and bending moments.
- The effect of corrosion on residual stress magnitudes and distributions was not addressed in the current study. The effect of other patterns of the residual stresses should be studied. This research assumed one pattern of residual stresses, however, other patterns of residual stresses have not been studied.
- Developing a closed-form mechanics based approach to predict the capacity of H-piles with localized corrosion that can be easily implemented in a design office may provide

more accurate predictions of the remaining capacity of existing piles than current design specification provisions.

- The developed numerical framework provided sufficiently accurate predictions of the axial capacity of corroded H-piles. However, it is impractical for engineers to build sophisticated numerical models and run time-consuming analyses for every case. Simplified design equations or curves that can be used to calculate the capacity could alternatively be derived semi-empirically from extensive FEA predictions.
- The findings of this study are limited to doubly-symmetric, I-shaped hot-rolled compression members that are generally designed to fail by inelastic global buckling prior to corrosion. However, the effect of corrosion on the remaining axial capacity of corroded members with different cross-sectional shapes, slenderness, geometries, and fabrication process requires further investigation.
- The numerical simulations indicated that the behavior of the grouted FRP jacket based repair system is sensitive to the properties of the steel/grout interface. Additional testing and simulation needs to be conducted to characterize the behavior of this interface and to completely understand its contribution to the overall behavior of the repaired piles.
- While the numerical simulations of the piles that were repaired with grouted FRP jackets provided important insight into the behavior of the piles, the predictions did not closely match the measured response in some cases. Specifically, the cases in which the repair system included headed stud anchors resulted in under-prediction of the capacity of up to 70%. The numerical framework should be refined to minimize this discrepancy.
- Alternative coatings to be applied on the steel plates of the repair systems should be evaluated. As stated in the findings, the second layer of coating exhibited brittle behavior

during testing, which may result in durability defects of the pile. Therefore, other types of coatings should be evaluated to obtain alternatives that are durable, and can provide corrosion resistance and the required slip resistance.

- The repaired piles in the experimental program were retrofitted in the situation with no axial load. However, piles in the field are subjected to load before and during rehabilitation. The design of the repair system for loaded piles should be investigated further.
- The field installation indicated that rupture of unlubricated, mechanically galvanized bolts could limit the usefulness of the steel plate-based repair system. A rigorous evaluation of the tension-torque relationships of lubricated and unlubricated, mechanically galvanized, and hot-dip galvanized bolts should be conducted to ensure that the steel-based repair system can be safely and effectively installed in practical applications.

Both FRP repair systems described in this study are patented by Professor Mo Ehsani; U.S. Patent #8,650,831 and #9,376,782

References

- AASHTO. (2012). Bridge Design Specifications (LRFD). American Association of State Highway and Transportation Officials.
- ACI318. (2014). Building Code Requirement for Structural Concrete. American Concrete Institute.
- ACI440.2R. (2008). Guide for the Design and Construction of Externally Bonded FRP Systems for Strengthening Concrete Structures. Farmington Hills, MI: American Concrete Institute.
- AISC. (2010). Steel Construction Manual (14th ed.). American Institute of Steel Construction.
- AISI. (2012). North American Specification for the Design of Cold-Formed Steel Structural Members. Washington, DC: American Iron and Steel Institute.
- Appuhamy, J., Ohga, M., Kaita, T., Fujii, K., and Dissanayake, P. (2011). Development of Analytical Method for Predicting Residual Mechanical Properties of Corroded Steel Plates. International Journal of Corrosion, 2011, 1-10.
- ARAMIS User Manual - Software. (2011). Braunschweig, Germany: GOM mbH, Optical Measuring Techniques.
- ASTM 370-13. (2013). Standard Test Methods and Definitions for Mechanical Testing of Steel Products. American Society for Testing and Materials.
- ASTM 706-14. (2014). Standard Specification for Deformed and Plain Low-Alloy Steel Bars for Concrete Reinforcement. American Society for Testing and Materials.

- ASTM C39-14a (2014). Standard Test Method for Compressive Strength of Cylindrical Concrete Specimens. American Society for Testing and Materials.
- ASTM C469-14 (2014). Standard Test Method for Static Modulus of Elasticity and Poisson's Ratio of Concrete in Compression. American Society for Testing and Materials.
- Avery, P. and Mahendran, M. (2000). Distributed Plasticity Analysis of Steel Frame Structures Comprising Non-Compact Section. *Engineering Structures*, 22, 901-919.
- Bahrami, A., Wan Badaruzzaman, W., and Osman, S. (2013). Behaviour of Stiffened Concrete-Filled Steel Composite (CFSC) Stub Columns. *Latin American Journal of Solids and Structures*, 10(2), 409-440.
- Bambach, M. and Elchalakani, M. (2007). Plastic Mechanism Analysis of Steel SHS Strengthened with CFRP under Large Axial Deformation. *Thin-Walled Structures*, 45(2), 159-170.
- Barringer Paul H., P.E.(2003), Barringer & Associates, Inc., "A Life Cycle Cost Summary", International Conference of Maintenance Societies (ICOMS).
- Beaulieu, L.V., Legeron, F., and Langlois, S. (2010). Compression Strength of Corroded Steel Angle Members. *Journal of Constructional Steel Research*, 66, 1366-1373.
- Berg A.C., Bank L.C., Oliva M.G., Russell J.S. (2005), "Construction and cost analysis of an FRP reinforced concrete bridge deck", *Construction and Building Materials*, Elsevier, 20, pp.515–526.
- Bethlehem Steel Corp. Steel H-Piles. Retrieved from <https://archive.org/details/steelhpiles00beth>

- Biondini and Frangopol (2008), "Life-Cycle Civil Engineering", Taylor&Francis Group, London, ISBN 978-0-415-46857-2.
- Bisagni, C. (2000). Numerical Analysis and Experimental Correlation of Composite Shell Buckling and Post-Buckling. *Composites Part B: Engineering*, 31(8), 655-667.
- Bjorhovde, R. (1972). Deterministic and Probabilistic Approaches to the Strength of Steel Columns (Doctoral Dissertation). Bethlehem, PA: Lehigh University.
- Bjorhovde, R. (1988). Columns: From Theory to Practice. *Engineering Journal*, 25(1), 21-34.
- Chan, T.M. and Gardner, L. (2008). Compressive Resistance of Hot-Rolled Elliptical Hollow Sections. *Engineering Structures*, 30, 522-532.
- Chan A., Keoleian G., Gabler E., (2008), "Evaluation of Life-Cycle Cost Analysis Practices Used by the Michigan Department of Transportation", *Journal of Transportation Engineering*, Vol.134, No. 6.
- Caltrans, (2007), "Life-Cycle Cost Analysis Procedures Manual", Pavement Standards Team & Division of Design, State of California Department of Transportation.
- Chen, Y. (1997). Assessment on Pile Effective Lengths and Their Effects on Design-I.Assessment. *Computers and Structures*, 62(2), 265-286.
- Chen, Y., Cheng, X., and Nethercot, D. (2013). An Overview Study on Cross-Section Classification of Steel H-Sections. *Journal of Constructional Steel Research*, 80, 386-393.
- Cinitha, A., Umesha, P.K., Iyer, R. (2014). An Overview of Corrosion and Experimental Studies on Corroded Mild Steel Compression Members. *KSCE Journal of Civil Engineering*, 18(6), 1735-1744.

- Collins Engineers. (2010). Underwater Bridge Inspection (Report No. FHWA-NHI-10-027).
Federal Highway Administration, U.S. Department of Transportation.
- Davisson, M. T. and Robinson, K. E. (1965). Bending and Buckling of Partially Embedded Piles.
Proceedings of the 6th International Conference on Soil Mechanics and Foundation
Engineering, 243-246. Montreal, Canada.
- Demos, G., (2006), "Life Cycle Cost Analysis and Discount Rate on Pavement for the Colorado
Department of Transportation", Report No. CDOT-2006-17, Colorado Department of
Transportation.
- Dinis, P.B., Camotim, D., Silvestre, N. (2007). FEM-Based Analysis of the Local-
Plate/Distortional Mode Interaction in Cold-Formed Steel Lipped Channel Columns.
Computers and Structures, 85, 1461-1474.
- Dinis, P.B. and Camotim, D. (2011). Post-Buckling Behavior and Strength of Cold-Formed Steel
Lipped Channel Columns Experiencing Distortional/Global Interaction. Computers and
Structures, 89, 422-434.
- Ehlen, M. A. (2003). "BridgeLCC 2.0 Users Manual", National Institute of Standards and
Technology (NIST), Gaithersburg, MD.
- Ehsani, M., Croarkin, M., (2011), "A Novel Solution for Restriction of Deteriorated Piles",
Government Engineering Journal, Waldwick, NJ;
- Ekiz, E. and El-Tawil, S. (2006). Inhibiting Steel Brace Buckling Using CFRP Wraps.
Proceedings of the 8th U.S. National Conference on Earthquake Engineering. San Francisco,
CA.

- Ellobody, E. and Young, B. (2006). Nonlinear Analysis of Concrete-Filled Steel SHS and RHS Columns. *Thin-walled structures*, 44(8), 919-930.
- El-Tawil, S. and Ekiz, E. (2009). Inhibiting Steel Brace Buckling Using Carbon Fiber-Reinforced Polymers: Large-Scale Tests. *Journal of Structural Engineering*, 135(5), 530-538.
- Federal Highway Administration(FHWA), (1998), "Life-Cycle Cost Analysis in Pavement Design ", -Pavement Division Interim Technical Bulletin, Washington, D.C.
- Federal Highway Administration (FHWA) (2004). "Life-Cycle Cost Analysis RealCost 2.5 User Manual", Washington, D.C.
- Federal Highway Administration(FHWA), (2010), "Highway Capacity Manual", Transportation Research Board, Washington, D.C.
- Feng, P., Zhang, Y., Bai, Y., and Ye, L. (2013a). Combination of Bamboo Filling and FRP Wrapping to Strengthen Steel Members in Compression. *Journal of Composites for Construction*, 17(3), 347-356.
- Feng, P., Zhang, Y., Bai, Y., and Ye, L. (2013b). Strengthening of Steel Members in Compression by Mortar-Filled FRP Tubes. *Thin-Walled Structures*, 64, 1-12.
- Five Star Products, Inc. Retrieved from <http://www.fivestarproducts.com/products/marine/marine-pilerestore/pilecap-h-pile.html>
- Flanagan, D. P., and Belytschko, T. (1981). A Uniform Strain Hexahedron and Quadrilateral with Orthogonal Hourglass Control. *International Journal for Numerical Methods in Engineering*, 17(5), 679-706.

- Frauenberger, A., Liu, X., Meyyappan, L., Mata, J., and Gupta, T. (2003). FRP Repair and Health Monitoring of Railroad Steel Bridges. Rolla, MO: The Center for Infrastructure Engineering Studies, University of Missouri-Rolla.
- Fyfe Co. LLC. Product Dta Sheet, Tyfo PR System Using Tyfo SEH-51A and Tyfo S Epoxy. Retrieved from <http://www.fyfeco.com/Products/Composite-Systems.aspx>
- Fyfe Co. LLC. Product Data Sheet, Tyfo SCH-41 Composite Using Tyfo SW-1(S) Underwater Epoxy. Retrieved from <http://www.fyfeco.com/Products/Composite-Systems.aspx>
- Fyfe Co. LLC. Product Data Sheet, Tyfo SW-1 Epoxy, Underwater Epoxy. Retrieved from <http://www.fyfeco.com/Products/Composite-Systems.aspx>
- Galambos, T. (1998). Guide to Stability Design Criteria for Metal Strutures. John Wiley and Sons, Inc.
- Galambos, T. V., and Surovek, A. E. (2008). Structural Stability of Steel: Concepts and Applications for Structural Engineers. Hoboken, NJ: Jonh Wiley and Sons, Inc.
- Gardner, L. and Nethercot, D.A. (2004). Numerical Modeling of Stainless Steel Structural Components- A Consistent Approach. Journal of Structural Engineering, 130, 1586-1601.
- Gillespie, J. W., Mertz, D. R., Edberg, W. M., Demitz, J. R., Kasai, K., and Hodgson, I. (1996). Rehabilitation of Steel Bridge Girders: Large Scale Testing. Proceedings of the American Society for Composites 11th Technical Conference on Composite Materials, 231-240.
- Griggs, D. (2014). Development of FEA Models to Predict the Behavior of Steel Bridge Piles Strengthened with FRP Jackets and Grout (M.Sc. Thesis). Texas Tech University.

- Gupta, P., Ahuja, A., and Khaudhair, Z. (2014). Modelling, Verification and Investigation of Behaviour of Circular CFST Columns. *Structural Concrete*, 15(3), 340-349.
- Harries, K. A., Peck, A. J., and Abraham, E. J. (2009). Enhancing Stability of Structural Steel Sections Using FRP. *Thin-Walled Structures*, 47(10), 1092-1101.
- Hawk, H. (2003). "Bridge Life-Cycle Cost Analysis", National Cooperative Highway Research Program (NCHRP) Report 483, Transportation Research Board (TRB), Washington, D.C.
- Hollaway, L. (2010). A Review of the Present and Future Utilisation of FRP Composites in the Civil Infrastructure with Reference to Their Important In-Service Properties. *Construction and Building Materials*, 24(12), 2419-2445.
- Hollaway, L., and Cadei, J. (2002). Progress in the Technique of Upgrading Metallic Structures with Advanced Polymer Composites. *Progress in Structural Engineering and Materials*, 4(2), 131–148.
- Hu, H. T., and Su, F. C. (2011). Nonlinear Analysis of Short Concrete-Filled Double Skin Tube Columns Subjected to Axial Compressive Forces. *Marine Structures*, 24(4), 319-337.
- Hu, H. T., Huang, C. S., and Chen, Z. L. (2005). Finite Element Analysis of CFT Columns Subjected to an Axial Compressive Force and Bending Moment in Combination. *Journal of Constructional Steel Research*, 61(12), 1692-1712.
- Huang, Y., Zhang, Y., Liu, G., & Zhang, Q. (2010). Ultimate Strength Assessment of Hull Structural Plate with Pitting Corrosion Damification under Biaxial Compression. *Ocean Engineering*, 37(17-18), 1503-1512.

- Hughes, D., Ramey, G. E., and Hughes, M. L. (2007). Effects of Extreme Scour and Soil Subgrade Modulus on Bridge Pile Bent Buckling. *Practice Periodical on Structural Design and Construction*, 12(2), 96-108.
- Jiang, X. and Soares, C. (2012a). Ultimate Capacity of Rectangular Plates with Partial Depth Pits under Uniaxial Loads. *Marine Structures*, 26(1), 27-41.
- Jiang, X. and Soares, C. (2012b). A Closed Form Formula to Predict the Ultimate Capacity of Pitted Mild Steel Plate under Biaxial Compression. *Thin-Walled Structures*, 59, 27-34.
- Johnson, D. (1985). An Investigation into the Interaction of Flanges and Webs in Wide Flange Shapes. *Proceedings of the Annual Technical Session and Meeting*, 397-405. Cleveland, OH.
- Karagah, H., Shi, C., Dawood, M., and Belarbi, A. (2015). Experimental Investigation of Short Steel Columns with Localized Corrosion. *Thin-Walled Structures*, 87, 191-199.
- Karimi, K., Tait, M. J., and El-Dakhakhni, W. W. (2012). Influence of Slenderness on the Behavior of a FRP-Encased Steel-Concrete Composite Column. *Journal of Composites for Construction*, 16(1), 100-109.
- Karimi, K., Tait, M., and El-Dakhakhni, W. (2011). Testing and Modeling of a Novel FRP-Encased Steel-Concrete Composite Column. *Composite Structures*, 93(5), 1463-1473.
- Karimi, K., Tait, M., and El-Dakhakhni, W. (2013). Analytical Modeling and Axial Load Design of a Novel FRP-Encased Steel-Concrete Composite Column for Various Slenderness Ratios. *Engineering Structures*, 44, 526-534.

- Kaya, A., Dawood, M., and Gencturk, B. (2015). Repair of Corroded and Buckled Short Steel Columns Using Concrete-Filled GFRP Jackets. *Construction and Building Materials*, 94, 20-27.
- Khedmati, M.R., Roshanali, M.M., Nouri, Z.H.M.E. (2011). Strength of Steel Plates with Both-Sides Randomly Distributed with Corrosion Wastage under Uniaxial Compression. *Thin-Walled Structures*, 49, 325-342.
- Kim, Y. J. and Harries, K. A. (2011). Behavior of Tee-Section Bracing Members Retrofitted with CFRP Strips Subjected to Axial Compression. *Composites Part B: Engineering*, 42(4), 789-800.
- Kirk, S., and Dell’Isola, A. (1995), "Life cycle costing for design professionals", McGraw-Hill, New York.
- Lai, Z. and Varma, A. H. (2015). Noncompact and Slender Circular CFT Members: Experimental Database, Analysis, and Design. *Journal of Constructional Steel Research*, 106, 220-233.
- Lamptey, G., Ahmad, M., Labi, S., Siha, K., (2004), "Life Cycle Cost Analysis for INDOT Pavement Design Procedures", Report No.FHWA/IN/JTRP-2004/28, Indiana Department of Transportation.
- Landers, Richard R., (1996), "Product Assurance Dictionary", Marlton Publishers, 169 Vista Drive, Marlton, NJ 08053.

- Liu, X., Nanni, A., and Silva, P. (2005). Rehabilitation of Compression Steel Members Using FRP Pipes Filled with Non-expansive and Expansive Light-weight Concrete. *Advances in Structural Engineering*, 8(2), 129-142.
- Lundquist, E. (1939). Local Instability of Symmetrical Rectangular Tubes under Axial Compression (Report No. NACA-TN-686). National Advisory Committee for Aeronautics, Langley Aeronautical Laboratory, Langley Field, VA.
- Lundquist, E. and Stowell, E. (1942a). Critical Compressive Stress for Flat Rectangular Plates Supported Along All Edges and Elastically Restrained Against Rotation Along the Unloaded Edges (Report No. NACA-TR-733). National Advisory Committee for Aeronautics, Langley Aeronautical Laboratory, Langley Field, VA.
- Lundquist, E. and Stowell, E. (1942b). Critical Compressive Stress for Outstanding Flanges (Report No. NACA-TR-734). National Advisory Committee for Aeronautics, Langley Aeronautical Laboratory, Langley Field, VA.
- Lundquist, E. and Stowell, E. (1942c). Restraint Provided a Flat Rectangular Plate by a Sturdy Stiffener Along an Edge of the Plate (Report No. NACA-TR-735). National Advisory Committee for Aeronautics, Langley Aeronautical Laboratory, Langley Field, VA.
- Mateus, A.F., & Witz, J.A. (1998). On the Post-Buckling of Corroded Steel Plates Used in Marine Structures. *RINA Transactions*, 140, 165-183.
- Mindlin, R.D. (1951). Influence of Rotatory Inertia and Shear on Flexural Motions of Isotropic Elastic Plates. *ASME Journal of Applied Mechanics*, 18, 31–38.

- Moen, C., & Schafer, B. (2008). Experiments on Cold-Formed Steel Columns with Holes. *Thin-Walled Structures*, 46(10), 1164-1182.
- Moen, C., & Schafer, B. (2011). Direct Strength Method for Design of Cold-Formed Steel Columns with Holes. *Journal of Structural Engineering*, 137(5), 559-570.
- Mohammadi, J., Guralnick, S.A., and Yan, L. (1995), "Incorporating Life-Cycle Costs in Highway-Bridge Planning and Design", *ASCE Journal of Transportation Engineering* 121(5), 417-424.
- NACE. (2013). Highways and Bridges. Corrosion Central. Retrieved from <https://www.nace.org/Corrosion-Central/Industries/Highways-and-Bridges/>
- Nakai, T., Matsushita, H., Yamamoto, N., Arai, H. (2004). Effect of Pitting Corrosion on Local Strength of Hold Frames of Bulk Carriers. *Marine Structures*, 17, 403-432.
- Ok, D., Pu, Y., Incecik, A. (2007). Computation of Ultimate Strength of Locally Corroded Unstiffened Plates under Uniaxial Compression. *Marine Structures*, 20, 100-114.
- Oszvald, K., Dunai, L. (2012). Effect of Corrosion on the Buckling of Steel Angle Members- Experimental Study. *Civil Engineering*, 56, 175-183.
- Oszvald, K., Dunai, L. (2013). Behavior of Corroded Steel Angle Compression Members- Numerical Study. *Civil Engineering*, 57, 63-75.
- Paik, J.K., Lee, J.M., and Ko, M.J. (2003). Ultimate Compressive Strength of Plate Elements with Pit Corrosion Wastage. *Proceeding of the Institution of Mechanical Engineers, Part M: Journal of Engineering for the Maritime Environment*, 217, 185-200.

- Paik, J.K., Lee, J.M., and Lee, D.H. (2003). Ultimate Strength of Dented Steel Plates under Compressive Loads. *International Journal of Mechanical Sciences*, 45, 433-448.
- Paik, J.K., Lee, J.M., and Ko, M.J. (2004). Ultimate Shear Strength of Plate Elements with Pit Corrosion Wastage. *Thin-Walled Structures*, 42, 1161-1176.
- Paik, J.K. (2007). Ultimate Strength of Perforated Steel Plates under Edge Shear Loading. *Thin-Walled Structures*, 46, 207-213.
- Paik, J.K. (2008). Ultimate Strength of Perforated Steel Plates under Combined Biaxial Compression and Edge Shear Loads. *Thin-Walled Structures*, 45, 301-306.
- Petrus, C., Abdul Hamid, H., Ibrahim, A., and Nyuin, J. (2011). Bond Strength in Concrete Filled Built-Up Steel Tube Columns with Tab Stiffeners. *Canadian Journal of Civil Engineerin*, 38(6), 627-637.
- PileMedic LLC. Product data sheet, PileMedic PLC100.60 for Structural Strengthening of Columns and Submerged Piles. Retrieved from http://www.pilemedic.com/product_data_sheets.php
- Pu, Y., Godley, M.H.R., Beale R.G., and Lau, H.H. (1999). Prediction of Ultimate Capacity of Perforated Lipped Channels. *Journal of Structural Engineering*, 125(5), 510-514.
- Purvis, R.L., Babaei, K., Clear, K.C., and Markow, M.J. (1994), "Life-Cycle Cost Analysis for Protection and Rehabilitation of Concrete Bridges Relative to Reinforcement Corrosion", SHRP-S-377, National Academies Press, Washington, D.C.
- QuakeWrap LLC. Product Data Sheet, QuakeBond 220UR Underwater Resin. Retrieved from http://www.pilemedic.com/product_data_sheets.php

- Rangaraju, P., Amirkhanian, S., Guven, Z., (2008), "Life Cycle Cost Analysis for Pavement Type Selection", Report No. FHWA-SC-08-01, South Carolina Department of Transportation.
- Rhodes, J. and Schneider, F.D. (1994). The Compression Behavior of Perforated Elements. Twelfth International Specialty Conference on Cold-Formed Steel Structures, St. Louis, MO, 11-28.
- Rhodes, J. and Macdonald, M. (1996). The Effects of Perforation Length on the Behavior of Perforated Elements in Compression. Thirteenth International Specialty Conference on Cold-Formed Steel Structures, St. Louis, MO, 91-101.
- Riks, E. (1979). An Incremental Approach to the Solution of Snapping and Buckling Problems. International Journal of Solids and Structures, 15(7), 529-551.
- Saad-Eldeen, S., Garbatov, Y., and Soares, C. G. (2010). Experimental Assessment of the Ultimate Strength of a Box Girder Subjected to Four-Point Bending Moment. Proceedings of the 11th International Symposium on Practical Design of Ships and Other Floating Structures (PRADS2010). Houston, TX.
- Saad-Eldeen, S., Garbatov, Y., and Soares, C. (2011). Experimental Assessment of the Ultimate Strength of a Box Girder Subjected to Severe Corrosion. Marine Structures, 24(4), 338-357.
- Saad-Eldeen, S., Garbatov, Y., and Soares, C. G. (2014). Strength Assessment of a Severely Corroded Box Girder Subjected to Bending Moment. Journal of Constructional Steel Research, 92(1), 90-102.
- Sadovsky, Z. and Drdacky, M. (2001). Buckling of Plate Strip Subjected to Localized Corrosion-a Stochastic Model. Thin-Walled Structures, 39, 247-259.

- Salem, O., Genaidy, A., (2008), "Improved Models for User Costs Analysis", Report No.FHWA/OH-2008/3, Ohio Department of Transportation.
- Sarawit, A.T., Kim, Y., Bakker, M.C.M., and Pekoz, T. (2003). The Finite Element Method for Thin-Walled Members- Applications. *Thin-Walled Structures*, 41, 191-206
- Schafer, B. W. (2002). Local Distortional and Euler Buckling of Thin-walled Columns. *Journal of Structural Engineering*, 128(3), 289-299.
- Schafer, B. W. (2008). Review: The Direct Strength Method of Cold-Formed Steel Member Design. *Journal of Constructional Steel Research*, 64, 766-778.
- Seif, M. and Schafer, B. W. (2010a). Local Buckling of Structural Steel Shapes. *Journal of Constructional Steel Research*, 66(10), 1232-1247.
- Seif, M. and Schafer, B. W. (2010b). Design Methods for Local-Global Interaction of Locally Slender Steel Members. *Proceedings of the Annual Stability Conference*, 553-572.
- Seif, M. and Schafer, B. W. (2011). Towards a Strain Energy Based Strength Prediction for Locally Slender Steel Columns. *Annual Stability Conference Proceedings* 344-357.
- Seif, M., and Schafer, B. (2013). Design of Locally Slender Structural Steel Columns. *Journal of Structural Engineering*, 140(4), 04013086.
- Seo, J., Kim, B., Ryu, H., Ha, Y., and Paik, J. (2011). Validation of the Equivalent Plate Thickness Approach for Ultimate Strength Analysis of Stiffened Panels with Non-Uniform Plate Thickness. *Thin-Walled Structures*, 49, 753-761.

- Shaat, A. and Fam, A. (2006a). Axial Loading Tests on Short and Long Hollow Structural Steel Columns Retrofitted Using Carbon Fibre Reinforced Polymers. *Canadian Journal of Civil Engineering*, 33(4), 458-470.
- Shaat, A. and Fam, A. (2006b). Numerical Modeling of FRP-Strengthened Long HSS Columns. *Tubular Structures-International Symposium*, 11, 375-382.
- Shaat, A. and Fam, A. (2007a). Fiber-Element Model for Slender HSS Columns Retrofitted with Bonded High-Modulus Composites. *Journal of Structural Engineering*, 133(1), 85-95.
- Shaat, A. and Fam, A. (2007b). Finite Element Analysis of Slender HSS Columns Strengthened with High Modulus Composites. *Steel and Composite Structures*, 7(1), 19-34.
- Shaat, A. and Fam, A. (2009). Slender Steel Columns Strengthened Using High-Modulus CFRP Plates for Buckling Control. *Journal of Composites for Construction*, 13(1), 2-12.
- Shaat, A., Sayed, W. S., and Fam, A. (2006). Modeling of Axially Loaded HSS Slender Steel Members Retrofitted with Composites. *Advances in Engineering Structures, Mechanics & Construction*, 140, 227-238.
- Shaat, A., Schnerch, D., Fam, A., and Rizkalla, S. (2004). Retrofit of Steel Structures Using Fiber-Reinforced Polymers (FRP): State-of-the-art. *Transportation Research Board (TRB) Annual Meeting*, CD-ROM (04-4063).
- Shan, J., Chen, R., Zhang, W., Xiao, Y., Yi, W., and Lu, F. (2007). Behavior of Concrete Filled Tubes and Confined Concrete Filled Tubes under High Speed Impact. *Advances in Structural Engineering*, 10(2), 209-218.

- Shanley, F. R. (1947). Inelastic Column Theory. *Journal of Aeronautical Science*, 14(5), 261-268.
- Shi, C., Karagah, H., Dawood, M., and Belarbi, A. (2014). Numerical Investigation of H-shaped Short Steel Piles with Localized Severe Corrosion. *Engineering Structures*, 73, 114-124.
- Shi, C., Karagah, H., Belarbi, A., and Dawood, M. (2015). Inelastic Buckling Behavior of Steel H-Piles with Localized Severe Corrosion. *ASCE Journal of Bridge Engineering*. (Accepted).
- Shulley, S. B., Huang, X., Karbhari, V. M., and Gillespie, J. W. (1994). Fundamental Considerations of Design and Durability in Composite Rehabilitation Schemes for Steel Girders with Web Distress. *Proceedings of the Third Materials Engineering Conference*, 1187-1194. San Diego, CA.
- Silvestre, N., Young, B., and Camotim, D. (2008). Non-linear Behaviour and Load-Carrying Capacity of CFRP-Strengthened Lipped Channel Steel Columns. *Engineering Structures*, 30(10), 2613-2630.
- SIMULIA. (2012). ABAQUS User's Manual Version 6.12. Providence, RI: Dassault Systemes Simulia Corporation.
- Smith, C.S., Davidson, P.C., Chapman, J.C., and Dowling, P.J. (1988). Strength and Stiffness of Ships' Plating under In-Plane Compression and Tension. *RINA Trans*, 130, 277-296.
- Sundarraja, M. C. and Sriram, P. (2014). Investigation on Corroded HSS Tubular Members under Compression Strengthened with CFRP Composites. *Archives of Civil Engineering*, 60(1), 145-159.

- Tall, L., Huber, A., and Beedle, L. (1960). Residual Stress and the Instability of Axial Loaded Columns (Report No. 220A.35). Lehigh University Institute of Research.
- Tao, Z. and Han, L. (2007a). Behaviour of Fire-Exposed Concrete-Filled Steel Tubular Beam Columns Repaired with CFRP Wraps. *Thin-Walled Structures*, 45(1), 63-76.
- Tao, Z., Han, L., and Wang, L. (2007b). Compressive and Flexural Behaviour of CFRP-Repaired Concrete-Filled Steel Tubes after Exposure to Fire. *Journal of Constructional Steel Research*, 63(8), 1116-1126.
- Tao, Z., Han, L., and Zhuang, J. (2008). Cyclic Performance of Fire-Damaged Concrete-Filled Steel Tubular Beam-Columns Repaired with CFRP Wraps. *Journal of Constructional Steel Research*, 64(1), 37-50.
- Tavakkolizadeh, M. and Saadatmanesh, H. (2001). Repair of Cracked Steel Girder Using CFRP Sheet. *Creative systems in structural and construction engineering*, 461-466.
- Teng, J. G. and Hu, Y. M. (2005). Enhancement of Seismic Resistance of Steel Tubular Columns by FRP Jacketing. *Proceedings, 3rd international conference on composites in construction*. Lyon, France.
- Teng, J. and Hu, Y. (2007). Behaviour of FRP-Jacketed Circular Steel Tubes and Cylindrical Shells under Axial Compression. *Construction and Building Materials*, 21(4), 827-838.
- Teng, J., Yu, T., and Fernando, D. (2012). Strengthening of Steel Structures with Fiber-Reinforced Polymer Composites. *Journal of Constructional Steel Research*, 78, 131-143.
- Tide, R. H. (2001). A Technical Note: Derivation of the LRFD Column Design Equations. *Engineering Journal*, 38(3), 137-139.

- Timoshenko and Gere. (1961). Theory of Elastic Stability. New York: McGraw-Hill Book.
- Texas Department of Transportation (2014). Guidelines for the Use of Steel Piling for Bridge Foundations.
- The Castle Group. Retrieved from <http://www.wjcastlegroup.com/pdf/CastleinSeptOctInlandPort.pdf>
- Vani, G., Jayabalan, P., Joseph, J. (2013). Numerical Analysis of Cold Formed Steel Plain Angle Compression Members. International Journal of Emerging Technology and Advanced Engineering, 3, 22-29.
- Verma, K. and Garg, H.K. (2012). Underwater Welding- Recent Trends and Future Scope. International Journal on Emerging Technologies, 3(2), 115-120.
- Vishay. (2011). System 7000 Instruction Manual Version 1.10. Raleigh, NC.
- Yan, J., Young, B. (2002). Column Tests of Cold-Formed Steel Channels with Complex Stiffeners. Journal of Structural Engineering, 128(6), 737-745.
- Walls, J., Smith, M., (1998), "Life-Cycle Cost Analysis in Pavement Design-Interim Technical Bulletin", Report No. FHWA-SA-98-079, Federal Highway Administration.
- Wiswell, G. (1972). Patent No.US3690110 A. US. Retrieved from <https://www.google.com/patents/US3690110#backward-citations>
- Xiao, Y., He, W., and Choi, K. (2005). Confined Concrete-Filled Tubular Columns. Journal of Structural Engineering, 131(3), 488-497.
- Yan, J., Young, B. (2002). Column Tests of Cold-Formed Steel Channels with Complex Stiffeners. Journal of Structural Engineering, 128(6), 737-745.

- Yan, J., Young, B. (2004). Numerical Investigation of Channel Columns with Complex Stiffeners-Part I: Test Verification. *Thin-Walled Structure*, 42(6), 883-893.
- Zhao, X. and Zhang, L. (2007). State-of-the-Art Review on FRP Strengthened Steel Structures. *Engineering Structures*, 29(8), 1808-1823.
- Zhu, J. and Young, B. (2006). Aluminum Alloy Tubular Columns-Part I: Finite Element Modeling and Test Verification. *Thin-Walled Structures*, 44(9), 961-968.
- Zhu, J. and Young, B. (2010). Cold-Formed-Steel Oval Hollow Sections under Axial Compression. *Journal of Structural Engineering*, 137, 719-727.
- Zhu, J. and Young, B. (2012). Design of Cold-Formed Steel Oval Hollow Section Columns. *Journal of Constructional Steel Research*, 71, 26-37.
- Ziemian, R. D. (2010). *Guide to Stability Design Criteria for Metal Structures* (6th ed.). Hoboken, NJ: John Wiley and Sons, Inc.